Synthesis and Characterisation of Halogen-Bonded Networks and Photoresponsive Dissipative Systems

Inaugural-Dissertation

zur Erlangung des Doktorgrades
der Mathematisch-Naturwissenschaftlichen Fakultät
der Heinrich-Heine-Universität Düsseldorf

vorgelegt von

Esther Johanna Gisa Nieland
aus Düsseldorf

Düsseldorf, Mai 2023

aus dem Institut für Organische und Makromolekulare Chemie
der Heinrich-Heine-Universität Düsseldorf

Gedruckt mit der Genehmigung der
Mathematisch-Naturwissenschaftlichen Fakultät der
Heinrich-Heine-Universität Düsseldorf

Berichterstatter:

1. Dr. Bernd M. Schmidt

2. Prof. Dr. Constantin Czekelius

Tag der mündlichen Prüfung: 15.08.2023

Die vorliegende Arbeit wurde in der Zeit von Januar 2020 bis April 2023 am Institut für Organische Chemie und Makromolekulare Chemie I der Heinrich-Heine-Universität Düsseldorf unter der Anleitung von Dr. Bernd M. Schmidt angefertigt.

Publications by the author during the work on this thesis

1) E. Nieland, J. Voss, B. M. Schmidt, *Synlett* **2023**, *34*, 975–982.
   E. Nieland and J. Voss wrote the manuscript with B. M. Schmidt.
2) E. Nieland, J. Voss, A. Mix, B. M. Schmidt, *Angew. Chem. Int. Ed.* **2022**, *61*, e202212745.
   E. Nieland and B. M. Schmidt conceived the project and designed the experiments; E. Nieland and J. Voss performed all experimental work and analysed the data; A. Mix performed all ^{19}F DOSY NMR measurements; E. Nieland and B. M. Schmidt wrote the manuscript.
3) E. Nieland, D. Komisarek, S. Hohloch, K. Wurst, V. Vasylyeva, O. Weingart, B. M. Schmidt, *Chem. Commun.* **2022**, *58*, 5233–5236.
   E. Nieland and B. M. Schmidt conceived the project and designed the experiments; E. Nieland performed all experimental work and analysed the data; E. Nieland performed the PXRD measurements with support from D. Komisarek and V. Vasylyeva; S. Hohloch, K. Wurst and B. M. Schmidt performed and analysed all SXRD measurements; O. Weingart performed all DFT computations; E. Nieland and B. M. Schmidt wrote the manuscript.

Posters

E. Nieland, J. Voss, B. M. Schmidt: “Photoresponsive Dissipative Macrocycles Using Visible-Light Switchable Azobenzenes”, Macrocyclic and Supramolecular Chemistry Meeting 2022, Nottingham, United Kingdom.

E. Nieland, O. Weingart, B. M. Schmidt: “Supramolecular networks by imine halogen bonding”, SupraChem 2022, Mainz, Germany.

Danksagung

Ich möchte mich gerne, bei den Menschen bedanken, die mich während oder vor meiner Promotion unterstützt haben und diese Arbeit in dieser Form erst möglich gemacht haben.
Zuerst möchte ich mich bei Dr. Bernd M. Schmidt für die Möglichkeit bedanken, seit 2018 in seinem Arbeitskreis an den unterschiedlichsten Projekten arbeiten zu können. Danke, dass du mir schon früh ermöglicht hast mich selbst kreativ einzubringen und mich in allen Situationen unterstützt hast. Vom ersten Forschungspraktikum bis zum Abschluss der Dissertation war es viel Arbeit und ich bin sehr froh, diese mit deiner Hilfe und als Teil deines Arbeitskreises absolviert zu haben.
Für die vielen schönen Momente in und außerhalb des Labors möchte ich insbesondere Tobi, Robin und Tom danken. Ohne Euch wären die letzten Jahre deutlich langweiliger gewesen.
Ich möchte mich bei Tom bedanken, der mir den erfolgreichen Einstieg in den Arbeitskreis ermöglicht hat und der mit Bernd zusammen meine Neugier und Begeisterung für supramolekulare Chemie geweckt hat. Danke an Tobi, dass ich immer zu dir kommen konnte, wenn ich eine spontane und eventuell verrückte Projektidee hatte, die eine zweite Meinung oder noch mehr kreative Köpfe brauchte! Robin, du bist der beste Abzugsnachbar, den ich mir wünschen konnte und ich werde die Zeit mit dir im Labor sicherlich vermissen. Auch wenn meine gemeinsame Zeit mit euch kürzer war, möchte ich mich auch bei Jona, Tim D. und Viviana für die schöne gemeinsame Zeit bedanken.
Jona, es hat unendlich viel Spaß gemacht mit dir zusammen zu arbeiten. Deine Begeisterung und gute Arbeit haben unser gemeinsames Projekt enorm nach vorn gebracht. Danke auch, dass du mich zur Konferenz nach England begleitet hast, das war ein gelungener Abschluss einer großartigen Zusammenarbeit.
Danke auch an die Bachelorstudenten, die ich während meiner Arbeit betreuen durfte. Danke an David, Tim C. und Alexander für die gemeinsame Zeit.
Dem Team des CeMSAs an der HHU möchte ich für die vielen aufgenommenen NMR und Massenspektren danken. Insbesondere möchte ich Maria Beuer, Mohanad Aian, Tanja Muth, Dr. Peter Tommes und Ralf Bürgel für ihre Flexibilität und ihren großartigen Service danken!
Des Weiteren möchte ich Tobias Heinen für die Aufnahme von TGAs und Daniel für die Unterstützung bei dem Messen von PXRD Spektren danken, sowie Dr. Vera Vasylyeva und Prof. Dr. Christoph Janiak für die Möglichkeit, diese Spektren in ihrem Arbeitskreis zu messen.
Prof. Dr. Constantin Czekelius möchte ich für seine Unterstützung danken und dafür, dass er die Rolle des 2. Gutachters für diese Arbeit übernimmt.
Prof. Dr. Klaus Wurst und Prof. Dr. Stefan Hohloch möchte ich für die Messung der Kristallstrukturen einiger meiner kristallinen Proben danken. Dr. Andreas Mix möchte ich für die Aufnahme von verschiedenen DOSY Spektren danken, ohne die die Analytik in einigen Projekten deutlich schwieriger gewesen wäre. Danke auch an Dr. Oliver Weingart für die vielen

theoretischen Berechnungen, die unsere Ergebnisse bestätigen konnten und eine Bereicherung für unser Projekt waren.
Ich möchte meinen Eltern und meiner Schwester danken. Danke, dass ihr immer für mich da seid, ohne euch wäre ich nicht die, die ich heute bin! Dafür, dass ihr meine Neugier und meinen Wissensdurst immer unterstützt habt und ich mir eurer Liebe und Fürsorge zu jeder Zeit bewusst sein konnte. Kathi, an dir konnte ich mehr oder weniger erfolgreich üben, anderen etwas beizubringen und mit dir zusammen groß zu werden und gemeinsam neue Dinge zu entdecken war großartig. Du bist die beste kleine Schwester, die ich mir hätte wünschen können.
Zuletzt möchte ich mich bei Martin bedanken! Danke für deine Liebe und deine Unterstützung. Du hast alle Höhen und Tiefen mitgemacht, die ich während dieser Arbeit und außerhalb durchlebt habe, bist immer für mich da und hältst mir den Rücken frei. Du hast mit mir meine Erfolge gefeiert und mich an schlechten Tagen aufgeheitert. Ohne dich wäre diese Arbeit in dieser Form nicht möglich gewesen.

Abstract

This thesis is divided into two major parts, focusing on the application of imine halogen bonding to generate supramolecular networks and on the generation of photoresponsive, dynamic, and dissipative supramolecular assemblies.

For the first time, imine halogen bonding was thoroughly examined in this work and employed to generate halogen-bonded frameworks. Networks with various topologies were created by combining two different imine cages with several electron-poor halogen bond donors. Box-like structures and infinite networks were among the structures studied using single-crystal X-ray analysis in conjunction with plane-wave DFT calculations and QTAIM investigations. While the structures are fascinating, imine halogen bonding is also a practical method for modifying the solid-state packing of porous organic cages. Additionally, by adding iodine as a heavy atom, this method facilitates the single-crystal X-ray structure analysis of these cages.

In the second part of this thesis, the structural differences between two azobenzene isomers were exploited to generate topologically different assemblies that can be transformed into each other using light. Among those systems is an azobenzene-based trianglimine, which can transiently undergo ring contraction under irradiation. Mixtures of oligomeric imines based on aliphatic diamines were utilised as starting materials to selectively generate macrocyclic structures. During those studies, two photoresponsive supramolecular macrocycles and one cage were also synthesised that underwent no structural rearrangements upon isomerisation making them interesting target structures in the generation of photoresponsive host-guest systems.

Finally, mixtures of the different employed amines were combined with the aldehyde photoswitch to investigate the possibility of a photo-induced building block exchange. During these studies, it was shown that the trianglimine as well as the azobenzene cage could be irreversibly transferred into discrete structures composed of different building blocks, which then over time were transformed into mixed species containing both building blocks.

This thesis gives a detailed insight into the nature and possibilities of imine halogen bonding while also shedding light on different dissipative dynamic systems and the variety of structures accessible by employing both isomers of an azobenzene building block.

Zusammenfassung

Diese Arbeit ist in zwei Teile gegliedert, die sich mit der Anwendung von Imin-Halogen-Bindungen zur Erzeugung von supramolekularen Netzwerken und mit der Synthese von photoresponsiven, dynamischen und dissipativen Systemen beschäftigen.

In dieser Arbeit wurde die Ausbildung von Halogen-Bindungen mit Iminen das erste Mal gründlich untersucht und zur Erzeugung von halogengebundenen Gerüsten eingesetzt. Durch die Kombination von zwei verschiedenen Iminkäfigen mit mehreren elektronenarmen Halogenbindungsdonoren wurden Netzwerke mit unterschiedlichen Topologien geschaffen. Zu den untersuchten Strukturen gehörten kastenförmige Strukturen und unendliche Netzwerke, die mit Hilfe der Einkristall-Röntgenanalyse in Verbindung mit DFT-Rechnungen und QTAIM-Analysen untersucht wurden. Auch wenn die Strukturen an sich faszinierend sind, ist die Imin-Halogen-Bindung zusätzlich eine praktische Methode, um die Festkörperpackung von porösen organischen Käfigen zu verändern. Durch das Eingbringen von Iod als schweres Atom erleichtert diese Methode außerdem die Röntgenstrukturanalyse dieser Käfige.

Im zweiten Teil dieser Arbeit wurden die strukturellen Unterschiede zwischen zwei Azobenzol-Isomeren ausgenutzt, um topologisch unterschiedliche Einheiten zu erzeugen, die mit Hilfe von Licht ineinander umgewandelt werden können. Zu diesen Systemen gehört ein auf Azobenzol basierendes Trianglimin, das bei Bestrahlung eine vorübergehende Ringkontraktion durchlaufen kann. Verschiedene Iminoligomere, die auf aliphatischen Diaminen basieren, wurden als Ausgangsmaterial für die selektive Erzeugung makrocyclischer Strukturen verwendet. Im Rahmen dieser Studien wurden auch zwei photoresponsive supramolekulare Makrocyclen und ein Käfig synthetisiert, die bei der Isomerisierung keine strukturellen Umlagerungen erfahren, was sie zu interessanten Zielstrukturen für die Erzeugung photoresponsiver Wirt-Gast-Systeme macht.

Schließlich wurden Mischungen der verschiedenen eingesetzten Amine mit dem Aldehydphotoschalter kombiniert, um die Möglichkeit eines photoinduzierten Bausteinaustauschs zu untersuchen. Dabei zeigte sich, dass sowohl der Trianglimin- als auch der Azobenzolkäfig irreversibel in diskrete Strukturen aus verschiedenen Bausteinen überführt werden können, die sich dann im Laufe der Zeit in gemischte Spezies mit beiden Bausteinen umwandeln.

Diese Arbeit gibt einen detaillierten Einblick in die Natur und die Möglichkeiten der Imin-Halogen-Bindung und beleuchtet gleichzeitig verschiedene dissipative dynamische Systeme und die Vielfalt der Strukturen, die durch die Verwendung der beiden Isomere eines Azobenzol-Bausteins zugänglich sind.

Table of Contents

1. Introduction

1.1 General introduction into supramolecular chemistry

Since the first syntheses, the possibilities in molecular chemistry have evolved, rapidly creating sophisticated methods to generate molecules of increasing complexity. The molecular chemistry that focuses on covalent bonds as well as the supramolecular chemistry, which has a focus on assemblies and intermolecular bonds both deal with molecular or supramolecular entities with well-defined characteristics. As supramolecular chemistry is not limited to single molecules, it is also called “chemistry beyond the molecule”.[1]

The term supramolecular chemistry was coined after the pioneering works of Pedersen, Lehn, and Cram on crown ethers, bi- and tricyclic cryptands, and chiral crown ethers, highlighting their potential for substrate binding and recognition.[2] From these first examples, supramolecular chemistry has further evolved and enabled the synthesis of structures like macrocycles, cages, catenanes, molecular knots, and rotaxanes.[3]

Supramolecular systems have found applications in different fields such as sensing, molecular imaging, metal extraction, and the separation and storage of molecules.[4] The scope of possible applications as well as the complexity of the systems were further increased by the generation of responsive and adaptive supramolecular systems. Applying an external stimulus to these systems leads to changes at the molecular level, often altering the macroscopic properties of the system. The systems can either be influenced by light, mechanical force, heat, or chemical stimuli, like, for example, a change in solvent or pH. The construction or destruction of systems can be triggered, the solubility can be adjusted, or a structural transformation can be induced, to name a few possible transformations in responsive architectures.[5] The variety of designs and applications is extensive and not limited to supramolecular chemistry.

Systems can also be designed to be dissipative or dynamic. A resting state is transferred into a transient, less stable state by using light or a chemical fuel as a stimulus. The transient, sometimes also called an activated state, is typically metastable and decomposes, yielding the precursor. This process can happen spontaneously over time due to the decay of the added fuel, normally producing waste. Alternatively, the process can be triggered by the addition of another fuel or irradiation with light (Figure 1).[6]

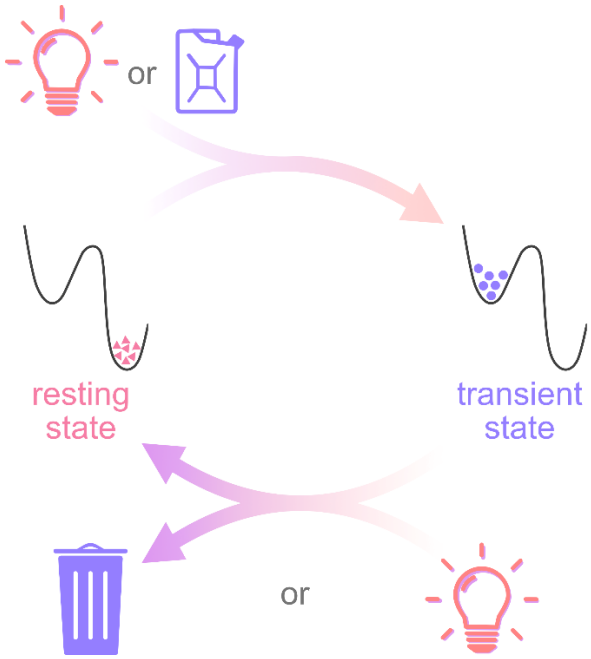

Figure 1: Transformation of a resting state into a transient state by addition of a chemical fuel or light. The resting state can be regained by exposure to light, by the addition of another fuel, or over time by producing waste.

Most biological processes are of a dissipative nature, but there are also many examples of artificial systems that can be transiently transformed into a metastable active state.[6b] Our group designed halogen-bonded boxes, each with two photoswitchable azobenzene units. While these moieties could be photoisomerised, the anticipated dissipative behaviour of the system could not be investigated, as the strength of the halogen bond formed in the system was weak in solution.[7] These findings sparked the curiosity to investigate methods to employ halogen bonding in combination with supramolecular structures in the solid-state, along with the interest to generate a dissipative supramolecular metal-free system based on stronger interactions.

The focus of this work will be on those two objectives. Accordingly, the thesis is divided into two major parts, with the first one focusing on a general investigation into imine halogen bonding and the potential to utilise this interaction to generate halogen-bonded networks in combination with imine cages, paving the way to reversibly alter the crystallisation behaviour and potentially influencing the solid-state properties (Section 3.1). While the second, larger part of this thesis concentrates on the generation of photoresponsive dynamic imine systems, starting with a thorough investigation of a potential light switchable building block (Section 3.2.1). This is followed by the synthesis of macrocyclic responsive systems based on either stiff diamines (Section 3.2.2), which allow the dissipative generation of a mixture of macrocycles from a precursor trianglimine, or flexible diamines (Section 3.2.3), that enable the switching between linear oligomeric species and metastable macrocycles. The synthesis and analysis of photoresponsive cages will be discussed in Section 3.2.4 while the possibility of

triggering the interconversion between the aforementioned systems photochemically will be discussed in Section 3.2.5. The theoretical foundations needed for these studies will be explained in the following introductory sections.

1.2 Bond formation in supramolecular chemistry

To generate complex, artificial architectures utilising covalent, irreversible bond formation, it often takes a high synthetic effort with typically low overall yields. To enhance the efficiency of the syntheses and to access more sophisticated systems, the formation of non-covalent interactions, dative bonds, or reversible bonds was utilised as they allow for “error correction” while leading to the thermodynamically or kinetically preferred product, depending on the reaction set up.[8] Some of these interactions are exemplarily discussed in the following sections.

1.2.1 Hydrogen and halogen bonding

Hydrogen bonds are ubiquitous in chemistry and biology and are defined as the interaction of a donor proton H covalently bound to a residue R, which interacts with the electron-rich region of an acceptor atom.[9] Being essential in governing the structure of complex structures such as proteins, hydrogen bonds also have numerous applications in artificial systems and have been employed to generate supramolecular structures.[3a,10]

One of these supramolecular structures is an Archimedean cage assembled by 72 hydrogen bonds, as reported by Ward *et al.* The truncated octahedron (**1**) is constructed out of two different hexagonal molecular tiles, one being a tris(guanidinium)nitrate cluster and the other a hexa(4-sulfonatophenyl)benzene in the solid-state (Figure 2).[11]

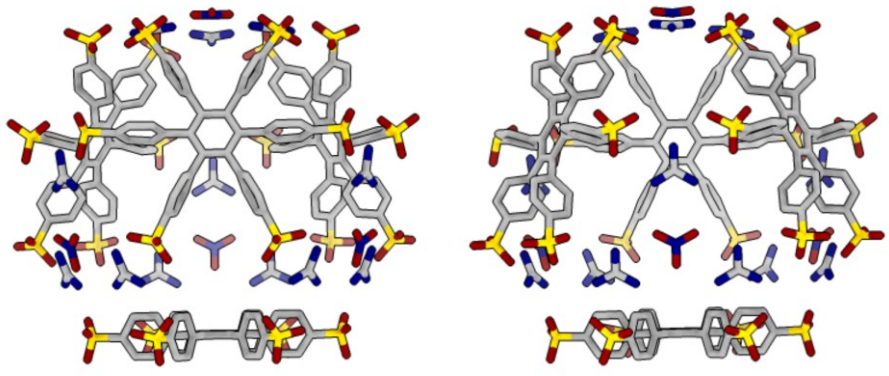

1

Figure 2: Hydrogen-bonded truncated octahedron cage **1**, reported by the group of Ward, as seen from two different orientations.

A halogen bond is defined as the interaction of a polarised halogen atom (donor) with an electron-rich Lewis basic halogen bond acceptor.[12] The neutral halogen bonding interaction can be described as R–X···Y, with R being covalently bound to the halogen atom X and Y being the halogen bond acceptor. Different molecular entities can act as halogen bond acceptors, such as π-systems, ions, or lone pair possessing molecules like phosphines,[13e,f] isocyanides,[13d] thiocarbonyls,[13c] dithianes[13b] and amines.[13a] Halogen bonds can also be constructed from halonium ions, leading to three-centre-four-electron bonds with two halogen bond acceptors [N···I$^+$···N].[12e,h] The large variety of possible building blocks as well as the tuneability and high directionality of halogen bonds make them a valuable tool in the construction of supramolecular architectures.

Discrete supramolecular structures like macrocycles,[14] boxes[7,15] and capsules[12b,e,16] as well as helicates[17] were synthesised using halogen bonding interactions. With the most prominent examples for capsules being reported by the groups of Diederich and Rissanen. Resorcin[4]arene based capsule halves were generated, forming different capsules by connection *via* 4 halogen bonds, of which one is shown in Figure 3a.[16b,g] The capsules, with an overall structure resembling the container published by Pilati and co-workers,[16h] were intensively studied in the solid-state, in solution, and in the gas phase, including the generation of different derivatives and revealing a significant solvent dependency of the strength of the observed halogen bonds.[16b]

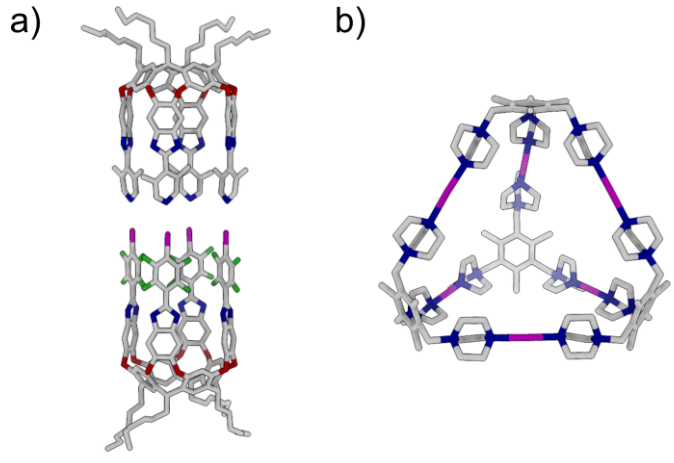

Figure 3: Halogen-bonded capsules synthesised by a) Diederich and co-workers and b) the group of Rissanen.

Rissanen and co-workers generated different-sized supramolecular capsules based on halonium ions.[12e,16a,c-f] Halogen bond acceptors were combined with Ag^I salts, generating dimeric, terameric (Figure 3b), or hexameric capsules, which were transferred into the

corresponding iodonium cages by the addition of iodine. The largest, hexameric capsule was found to have a diameter of 4.5 nm.[16c]

Halogen bonding was used in crystal engineering[12c,g] as well as in the generation of polymers[12a,f,j] and network structures.[12i,18] Halogen bonding using halonium ions was utilised by the groups of Chen and Kukushkin to generate halogen-bonded networks. While the example reported by Chen *et al.* was constructed by the combination of the halogen bond acceptor with Ag^{I} followed by the addition of iodine to generate halonium ions,[18b] the structure reported by Kukushkin is based on one zwitterionic building block. The latter was also shown to be porous, but the measured BET surface was relatively low due to remaining solvent molecules.[18a] A halogen-bonded framework, based on neutral halogen bonds, that showed room-temperature phosphorescence was reported by Wu *et al.*,[18c] while the group of Barbour reported on a network that underwent structural transformation upon guest encapsulation.[18f]

1.2.2 Metal-organic assemblies

The dative bonds between organic ligands and metals that are used to form supramolecular assemblies are in general stronger than the typical hydrogen or halogen bond. These interactions will only be briefly discussed as they were not employed in this thesis. The structures accessible range from infinite networks to discrete systems, including macrocycles and cages.[19] The potential of these metal-organic frameworks (MOFs) for gas adsorption and other applications has been extensively studied but will not be discussed further.[20]

A large variety of metal-organic cages and macrocyclic structures has been obtained based on different metals and linkers. One of the most famously known and well-studied metal-organic cages are the octahedral palladium cages synthesised by Fujita *et al.*[21] (Figure 4), which were shown to have a variety of different applications.[22]

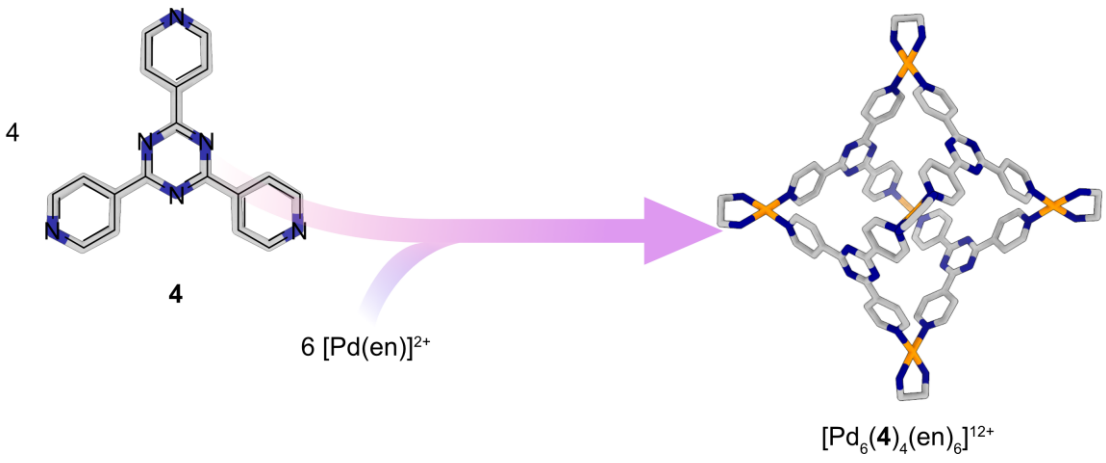

Figure 4: A metal-organic coordination cage $[Pd_6(en)_6(\mathbf{4})_4]^{12+}$ synthesised by the group of Fujita.

Yaghi *et al.* analysed the structures of existing metal-organic cages and polyhedra to derive essential criteria for the generation of cages of different shapes, highlighting that the shapes of the targeted cages can be predicted by the type of metal employed and by the shape of the linker used.[19g] Choe *et al*. additionally summarised the variety of different metal-organic assemblies sorted by shapes, featuring more recent examples.[19a]

1.2.3 Dynamic covalent bond formation

The reversible formation of covalent bonds allows “error-checking” or “proof-reading” in synthesis. These formations are often summarised under the term dynamic covalent chemistry (DCC). During the formation of the thermodynamically or kinetically preferred product, depending on the conditions, the reversibility in the bond formation can increase the yields of the desired product, and the product distribution can in some cases be re-adjusted, even retrospectively, by changing the reaction environment.[8]

The reaction conditions, such as concentration, temperature, and the presence or absence of templates, influence whether a discrete supramolecular structure, such as a macrocycle or cage, or an oligomeric or polymeric structure is formed. The shape of both building blocks and especially the valence angles present in the different building blocks define the shape and topology of the assembled structure.

The group of Jelfs investigated this relation and introduced a nomenclature to clearly describe the structure of different cages. The different building blocks are classified using the number of reactive end groups as either ditopic (Di), tritopic (Tri), or tetratopic (Tet). Combining these precursors leads to different topologies, of which the Jelfs group analysed the most probable ones and discussed the factors that lead to their formation as well as the challenges and limitations of predicting them by computational methods.[23] The nomenclature defined by Jelfs *et al.* describes structures as $X_p^mY^n$, with X and Y being the different building blocks from which the cage is assembled, and the superscripts m and n denoting the number of the respective building blocks in the cage. The subscript p is used to give the number of double connections between the building blocks and is only used if it is larger than one and if the cage does not consist of only two building blocks.[23] As this nomenclature allows for a definite description of supramolecular structures, it will be adapted in this thesis.

The reversible bond types that are most commonly employed in the construction of macrocycles and cage compounds are the formation of boronate esters and imines, while other reactions like the reversible formation of disulfides or orthoesters have also been employed to generate discrete supramolecular structures (Figure 5).[24] Focusing on the most prevalent types of bond formation in covalent organic cages, the formation of boronate esters and imines will be discussed in more detail.

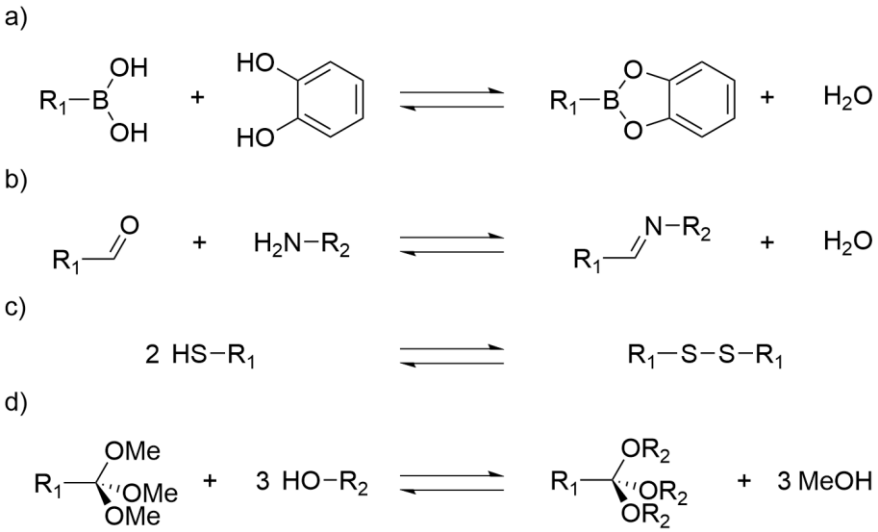

Figure 5: Exemplary reactions that have been used to generate supramolecular cages: a) formation of boronate esters; b) imine formation; c) disulfide formation; d) orthoester formation.

The condensation of a boronic acid and a diol leads to the formation of boronate esters. This reaction has been employed to generate infinite structures such as covalent organic frameworks (COFs) and discrete structures such as cages.[24b,25] The formation of the cyclic boronate ester introduces a rigidity in the structure that was utilised by the group of Mastalerz to generate a shape persistent cage that was shown to be capable of adsorbing various gases (Figure 6).[25c]

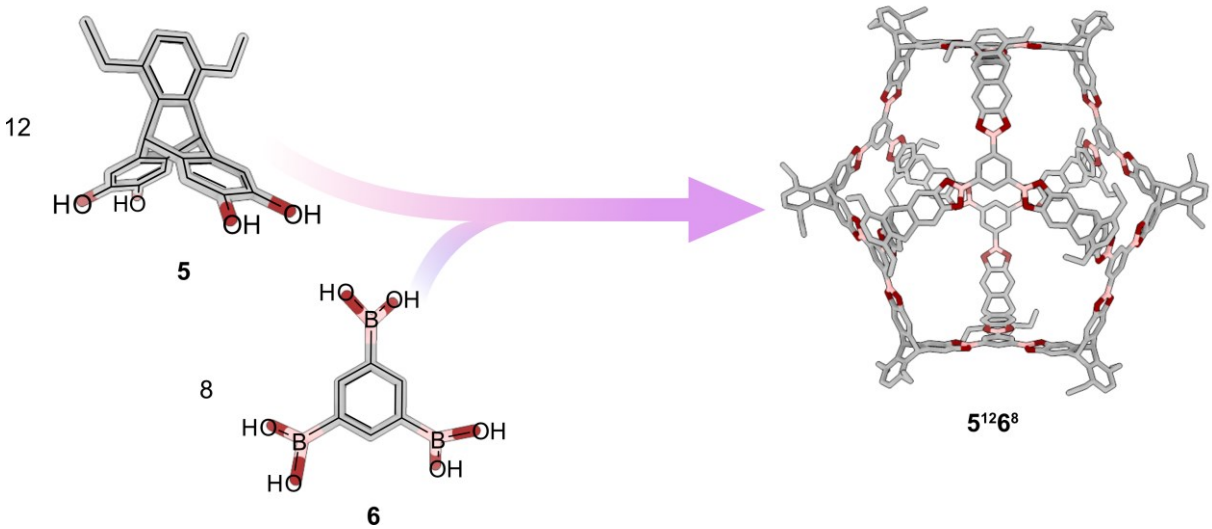

Figure 6: Cage formation of a large boronate ester cage ($\mathbf{5^{12}6^8}$) as reported by the group of Mastalerz.

While the rigidity introduced might be an advantage in the generation of porous systems, the corresponding planarity of the bond as well as the need for two adjacent alcohol functionalities also severely limits the number of possible building blocks.

Ultimately, forming an imine is fairly similar to the formation of the above described boronate esters, but instead of three functional groups required to form the reversible bond, this number is reduced to two. [24e] The dynamic covalent reaction of aldehydes and amines to form imines can be used, just as the formation of boronate esters, to generate COFs or discrete systems such as macrocycles and cages.[24] One of the most famous imine cages was first synthesised by the group of Gawroński and later studied by the group of Cooper, who unravelled its exceptional potential to encapsulate gases (Figure 7).[26]

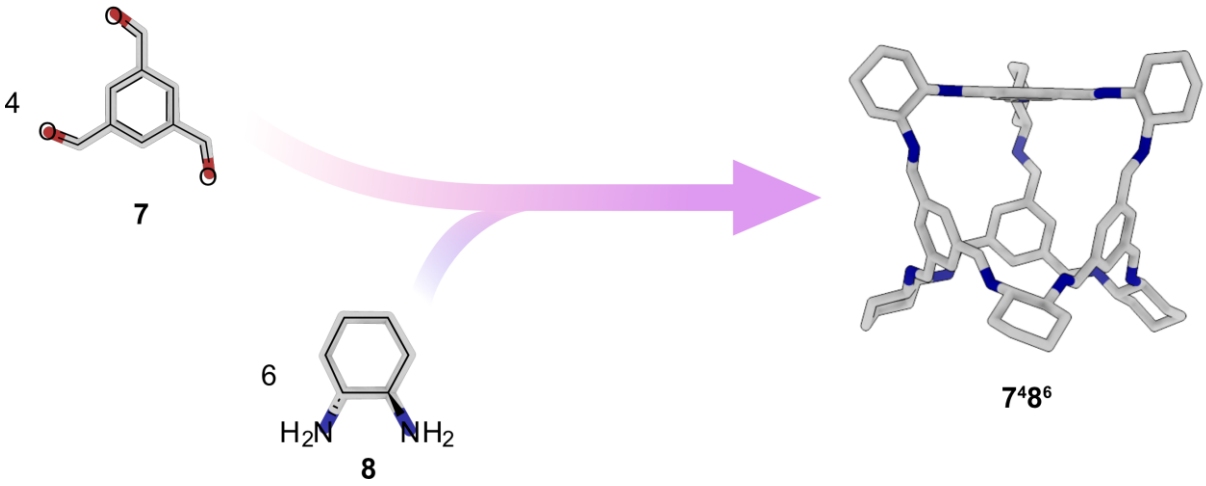

Figure 7: Imine cage $\mathbf{7^4 8^6}$ studied by the groups of Gawroński and Cooper.

The variety of different amines and aldehydes leads to numerous imine compounds varying in size, shape, and topology, as well as their potential applications.

1.3 Photoswitches and photoswitchable systems

The employment of DCC made the synthesis of highly complex structures more accessible, which were previously hardly accessible or impossible to synthesise using typical synthetic methods. By altering the building blocks for the supramolecular structures stimuli-responsive the complexity of the systems can be further enhanced. As initially mentioned, systems can be designed to react to different stimuli like mechanical force, heat, varying chemical stimuli, or light.[5] The latter is of special interest due to its high spatio-temporal resolution. Additionally, light is cheap and can be easily adjusted to match the adsorption spectrum of a photoresponsive molecule, while simultaneously not producing any waste.

1.3.1 Introduction into photoswitches

Photochromism describes the reversible, light-induced transformation between two structurally different forms, A and B, of a molecule. These forms can be further distinguished by their different absorption spectra and physicochemical properties, and the transformation of the thermodynamically more stable form A to B can be triggered by irradiation and *vice versa*, induced photochemically or thermally.[27] Small organic molecules that show photochromic behaviour, so-called photoswitches, can be implemented into materials, enabling the light-induced change of macroscopic material properties.[28] The major isomerisation reaction mechanisms in photoswitches are *E* to *Z*-isomerisations or electrocyclisations.

Among the most commonly employed photoswitches are diarylethenes,[29] and spiropyranes,[30] that undergo electrocyclisation, and alkene-based motors,[31] indigoids,[32] stilbenes,[33] and azobenzenes,[34] which undergo *E*/*Z*-isomerisation (Figure 8).

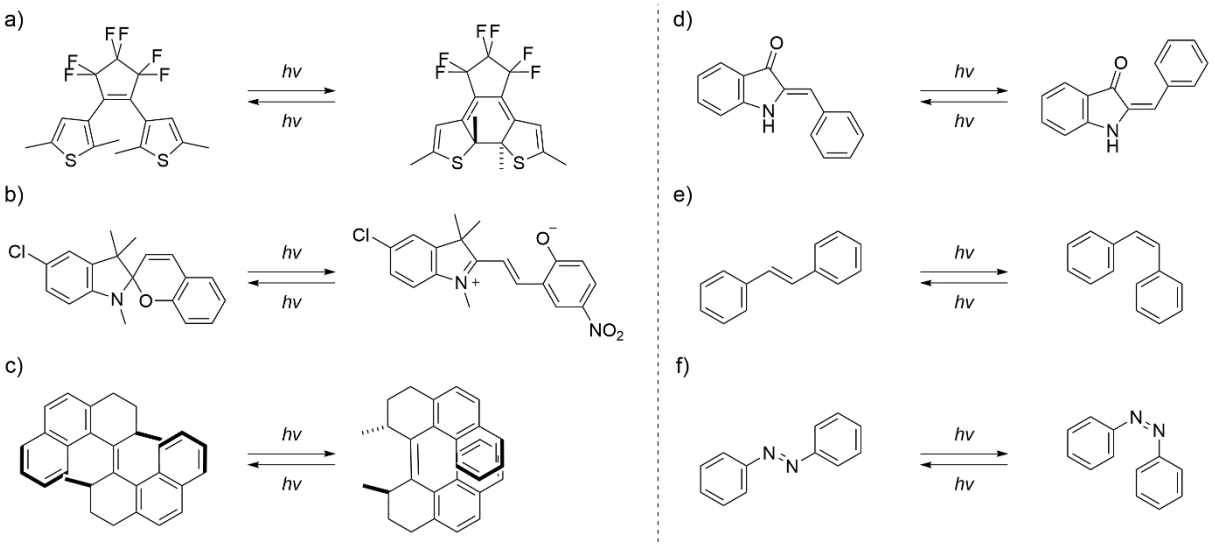

Figure 8: Photochromic reactions of different examples from classes of commonly employed photoswitches, including: a) diarylethene; b) spiropyran; c) overcrowded alkene rotor; d) indigoid; e) stilbene and f) azobenzene.

Diarylethenes, first discovered in 1988,[35] undergo a 6π electrocyclisation upon irradiation, accompanied by a distinctive colour change and a small anisotropic shape change from the flexible open form to the more rigid conjugated form.[29] The irradiation of spiropyran leads to the ring-opening and formation of merocyanine, which is metastable and zwitterionic.[30] Overcrowded alkene-based rotors were first introduced by the group of Feringa and allow an unidirectional rotary motion upon irradiation.[31,36] Derived from the parent compound indigo, indigo photoswitches, especially hemiindigo and hemithioindigo, show a pronounced geometry change upon photoisomerisation, while being bidirectionally switchable with visible light, with quantum yields that are often high, and, additionally, a metastable form with a comparably long

half-life.[32] Stilbenes can be photoisomerised from *E* to *Z* using UV light. However, the application of stilbene as a photoswitch is hindered by the fact that, instead of the reverse photoisomerisation yielding *E*-stilbene, electrocyclisation yielding dihydrophenanthrene can occur.[33]

Azobenzenes have been used as molecular switches in a variety of different applications due to the distinct geometry change upon irradiation and the minimal photobleaching that occurs upon switching. In general, the more stable *E*-isomer undergoes photoisomerisation by inversion or rotation, yielding the metastable *Z*-isomer.[34] The photochemical properties of the photoswitches can be tuned by introducing different substituents, leading to a high adaptability, by changing the half-life of the photoswitch and the wavelength needed for isomerisation.[37] The groups of Hecht and Woolley introduced electron-rich substituents like methoxy[38b,c] or electron-deficient substituents like fluorine[39] or chlorine[38b] in *ortho*-position to generate azobenzene derivatives that have half-lives of up to two years for the *Z*-isomer at room temperature and that can be switched with visible light.[38,39] Heteroaryl azo compounds have been introduced by different groups.[40] Among those, the arylazopyrazoles have been extensively studied by the group of Fuchter.[41] Typically, the *E*-isomer of azobenzenes is more stable than the *Z*-isomer. This stability trend was inverted by generating bridged azobenzene derivatives, the so-called diazocines, which were first introduced by the group of Herges.[42]

Bidirectional switching using visible light was achieved by introducing different substituents. This is beneficial, especially for biological applications, as the isomerisation with UV light is toxic and deleterious to cells, and visible light irradiation also reduces the possibility of decomposition reactions of other compounds that are used together with the photoswitches.[28a,43]

1.3.2 Photoresponsive supramolecular systems

Implementing those photoswitches into supramolecular systems led to an enormous number of exciting photoresponsive and functional systems.[5d,28] While there are numerous intriguing examples, like among others light responsive polymers,[44] or other materials,[28b,d] the focus will be on photoresponsive macrocycles and cages.[5c,45,46] A macrocycle or cage can be functionalised with the photoswitching unit, enabling the alteration of the exterior or interior of the system, or the photoswitches can be implemented directly into the architecture of the system, typically allowing for pronounced geometry changes upon isomerisation. Another method to generate a photoresponsive supramolecular system is the combination of a cage or macrocycle with a photoresponsive guest.[46c,47]

The latter technique was employed by different groups with diverse and exciting outcomes, such as the light-triggered crystallisation by photoisomerisation of an azobenzene guest[47c] or

the switching of different azobenzenes in a coordination cage dissolved in water.[47b] While these applications as well as the numerous additional examples are intriguing, the further discussion will be limited to supramolecular cages and macrocycles that incorporate photoswitchable moieties in their structures.

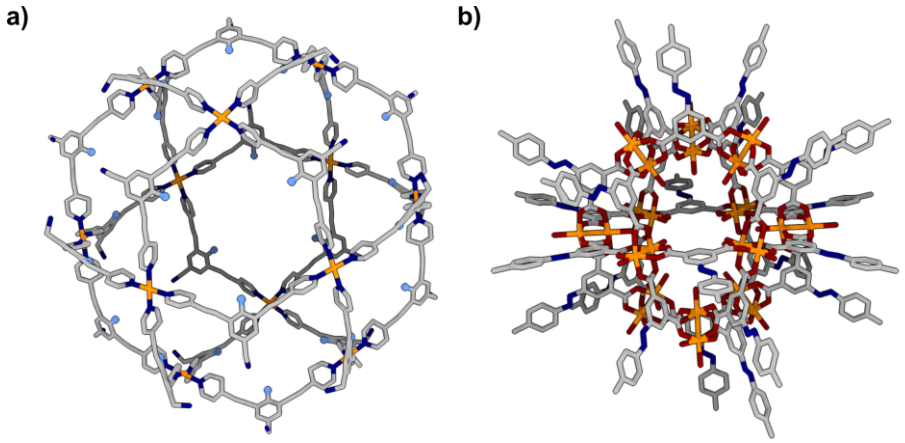

Figure 9: Structures of a) the intrinsically functionalised metal-organic cage with azobenzene groups replaced by light blue dots for better visibility synthesised by the group of Fujita and b) the extrinsically functionalised cage employed by Zhou and co-workers.

Fujita and co-workers synthesised a spherical metal-organic complex (**9**) whose 24 ligands were functionalised with azobenzenes, enabling the control of the interior hydrophobicity by photoisomerisation (Figure 9a). The isomerisation process, which could be reversed thermally or photochemically, influenced the affinity of the $[Pd_{12}(\mathbf{9})_{24}]^{24+}$ cage to act as a host, with the guest being encapsulated in the cavity when the *E*-isomer is present and the guest being released upon irradiation.[48] In addition to that, a copper-based metal-organic cage whose solubility can be controlled by light was reported by the group of Zhou (Figure 9b). The *E*-isomer can be used to trap methylene blue among the different cages. Irradiation with UV light releases the guest and dissolves the crystalline cage.[49b] Later, the same group enhanced the photoresponsive efficiency by isolating the metal-organic assembly in mesoporous silica.[49a] Silsesquioxane cages, also functionalised with azobenzene moieties on the exterior, were reported by the group of Liu in 2015. The cages showed good thermal stability and were fluorescent, with an emission maximum at 400 nm.[50]

If the photoresponsive moiety is incorporated into the structure of the assembly the isomerisation of the photoswitch can either lead to a geometry change, to the disassembly, or to the disassembly and reassembly of a structurally different assembly (Figure 10).

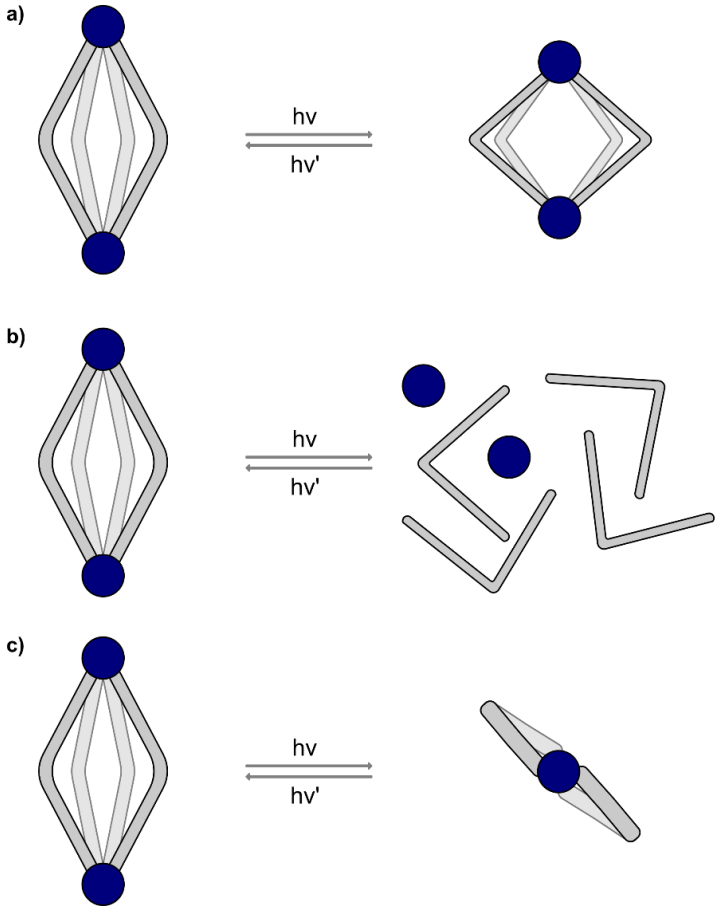

Figure 10: Different modes of isomerism upon photoisomerisation: a) change in geometry; b) disassembly; c) alteration in geometry accompanied by a change in absolute stochiometry.

Macrocycles that undergo geometry changes without disassembly or reconfiguration have been reported by various groups.[5c,45] Among those are covalent macrocycles with one[51] or multiple[52] azobenzene moieties. The photoisomerisation of a “Texas-sized” box reported by the group of Sessler significantly influences the shape of the macrocycle, which, depending on the isomer, either hosts a small or a large guest.[52c] The groups of Yoshida[52i] and Wegner[52g] used the geometry change occurring upon photoisomerisation to trigger the assembly or disassembly of stacks of macrocycles. Recently, Adamson and co-workers reported on the synthesis and properties of different, large azobenzene-based macrocycles, containing between two and eight azobenzene moieties. Varying the reaction conditions either led to the preferred formation of smaller or larger macrocycles from the precursors.[53a] A platinum based metal-organic macrocycle was reported by Zhu *et al.*, which, depending on the type of platinum acceptor employed, consists of three or six diarylethene units. These can be photoisomerised, slightly changing the shape of the macrocycle.[53b]

A number of diarylethene-based photoresponsive palladium cages that change geometry upon irradiation have been synthesised and thoroughly investigated by the group of Clever (Figure 11).[54] The first cage, reported in 2013, was constructed of four diarylethene photoswitches that were connected to pyridine units by acetylene linkers and two Pd^{II}-ions.

Irradiation with UV light (565 nm) of the more flexible cage led to electrocyclisation in the photoswitching units, generating a more rigid metal-organic cage. The process could be reversed by irradiation with white light and was used to gain control over the formation of a host-guest complex. While the more flexible cage is able to host a dianionic guest, isomerisation of the cage leads to the release of the guest.[54f] Similar cages have been used to investigate the switching behaviour,[54d] the mechanism of guest encapsulation and release[54c,e] and to generate a multi-stimuli responsive system.[54b]

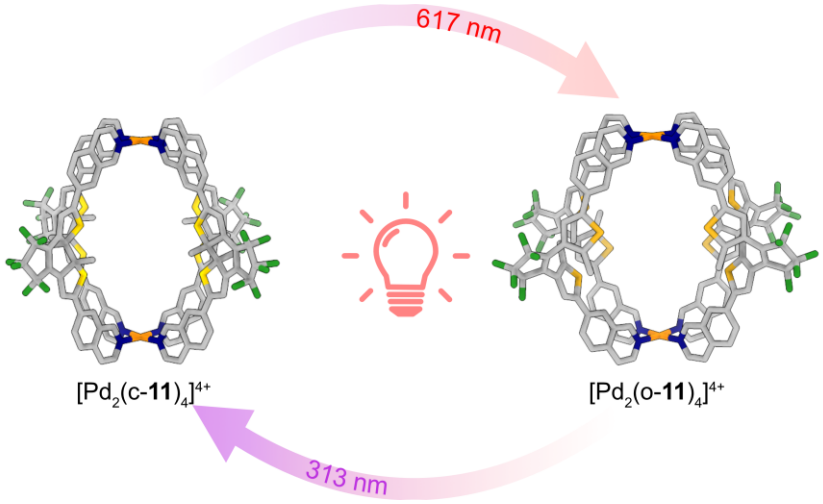

Figure 11: Structure and isomerisation of one of the diarylethene-based cages reported by the group of Clever. The open cage $[Pd_2(o\text{-}\mathbf{11})_4]^{4+}$ can be transformed into the closed cage $[Pd_2(o\text{-}\mathbf{11})_4]^{4+}$ by irradiation with UV light, and the reverse reaction can be triggered by irradiation with red light.

An azobenzene-based gold macrocycle has been reported by Yam *et al.*,[55c] while metal-organic cages that are able to undergo a geometry change upon irradiation include the palladium cage based on overcrowded alkenes reported by the group of Feringa[55a] or the iridium cage based on azobenzene photoswitches reported by the Hardie group.[55b]

The geometry change in the photoswitch can lead to an overall geometry change in the supramolecular structure or in the disassembly of the systems. Examples in which a reassembly with the isomerised building block occurs afterwards will be discussed separately in Section 1.4.2.

A rhenium square was reported by the group of Lees, which underwent decomposition upon irradiation with UV light.[56] A palladium derivative that can undergo disassembly and reassembly was also reported in the same publication and will be discussed later on. The group led by Liu used a bis-pyridyl ligand containing azobenzene moieties in a reaction with Pd^{II}, leading to the formation of a lantern-shaped cage. Irradiation with UV light leads to the *E* to *Z* isomerisation of the azobenzenes in the cage, which contains eight photoswitches in total, and to the disassembly of the cage. The reassembly of the cage can be obtained by irradiation with visible light.[57]

Recently, the group of Nitschke reported a metal-organic zinc cage that was functionalised with azobenzene moieties on its vertices. Irradiation with UV light led to the consecutive isomerisation of the different photoswitches, generating a steric clash and leading to the disassembly of the cage. *Z* to *E* isomerisation can be achieved photochemically, by irradiation with green light (500 nm), or thermally, leading to the reformation of the cage. As the cage can be used to host anionic guests, the disassembly and reassembly of the cage can be used to control the encapsulation, and the release of the guest can be controlled by light.[58]

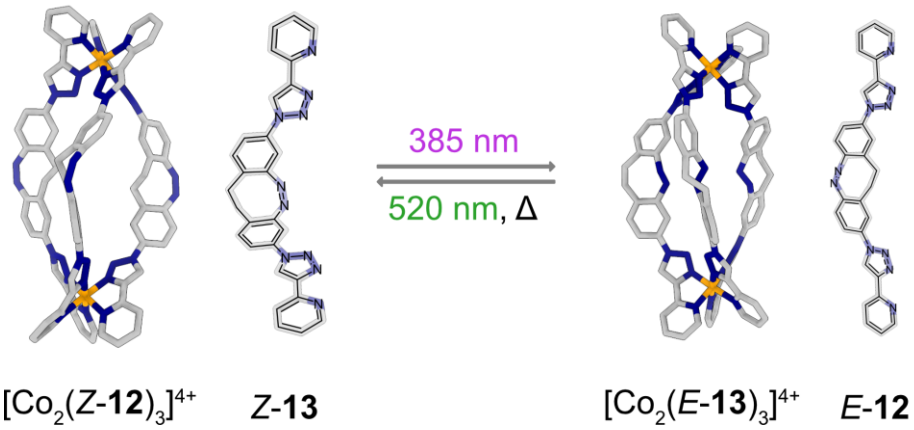

Figure 12: Photo-controlled ligand exchange investigated by the group of Herges. This figure was reproduced from reference 59 with permission.

Another system that shows disassembly upon irradiation was reported by the groups of McConell and Herges. The complexity of the system was enhanced by using two different, regioisomeric 2-pyridyltriazole functionalised diazocine ligands to form metal-organic helical assemblies. The isomeric ligands vary slightly in their biting angle, 61° and 63° for *Z*-**12** and *Z*-**13**, respectively, which has a significant impact on their macrocycle formation behaviour. The more stable *Z*-isomer of **12** readily forms $[Co_2(Z\text{-}\mathbf{12})_3]^{4+}$ assemblies in combination with Co^{II}, while the corresponding less stable *E*-**12** does not form defined helical structures. In contrast, the regioisomer **13** shows the inverse assembly behaviour, with the less stable *E*-**13** forming metal-organic helices, while the more stable *Z*-isomer does not. In summary, when isomerising the photoswitches, the disassembly of one system is triggered while the other shows the reverse behaviour. Mixing both ligands with Co^{II} resulted in a system that can be photochemically switched between structurally similar helices composed of different ligands using UV light (385 nm) and green light (520 nm) or heat (Figure 12). The alternating exchange over numerous switching cycles was studied by NMR and UV/VIS spectroscopy and supported by DFT calculations.[60]

1.4 Dissipative systems

As initially mentioned, dissipative systems are generally described as systems in which a dormant state is transformed into a metastable transient or active state by a trigger. This active state slowly transforms back into the initial state over time. The activation of these systems is often achieved by adding a chemical fuel, producing waste in the process, or by irradiation with light. The deactivation of the system can occur spontaneously over time or be triggered by the addition of fuel or irradiation.[6]

While dissipative systems are ubiquitous in nature and the use of chemical fuels in these systems is highly effective, there are also numerous advantages and disadvantages of using light as a fuel in synthetic systems. Due to its high-spatio temporal resolution, the precision of fuel delivery by irradiation is very high, and the time in which it can be employed, even without disturbing a closed system, can be controlled easily. However, the efficiency of light as a fuel is highly dependent on the photochemical properties, especially the photostationary state (PSS), of the employed photoswitch. The diversity of possible chemical fuels is in theory much larger than that of light, but the use of light does not produce waste that accumulates during the process.[6a] Both methods of activating systems have different advantages and have been successfully used to create dissipative supramolecular systems. While the variety of the systems is high, including many dissipative materials,[6b] the focus in the following section will be on supramolecular cages and macrocycles, as well as similar assemblies.

1.4.1 Chemical fuel-based dissipative supramolecular systems

While there has been a recent discussion of whether the term fuel is misleading due to the different mechanisms by which it works, it will be used in the following as it is commonly used in literature.[61] Chemical fuels have been used to trigger the formation or transformation of different metal-organic or organic assemblies.[62,63]

The group of Otto generated a thiol-based catenane, which undergoes structural rearrangement, forming a square-shaped tetramer, upon addition of a chemical fuel that acts as a template. This tetramer catalyses the decay of the fuel, leading to the reformation of the catenane structure.[62c] Shortly after, the group of Nitschke reported on a system that can be used to transform different metal-organic structures into each other by the addition of a fuel mixture. The reaction system was used to control the threading and dethreading of a pseudorotaxane as well as the uptake and release of a fullerene guest.[62b]

Employing a metastable acid that leads to the temporary protonation of an amine building block and therefore its unavailability for imine formation reactions or other interactions is a technique that has been used to create dissipative systems.[63]

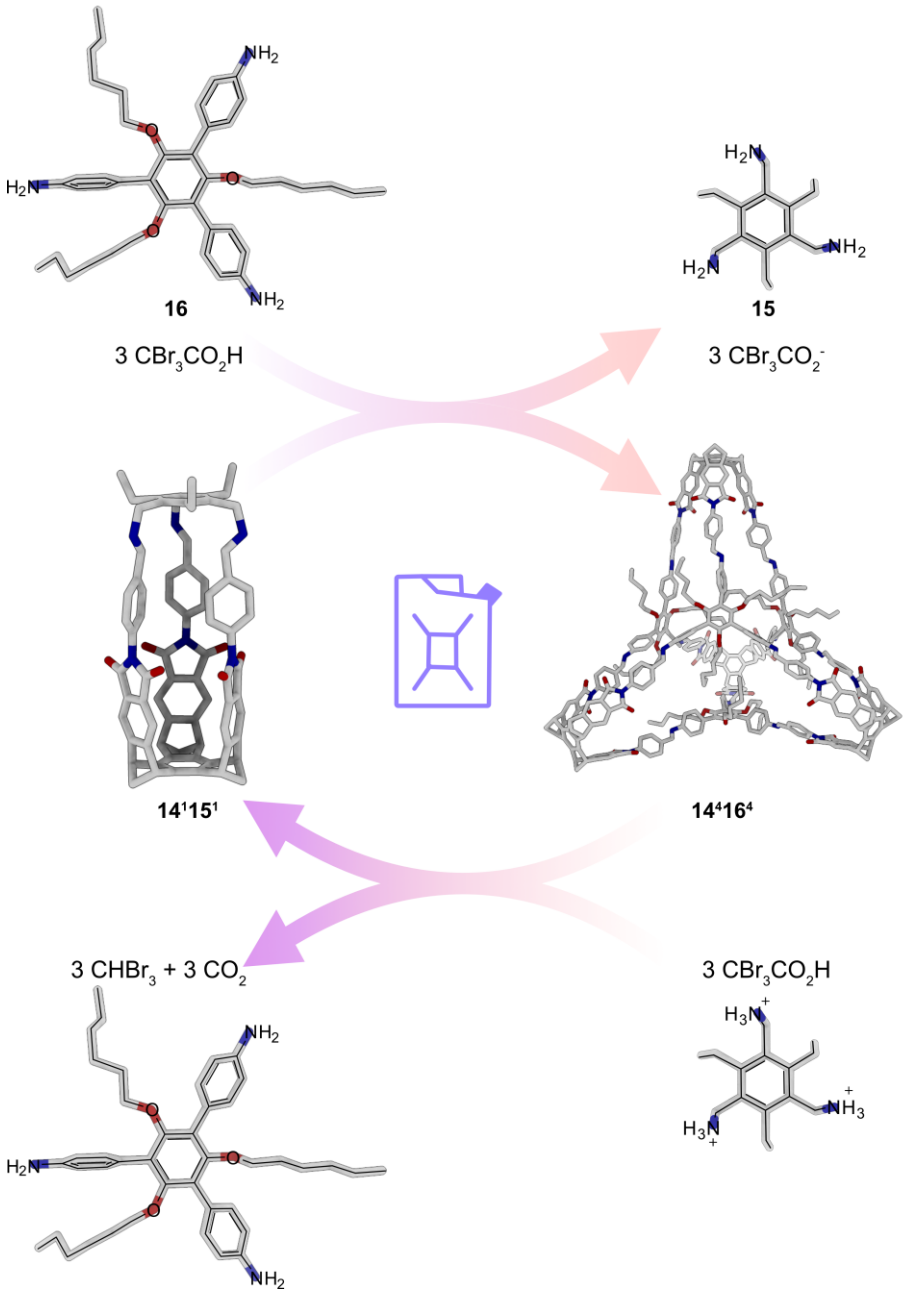

Figure 13: The Tri[1]Tri[1] cage (**14[1]15[1]**) that is formed from the basket aldehyde and the aliphatic tris-amine can be transferred into the Tri[4]Tri[4] cage (**14[4]16[4]**) by the addition of tribromoacetic acid. The decomposition of the metastable acid leads to the deprotonation of the aliphatic tris-amine and the concomitant decay of the Tri[4]Tri[4] cage, followed by the reformation of the Tri[1]Tri[1] cage.

A dynamic imine system in which the addition of a fuel triggers the disassembly and reassembly of a cage coupled with a topology change and an imine exchange was recently reported by the group of Badjić. The employed basket-shaped aldehyde (**14**) was able to form either the Tri[1]Tri[1] cage (**14[1]15[1]**) or the Tri[4]Tri[4] cage (**14[4]16[4]**), depending on the amine employed. Combining the aromatic tris-amine **16** with the aldehyde **14** and an excess of the aliphatic tris-amine **15** led to the preferred formation of **14[1]15[1]**. The addition of the meta-stable

acid tribromoacetic acid (TBA) led to the protonation of the **15** and the disassembly of the cage. As only amine **16** is available as a building block cage $\mathbf{14^4 16^4}$ is formed. The meta stable TBA decomposes over time, forming bromoform and carbon dioxide, and as the aliphatic diamine is now again available for cage formation, $\mathbf{14^4 16^4}$ is transformed into $\mathbf{14^1 15^1}$ (Figure 13).[63b]

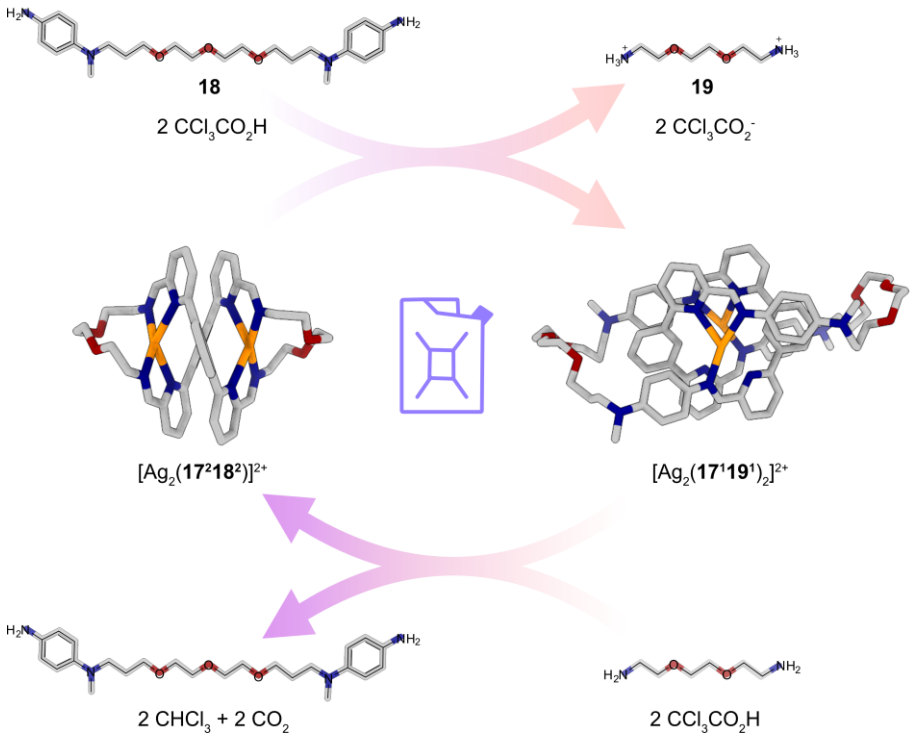

Figure 14: An imine ligand based on aliphatic diamine **18** forms a helical structure in combination with Ag^I. Upon addition of the metastable fuel, trichloracetic, the aliphatic amine is protonated, leading to the decomposition of the ligand and the formation of an imine ligand based on the aromatic diamine. The new ligand forms a 2-catenane with Ag^I. As the acid decays over time, forming chloroform and carbon dioxide, the aliphatic diamine is again capable of forming the helical assembly.

A similar approach was employed by Ayme and co-workers, who also utilised the different basicity of arylamines and alkylamines in combination with a metastable acid to induce rearrangements. Imine ligands, capable of forming metal-organic assemblies, were generated by mixing one aldehyde with two different amines. The more basic amine in combination with the aldehyde led to the formation of the ligand, that formed the most stable complex with Cu^I or Ag^I. Adding trichloroacetic acid (TCA) led to the disassembly of the ligand and the formation of a new ligand based on the amine with the less basic amine. A new metal-organic complex is formed, which as a result of the decarboxylation of TCA over time, decomposes resulting in the reformation of the precursor assembly. This concept was used to switch between different metal-organic assemblies and was also transferred on a helical macrocycle based on Ag^I that can be temporarily transformed into a catenane (Figure 14).[63a]

Severin *et al.* used a combination of light and chemical fuel to drive the system out of equilibrium by using a metastable state photoacid. The photocontrolled transformation of a merocyanine into a spiropyrane sets a proton free. This process was used to trigger the disassembly and reassembly of a palladium cage over several cycles by reversibly protonating the ligands.[64]

1.4.2 Photoresponsive dissipative supramolecular systems

By employing different kinds of photoswitches, a variety of dissipative systems fuelled by light have been created, with several exciting examples being published in the last few years.
A palladium-based macrocycle that was able to undergo dissipative rearrangement was published by the group of Lees.[56] The square-shaped complex, which contained four azobenzene units, underwent a rearrangement upon irradiation with UV light, forming a smaller square based on only two azobenzene units. Another azobenzene-based system was reported by the group of Sleiman. The azobenzene units formed tape-like structures by intermolecular hydrogen bonding with the *E*-isomer, while the *Z*-isomer formed square-shaped structures.[65]
The group of Clever utilised a similar diarylethene functionalised with pyridyl units to generate a photoresponsive system that underwent a geometry change coupled with a topology change of the assembly upon irradiation (Figure 15a). The open ligand o-**20**, which was more flexible than its corresponding isomer, formed two different symmetric products in combination with Pd^{II}, which the group of Clever identified as a triangular, three-membered $[Pd_3(o\text{-}\mathbf{20})_6]^{6+}$ and a four-membered $[Pd_4(o\text{-}\mathbf{20})_8]^{8+}$ ring in a 3 to 1 ratio. Irradiation of o-**20** with UV light (313 nm) gave the closed photoswitch c-**20** in 96% yield, while the reverse process could be achieved quantitatively by irradiation with red light (617 nm). Combining c-**20** with Pd^{II} yielded an enormous supramolecular cage with a radius of 35 Å as determined by ^{1}H DOSY NMR experiments, which corresponded well to the formation of a cuboctahedral $[Pd_{24}(c\text{-}\mathbf{20})_{48}]^{48+}$ cage. The irradiation of the mixture formed by the reaction of o-**20** also yielded the large cage.[66]

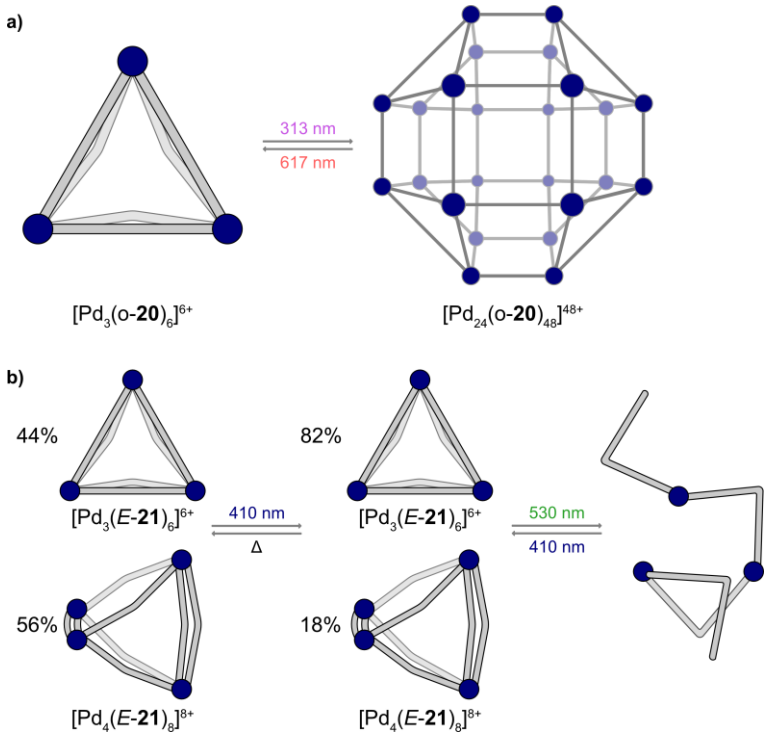

Figure 15: Schematic representations of a) a triangular metal-organic assembly that transformed into a rhombicuboctahedral sphere upon irradiation with UV light (313 nm), as reported by Clever *et al.*, and b) a mixture of a double-walled triangle and a distorted tetrahedron that reversibly changed composition during the irradiation with UV light, as published by the group of Beves. The mixture can be transformed into a polymeric structure upon irradiation with green light.

A photoswitchable fluorinated azobenzene **21** was combined with Pd^{II} by the group of Beves, yielded a mixture of two metal-organic assemblies, namely $[Pd_3(E\text{-}\mathbf{21})_6]^{6+}$ and $[Pd_4(E\text{-}\mathbf{21})_8]^{8+}$, which corresponds most likely to metal-organic complexes in the shape of a double-walled triangle and a distorted tetrahedron (Figure 15b). The mixture was pumped out of equilibrium, enriching the less stable double-walled triangle $[Pd_3(E\text{-}\mathbf{21})_6]^{6+}$, by irradiation with light of a wavelength of 410 nm. This process was reversed by heating the mixture. Irradiation with green light (530 nm) results in the decomposition of the structures and the formation of ill-defined oligomeric species. Beves *et al.* propose that upon irradiation with UV light, a free azobenzene *E*-**21** unit, which is formed by dissociation from the tetrahedral structure $[Pd_4(E\text{-}\mathbf{21})_8]^{8+}$, isomerises and the resulting *Z*-**21** can no longer be incorporated in the structure. It is further theorised that the metastable $[Pd_4(E\text{-}\mathbf{21})_7]^{8+}$ rearranges to form the double-walled triangle $[Pd_3(E\text{-}\mathbf{21})_6]^{6+}$.[67b]

The groups of Clever and Herges combined the isomers of a diazocine ligand (**22**), which consists of two pyridine units that are connected to the photoswitching moiety by ethinyl linkers and Pd^{II} ions to generate metal-organic cages. While the more stable *Z*-isomer led to the formation of a mixture of cages of the general formula $[Pd_n(Z\text{-}\mathbf{22})_{2n}]^{2n+}$, the reaction of the *E*-isomer selectively formed the $[Pd_2(E\text{-}\mathbf{22})_4]^{4+}$ cage. As the *Z* to *E* isomerisation occured not

quantitatively after irradiation with UV light (385 nm), but approximately 62% of *E*-**22** was formed, the formation of $[Pd_2(E\text{-}\mathbf{22})_4]^{4+}$ was accompanied by the formation of the $[Pd_n(Z\text{-}\mathbf{22})_{2n}]$ mixture. The *E*-isomer of the cage was transferred into the mixture of cages either thermally or by irradiation with green light (530 nm) or *vice versa* by irradiation with UV light. Due to their different shape and cavity size, the *E*-cage was able to encapsulate the dianionic guest, 2,6-naphtalenedisulfonate. Irradiation or heating of the host-guest complex triggered the *E* to *Z* isomerisation and the formation of the cage mixture. The guest was concurrently released as the smaller *Z*-cages were not capable of acting as hosts (Figure 16).[68]

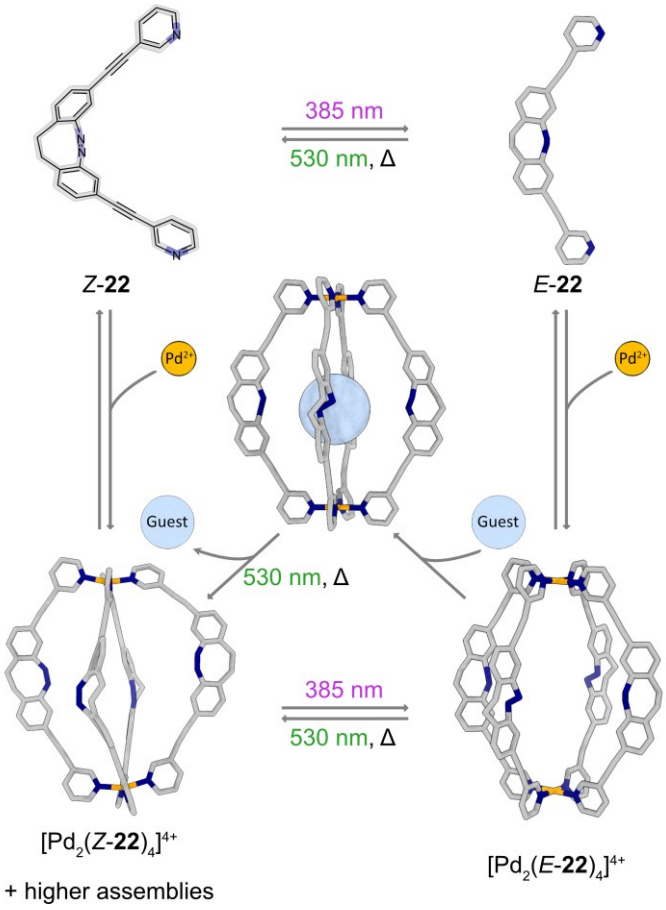

Figure 16: Photoswitching of the ligands *Z*- and *E*-**22**, as well as between the self-assembled $[Pd_2(Z\text{-}\mathbf{22})_4]^{4+}$ cage mixture and $[Pd_2(E\text{-}\mathbf{22})_4]^{4+}$ cage as synthesised by Clever and co-workers. The $[Pd_2(E\text{-}\mathbf{22})_4]^{4+}$ is capable of taking up a guest, which can be released by the photochemical or thermal reformation of the assembled $[Pd_2(Z\text{-}\mathbf{22})_4]^{4+}$ cage mixture. The figure was copied from reference 59 with permission.

A metal-organic system in which the geometrical change is accompanied by a change in the stoichiometry of the monomers was recently reported by Beves and co-workers (Figure 17). The *ortho*-fluorinated azobenzene photoswitch connected to two isoquinoline units was photoisomerised from *E* to *Z* using green (530 nm) or red (617 nm) light, while the reformation of the *E*-isomer was induced thermally or photochemically by irradiation with UV light (405 nm).

In combination with Pd^{II} ions, *E*-**23** formed the twisted $[Pd_2(E\text{-}\mathbf{23})_4]^{4+}$ cage. In contrast, the smaller $[Pd(Z\text{-}\mathbf{23})_2]^{2+}$ assembly was formed when *Z*-**23** was used as a starting material. The interconversion between the different metal-organic assemblies was achieved photochemically and thermally. The coordination of **23** to a Pd^{II} ion changed the photochemical properties of the photoswitch, altering the wavelength needed for *E* to *Z* isomerisation and significantly improving the thermal stability and *Z* ratio in the PSS of the $[Pd_2(Z\text{-}\mathbf{23})_2]^{2+}$ (850 days, 95%) in comparison to the unbound ligand *Z*-**23** (40 days, 52%).[67a]

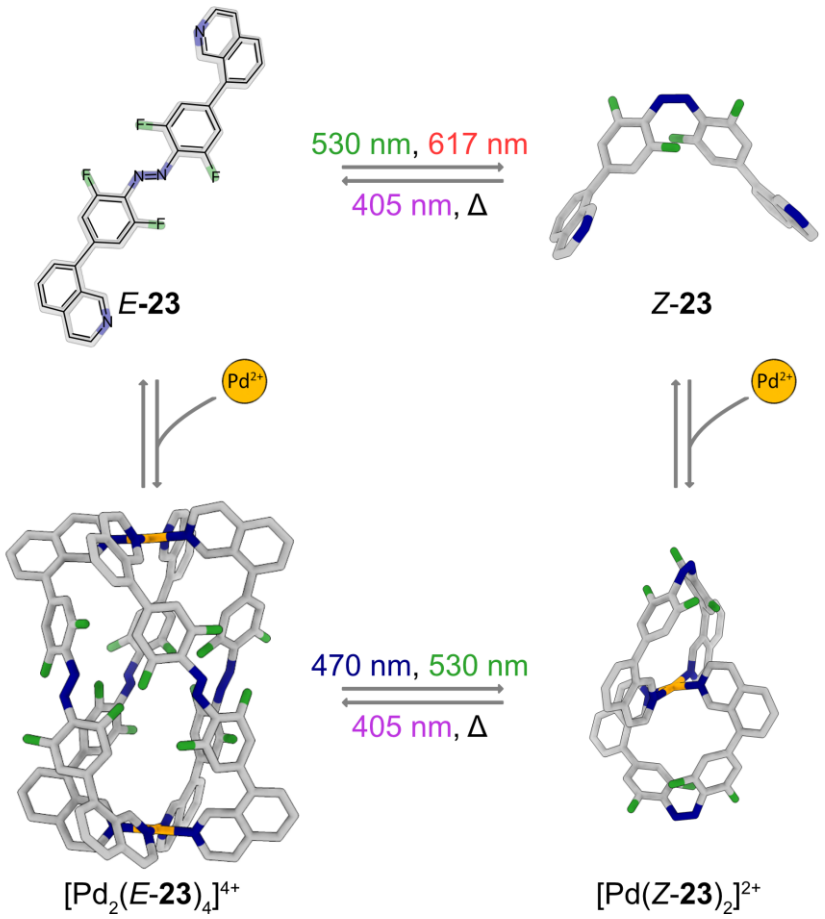

Figure 17: Photoswitching of the ligands *E*- and *Z*-**23**, as well as between the self-assembled cages $[Pd_2(E\text{-}\mathbf{23})_4]^{4+}$ and $[Pd(Z\text{-}\mathbf{23})_2]^{2+}$, as reported by the group of Beves. The figure was copied from reference 59 with permission.

Shortly after, a similar system was published by the group of Wang that features an azobenzene ligand with two picolyl units that, in combination with Pd^{II}, formed metal-organic assemblies with varying stoichiometries depending on the isomer of **24** employed. The ligand was isomerised from *E* to *Z* using UV light (365 nm) with a ratio of 94% *Z*-isomer in the PSS and *vice versa* with 77% *E*-isomer in the PSS after irradiation with blue light (420 nm). Irradiation of the $[Pd_2(E\text{-}\mathbf{24})_4]^{4+}$ cage, structurally similar to the cage reported by Beves *et al.*, also leads to the formation of a smaller $[Pd\ (Z\text{-}\mathbf{24})_2]^{2+}$ structure.[69]

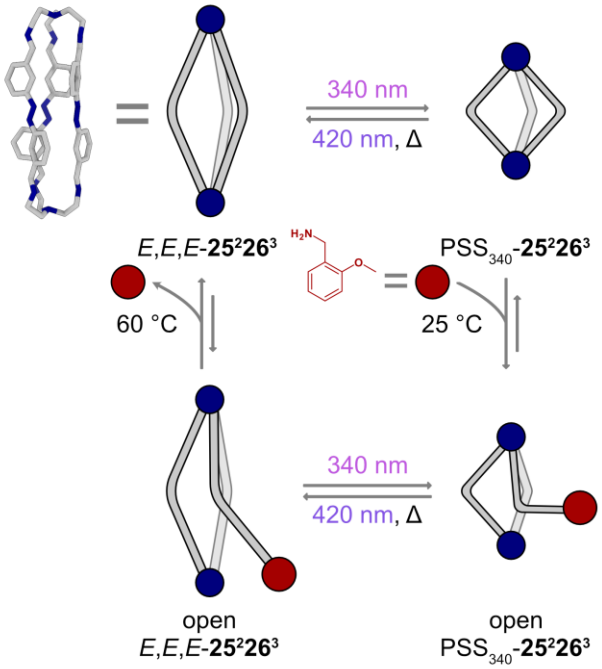

Figure 18: Structures of one of the azobenzene cages synthesised by Vögtle *et al.* and utilised in exchange reactions by Feringa *et al.* This figure was reproduced from reference 59 with permission.

At the same time, the group of Feringa showed that an azobenzene imine cage, which was first reported in 1992 by Bauer and Vögtle,[70] can be used to induce an amine exchange by light (Figure 18). The *E,E,E*-**25²26³** cage can be photoisomerised, yielding a mixture that contains the different isomers of **25²26³**, by using light with a wavelength of 340 nm. Employing light with a wavelength of 420 nm or heat leads to the reformation of *E,E,E*-**25²26³**. The *Z,Z,Z*-isomer of **25²26³** can undergo reversible opening of the cage, and the resulting free aldehyde group can be capped by the addition of (2-methoxyphenyl)methanamine. The *Z*-isomers of the open cage can then be photochemically transferred to the open *E*-isomer, which is less stable than its closed counterpart. Heating the open species to 60 °C again leads to the formation of *E,E,E*-**25²26³**. The extensive studies showed that the open species cannot be obtained by the combination of *E,E,E*-**25²26³** and (2-methoxyphenyl)methanamine. Additionally, the combination of PSS_{340}-**25²26³** with isophthalaldehyde leads to irreversible amine exchange and the formation of a new cage.[71]

2. Motivation

While there are numerous exciting examples of photoresponsive and dissipative metal-organic cages and macrocycles, the number of metal-free systems is significantly lower. In 2019, our group designed different halogen-bonded boxes based on photoswitchable azobenzene donors and U-shaped halogen bond acceptors (Figure 19).[7] We anticipated that the clear geometry change that occurs upon photoisomerisation should lead to a change in the structure and topology of the assembly, which should be reversible by irradiation with an alternative light source. While the formation was thoroughly investigated in the solid-state, the investigations in solution were of increased difficulty due to the weak nature of the halogen bonding interactions in the system. The association in solution was observed, but investigations into whether the composition of the formed structures changed upon isomerisation of the photoswitch were inconclusive.

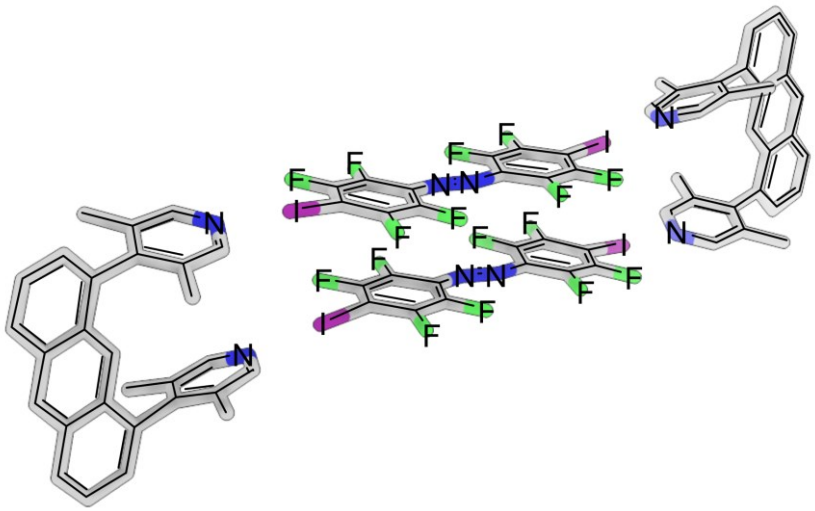

Figure 19: One of the halogen-bonded boxes investigated by our group.

Although this example further highlights the diverse applications of halogen bonds in the creation of supramolecular structures, halogen bonding using neutral halogen bond donors is a more suitable tool to generate architectures in the solid-state, while the generation of photoresponsive systems in solution is in need of stronger intermolecular interactions. Halogen bonding donors have been employed in combination with a variety of different Lewis basic acceptor motifs. Among those, many of the acceptors are nitrogen-based, which led to the idea to investigate whether imine halogen bonding could be utilised to build supramolecular structures. The halogen bonding of imines was only used once to generate a supramolecular structure, and apart from that, only rarely employed in catalysis, but until now not thoroughly investigated. Imines as a structure motif are highly interesting, as they are one of the most

common structure motifs in cages generated by dynamic covalent chemistry. Building structures based on imine cages and different halogen bond donors could be a useful tool to alter the solid-state structure and therefore the properties of the obtained compounds, as well as facilitate the crystallisation and structure determination of large cage compounds, which is inherently difficult.

The first part of this work will investigate the suitability of imines as halogen bond donors and the variety of networks accessible using supramolecular imine compounds. Using a model system, the properties of the imine halogen bond were examined in solution by binding titrations and in the gas phase by DFT computations. Halogen-bonded networks were obtained by combining two imine cages that vary in size and structure with seven different halogen bond donors. The formation of a halogen-bonded structure or the absence thereof gave an indication of the possible structural prerequisites necessary for the successful generation. The single crystal structures obtained for some of the frameworks gave further insight into the nature of the imine halogen bond, supported by computational analyses of the obtained structures. A different synthetic approach to the obtained structures was also investigated, as were the structural features of the obtained networks, such as stability and gas adsorption properties.

The second part of this thesis will focus on the generation of different photoresponsive systems that might undergo dissipative interconversion. As initially mentioned, a stronger interaction than halogen bonding is needed to enable a detailed analysis of the compound in solution as well as the changes in geometry or composition that occur upon photoisomerisation. The reversibility in the formation of imines should enable the interconversion between different systems, while the imine bond itself is stable enough to allow for the analysis of the generated samples. A suitable azobenzene building block, that was recently published by the group of Pianowski *et al.*,[72] was synthesised, and its photochemical properties as well as its reactivity towards imine formation were investigated. As the formation and topology of supramolecular cages and macrocycles highly depend on the geometry of the employed building blocks and the azobenzene building block undergoes a major geometrical change upon isomerisation, the formation of different structures based on both isomers should be possible. Combination with rigid or more flexible aliphatic diamines showcased the diverse structures accessible by the employment of the different isomers, ranging from oligo- and polymers to macrocycles, even containing highly strained or metastable structures. The interconversion between the obtained distinct structures could be achieved by photoisomerisation with visible light, giving access to the first photoresponsive dissipative imine system. A photoresponsive cage was also generated by combining the azobenzene building block with a triamine.

Finally, the possibility of utilising the differing tendency of the two isomers to form distinct supramolecular structures to generate a system in which the exchange of the amine building block could be reversibly triggered by light was investigated.

3. Results and discussion

3.1 Halogen-bonded networks

3.1.1 Imine halogen bonding

Introduction

Halogen bonding as a weak, non-covalent interaction has been used to generate several exciting structures in solution, such as macrocycles,[14] boxes,[15] and capsules,[12b,e,16] as well as in the solid-state for example to generate frameworks.[12i,18]

While the variety of commonly used, nitrogen-based halogen bond acceptors is large, imines have been until now rarely employed. There are few examples in which an imine is activated by halogen bonding with a catalyst,[73] but apart from one example, there are no supramolecular structures constructed by imine halogen bonding[12h, 74] and the properties of imine halogen bonds have not been further investigated yet. Imines could be an interesting donor motif, as a large part of supramolecular cages generated by dynamic covalent chemistry has imine groups. Building solid-state structures based on imine cages and halogen bond donors would offer a reversible and easy technique to alter the solid-state packing of supramolecular cages and the dependent macroscopic properties. To evaluate the imine motif as a halogen bond donor, an imine model compound was generated and investigated in solution. Those studies have been supported by computational analyses.[1]

Imine halogen bonding in solution

To investigate the suitability and evaluate the strength of imines as halogen bond donors, a model compound was employed in an NMR association experiment. The commercially available *N*-benzylideneaniline (**28**) was used. Pentafluoroiodobenzene (**IF_5**) was chosen to be the monotopic halogen bond donor. As the formation of halogen bonds is also highly dependent on the solvent that is used, cyclohexane was employed as a non-coordinating solvent that was found to be most suitable for the development of halogen bonds.[12d,k,l] The halogen bond acceptor was successively added to a solution of the donor, varying the concentration of the acceptor while keeping the total concentration of the donor constant. The titration was carried out twice, and the shift of the signals in the $^{19}F\{^{1}H\}$ NMR that occurs upon

[1] Large parts of this work have been published: E. Nieland, D. Komisarek, S. Hohloch, K. Wurst, V. Vasylyeva, O. Weingart, B. M. Schmidt, *Chem. Commun*. **2022**, *58*, 5233-5236.

addition of the acceptor is monitored and later plotted against the concentration of the acceptor. The obtained values were fitted to the following equation using the orthogonal distance regression iteration algorithm.

$$\Delta\delta = \frac{\Delta\delta_{sat}}{2}\left[\left(\frac{[G]_0}{[H]_0} + 1 + \frac{1}{K_a[H]_0}\right) - \sqrt{\left(\frac{[G]_0}{[H]_0} + 1 + \frac{1}{K_a[H]_0}\right)^2 - 4\frac{[G]_0}{[H]_0}}\right] \quad (1)$$

While the total concentration of the host $[H]_0$ is kept constant, the total concentration of the guest $[G]_0$ is varied. The association constant K_α as well as the change in chemical shift for a saturated system $\Delta\delta_{sat}$ are obtained by curve fitting. While similar binding titrations are often performed at lower temperatures[7,16b,g] the shift of the signals in the $^{19}F\{^1H\}$ NMR spectrum was already observable at room temperature, even though it was diminutive. As indicated by the small shifts, the determined association constant for the two titrations were 1.69 and 2.48 M^{-1}, suggesting that the binding in the chosen system is very weak (Figures S1-S2 and table S1). The large variation in the determined value is a result of the small shifts, which introduced large errors, as well as the poor fit of the curves to the obtained values.

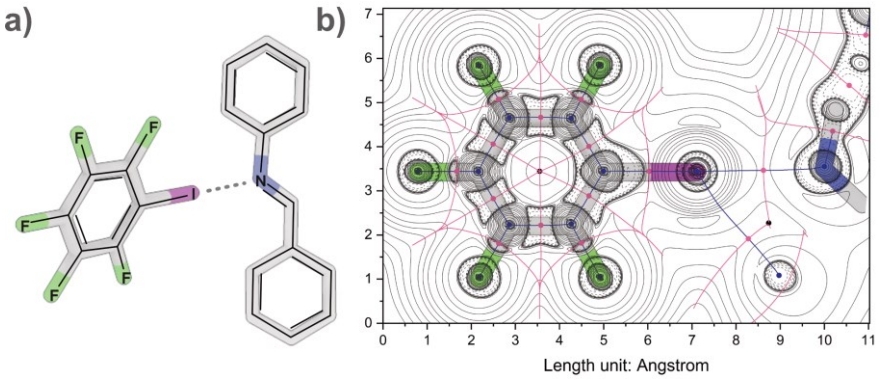

Figure 20: a) Imine halogen bonding in the **28···IF$_5$** model system; b) corresponding Laplacian of electron density with critical points and bond paths. Bond critical (3,-1) points are depicted in pink, nuclear critical (3,-3) points in blue, ring critical (3,+1) points in black, paths and zero-flux surfaces as blue and pink lines. DFT computations were performed by Dr. Oliver Weingart. This figure was reproduced from reference 75 with permission.

The model system based on **28** was also investigated in the gas phase by DFT computations that were performed by Dr. Oliver Weingart. The analysis of the DFT-computed density of the **28···IF$_5$** model system revealed an interaction energy between 18.62 and 29.07 kJ mol^{-1} for the halogen bond that is computed to be 2.89 Å long. Depending on the chosen donors and acceptors, typical values for halogen bonds lie between 10 and 150 kJ mol^{-1}, supporting the initial conclusion that the halogen bonding of imines is comparably weak.[12h,76] The density

analysis also showed additional H···I interactions between the donor and the acceptor (3.00 Å, 5.40–9.34 kJ mol^{-1}).

Synthesis of halogen bond donors

In the following sections, the commercially available fluorinated halogen bond donors pentafluoroiodobenzene (**IF_5**), and 1,2-diiodotetrafluoroethane (**I_2F_4Et**) were employed, as well as 1,2-diiodotetrafluorobenzene (***o*-I_2F_4**), 1,3-diiodotetrafluorobenzene (***m*-I_2F_4**), and 1,4-diiodotetrafluorobenzene (***p*-I_2F_4**). The aforementioned compounds were synthesised by iodination of the corresponding tetrafluorobenzene precursors with periodic acid and potassium iodide in concentrated sulfuric acid, adapting an established literature procedure.[77] The ***o*-I_2F_4** and ***p*-I_2F_4** were further purified by recrystallisation. All three compounds could be isolated with satisfying yields and large scopes (Figure 21).

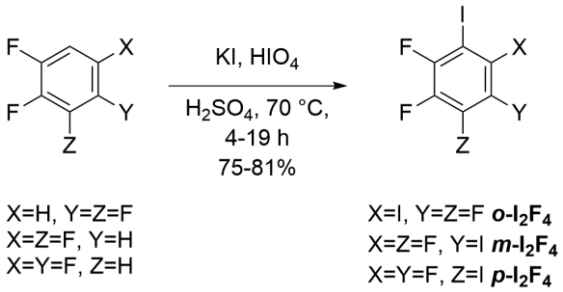

Figure 21: Synthesis of ***o*-I_2F_4**, ***m*-I_2F_4**, and ***p*-I_2F_4**.

Another ditopic halogen bond donor, previously employed, among others, in the synthesis of photoresponsive liquid crystals[78b,c] or in the construction of halogen-bonded boxes[7] was synthesised starting from 2,3,5,6-tetrafluoroaniline. Iodination using red mercury oxide and iodine led to the formation of aniline **29**, which could be coupled using *N*-chlorosuccinimide and 1,8-diazabicyclo[5.4.0]undec-7-ene (DBU), yielding the corresponding azobenzene **I_2F_8** following the procedure established by John and Lin (Figure 22).[79]

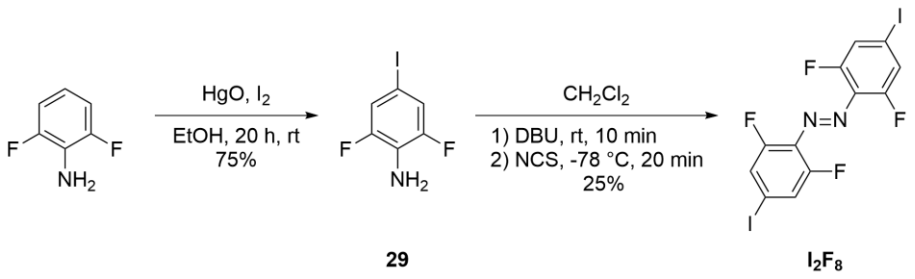

Figure 22: Synthesis of **I_2F_8**.

A tritopic donor was synthesised analogous to the iodination of the ditopic donors followed by recrystallisation yielding 1,3,5-trifluorotriiodobenzene (**I_3F_3**) as colourless needles in an appropriate yield in a large scope (Figure 23).[77]

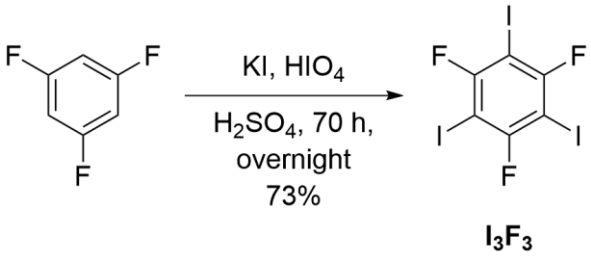

I_3F_3

Figure 23: Synthesis of **I_3F_3**.

The different donors were employed in the formation or attempted formation of halogen-bonded imine networks in the following chapters.

3.1.2 Halogen-bonded networks based on a Tri^2Di^3 cage

Introduction and synthesis of the Tri^2Di^3 halogen bond acceptor

There is a large variety of different imine cages that could possibly be employed in the generation of halogen-bonded networks.[24] To facilitate the analysis and evaluate whether the targeted networks can be synthesised in the first place, a small Tri^2Di^3 cage was chosen as the structure motif. The shape persistency and stability of the Tri^2Di^3 as well as the comparably easy synthesis in larger scopes make them attractive building blocks. The cage itself should have no functional groups that can act as halogen bond acceptors or donors to not hinder the halogen bonding of the imine with the added donor.

The group of Cooper investigated the formation of different Tri^2Di^3, Tri^4Tri^4, and Tri^4Di^6 cages with three different amines and 26 different aldehydes in a high-throughput screening, showcasing among other findings, the effect of the substituents on the triamines on the capability to form cages.[80] While the non-substituted 1,3,5-tris-(aminomethyl)-benzene is found to, in most cases, not form the targeted cage or to show incomplete or impure conversion with the different aldehydes, the substituted triamines (2,4,6-trimethylbenzene-1,3,5-triyl)trimethanamine (**Me**) and (2,4,6-triethylbenzene-1,3,5-triyl)trimethanamine (**Et**) are more likely to form the cages selectively. While some cages that were not formed under the conditions chosen in the high-throughput screening were already synthesised by other groups, the systematic investigation of the cage formations in combination with a computational screening gives an insight into the different structural and electronic effects that need to be considered in the design of imine cages. The cages based on isophthalaldehyde (**Iso**) and the amines **Me** or **Et**, **Me^2Iso^3** and **Et^2Iso^3**, both form cleanly and can be easily synthesised in larger scales. As they have no additional functional groups that could act as halogen bond acceptors both cages would be suitable halogen bond acceptors for the generation of networks. **Me^2Iso^3** was chosen as the acceptor employed in the following framework syntheses as it is assumed that the ethyl groups of **Et^2Iso^3** could hinder crystallisation (Figure 24).[2]

Following an established procedure,[81] **Me** was synthesised starting from mesitylene in three steps. Using paraformaldehyde, zinc bromide, and hydrogen bromide in acetic acid, mesitylene was transformed into **30** with a yield of 75%. Using sodium azide in dimethylformamide, bromide **31** was transformed into the corresponding azide, which could be isolated in 93% yield. The following reduction using hydrogen and palladium on charcoal yielded the targeted triamine **Me** in 92% yield after a total reaction time of approximately five days.

[2] Large parts of this work have been published: E. Nieland, D. Komisarek, S. Hohloch, K. Wurst, V. Vasylyeva, O. Weingart, B. M. Schmidt, *Chem. Commun*. **2022**, *58*, 5233-5236.

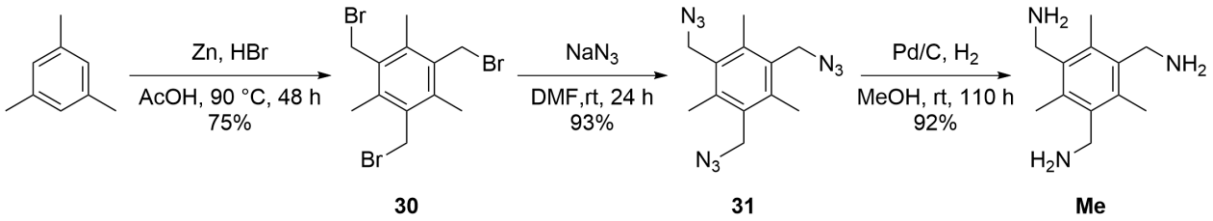

Figure 24: Synthesis of **Me** starting from mesitylene.

Employing commercially available **Iso** and **Me** following a procedure published by Cooper *et al.*[80] imine cage **Me²Iso³** was synthesised in 38% yield (Figure 25).

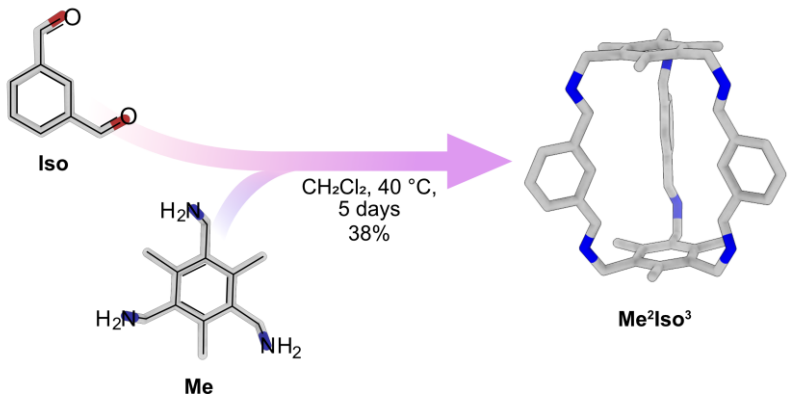

Figure 25: Synthesis of **Me²Iso³**.

The obtained analytical data were in accordance with literature, confirming the clean formation of a Tri²Di³ cage that could be employed in the generation of halogen-bonded networks.

Halogen bonding of Me²Iso³ with a monotopic halogen bond donor

The imine cage was first combined with the simplest halogen bond donor **IF₅**, which has shown to be able to form imine halogen bonds with the model compound, leading to the formation of a halogen-bonded system. The starting materials were dissolved in a mixture of methanol and chloroform, and slow evaporation of the solvents led to the formation of **Me²Iso³···IF₅** as a crystalline material suitable for single-crystal X-ray crystallography. The halogen-bonded structure **Me²Iso³···IF₅** consists of one **Me²Iso³** cage as well as one **IF₅** donor. The formation of the structure in this ratio is surprising, as the number of possible halogen bond acceptor sites of **Me²Iso³** in combination with the monotopic halogen bond donor should suggest that the formation of a halogen bonding adduct with the cage-to-donor ratio of one-to-six should be possible. However, varying the equivalents of donor, always led to the formation of the same structure.

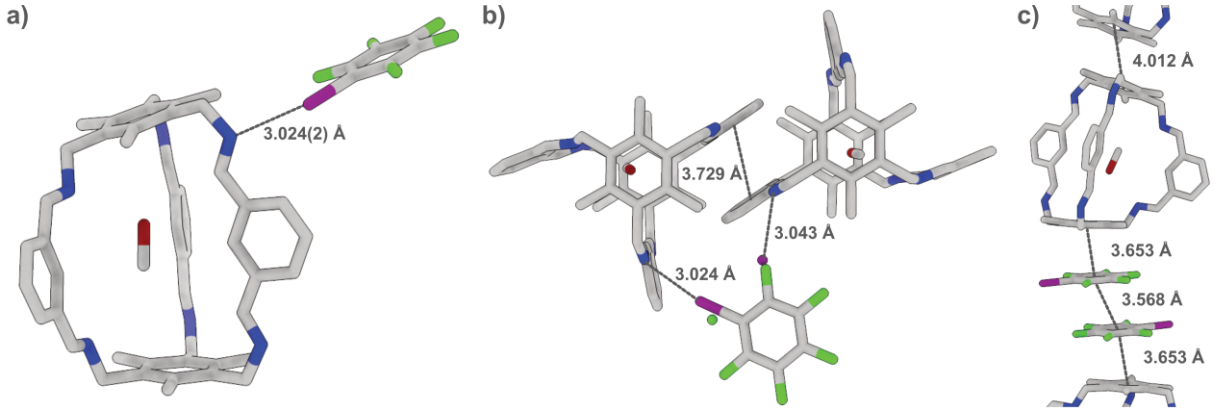

Figure 26: Single-crystal X-ray structure of **Me²Iso³···IF₅** showing a) the asymmetric unit bearing one **Me²Iso³** cage connected to one **IF₅** donor by a halogen bond (shown as a grey dotted line) and one ordered methanol solvent molecule. b) the rotational disorder (60°, 88:12) of the halogen bond donor; c) the formation of columnar stacks in the single-crystal structure by (distant) π-stacking (depicted by grey dotted lines). Hydrogen atoms are omitted for clarity. The crystal structure was measured by Prof. Dr. Stephan Hohloch and refined by Dr. Bernd M. Schmidt and Prof. Dr. Stephan Hohloch. This figure was adapted from reference 75 with permission.

The interaction between the imine group of the cage and the iodine of the donor can be seen in the crystal structure of **Me²Iso³···IF₅** (Figure 26) suggesting the presence of a halogen bond with an N···I distance of 3.024(2) Å an N···I–C angle of 166.17(9)°. The length of iodine halogen bonds with nitrogen containing acceptors range between approximately 2.7 and 3.5 Å with a bonding angle being between 140 and 180°; a stronger interaction is often accompanied by shorter bonds with angles close to 180°, while weaker interactions lead to longer bonds with varying angles. The observed halogen bond between **Me²Iso³** and **IF₅** is of mediocre strength according to its length and angle. The halogen bond donor **IF₅** shows a rotational disorder of 60° with an occupancy of 88 to 12. This is a result of an imine moiety of a neighbouring cage being in close proximity to the halogen bond donor, offering an alternative halogen bonding site. The cage is connected to the disordered halogen bond donor by a halogen bond interaction with a similar N···I distance length of 3.043(4) Å and an N···I–C angle of 162.9(3). The two neighbouring cages are connected by π-stacking.

Each **Me²Iso³** is slightly deformed, with two imine units pointing inwards and four pointing outwards. The deformation is a result of hydrogen bonding of one of the imine groups with the ordered methanol solvent molecule that is encapsulated in each cage. Columnar stacks containing **Me²Iso³** cages and **IF₅** are formed by π-stacking and distant π-stacking. The interaction between two **Me²Iso³** is very weak (4.012 Å), while the π-stacking distance of **Me²Iso³** with **IF₅** is significantly shorter (3.653 Å). Surprisingly, the shortest distance in the stack can be measured between two **IF₅** molecules that are ordered in opposite directions (3.568 Å).

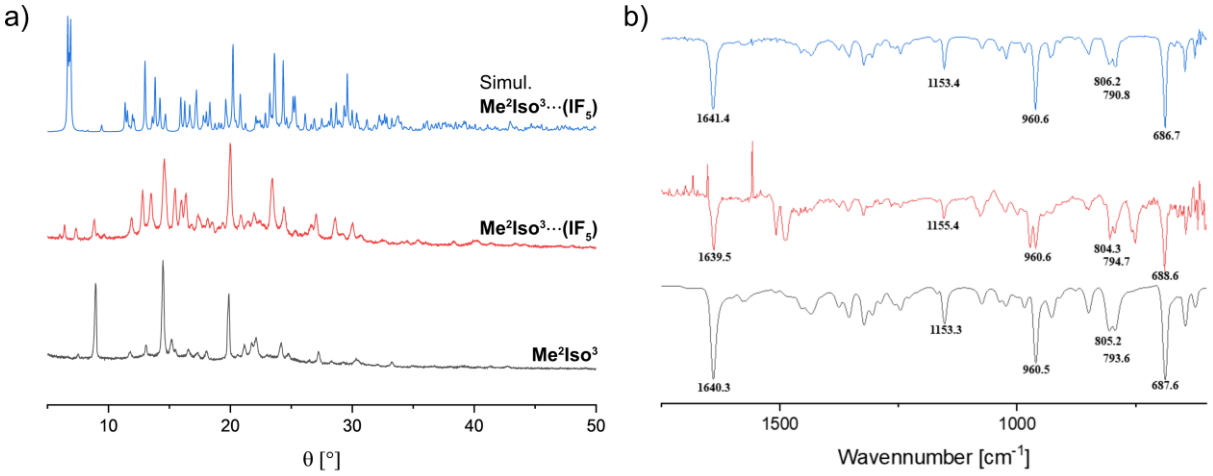

Figure 27: a) Comparison of the simulated diffractogram of **Me²Iso³···IF₅** (blue) obtained from the single-crystal X-ray diffraction data with the measured powder X-ray diffractograms of **Me²Iso³···IF₅** (red) and **Me²Iso³** (black). No reference diffractogram for **IF₅** is given as the compound is liquid at room temperature; b) Excerpts of the IR spectra of acceptor **Me²Iso³** (blue), **Me²Iso³···IF₅** synthesised by liquid assisted grinding (red) and **Me²Iso³···IF₅** obtained by slow evaporation (black).

The formation of the halogen-bonded compound can also be observed by powder X-ray diffraction. The comparison of the simulated diffractogram obtained from the crystal structure of **Me²Iso³···IF₅** with the one measured for **Me²Iso³···IF₅** shows large similarities while distinct differences to the measured diffractogram of **Me²Iso³···IF₅** can be seen (Figure 27a).

Due to the mediocre solubility of the **Me²Iso³** cage compound, large amounts of solvents need to be used to generate the halogen-bonded structures. Halogen-bonded compounds can also be generated by neat or liquid-assisted grinding (LAG, also known as solvent drop grind).[82] To do that, the different compounds are mixed in the desired ratio; in the case of LAG, a small amount of solvent is added, and the mixture is ground in a ball mill. This does not only significantly reduce the amount of solvent needed and waste produced, but the compounds can also typically be obtained after a short time.[83] An attempt was made to synthesise **Me²Iso³···IF₅** by liquid-assisted grinding in a ball mill. The powder diffractogram of the homogenous product obtained by grinding could not be analysed due to a very high amorphous percentage. The comparison of IR spectra is another commonly used method to investigate halogen-bonded structures.[82d] The IR spectra recorded of the starting material, and the compounds obtained by slow evaporation and LAG indicated the successful formation, as shown by the shifts of the bands (Figure 27b). The observed shifts of the compound obtained by LAG in comparison to the precursor are marginal, which is in accordance with the shifts of the crystalline material obtained by slow evaporation.

A box-shaped structure based on Me^2Iso^3 and a ditopic halogen bond donor

After investigating the formation of a halogen-bonded structure with a monotopic halogen bond donor, different ditopic halogen bond donors were combined with **Me^2Iso^3** to form structures of higher complexity. As only one of the combinations yielded crystals that were suitable for single-crystal X-ray crystallography, this structure will be discussed in this section, while the possible halogen bonding of the other donors will be evaluated later on. The slow evaporation of a chloroform solution of **Me^2Iso^3** and ***p*-I_2F_4** yielded crystalline **$Me^2Iso^3\cdots2(p\text{-}I_2F_4)$**. Single-crystal X-ray crystallography revealed a box-like structure formed by the interaction of two imine cages and four donors (Figure 28). The structure was surprisingly not formed in the ratio that was initially expected, and other structures were not accessible by changing the ratio of starting materials, rendering the box-like structure obtained the predominant form.

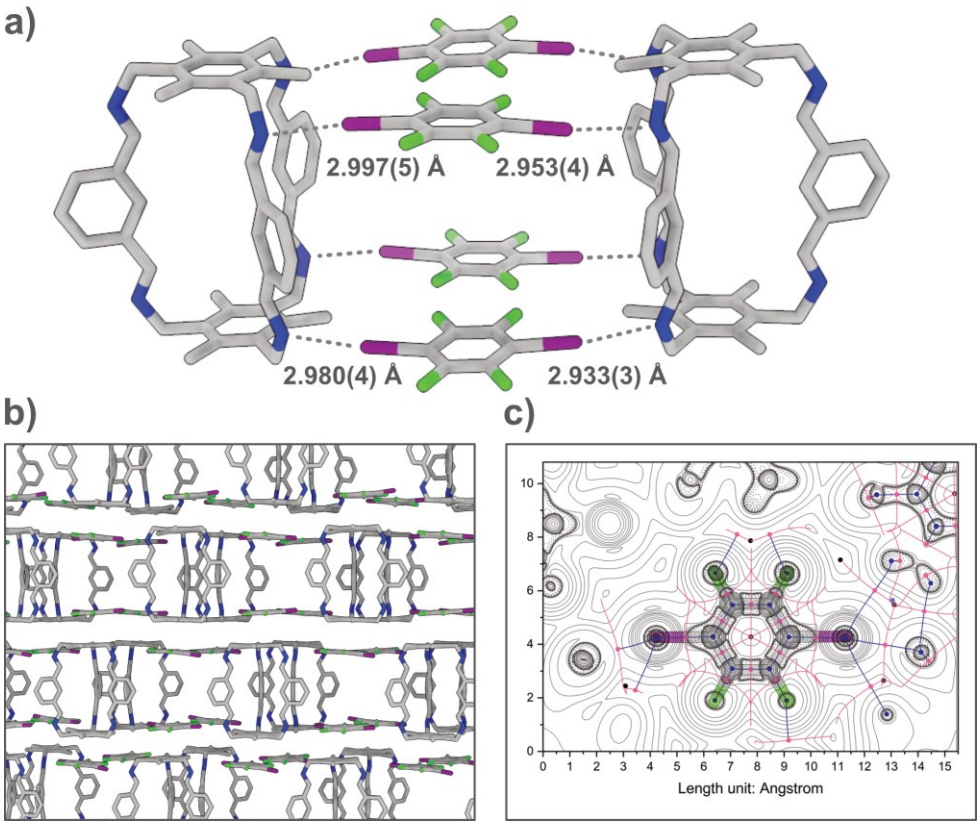

Figure 28: Single-crystal X-ray structure of **$Me^2Iso^3\cdots2(p\text{-}I_2F_4)$** showing a) the structure resembling a box formed by the interaction of two **Me^2Iso^3** cages with four ***p*-I_2F_4** donors. N···I halogen bonds are depicted as grey dotted lines; b) packing of **$Me^2Iso^3\cdots2(p\text{-}I_2F_4)$** along the crystallographic *b* axis; c) corresponding Laplacian of electron density with critical points and bond paths. Bond critical (3, -1) points are depicted in pink, nuclear critical (3, -3) points in blue, ring critical (3, +1) points in black, paths and zero-flux surfaces as blue and pink lines. Hydrogen atoms and solvent molecules are omitted for clarity. The crystal structure was measured by Prof. Dr. Stephan Hohloch and refined by Prof. Dr. Klaus Wurst and Prof. Dr. Stephan Hohloch. DFT computations were performed by Dr. Oliver Weingart. This figure was reproduced from reference 75 with permission.

The four different halogen bonds connecting the two cages are of similar strength, with N···I distances between 2.933(3) and 2.997(5) Å and N···I–C angles between 164.6(2) and 171.6(2). The cage in **Me²Iso³···2(*p*-I₂F₄)** is not distorted with all six imine groups pointing outwards. While four of the six possible halogen bonding sites are occupied by donors, the unoccupied side of the cage interacts with two other cages, each forming its own box *via* π-stacking and distant π-stacking. The interaction of the different boxes leads to the formation of a 2D lattice that can be observed along the crystallographic *b* axis (Figure 28b). With the N···I contacts being significantly shorter and in general closer to an angle of 180°, the interactions observed in this structure are stronger than in the previously discussed **Me²Iso³···IF₅**. The geometrical parameters suggest that the interactions observed are indeed halogen bonds, and to confirm this DFT-D3 calculations[84] and QTAIM analyses[85] were performed. The crystal structure of **Me²Iso³···2(*p*-I₂F₄)** was geometry optimised resulting in a minor shortening of the N···I bonds to 2.84 and 2.89 Å, and QTAIM analyses showed the relevant bond critical points (3, -1) for the N···I contacts, confirming that the interactions are indeed halogen bonds. The interaction energies computed for the N···I bonds in **Me²Iso³···2(*p*-I₂F₄)** lie between 15.64 and 24.43 kJ mol^{-1} and 17.66 and 27.58 kJ mol^{-1}. The interactions were also investigated in the gas phase by the generation of a simplified model system yielding bond lengths and interaction energies that resemble those obtained before (2.87 Å, 19.63–30.65 kJ mol^{-1}) (Figure 29).

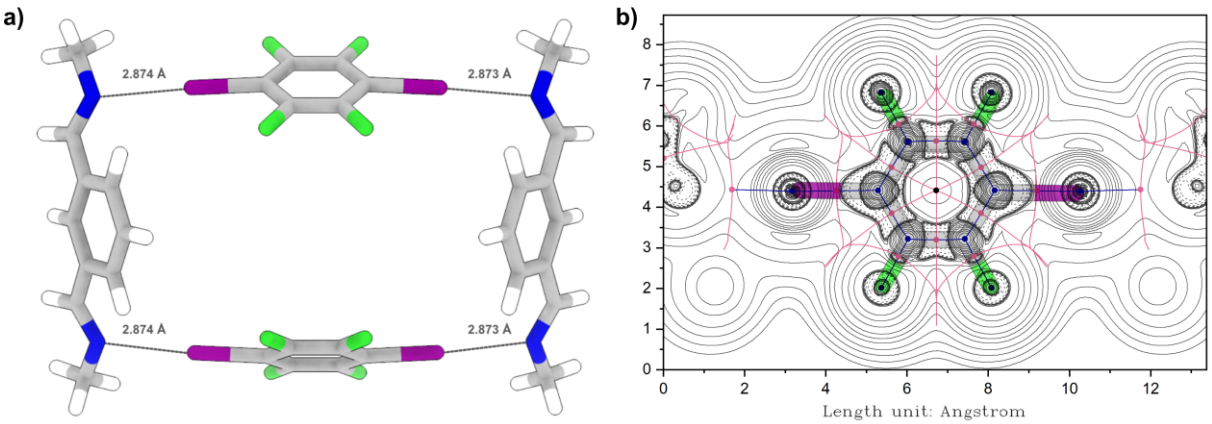

Figure 29: a) Structure of the simplified model system resembling the structure of **Me²Iso³···2(*p*-I₂F₄)**. Halogen-bonds are depicted as grey dotted lines; b) Laplacian of electron density with critical points and bond paths. Bond critical (3, -1) points are depicted in pink, nuclear critical (3, -3) points in blue, ring critical (3, +1) points in black, paths and zero-flux surfaces as blue and pink lines. DFT computations were performed by Dr. Oliver Weingart.

The formation of the networks could again be observed by the comparison of the powder X-ray diffractograms that were computed based on the crystal structure and those that were measured of **Me²Iso³···2(*p*-I₂F₄)**, **Me²Iso³**, and ***p*-I₂F₄**. The measured diffractogram of **Me²Iso³···2(*p*-I₂F₄)** coincides well with the predicted diffractogram, while both show distinct

differences from the diffractograms measured for the starting materials (Figure 30a). The structure was also synthesised by LAG, and comparison of the IR data of the precursors as well as of the halogen-bonded structures obtained by slow evaporation and LAG confirmed the successful synthesis (Figure 30b).

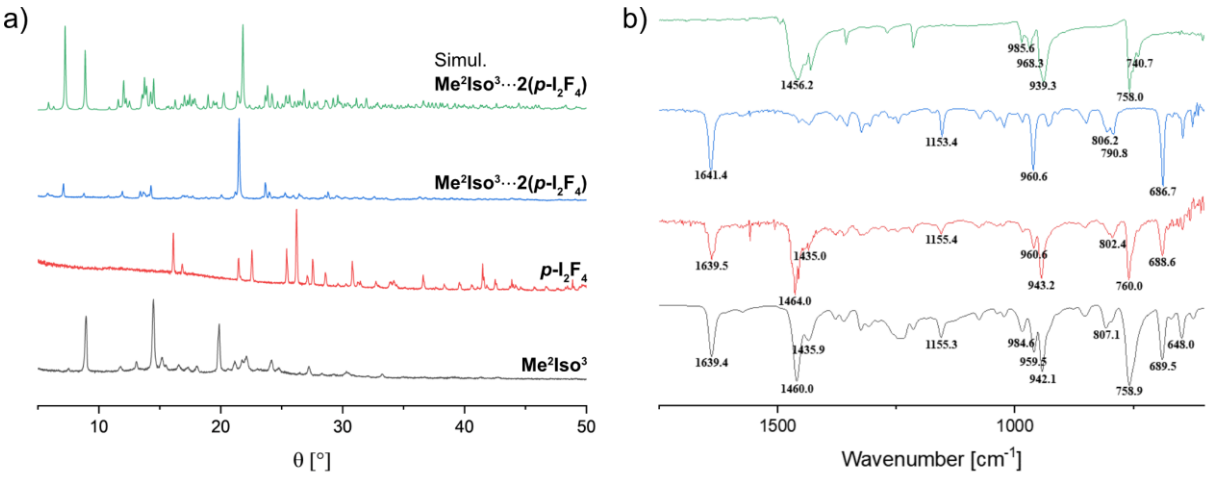

Figure 30: a) Comparison of the simulated diffractogram of **Me²Iso³···2(*p*-I₂F₄)** obtained from the single-crystal X-ray diffraction data (green) with the measured powder X-ray diffractograms of **Me²Iso³···2(*p*-I₂F₄)** (blue), ***p*-I₂F₄** (red) and **Me²Iso³** (black); b) excerpts of the IR spectra of acceptor ***p*-I₂F₄** (green), **Me²Iso³** (blue) and **Me²Iso³···2(*p*-I₂F₄)** synthesised by liquid assisted grinding (red) and **Me²Iso³···2(*p*-I₂F₄)** obtained by slow evaporation (black).

While the signals observed for the crystalline compound and the compound obtained by grinding were not identical, the shifts in comparison to the signals for the starting materials were large enough that a halogen-bonded structure was obtained by LAG. To investigate the stability of the generated structure, thermogravimetric analysis (TGA) was performed on a crystalline sample of **Me²Iso³···2(*p*-I₂F₄)**, revealing an onset temperature of 111.65 °C for the first step (Figure 31a). The decomposition of **Me²Iso³···2(*p*-I₂F₄)** occurs in several steps, but the mass losses could not be assigned to specific decomposition processes.

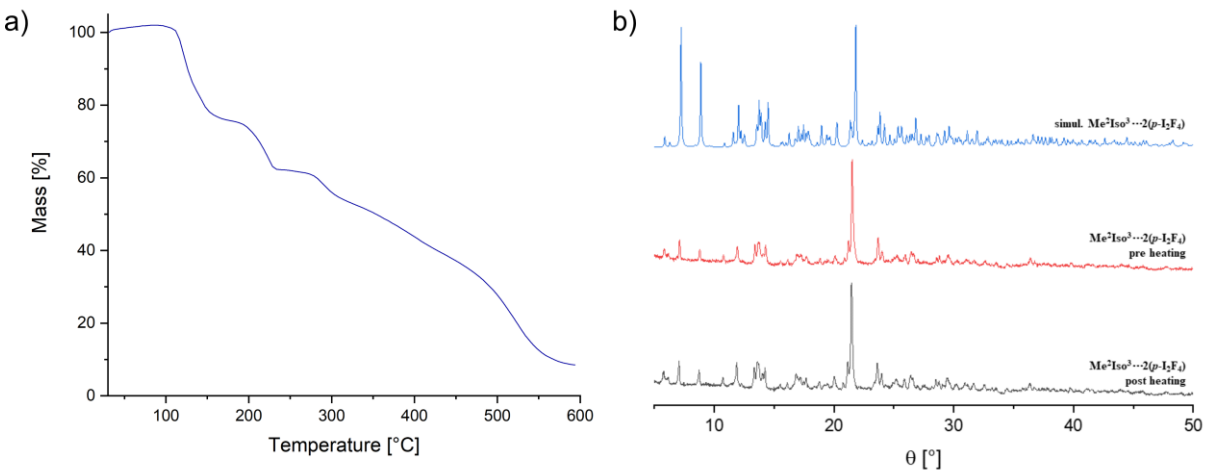

Figure 31: a) Measured TGA spectrum of **Me²Iso³···2(*p*-I₂F₄)** obtained by slow evaporation. The onset decomposition temperature obtained by tangent evaluation is 111.65 °C; b) simulated diffractogram of **Me²Iso³···2(*p*-I₂F₄)** obtained from the single-crystal X-ray diffraction data (blue) with the measured powder X-ray diffractograms of **Me²Iso³···2(*p*-I₂F₄)** obtained by slow evaporation before (red) and after (black) being kept at elevated temperature under high vacuum. The thermogravimetric analyses were performed by Tobias Heinen.

Additionally, a sample obtained by slow evaporation was kept under high vacuum at 60 °C for several hours. The highly fluorinated donors are known to be easily sublimed, but embedded in **Me²Iso³···2(*p*-I₂F₄)** the recorded powder X-ray diffractograms show no decomposition (Figure 31b).

Generation of a network based on Me²Iso³ and a tritopic donor

After generating a structure in which one donor interacts with one cage based on a monotopic donor and a box-like structure based on ditopic donors, a tritopic donor was employed in combination with the **Me²Iso³** cage. The slow evaporation of a solution of **Me²Iso³** and **I₃F₃** in chloroform yielded crystalline **Me²Iso³···4(I₃F₃)**. While the previously discussed structures formed by **Me²Iso³** were halogen-bonded structures with fewer donors than expected, leaving possible halogen bonding acceptor sites unoccupied, the halogen-bonded network formed by **Me²Iso³** and **I₃F₃** is in a one-to-four cage-to-donor ratio instead of the expected one-to-two ratio. Two of the **I₃F₃** donors interact in halogen bonds with the cage acceptor, while the other two **I₃F₃** take on a solvent-like role in the crystal structure.

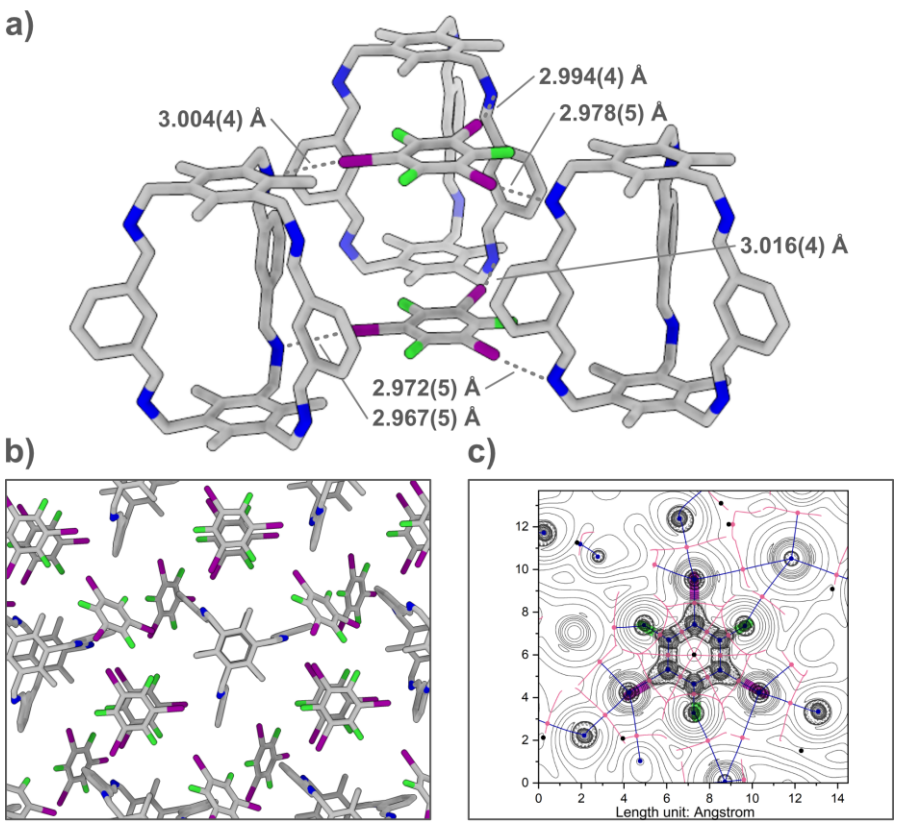

Figure 32: Single-crystal X-ray structure of **Me²Iso³···4(I_3F_3)** showing a) the lattice building motif with the six different halogen bonds depicted as grey dotted lines. **I_3F_3** that form no halogen bonds with the cage are not shown for clarity; and b) the infinite network pictured along the crystallographic *c* axis. c) The corresponding Laplacian of electron density with critical points and bond paths. Bond critical (3, -1) points are depicted in pink, nuclear critical (3, -3) points in blue, ring critical (3, +1) points in black, paths and zero-flux surfaces as blue and pink lines. Hydrogen atoms and solvent molecules are omitted for clarity. The crystal structure was measured and refined by Dr. Bernd M. Schmidt. DFT computations were performed by Dr. Oliver Weingart. This figure was adapted from reference 75 with permission.

Two donors are situated between three cages connected by six different halogen bonds with N···I distances ranging from 2.967(5) to 3.016(4) Å and N···I–C angles between 163.3(1) and 166.4(1)° (Figure 32a). Each cage is in total connected to six different **I_3F_3** donors, forming an infinite 2D lattice that can be observed along the crystallographic *c*-axis (Figure 32b). The presence of the appropriate bond critical points (3, -1) in the QTAIM analysis confirms the presence of halogen bonds between the cage and the donor (Figure 32c). The calculated N···I distances ranging between 2.90 and 2.93 Å resemble the experimental results, and the calculated interaction energies between 14.45 and 24.22 kJ mol^{-1} are, as indicated by the slightly longer halogen bonds, slightly lower than those of **Me²Iso³···2(*p*-I_2F_4)**.

While two of the four **I_3F_3** donors form the 2D-lattice through halogen bonding interactions with the cage, the other two donors engage in no halogen bonding with the cage and additionally show only minor interactions with the cage at all. These **I_3F_3** act as “solvent molecules”,

interconnecting the different lattice layers. I···I halogen bonds between lattice-building donors and solvent-like donors can be observed with I···I distances between 3.798(1) and 3.826(1) (Figure 33). Desiraju and Parthasarathy introduced the differentiation for X···X halogen interactions between type I interactions, which are symmetric and have the same I···I–C angles ($\theta_1 = \theta_2$) and type II interactions, which are bent and have different I···I–C angles ($\theta_1 \approx 90°$, $\theta_2 \approx 180°$).[86, 12h] While the first are not true halogen bonds and are only a result of close proximity in the crystal structure, the latter are halogen bonds according to the definition of the IUPAC[87] and result from an interaction of the electrophilic area of one halogen atom with the nucleophilic area of another halogen bond atom. As the I···I–C observed angles for the interactions between two **I_3F_3** lie between 159.34° and 160.90° and 102.23° and 103.09°, the presence of halogen bonds is likely. This was further confirmed by QTAIM analysis, which revealed the necessary bond critical points and gave calculated bond lengths between 3.86 Å and 4.67 Å and interaction energies between 1.13 kJ mol^{-1} and 7.39 kJ mol^{-1}. The solvent-like **I_3F_3** also interact with each other by π-stacking. The different 2D-layers are additionally interconnected by π-stacking of the lattice building donors with the cages of the neighbouring layer.

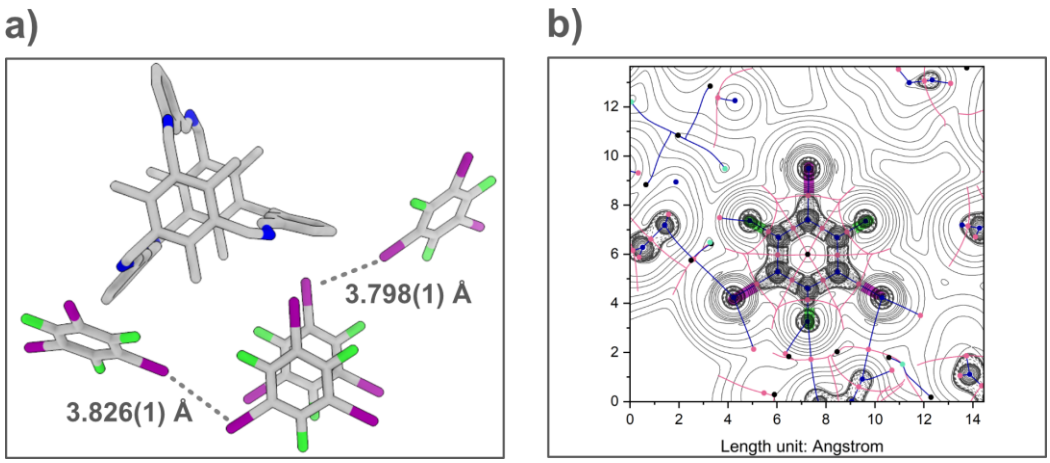

Figure 33: a) Single-crystal X-ray structure of **Me^{2}Iso^3···4(I_3F_3)** with lattice building and solvent-like **I_3F_3**, the I···I halogen bonds are shown as grey dotted lines, b) the corresponding Laplacian of electron density with critical points and bond paths. Bond critical (3, -1) points are depicted in pink, nuclear critical (3, -3) points in blue, ring critical (3, +1) points in black, paths and zero-flux surfaces as blue and pink lines. Hydrogen atoms and solvent molecules are omitted for clarity. The crystal structure was measured and refined by Dr. Bernd M. Schmidt. DFT computations were performed by Dr. Oliver Weingart. This figure was adapted from reference 75 with permission.

The formation of the network by slow evaporation was again observed by powder X-ray diffractometry and IR analysis. The latter also confirmed the successful formation of **Me^{2}Iso^3···2(*p*-I_2F_4)** by LAG (Figure 34).

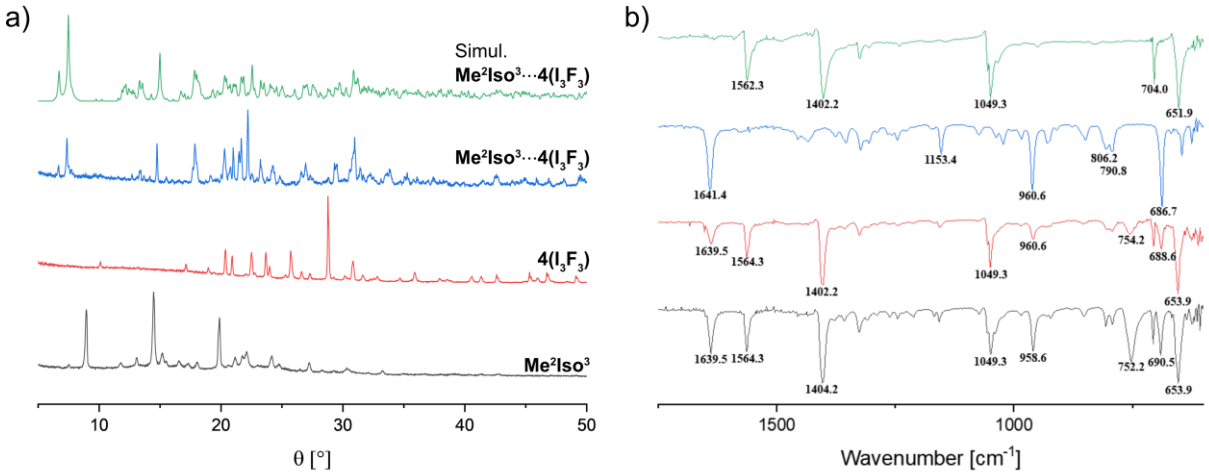

Figure 34: a) Comparison of the simulated diffractogram of **Me²Iso³···4(I_3F_3)** obtained from the single-crystal X-ray diffraction data (green) with the measured powder X-ray diffractograms of **Me²Iso³···4(I_3F_3)** (blue), **I_3F_3** (red) and **Me²Iso³** (black); b) excerpts of the IR spectra of acceptor **I_3F_3** (green), **Me²Iso³** (blue),and **Me²Iso³···4(I_3F_3)** synthesised by LAG (red) and **Me²Iso³···4(I_3F_3)** obtained by slow evaporation (black).

The measured and the predicted diffractograms of **Me²Iso³···4(I_3F_3)** are very similar, while the diffractograms recorded for the starting materials **Me²Iso³** and **I_3F_3** are distinctively different, with the most prominent reflexes visible in the diffractograms not being visible in the diffractograms of the product. The shifts in the IR spectrum are again very similar for the halogen-bonded structure obtained by grinding and slow evaporation.

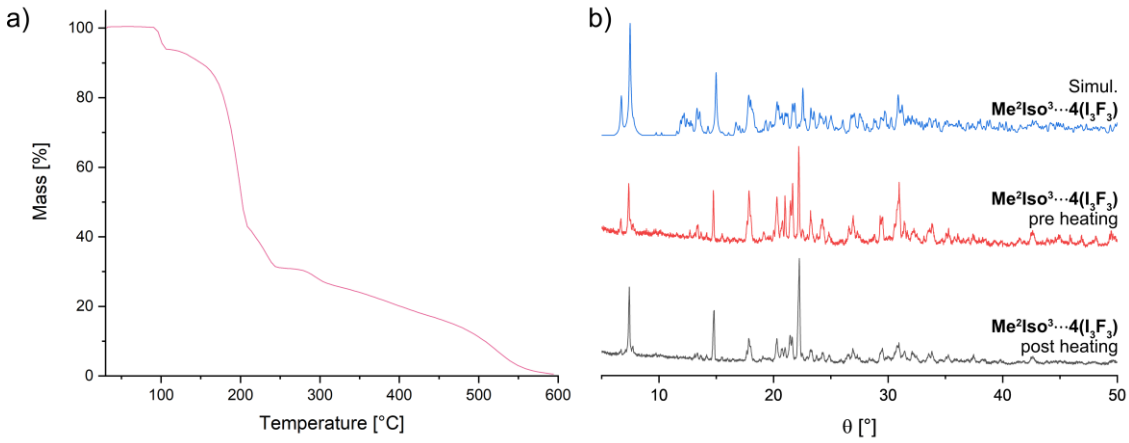

Figure 35: a) Measured TGA spectrum of **Me²Iso³···4(I_3F_3)** obtained by slow evaporation. The onset decomposition temperature obtained by tangent evaluation is 91.33 °C; b) simulated diffractogram of **Me²Iso³···4(I_3F_3)** obtained from the single-crystal X-ray diffraction data (blue) with the measured powder X-ray diffractograms of **Me²Iso³···4(I_3F_3)** obtained by slow evaporation before (red) and after (black) being kept at elevated temperature under high vacuum. The thermogravimetric analyses were performed by Tobias Heinen.

The TGA of this compound showed an onset decomposition temperature of 91.33 °C, which is significantly lower than that of **Me^{2}Iso^3···2(*p*-I$_2$F$_4$)** (Figure 35a). However, the mass loss happens in several steps, with the first one being relatively small and significantly smaller than that of the box-like structure, probably due to the loss of solvent that was remaining in the structure. Keeping the halogen-bonded network under high vacuum at an elevated temperature for several hours led to a decrease in some of the peaks in the powder X-ray diffractogram (Figure 35b). This might be due to solvent loss or the sublimation of some of the **I^{3}F^3**, probably those that are not connected to the cages by halogen bonding interactions. While partial decomposition occurs no complete destruction of the structure was observed.

Investigation into the possibility to generate more halogen-bonded networks

As initially mentioned, the generation of single-crystals suitable for X-ray crystallography was only possible in the discussed examples, while the attempts with other donors were not successful. The large difference in the solubility of the different compounds further hindered the crystallisation. While the solubility of the different donors was typically very high, the cage compounds only showed mediocre solubility. However, once the compounds were mixed, the solubility of the cage increased, and solids, either crystals, powder, or glass like solids, only formed when there was little to no solvent left. The addition of some precipitating solvents to the chloroform solutions led to the formation of single-crystals that only contained the cage compound, showing that this method is also not feasible for the generation of single-crystals or needs intensive optimisation.

To systematically investigate if the formation of halogen-bonded structures is possible with ***o*-I$_2$F$_4$** and ***m*-I$_2$F$_4$**, as well as with **I$_2$F$_4$Et** and **I$_2$F$_8$**, mixtures of the different donors and imine cage **Me^{2}Iso^3** were prepared in chloroform to slowly evaporate over a few days. While no formation of crystalline materials was observed during this experiment, IR analysis of all obtained homogenous solids was measured to determine whether the shift of any signals indicates the formation of halogen-bonded materials (Table S12).

The shifts that were observed, especially for the imine band at 1641.4 cm^{-1}, indicate that the formation of halogen-bonded networks could be possible with **I$_2$F$_4$Et** and **I$_2$F$_8$**, as the shifts are relatively small but present. Additionally, the isomers of **I$_2$F$_4$** seem to be suitable donors, as shifts in the IR-spectrum were also observed, for some bands even larger than those for **I$_2$F$_4$Et** and **I$_2$F$_8$**. To get further insight into the stoichiometry of the formed assemblies or the structure, the measurement of single crystal structures is essential.

Summary

Based on the small **Me²Iso³**, three different structures with totally different topologies could be generated, and the possibility of generating structures with four more donors was investigated. The different structures feature a combination in which a single cage and donor interact, forming columnar stacks in the single-crystal X-ray structure; a structure in which two cages form boxes with four donors, while those are connected by interactions forming a lattice-like structure; and lastly, an infinite 2D network in which each cage is connected to six different cages by the halogen bonding of six different donors surrounding the cage; the layers formed are connected by additional donors that act solvent-like (Figure 36). Surprisingly, none of the structures formed in the ratio that was initially expected regarding the number of possible acceptor and donor sites. Additional interactions such as, for example, π-stacking and packing effects govern the structure formed in the solid-state together with the halogen bonds, leading to the formation of the most stable structure. The selectivity to form the structures is very high, resulting in the formation of only one structure for each combination even if a large excess of donor or cage is used.

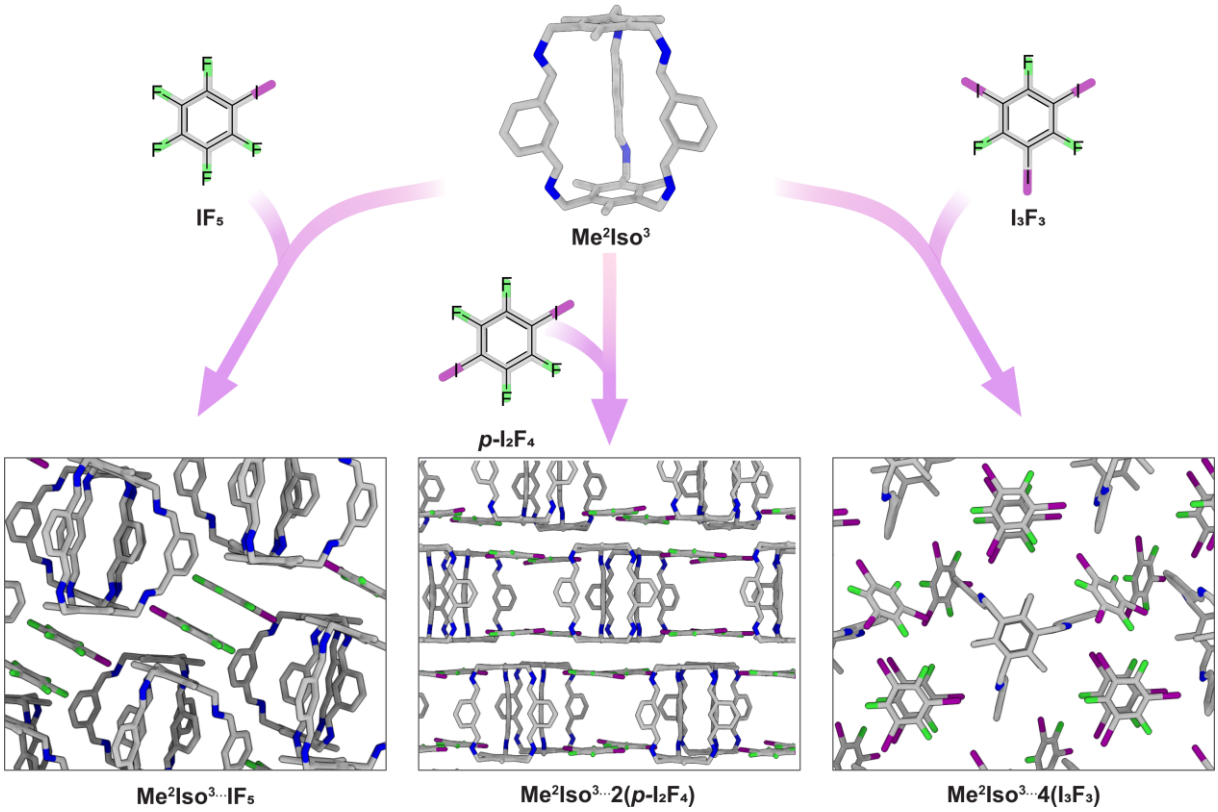

Figure 36: Overview over the halogen bond acceptor **Me²Iso³**, and the halogen bond donors **IF₅**, ***p*-I₂F₄**, and **I₃F₃**, that were employed in the synthesis of the corresponding halogen-bonded structures: **Me²Iso³···IF₅** (view along c axis, solvent molecules, hydrogens and disorder omitted for clarity), **Me²Iso³···2(*p*-I₂F₄)** (view along b axis, solvent molecules and hydrogens omitted for clarity), and **Me²Iso³···4(I₃F₃)** (view along c axis, hydrogens omitted for clarity).

DFT calculations and detailed QTAIM-analyses confirmed that the interactions that were suggested to be halogen bonds regarding their geometrical parameters were indeed halogen bonds, and the calculated interaction energies gave further insights into imines as halogen bond acceptors and the classification of imine halogen bonding as a comparably weak non-covalent interaction. The analysis of measured powder X-ray diffractograms and the IR spectra further confirmed the formation of networks, and the latter showed, that the targeted networks are even accessible by LAG, enabling a much more efficient and economical synthesis. The stability of the networks is high, especially considering the fact that the donors can be easily sublimed normally.

The different structures accessible with just one cage and three different donors as well as the finding that four additional donors are also possibly capable of forming halogen bonds with **Me^{2}Iso^3** highlight the variety of structures that are already accessible and could be accessed by imine halogen bonding in the future.

3.1.3 A halogen-bonded network based on a Tri^{4}Di^6 cage

Introduction and synthesis of a Tri^{4}Di^6 cage

After accessing a variety of different structures based on the Tri^{2}Di^3 cage **Me^{2}Iso^3**, a larger cage was targeted. Cage compounds, especially those with topologies like Tri^{4}Tri^4, Tri^{4}Di^6, or larger, often have large hollow cavities. In the solid-state, these cavities are often filled with disordered solvent molecules. This, in addition to the fact that the cages are solely organic, often leads to difficulties during single-crystal X-ray measurements with diffuse diffraction within the reciprocal space at higher resolutions.

As the generation of halogen-bonded networks introduces well-ordered, iodine-containing halogen bond donors into the crystal structure, the scattering could be significantly enhanced, facilitating the structure determination of large hollow compounds. After removing the solvent from the cavities, a variety of larger cages have been utilised to store or separate different gases.[88] Whether the intrinsic pores of a structure can be accessed and used is, among other factors, highly dependent on the solid-state packing, as this governs whether the pores are connected to each other and accessible for potential guests.[88b] The use of imine halogen bonding changes the solid-state packing as seen in the previously discussed examples and could be a tool to change the gas adsorption properties of a cage compound.[3]

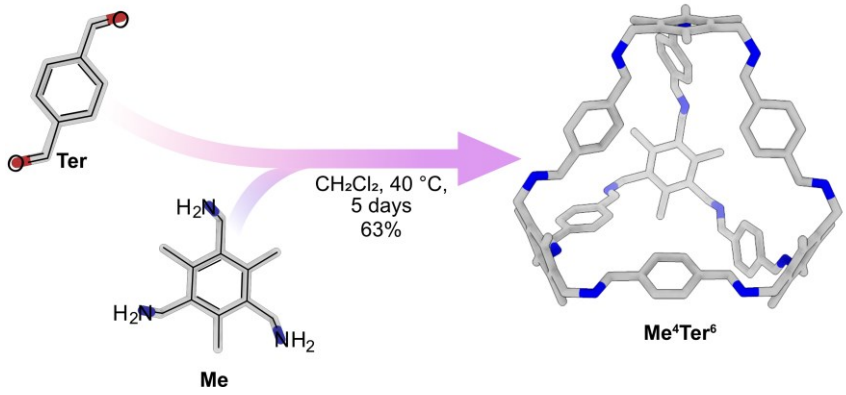

Figure 37: Synthesis of **Me^{4}Ter^6**.

To examine whether the formation of halogen-bonded networks based on larger imine cages is possible, the Tri^{4}Di^6 cage compound based on (2,4,6-trimethylbenzene-1,3,5-triyl)trimethanamine (**Me**) and terephthalaldehyde (**Ter**), which was reported by the group of Cooper, was chosen as a model and synthesised according to the published procedure (Figure 37).[80] The compound was obtained in a satisfactory yield, with the analytical data

[3] Large parts of this work have been published: E. Nieland, D. Komisarek, S. Hohloch, K. Wurst, V. Vasylyeva, O. Weingart, B. M. Schmidt, *Chem. Commun*. **2022**, *58*, 5233-5236.

confirming the formation of the targeted **Me^{4}Ter^6** imine cage. **Ter** is commercially available, and the synthesis of **Me** was described in the previous section.

Generation of a halogen-bonded structure based on Me^{4}Ter^6

Combining the imine cage **Me^{4}Ter^6** with the different donors that were introduced in the previous chapters only led to the formation of single-crystals suitable for single-crystal X-ray crystallography in combination with ***p*-I$_2$F$_4$**. Similar to the previously discussed cases, the formation of the halogen-bonded structure **Me^{4}Ter^6···2(*p*-I$_2$F$_4$)** did not occur in the expected ratio of one-to-six (cage-to-donor), as suggested by the number of imine functionalities of the cage and the use of a ditopic donor. The crystals formed from a solvent mixture of chloroform and acetonitrile contain the cage and the donor in a one-to-two ratio.

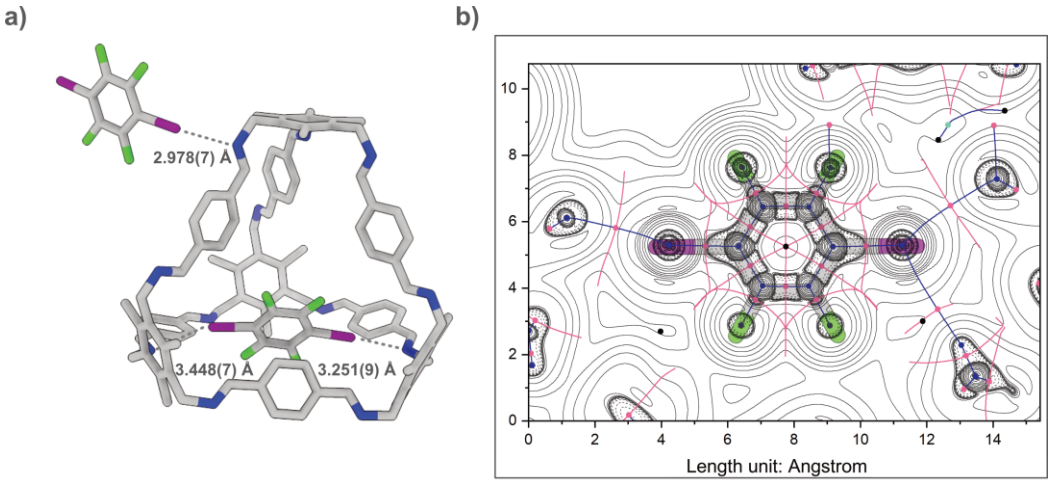

Figure 38: Single-crystal structure of **Me^{4}Ter^6···2(*p*-I$_2$F$_4$)**, a) showing the cage with the two different donors, and b) Laplacian of electron density with critical points and bond paths of the donor inside the **Me^{4}Ter^6** cage. Bond critical (3, -1) points are depicted in pink, nuclear critical (3, -3) points in blue, ring critical (3, +1) points in black, paths and zero-flux surfaces as blue and pink lines. Hydrogen atoms are omitted for clarity. The crystal structure was measured by Prof. Dr. Stephan Hohloch and refined by Prof. Dr. Klaus Wurst and Prof. Dr. Stephan Hohloch. DFT computations were performed by Dr. Oliver Weingart. This figure was adapted from reference 75 with permission.

The single-crystal structure shows that the cavity of **Me^{4}Ter^6** is occupied by one ***p*-I$_2$F$_4$** that is situated between and interacts with two imine groups. While the N···I distance of 3.251(9) Å and the corresponding N···I–C angle of 164.6(3)° suggest the presence of a halogen bond, the other contact observed with a N···I distance of 3.448(7) Å and an N···I–C angle of 142.1(3)° seems to be very weak. These findings are again supported by QTAIM analysis, which shows interaction energies between 8.37 and 13.35 kJ mol^{-1} for the first contact and between 4.85 and 8.13 kJ mol^{-1} for the second contact, confirming the presence of one halogen bond and an additional weak interaction. The large distance between the imine functionalities in the cage is

probably the reason that only one halogen bond was formed, and the N···I distance of both contacts is comparably long. Of the twelve imine groups in the cage, seven are directed outward and five are directed inward. The other ***p*-I$_2$F$_4$** is located on the outside of the cage and interacts with one of the outward-pointing imine groups. QTAIM analysis shows appropriate bond critical points (3, -1) for the interaction, confirming that a halogen bond is formed. The N···I distance of 2.978(7) Å is significantly shorter than the distance for the other N···I contacts, and the N···I–C angle of 161.2(3)° is close to 180°. The assumption that this halogen bond is stronger than the other N···I halogen bonds in this structure is confirmed, revealing an interaction energy between 14.59 and 22.78 kJ mol^{-1}. While one side of the donor is connected to the cage by imine halogen bonding, the other side engages in a halogen bond with the π-system of a neighbouring cage. The distance of the donor to the centroid of the nearest double bond of 3.281 Å and the π···I–C angle of 171.32° are in accordance with geometrical parameters for π-halogen bonds (Figure 38).[12h,87]

The formation of the system was again observed by powder X-ray diffractometry and IR analysis. As the obtained **Me^{4}Ter^6** was mostly amorphous, there were only very broad signals in the diffractograms that were visible. The comparison of the predicted and the measured diffractogram of **Me^{4}Ter^6···2(*p*-I$_2$F$_4$)** showed similarities and clear differences to the diffractogram recorded for the precursor ***p*-I$_2$F$_4$** (Figure 39a).

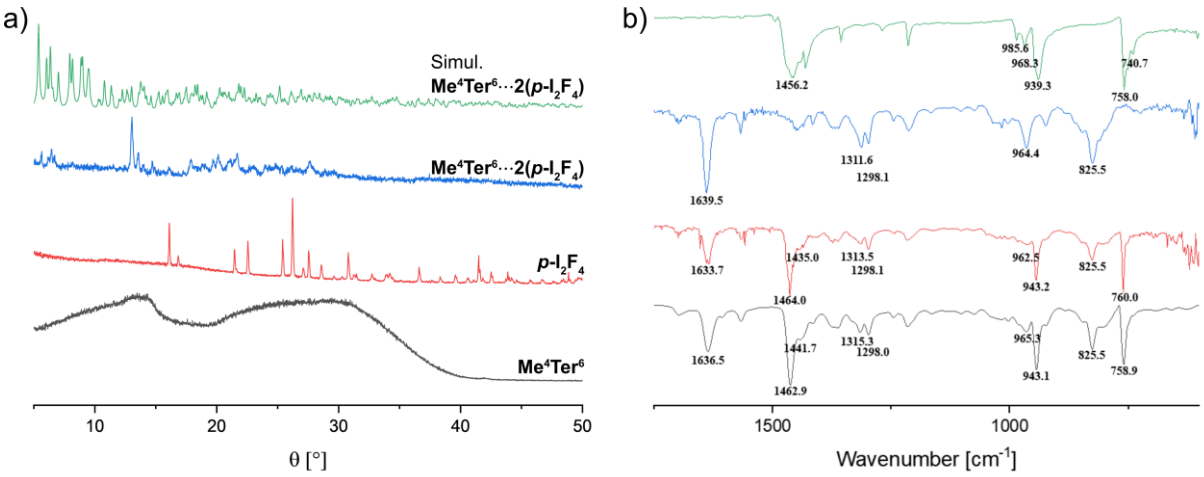

Figure 39: a) Comparison of the simulated diffractogram of **Me^{4}Ter^6···2(*p*-I$_2$F$_4$)** obtained from the single-crystal X-ray diffraction data (green) with the measured powder X-ray diffractograms of **Me^{4}Ter^6···2(*p*-I$_2$F$_4$)** (blue), ***p*-I$_2$F$_4$** (red) and **Me^{4}Ter^6** (black); b) Excerpts of the IR spectra of acceptor ***p*-I$_2$F$_4$** (green), **Me^{4}Ter^6** (blue), and **Me^{4}Ter^6···2(*p*-I$_2$F$_4$)** synthesised by liquid assisted grinding (red) and **Me^{4}Ter^6···2(*p*-I$_2$F$_4$)** obtained by slow evaporation (black).

The bands in the IR undergo significant changes upon network formation. Both of the precursor spectra show distinct changes in comparison to both spectra of **Me^{4}Ter^6···2(*p*-I$_2$F$_4$)** (Figure 39b). The bands observed for the samples obtained by slow evaporation and LAG

confirm the formation of the network by grinding. Thermogravimetric analyses of **Me^{4}Ter^6···2(*p*-I$_2$F$_4$)** obtained by both methods were performed, showing different onset decomposition temperatures for the two samples (Figure 40a). While the sample obtained by slow evaporation has a determined onset decomposition temperature of 108.67 °C, the temperature for the sample obtained by LAG is 128.28 °C.

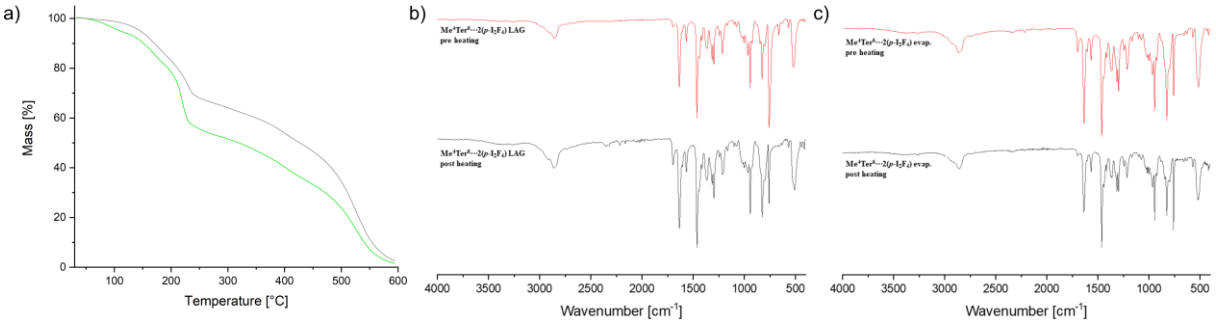

Figure 40: a) Measured TGA spectrum of **Me^{4}Ter^6···2(*p*-I$_2$F$_4$)** obtained by slow evaporation (green) and by LAG (grey). The onset decomposition temperatures obtained by tangent evaluation are 108.67 and 128.28 °C, respectively. IR spectra of samples of **Me^{4}Ter^6···2(*p*-I$_2$F$_4$)** obtained by b) slow evaporation and c) liquid assisted grinding. Before (red) and after (black) being kept at an elevated temperature under high vacuum. The thermogravimetric analyses were performed by Tobias Heinen.

The continuous slow decline at low temperatures indicates that the processes of solvent loss and decomposition overlap at some temperatures, impeding the accurate determination of the onset decomposition temperature. As the amount of residual solvent in **Me^{4}Ter^6···2(*p*-I$_2$F$_4$)** obtained by slow evaporation is significantly higher than in the sample obtained by LAG, the initial decline is larger, giving a possible explanation for the smaller onset decomposition temperature. The stability of the sample was further investigated to see whether the structure could possibly be activated for gas sorption measurements. A crystalline sample and a sample obtained by grinding were soaked in *n*-pentane for three days, with the solvent being changed twice a day. After this time, the solvent was allowed to evaporate, and the sample was kept under high vacuum at 60 °C for at least 10 hours. Before and after this procedure, IR spectra of the samples were measured to show if any decomposition had taken place (Figure 40b-c). No changes could be observed for the sample obtained by slow evaporation, and only small changes, especially the decrease of the intensity of one band, were observed for the sample generated by LAG. This is most likely due to the removal of unbound ***p*-I$_2$F$_4$**.

As pores are visible in the crystal structure of **Me^{4}Ter^6···2(*p*-I$_2$F$_4$)**, additional gas sorption measurements of both samples were performed to see whether the formation of a halogen-bonded network changed the gas sorption properties of the compound (Figure 41).

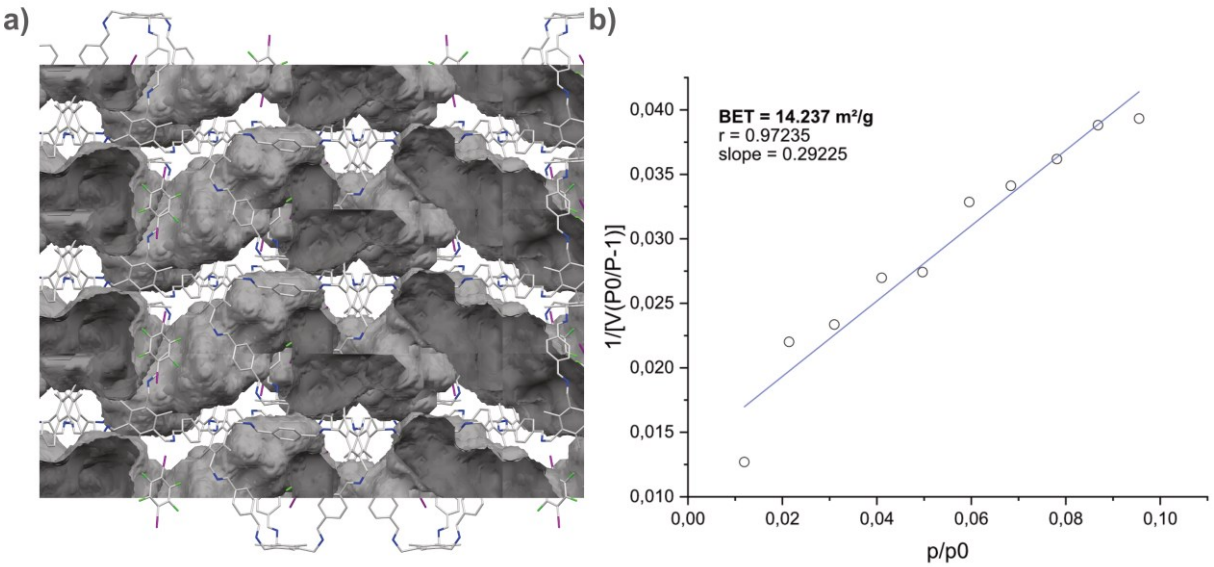

Figure 41: a) Single-crystal structure of **Me^{4}Ter^6···2(*p*-I$_2$F$_4$)** depicting the porous inside the structure after solvent removal. b) corresponding BET plot measured for the crystalline sample in the area between p/p$_0$ 0.001–0.1.

The BET surface reported for **Me^{4}Ter^6** by Cooper *et al.* is 131 m^2 g^{-1}, however, the formation of a halogen-bonded network significantly lowered the obtained value to 14 m^2 g^{-1} for the crystalline sample and 3 m^2 g^{-1} for the sample obtained by LAG. Even when factoring in the higher molecular weight of the halogen-bonded structure, the value for the single cage is significantly higher. The decrease in the pore size was anticipated as each pore is occupied by one donor molecule. While the nitrogen uptake is lower, the smaller pore might be more capable of selectively encapsulating gases like hydrogen.

Summary

While four different examples of halogen-bonded structures were obtained from the smaller **Me^{2}Iso^3** cage, the combination with **Me^{4}Ter^6** only led to the formation of single-crystals suitable for X-ray crystallography in combination with ***p*-I$_2$F$_4$**. While one donor is encapsulated in the inside of the cage, another donor connects different cages by the halogen bonding of an imine and a π-system. The size of the pores in **Me^{4}Ter^6** is significantly smaller in comparison to the sole cage, lowering the gas adsorption properties while also decreasing the space in which disordered solvent molecules could be. The generation of halogen-bonded networks from large hollow cages could therefore be a viable tool to improve and facilitate the measurement of single-crystal X-ray structures.

3.1.4 Conclusion

In this work, imine halogen bonding has been thoroughly investigated for the first time by NMR titrations and DFT calculations, showing that the interaction is of mediocre strength and therefore ideal for the reversible formation of halogen-bonded structures in the solid-state.

In combination with the small Tri^2Di^3 imine cage, three different networks with completely different topologies could be obtained. The combination of **Me^2Iso^3** with **IF_5** led to the formation of column-like stacks in the solid-state, while small boxes, building a 2D lattice by π-stacking, were generated from **Me^2Iso^3** and ***p*-I_2F_4**. The tritopic donor **I_3F_3** could be used to generate infinite networks connecting each imine cage to six different cages. While the variety of the structures obtained was large, IR analysis of powders obtained by combining **Me^2Iso^3** with different donors indicated that the formation of even more structures was possible.

A larger cage, **Me^4Ter^6**, was utilised as a building block and formed a halogen-bonded network in combination with ***p*-I_2F_4**, showing that the formation of larger structures is possible and that imine halogen bonding could be used in the future to alter the crystallisation behaviour of compounds with large, hollow pores.

Apart from single-crystal X-ray structures, the formation of the networks was also confirmed by PXRD diffractometry and IR spectroscopy. The latter was also used to evaluate the homogenous powders that were obtained by LAG, confirming that the halogen-bonded structures could also be obtained in a more time-efficient synthesis using nearly no solvent.

Investigations into the stability of the networks revealed that, even though the donors can normally be easily sublimed, the obtained halogen-bonded structures are surprisingly stable. As the halogen bond donors occupied the cavity, the BET surface obtained for **Me^4Ter^6** decreased upon network formation, but the smaller pores could lead to a higher selectivity for smaller guest molecules.

As no significant changes in the solid-state properties of the halogen-bonded architectures were observed, imine halogen bonding presents itself as a viable tool in obtaining single-crystal X-ray structures of porous organic cages, as the introduction of heavy atoms significantly facilitates the measurement.

3.2 Photoresponsive Dissipative Imine Systems

3.2.1 Synthesis and characterisation of a photoresponsive building block

Introduction

As the investigations into a suitable solid-state application for halogen bonds were concluded, the focus fell again on the generation of dissipative systems based on stronger interactions. There are several characteristics that must be present in a building block before it can be utilised to create photoresponsive dissipative systems. Ideally, the compound should be bidirectionally switchable with light of different wavelengths and with high yields to prevent the formation of product mixtures upon irradiation. The half-life of the less stable isomer should be long on a laboratory time scale to facilitate analysis and handling, while the building block also needs to be functionalised with groups that allow the reversible formation of bonds. Azobenzenes, as initially mentioned, undergo a distinct geometry change upon irradiation, and their photochemical properties can be tuned by generating bridged[42] or heteroarene[41] derivatives or introducing, among others,[38] methoxy,[38c] or fluorine[39] substituents in *ortho*-positon (Figure 42). 4,4'-(Diazene-1,2-diyl)bis(3,5-difluorobenzaldehyde) (**A**), which was recently published by the group of Pianowski,[72] has beneficial photochemical properties and can be, in combination with different amine building blocks, used in the reversible formation of imines.

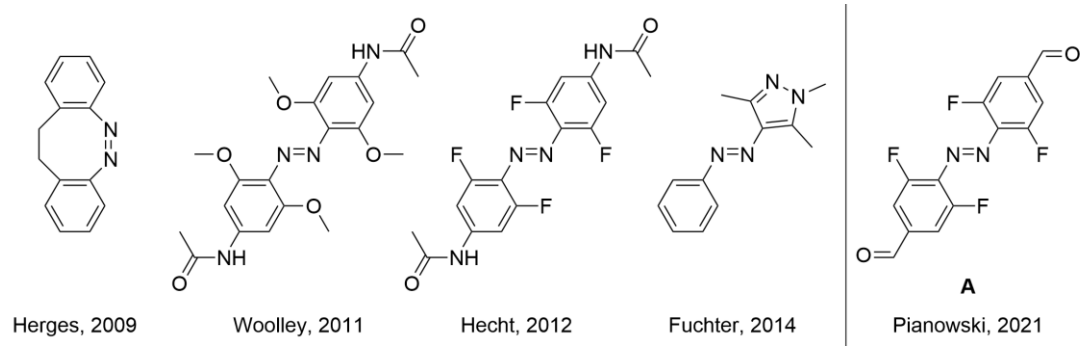

Figure 42: Bridged and heteroarene azobenzene derivatives by the groups of Herges and Fuchter, and *ortho*-substituted azobenzenes by the groups of Woolley, Hecht, and Pianowski.

The fact that the initial photoswitchable building block changes during its incorporation into a supramolecular structure is a common issue in the design of photoresponsive systems. The substituents changing during a reaction or the generation of a strained or geometrically hindered system can change the photochemical properties or even prevent photoswitching.

The group of Beves recently showed that coordination of a quinoline functionalised azobenzene to Pd^{2+} improves the photoswitching and increases the thermal half-life.[67a] The photochemical properties of an azobenzene that, when embedded in an amine cage improved in comparison to the free analogue.[89] The Nabeshima group demonstrated that the formation of a macrocyclic structure can, in some cases, prevent photoisomerization.[90] While the precursor and the acyclic compound in their study can be photoisomerised, the formed macrocycles show no photoisomerisation upon irradiation. To conclude, a building block's photochemical characteristics should not only be beneficial, but they also should not fundamentally change during a reaction. **A** as well as an imine model compound (**AC²**) were synthesised, and their photoswitching behaviour was thoroughly investigated.[4]

Synthesis of azobenzene A and model compound AC²

Azobenzene **A** was synthesised according to a modified procedure[72] (Figure 43). The bromination of 2,6-difluoroaniline using *N*-bromosuccinimide (NBS) yielded aniline **32** in high yields, and the following Rosenmund-von Braun reaction with copper(I) cyanide gave nitrile **33** in good yields in comparison to literature procedures.[39] The hydrolysis of **33** yielded the acid **34**, which was precipitated as its hydrochloric salt.

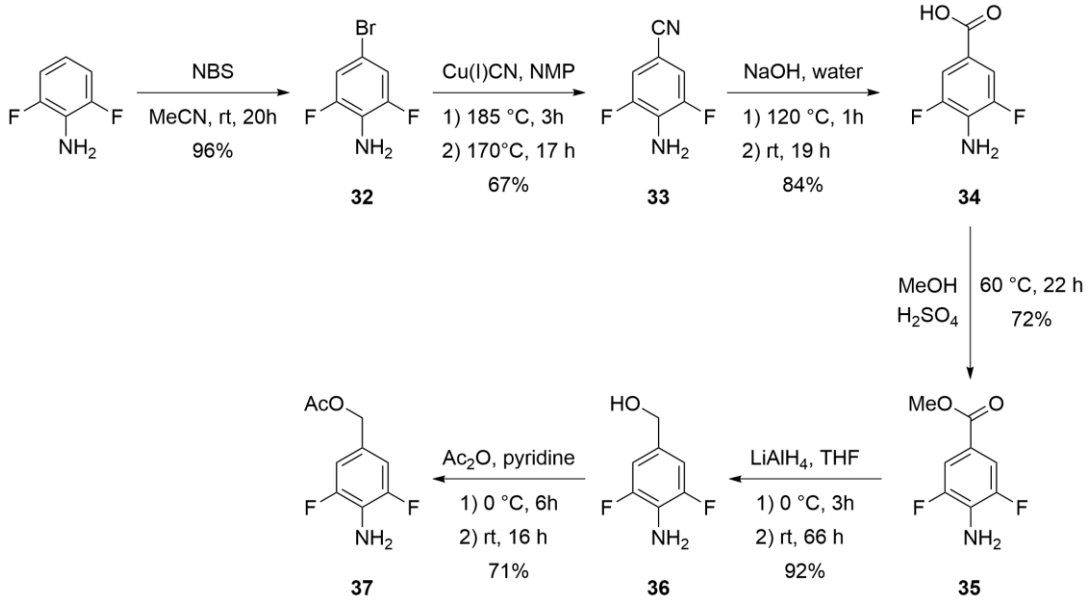

Figure 43: Synthesis of 4-amino-3,5-difluorobenzyl acetate (**37**) starting from 2,6-difluoroaniline.

Ester **35** was synthesised, which was then reduced to alcohol **36** using lithium aluminium hydride following a modified literature procedure.[91] Even though the mixture gelled during the reaction and needed to be stirred manually, the compound was obtained in high yields. The

[4] Large parts of this work have been published: E. Nieland, J. Voss, A. Mix, B. M. Schmidt, *Angew. Chem. Int. Ed.* **2022**, *61*, e202212745.

acetylation of **37** following the procedure published by Leistner *et al.*[72] involves a short reaction time of 2 hours at 0 °C to prevent the formation of the N-acetylated side product, resulting in incomplete conversion. To minimise the amount of undesired side product and increase the yield, the original procedure was modified. A solution of acetic anhydride in pyridine was added to a solution of alcohol **36** at 0 °C over the course of 90 minutes. The mixture was stirred at 0 °C for 6 hours, and as the TLC indicated incomplete conversion, it was kept at room temperature for an additional 16 hours. Following this procedure, the yield of acetate **37** was slightly increased to 71%.

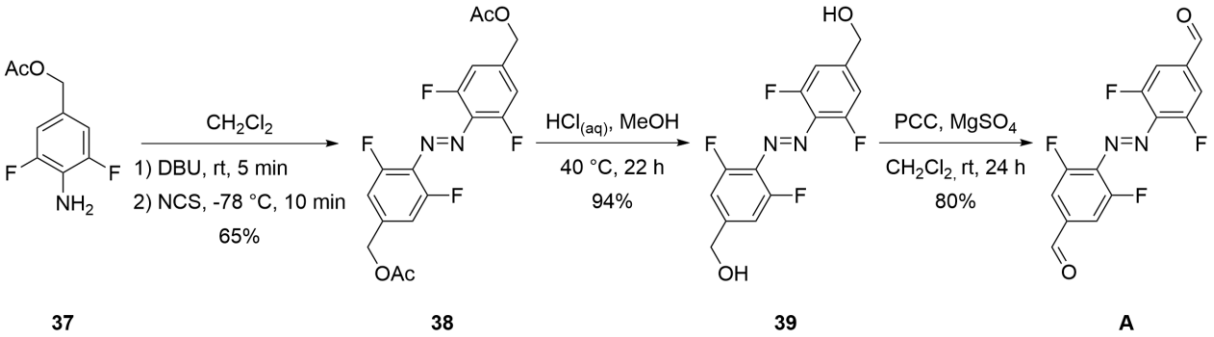

Figure 44: Synthesis of *E*-4,4'-(diazene-1,2-diyl)bis(3,5-difluorobenzaldehyde) (*E*-**A**) starting from acetate **37**.

The following azobenzene coupling utilising 1,8-diazabicyclo[5.4.0]undec-7-ene (DBU) and *N*-chlorosuccinimide (NCS) is a method that was first published by John and Lin[79] and later used by Leistner *et al.*[72] As the acetate groups of azobenzene **38** can be cleaved by acids, leading to the formation of a product mixture and an overall lower yield, the initial work-up was alternated accordingly, and instead of washing with diluted hydrochloric acid, the mixture was repeatedly washed with water and brine. The purified product contained significant amounts of succinimide, which was removed in the following step. Alcohol **39** was obtained in high yields by stirring **38** in a mixture of concentrated hydrochloric acid and methanol at 40 °C. The following oxidation with pyridinium chlorochromate (PCC) in the presence of magnesium sulfate led to the formation of aldehyde **A** in significantly higher yields than those of the published oxidation with activated manganese dioxide (Figure 44).[72]

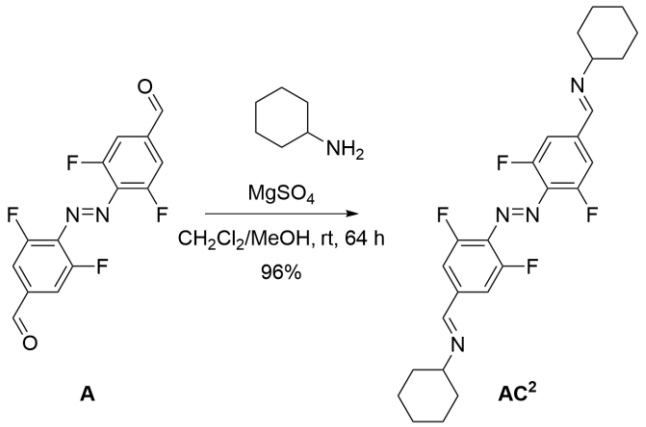

Figure 45: Synthesis of **AC²** starting from **A**.

The model compound **AC²** could then be obtained by stirring cyclohexylamine (**C**) and azobenzene **A** in a mixture of methanol and dichloromethane. As the formation is in equilibrium, an excess of **C** was used, and magnesium sulfate was added as a desiccant to favour the formation of imine **AC²**, giving the product in nearly quantitative yields (Figure 45).

Evaluation of A as a photoswitch and building block

After both photoswitchable compounds **A** and **AC²** were successfully synthesised, their photochemistry as well as the reactivity of **A** towards imine formation were investigated to evaluate the suitability of **A** as a building block in the formation of supramolecular systems. Solutions of the photoswitch in dichloromethane were irradiated with light of different wavelengths, and UV/VIS spectra were recorded to monitor the isomerisation of the compound. The *ortho*-fluorination of azobenzenes leads to a distinct separation of the n→π* bands of the *E*- and *Z*-isomer, enabling the isomerisation with visible light.[39] The extended π-system of **A** leads to a bathochromic shift of the n→π* band of *E*-**A** facilitating the switching of the azobenzene with red light.[72, 28a] While the *E*- to *Z*-isomerisation of **A** with red light (660 nm) occurs in high yields, the low absorbance at higher wavelengths leads to longer irradiation times (Figure 46). In contrast, the photostationary state of the irradiation with green light (565 nm) is reached more rapidly, as the absorbance in this wavelength area is higher. This is accompanied by a lower ratio of *Z*-**A**, as observable by comparison of the UV/VIS spectra, because the overlap of the n→π* bands of *E*-**A** and *Z*-**A** is larger. The *Z* to *E* isomerisation of **A** can be achieved by irradiation with light with the wavelengths of 405 nm and 470 nm. Due to the higher absorbance of the n→π* band *Z*-**A** in this wavelength area alongside the smaller overlap with the band for *E*-**A**, the isomerisation using light of a wavelength of 405 nm occurs faster, and with higher yields than with light of a wavelength of 470 nm. The *Z* to *E* isomerisation occurs significantly faster because of the higher thermal stability of the *E*-isomer and the low kinetic barrier.[92] The slightly shifted curve for the irradiation with 470 nm, which

does not cross the isosbestic points, can be attributed to the solvent loss occurred during the experiment leading to a slightly higher concentration in comparison to the other samples.

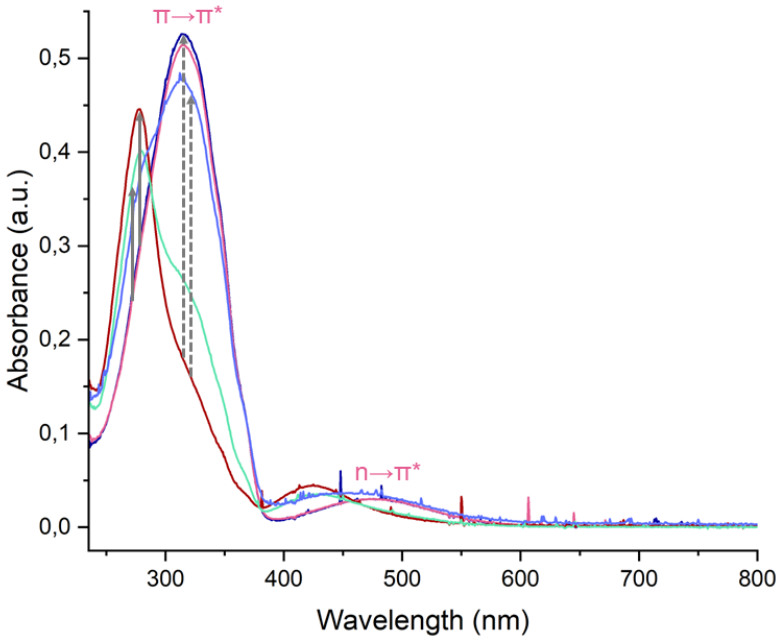

Figure 46: UV/VIS spectrum of **A** after irradiation with light of different wavelengths. The initial spectrum of *E*-**A** is depicted in pink, a solution of *E*-**A** was irradiated with green light (565 nm) for 80 minutes (turquoise curve) or with red light (660 nm) for 300 minutes (dark red curve). A *Z*-enriched solution of **A** was irradiated with blue light (470 nm) for 2 minutes (light blue curve) or with light of a wavelength of 405 nm for 1 minute (dark blue curve). The solid grey arrows indicate *E* to *Z* isomerisation while the dashed arrows indicate *Z* to *E* isomerisation.

To confirm that the photochemical properties of **A** undergo no major changes upon imine formation the photochemistry of **AC²** was also investigated. The isomerisation of **AC²** follows the same trends. Irradiation with red light (660 nm) leads to higher ratios of the *Z*-isomer while taking significantly longer than irradiation with green light (565 nm) (Figure 47). As irradiation with blue light (470 nm) led to incomplete isomerisation and took longer for compound **A**, following *Z* to *E* isomerisation experiments were mostly only performed with light having a wavelength of 405 nm. The irradiation of a *Z*-enriched solution of **AC²** with light of a wavelength of 405 nm led, as expected, to rapid isomerisation.

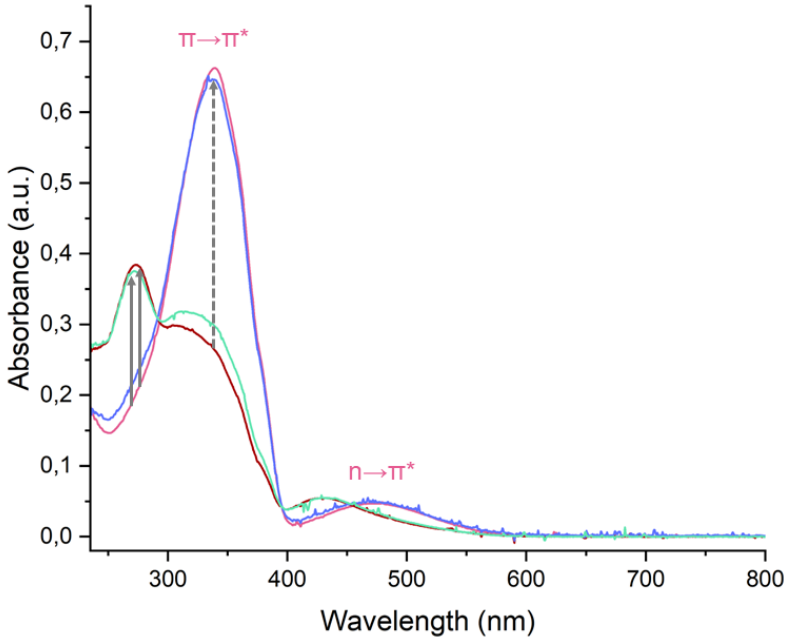

Figure 47: UV/VIS spectrum of **AC²** after irradiation with light of different wavelengths. The initial spectrum of *E*-**AC²** is depicted in pink, a solution of *E*-**AC²** was irradiated with green light (565 nm) for 15 minutes (turquoise curve), or with red light (660 nm) for 1000 minutes (dark red curve). A *Z*-enriched solution of **AC²** was irradiated with light of a wavelength of 405 nm for 1 minute (light blue curve). The solid grey arrows indicate *E* to *Z* isomerisation while the dashed arrows indicate *Z* to *E* isomerisation.

The comparison of the UV/VIS spectra for the isomerisation of **A** and **AC²** with red light (660 nm) reveals differences in the absorbance curves for both compounds (Figure 48). The π→π* band of *E*-**AC²** undergoes a bathochromic and hypochromic shift, a shift to higher wavelength and a lowered absorbance, in comparison to *E*-**A**. The irradiation time of the sample of *E*-**AC²** was one hour longer than that of *E*-**A** while the ratio of *Z* for the latter seems to be significantly higher. This is due to the differing concentrations of the samples used as well as possible experimental inaccuracies regarding the distance and position of the employed LED lamp in relation to the sample. The position of the π→π* band for *Z*-**AC²** seems to undergo no major positional changes, but a hypochromic shift is also visible for this band. The n→π* bands for the *E*- and *Z*-isomer, in contrast do not shift upon imine formation and the intensity declines only slightly.

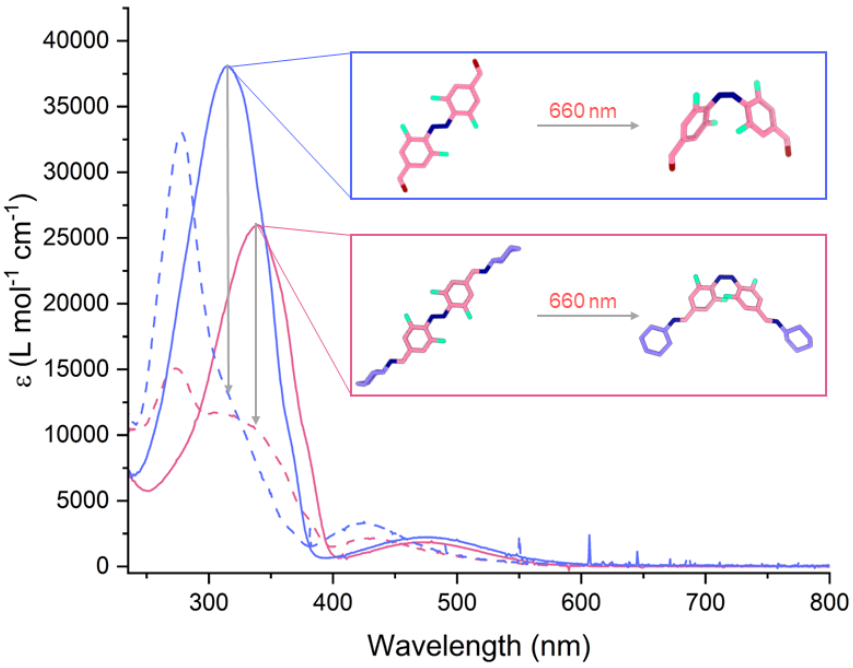

Figure 48: UV/VIS/spectra of the isomerisation of **A** and **AC²** after irradiation with red light (660 nm). The curves for compound *E*-**A** (solid line) and **A** after irradiation for 5 hours (dashed line) are depicted in blue, while the pink curves are for *E*-**AC²** (solid line) and **AC²** after 6 hours of irradiation (dashed line). The molar attenuation coefficient is plotted against the wavelength to allow a better comparison between **A** and **AC²**.

As initially mentioned, a building block needs to be bidirectionally switchable with high ratios of the desired isomer in the photostationary state (PSS). Whether the isomerisation of the photoswitch leads to high yields of *E*- or *Z*-azobenzene, respectively, depends on the absorbance of the compound and the irradiation wavelengths. While most azobenzenes can be isomerised from *E* to *Z* with UV light, yielding high ratios of the *Z*-isomer in the PSS_Z, the reverse isomerisation often occurs with low yields in the PSS_E due to an overlap of the n→π* bands. Substitutions like *ortho*-fluorination can lead to a clear separation of the n→π* bands and therefore to the possibility to bidirectionally isomerise the compounds with visible light. The UV/VIS spectra and the irradiation experiments performed with **A** and **AC²** showed that the compounds are indeed switchable with visible light and gave an indication that the yields in the PSS_Z after irradiation with red light (660 nm) and in the PSS_E after irradiation with light with a wavelength of 405 nm are high. To further establish and quantify this, solutions of both photoswitches in CD_2Cl_2 were irradiated with light of different wavelengths, and the amount of *Z*- and *E*-isomer was determined afterwards by ^1H and $^{19}F\{^1H\}$ NMR. The *E* to *Z* isomerisation of **A** after irradiation with red light (660 nm) is exemplified in Figure 49.

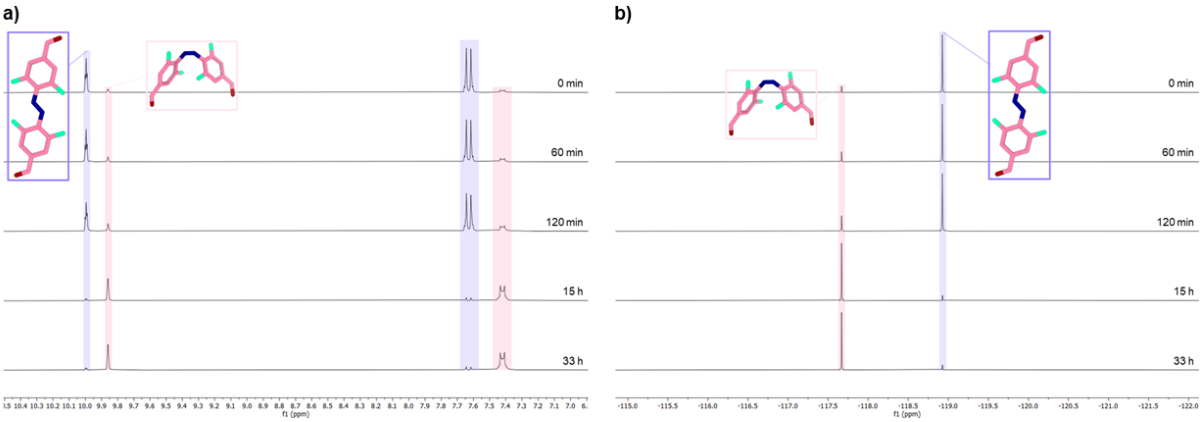

Figure 49: The *E*- to *Z* isomerisation of **A** after irradiation with light of a wavelength of 660 nm. The signals of the *E*- and the *Z*-isomer are highlighted in blue and respectively: a) ^{1}H NMR (CD_2Cl_2, 300 MHz); b) $^{19}F\{^{1}H\}$ NMR (CD_2Cl_2, 282 MHz).

Both compounds, **A** and **AC²**, could be isomerised from *E* to *Z* with either green (565 nm) or red (660 nm) light, and *vice versa* with light having a wavelengths of 405 nm. The *E* to *Z* ratios for the photostationary state were determined using the imine signal and the aromatic signal in the ^{1}H NMR and the fluorine signal in the ^{19}F NMR and the average for each wavelength is shown in table 1 (all values are listed in the tables S19 and S20).

Table 1: Average *E* to *Z* ratios after irradiation with 660 nm, 565 nm, or 405 nm for the compounds **A** and **AC²**.

Irradiation Wavelength	**A** (*E*:*Z* ratio)	**AC²** (*E*:*Z* ratio)
660 nm (*E*→*Z*)	10:90	14:86
565 nm (*E*→*Z*)	29:71	25:75
405 nm (*Z*→*E*)	96:4	90:10

Upon imine formation, the switchability undergoes minor changes. While the ratio of the *Z*-isomer after irradiation with green light (565 nm) is slightly higher for **AC²** than for **A**, the *Z*- and *E*-ratios after irradiation with red light (660 nm) or light of a wavelength of 405 nm, respectively, are higher for **A**. To conclude, as the values in each case are fairly similar and both compounds can be switched rather selectively to *E* and *Z*, the aldehyde **A** as well as the corresponding imine **AC²** seem to be suitable building blocks in the generation of photoresponsive and dissipative systems.

To determine whether the reactivity of **A** changes upon photoisomerisation, the reactions of the different isomers of **A** with **C** were observed by ^{1}H and $^{19}F\{^{1}H\}$ NMR over time. The formation of **AC²** is, as initially mentioned, an equilibrium. At first, the monosubstituted species **AC** is formed, which reacts with **C** to form the model compound **AC²** (Figure 50).

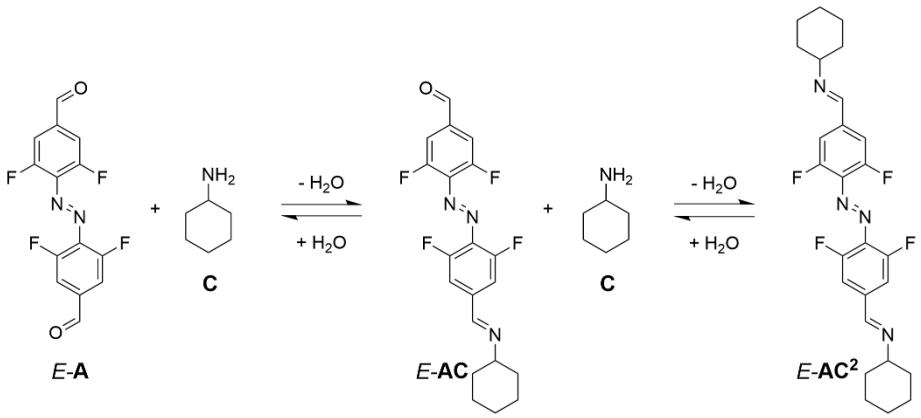

Figure 50: Reaction of *E*-**A** and **C** forming the monosubstituted *E*-**AC** and the bis-imine **AC²**.

While the signals of the different species overlap in the ^{1}H NMR spectra (Figures S63 and S66), rendering analysis difficult, the reaction can be easily followed by ^{19}F{^{1}H} NMR. While the signal for *E*-**A** steadily decreases over time, the intensity of the signal for *E*-**AC** initially rises and later on declines with the concomitant formation of *E*-**AC²** (Figure 51a). The shapes of the resulting kinetic curves for the formation of **AC²** are in agreement with a second-order kinetic model, as already observed for similar imine formations (Figure 51b).[93]

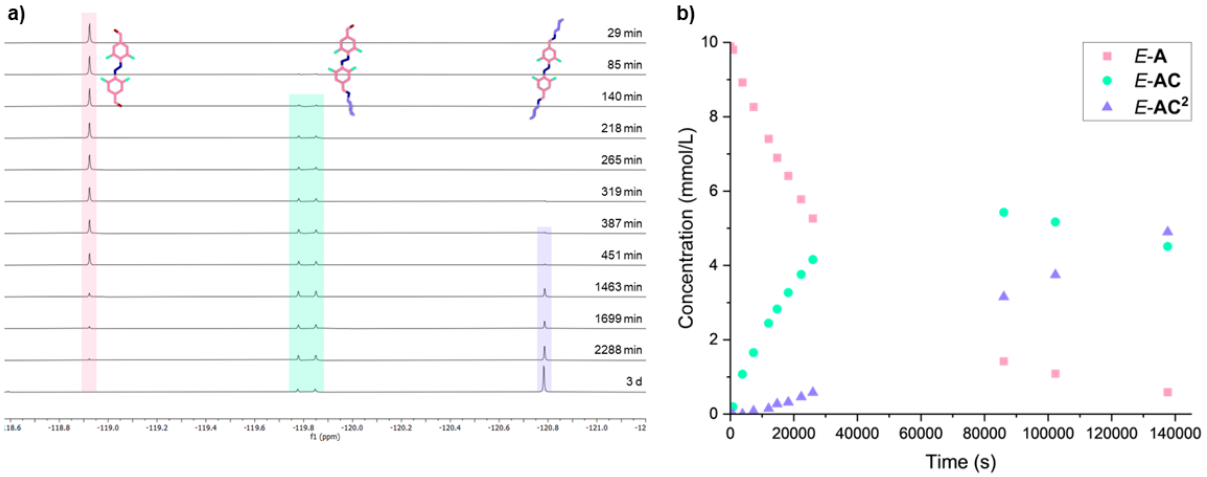

Figure 51: a) ^{19}F{^{1}H} NMR of the reaction of **C** and *E*-**A** (pink) forming the mono-imine *E*-**AC** (turquoise) and the bis-imine *E*-**AC²** (blue) (CD_2Cl_2, 282 MHz); b) observed concentrations of *E*-**A** (pink), *E*-**AC** and *E*-**AC²** (blue) as determined from the ^{19}F{^{1}H} NMR spectra.

Starting from *Z*-**A**, the imine formation with **C** was again observed by ^{1}H and ^{19}F{^{1}H} NMR. A solution of the azobenzene was irradiated with red light (660 nm) until the PSS was reached, generating a *Z*-enriched solution of **A**, to which amine **C** was added. The solution was not continuously irradiated during the reaction but kept in the dark during the acquisition of the data points. As a result, not only *Z*-**AC** and *Z*-**AC²** were formed but, over time, also the corresponding *E*-isomers (Figure 52). As the initial amount of *E*-**A** after irradiation is very small

(around 10%), the side reaction of the remaining *E*-**A** forming *E*-**AC** and *E*-**AC²** will not be considered for the following analysis.

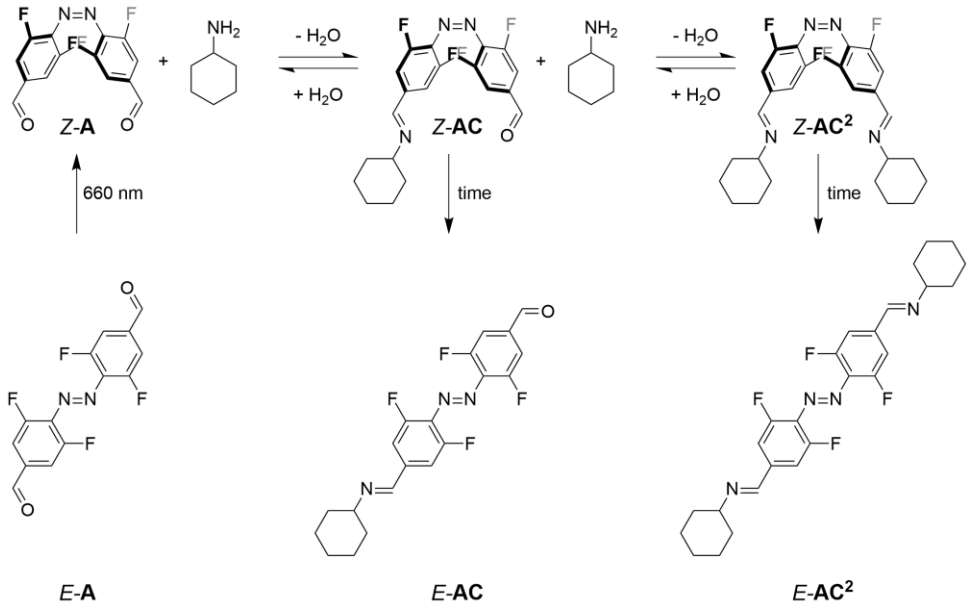

Figure 52: Initial irradiation of *E*-**A** with red light (660 nm) leads to the formation of *Z*-**A**, followed by the reaction of *Z*-**A** with **C** forming the imines *Z*-**AC** and *E*-**AC²**. As the mixture is not continuously irradiated during the reaction the corresponding *E*-imines are also formed over time.

The formation of the different compounds can again be clearly observed in the $^{19}F\{^{1}H\}$ NMR, in which only the signal of *Z*-**AC²** and one of the signals for *E*-**AC** overlap (Figure 53a), while the signals of the six different compounds present in the reaction mixtures show several overlaps of different signals in the ^{1}H NMR (Figures S70 and S73).

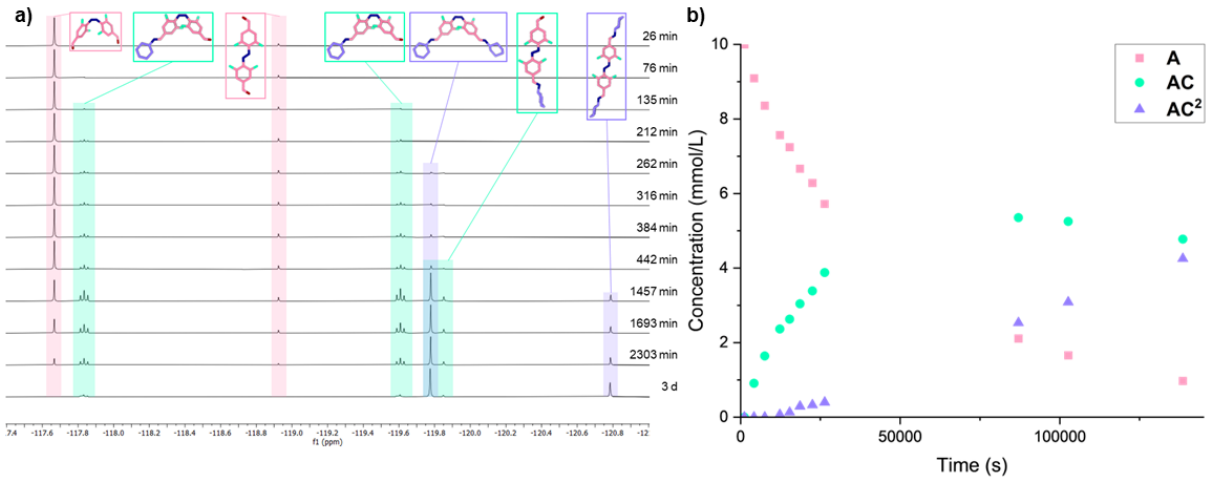

Figure 53: a) $^{19}F\{^{1}H\}$ NMR of the reaction of **C** and *Z*-**A** (pink) forming the mono-imine *Z*-**AC** (turquoise) and the bis-imine *Z*-**AC²** (blue) (CD_2Cl_2, 282 MHz). Because the mixture is not continuously irradiated, the corresponding *E*-isomers are also formed and highlighted in the respective colour; b) observed concentrations of **A** (pink square), **AC** (turquoise circle) and **AC²** (blue triangle) as determined from the $^{19}F\{^{1}H\}$ NMR spectra.

As the thermal relaxation of the *Z*-isomers leads to the formation of the corresponding *E*-compounds during the observation time, the concentrations depicted are the sum of the amounts of the *E*- and *Z*-isomers of each compound. The shapes of the resulting curves are again in accordance with a second-order kinetic model (Figure 53b).[93] Keeping the sample in the dark between the acquisition of the different data points leads to possible side reactions as the *E*-compounds that are formed over time could also undergo reversible reactions. Yet, the comparison of the development of the concentration over the observation time shows only minor differences, showing that the reactivity of **A** to imine formation undergoes no major changes upon isomerisation.

Summary

The photochemical properties of **A** in dichloromethane have been thoroughly investigated, showing that **A** is bidirectionally switchable with light of different wavelengths. High *Z* or *E* ratios in the photostationary state were observed after irradiation with red (660 nm) or UV light (405 nm), respectively. The synthesis and the photochemical analysis of the model compound **AC²** revealed that the photochemical properties undergo no major change upon imine formation, showing that the compound is still switchable with red light, and the ratios in the photostationary state are similar to those observed for **A**. The half-life of the compound was not investigated as initial experiments indicated the partial decomposition of **AC²** at elevated temperatures, however the high comparatively high stability of the parent compound **A**, which was investigated by Leistner et al.,[72] and the observation made in the NMR and UV/VIS measurements indicate that the stability of might be high on a laboratory time scale. The

formation of **AC²** starting from both azobenzene isomers was investigated, showing a very similar that the reactivity of the different isomers *E*- and *Z*-**A**. The bidirectional switchability of **A** in high yields accompanied by a high degree of stability for the *Z*-isomer on a laboratory time scale alongside the observation that these properties undergo no major changes upon imine formation render **A** to be an ideal building block to generate photoswitchable and dissipative imine systems.

3.2.2 Macrocycles based on stiff diamines

Introduction

The topologies, shapes and corresponding properties of supramolecular cages and macrocycles is highly dependent on the building blocks employed.[24] The enantiomers of 1,2-diaminocyclohexane (**D**) are two of the several diamine building blocks that have been successfully utilised to construct imine macrocycles[94,95] and cages[24] because of their advantageous structural features such as their rigidity and their quasi-valence angle of 60°, which equals the internal angle of an equilateral triangle.[94] When combining **D** with different dialdehydes the angle formed between the aldehyde groups defines the structure of the formed macrocycle with the utilisation of linear dialdehydes leading to the formation of trianglimines (Figure 54).[94]

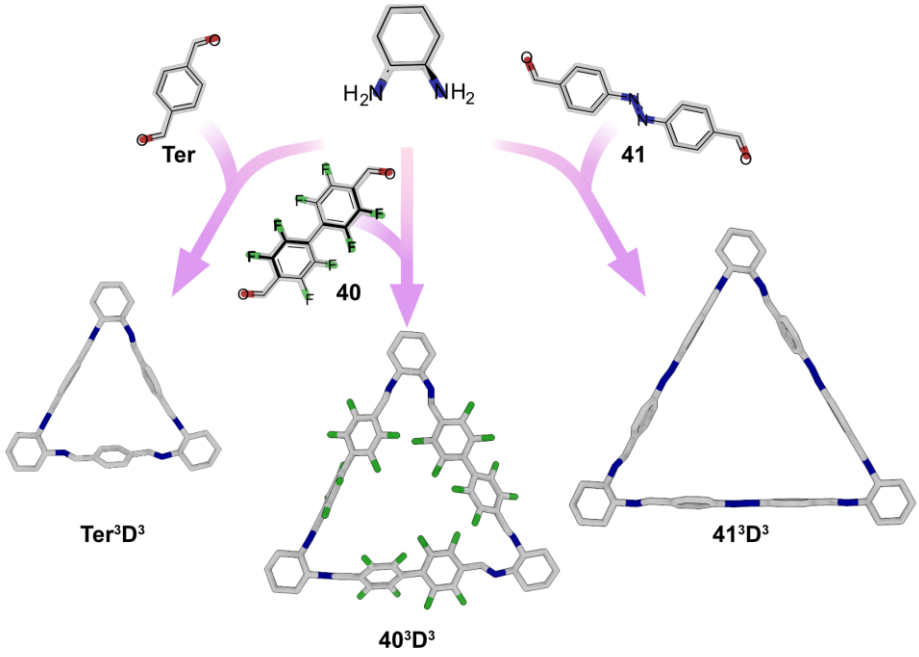

Figure 54: Examples of different trianglimines based on **D** that have previously been studied by the groups of Gawroński and Cooper (left), our group (middle) and Tanaka (right).

A macrocycle based on terephthalaldehyde (**Ter**) and **D** has been reported by the group of Gawroński in 2001[96d] has been recently utilised by Cooper *et al.* to separate ethyl acetate from an azeotropic mixture.[96b] Our group has used a fluorinated macrocycle (**40^{3}D^3**) to build supramolecular organic frameworks capable of taking up gas molecules.[96a] Tanaka *et al.* generated an azobenzene-based trianglimine (**41^{3}D^3**) which was utilised to generate a gel in combination with benzene.[96c] As the structure of the linear azobenzene is nearly identical to that of **A**, it is expected that *E*- **A** and **D** should also form Di^{3}Di^3-type macrocycles. The excellent photochemical properties of **A** also allow the use of *Z*-**A** as a building block, which, due to the

distinct geometrical difference, should lead to the formation of macrocycles with different structures or stoichiometries. Due to the reversibility of the imine formation, the light-controlled interconversion of the products should be possible, generating a photoswitchable dissipative systems.[5]

In the following chapters **D**, exclusively refers to *R,R*-1,2-diaminocyclohexane, as this is the enantiomer that was employed for the macrocycle formation and isomerisation experiments. If *S,S-1,2*-diaminocyclohexane is utilised, it will be explicitly mentioned. While the synthesis of the trianglimine using *S,S-1,2*-diaminocyclohexane is possible, this enantiomer of the building block itself is significantly more expensive than the *R,R*-enantiomer.

Synthesis and characterisation of an azobenzene trianglimine

To find suitable reaction conditions for the formation of *E,E,E*-$\mathbf{A^3D^3}$, the solvent, concentrations, and work-up method were evaluated. In supramolecular imine chemistry, one can differentiate between two major reaction set-ups regarding the solvent. If the reaction is kinetically controlled, a solvent is chosen in which the precursors are soluble but the supramolecular cage or macrocycle precipitates during the reaction. Typical solvents in this cage are often polar solvents like methanol or acetonitrile. In a thermodynamically controlled reaction, both the precursors and the products are soluble in the solvent chosen. As it would be beneficial for further transformations if the macrocycle would stay in solution after being formed; the initial focus fell on dichloromethane as a solvent. The selective formation of $\mathbf{A^3D^3}$ was observed by MALDI-mass spectrometry in dichloromethane at concentrations of 5 and 10 mM, as well as in a mixture of dichloromethane and acetonitrile (5 mM). Attempts to isolate the formed macrocycle by adding cyclohexane or toluene to the reaction mixture and removing the more volatile solvent at low temperatures failed and produced mainly a mixture of oligomers and starting material **A**.

[5] Large parts of this work have been published: E. Nieland, J. Voss, A. Mix, B. M. Schmidt, *Angew. Chem. Int. Ed.* **2022**, *61*, e202212745. Some conclusion in this report were drawn from the research report “Dynamic covalent assembly of azobenzene containing macorcycles photoswitchable with red light” by Jona Voss.

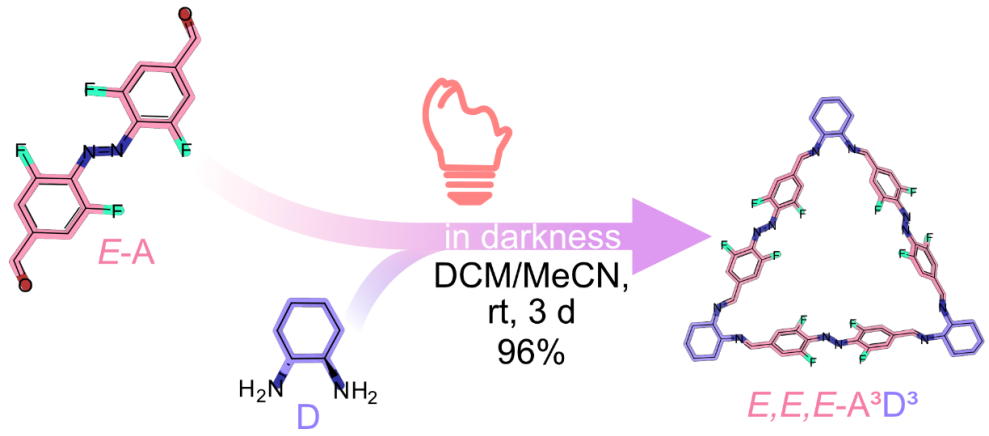

Figure 55: Formation of **A³D³** starting from *E*-**A** and **D**.

Testing different work-up conditions, the addition of EtOH followed by the removal of the solvent under reduced pressure at 30 °C led to the isolation of pure *E,E,E*-**A³D³**. As the starting material was still present after the work-up of the initial reactions, 1.2 equivalents of amine **D** were used for the formation of *E,E,E*-**A³D³** (Figure 55). As observed by the group of Cooper, using a small excess of amine enhances the yield in the formation of imine cages.[80] The formation of an imine compound was confirmed by a distinct shift of the signals in the ^{1}H and ^{19}F{^{1}H} NMR in *d*-dichloromethane (Figure 56). Upon imine formation, the signal for the proton of the aldehyde group shifts from 10.00 ppm to 8.08 ppm, while the signal for the aromatic protons shifts from 7.63 ppm to 7.31 ppm. The fluorine signal also undergoes an upfield shift from -118.93 ppm to -120.37 ppm.

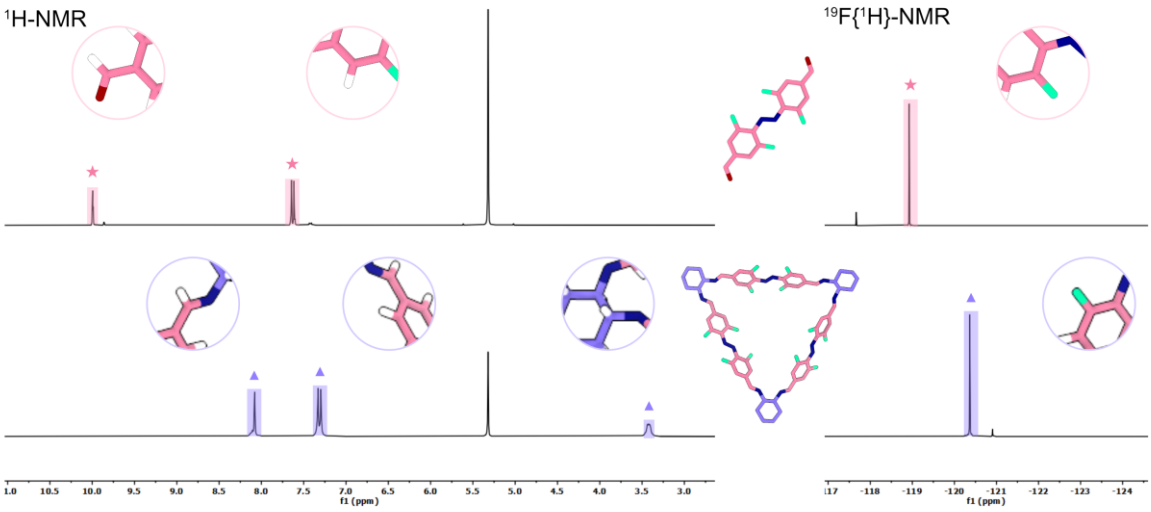

Figure 56: Excerpts of ^{1}H and ^{19}F{^{1}H} NMR spectra of azobenzene **A** (top) and *E,E,E*-**A³D³** (bottom) (CD_2Cl_2, 300 and 282 MHz, respectively). The signals for **A** are highlighted in pink (star) while the signals for *E,E,E*-**A³D³** are highlighted in blue (triangle).

That the formed macrocycle is indeed the targeted *E,E,E*-**A^{3}D^3** species, was confirmed by MALDI-mass spectrometry as well as by ^{1}H and ^{19}F DOSY NMR experiments (Figure 57). The observed mass of 1165.498 corresponds very well to the mass of 1165.441 that was calculated for the protonated **A^{3}D^3** macrocycle. As the diffusion coefficient correlates with the temperature-dependent viscosity of the used solvent, the diffusion coefficients determined in the DOSY NMR experiments differ significantly. While the ^{1}H NMR was measured in *d*-chloroform at 25 °C, the ^{19}F DOSY NMR was recorded in *d*-dichloromethane at 20 °C, leading to diffusion coefficients of $5.21 \cdot 10^{-10}$ and $6.02 \cdot 10^{-10}$ m^2s^{-1}, respectively. The resulting solvodynamic values of 7.81 and 8.29 Å are similar in size and are in accordance with values for a macrocycle of a similar size.[96a]

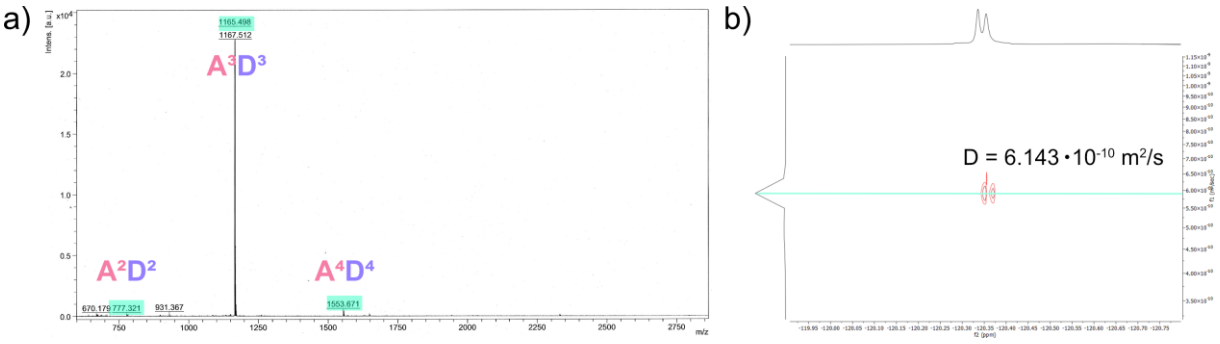

Figure 57: a) MALDI-mass spectrum of *E,E,E*-**A^{3}D^3**; b) ^{19}F DOSY NMR of *E,E,E*-**A^{3}D^3** (CD_2Cl_2, 565 MHz). The ^{19}F NMR was kindly measured and analysed by Dr. Andreas Mix.

The discrepancy in the calculated solvodynamic radii can most likely be explained by the different execution of the measurements. While the ^{1}H DOSY NMR was recorded using a method that is intended to be routinely used for cages and macrocycles, the fluorine measurement was adapted to this specific compound, and the obtained value was corrected using a predefined coefficient. Considering the discrepancy, both values are in accordance with the size of *E,E,E*-**A^{3}D^3**, which therefore further proves the formation of the macrocycle.
Even though **A^{3}D^3** could be synthesised in high yields and purity, no single-crystal X-ray structure could be obtained. Slow evaporation of a solvent or a solvent mixture, as well as vapor-liquid and liquid-liquid diffusion, only led to the formation of powders or, more often, films. The insolubility of the films indicates that the macrocycle decomposed, forming an oligomeric or polymeric species. While the macrocycle based on *S,S*-1,2-diaminocyclohexane and *E*-**A** could also be synthesised and isolated, as confirmed by ^{1}H and ^{19}F{^{1}H} NMR spectroscopy as well as by MALDI-mass spectrometry, further syntheses and experiments are all carried out with *R,R*-diaminocyclohexane (**D**) and its corresponding macrocycle *E,E,E*-**A^{3}D^3**. The photoswitching of *E,E,E*-**A^{3}D^3** was studied in dichloromethane by UV/VIS spectroscopy after irradiation with light of different wavelengths, showing that the macrocycle, like the precursor **A** and the imine model compound **AC^2**, can be isomerised from *E* to *Z* using red

(660 nm) or green (565 nm) light, and *vice versa* using light of the wavelength of 405 or 470 nm (Figure 58). As the spectra were in part recorded with samples of different concentrations, the molar attenuation coefficient is plotted against the wavelength instead of the absorbance for better comparability.

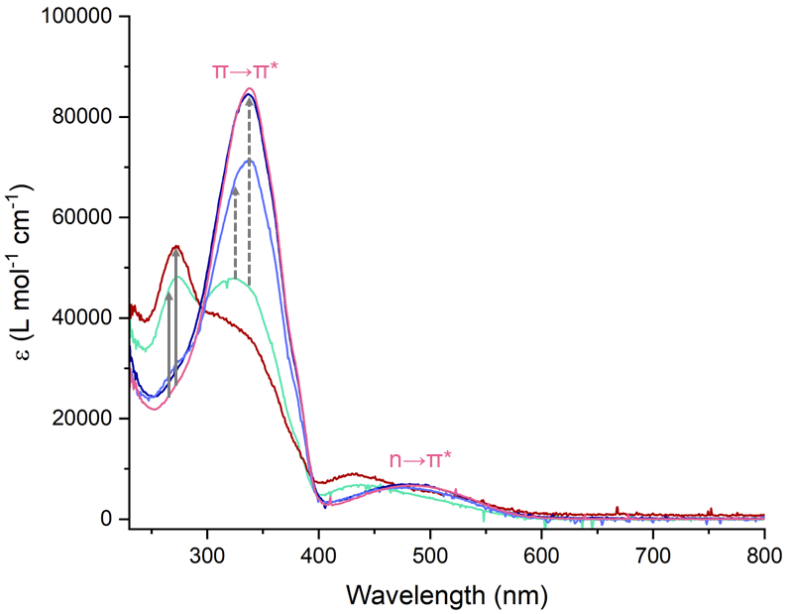

Figure 58: UV/VIS spectra of *E,E,E*-**A^{3}D^3** (pink curve), after irradiation with light of a wavelength of 660 nm for 1000 minutes (dark red curve) and 565 nm for 650 seconds (turquoise curve). A solution that was *Z*-enriched by irradiation with green light (565 nm) was irradiated with light of a wavelength of 405 nm (dark blue curve) for 55 seconds and 470 nm (light blue curve) for 110 seconds. The curve for the irradiation with red light (660 nm) misses the isosbestic point most likely due to evaporation during the prolonged irradiation time (Figure S75). The solid grey arrows indicate *E* to *Z* isomerisation while the dashed arrows indicate *Z* to *E* isomerisation.

The isomerisation behaviour is also similar to that of the previously investigated compounds, with red light (660 nm) having the highest yields of *Z*-isomer but being significantly slower than the isomerisation with green light (565 nm) and the *Z* to *E* isomerisation being faster and with higher ratios of *E*-isomer when light of a wavelength of 405 nm is used instead of 470 nm. Comparing the spectra recorded for **A^{3}D^3** and the previously synthesised compounds **A** and **AC^2** the significantly higher molar attenuation coefficient of **A^{3}D^3** stands out (Figure 59).

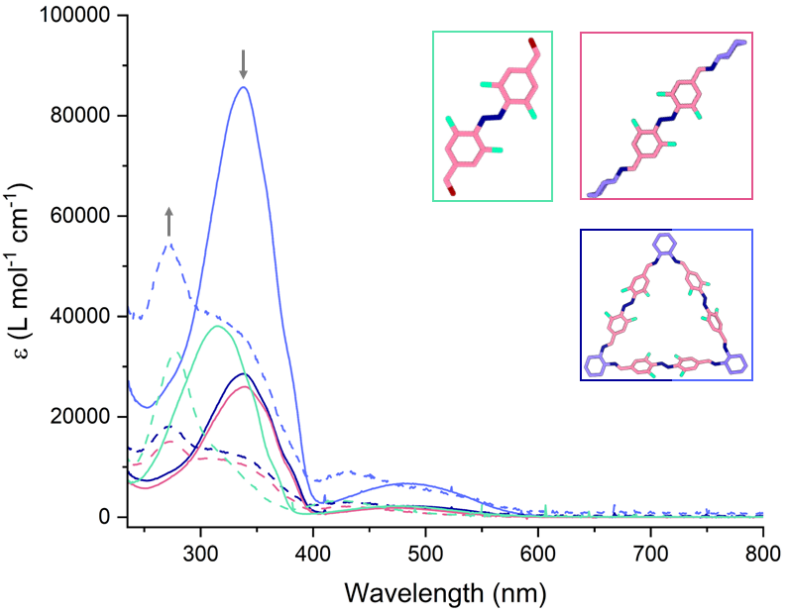

Figure 59: Comparison of the UV/VIS spectra of **A** (turquoise curve), **AC²** (pink curve) and **A³D³** (light blue curve). The molar attenuation coefficient for **A³D³** is significantly larger as each molecule contains three azobenzenes. For better comparability a curve of **A³D³** with an attenuation coefficient that was divided by three is depicted in dark blue. The solid curves show the UV/VIS spectra *E*-compounds while the dashed lines show the spectra after irradiation with red light (660 nm).

This is because **A³D³** bears three azobenzene moieties, while the other compounds only have one. To facilitate comparison the values for the curve of **A³D³** were divided by three, showing that the absorbance of the π→π* band of **A³D³** is lower than that of the precursor **A**, just as the absorbance of the π→π* band of the model compound **AC²**. Both the π→π* band of **A³D³** and **AC²** undergo a bathochromic shift in comparison to the π→π* band of **A**. The position of the band after irradiation with red light is also very similar for both imine compounds. The n→π* band of the **A³D³** macrocycle undergoes a bathochromic shift in comparison to both **A** and **AC²**. These observations show only minor differences between the photochemical properties of the model compound **AC²** and of the azobenzenes in **A³D³** and therefore confirm the suitability of **AC²** as an appropriate model. The corresponding absorbance maxima and molar attenuation coefficients are listed in table 2.

Table 2: Comparison of the wavelengths of absorbance maxima λ_{max} and molar attenuation coefficients ε of *E,E,E*-**A³D³**, *E*-**AC²** and *E*-**A**.

	E,E,E-**A³D³**		*E*-**AC²**		*E*-**A**	
	π→π*	n→π*	π→π*	n→π*	π→π*	n→π*
λ_{max} / nm	339	495	340	475	314	475
ε / 10^3 L mol^{-1} cm^{-1}	86.8	7.52	26.0	1.84	37.8	2.11

A sample of *E,E,E*-**A³D³** was subjected to alternate irradiation with light of a wavelength of 660 and 405 nm, confirming that the switching between the isomers can be repeated over several cycles without major photodegradation. The absorbance at 339 nm was measured after each irradiation (Figure 60). While the values recorded after the irradiation with light of a wavelength of 405 nm show nearly no deviation, the absorbance after red light irradiation varies. This is not the result of decay, as this would be visible by a trend of continuously rising absorbance and not by alternating higher and lower values. The discrepancy is most likely due to the varying irradiation times that were between 8 and 15 hours, while the irradiation time for the *Z* to *E* isomerisation was 5 minutes, and experimental inaccuracies, such as, for example, a different orientation of the sample to the light source.

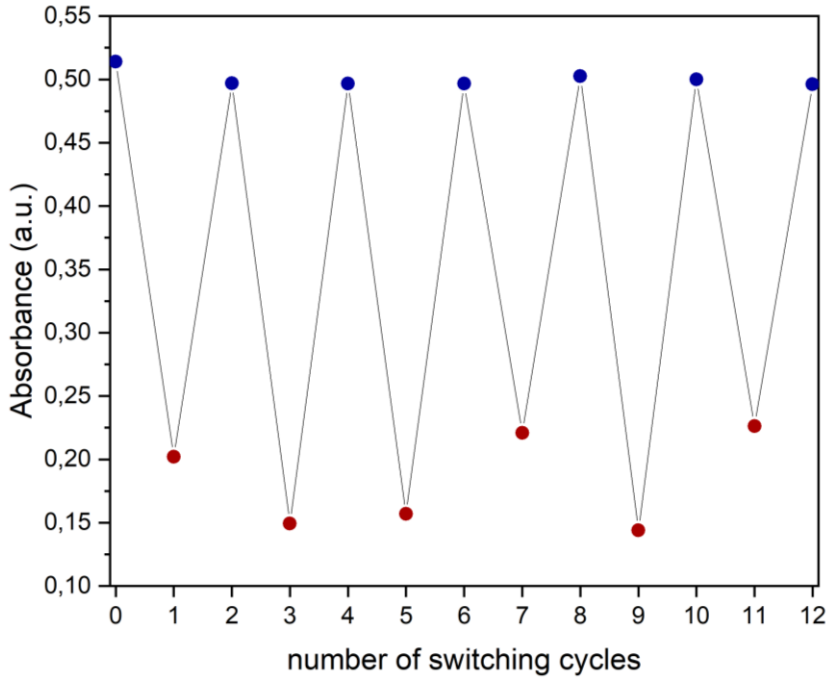

Figure 60: Absorbance at 339 nm after alternating irradiation with red light (660 nm, dark red points) and light of a wavelength of 405 nm (dark blue points). The absorbance spectra used to determine the plot are depicted in Figure S77.

To study whether the isomerisation of the different photoswitchable units is independent from each other or if the photoisomerisation of one unit affects the photochemical properties of the

others, the absorbance at 339 nm after the irradiation with light of different wavelengths was plotted against the time. The values were fitted to a curve using first-order exponential regression (Figure 61).

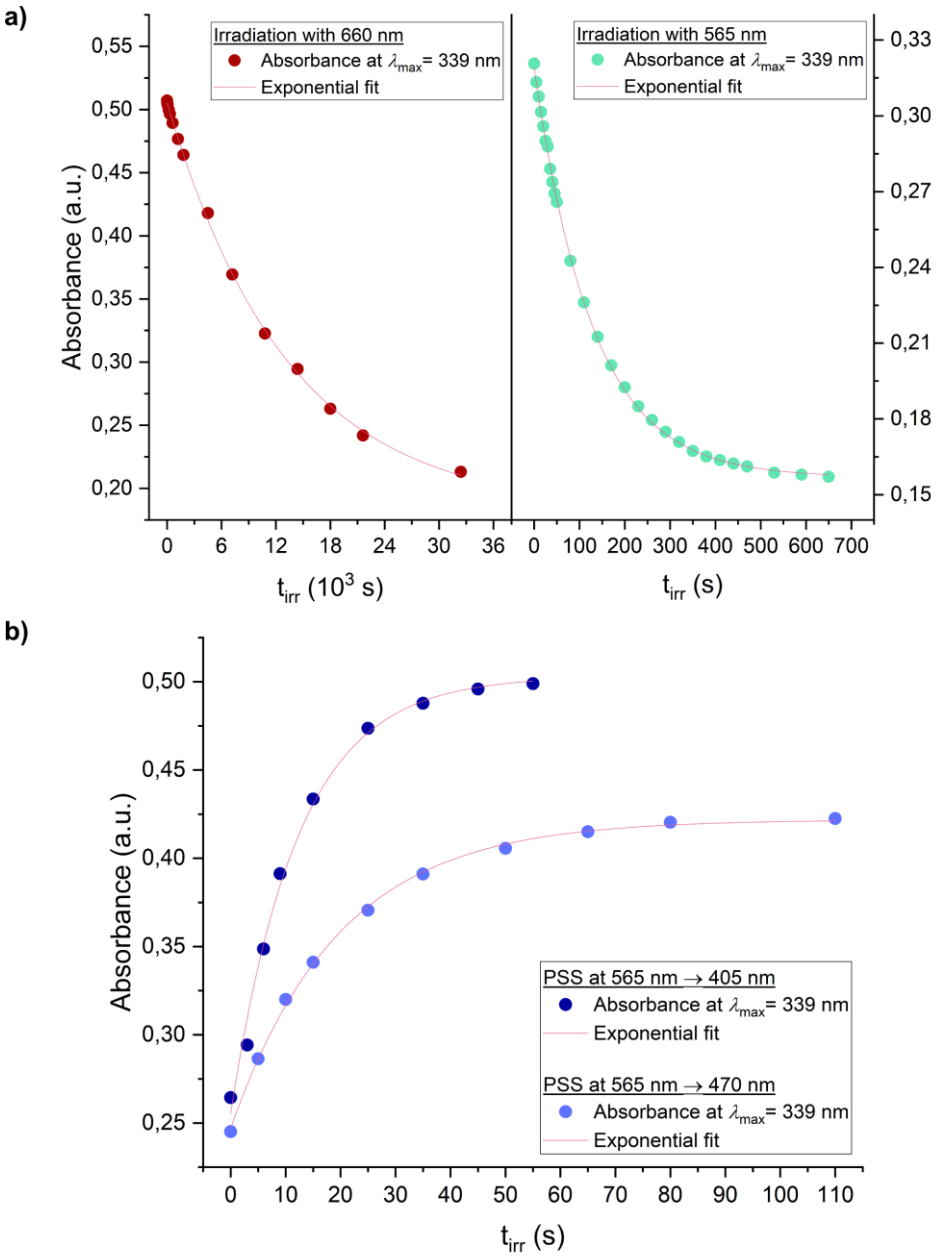

Figure 61: a) The absorbance at 339 nm of a solution of *E,E,E*-**A^{3}D^3** that was irradiated with red light (red dots) or green light (turquoise) is plotted against the irradiation time. b) A solution of **A^{3}D^3** that was *Z*-enriched by irradiation with green light was irradiated with light of the wavelength of 405 nm (dark blue) or 470 nm (light blue dots). The absorbance was plotted against the irradiation time. The regression curves are plotted in pink.

As the regression curves for both *E* to *Z* isomerisations as well as for both *Z* to *E* isomerisations are in good accordance with the experimental data, it can be suggested that the azobenzene units can be switched independently, with the partial isomerisation of other units not having a

major effect on the process. The calculated isomerisation rates reflect the trends observed for the different wavelengths (Table 3), however it should be noted that, comparing these values is difficult due to the varying concentrations (3.45 µM for 565 nm and 5.92 µM for other wavelengths) and the different properties such as the differing output power and the resulting maximum irradiance of the employed LED lamps.

Table 3: Isomerisation reaction rates k and their calculated standard deviations at different irradiation wavelengths λ_{irr}. The isomerisation reaction rates k_{Z-E} were determined by irradiation of a solution of **A^{3}D^3** after reaching PSS$_{565nm}$.

k_{E-Z} at 660 nm	k_{E-Z} at 565 nm	k_{Z-E} at 405 nm	k_{Z-E} at 470 nm
(7.55 ± 0.08) · 10^{-5} s^{-1}	(7.75 ± 0.04) · 10^{-3} s^{-1}	(82.0 ± 1.1) · 10^{-3} s^{-1}	(50.8 ± 0.9) · 10^{-3} s^{-1}

Due to the reversibility of the imine bond formation, the isomerisation process of **A^{3}D^3** might proceed by opening the imine ring. As there are many examples of covalent azobenzene macrocycles that can undergo *E* to *Z* isomerisation[5c,d,45] it would be interesting to see if a macrocycle with a structural motif similar to **A^{3}D^3**, which cannot undergo dynamic covalent exchange, can also be photoisomerised. Following the procedure by Tanaka *et al.*,[96c] the imine macrocycle *E,E,E*-**A^{3}D^3** was reduced to the corresponding amine macrocycle *E,E,E*-**A^{3}D$^3_{red}$** using sodium borohydride in a solvent mixture of chloroform and methanol with a 93% yield (Figure 62).

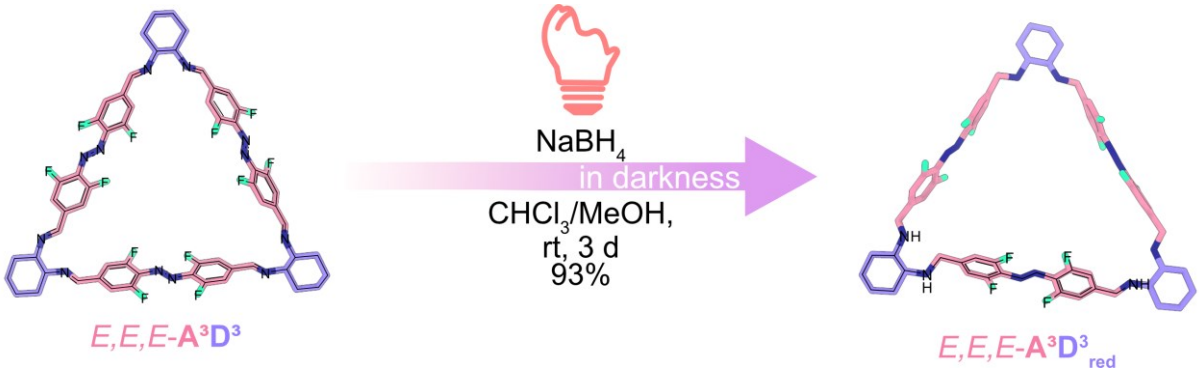

Figure 62: Synthesis of *E,E,E*-**A^{3}D$^3_{red}$** starting from *E,E,E*-**A^{3}D^3**.

The amine compound is still photoswitchable, but *E* to *Z* isomerisation is only possible using green light (565 nm), while prolonged irradiation with red light leads to nearly no conversion (see Figures S79 and S80). The *Z* to *E* isomerisation of a solution that was initially irradiated with green light is also possible using light with a wavelength of 405 nm or 470 nm (see Figure S81).

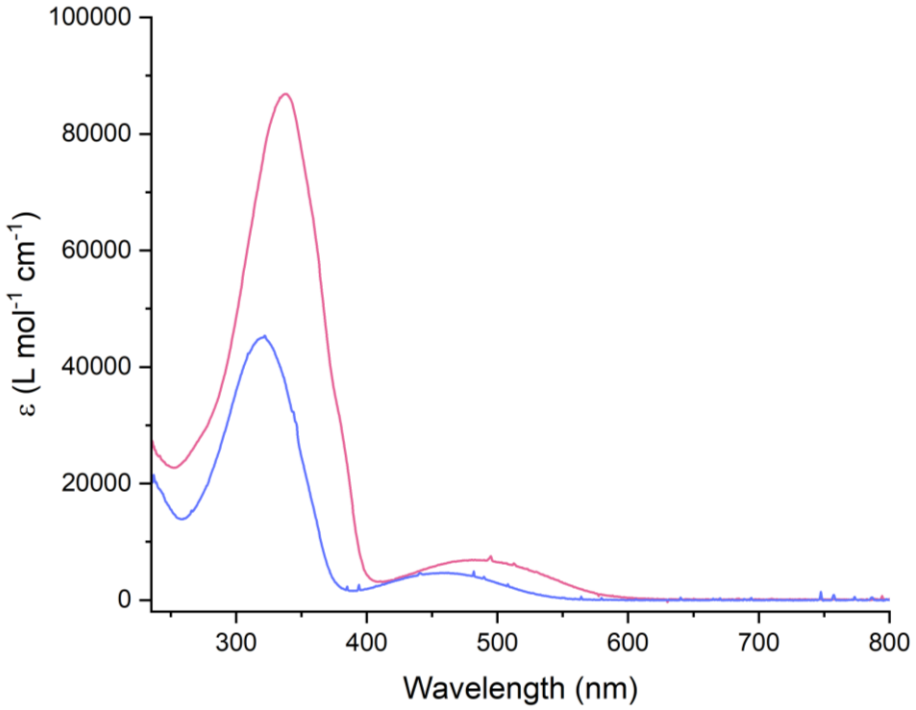

Figure 63: Comparison of the UV/VIS curves of *E,E,E*-$\mathbf{A^3D^3}$ (pink curve) and *E,E,E*-$\mathbf{A^3D^3_{red}}$ (light blue curve).

The hypsochromic shift of the n→π* band of *E,E,E*-$\mathbf{A^3D^3_{red}}$ in comparison to the imine compound *E,E,E*-$\mathbf{A^3D^3}$ explains the loss of the red light switchability of the amine (Figure 63). While the curve for the imine still shows a minor absorbance in the wavelength range of the red light source, *E,E,E*-$\mathbf{A^3D^3_{red}}$ shows no absorbance. The π→π* also undergoes a small hypsochromic shift upon reduction, and both bands undergo a significant hypochromic shift. Due to the structural similarity between $\mathbf{A^3D^3}$ and $\mathbf{A^3D^3_{red}}$ the photoswitchability of the amine, that cannot undergo reversible opening of the macrocycle, could be an indicator that the isomerisation of $\mathbf{A^3D^3}$ might can occurs without breakage of imine bonds. However, while the azobenzenes of both macrocycles might be affected by steric hindrance and possible ring strain, the amine system is more flexible than the imine system.

Combination of rigid diamine D with bent azobenzene isomer *Z*-A

While *E*-**A** and **D** form the trianglimine *E,E,E*-$\mathbf{A^3D^3}$, as anticipated, the product of the reaction between *Z*-**A** and **D** is not as easily predictable. The different geometry of the *Z*-isomer might lead to the formation of different macrocycles or might hinder the formation of closed macrocycles at all. As discussed in chapter 3.2.1, irradiation with red light (660 nm) leads to the highest ratio of *Z*-isomer in the photostationary state; therefore, a solution of *E*-**A** in *d*-dichloromethane was irradiated with red light for a prolonged time before a solution of **D** was added. The mixture was continuously irradiated with red light (660 nm) for several days, followed by a period in which the mixture was stirred in the dark, during both monitoring was

conducted by MALDI-mass spectrometry, ^{1}H, and $^{19}F\{^{1}H\}$ NMR spectroscopy. The recorded spectra show that a mixture of different macrocycles is formed. The signals for the mixture in the $^{19}F\{^{1}H\}$ NMR are well resolved (Figure 64) in comparison to the signals in the corresponding ^{1}H NMR spectrum that overlap, making the analysis of specific species difficult, but the absence of aldehyde signals strongly suggests that no open species are formed over the course of the reaction (Figure S85).

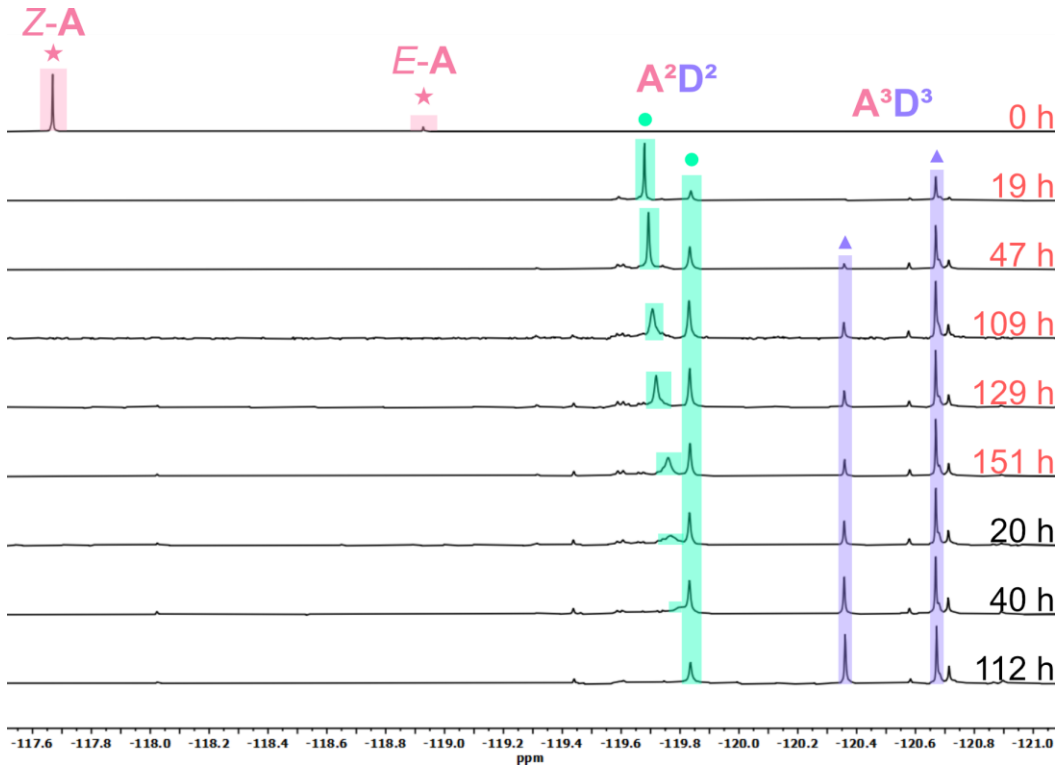

Figure 64: Excerpts of the $^{19}F\{^{1}H\}$ NMR-spectra of the reaction of *Z*-**A** and **D** during the continuous irradiation with red light (times highlighted in red) and the following time in the dark (times highlighted in black) (CD_2Cl_2, 282 MHz). Signals of azobenzene isomers are highlighted in pink (star), signals for the **A²D²** macrocycles in turquoise (circle) and signals for the **A³D³** macrocycle in blue (triangle). This figure was adapted from reference 97 with permission.

After continuous irradiation for 19 hours after the addition of diamine **D**, the formation of three signals was observed. To assist in the assignment of the different signals to macrocyclic species of different sizes, DOSY NMR experiments were performed. While the ^{1}H DOSY NMR showed the presence of macrocyclic species with two different sizes (10.5 Å and 6.46 Å) the assignment to the different signals was hindered by the overlapping of the signals (Figure S97). To circumvent this problem, ^{19}F DOSY NMR spectra were recorded by Dr. Andreas Mix at the University of Bielefeld, enabling the analysis of the $^{19}F\{^{1}H\}$ NMR spectra (Figures S101 and S102). The signal with the highest intensity at -119.68 ppm, shifts during the irradiation, broadens, and, during the time in the dark, merges with the signal at -119.84 ppm. This signal appears after 19 hours of irradiation, the intensity of the peak rises during the irradiation and

declines during the time in the dark. Both signals can be assigned to an **A²D²** macrocycle according to the determined solvodynamic radii of 5.93 Å for the signal at -119.68 ppm and 6.02 Å for the signal at -119.84 ppm. The initial assumption was that the first signal at -119.68 ppm could be assigned to the *Z*-isomer of **A²D²**, that the second signal might be assigned to an *E*-isomer which forms later. The reasons why this assumption is highly improbable will be explained subsequently. The third signal with a chemical shift of -120.67 ppm that can be observed after 19 hours can be associated with an **A³D³** macrocycle according to its size of 6.98 Å. After 47 hours, a signal with the same chemical shift as *E,E,E*-**A³D³**, -120.36 ppm, can be observed. This signal slightly inclines during the irradiation with red light and shows a larger growth during the time in the dark. This suggests that any *E*-**A** that forms assembles into the product that is most stable for this isomer, the **A³D³** macrocycle. The mixture of products formed by the reaction of *Z*-**A** and **D** is depicted in Figure 65a.

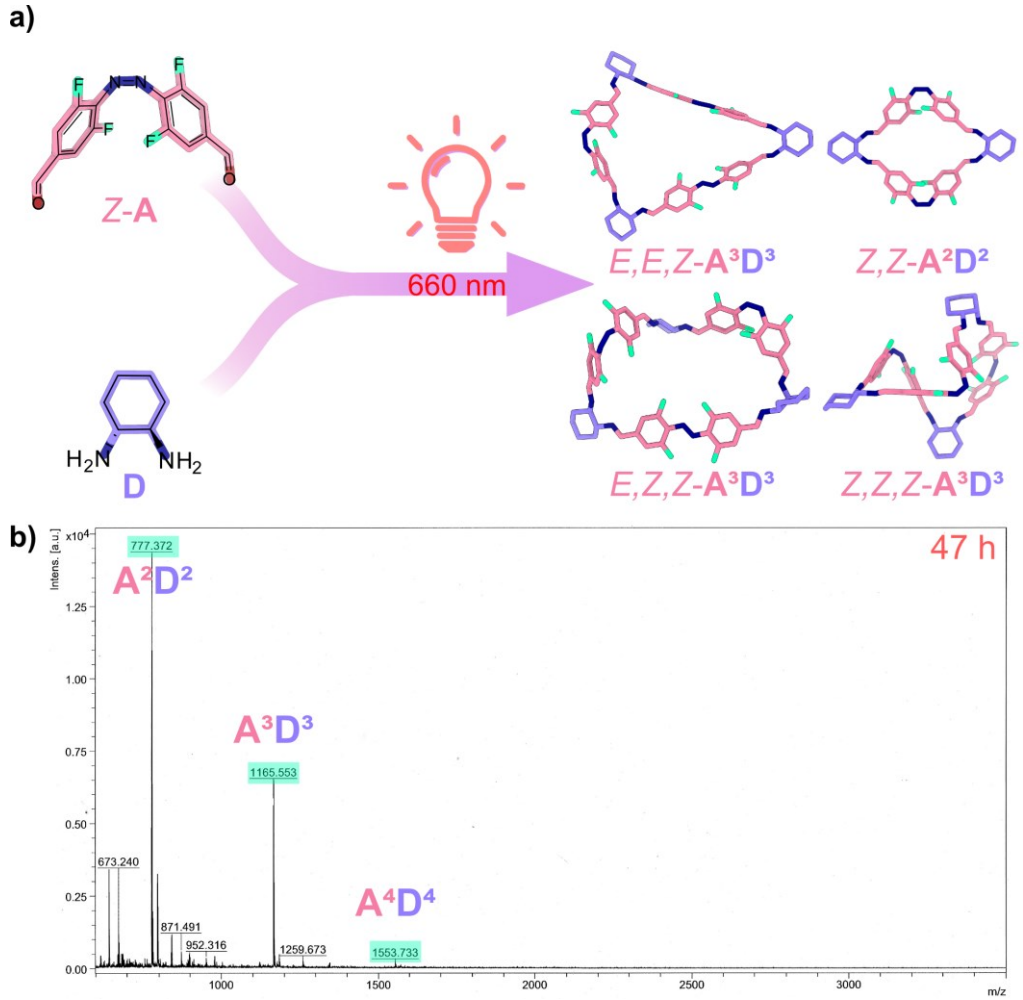

Figure 65: a) Reaction of *Z*-**A** and **D** forming a mixture of macrocycles; b) MALDI-mass spectrum after 19 hours of irradiation with red light (660 nm).

It is difficult to make a quantitative analysis based on peaks in the MALDI-mass spectrum, as the height of the peaks depends on different factors, for example, how easily the molecule can

be ionised. Nonetheless, the trends that are visible in the recorded spectra align with the product distribution observed in the $^{19}F\{^{1}H\}$ NMR spectrum (Figure 65b and Figure S89). According to the MALDI-mass spectrum, the major product that is initially formed after 19 hours is an **A^2D^2** macrocycle. The peak for the **A^3D^3** macrocycle is also visible from the beginning and steadily increases in height during the period in the dark, concomitantly with the decline in intensity of the peak of the **A^2D^2** macrocycle. In some of the mass spectra, a minor peak for the **A^4D^4** macrocycle is visible. Either this macrocycle is formed in small quantities and was therefore not observed in the NMR study, or the peak is the result of aggregation. In collaboration with the Clever group, attempts were made to get further insight into the number and nature of the different **A^3D^3** isomers formed under different conditions by ion mass mobility measurements. As the cross-collision sections should be different depending on the isomer, these measurements should allow the identification of the isomers formed; unfortunately, the measurements conducted with isolated samples were not successful.

Dissipative reaction of A^3D^3

The generation of a mixture of different macrocycles starting from *Z*-**A** and **D**, and the subsequent formation of **A^3D^3** in the absence of light led to the idea of generating a dissipative system based on **A^3D^3**. The activation of a precursor in a dissipative system by the addition of a chemical fuel, which is then turned into waste, or by light leads to a reversible assembly. This formation process competes with a deactivation process that can happen spontaneously or be triggered by the addition of a chemical fuel and reproduces the precursor. A solution of **A^3D^3** in *d*-dichloromethane was irradiated with red light (660 nm) and monitored again by MALDI-mass spectrometry, ^{1}H and $^{19}F\{^{1}H\}$ NMR spectroscopy (Figure 66 and Figure S88). The assignment of the signals was based on the previous measurement, and supported by additional ^{19}F DOSY NMR measurements (Figures S98-S100).

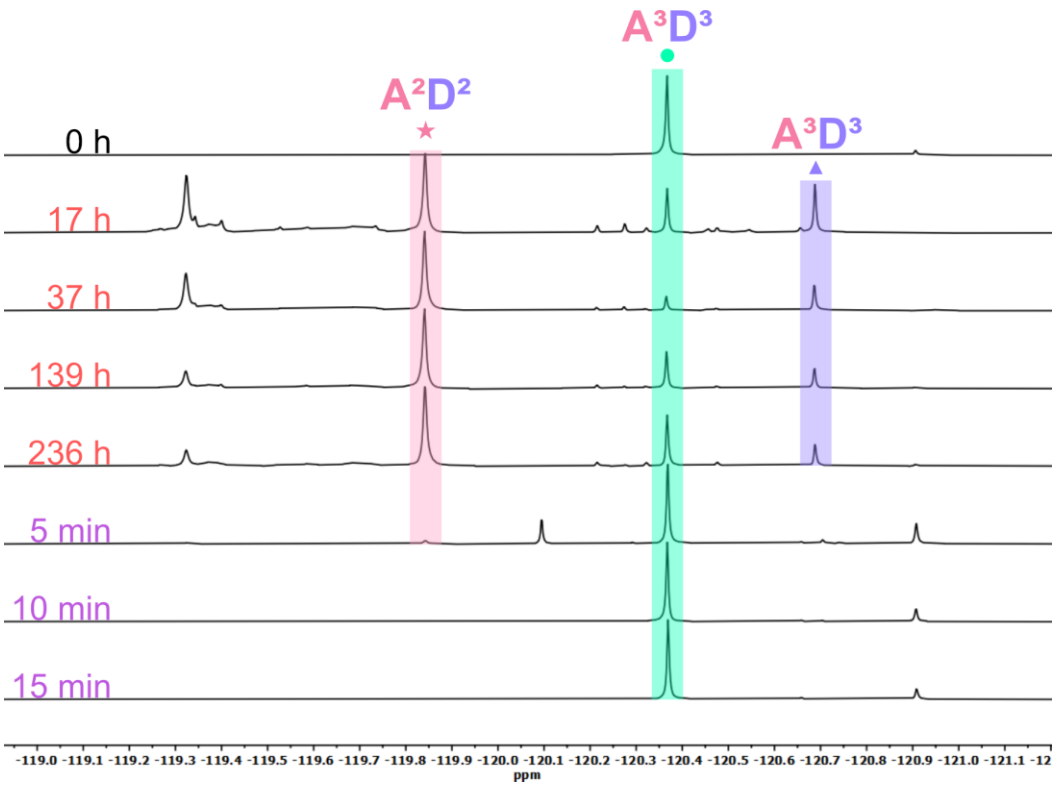

Figure 66: Excerpts of the $^{19}F\{^{1}H\}$ NMR-spectra of the continuous irradiation of *E,E,E*-**A³D³** with red light (times highlighted in red) and the following irradiation with light of a wavelength of 405 nm (times highlighted in violet) (CD_2Cl_2, 282 MHz). Signals of **A²D²** are highlighted in pink (star) while signals for the **A³D³** macrocycle are highlighted in turquoise (circle) and blue (triangle). This figure was adapted from reference 97 with permission.

Upon irradiation with red light (660 nm), four different major signals can be observed after 17 hours. The signal at -120.37 ppm can be assigned to *E,E,E*-**A³D³** in accordance with the determined solvodynamic radius of 8.24 nm. This signal decreases in intensity in relation to the other signals at first. After 37 hours, the intensity of the signal rises slowly during the irradiation with red light and then rapidly upon irradiation with UV light (405 nm). The signal at -120.68 ppm can again be assigned to an **A³D³** macrocycle. The solvodynamic radii that were observed in the different ^{19}F DOSY measurements are different even if the signal has the same chemical shift. As the signals observed in the DOSY are comparably broad, they might be caused by compounds that cause signals with similar chemical shifts but are of slightly different sizes. While there are only two major signals observable that can be assigned to the **A³D³** macrocycles according to their size, it can be assumed that more **A³D³** species are formed and that the signals of the different possible isomers, *E,E,E*, *E,E,Z*, *E,Z,Z*, and *Z,Z,Z* overlap, forming the two observable signals. In contrast to the previous measurement, only one signal for the **A²D²** macrocycle can be observed. The signal at -119.84 ppm correlates to a macrocycle with a solvodynamic radius of 5.64 nm, according to the analysis of the ^{19}F DOSY NMR. This signal has the highest intensity in comparison to the other signals and disappears

upon irradiation with light of a wavelength of 405 nm. The chemical shift of this signal is not identical to the signal of the compound that is initially formed by the reaction of *Z*-**A** and **D** but to the signal that is formed subsequently (Figure 67a-b). As a result, it can be assumed that in the reaction of *Z*-**A** and **D**, two different types of *Z,Z*-$\mathbf{A^2D^2}$ macrocycles are formed.

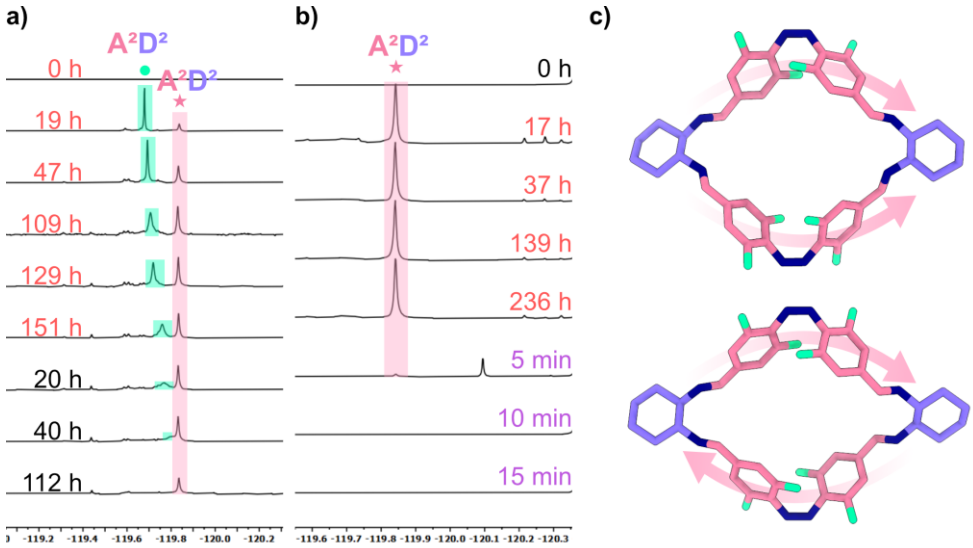

Figure 67: Comparison of excerpts of $^{19}F\{^1H\}$ NMR spectra of a) the reaction of *Z*-**A** and **D** under continuous irradiation (CD_2Cl_2, 282 MHz) and b) of the irradiation of *E,E,E*-$\mathbf{A^3D^3}$ with red light (660 nm) and light of the wavelength of 405 nm (CD_2Cl_2, 282 MHz); c) possible different structures of *Z,Z*-$\mathbf{A^2D^2}$ macrocycles as seen from the top with structures obtain from force field optimisations.

The two different types of *Z,Z*-$\mathbf{A^2D^2}$ might differ in their geometry (Figure 67c). While the first of the possible structures contains two azobenzene units that are mirrored, the whole macrocycle is of C_1 symmetry due to the diamines. The second possible structure could be D_2-symmetric if depicted as above. One of the structures is the kinetic product of the reaction of *Z*-**A** and **D**, which is primarily formed and later converts into the second, more stable structure. The formation of $\mathbf{A^2D^2}$ would then only lead to the formation of the more stable product; this might be due to the fact that the building blocks are preorganised in the $\mathbf{A^3D^3}$ macrocycle that undergoes ring contraction upon irradiation.

The last signal that can be observed after 17 hours of reaction time has a chemical shift of -119.32 ppm and cannot be assigned to a macrocycle of a specific size. At first, it was expected that this signal belongs to an open species, but as the corresponding ^1H NMR-spectra show no aldehyde signal, this is rather unlikely. The size of the signal could not be determined by ^{19}F DOSY NMR measurements, because even though the signal shows a high intensity in the $^{19}F\{^1H\}$ NMR in the corresponding ^{19}F NMR it presents itself as a broad signal with a lower visibility.

While the isomerisation of *E,E,E*-$\mathbf{A^3D^3}$ with light of different wavelengths was also studied by UV/VIS-spectroscopy in a previous section, it is assumed that the reactions observed deviate

due to the differing concentrations of 3.45 to 5.92 µM for the UV/VIS experiments and 2.79 mM for the NMR study. During the comparably short reaction times and the low concentrations in the UV/VIS experiments, only the isomerisation of the macrocycle was observable. This is in accordance with the spectra that show clear isosbestic points. In contrast, the longer reaction times and higher concentrations in the NMR-studies should favour the formation of other species such as the $\mathbf{A^2D^2}$ macrocycle. The proposed reversible isomerisation and transformation of *E,E,E*-$\mathbf{A^3D^3}$ is depicted in Figure 68a.

The MALDI-spectra that were recorded, again show a trend similar to the one observable by NMR-spectroscopy. In the spectrum that was recorded before irradiation, $\mathbf{A^3D^3}$ is the major product, with only minor amounts of $\mathbf{A^2D^2}$ and $\mathbf{A^4D^4}$ present. After irradiation with red light, the amount of $\mathbf{A^2D^2}$ rises significantly, and in each spectrum recorded during the irradiation, either this macrocycle or $\mathbf{A^3D^3}$ can be assigned to the peak with the highest intensity. The signal for the smaller ring decreases and disappears during the irradiation with light of a wavelength of 405 nm. Additionally, in the spectra that were recorded during the irradiation with red light (660 nm) and during the following *Z* to *E* isomerisation masses of larger macrocycles up to $\mathbf{A^8D^8}$ were observed (Figure 68b and Figure S89). Either those macrocycles are formed in concentrations that are too small to be seen in the NMR spectrum, or more likely, those peaks are the result of aggregate formation. Catenation is an unlikely explanation for the formation of those signals, as the diameter of the different macrocycles is comparably small and more complex NMR spectra with distinct shifts would be expected in this case.

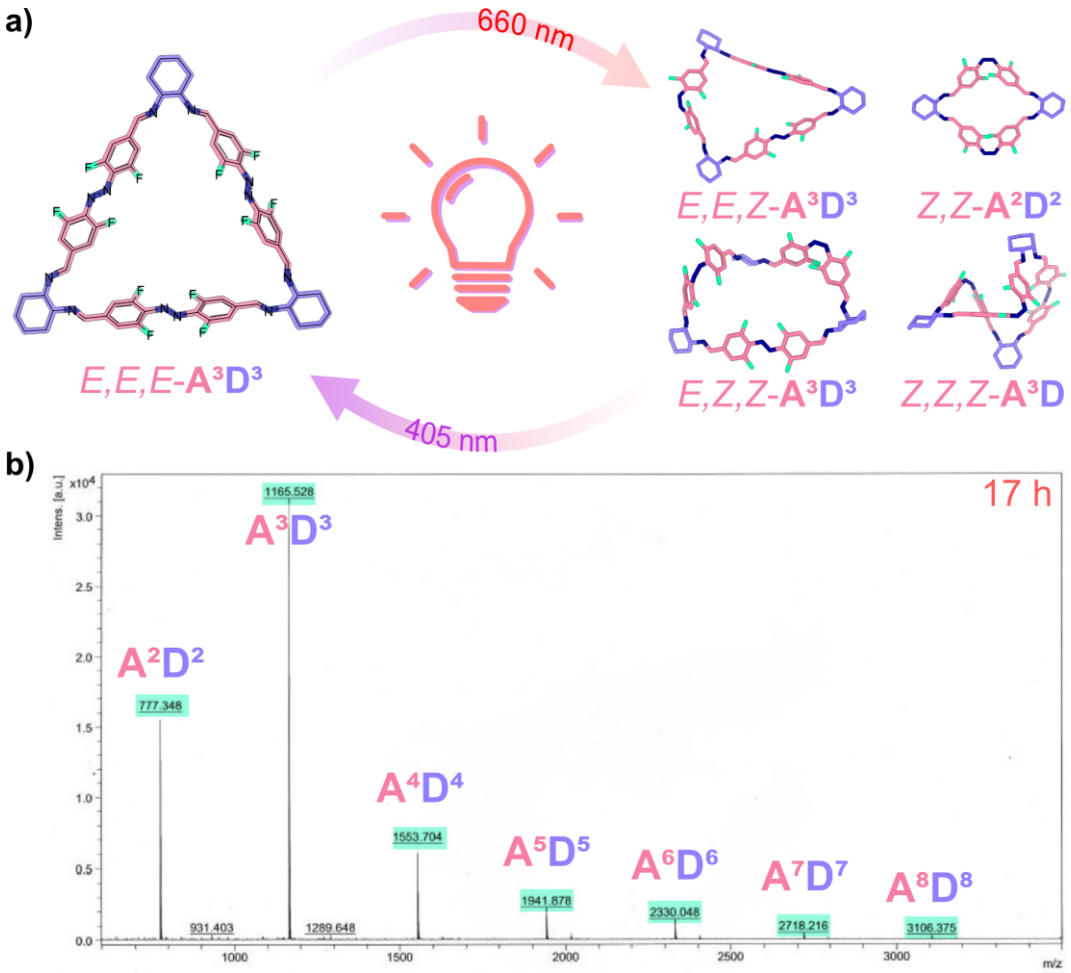

Figure 68: a) Irradiation of *E,E,E*-**A³D³** with red light leading to a mixture of macrocycles; b) exemplary MALDI-mass spectrum obtained after 17 hours of irradiation with red light (660 nm) in *d*-dichloromethane. This figure was adapted from reference 97 with permission.

The irradiation of *E,E,E*-**A³D³** leads to the formation of a mixture of macrocycles containing mostly **A²D²** and **A³D³** macrocycles. The precursor can be easily and rapidly regained by irradiation with UV light, making this system the first photoresponsive dissipative system based on an imine macrocycle.

Macrocycle formation attempts with other stiff diamines

Other rigid diamines that are sometimes employed in macrocycle or cage formation are the enantiomers of 1,2-diphenylethylenediamine, in which the amine groups adapt a *gauche* conformation that closely mimics the structural features of **DACH** while giving the system a little bit more freedom.[94] The reaction of *R,R*-1,2-diphenylethylenediamine (**DPEN**) and both azobenzene isomers *E*-**A** and *Z*-**A** was carried out in *d*-chloroform and observed by MALDI-mass spectrometry and ^{1}H and ^{19}F{^{1}H} NMR spectroscopy to investigate whether the increased flexibility of the acyclic **DPEN** in comparison to **DACH** has an effect on the products formed (Figure 69).

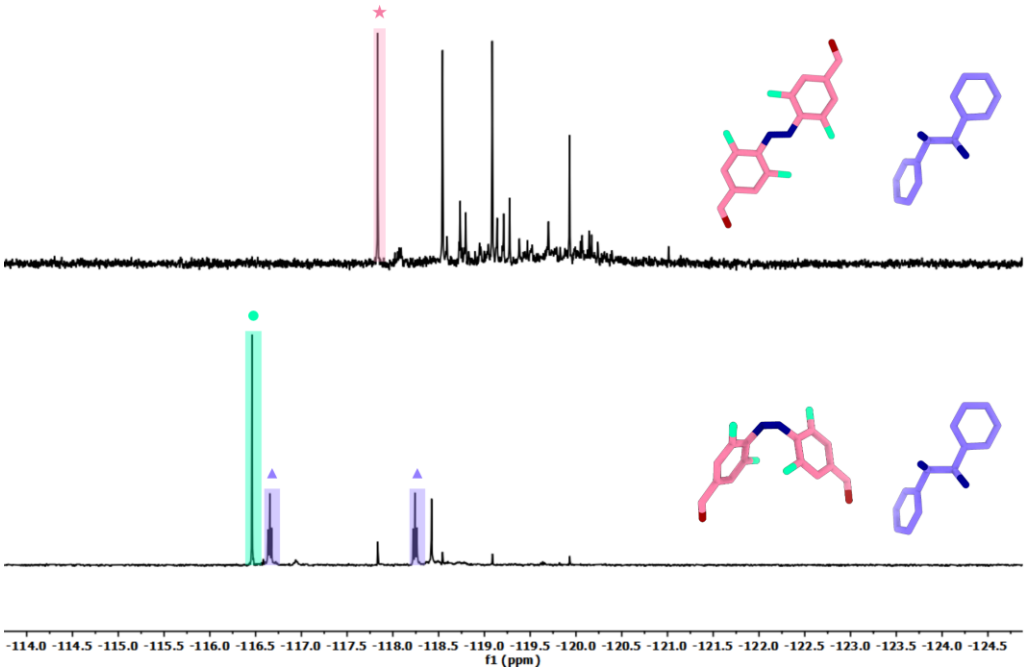

Figure 69: Excerpts of $^{19}F\{^{1}H\}$ NMR spectra showing the reaction of *E*-**A** and **DPEN** forming different probably oligomeric species, and the reaction of *Z*-**A** and **DPEN** yielding mostly unreacted azobenzene starting materials and monofunctionalised *Z* azobenzene ($CDCl_3$, 282 MHz). Signals of *E*-**A** are highlighted in pink (star), *Z*-**A** is highlighted in turquoise (circle) and monofunctionalised *Z*-**A** is highlighted in blue (triangle).

After three days of stirring *E*-**A** and **DPEN** at room temperature in the dark, peaks that can be assigned to different species can be observed in the $^{19}F\{^{1}H\}$ NMR. Residues of *E*-**A** as well as different species that could be oligomeric or macrocyclic species had formed. The broad signals in the ^{1}H NMR between 9.9 and 10.1 ppm and the equally broad signals with lower intensity between 8.2 and 8.4 ppm show that the different products formed are different aldehyde and imine species, confirming the formation of mostly oligomeric species (Figure S90). The MALDI-mass spectra that were recorded show the formation of $\mathbf{A^1DPEN^1}$ macrocycles. The formation of these macrocyclic structures is highly unlikely due to the geometry of both precursors; either the species are formed during the measurement or these are larger macrocycles with multiple charges. Signals for the open $\mathbf{A^1DPEN^1}$ species can also be observed. Using a *Z*-enriched solution of **A** in combination with **DPEN** resulted in large amounts of unreacted *Z*-**A** and signals that can most likely be assigned to the *Z*-isomer of monofunctionalised **A**, which causes two multiplets that appear with a comparably large distance from each other. A mass that can be assigned to the $\mathbf{A^1DPEN^1}$ compound can again be observed in the corresponding MALDI-mass spectrum, and a peak with low intensity can be assigned to an open $\mathbf{A^2DPEN^2}$ compound (Figure S92). As no macrocyclic species was observed as the major product with either of the isomers, the attempts to synthesise a **DPEN**-

based dissipative macrocycle were discarded. To successfully generate a system that can be switched back and forth between different states, at least one stable state is required.

The literature-known macrocycles based on **DPEN** are often synthesised in lower yields than their corresponding **D** analogues due to their increased flexibility.[94,98] The decay of the isolated **DPEN** macrocycles after a few days in solution was also observed, indicating that the **DPEN**-based structures are the kinetical and not the thermodynamical products further rendering **DPEN** macrocycles unsuitable.[98] To favour the formation of macrocycles based on **DPEN**, different 2-hydroxyisopthalaldehydes or other hydroxy functionalised isophthalaldehydes and terepthalaldehydes were employed as building blocks, as the hydrogen bond between the hydroxy group and the adjacent imine units stabilised the macrocycle.[99] The imine cage based on **DPEN** introduced by the Cooper group was also synthesised under adapted conditions using lowered temperatures and catalytic amounts of trifluoroacetic acid while additionally stopping the reaction before the equilibrium state was reached.[100]

Another building block that might be suitable for the formation of macrocycles in combination with **A** is 1,3-phenylenedimethanamine (**mP**). Mixing *E*-**A** and **mP** in *d*-chloroform and monitoring the reaction by MALDI-mass spectrometry and ^{1}H and $^{19}F\{^{1}H\}$ spectroscopy revealed the formation of *E,E*-$\mathbf{A^2mP^2}$ (-119.18 ppm) and residual *E*-**A** (-117.84 ppm) (Figure 70). Additional signals of smaller intensity between -118.57 and -118.80 ppm and between -119.56 and -199.64 ppm can most probably be assigned to monofunctionalised **A** and oligomeric bis-imine species, respectively. Irradiation of the mixture with red light (660 nm) led to the formation of a signal at -118.39 ppm that can be assigned to a *Z,Z*-$\mathbf{A^2mP^2}$ macrocycle. This spectrum contains residues of the *E*-macrocycle, indicating incomplete conversion. The reaction of *Z*-**A** and **mP** also gives access to the *Z*-macrocycle with minor amounts of residual **A** and monofunctionalised **A**.

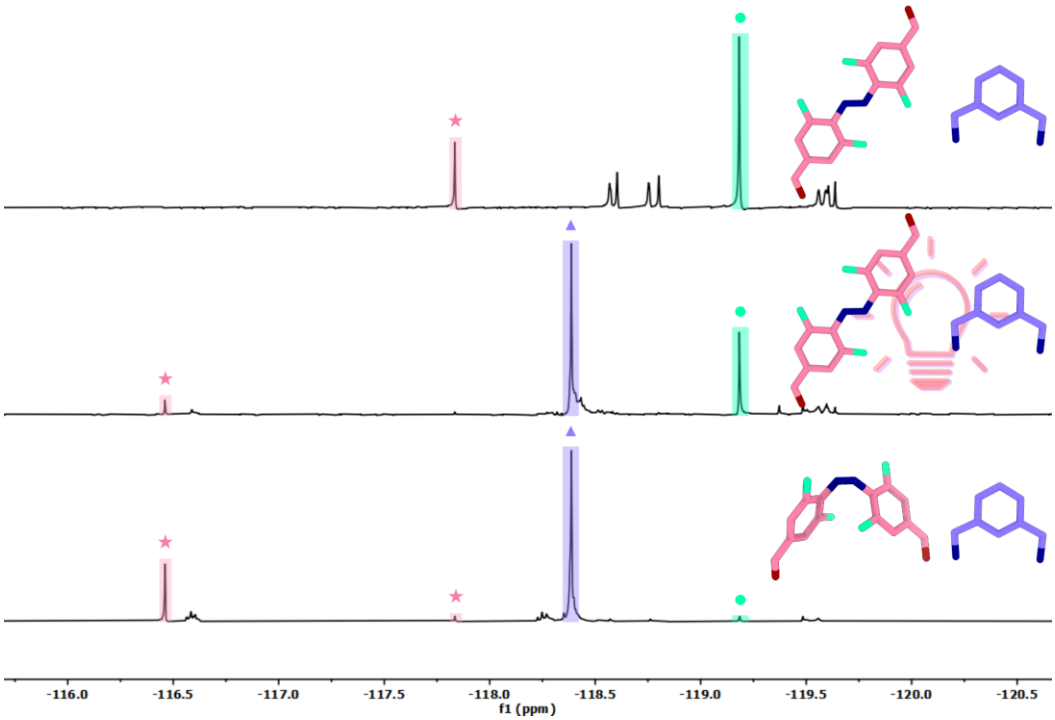

Figure 70: Excerpts of $^{19}F\{^{1}H\}$ NMR spectra showing the reaction of *E*-**A** and **mP** forming the macrocycle *E,E*-**A²mP²** in the dark, irradiation of the mixture led to the formation of a *Z,Z*- **A²mP²** macrocycle. The same macrocycle can be obtained by the reaction of *Z*-**A** and **mP** ($CDCl_3$, 282 MHz). Signals of **A** are highlighted in pink (star), *E,E*-**A²mP²** is highlighted in turquoise (circle) and *Z,Z*-**A²mP²** is highlighted in blue (triangle).

The size of the macrocycle was confirmed by the analysis of the corresponding MALDI-mass spectra, which showed peaks with masses that can be assigned to macrocycles between the sizes of **A²mP²** and **A⁶mP⁶** with the first having the highest intensity in all recorded spectra (Figure S95).

Summary

In summary experiments in which the sterically constrained **DPEN** building block was used, at most only led to the formation of macrocycles as byproducts, while the use of **mP** in combination with *E*-**A** and *Z*-**A** led to the clean formation of an **A²mP²** macrocycle that, according to the recorded NMR spectra can be generated and isomerised selectively. While the formation of the macrocycle was observed in *d*-chloroform, it was not isolated yet, and further measurements confirming its size have not been performed yet.

Employing the cyclic building block **D** as a precursor in combination with *E*-**A** led to the clean formation of trianglimine *E,E,E*-**A³D³** in high yields. The macrocycle can be photoisomerised from *E* to *Z* in low concentrations using red or green light, and *vice versa* using blue or UV light. In higher concentrations, the formation of a mixture could be observed by MALDI-mass spectrometry and ^{1}H and $^{19}F\{^{1}H\}$ NMR spectroscopy. ^{19}F DOSY NMR measurements revealed

that, in addition to the different isomers of **A^{3}D^3**, the irradiation with red light leads to a ring contraction, forming the smaller *Z,Z*-**A^{2}D^2** macrocycle. The precursor *E,E,E*-**A^{3}D^3** can be regained by irradiation with UV light, making this system the first photoresponsive, dissipative system based on imine macrocycles. Employing *Z*-**A**, generated by irradiation with red light, in combination with diamine **D** yields a mixture with a slightly different composition. Instead of one *Z,Z*-**A^{2}D^2**, two different types of macrocycles were formed, with one being metastable and slowly transforming into the more stable structure. The possibility to employ both structurally different azobenzene isomers in the generation of supramolecular imine systems further widens the scope of structures that can be accessed. The variety of structures accessible by combining **A** and **D** is highlighted in Figure 71.

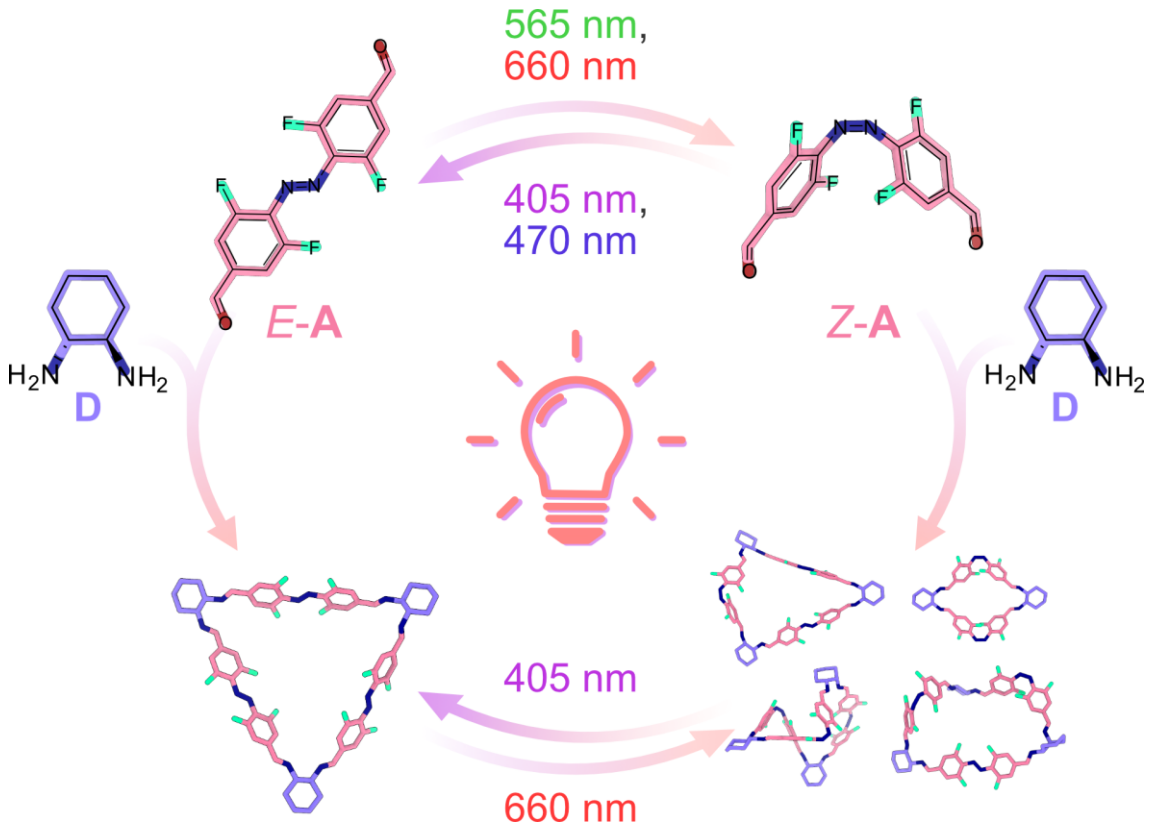

Figure 71: Overview of structures and reactions accessible by employing azobenzene isomers *E*-**A** and *Z*-**A** in combination with diamine **D** and dissipative interconversion of the obtained products.

E,E,E-**A^{3}D^3** can also be transformed into the amine derivate *E,E,E*-**A^{3}D^3$_{red}$**. The amine macrocycle can no longer undergo reversible ring opening or ring contraction but can still be isomerised from *E* to *Z* using green light and *vice versa* using blue and UV light. While (symmetrical) covalent macrocycles containing several diamines are often synthesised in several steps with moderate yields,[5d,45] *E,E,E*-**A^{3}D^3$_{red}$** can be obtained in two steps with high yields. The synthetical effort could also be further reduced by performing these steps consecutively by directly adding the reducing agent to the reaction mixture. Photoswitchable

macrocycles are highly interesting targets as they can be employed, among others, in guest encapsulation and controlled release, sensing and imaging, or in photocontrolled catalysis.[5d,45] The convenient synthesis and the good photochemical properties could make the macrocycle or possible amine derivatives obtained from different diamines interesting structures for a variety of applications.

3.2.3 Macrocycles based on flexible diamines

Introduction

In the formation of macrocycles based on **A** and **D**, the structure was highly influenced by the structure encoded in the diamine. To generate a system that is majorly affected by the structure of the azobenzene **A** and, as a result, allow the formation of very diverse products with the different azobenzene isomers, an amine with little to no intrinsic precoordination needs to be used. The focus fell on linear aliphatic diamines, as their flexibility should lead to structures governed mostly by the structure of azobenzene **A**. Employing those diamines in the generation of cages or macrocycles, different techniques have been utilised to favour the formation or enable the isolation of the product. The group of Warmuth used ethylenediamine (**E**) in combination with a rigid functionalised aldehyde cavitand to generate different capsules.[101] Another strategy to generate cages based on **E** is the addition of molecules that act as templates, as published by the group of Zonta.[102] After synthesising the ethylenediamine-based cage CC1,[26a,103] the group of Cooper also synthesised other cages based on different aliphatic diamines, studying the influence of the diamine's length on the topology of the formed cage. While the ethylene (**E**) and pentandiamine (**Pe**) derivatives were isolated, the other cages in the study were only stable in solution (Figure 72).[104] Cao and co-workers reported on a chiral cage based on **E**, which can be partially disassembled and converted into the other enantiomer.[105]

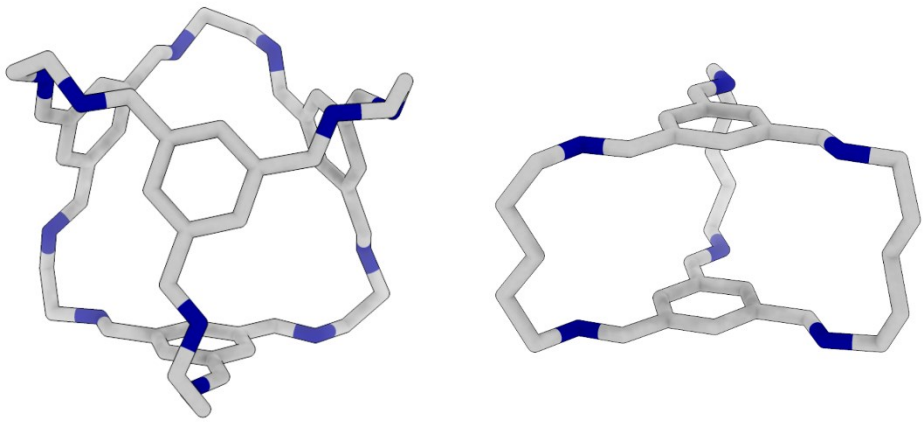

42^4E^6 42^2Pe^3

Figure 72: Examples for cages based on aliphatic diamines synthesised by the group of Cooper.

Imine macrocycles based on **E** or other aliphatic diamines are often constructed using bent aldehydes and additional hydrogen bonding interactions, generating salen-based macrocycles to favour the ring formation.[99c,106]

Considering the known structures, *E*-**A** and the linear aliphatic amines should most likely generate oligomeric or polymeric structures, while the *Z*-isomer should be able to form

macrocycles, due to its bent structure. These macrocycles should also be accessible in a dissipative reaction using the oligomers or polymers as precursors.[6]

Oligomers and macrocycles based on a short aliphatic diamine

The reaction of *E*-**A** and **E** in dichloromethane led to the formation of an oligomeric or polymeric product $\mathbf{A^nE^n}$, that precipitated out of solution after three days, leaving the supernatant solution nearly colourless (Figure 73). The red powder was insoluble in any organic solvent tested, while the addition of large amounts of trifluoroacetic acid yielded a coloured supernatant solution over the partially still insoluble powder, most likely by decomposing the formed polymer. The insolubility hindered further analysis, yet the recorded IR spectrum of $\mathbf{A^nE^n}$ confirmed the formation of an imine species.

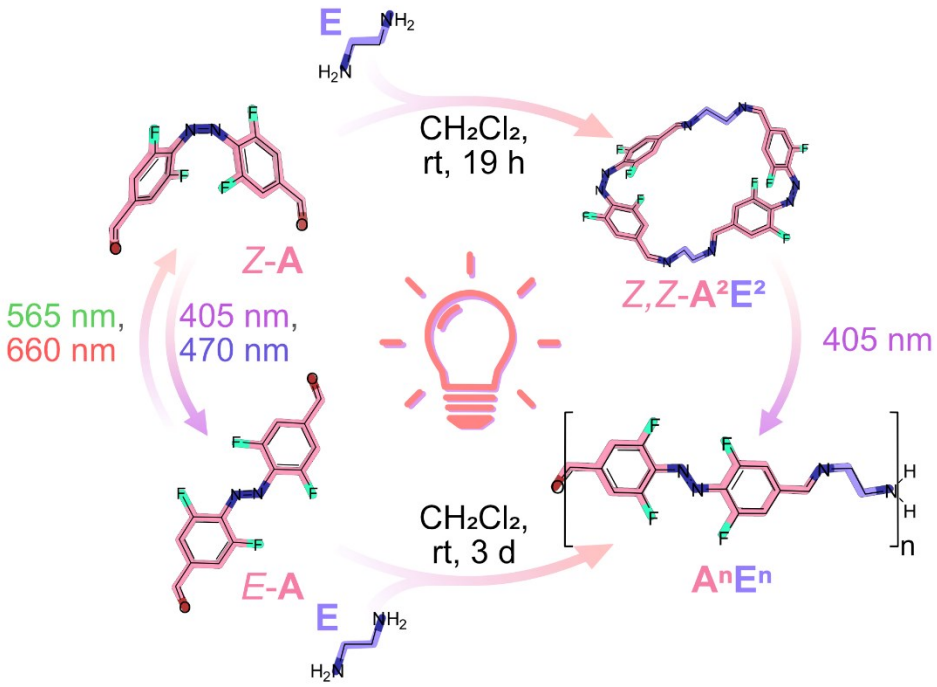

Figure 73: Reactions of **E** with *Z*-**A** forming an $\mathbf{A^2D^2}$ macrocycle and with *E*-**A** forming an $\mathbf{A^nE^n}$ oligomer. This figure was adapted from reference 97 with permission.

As $\mathbf{A^nE^n}$ could not be used as a precursor for macrocycle formation, the formation of macrocycles was attempted using *Z*-**A** and **E** as starting materials. The addition of **E** to a solution of **A** that had previously been irradiated with red light yielded an imine macrocycle. As the reaction was performed in *d*-dichloromethane, the formation could be observed by ^{1}H and ^{19}F{^{1}H} NMR (Figure 74). The distinct shifts of the signals of the protons for *Z*-**A** from 9.86 ppm to 8.18 ppm, as well as from 7.42 ppm to 7.23 ppm, confirmed the imine formation.

[6] Some parts of this work have been published: E. Nieland, J. Voss, A. Mix, B. M. Schmidt, *Angew. Chem. Int. Ed.* **2022**, *61*, e202212745.

Additionally, a significant upfield shift of the signals in the $^{19}F\{^{1}H\}$-spectrum shift from -117.67 ppm to -119.49 ppm was also observed.

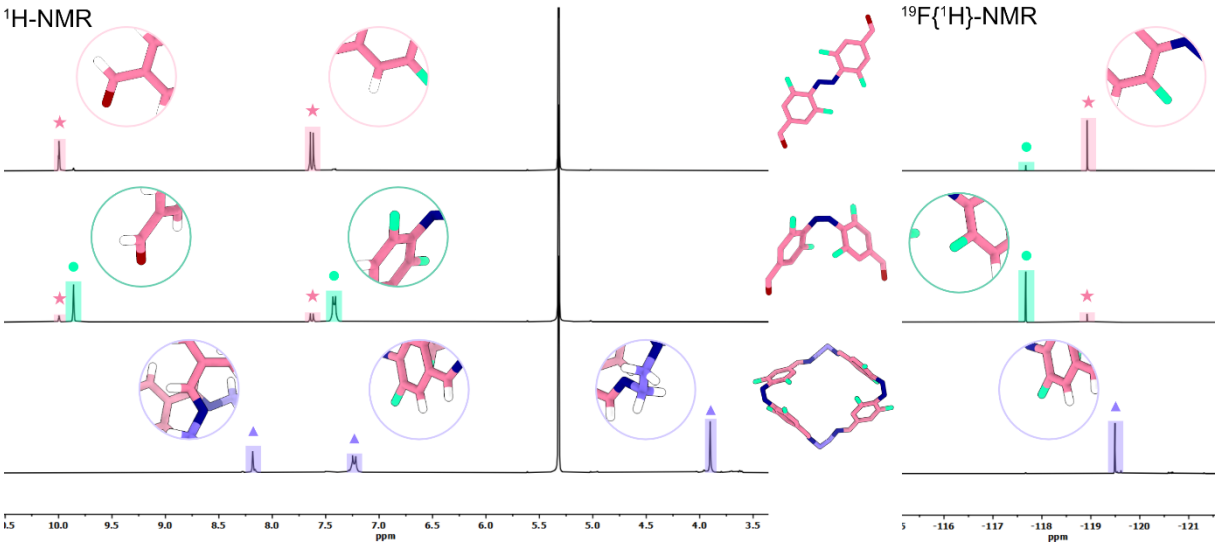

Figure 74: Excerpts of ^{1}H NMR and $^{19}F\{^{1}H\}$ NMR spectra showing the isomerisation of *E*-**A** (pink star) to *Z*-**A** (turquoise circle) after irradiation with red light (660 nm) and the following imine formation yielding *Z,Z*-$\mathbf{A^2E^2}$ 19 hours after the addition of **E** (CD_2Cl_2, 300 and 282 MHz, respectively). This figure was adapted from reference 59 with permission.

The mass of the macrocycle as determined by MALDI-mass spectrometry, 669.272, corresponds very well to the calculated mass of 669.176 for a protonated $\mathbf{A^2E^2}$ macrocycle (Figure S112). Slow liquid-liquid diffusion of EtOH into the reaction mixture led to the formation of dark red prismatic crystals that were suitable for single-crystal X-ray crystallography and gave further insight into the structure of *Z,Z*-$\mathbf{A^2E^2}$ (Figure 75). The asymmetric unit contains three *Z,Z*-$\mathbf{A^2E^2}$ macrocycles with very similar structures. Each bowl-shaped macrocycle consists of two azobenzene units that are pointing upwards, while the amine units are pointing downwards. The torsion angles for **E** are between 68.5° and 73.6°, being close to the stable *gauche* conformation (60°). The torsion angles for the azobenzenes lie between 7.25° and 12.38° and are in accordance with literature-known values of the *Z*-isomers of difluoro-,[78a] pentafluoro-,[78b] and various octafluoroazobenzenes[78c] whose torsion angles are between 8.88° and 12.07°. Hence, the bowl-shaped structure in the solid-state is a result of *Z*-**A**, and **E** being in the most stable conformation.

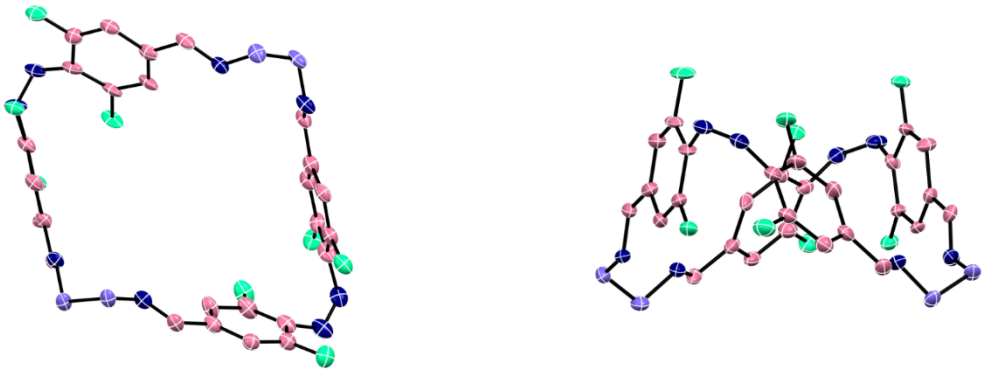

Z,Z-**A²E²**
top view

Z,Z-**A²E²**
side view

Figure 75: Single-crystal X-ray structure of one *Z*,*Z*-**A²E²** macrocycle as seen from the top and from the side. Thermal ellipsoid representation with 50% probability ellipsoids. Hydrogen atoms and solvent molecules are omitted for clarity. The crystal structure was obtained and refined by Dr. Bernd M. Schmidt. This figure was adapted from reference 97 with permission.

In solution, *Z*,*Z*-**A²E²** is metastable when kept in the dark. After a few days, a precipitate starts to form due to the slow thermal *Z* to *E* isomerisation and the concomitant decay of the *Z*-macrocycle, and the subsequently formed *E*-oligomers and polymers start to precipitate. The stability of the macrocycle can be enhanced by continuous irradiation with red light (660 nm), or the macrocycle can be deliberately destroyed by irradiation with UV light (405 nm). Judging by the distinctive colour change from orange to dark red after 5 minutes of irradiation with light of a wavelength of 405 nm, the former *Z*-enriched solution consisted of mostly *E*-isomers at that point. However, only a small amount of precipitate had formed. The irradiation was continued, and after 19 hours, a large amount of solid had precipitated out of solution and the supernatant solution was only lightly coloured. While the *Z* to *E* isomerisation can be induced quickly by irradiation with UV light, the formation of the oligomeric structure, with a length that causes precipitation, takes longer (Figures S155-S157).

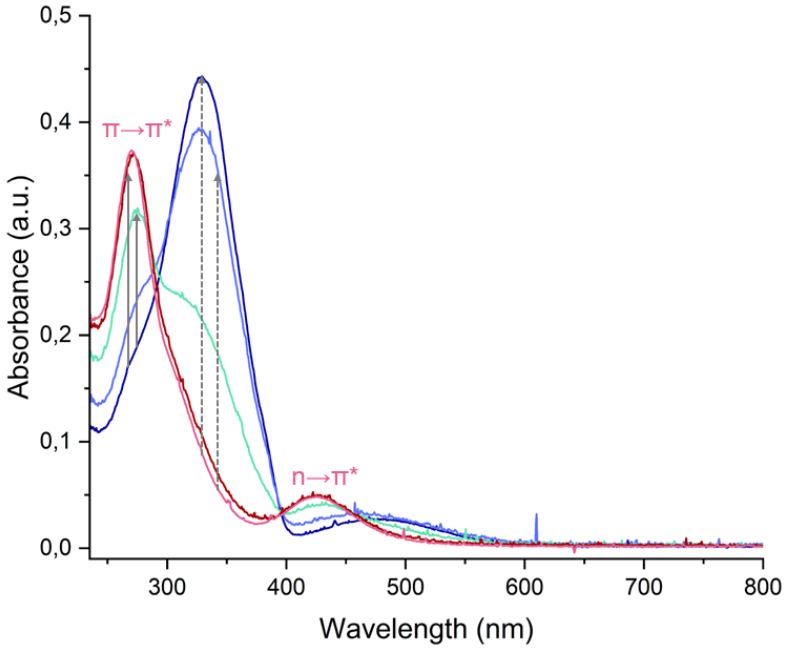

Figure 76: UV/VIS spectra of *Z*,*Z*-**A²E²** (pink curve), after irradiation with light of a wavelength of 405 nm (dark blue curve) for 120 seconds and 470 nm (light blue curve) for 120 seconds. A solution that was *E*-enriched by irradiation with UV light (405 nm) was irradiated with light of a wavelength of 660 nm for 21 hours (dark red curve) and 565 nm for 10 minutes (turquoise curve). The solid grey arrows indicate *E* to *Z* isomerisation while the dashed arrows indicate *Z* to *E* isomerisation.

In small concentrations (6.98 µmol), the azobenzenes in *Z*,*Z*-**A²E²** can be isomerised using light of a wavelength of 405 nm or 470 nm, and *vice versa* using 565 nm or 660 nm (Figure 76). *Z* to *E* isomerisation using UV light (405 nm) leads to a higher ratio of *E*-isomers, judging by the shape of the UV/VIS spectrum. This is due to the significant higher absorption of the n→π* band of *Z*,*Z*-**A²E²** in comparison to the n→π* of the *E*-isomer which is shifted to higher wavelengths. Using either green (565 nm) or red light (660 nm), the compound can be isomerised back to *Z*,*Z*-**A²E²**, with both processes taking significantly longer than the reversed isomerisations. The irradiation with red light again yields the higher ratio of *Z*-azobenzene, producing a spectrum that is very similar to the starting material. The *Z* to *E* isomerisation is again significantly faster than the reverse isomerisations. While it can be assumed that the *Z,Z*-**A²E²** macrocycle should be more stable than the *E,Z*-**A²E²** or *E,E*-**A²E²** isomers, which could possibly slow down or hinder the formation of these species, the dynamic nature of the imine bond allows the opening of the macrocycle and therefore prevents that steric hindrance or ring strain hinders the *Z* to *E* isomerisation. In comparison to the UV/VIS spectra of other azobenzene derivatives studied in this thesis, fewer isosbestic points are observable. There is no isosbestic point in the region of 290 nm, and the isosbestic point in the region of 460 nm is less defined. This further indicates that more processes than simple isomerisation take place upon irradiation. While no obvious precipitation could be observed during the isomerisation experiments, the formation of open and oligomeric species is very likely.

Conversion of oligomers into discrete macrocycles

The initial experiments with the aliphatic diamine, **E**, highlighted the distinct differences between the structures that are accessible when either *E*-**A** or *Z*-**A** are employed. The obtained *Z,Z*-$\mathbf{A^2E^2}$ macrocycle could be transformed into the imine oligomer. Due to the insolubility of the *E*-**A**-based oligomer, reversible switching between the two structures obtained was not possible. To generate more soluble systems, the longer aliphatic diamines 1,3-diaminopropane (**Pr**), 1,4-diaminobutane (**B**), and 1,6-diaminohexane (**H**) were chosen as building blocks. The anticipated change in the solubility of the products should enable the synthesis of two distinctively different products, depending on the isomer employed and the switching between oligomeric and macrocyclic (Figure 77).

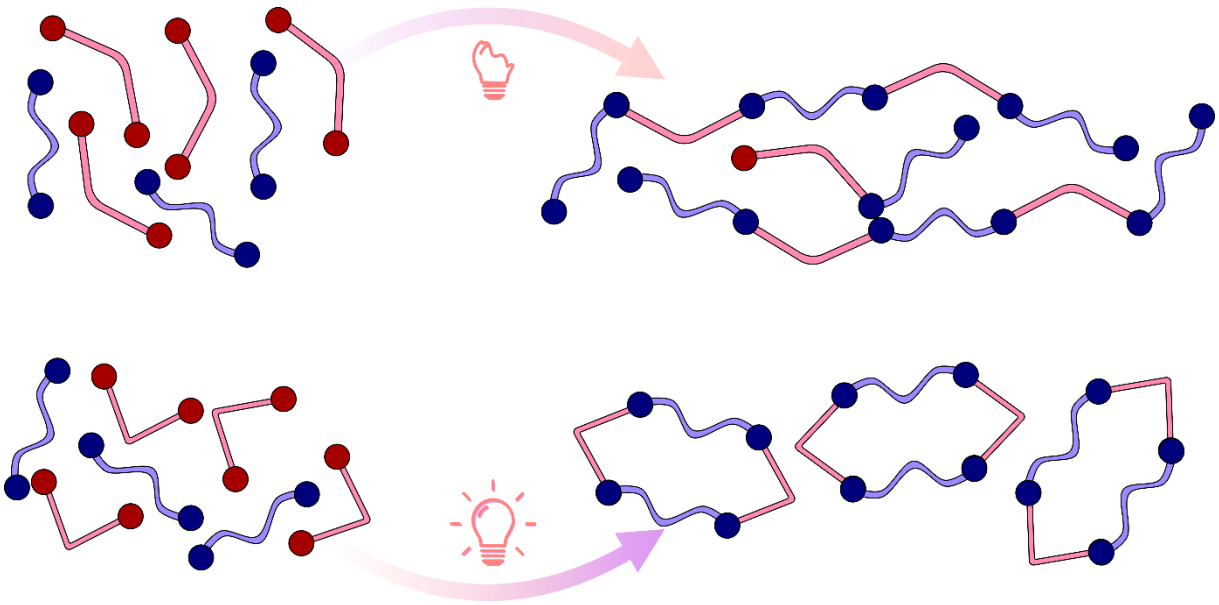

Figure 77: Schematic representation of the anticipated reactions of the azobenzene isomer *E*-**A** with either **Pr**, **B**, or **H** to form oligomeric species (top) and of *Z*-**A** with the same amines to form discrete macrocyclic species (bottom). The enhanced solubility should enable switching between both products. The azobenzene isomers are depicted as pink sticks, while the amines are depicted in blue.

As anticipated, the reaction of azobenzene *E*-**A** and diamine **B** in *d*-chloroform led to the formation of acyclic products, as monitored by ^{1}H and ^{19}F{^{1}H} NMR (Figure S116 and 78). A signal for the residues of unreacted starting material *E*-**A** was observed at -117.84 ppm. Based on the observations made during the formation of the model compound $\mathbf{AC^2}$ (Section 3.2.1), the signals -118.65 ppm and -118.81 ppm were assigned to a monofunctionalised azobenzene, and the signals in the region between -119.67 ppm and -119.72 ppm to bisimine species. The defined shape of the first indicated that the product formed is most likely **AB** instead of different species with the general formula of $\mathbf{A^nB^n}$, while the different overlapping signals for the latter indicated the formation of different $\mathbf{A^nB^{n+1}}$ bisimine species. The products are formed in a ratio of 8:40:42 (aldehyde:monoamine:bisimine). The product distribution

depends, among others, on the concentration of the starting materials, with lower concentrations leading to a higher amount of residual starting materials and higher concentrations to more oligomeric bisimine species after the same reaction time (Figure S131-S133).

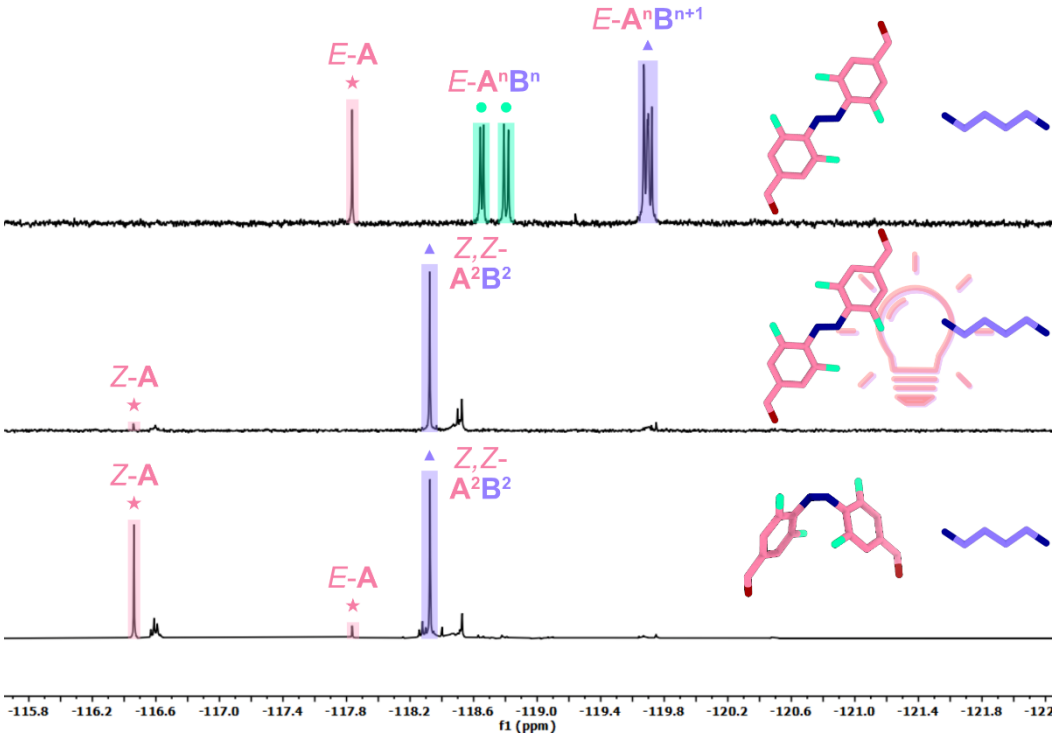

Figure 78: Excerpts of $^{19}F\{^{1}H\}$ NMR spectra showing the reaction of *E*-**A** and **B** forming oligomers, the **A²B²** macrocycle that is formed by irradiation of the oligomeric mixture with red light (660 nm), and the macrocycle formation starting from *Z*-**A** and **B** ($CDCl_3$, 282 MHz). Signals of **A** are highlighted in pink (star), monofunctionalised species are highlighted in turquoise (circle) and bisimine species and macrocycles are highlighted in blue (triangle).

To see whether the combination of *Z*-**A** and diamine **B** also led to the formation of macrocycles comparable to the formation of the macrocycle *Z,Z*-**A²E²** based on azobenzene **A** and ethylenediamine **E**, the reaction was monitored in *d*-chloroform. The resulting $^{19}F\{^{1}H\}$ NMR spectra revealed the remains of unreacted starting material (-116.46 ppm) and the formation of one major product (-118.32 ppm). A MALDI-mass spectrum that was recorded confirmed that the preferred macrocyclic species that is formed is an *Z,Z*-**A²B²** macrocycle. The irradiation of the acyclic product mixture, obtained by the reaction of azobenze *E*-**A** and diamine **B**, also led to the formation of the macrocyclic product *Z,Z*-**A²B²** with only minor amounts of residual *Z*-**A**, demonstrating that it is possible to use a mixture of unreacted azobenzene and different products to generate the macrocyclic product *Z,Z*-**A²B²** with high selectivity.

The employment of the longer aliphatic diamine analogue, 1,6-diaminohexane **H**, also led to the formation of acyclic species in combination with *E*-**A** in *d*-chloroform (Figures S122 and

79). Residues of the azobenzene starting material (*E*-**A**) were again observed at -117.84 ppm, while signals for the monosubstituted azobenzene were visible at -118.67 ppm and -118.82 ppm. In contrast to the previously discussed reaction of *E*-**A** and **B**, different overlapping signals were observed, indicating that with **H**, not only the acyclic monosubstituted species **AH** was formed but probably species of different lengths with the general formula of $\mathbf{A^nH^n}$. Difunctionalised azobenzenes, described with the general formular of $\mathbf{A^nH^{n+1}}$, were formed as the major product with a percentage of 58% and cause different overlapping signals at -119.75 ppm. Again, the distribution of the products after a specific reaction time can be altered by changing the concentration of the samples (Figures S143-S145)

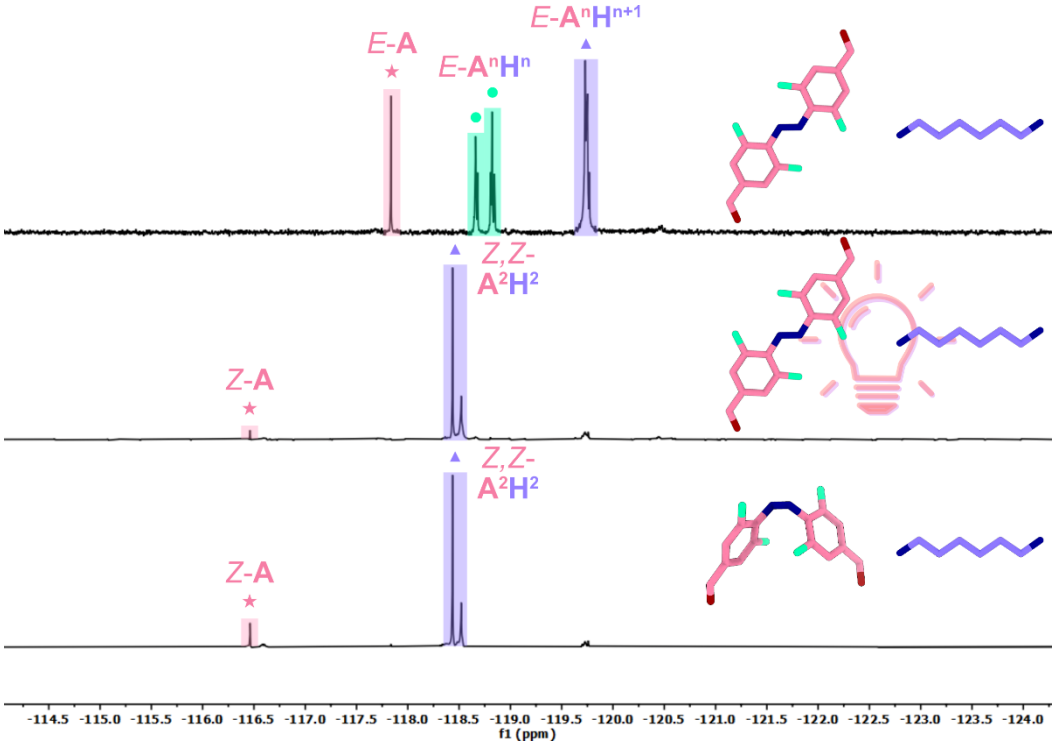

Figure 79: Excerpts of $^{19}F\{^1H\}$ NMR spectra showing the reaction of *E*-**A** and **H** forming oligomers, the $\mathbf{A^2H^2}$ macrocycle that is formed by irradiation of the oligomeric mixture with red light (660 nm), and the macrocycle formation starting from *Z*-**A** and **H** ($CDCl_3$, 282 MHz). Signals of **A** are highlighted in pink (star), monofunctionalised species are highlighted in turquoise (circle) and bisimine species and macrocycles are highlighted in blue (triangle).

Employing the other azobenzene isomer, *Z*-**A**, in combination with **H** led to the formation of a macrocyclic species, as anticipated. According to the MALDI-mass spectra that were recorded for the sample, the signal at -118.44 ppm can most likely be assigned to a *Z,Z*-$\mathbf{A^2H^2}$ macrocycle (Figure S124). Again, the macrocyclic species was also accessible by irradiation with red light (660 nm) of the oligomeric mixture obtained in the dark. The additional smaller signal at -118.52 ppm that is formed in both cases could be due to the increased flexibility of the macrocycle, allowing it to adapt different conformations in solution, or it could be due to another

macrocycle that varies in size. In both reactions, signals that were assigned to unreacted *Z*-**A** azobenzene were visible at -116.46 ppm.

1,3-Diaminopropane, **Pr**, was also combined with *E*-**A** to generate oligomeric structures. While signals for the unreacted azobenzene *E*-**A** (-117.84 ppm), the monofunctionalised aldehydes (-119.00 and -119.07 ppm), and the bisimines (-120.36 ppm) were observed in *d*-chloroform, additional signals were also visible indicating the formation of other products (Figure 80). These signals cannot be conclusively assigned to specific products, but their formation seems to be favourably affected by employing a slight excess of diamine (1.2 equivalents) and by higher concentrations, as these signals are significantly smaller when using only 1.0 equivalent and decreasing the concentration (Figure S128-S130).

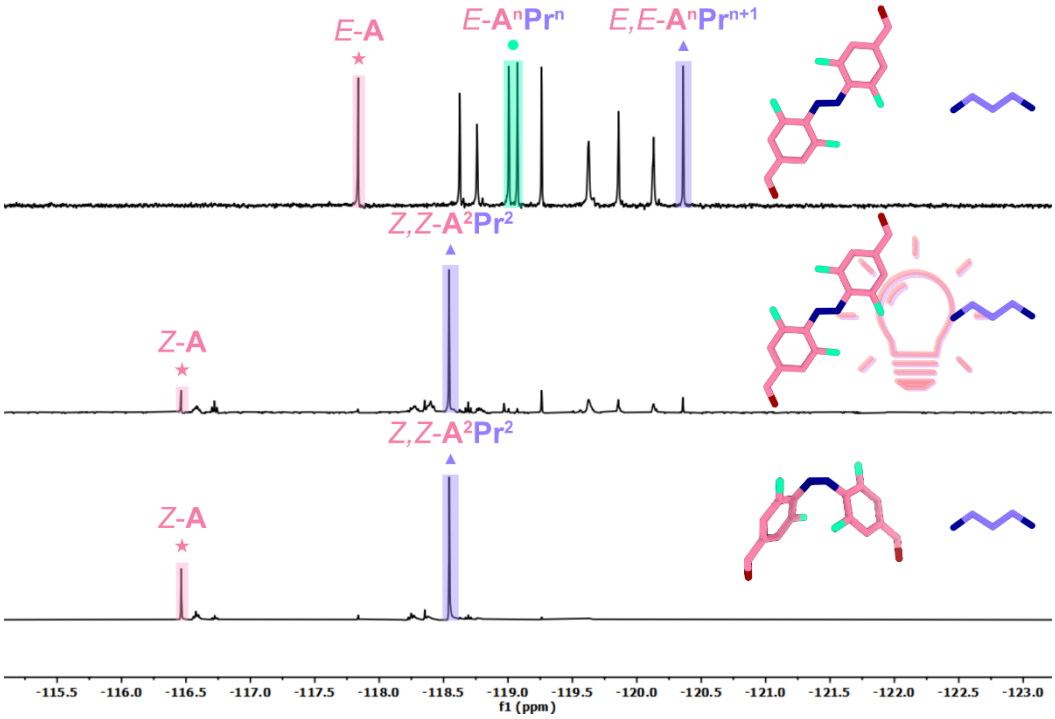

Figure 80: Excerpts of $^{19}F\{^{1}H\}$ NMR spectra of the azobenzene isomers *E*-**A** and *Z*-**A**, the reaction of *E*-**A** with **Pr**, forming a mixture of products, and the irradiation of the mixture with red light (660 nm), yielding the macrocycle **A²Pr²**, and the formation of **A²Pr²** starting from *Z*-**A** and **Pr** ($CDCl_3$, 282 MHz). Signals of **A** are highlighted in pink (star), monofunctionalised species are highlighted in turquoise (circle) and bisimine species and macrocycles are highlighted in blue (triangle).

The combination of a *Z*-enriched solution of **A** with **Pr** led to the formation of a macrocyclic species after three days under continuous irradiation with red light (660 nm), as visible by the formation of a sharp signal at -118.54 ppm. MALDI-mass spectrometry revealed the composition of the macrocycle to be *Z;Z*-**A²Pr²** (Figure S115). This macrocycle could also be synthesised by irradiating the oligomeric mixture with red light for three days.

To conclude, employing the different diamines **Pr**, **B**, and **H** in combination with *E*-**A** led to the formation of acyclic species, while using the other azobenzene isomer *Z*-**A** with the same diamines led to the preferred formation of *Z,Z*-$\mathbf{X^2Y^2}$ macrocycles. Attempts to either isolate or crystallise these macrocycles have not been successful yet, and the prolonged and continuous malfunctioning of the NMR in Düsseldorf unfortunately prevented the recording of DOSY NMR spectra to conclusively verify the composition of the macrocycles. Even though a small excess of diamine is employed in all reactions, unreacted azobenzene, either *E*- or *Z*-**A**, can be observed in all reactions. As the formation of the imine species is in equilibrium, it was shown that the product distribution can be altered by changing the concentration of the solution. This is in accordance with observations made in the formation of supramolecular polymers. The ring-chain equilibrium describes the preferred formation of macrocyclic species in low concentrations and the formation of oligomers and polymers in higher concentrations.[107] The systems investigated allow the transient generation of discrete macrocycles with high selectivity, starting from a mixture of different acyclic species by irradiation.

The macrocycles discussed in this section are all composed of an aliphatic diamine and *Z*-**A**. Upon *Z* to *E* isomerisation, the macrocycles decompose, forming oligomers of different lengths. Attempts were made to prevent this decomposition and transform the metastable imine macrocycles into more stable amine macrocycles. The photochemical properties of the macrocycle and the stability of the respective *Z*-isomer should be dependent on the length of the employed diamine, with $\mathbf{A^2E^2_{red}}$ probably showing a significantly higher degree of stability for the *Z*-isomer than $\mathbf{A^2H^2_{red}}$. Even though there are already several examples of macrocycles based on *Z*-azobenzenes[108] and even a whole class of photoswitches, the diazocines,[42] whose *Z*-isomers show a higher stability, the easy access to a variety of different macrocycles composed of different diamines would allow a systematic investigation of the influence of flexibility and ring strain in the macrocycles on the photochemical properties.

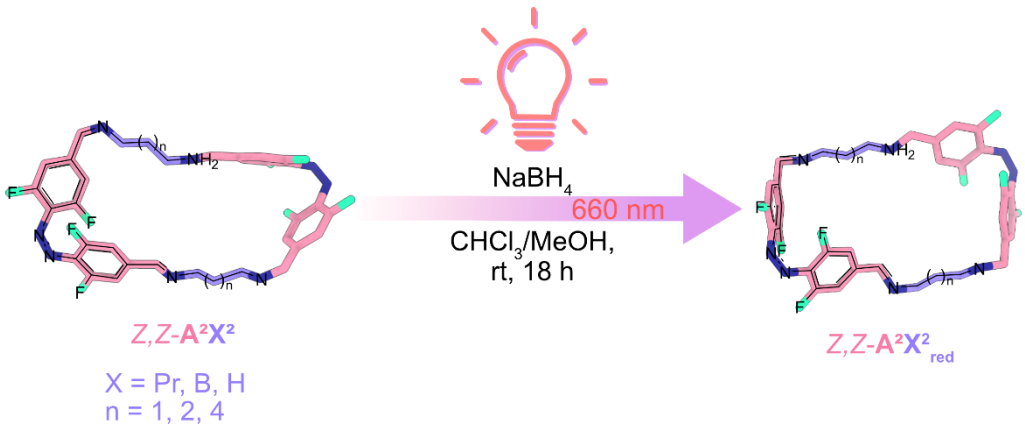

Figure 81: Reduction of imine macrocycles $\mathbf{A^2X^2}$ to the corresponding amine macrocycles $\mathbf{A^2X^2_{red}}$.

To prevent the dynamic covalent formation of the oligomers, an attempt was made to reduce the macrocycles to their corresponding amine compounds. The conditions and the reducing agent were chosen based on the procedure published by Tanaka *et al.*[96c] and previous experiences with the reduction of **A^{3}D^3** to **A^{3}D$^3_{red}$**. As there is no established method to isolate the *Z*-macrocycles yet, **A^{2}Pr^2**, **A^{2}B^2**, and **A^{2}H^2** were generated *in situ* in chloroform, and methanol and sodium borohydride were added once the ^{19}F{^{1}H} NMR spectra showed the formation of the targeted macrocycle (Figure 81). Due to the lower concentration of the *Z*-macrocycles in comparison to the literature procedures, two attempts were made to generate the amines with differing numbers of equivalents of sodium borohydride.

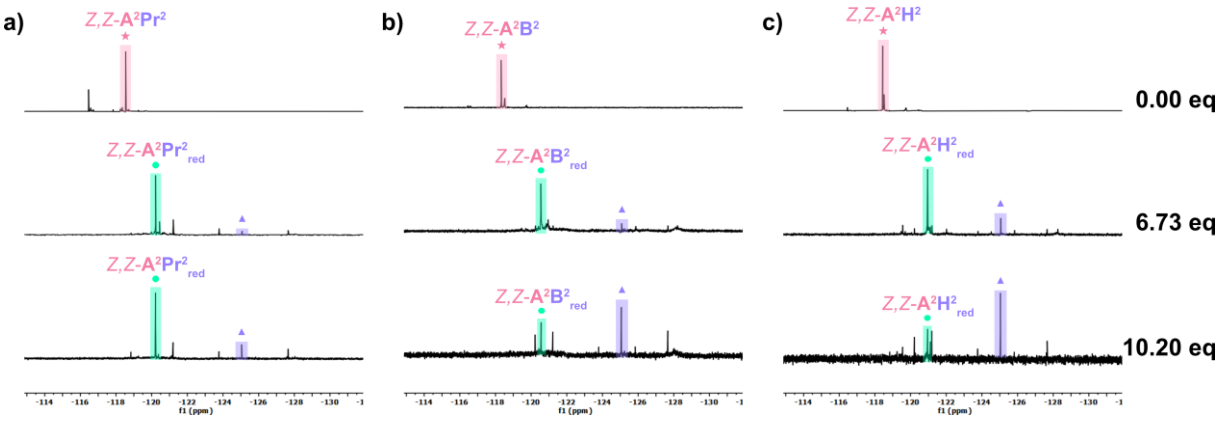

Figure 82: Excerpts of the ^{19}F{^{1}H} NMR spectra of a) **A^{2}Pr^2**, b) **A^{2}B^2**, c) **A^{2}H^2**, and their respective, attempted reductions using either 6.73 or 10.2 equivalents of sodium borohydride ($CDCl_3$, 282 MHz). Imine macrocycles are highlighted in pink (star), signals for amine macrocycles are highlighted in turquoise (circle) and signals that can possibly be assigned to hydrazines are highlighted in blue (triangle).

The reactions were carried out for 18 hours under continuous irradiation with red light to minimise possible oligomer formation during the course of the reaction. The ^{19}F NMR spectra that were obtained after work-up showed that using differing amounts of sodium borohydride indeed led to the formation of an amine macrocycle, while using larger amounts also led to the formation of signals that can most likely be assigned to azobenzene species that have been reduced to hydrazines (Figure 82). The yields in the different attempts were all low, and the product formation was accompanied by the formation of large amounts of insoluble, possible oligomeric or polymeric species. As no precipitate formation was observed during the reaction, the insoluble species are most likely imine species that formed during the work-up procedure, indicating incomplete conversion; prolonging the reaction times could prevent this. Carrying the reaction out at lower temperatures and choosing a reaction setup in which the sodium borohydride is added to the mixture over a longer period should favour the reduction of the imine bond, preventing further reductions and improving the yield. Alternatively, the use of

other less reactive reducing agents like sodium cyanoborohydride could lead to the selective formation of the amine macrocycles. Arylhydrazines in general can also be converted to azobenzenes using different oxidants,[109] but to generate the targeted amine macrocycle, this oxidation would need to be very selective.

Generating box like macrocycles

The aliphatic diamines 1,3-propanediamine **Pr**, 1,4-butanediamine **B**, and 1,6-hexanediamine **H** were able to either form a mixture of acyclic products or macrocycles depending on the isomer employed in the reaction. To see whether other diamines show the same behaviour, structurally similar diamines 1,5-pentanediamine **Pe** and ethylenglycoldiamine (**O**) were both employed with the different azobenzene isomers.

The reaction of *E*-**A** with **Pe** in *d*-chloroform was monitored by ^{1}H and $^{19}F\{^{1}H\}$ spectroscopy, revealing that the product mixture obtained contained residues of the starting material *E*-**A** (-117.83 ppm), as well as minor amounts of monosubstituted imine species of the general formula of $\mathbf{A^nPe^n}$ (-118.65 ppm and -118.81 ppm) (Figures S119 and 83). The major product of the reaction caused a sharp singlet at -119.15 ppm. The shape of the signal as well as the smaller upfield shift, in comparison to the signals for the $\mathbf{A^nPe^n}$ species, varied distinctively from the results obtained from the reactions of the other aliphatic diamines, which led to different overlapping signals with a larger upfield shift. This indicated that the preferred product of the reaction of diamine **Pe** and azobenzene isomer *E*-**A** is not a mixture of different bisimine species but might be a distinct macrocycle. This was further confirmed by MALDI-mass spectrometry, which showed a signal at 753.323, which aligns with the calculated mass of 753.270 for a protonated $\mathbf{A^2Pe^2}$ macrocycle.

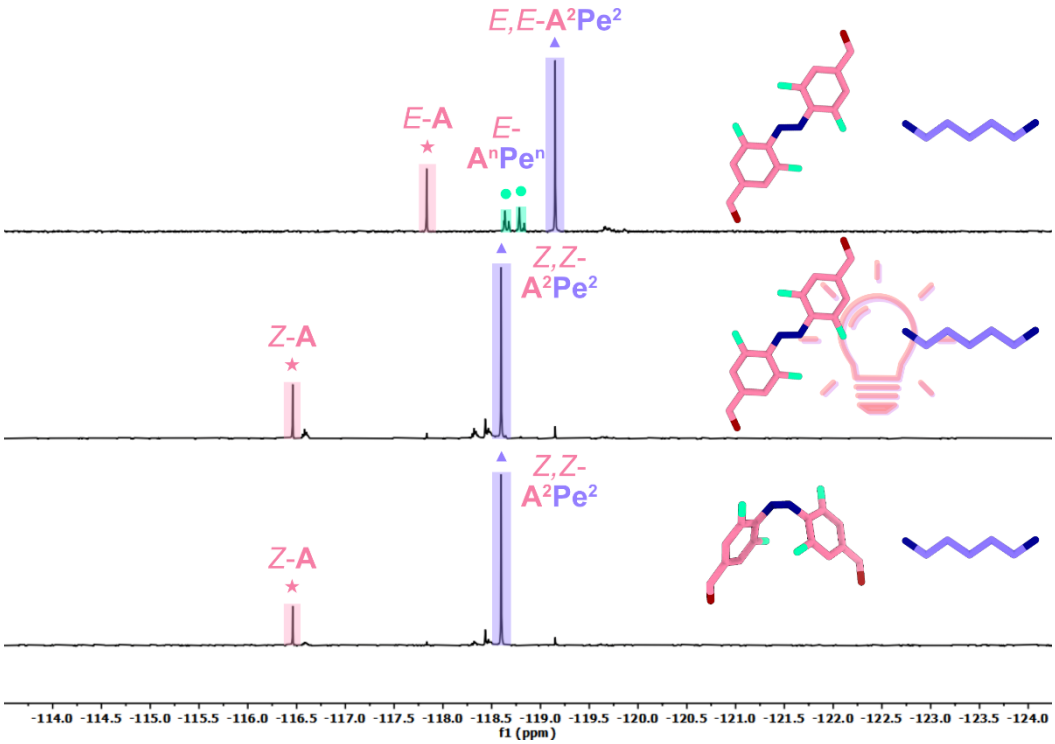

Figure 83: Excerpts of $^{19}F\{^{1}H\}$ NMR spectra showing the reaction of *E*-**A** and **Pe** forming a mixture of products, the **A²Pe²** macrocycle that is formed by irradiation of the mixture with red light (660 nm), and the macrocycle formation starting from *Z*-**A** and **B** ($CDCl_3$, 282 MHz). Signals of **A** are highlighted in pink (star), monofunctionalised species are highlighted in turquoise (circle) and bisimine species and macrocycles are highlighted in blue (triangle).

Diamine **Pe** was then combined with the other azobenzene isomer, *Z*-**A**, also yielding one preferred, probably macrocyclic product (-118.60 ppm) accompanied by residues of *Z*-**A** (-116.46 ppm). MALDI-mass spectrometry confirmed the preferred product to be the *Z,Z*-**A²Pe²** macrocycle. Irradiation of the initially formed *E,E*-**A²Pe²** with red light (660 nm) showed the isomerisation of the formed macrocycle without any changes in the stoichiometry of the monomers. Decreasing or increasing the concentration of the starting materials always led to the formation of the above-mentioned products, with lower concentrations leading to higher ratios of residual starting material and monofunctionalised species after the same reaction time. In higher concentrations, the **A²Pe²** macrocycle was the major product after three or four days, respectively (Figures S138-S140).

As the reaction of both isomers of **A** with **Pe** led to the selective formation of an **A²Pe²** macrocycle, it should be possible to generate other similar macrocycles based on **A**. These structurally similar macrocycles are anticipated to also undergo geometrical changes without a change in stoichiometry. To possibly alter the properties of the obtained macrocycle, the structure of the employed diamine was varied. Diethylene glycol bisamine (**O**) was synthesised following an established procedure.[110] Ethylene glycol was reacted with triethylamine and tosylchloride, forming tosylate **43**. As tosyl groups are good leaving groups, these can be

replaced in a nucleophilic substitution using sodium azide. The obtained azido compound **44** can be reduced using palladium on charcoal and hydrogen, giving the targeted amine **O** with an overall yield of approximately 66% (Figure 84).

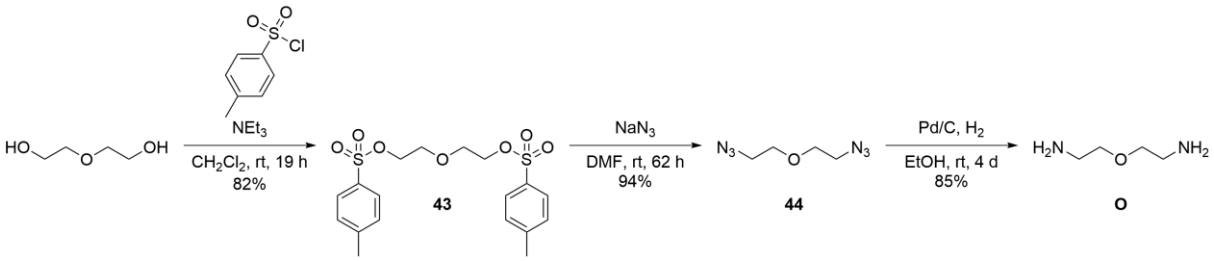

Figure 84: Synthesis of **O** starting from ethylene glycol.

Due to the poor solubility of **O** in dichloromethane or chloroform and the reduced solubility of the azobenzene compound **A** in methanol or ethanol, the reaction needed to be performed in a mixture of dichloromethane and ethanol (Figure 85). The composition of the macrocycle was confirmed to be *E,E*-$\mathbf{A^2O^2}$ by mass spectrometry, while further methods like DOSY NMR experiments were hindered by the reduced solubility of the product.

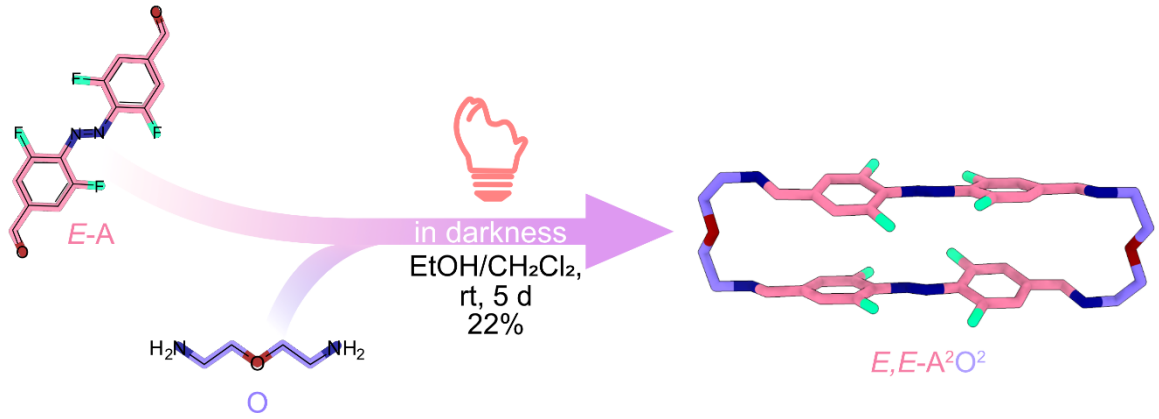

Figure 85: Synthesis of $\mathbf{A^2O^2}$.

The obtained macrocycle can be photoisomerised from *E* to *Z* using red (660 nm) or green light (565 nm), and *vice versa* using UV light (405 nm). Following the same trends regarding speed and efficiency as the previously discussed macrocyclic structures (Figure 86).

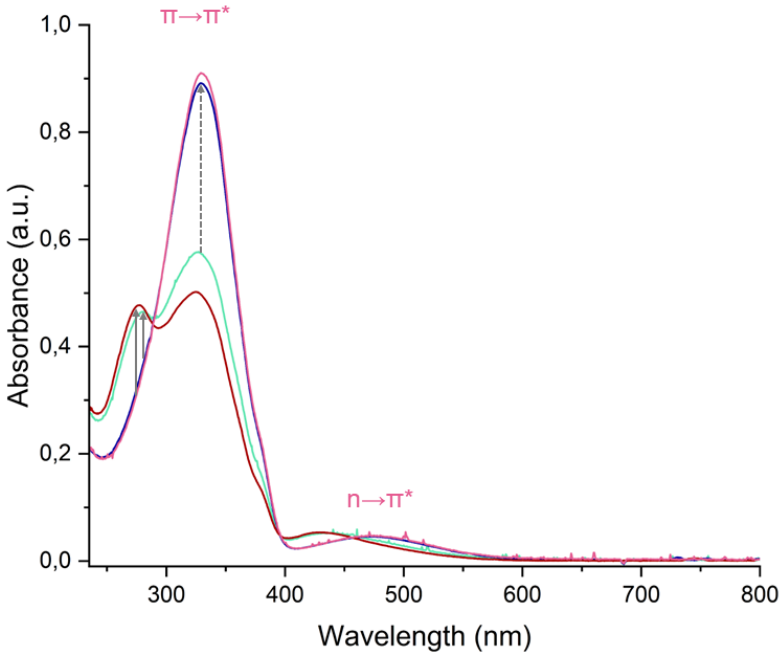

Figure 86: UV/VIS spectra of *E,E*-**A²O²** (pink curve), after irradiation with light of a wavelength of with light of a wavelength of 660 nm for 240 minutes (dark red curve) and 565 nm for 20 minutes (turquoise curve). A solution that was *E*-enriched by irradiation with green light (565 nm) was irradiated with light of a wavelength of 405 nm (dark blue curve) for 60 seconds. The solid grey arrows indicate *E* to *Z* isomerisation while the dashed arrows indicate *Z* to *E* isomerisation.

Vapor diffusion of diethyl ether into a mixture of dichloromethane and ethanol led to the formation of crystals suitable for X-ray crystallography. While the first modification shows one box-shaped *E,E*-**A²O²**, macrocycle, the second modification contains two *E,E*-**A²O²** macrocycles that slightly vary in their shape (Figure 87). One of those macrocycles, as well as the structure obtained from the first measurement, contains slightly twisted azobenzene units, leading to an overall twisted structure of the macrocycle. The second macrocycle, in contrast, is constructed of azobenzenes that are much less twisted.

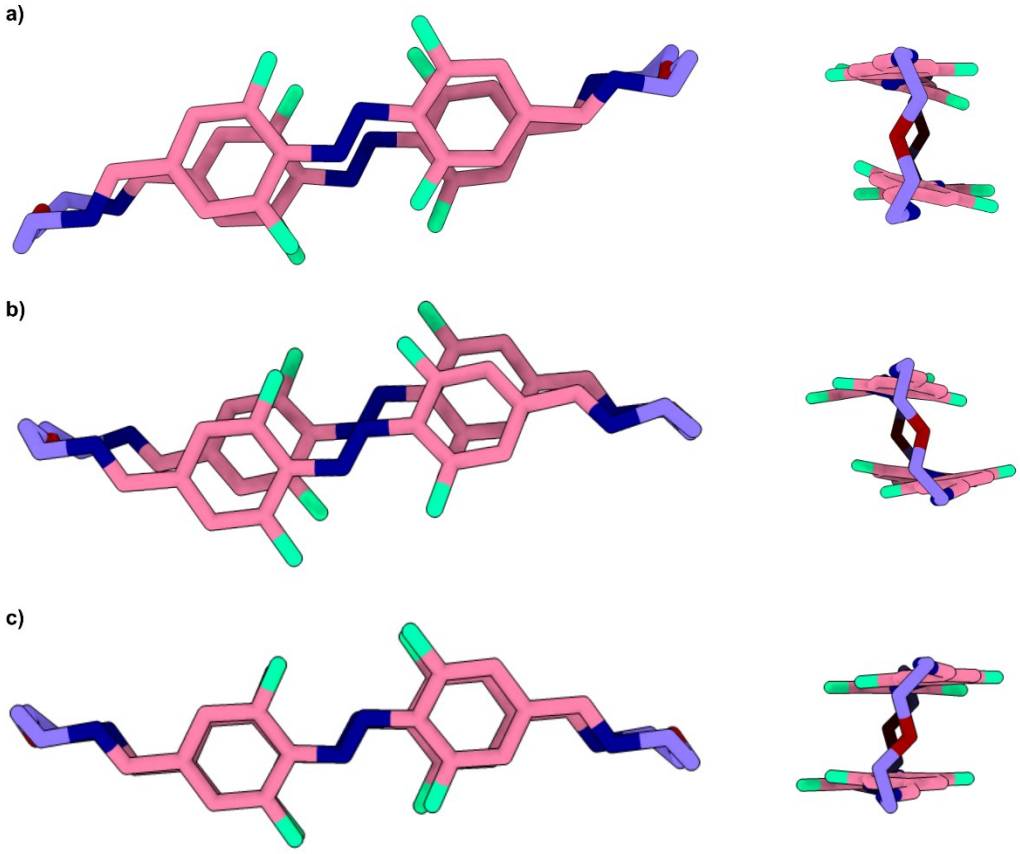

Figure 87: Crystal structures obtained for the *E,E*-**A²O²** macrocycle a) as observed in the first modification b) and c) structures of *E,E*-**A²O²** as obtained from the second modification.

Focusing on the ethylene glycol units in the obtained crystal structures reveals the reason why the formation of this macrocyclic structure, and the formation of *E,E*-**A²Pe²** are preferred. The torsion angles in all macrocycles range between 58.7 and 70.8°, which is very close to the stable gauche conformation of 60°. The gauche effect, which was thoroughly studied for similar structures like polyethylene oxide,[111b] leads to a higher stability of the gauche conformation in comparison to the normally preferred *anti* conformation due to sterio-electronic effects.[111] This introduces a certain precoordination in otherwise flexible building blocks like **O**, making them suitable building blocks for the formation of macrocycles, as already observed by the group of Lehn.[112]

Summary

Employing flexible diamines of different lengths in combination with both azobenzene isomers *E*-**A** and *Z*-**A** makes a variety of oligomers and macrocycles accessible. The combination of **E** and **A** either led to the formation of an insoluble imine oligomer when the starting materials and the reaction were kept in the dark or to the formation of metastable azobenzene macrocycles. *Z,Z*-**A²E²** adapts a bowl-like structure in the solid-state as observed by single-crystal X-ray crystallography and can be selectively stabilised by irradiation with red light (660 nm) or transformed into the insoluble oligomer **AⁿEⁿ** by irradiation with UV light (405 nm).

Unfortunately, the initial goal of using the *E*-**A**-based oligomer as a resting state that can be transformed into the strained macrocycle was hindered by the insolubility of the formed species. To enhance the solubility without introducing groups that induce a large amount of precoordination, the focus shifted to longer diamines. While employing **Pr** and *E*-**A**, the formation of several possibly oligomeric species was observed, as confirmed by NMR and MALDI-mass spectrometry, but the large number of products and the accompanying formation of precipitates were not ideal, even though the mixture could be selectively converted into one macrocyclic species by irradiation with red light. The *Z,Z*-$\mathbf{A^2Pr^2}$ macrocycle was also accessible by using *Z*-**A** as a starting material. Longer diamines like **B** and **H** allowed the formation of oligomeric species, which did not precipitate from solution and can also be transformed into *Z,Z*-$\mathbf{A^2B^2}$, and *Z,Z*-$\mathbf{A^2H^2}$ macrocycles, respectively. The formation of more than one peak upon irradiation of the mixture and when employing *Z*-**A** as a starting material is possibly due to the formation of different-sized macrocycles, as indicated by the analysis of the recorded MALDI-mass spectra showing peaks for macrocycles between $\mathbf{A^2B^2}$ and $\mathbf{A^6B^6}$, and $\mathbf{A^2H^2}$ and $\mathbf{A^7H^7}$, respectively. Another possible reason for the presence of two signals with very similar shifts for both diamines could be a macrocycle that adapts different conformations due to its comparably flexible diamine.

When employing the diamines of different lengths, the group of Cooper could observe an odd-even effect with the lengths of the diamine having an impact on the formed cage topology, which can be rationalised by the adapted zigzag structure of alkyl chains leading towards the amines being located on the same side without introducing strain into the alkyl chain.[104] The macrocycle formation behaviour of **Pe**, which has an odd chain length, also varies from that of **E**, **B**, and **H**. Instead of an oligomeric or polymeric product, the combination of **Pe** and *E*-**A** led to the clean formation of an *E,E*-$\mathbf{A^2Pe^2}$ macrocycle. The isomerisation of the mixture or the use of *Z*-**A** as a starting material also led to the formation of an $\mathbf{A^2Pe^2}$ macrocycle as the preferred product. Further investigations into the product distribution obtained from the different diamines as well as experiments with longer aliphatic diamines having an odd and even number of carbon atoms could show whether the trend in the formations observed can also be applied to other diamines. The structurally similar macrocycle *E,E*-$\mathbf{A^2O^2}$, could be synthesised, and the obtained crystal structures give an interesting insight into the structure, showing that the gauche conformation of **O** is beneficial for the construction of macrocycles.

To conclude, two structurally similar macrocycles, $\mathbf{A^2Pe^2}$ and $\mathbf{A^2O^2}$, were synthesised, whose ability to isomerise without decomposing or undergoing rearrangements could make them convenient targets for applications like photocontrolled guest release. The combination of azobenzene **A** with linear diamines enabled the selective formation of different macrocycles out of mixtures containing several different products.

3.2.4 Synthesis of photoresponsive imine cages

Introduction

Cages, just like macrocycles, can be designed to be photoresponsive by the implementation of photoswitches.[5d] While the first photoswitchable imine cages based on azobenzenes were synthesised by the group of Vögtle in 1992,[70] the structures were recently rediscovered by different groups.[71,89,113] The cage based on 4,4'-(diazene-1,2-diyl)dibenzaldehyde was recently used by Khashab *et al.* to separate *p*-xylene from its isomers by crystallisation,[113] while the group of Wang reduced the same cage and showed that the amine cage has an improved photoisomerisation efficiency in comparison to the corresponding individual amine azobenzene.[89]

The group of Feringa employed another cage reported by Vögtle based on the regioisomeric 3,3'-(diazene-1,2-diyl)dibenzaldehyde, showing that the isomerisation enabled the opening of the cage and even the irreversible transformation into another, non-switchable imine cage, which would not be accessible from the *E*-isomer.[71] This example is more thoroughly discussed in Section 1.4.2.

Cages based on a photoswitch with more beneficial photochemical properties should allow an isomerisation with a higher ratio of *Z*-isomers in the photostationary state and a longer half-life, facilitating analysis. To investigate whether the implementation of **A** into an imine cage could also lead to the formation of cages with other stoichiometries upon irradiation, analogous to the transformation of $\mathbf{A^3D^3}$ to $\mathbf{A^2D^2}$, cage synthesis was attempted with tris(2-aminoethyl)amine (**Tren**) as well as with the more rigid amine (2,4,6-triethylbenzene-1,3,5-triyl)trimethanamine (**Et**).

Synthesis of a $\mathbf{Tri^2Di^3}$ cage based on *E*-A

The initial proposed synthesis of the non-fluorinated analogue uses a Soxhlet extractor, elevated reaction temperatures, and comparably short reaction times,[70] yielding the cage in comparably low yields. The group of Khashab adapted the procedure, increasing the yield from 22 to 73%.[113] The procedure for the reaction of **Tren** and *E*-**A** was based on this procedure. Using a solvent mixture of ethanol and chloroform led to the precipitation of the imine cage *E,E,E*-$\mathbf{A^3Tren^2}$ after 18 hours with a yield of 71% (Figure 88).

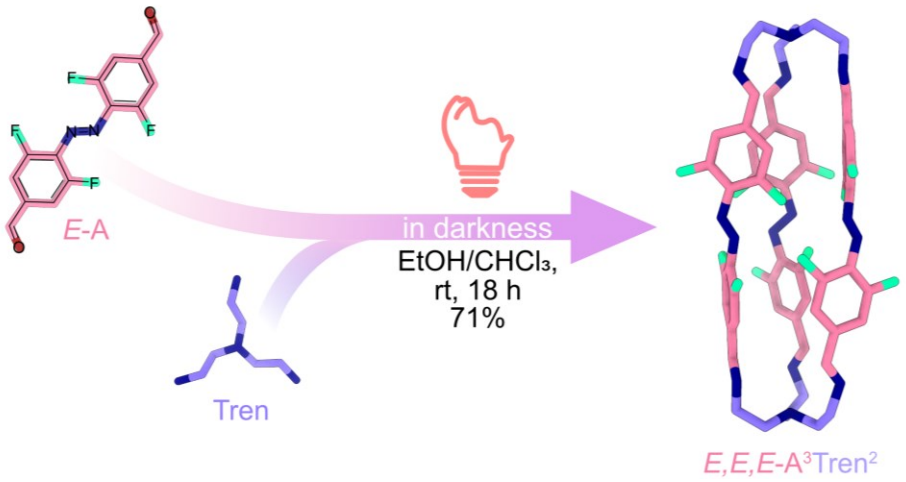

Figure 88: Synthesis of *E,E,E*-**A^{3}Tren^2**.

The formation of the supramolecular structure could again be observed by distinct shifts of the signals in the ^{1}H and ^{19}F{^{1}H} NMR. The aldehyde signals in the ^{1}H NMR show a significant shift upon imine formation from 10.00 to 8.04 ppm, while the signal for the aromatic protons shifts from 7.62 to 6.95 ppm. The signals in the ^{19}F{^{1}H} NMR also undergo a upfield shift from -117.84 to -118.11 ppm (Figure 89). The composition of the formed cage was confirmed by high-resolution mass spectrometry.

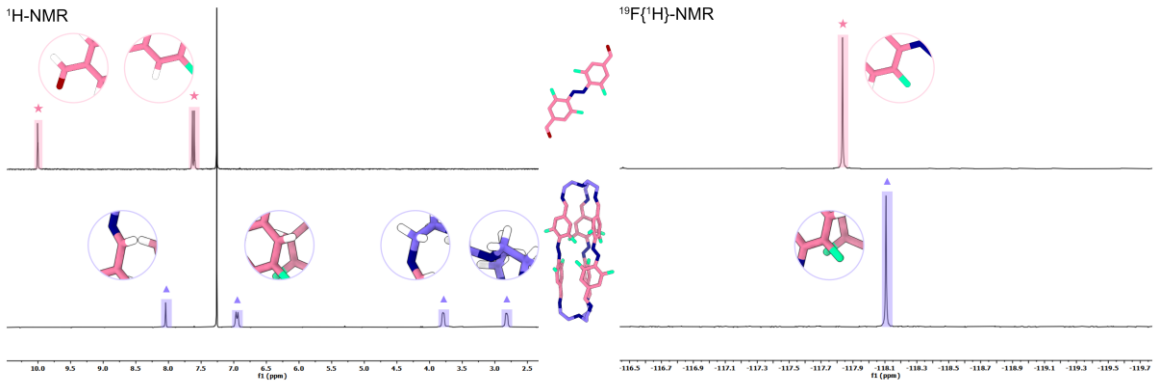

Figure 89: Comparison of the ^{1}H and ^{19}F{^{1}H} NMR spectra of *E*-**A** (pink star) and the **A^{3}Tren^2** cage (blue triangle) ($CDCl_3$, 300 and 282 MHz, respectively).

Liquid-liquid diffusion of ethanol and chloroform followed by slow evaporation of the mixture led to the formation of red prismatic crystals that were suitable for single-crystal X-ray crystallography (Figure 90). The *ortho*-fluorination of **A** leads to a twist in the azobenzenes, with the benzene rings being in a twisted position to each other. In comparison, the crystal structure of the non-fluorinated analogue depicts more planar azobenzene units. Apart from that, the structures of the two azobenzene cages are very similar, both featuring three azobenzene units that are slightly tilted with the imine bonds in a *s-trans* conformation. **A^{3}Tren^2** is more tilted than the other cage as the imine bonds are also in a *s-trans* conformation to the

diazenyl group, while in the crystal structure reported by the group of Khashab the imine groups are in a *s-cis*-conformation to the diazenyl functionality.

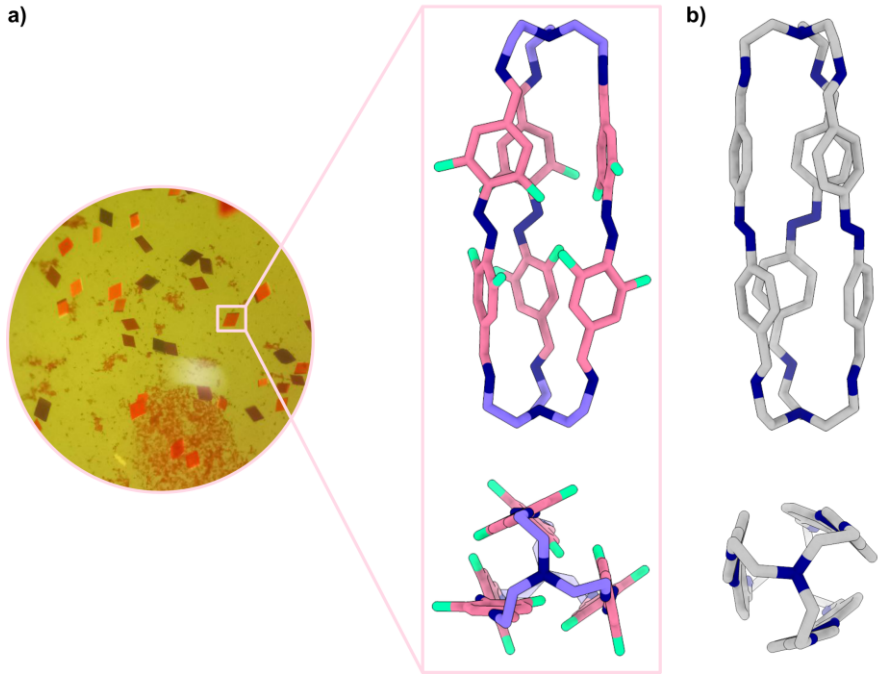

Figure 90: a) Single-crystals and crystal structure of **A^{3}Tren^2** as seen from the side and from the top Hydrogen atoms and solvent molecules are omitted for clarity. The crystal structure was obtained and refined by Dr. Bernd M. Schmidt. b) Single-crystal structure of the azobenzene cage published by the group of Khashab.[113]

The UV/VIS spectra recorded for **A^{3}Tren^2** show that the cage is switchable from *E* to *Z* using red or green light, and *vice versa* using UV light (Figure 91). Again, the isomerisation with green light is much faster but yields less *Z*-isomer in the PSS, while after 6 hours of irradiation with red light, a spectrum was obtained that, judging by the obtained curve, contains mostly *Z* isomeric species. The *Z* to *E* isomerisation with light of a wavelength of 405 nm occurred fast and in high yields.

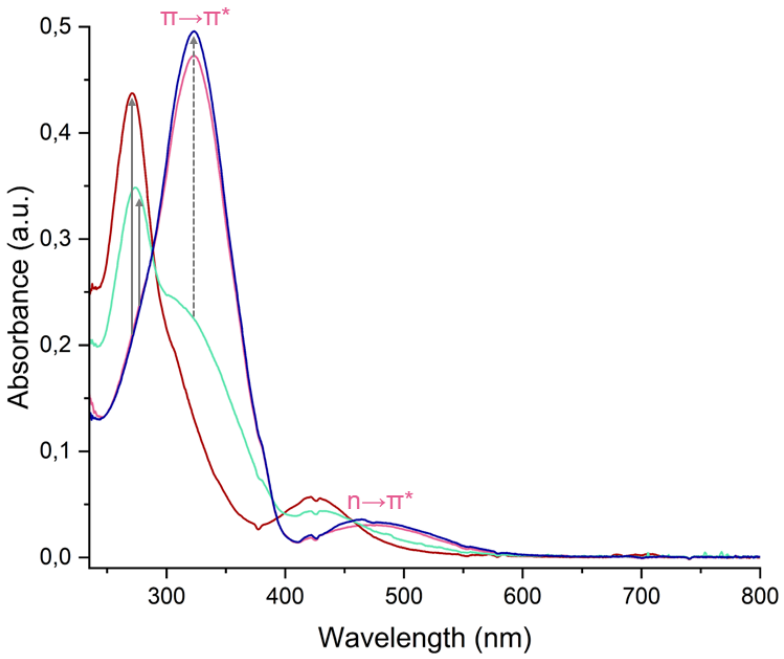

Figure 91: UV/VIS spectra of *E,E,E*-**A^{3}Tren^2** (pink curve), after irradiation with light of a wavelength of with light of a wavelength of 660 nm for 6 hours (dark red curve) and 565 nm for 15 minutes (turquoise curve). A solution that was *E*-enriched by irradiation with green light (565 nm) was irradiated with light of a wavelength of 405 nm (dark blue curve) for 30 seconds. The solid grey arrows indicate *E* to *Z* isomerisation while the dashed arrows indicate *Z* to *E* isomerisation.

As the photoswitchability of **A^{3}Tren^2** in low concentrations was investigated by UV/VIS spectroscopy, the cage was dissolved in *d*-chloroform and irradiated with red light in higher concentrations. This could lead to changes in the stoichiometry of the formed cage, comparable to the ring contraction observed for **A^{3}D^3**. ^{1}H and ^{19}F{^{1}H} NMR spectra as well as MALDI-mass spectra were recorded to investigate the potentially dissipative behaviour (Figure 92 and Figure S332-S334).

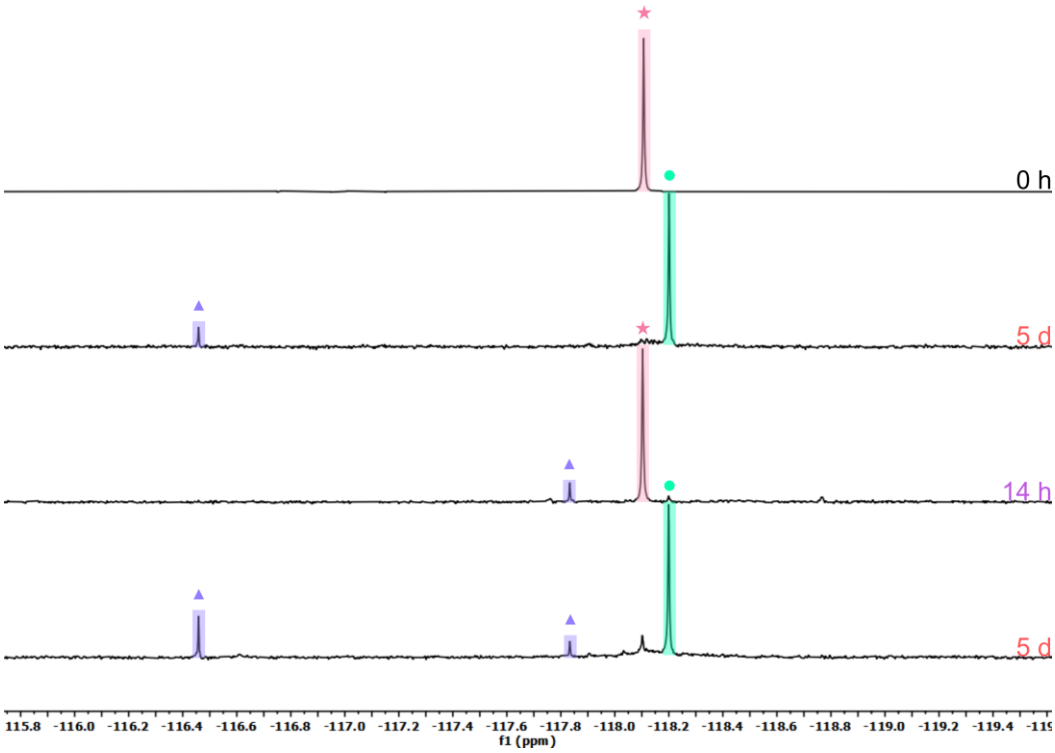

Figure 92: Excerpts of $^{19}F\{^{1}H\}$ NMR spectra showing the spectrum of **A^{3}Tren^{2}** (times highlighted in black), and the spectra for a solution of **A^{3}Tren^{2}** that was alternative irradiated with red light (660 nm, highlighted in red) and UV light (405 nm, highlighted in violet) ($CDCl_3$, 282 MHz). Signals of *E,E,E*-**A^{3}Tren^{2}** are highlighted in pink (star), the signals for the *Z*-isomer are highlighted in turquoise (circle) and the signals for both isomers of **A** are highlighted in blue (triangle).

Upon irradiation with red light (660 nm), the peak in the $^{19}F\{^{1}H\}$ NMR undergoes a small upfield shift from -118.11 to -118.20 ppm, and the corresponding signal for the aromatic protons also undergoes a highfield shift from 6.95 to 7.15 ppm, while the signal of the aldehyde protons only shifts minimally from 8.04 to 8.06 ppm. The presence of only two clear signals in the $^{19}F\{^{1}H\}$ NMR spectrum suggests that upon irradiation, only one isomer is formed, as well as a small amount of *Z*-**A**. The isomer formed by irradiation with red light is most likely the *Z,Z,Z*-**A^{3}Tren^{2}** cage judging by the small number of signals in the ^{1}H NMR, which indicates the formation of a symmetric species. The signals in the ^{1}H NMR spectrum confirm the presence of mostly imine species as well as some small signals that can be assigned to *Z*-**A** (Figure S332-S333). The observed signals are slightly broadened, which could be caused by the flexibility of the cage as well as by the formation of small amounts of byproducts, such as other isomers or oligomeric species. The latter is very likely, as during the reaction the formation of a dark red precipitate was observed and **Tren** is also frequently used in the formation of imine polymers.[114] The partial decay of **A^{3}Tren^{2}**, forming insoluble oligomers, would also be an explanation for the formed **A** signals.

The *Z*-isomer of **A^{3}Tren^{2}** can be transferred back to the *E,E,E*-**A^{3}Tren^{2}** cage by irradiation with UV light. Irradiation of the regained *E,E,E*- **A^{3}Tren^{2}** cage again led to the formation of the *Z*-

isomer, but the ratio of **A** in relation to the cage rose from approximately 8% after the first irradiation to 16% after the second irradiation, suggesting a consecutive decay during the irradiation due to the precipitation of imine rich species. The MALDI-mass spectrum that was recorded after the initial sample was irradiated with red light for 5 days shows a peak at 1115.411 with a high intensity, which, in comparison to the calculated mass of 1115.360 for the protonated cage, indicated that **A^{3}Tren^2** is still the major product of the reaction (Figure S334).

Attempts to generate a less flexible cage

The reaction of linear *E*-**A** and **Tren** led to the formation of a Tri^{2}Di^3 cage, which could be selectively isomerised using light of different wavelengths but showed no dissipative behaviour; this is probably due to the high flexibility of **Tren**. To generate a more rigid system that might undergo a transformation, another triamine, more specifically (2,4,6-triethylbenzene-1,3,5-triyl)trimethanamine (**Et**), was chosen as a building block. Based on the high-throughput screening and the supporting computations performed by Cooper *et al.*, the reaction of a linear dialdehyde like *E*-**A** and **Et** should probably lead to the formation of Tri^{4}Di^6 cages, while the usage of **Et** in combination with *meta*-aldehydes mostly leads to the formation of Tri^{2}Di^3 cages.[80]

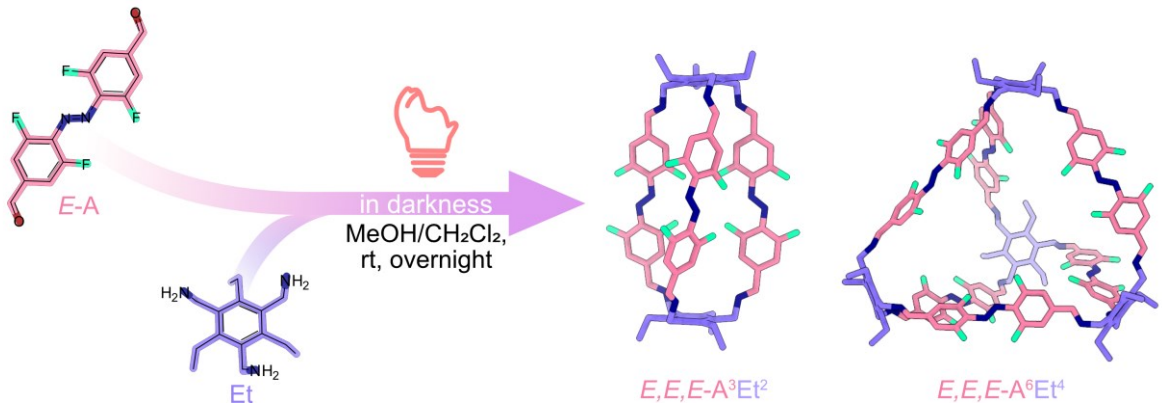

Figure 93: Attempted synthesis of imine cages based on *E*-**A** and **Et**.

Et was synthesised according to an established procedure,[115] which resembles the synthesis of **Me** discussed in Chapter 3.1.2. To synthesise a photoresponsive cage based on *E*-**A** and **Et**, similar conditions than those used for **A^{3}Tren^2** were utilised in a mixture of methanol and chloroform (Figure 93). The dark red powder that precipitated consisted mostly of insoluble species that are most likely oligomers and polymers. The small percentage of the sample that was soluble in *d*-chloroform consisted of the aldehyde starting material **A** and an imine compound. The broad signals observed indicate that if the cage formation was successful, it was at least accompanied by the formation of soluble oligomers. While the initial results show

that the synthesis of a cage based on **A** and **Et** might be possible, intensive optimisation of the reaction and an investigation into proper purification techniques would be necessary.

Summary

In summary, the photoswitchable imine cage **A^{3}Tren^2**, based on azobenzene **A**, was synthesised and thoroughly investigated. The single-crystal X-ray structure obtained gave insights into the structure of **A^{3}Tren^2**, showing that the fluorine substituents in *ortho*-position did not only impact the photochemical properties of the cage but also the structure, generating a highly twisted compound in comparison to the non-fluorinated analogue. **A^{3}Tren^2** can be isomerised from *E* to *Z* using red or green light, and *vice versa* using UV light. Judging by the irradiation experiments that were monitored by NMR spectroscopy, the bidirectional photoswitching of **A^{3}Tren^2** occurs nearly quantitatively when red light or UV light are employed. While the flexible nature of **Tren** might enable the excellent photoswitching it might also be one of the reasons that no structural rearrangements occur upon irradiation. Attempts to synthesise a more rigid cage based on **A** and **Et** that, upon irradiation might undergo a topological change have not been successful yet. Albeit no dissipative reorganisation comparable to those observed for the macrocyclic species could be triggered by irradiation, the beneficial photochemical properties and the easy synthesis that gives **A^{3}Tren^2** in appropriate yields and high purity make the imine cage an interesting synthetic target. The **Tren** units of the cage could be used to encapsulate cationic guests that could possibly be released by irradiation, and the possibility that **A^{3}Tren^2** might undergo a ligand exchange in combination with other amines could also be of interest and will be investigated in the next section.

3.2.5 Light-induced amine exchange

Introduction

In the preceding chapters, reactions with two different building blocks as starting materials formed different macrocycles, cages, oligomers, or mixtures thereof. If more than two different building blocks are employed, different types of sorting, the most common of which are narcissistic and social self-sorting, can occur and different products can be formed.[116] If building block **I** could either react with building block **II** or **III** and was mixed with both, narcissistic self-sorting would lead to the formation of binary products containing either **I** and **II** or **I** and **III**, while social self-sorting would lead to products containing all compounds (Figure 94). The process by which both building blocks are statistically incorporated into the structures that are formed is called scrambling.

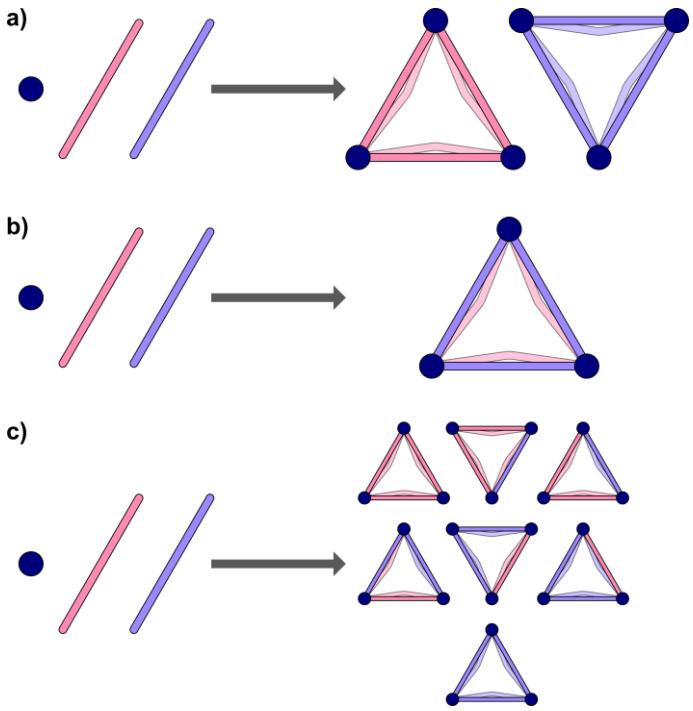

Figure 94: Schematic representation of a) narcissistic, and b) social self-sorting as well as c) scrambling.

A group of low-symmetry imine cages was generated by Slater *et al.* using social self-sorting in a combined experimental-computational approach.[117] The group of Mukherjee showed that in a mixture of two different aldehydes and two different amines, only two preferred cages formed in a self-sorting process called molecular marriage.[116a,118] Generating the less preferred cage structure first, the preferred cage could be accessed by the addition of the second building block to the preformed cage.[118c]

Another example of an irreversible cage-to-cage transformation was recently published by the group of Feringa, in which the aldehyde units in the Tri^2Di^3 cage could be irreversibly exchanged after irradiation with light.[71] The reversible dissipative interconversion between imines is mostly obtained by the addition of a fuel or a metastable acid,[63] while Herges *et al.* were able to achieve a photocontrolled ligand exchange in a metal-organic, cobalt-based system.[60] These examples are thoroughly discussed in the introductory section 1.4.2.

A photoswitchable system in which the incorporated building block can be controlled by light could be generated based on the results discussed in the previous sections if the combination of two structurally different amine building blocks with the *E*-isomer of the azobenzene would only lead to the formation of one homoleptic product (Figure 95a), while the combination of both building blocks with the other isomer would lead to a product based on the other amine (Figure 95b). As a result, a system could be generated in which the exchange of the amine can be triggered by light (Figure 95c).

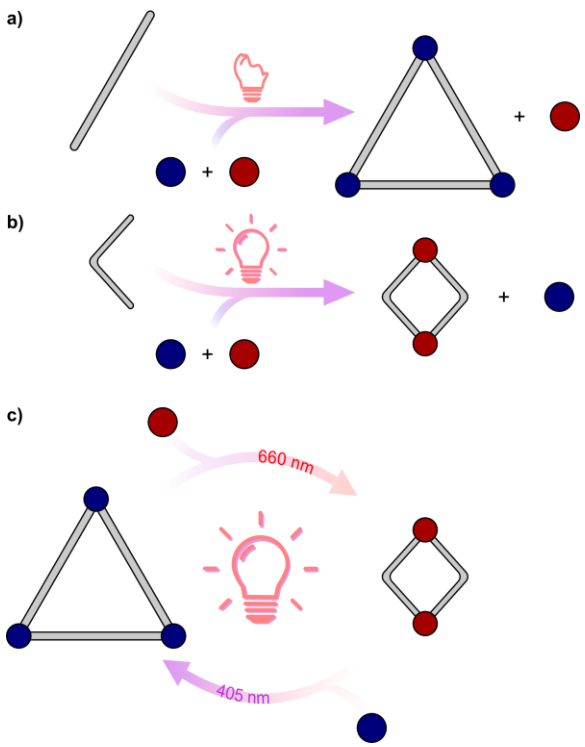

Figure 95: Schematic representations of the reaction of an azobenzene aldehyde (grey stick) with two different amine building blocks (blue and red balls). Reaction of a) the *E*-isomer with one amine building block forming one homoleptic product in the absence of light, b) the *Z*-isomer with another amine building block under continuous irradiation, and c) the light-triggered interconversion between two macrocyclic products based on different amine building blocks.

Considering the different behaviour of the more flexible and more rigid diamines and their tendency to form, in most cases, either a macrocycle or a mixture of different products depending on the azobenzene isomer employed, as discussed in Sections 3.2.2 and 3.2.3, the

combination of a building block such as **D** with one of the other rigid or flexible building blocks should create a system that can be photochemically switched between two macrocycles.

Competitive formation experiments with D

To generate a system that can be selectively switched between two binary macrocycles containing different amines, the formation of mixed macrocyclic structures formed by social self-sorting or scrambling needs to be avoided. Azobenzene *E*-**A**, and diaminocyclohexane **D** were mixed with different diamines to evaluate which combination would lead to binary products or preferably to the formation of only one product and would therefore be beneficial combinations for the generation of a system in which the amine can be exchanged by light.

While the initial macrocycle formation experiments based on diphenylethylenediamine **DPEN** were not successful with no obvious preference for the formation of a specific macrocyclic species, the combination of azobenzene *E*-**A** and phenylenedimethanamine **mP** led to the formation of an **A²mP²** macrocycle with both isomers of **A** as discussed in Section 3.2.2 (Figure 96). In contrast the reaction of **D** with *E*-**A** led to the formation of only *E,E,E*-**A³D³**, while the employment of *Z*-**A** or the isomerisation of the trianglimine yielded a mixture of different isomers of **A³D³** as well as of *Z,Z*-**A²D²** (Figure 96).

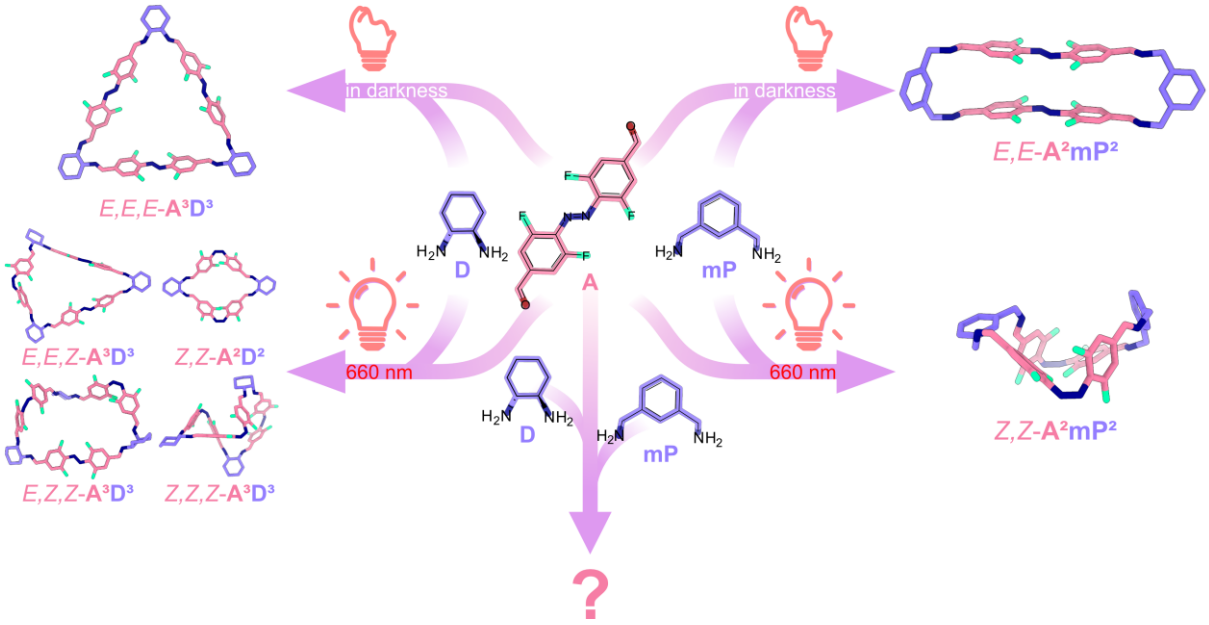

Figure 96: Reaction of **A** with either **D** or **mP** in the dark or under irradiation with red light leading to different products.

E-**A** was mixed with **D** and either **DPEN** or **mP**, and the mixture was stirred in the dark for 3 days and for 3 days under irradiation with red light (660 nm). A *Z*-enriched solution of **A** was generated by irradiation with red light and combined with **D** and with one of the other diamines,

respectively. The reactions were monitored by ^{1}H and $^{19}F\{^{1}H\}$ NMR spectroscopy and by MALDI-mass spectrometry (Figure 97 and Figure S175-S180).

When combining azobenzene *E*-**A** with diamines **D** and **DPEN**, the major product is formed by *E*-**A** and **DPEN**. This product is accompanied by several peaks that only appear when both amines are combined with **A**, suggesting that those can be assigned to mixed species. The formation of a mixed macrocycle can also be observed in the MALDI-mass spectrum recorded, which shows the formation of an $\mathbf{A^2D^1DPEN^1}$ macrocycle. *E,E,E*-$\mathbf{A^3D^3}$ is also formed in small quantities, as observed in the NMR and MALDI-mass spectra. The previously observed **DPEN** macrocycle and the mixed species are still present after irradiation of the mixture with red light, while the signal for *E,E,E*-$\mathbf{A^3D^3}$ disappears and a signal for an $\mathbf{A^2D^2}$ macrocycle can now be observed. A signal that can most likely be assigned to an *Z*-isomer of a **DPEN** macrocycle can also be observed, as can smaller multiplets possibly caused by oligomers or *Z*-isomers of the mixed macrocycle. Employing both diamines in combination with *Z*-**A** as starting materials only leads to the formation of macrocycles containing either **D** or **DPEN**. This might be an indication that starting from the *E*-isomer, the formation of binary macrocycles is not preferred in comparison to mixed macrocycles, while the different geometry of *Z*-**A** leads to the preferred formation of $\mathbf{A^nD^n}$ and $\mathbf{A^nDPEN^n}$ macrocycles.

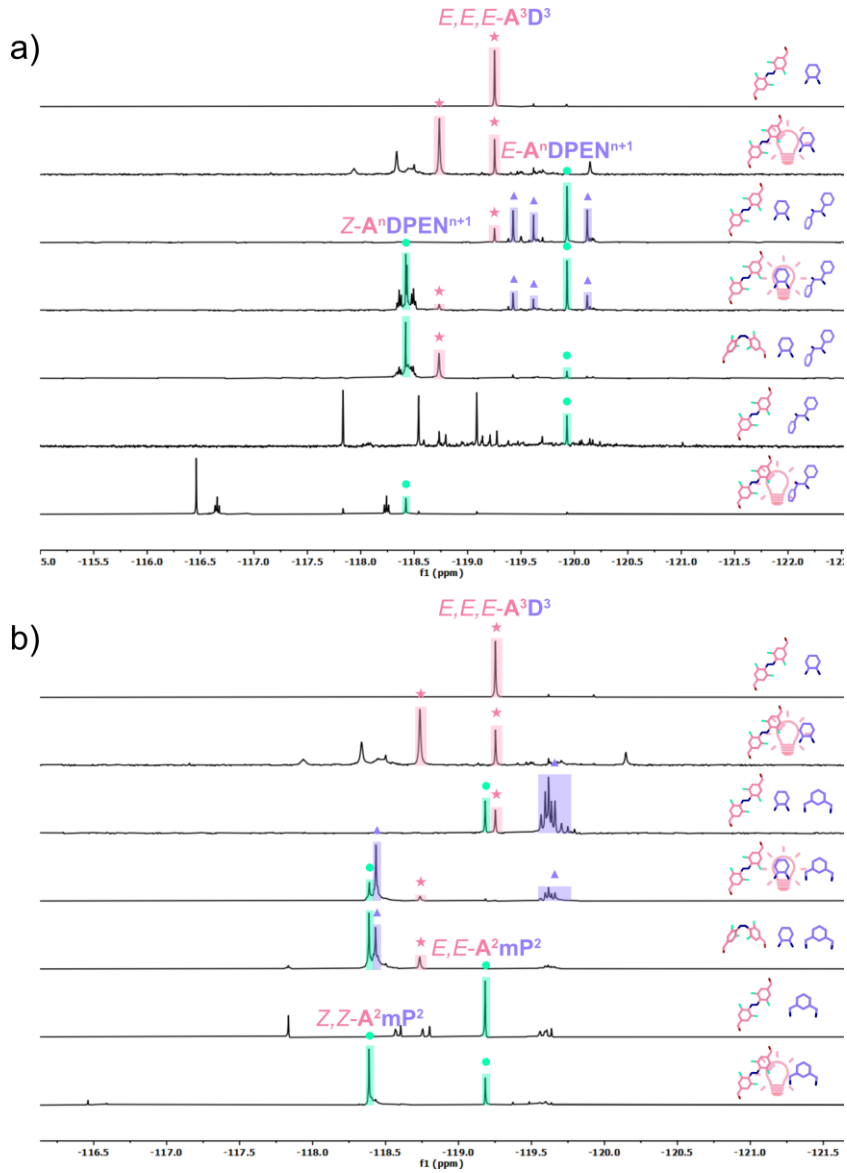

Figure 97: Comparison of the excerpts of the $^{19}F\{^{1}H\}$ NMR spectra of the reaction of *E*-**A** with **D** in the dark and after irradiation with red light (660 nm), of *E*-**A** with **D** and a) **DPEN** or b) **mP** in the dark and after irradiation with red light, of *Z*-**A** with **D** and a) **DPEN** or b) **mP**, and of the reaction of *E*-**A** with a) **DPEN** or b) **mP** in the dark and after irradiation with red light, as well as of the reaction of the respective amine with *E*-**A** in the dark and after irradiation with red light ($CDCl_3$, 282 MHz). Species that can be assigned to products formed by **A** and **D** are highlighted in pink (star), products formed by **A** with either **DPEN** or **mP** are highlighted in turquoise (circle) and the signals that cannot be assigned to either and are most likely mixed compounds are highlighted in blue (triangle).

If either **D** or **mP** is mixed with *E*-**A**, the formation of a macrocyclic species, more precisely *E,E,E*-$\mathbf{A^3D^3}$ or *E,E*-$\mathbf{A^2mP^2}$, can be observed as the major product. When all three compounds are combined, the macrocycles are formed in a small percentage, while the major product, judged by the broad overlapping signals, is an oligomer containing all three starting materials. In the corresponding MALDI-mass spectrum, peaks that can be assigned to the two binary macrocycles can be observed, as well as signals for open species such as $\mathbf{A^1D^2}$, $\mathbf{A^1mP^2}$, and

A³D¹mP². Irradiation of the mixture leads to the formation of *Z*,*Z*-**A²mP²**. Additionally, a new signal at -118.43 ppm can be observed that is not formed in the reaction of one of the single diamines with **A**. This signal might be the result of the formation of a mixed macrocycle; however, as those species would be less symmetric than the previously obtained macrocycles, it would be expected that more than one signal in the $^{19}F\{^{1}H\}$ NMR spectrum is observable. Additional measurements are needed to determine the nature of the formed species. The same signal can be observed in the spectrum of the reaction of *Z*-**A** and **mP**. In the MALDI spectra that were recorded for both reactions, one peak can be observed that is present in both spectra and can be assigned to an **A²mP²** macrocycle. Additionally, peaks of small intensity for the mixed macrocyclic species **A³D²mP¹** and **A⁴D²mP²** can be observed for the reaction of *Z*-**A**.

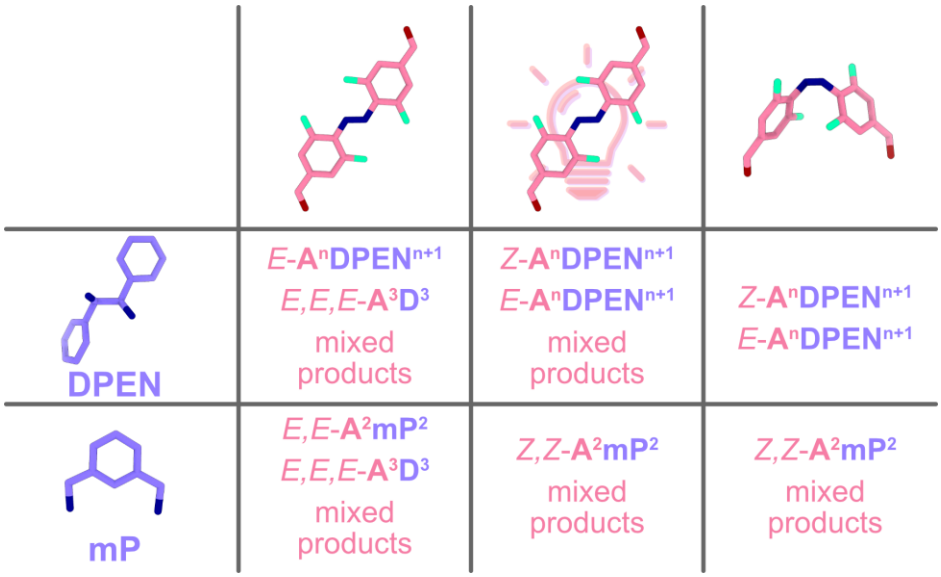

Figure 98: Summary of products formed from the reaction of *E*-**A** and **D** with diamines **DPEN** or **mP**, the products formed by the irradiation of the reaction mixture and the products formed by combining the same building blocks with *Z*-**A**.

The combination of **DPEN** and **D** with the isomers of **A** led to the formation of **DPEN**-based macrocycles as well as possibly mixed macrocycles when *E*-**A** was employed. As **A³D³** macrocycles are only formed as minor products independent of the azobenzene isomer employed and the reactions are accompanied by the formation of several different byproducts, this system seems not to be suitable for photo-controlled amine exchange. The combination of **D** with **mP** is equally unsuitable. While the reaction of *Z*-**A** and both diamines clearly favours the formation of an **A²mP²** macrocycle, another signal that cannot be definitely assigned to a specific macrocycle was also observed, and the reaction of *E*-**A** and the diamines leads to the formation of several oligomeric imine species (Figure 98).

As mentioned above and in Section 3.2.2, the combination of *E*-**A** and diaminocycohexane **D** led to the formation of trianglimine *E,E,E*-**A³D³**, while the utilisation of the other isomer *Z*-**A** led

to a mixture of different isomers of $\mathbf{A^3D^3}$ as well as the smaller macrocycle $\mathbf{A^2D^2}$. In contrast, the aliphatic diamines ethylenediamin **E**, propanediamin **Pr**, butanediamine **B**, and hexanediamine **H** yielded oligomeric and polymeric species in combination with *E*-**A** and macrocycles were only observed when *Z*-**A** was employed, as discussed in Section 3.2.3 (Figure 99).

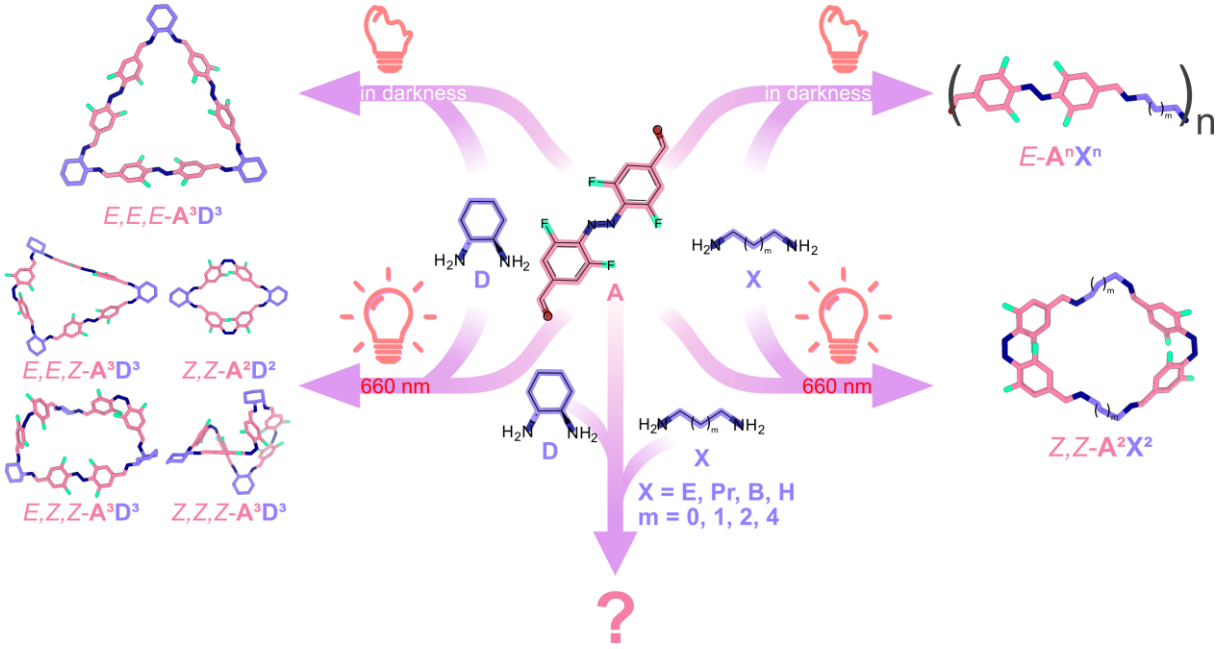

Figure 99: Reaction of **A** with either **D** or one of the aliphatic diamines **E**, **Pr**, **B**, or **H** in the dark or under irradiation with red light leading to different products.

Azobenzene **A** and 1,2-diaminocyclohexane **D** were combined with aliphatic diamines of different lengths to evaluate if these combinations could lead to the selective formation of one macrocycle. The reaction mixtures were either stirred in the dark and then irradiated with red light for three days, or a preirradiated solution of **A** was used. The combination of **A** with ethylenediamine **E** and **D** mostly favoured the formation of $\mathbf{A^nE^n}$ species, while mixed species and $\mathbf{A^nD^n}$ species were formed as byproducts (Figure 100a). It was accompanied by the formation of large amounts of oligomers that precipitated out of solution. The corresponding MALDI-mass spectra show peaks that can be assigned to the open species $\mathbf{A^1D^2}$, $\mathbf{A^1E^2}$, and $\mathbf{A^2D^1E^1}$ as well as to the macrocyclic species $\mathbf{A^3D^1E^2}$, $\mathbf{A^3D^2E^1}$, and $\mathbf{A^3D^3}$, underscoring the observation that mixed $\mathbf{A^nD^nE^n}$ species are also formed (Figure S165).

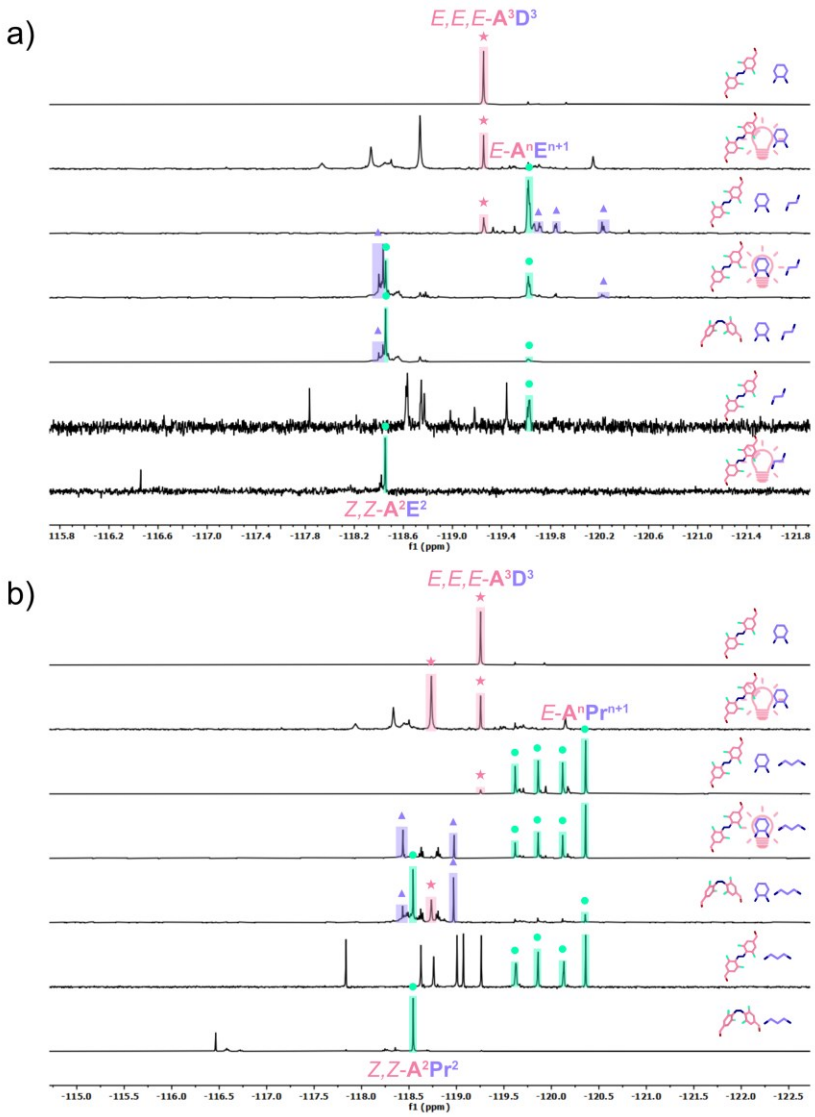

Figure 100: Comparison of the excerpts of the $^{19}F\{^{1}H\}$ NMR spectra of the reaction of **A** and **D** in the dark and under irradiation with red light (660 nm), of *E*-**A** with **D** and an aliphatic diamine in the dark and under irradiation, of *Z*-**A** with **D** and an aliphatic diamine under irradiation, and of *E*-**A** and an aliphatic diamine in the dark and under irradiation ($CDCl_3$, 282 MHz). The employed aliphatic diamines are a) **E** and b) **Pr**. Signals for species that are formed by **A** and **D** are highlighted in pink (star), species formed by **A** and the respective aliphatic diamine are highlighted in turquoise (circle), and signals that have not appeared before are highlighted in blue (triangle).

The utilisation of 1,3-propanediamine **Pr** mostly led to the formation of different products that were also observed in the reaction of **Pr** and *E*-**A** (Figure 100b). New signals that were previously not observed formed upon irradiation, while the $\mathbf{A^nD^n}$ species were again formed as byproducts at most. Employing *Z*-**A** and **Pr** led to the formation of *Z,Z*-$\mathbf{A^2Pr^2}$, and the products also formed by the irradiation of the *E* mixture.

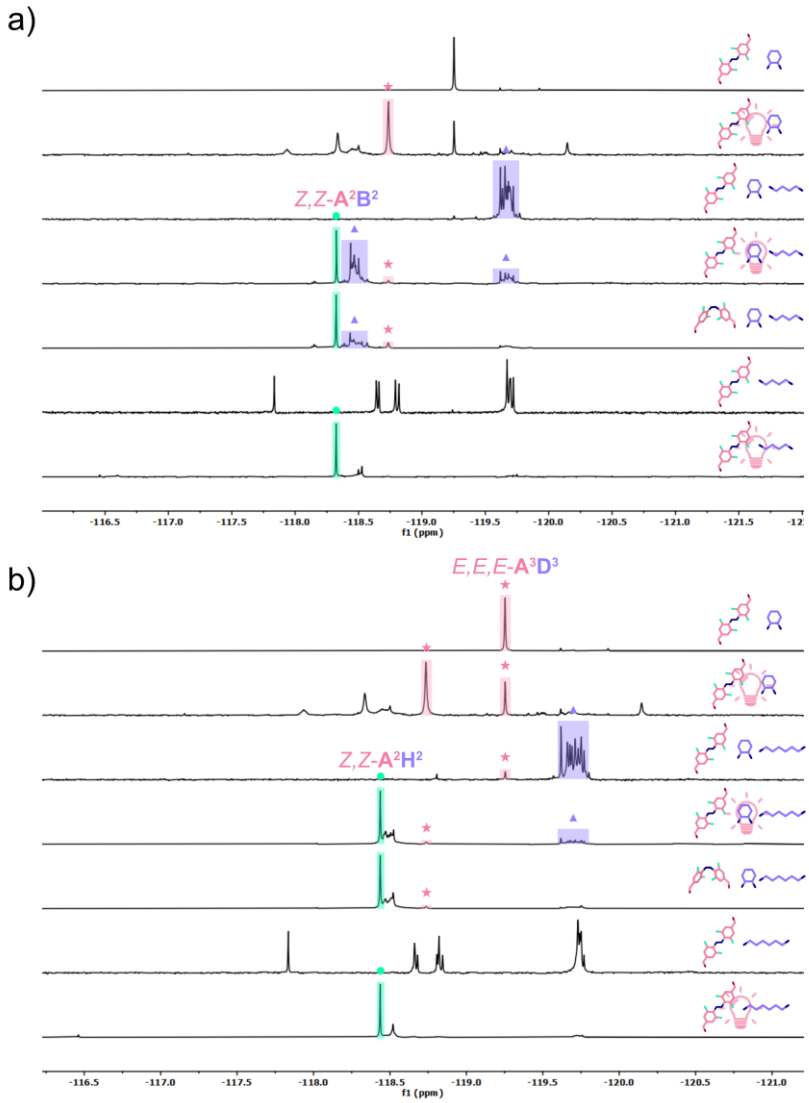

Figure 101: Comparison of the excerpts of the $^{19}F\{^{1}H\}$ NMR spectra of the reaction of **A** and **D** in the dark and under irradiation with red light (660 nm), of *E*-**A** with **D** and an aliphatic diamine, in the dark and under irradiation, of *Z*-**A** with **D** and an aliphatic diamine under irradiation and of *E*-**A** and an aliphatic diamine in the dark and under irradiation ($CDCl_3$, 282 MHz). The employed aliphatic diamines are a) **B** and b) **H**. Signals for species that are formed by **A** and **D** are highlighted in pink (star), species formed by **A** and the respective aliphatic diamine are highlighted in turquoise (circle) and signals that have not appeared before are highlighted in blue (triangle).

Employing the longer diamines 1,4-butanediamine **B** or 1,6-hexanediamine **H** in combination with **D** and *E*-**A**, the formation of different mixed imine species, probably oligomers judging by the number of overlapping signals, is the major process (Figure 101). Additionally, in the reaction using **H**, the formation of minor amounts of *E,E,E*-**A³D³** can be observed. When this mixture is irradiated with red light, or if *Z*-**A** is combined with **D** and the respective diamine, the formation of a *Z,Z*-**A²B²** or *Z,Z*-**A²H²** is the major product. While the formation of *Z,Z*-**A²B²** is accompanied by the formation of a substantial amount of different oligomers, fewer side products are formed in the reaction with **H**. These findings are again supported by the MALDI-

mass spectra that were recorded, showing the formation of different species containing one or both employed diamines for the reactions in the dark and the formation of the **A²B²** or **A²H²** macrocycles in the irradiated samples (Figure S171 and Figure S174).

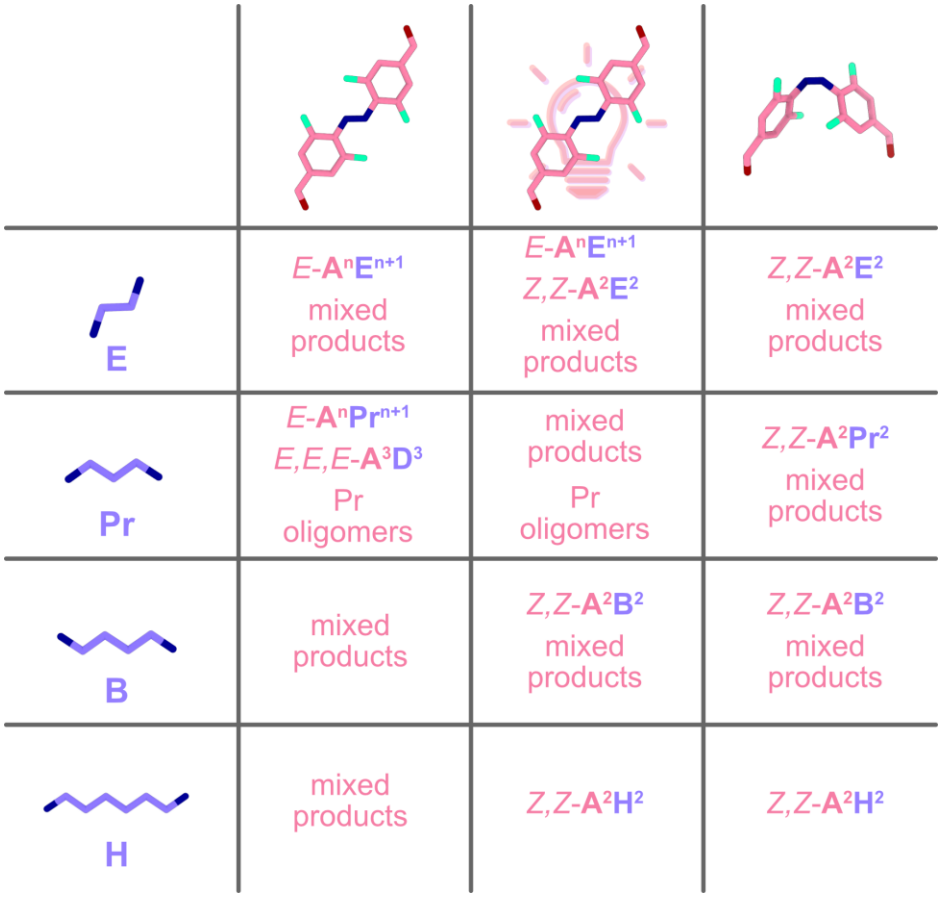

Figure 102: Summary of products formed from the reaction of *E*-**A** and **D** with diamines **E**, **Pr**, **B** or **H**, the products formed by the irradiation of the reaction mixture and the products formed by combining the same building blocks with *Z*-**A**.

While the assumption that the formation of aliphatic **A²X²** macrocycles based on *Z*-**A** might be preferred in comparison to the formation of the more strained **A²D²** was confirmed, the reactions were accompanied by the formation of several byproducts. Unfortunately, the reactions of all employed diamine mixtures in combination with *E*-**A** did not yield *E,E,E*-**A³D³** as the preferred product (Figure 102).

Exchange experiments based on *E,E,E*-A³D³

While none of the investigated reactions employing the different diamine mixtures favour the formation of binary **AⁿDⁿ** species, the use of *E,E,E*-**A³D³** as a starting material in combination with different diamines might enable the formation of different products upon irradiation or enable the reversible or irreversible transformation of the *E,E,E*-**A³D³** into another macrocycle. *E,E,E*-**A³D³** was combined with different diamines in a macrocycle-to-amine ratio of 1-to-3 and

irradiated with red light (660 nm) for 5 days. After NMR and MALDI-mass spectra were recorded, the mixture was irradiated with UV light for 14 hours to induce *Z* to *E* isomerisation and which could lead to the reformation of the precursor. The mixture was then again irradiated with red light for 5 days to check whether the products obtained from the mixture differed from those obtained from *E,E,E*-**A^{3}D^3** and the diamine. The *Z*-enriched mixture was stirred in the dark for 4 days at room temperature and 2 days at 45 °C**.**

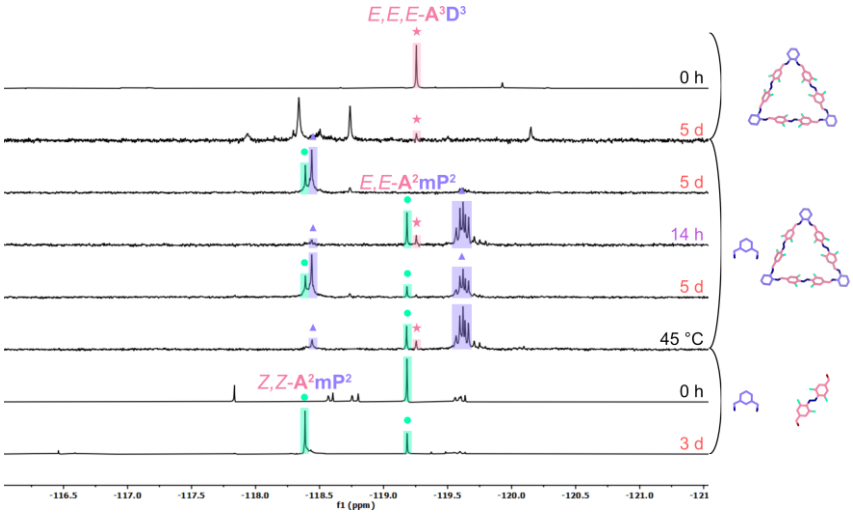

Figure 103: Comparison of the excerpts of the $^{19}F\{^1H\}$ NMR spectra of *E,E,E*-**A^{3}D^3** in the dark and after irradiation with red light (660 nm), of the reaction of *E,E,E*-**A^{3}D^3** with **mP**, after irradiation with red light for 5 days, followed by irradiation with UV light (405 nm) for 14 hours, irradiation with red light for 5 days and a period in which the reaction was stirred in the dark for 4 days at room temperature and for 2 days at 45 °C, and of the reaction of **mP** with *E*-**A** in the dark and after irradiation with red light ($CDCl_3$, 282 MHz). Signals that can be assigned to *E,E,E*-**A^{3}D^3** or products of the isomerisation thereof are highlighted in pink (star), species formed by the reaction of **A** and **mP** are highlighted in turquoise (circle) and signals that have not been observed before are highlighted in blue (triangle).

The spectra obtained for the combination of *E,E,E*-**A^{3}D^3**, and **mP** under irradiation with red light (660 nm) are very similar to those previously measured for the reaction of **mP**, **D** and *Z*-**A** (Figure 103). In both cases, the major products formed are a *Z,Z*-**A^{2}mP^2** macrocycle and another unidentified species that was only observed in the presence of both diamines. These species can also be observed in the second irradiation cycle, accompanied by some oligomers and an *E,E*-**A^{2}mP^2** macrocycle, indicating that the irradiation of the sample was incomplete. *Z* to *E* isomerisation using UV light or heat both led to the formation of a product mixture of the same composition, containing oligomers as well as *E,E*-**A^{2}mP^2** and traces of *E,E,E*-**A^{3}D^3**.

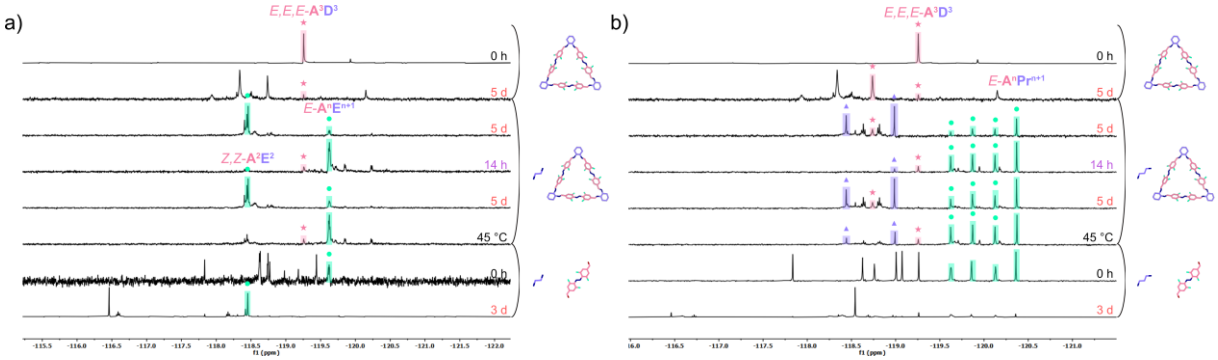

Figure 104: Comparison of the excerpts of the $^{19}F\{^{1}H\}$ NMR spectra of *E,E,E*-**A^{3}D^3** in the dark and after irradiation with red light (660 nm), of the reaction of *E,E,E*-**A^{3}D^3** with a) **E** or b) **Pr**, after irradiation with red light for 5 days, followed by irradiation with UV light (405 nm) for 14 hours, irradiation with red light for 5 days and a period in which the reaction was stirred in the dark for 4 days at room temperature and for 2 days at 45 °C, and of the reaction of a) **E** or b) **Pr** with *E*-**A** in the dark and after irradiation with red light ($CDCl_3$, 282 MHz). Signals that can be assigned to *E,E,E*-**A^{3}D^3** or products of the isomerisation thereof are highlighted in pink (star), species formed by the reaction of **A** and a) **E** or b) **Pr** are highlighted in turquoise (circle) and signals that have not been observed before are highlighted in blue (triangle).

Combining the macrocycle with the short aliphatic diamine **E** also led to results that did not differ from those obtained previously, with the preferred products being the binary, **E**-containing products and large amounts of precipitate forming during the observation period. A similar outcome was obtained by employing **Pr** and *E,E,E*-**A^{3}D^3**, which yielded spectra that closely matched those obtained in the experiments performed before (Figure 104).

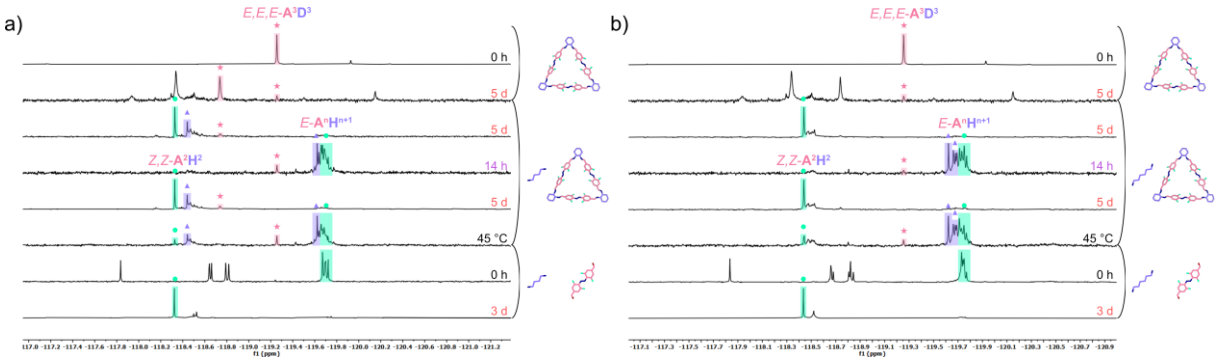

Figure 105: Comparison of the excerpts of the $^{19}F\{^{1}H\}$ NMR spectra of *E,E,E*-**A^{3}D^3** in the dark and after irradiation with red light (660 nm), of the reaction of *E,E,E*-**A^{3}D^3** with a) **B** or b) **H**, after irradiation with red light for 5 days, followed by irradiation with UV light (405 nm) for 14 hours, irradiation with red light for 5 days and a period in which the reaction was stirred in the dark for 4 days at room temperature and for 2 days at 45 °C, and of the reaction of a) **B** or b) **H** with *E*-**A** in the dark and after irradiation with red light ($CDCl_3$, 282 MHz). Signals that can be assigned to *E,E,E*-**A^{3}D^3** or products of the isomerisation thereof are highlighted in pink (star), species formed by the reaction of **A** and a) **B** or b) **H** are highlighted in turquoise (circle) and signals that have not been observed before are highlighted in blue (triangle).

The longer aliphatic diamines initially showed more promising results regarding the selectivity of the formation of only one binary product upon irradiation with red light (660 nm) (Figure 105). Combining those diamines, **B** and **H**, with *E,E,E*-$\mathbf{A^3D^3}$, and irradiating the mixture with red light led to the selective formation of *Z,Z*-$\mathbf{A^2B^2}$ or *Z,Z*-$\mathbf{A^2H^2}$, respectively. The formation of the **B**-containing species is accompanied by the formation of small amounts of byproducts. Thermal relaxation or irradiation with UV light only produced the precursor *E,E,E*-$\mathbf{A^3D^3}$ in a small percentage, while the preferred product seems to be oligomeric or polymeric, judging by the broad overlapping signals. Additionally, a signal at -119.62 ppm can be observed in both reactions and can most likely be assigned to a macrocyclic $\mathbf{A^nD^n}$ species as it is present in both reactions.

While the combination of the different diamines with macrocycle *E,E,E*-$\mathbf{A^3D^3}$ did not lead to results that were significantly different from those obtained by combining the building blocks, it was shown that the macrocycle can be transformed into different macrocyclic species by irradiation with red light (660 nm). In the cases of **B** and **H**, this transformation is very selective, leading to the clean formation of macrocyclic *Z,Z*-$\mathbf{A^2B^2}$, and *Z,Z*-$\mathbf{A^2H^2}$, respectively.

Attempts to achieve the reversible transformation between two different macrocycles

As the formation of *Z,Z*-$\mathbf{A^2H^2}$ from *E,E,E*-$\mathbf{A^3D^3}$ and **H** proceeds with only minor formation of side products under irradiation with red light, attempts were made to modify the system to favour the formation of an $\mathbf{A^3D^3}$ macrocycle with *E*-**A**. The azobenzene **A** was combined with 1.2 equivalents of **H** and varying equivalents of **D**.

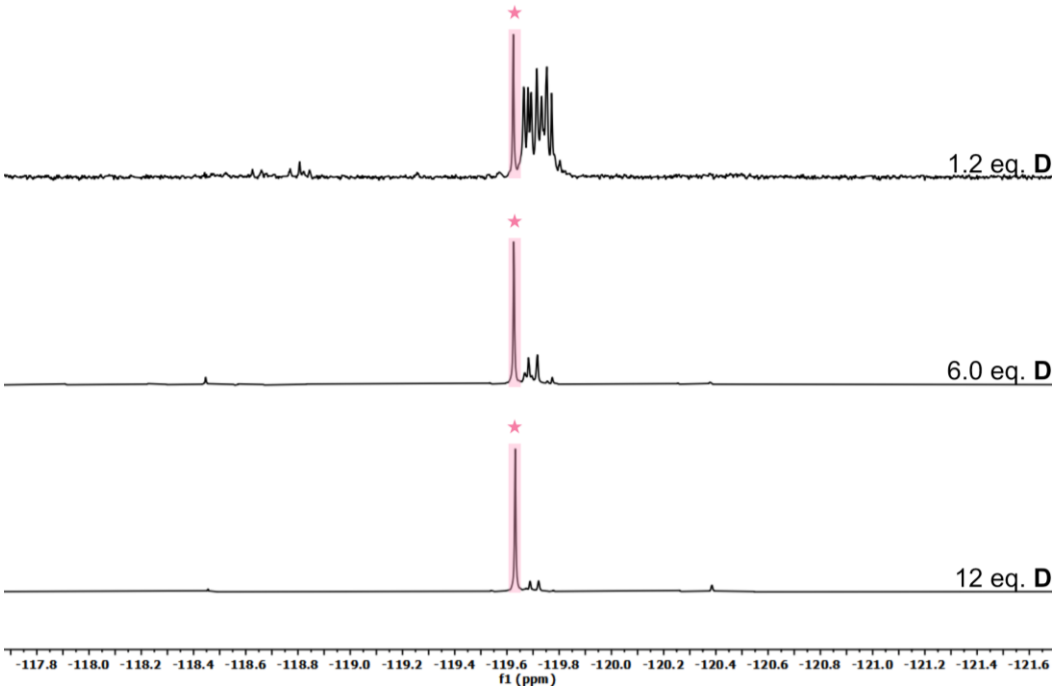

Figure 106: Comparison of the excerpts of the $^{19}F\{^{1}H\}$ NMR spectra of the reaction of *E*-**A** and **H** with, 1.2, 6.0 or 12 equivalents of **D** after 3 days ($CDCl_3$, 282 MHz). Signals that can be assigned to the newly formed species are highlighted in pink (star).

While increasing the equivalents of **D** employed, the number of oligomeric byproducts significantly decreased (Figure 106). The sharp signals in the $^{19}F\{^{1}H\}$ as well as in the ^{1}H NMR indicate the formation of only one product, as the formation of several or oligomeric products would lead to more broad signals. Surprisingly, the observed signals in the ^{1}H NMR are shifted downfield while the signals in the $^{19}F\{^{1}H\}$ NMR are shifted upfield in comparison to the signals of *E,E,E*-**A^{3}D^3**, indicating that instead of *E,E,E*-**A^{3}D^3**, another molecule was formed.

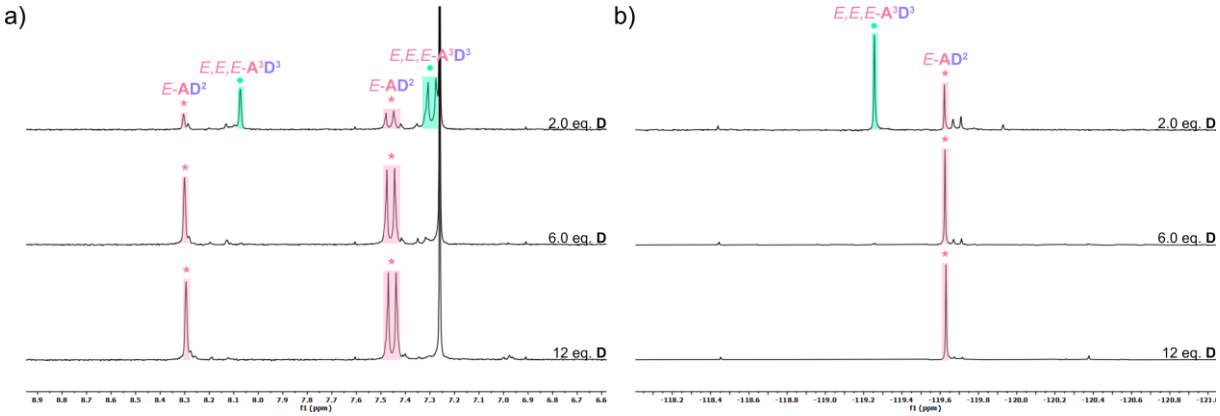

Figure 107: Comparison of the excerpts of a) the ^{1}H NMR and b) the $^{19}F\{^{1}H\}$ NMR spectra of the reaction of *E*-**A** different amounts of **D** ($CDCl_3$, 300 and 282 MHz). Signals that can be assigned to *E,E,E*-**A^{3}D^3** are highlighted in turquoise (circle), while the signals for the new species are highlighted in pink (star).

To further see whether this new species is also formed in the absence of **H**, *E*-**A** was combined with either two, six, or twelve equivalents of **D** and ^{1}H and ^{19}F{^{1}H} NMR spectra were recorded after the mixture was stirred for three days in the dark (Figure 107). While the reaction of *E*-**A** with two equivalents of **D** led to the formation of both products, the newly formed species and the *E,E,E*-$\mathbf{A^3D^3}$ macrocycle, utilising larger amounts of **D** only led to the formation of the other product. MALDI-mass spectra that were measured show peaks that can be assigned to an $\mathbf{AD^2}$ bisimine.

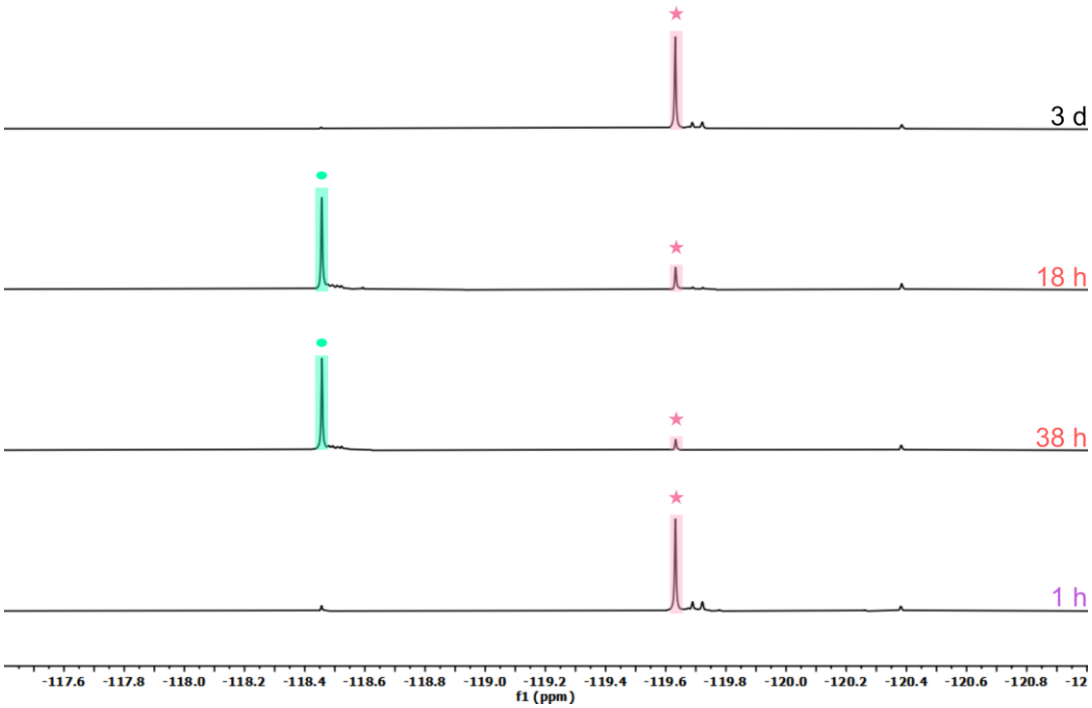

Figure 108: Comparison of the excerpts of the ^{19}F{^{1}H} NMR spectra of the reaction of *E*-**A** and **H** with 12 equivalents of **D** in the dark, after irradiation with red light (660 nm) for 18 and 38 hours and after irradiation with UV light for one hour ($CDCl_3$, 282 MHz). Signals that can be assigned to the newly formed $\mathbf{AD^2}$ species are highlighted in pink (star), while the signals for *Z*-$\mathbf{AD^2}$ are highlighted in turquoise (circle).

Irradiation of the mixture containing *E*-**A**, **D**, and **H** with red light (660 nm) was monitored by ^{1}H and ^{19}F{^{1}H} spectroscopy showing the formation of a signal at -118.46 ppm, independent of the equivalents of **D** added (see Figure 108 and Figures S177, S179, S181). While this signal is in accordance with the signal observed for the formation of *Z,Z*-$\mathbf{A^2H^2}$ (-118.44 ppm) it might also show the formation of *Z*-$\mathbf{AD^2}$ (-118.44 ppm). The comparison of the ^{1}H NMR spectra recorded for these compounds with the results show that the latter process occurs and while the transformation of an oligomeric product mixture into *Z,Z*-$\mathbf{A^2H^2}$ was possible the utilisation of an excess of **D** only led to the isomerisation of the newly formed $\mathbf{AD^2}$ species.

Attempts to photochemically induce a transformation from cage to macrocycle

The beneficial photochemical properties of **A^{3}Tren^2** and the promising exchange experiments with an azobenzene imine cage conducted by the group of Feringa[71] led to the idea to investigate whether **A^{3}Tren^2** could also undergo an imine exchange upon irradiation. Instead of a monoamine, different diamines were chosen as building blocks to enable the formation of macrocyclic structures, hopefully enabling a photoinduced change of geometry from a cage to a macrocycle (Figure 106).

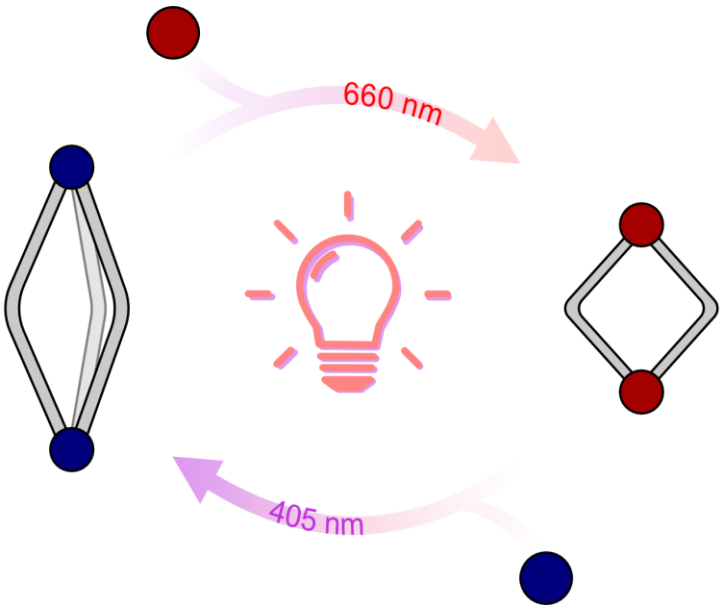

Figure 109: Targeted transformation of **A^{3}Tren^2** into a macrocycle.

A^{3}Tren^2 was combined with different diamines and stirred under continuous irradiation with red light (660 nm) for 5 days. After ^{1}H and ^{19}F{^{1}H} NMR as well as MALDI-mass measurements were conducted, the mixture was irradiated with UV light for 14 hours and again irradiated with red light for 5 days. Finally, the samples were stirred in the dark at room temperature for 4 days and heated in the dark to 45 °C for 2 days.

The combination of **A^{3}Tren^2** and **D** under irradiation with red light (660 nm) in *d*-chloroform led to the formation of two species that were not observed in the reactions of *E*-**A**, with either **Tren** or **D** producing signals at -118.44 ppm and -119.62 ppm as observed by ^{19}F{^{1}H} NMR spectroscopy (Figure 110). The latter signal was also observed in reactions of **D** with *E*-**A** and **B** or **H**, respectively, and can, according to MALDI-mass spectrometry, most likely be assigned to **AD^2**. An additional small signal is formed in low intensity at -118.74 ppm, which can most likely be assigned to an **A^{2}D^2** macrocycle, and is also formed in the irradiation of **A^{3}D^3**. Irradiation with UV light (405 nm) changed the ratio of the peaks of the newly observed macrocycle, with the peak at -119.62 ppm rising in intensity and the peak at -118.44 ppm declining, indicating that the first can be assigned to a *Z* species while the latter correlates to an *E* species. Peaks that can be assigned to *E,E,E*-**A^{3}Tren^2**, and *E,E,E*-**A^{3}D^3** could also be

observed at -118.10 ppm and -119.26 ppm, respectively. Irradiation with red light (660 nm) for 5 days yielded a spectrum that closely resembles the one initially obtained. Stirring the sample in the dark for a total of 6 days, two of those at 45 °C, again led to the formation of the new *E* compound as well of *E,E,E*-**A^{3}D^3**. While the irradiation with UV light only led to the formation of *E,E,E*-**A^{3}D^3** in minor amounts, heating the mixture formed *E,E,E*-**A^{3}D^3** as the major product, indicating that the bisimine **AD^2** might be the kinetic product while *E,E,E*-**A^{3}D^3** seems to be the thermodynamic product.

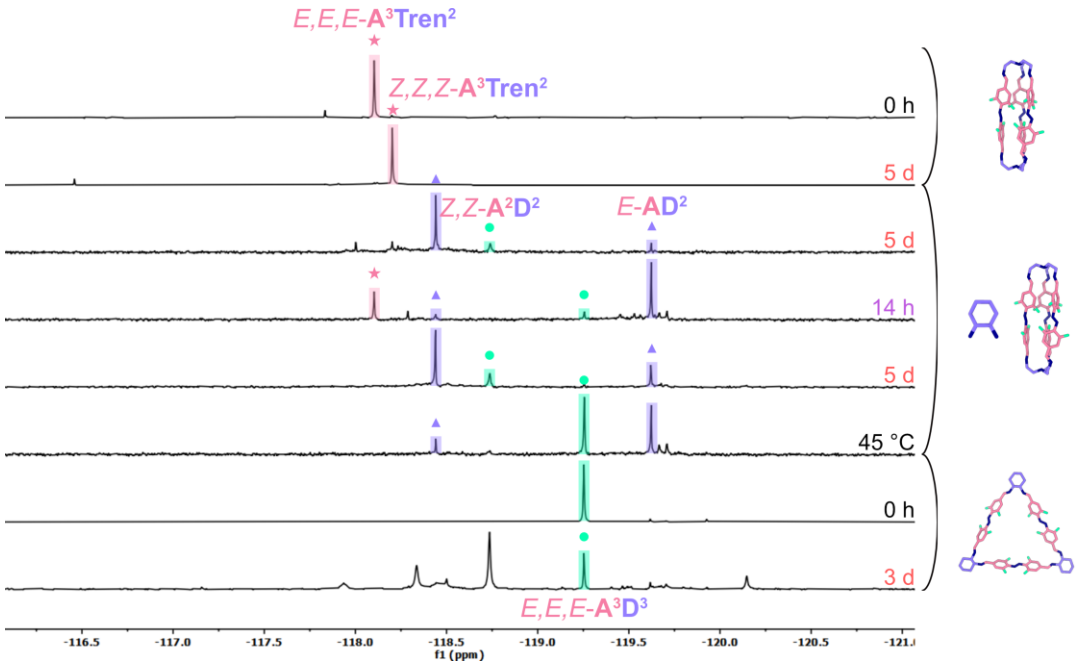

Figure 110: Excerpts of the $^{19}F\{^1H\}$ NMR spectra of *E,E,E*-**A^{3}Tren^2** in the dark (times highlighted in black) and after irradiation with red light (660 nm, times highlighted in red), spectra of a mixture of *E,E,E*-**A^{3}Tren^2** and **D** that was consecutively irradiated with red light, UV light (405 nm, times highlighted in violet), red light and stirred in the dark for 4 days at room temperature followed by 2 days at 45 °C, and spectra of *E,E,E*-**A^{3}D^3** in the dark and after irradiation with red light ($CDCl_3$, 282 MHz). Signals of **A^{3}Tren^2** cages are highlighted in pink (star), signals of **A^{3}D^3** and **A^{2}D^2** species are highlighted in turquoise (circle) and the newly observed signals are highlighted in blue (triangle).

Additional MALDI-mass spectrometry recorded after 5 days of irradiation with red light (660 nm) showed peaks for masses that can be assigned to **A^{3}Tren^2**, **A^{2}D^2**, and **A^{2}Tren^2**, indicating that the signal observed at -118.44 ppm could possibly be assigned to a *Z,Z*-**A^{2}Tren^2** macrocycle. This would be in accordance with similar macrocyclic species such as *Z,Z*-**A^{2}Pr^2**, *Z,Z*-**A^{2}B^2**, *Z,Z*-**A^{2}Pe^2**, and *Z,Z*-**A^{2}H^2** showing signals at a very similar chemical shift between -118.32 and -118.60 ppm. Additional measurements, such as DOSY NMR experiments, need to be conducted to further confirm the size of the formed macrocycle.

Combining the photoswitchable imine cage *E,E,E*-**A^{3}Tren^2** with another more rigid diamine (**mP**) under irradiation with red light (660 nm), the formation of *Z,Z*-**A^{2}mP^2** (-118.40 ppm) and

Z,Z-**A²Tren²** (-118.44 ppm) can be observed (Figure 111). Subsequent irradiation with UV light led to the reformation of the precursor *E,E,E*-**A³Tren²** (-118.10 ppm) as well as *E,E*-**A²mP²** (-119.18 ppm) and another probably larger macrocycle, which is most likely *E,E,E*-**A³mP³** (-119.64 ppm). Irradiation with red light again led to the formation of *Z,Z*-**A²mP²** and *Z,Z*-**A²mP²**, while the following period in the dark at room temperature and at 45 °C, which was hoped to produce *E,E,E*-**A³Tren²** with a higher yield, only led to the formation of *E,E*-**A²mP²**.

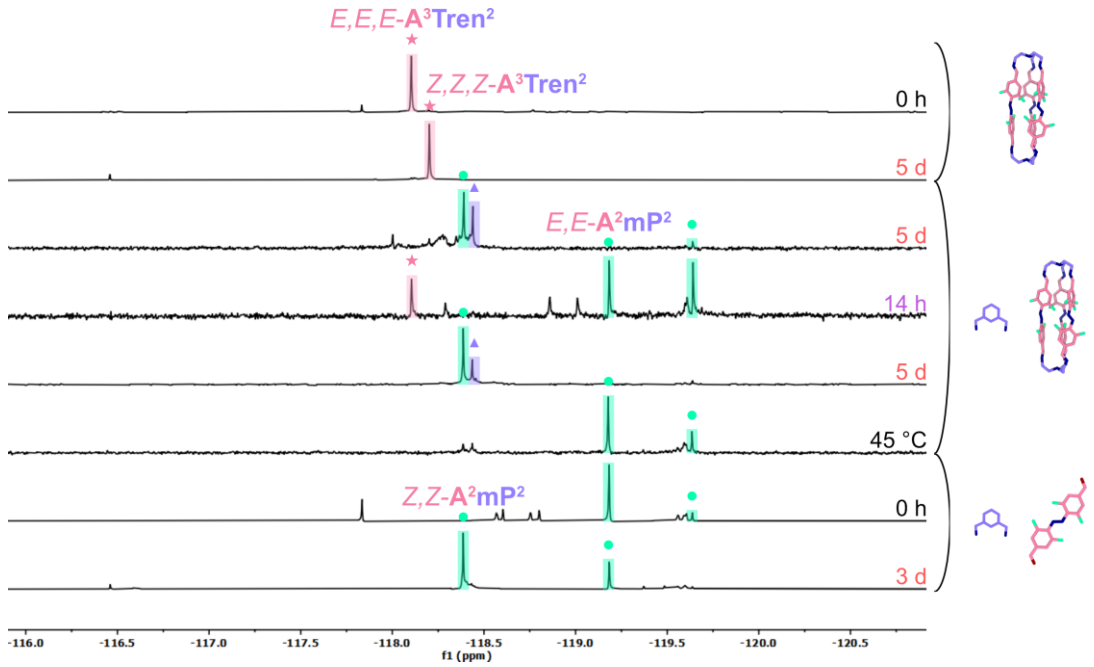

Figure 111: Excerpts of the $^{19}F\{^{1}H\}$ NMR spectra of *E,E,E*-**A³Tren²** in the dark (times highlighted in black) and after irradiation with red light (660 nm, times highlighted in red), spectra of a mixture of *E,E,E*-**A³Tren²** and **mP** that was consecutively irradiated with red light, UV light (405 nm, times highlighted in violet), red light and stirred in the dark for 4 days at room temperature followed by 2 days at 45 °C, and spectra of **A** and **mP** in the dark and after irradiation with red light ($CDCl_3$, 282 MHz). Signals of **A³Tren²** cages are highlighted in pink (star), signals of **AⁿmPⁿ** species are highlighted in turquoise (circle) and the newly observed signals are highlighted in blue (triangle).

E in combination with *E,E,E*-**A³Tren²** under irradiation resulted in the formation of **AⁿEⁿ** macrocycles, accompanied by the formation of precipitating byproducts (Figure 112a). The *Z* to *E* isomerisation with UV light or using heat led to a sharp signal at -119.63 ppm that was not previously observed. The MALDI-mass spectrum that was recorded after 5 days of irradiation with red light shows the formation of **A²E²** as well as peaks that can be assigned to **A³Tren²** and **A¹E¹Tren¹**. The reaction of **Pr** with imine cage *E,E,E*-**A³Tren²** led to the formation of an **AⁿPrⁿ** species that was previously observed but could not be assigned to a macrocycle or oligomer of a specific size (-120.37 ppm) and another species that was not previously observed (-119.00 ppm) (Figure 112b). Irradiation with UV light led to the formation of *E,E,E*-**A³Tren²** in a small percentage, while the decrease of the signal at -119.00 ppm and the concurrent

increase of the signal at -120.37 ppm were observed. After the repeated irradiation with red light, a signal that can be assigned to *Z,Z*-**A²Pr²** appeared along with the previously observed products.

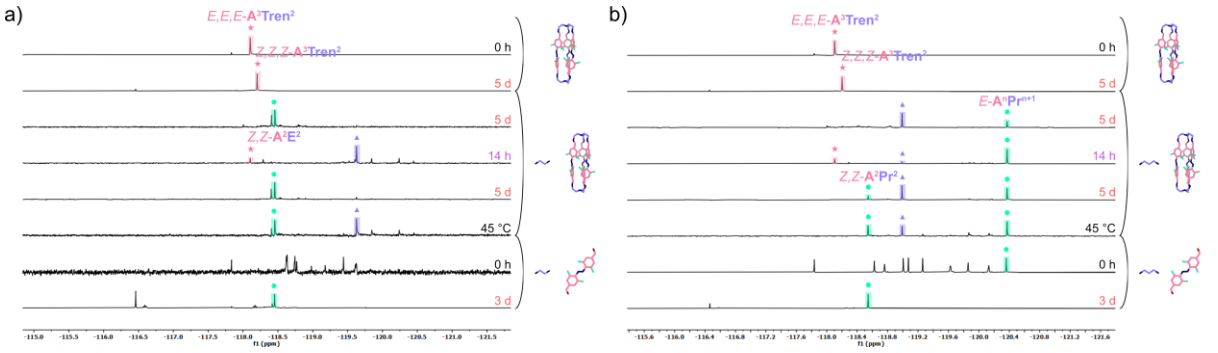

Figure 112: Excerpts of the $^{19}F\{^{1}H\}$ NMR spectra of *E,E,E*-**A³Tren²** in the dark (times highlighted in black) and after irradiation with red light (660 nm, times highlighted in red), spectra of a mixture of *E,E,E*-**A³Tren²** and a) **E** or b) **Pr** that was consecutively irradiated with red light, UV light (405 nm, times highlighted in violet), red light and stirred in the dark for 4 days at room temperature followed by 2 days at 45 °C, and spectra of **A** and a) **E** or b) **Pr** in the dark and after irradiation with red light ($CDCl_3$, 282 MHz). Signals of **A³Tren²** cages are highlighted in pink (star), signals of a) **AⁿEⁿ** or b) **AⁿPrⁿ** species are highlighted in turquoise (circle) and the newly observed signals are highlighted in blue (triangle).

The reactions of both **B** and **H** with *E,E,E*-**A³Tren²** under red light led to the formation of the respective *Z,Z*-macrocycle (Figure 113). After irradiation of the *Z,Z*-**A²B²** macrocycle with UV light signals at -118.10 ppm and -119.67 ppm, this indicated the formation of *E,E,E*-**A³Tren²** and a bisimine species based on **A** and **B**. A new signal at -119.24 ppm cannot be assigned to a specific macrocycle or oligomer and was not observed before. By triggering the *Z* to *E* isomerisation by heating the solution instead of using UV light, the formation of *E,E,E*-**A³Tren²** was not observed. *Z* to *E* isomerisation of the mixture containing *Z,Z*-**A²H²** by irradiation with UV light led to the formation of oligomeric bisimine species judging by the shape of the signals in the region of -119.75 ppm. Additionally, signals for *E,E,E*-**A³Tren²** at -118.10 ppm and a species that was not previously observed at -118.80 ppm were present. The spectrum obtained after thermal *Z* to *E* isomerisation are very similar only differing in still containing residues of *Z,Z*-**A²H²**, and not showing signals which can be assigned to *E,E,E*-**A³Tren²**.

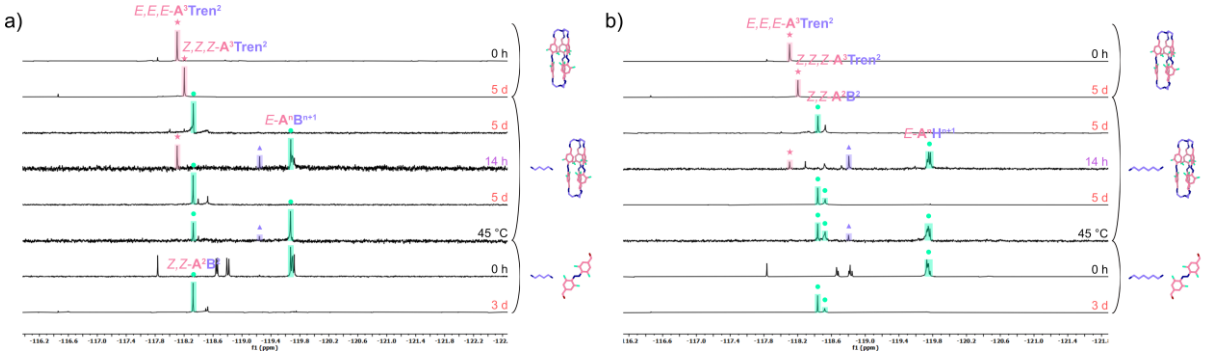

Figure 113: Excerpts of the $^{19}F\{^{1}H\}$ NMR spectra of *E,E,E*-**A³Tren²** in the dark (times highlighted in black) and after irradiation with red light (660 nm, times highlighted in red), spectra of a mixture of *E,E,E*-**A³Tren²** and a) **B** or b) **H** that was consecutively irradiated with red light, UV light (405 nm, times highlighted in violet), red light and stirred in the dark for 4 days at room temperature followed by 2 days at 45 °C, and spectra of **A** and a) **B** or b) **H** in the dark and after irradiation with red light ($CDCl_3$, 282 MHz). Signals of **A³Tren²** cages are highlighted in pink (star), signals of a) **AⁿBⁿ** or b) **AⁿHⁿ** species are highlighted in turquoise (circle) and the newly observed signals are highlighted in blue (triangle).

To summarise in combination with **B** and **H**, the imine cage was successfully transferred into a *Z*-macrocycle, the transformation into other macrocycles based on aliphatic diamines was less successful, and the formation of *Z,Z*-**A²mP²** was accompanied by the formation of *Z,Z*-**A²Tren²**. Unfortunately, the *Z* to *E* isomerisation of the obtained products or product mixtures yielded the precursor *E,E,E*-**A³Tren²** as a sideproduct at most. Attempts to heat the mixture to trigger the isomerisation and the formation of the most stable product also did not lead to the formation of the imine cage.

Summary

In this chapter the combination of **A** with **D** and different diamines as well as the combination of discrete supramolecular structures **A³Tren²** and **A³D³** with different diamines under irradiation or in the dark either led to the formation of other discrete structures or product mixtures. The rigid diamines **DPEN** and **mP** were combined with **D** and either *E*- or *Z*-**A**. For *E*-**A** and **DPEN**, the formation of a **DPEN** macrocycle as well as mixed species and small quantities of **A³D³** was observed, while the reaction with **mP** led to the formation of mixed oligomers as well as an **A²mP²** and **A³D³** macrocycle. Irradiating the mixtures or employing *Z*-**A** as a starting material caused the formation of the *Z*-isomer of a **DPEN** macrocycle as well as the formation of a *Z,Z*-**A²mP²** macrocycle. *Z,Z*-**A²D²** macrocycles were only observed in smaller percentages. Competitive experiments that combined **D** with different diamines and *Z*-**A** showed that in the case of the aliphatic diamines **E**, **Pr**, **B**, and **H**, the formation of the corresponding *Z*-macrocycles, which were in some cases accompanied by the formation of side products, were clearly preferred over the formation of the *Z,Z*-**A²D²** or **A³D³** macrocycles. The reactions using *E*-**A** as a starting material did not favour the formation of oligomers or

macrocycles containing solely **A** and **D**, but in the case of **E** and **Pr**, they favour the formation of binary macrocyclic or oligomeric species, and in the case of **B** and **H**, they lead to the formation of mixed oligomeric species containing both **D** and **B** or **H**, respectively.

In conclusion, while the formation of the respective *Z*-isomeric macrocycle is preferred over the formation of *Z,Z*-**A²D²**, as anticipated, the formation of **A³D³** starting from *E,E,E*-**A³D³** is not preferred in competitive conditions.

Combining *E,E,E*-**A³D³** with the different diamines under irradiation and triggering the *Z* to *E* isomerisation either by irradiation with UV light or thermally did not lead to the reformation of the precursor macrocycle. However, the reactions led to the irreversible transformation of the trianglimine into different metastable macrocycles (Figure 114) with a fairly high selectivity.

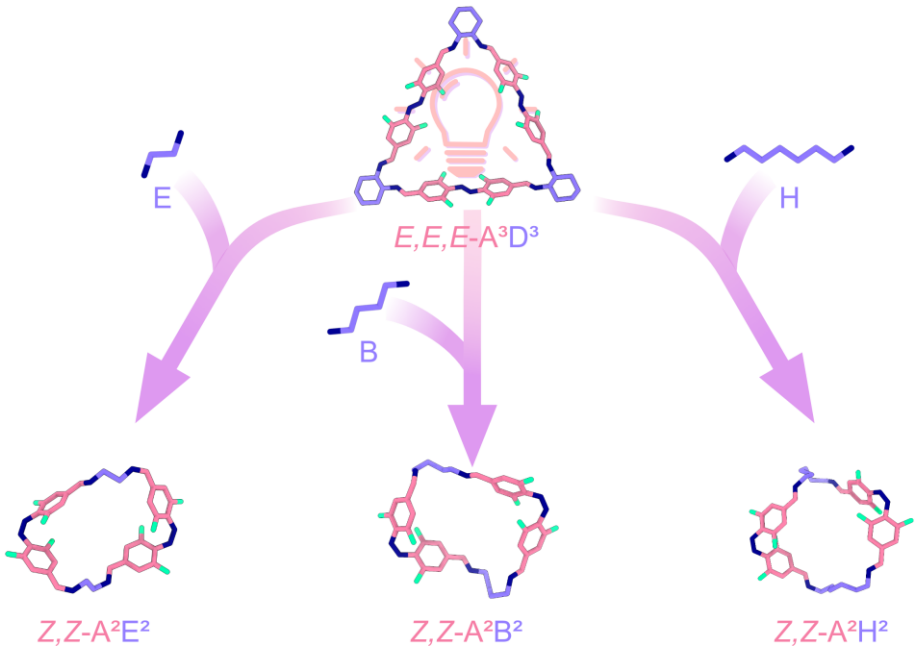

Figure 114: Transformation of *E,E,E*-**A³D³** to different *Z,Z*-macrocycles.

Employing an excess of **D** in combination with **A** and **H** did not lead to the selective formation of **A³D³** to but to the formation of the acyclic **AD²** species, which could not be transferred into the previously observed *Z,Z*-**A²H²** macrocycle.

The combination of the photoswitchable imine cage *E,E,E*-**A³Tren²** with different diamines under irradiation with red light led to the irreversible transformation into different imine macrocycles. Attempts to generate a dissipative system in which the precursor *E,E,E*-**A³Tren²** can be regained and again transformed were not successful, but the selective transformation could be achieved with diamines. Among the amines investigated, **B** and **H** were capable of leading to selective transformations upon irradiation, while the reactions of the other compounds often led to the formation of byproducts.

While the targeted reversible imine exchange leading to macrocycle to macrocycle transformation was not observed the irreversible transformation of the *E,E,E*-**A³D³** macrocycle

and the imine cage *E,E,E*-**A**^{3}**Tren**^{2} into other smaller macrocycles could be obtained by irradiation. These macrocycles were transient and transformed into a mixture of different products. The different mixtures of amines in combination with *E*-**A** often led to the formation of different binary and mixed products but upon applying light as a stimulus these mixtures could be reversibly and rather selectively transferred into distinct macrocyclic species.

3.2.6 Conclusion

In this work different dynamic and dissipative photoresponsive systems based on the dynamic covalent formation of imines were established. While many intriguing metal-based supramolecular systems have been reported that can undergo dissipative rearrangements, the number of metal-free systems is much smaller. Most imine based systems have until now been based on temporary pH changes by addition of metastable acids. During this work different dynamic formations could be observed and intensively studied and varying photoresponsive supramolecular structures have been synthesised.

The fluorinated photoswitchable building block **A** that was previously reported, was thoroughly investigated in regard to its photochemical properties and its reactivity towards imine formation. As the beneficial properties of **A** as a photoswitchable building block for imine systems was established a model compound $\mathbf{AC^2}$ was additionally synthesised and analysed to confirm that those properties undergo no major change upon imine formation.

The combination of **A** with rigid diamine **D** either led to the formation of an $\mathbf{A^3D^3}$ trianglimine or to a mixture of different macrocycles containing isomers of $\mathbf{A^3D^3}$ and the smaller macrocycle $\mathbf{A^2D^2}$, depending on the isomer of **A** that was employed. The irradiation of $\mathbf{A^3D^3}$ with red light also led to the formation of the product mixture, which could be reversibly transferred to precursing $\mathbf{A^3D^3}$. This is the first time that the dissipative transformation of an imine macrocycle was triggered photochemically. Additionally, the obtained macrocycle $\mathbf{A^3D^3}$ as well as its amine derivative $\mathbf{A^3D^3_{red}}$ could be interesting hosts in the future due to their exceptional photochemical properties and their switchability with visible light.

Two other rigid diamines, **DPEN** and **mP**, were also employed in combination with **A**, with the first not leading to any stable macrocyclic species and the second amine selectively forming the $\mathbf{A^2mP^2}$ macrocycle as a preferred product with both isomers of **A**.

The utilisation of more flexible aliphatic diamines **E**, **B** and **H**, with an even number of carbon atoms, led to the formation of insoluble or soluble oligomeric and polymeric structures with the *E*-isomer of **A** and to the formation of discrete macrocycles with the *Z*-isomers. Apart from the insoluble **E**-based imine oligomers the obtained product mixtures could be transformed selectively into the corresponding macrocyclic structures. In these cases the ring-chain equilibrium that is present in the formation of polymers can be reversibly controlled by light.

Aliphatic diamines **Pr** and **Pe**, as well as the derivate **O**, were also combined with *E*- and *Z*-**A**. While the first led to the formation of different products with the *E*-isomer and to a small macrocycle with the corresponding *Z*-isomer, the combination of both isomers with the other amines led to the formation of macrocyclic species $\mathbf{A^2Pe^2}$ or $\mathbf{A^2O^2}$ independent of the isomer employed. A single-crystal X-ray structure obtained for *E,E*-$\mathbf{A^2O^2}$ gave insights of the possible impact of the gauche effect on the structure formation.

A three-dimensional photoresponsive system was generated by combining **Tren** with **A** leading to the formation of *E,E,E*-**A^{3}Tren^2**. Upon irradiation this cage undergoes no dissipative rearrangement but can be isomerised in high yields. As a result of its bidirectional switchability and easy synthesis, as well as the distinct geometry change **A^{3}Tren^2** undergoes upon irradiation, the structure is an interesting target for further investigations.

To generate systems in which the exchange of a building block can be reversibly triggered by light the supramolecular structures **A^{3}D^3** and **A^{3}Tren^2** were combined with different diamines showing that the interconversion of one macrocycle or cage into another upon irradiation is possible, however the consecutive photochemically or thermally induced *Z* to *E* isomerisation did not lead to the formation of the precursor but to mixtures containing both compounds. However, the often ill-defined product mixtures obtained by the reaction of *E*-**A**, **D** and varying diamines could be reversibly transferred into distinct macrocyclic species, significantly simplifying the system by irradiation.

Employing both isomers of a photoswitchable building block made a variety of different structures with outstanding structural featuers accessible and allowed for the transient formation of different system and their reversible interconversion, all triggered by irradiation with light. Laying a foundation for the generation of photoresponsive imine systems these findings can be transferred to different systems enabling the synthesis of photoresponsive, dynamic and dissipative systems that are not based on metals.

4. Experimental details

4.1 General

Solvents and commercial starting materials were purchased from Sigma Aldrich, TCI, Fisher Scientific, J&K scientific, fluorochem, and abcr GmbH, and used as received. Dry solvents were obtained from an MBraun solvent purification system. Reactions were monitored by thin layer chromatography (TLC) carried out on silica gel plates (ALUGRAM® Xtra SIL G/UV254, Macherey Nagel) using UV light for detection. Column chromatography was carried out with silica gel (Silica 60 M, 0.04-0.063 mm, Macherey Nagel) using eluents as specified. Flash column chromatography was carried out on a Biotage® Selekt system using the SNAP Sphär60 columns. Compounds, that can photoisomerise were kept in the dark to avoid isomerisation unless otherwise stated. In addition, glassware used was wrapped in aluminium foil or amber glass variants were used.

NMR spectroscopy

NMR spectra were recorded on a Bruker Avance III 300 and a Bruker Avance III 600 spectrometer at 25 °C, using residual protonated solvent signals as internal standards for ^{1}H spectra (^{1}H: δ($CDCl_3$) = 7.26 ppm, δ(CD_2Cl_2) = 5.32 ppm).[119] Splitting patterns are abbreviated as follows: singlet (s), doublet (d), triplet (t), and multiplet (m). ^{19}F DOSY NMR spectra were recorded on a Bruker Avance NEO 600 spectrometer at 20 °C.

Crystallographic Details

Single-crystals were mounted using a microfabricated polymer film crystal-mounting tool (dual-thickness MicroMount, MiTeGen) using low viscosity oil (perfluoropolyalkylether; viscosity 1800 cSt, ABCR) to reduce the X-ray absorption and scattering. A Rigaku XtaLAB Synergy diffractometer or Bruker D8 QUEST single-crystal X-ray diffractometer using Mo-K_α (λ = 0.71073 Å) radiation or a Bruker D8 Venture single-crystal X-ray diffractometer using Cu-K_α (λ = 1.54178 Å) radiation were used for data collection at the temperature stated for each compound. The structures were refined by full-matrix least-squares methods on F^2 (SHELXL-2018)[120] or by intrinsic phasing (SHELXT-2013) and refined by full-matrix least-squares methods on F^2 (SHELXL-2014).[121] The hydrogen atoms were placed at calculated positions and refined by using a riding model. CCDC 2115251 (**Me^{2}Iso^3···IF$_5$**) CCDC 2115253 (**Me^{2}Iso^3···2(*p*-I$_2$F$_4$)**) CCDC 2115252 (**Me^{2}Iso^3···4(I$_3$F$_3$)**), CCDC 2115254 (**Me^{4}Ter^6···2(*p*-I$_2$F$_4$)**) and CCDC 2203711 (*Z*,*Z*-**A^{2}E^2**) contain the supplementary crystallographic data for the crystal

structures. These data can be obtained free of charge from The Cambridge Crystallographic Data Centre.

Computational Details

DFT-calculations were performed using QuantumEspresso[84b] for periodic crystals of **A···2(*p*-I_2F_4)**, **A···4(I_3F_3)** and **B···2(*p*-I_2F_4)**. Gaussian16[122] was used for the simplified model systems 1 and 2 in vacuum. The unit-cell structures of **A···2(*p*-I_2F_4)**, **A···4(I_3F_3)** and **B···2(*p*-I_2F_4)** were geometry-optimized using the Broyden-Fletcher-Goldfarb-Shanno (BFGS) scheme using the experimentally obtained unit cells as starting configuration. Atoms were described with ultrasoft Rappe-Rabe-Kaxiras-Joannopoulos(RRKJ)-type pseudopotentials. Periodic plane-wave DFT computations were performed using the generalized gradient approximation (GGA) with Perdew-Burke-Enzerhof (PBE) exchange correlation and the Monkhorst pack scheme with a 2 x 2 x 2 k-point mesh for **Me^2Iso^3 ···2(*p*-I_2F_4)** and **Me^2Iso^3···4(I_3F_3)** structures. The unit cell of **Me^4Ter^6···2(*p*-I_2F_4)** was evaluated using only the Γ-point. An energy cutoff of 70 Rydberg and a charge cutoff of 700 Rydberg was applied. To account for dispersion effects, the semi-empirical Grimme D3-correction scheme[123] was adopted. For QTAIM-analysis, a single point computation on the optimized structures was performed using CP2K[84a] with the DZVP-MOLOPT-GTH basis set and corresponding GTH-PBE pseudopotentials.

A simplified model of **Me^2Iso^3···2(*p*-I_2F_4)** was created from the optimized structure of **Me^2Iso^3···2(*p*-I_2F_4)** by cutting the cages to keep two bis-aminomethyl-benzenes that bind two ***p*-I_2F_4** donors. This model structure, as well as the other one investigated, were geometry-optimized *in vacuo* with the M062X density functional[124] and the CEP-121G basis set. The nature of stationary points was verified through vibrational analysis yielding no imaginary frequencies. Wavefunction analysis was performed for all computed structures with Multiwfn.[85] Approximate interaction energies between halogen bond donor and acceptor atoms were obtained by a) computing the kinetic energy density β·G(r) and b) by calculating the potential energy density -γ·V(r) of the electrons at the X-B bond critical point. Here, the coefficients β and γ denote proportionality factors. Interaction energies computed with the proportionality coefficients used by Espinosa *et al.* (β=0.429, γ=0.5)[125,126] and atom specific parameters reported by Bartashevich and Tsirelson (β=0.67, γ=0.68)[127] are listed in the respective table in each section.

Powder X-ray diffractogram measurements

PXRD measurements were obtained using a Rigaku Miniflex 600 with Cu-K_α radiation (40 kV, 15mA). The samples were measured at 2θ angles from 5-50 °. The most intense reflection in each diffractogram was normalized to 1 for better visibility.

IR analysis

Infrared spectra were recorded with a Shimadzu IR Affinity-1 with ATR sampling technique. Some of the spectra were standardized for better comparability.

Thermogravimetric analysis (TGA)

Thermogravimetric analysis was carried out under synthetic air using a Netzsch TG 209 F3 Tarsus in a temperature range from 30 °C to 600 °C at a step rate of 5 °C/min Onset decomposition temperatures were derived from thermogravimetric analysis curves by tangent evaluation.

Mass spectrometry

Matrix-assisted Laser Desorption/Ionization mass spectrometry was performed on a MALDI-TOF/TOF UltrafleXtreme (Bruker Daltonics) using dithranol as matrix. High resolution electrospray ionisation mass spectrometry was performed on a UHR-QTOF maXis 4G (Bruker Daltonics) instrument.

Irradiation experiments

A 405 nm LED (M405L3), a 470 nm LED (M470L3), a 565 nm LED (M565L3) and a 660 nm LED (M660L4), together with a LED driver (LEDD1B), from Thorlabs were applied for photoisomerisation. Irradiation times were determined using a stopwatch.

UV/VIS Spectroscopy

UV/VIS spectroscopy was performed on a Cary 60 equipped with a Peltier thermostatted cell holder. Quartz cuvettes (d = 10 mm) and solvents of spectrophotometric grade were used. Irradiation times were determined using a stopwatch. UV vis spectra were recorded at 25 °C unless otherwise stated. The concentrations of the measured samples are listed in a table in each section.

Absorption maxima λ_{max} were determined using the Origin Lab 2021b peak picking tool, molar attenuation coefficients ε were determined using the Lambert-Beer law (equation (2)), where *A* is the measured absorbance, *c* is the concentration of the analyte and *d* is the optical path length.

$$A = \varepsilon * c * d \tag{2}$$

4.2 Experimental details for halogen-bonded networks

4.2.1 Experimental details for part 3.1.1

Syntheses

Synthesis of tetrafluoro diiodobenzenes

General Procedure

Potassium iodide was added very slowly to a suspension of periodic acid in concentrated H_2SO_4 at 0 °C. To the dark mixture, tetrafluorobenzene was added dropwise. The suspension was heated to 70 °C for the indicated time. The mixture was allowed to cool to room temperature and then poured onto ice. The aqueous solution was extracted with diethyl ether and the combined organic phases were washed with aqueous, saturated $Na_2S_2O_3$ solution and water. The organic solution was dried over $MgSO_4$ and concentrated under reduced pressure.

1,2,3,4-tetrafluoro-5,6-diiodobenzene (*o*-I_2F_4)

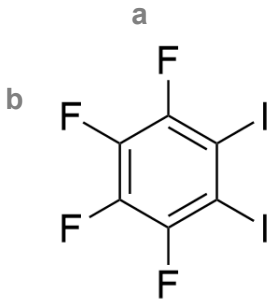

The product was prepared according to the general procedure using potassium iodide (4.43 g, 26.7 mmol, 3.01 eq.), periodic acid (1.70 g, 8.86 mmol, 1.00 eq.), concentrated H_2SO_4 (10 mL), and 1,2,3,4-tetrafluorobenzene (0.950 mL, 8.86 mmol, 1.00 eq.), at 70 °C for 4 h. The crude product was purified by recrystallization from CyHex yielding ***o*-I_2F_4** (2.68 g, 6.68 mmol, 75%) as dark orange crystals.

$^{19}F\{^1H\}$ NMR (282 MHz, $CDCl_3$): δ = -104.04 – -104.28 (m, 2F, F_a), -151.02 – -151.25 (m, 2F, F_b).

Analytical data was in accordance with literature.[128]

1,2,3,5-tetrafluoro-4,6-diiodobenzene (*m*-I_2F_4)

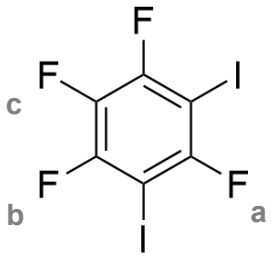

The product was prepared according to the general procedure using potassium iodide (4.43 g, 26.7 mmol, 3.33 eq.), periodic acid (1.54 g, 8.00 mmol, 1.00 eq.), concentrated H_2SO_4 (20 mL), and 1,2,3,5-tetrafluorobenzene (0.862 mL, 8.00 mmol, 1.00 eq.), at 70 °C for 19 h. The product ***m*-I_2F_4** (2.59 g, 6.44 mmol, 81 %) was isolated as a light pink oil.

$^{19}F\{^1H\}$ NMR (282 MHz, $CDCl_3$): δ = -76.46 (d, *J* = 8.7 Hz, 1F, F_a), -110.63 (d, *J* = 22 Hz, 2F, F_b), -158.27 (td, *J* = 22 Hz, *J* = 9.2 Hz, 1F, F_c).

1,2,4,5-tetrafluoro-3,6-diiodobenzene (*p*-I_2F_4)

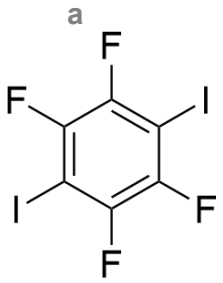

The product was prepared according to the general procedure using potassium iodide (4.98 g, 30.0 mmol, 3.30 eq.), periodic acid (1.73 g, 9.00 mmol, 1.00 eq.), concentrated H_2SO_4 (20 mL), and 1,2,4,5-tetrafluorobenzene (1.10 mL, 9.00 mmol, 1.00 eq.), at 70 °C for 4 h. The crude product was purified by recrystallization from CyHex yielding ***p*-I_2F_4** (2.82 g, 7.00 mmol, 78%) as colourless crystals.

$^{19}F\{^1H\}$ NMR (282 MHz, $CDCl_3$): δ = -118.06 (s, 4F, F_a) ppm.
Analytical data was in accordance with literature.[129]

2,3,5,6-tetrafluoro-4-iodoaniline (29)

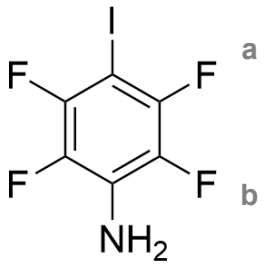

2,3,5,6-Tetrafluoroaniline (1.16 g, 7.00 mmol, 1.00 eq.) was dissolved in EtOH (60 mL). To this mixture red mercury oxide (1.52 g, 7.00 mmol, 1.00 eq.) was added and the resulting mixture was stirred for 20 minutes at room temperature. Iodine (1.78 g, 7.00 mmol, 1.00 eq.) was added and the resulting suspension suspension was stirred for 20 hours at room temperature. After filtration over a small silica plug, the solution was concentrated and the crude product was redissolved in CH_2Cl_2. The organic phase was washed with an aqueous solution of Na_2SO_3 (10 wt%, 20 mL) and dried over $MgSO_4$. After evaporation of the solvent, the crude product was purified by recrystallization from CyHex yielding aniline **29** (1.53 g, 5.26 mmol, 75%) as dark orange to brown crystals.

^{19}F NMR (565 MHz, $CDCl_3$, 298 K): δ = -123.29 – -123.41 (m, 2F, F_a), -158.91 – -159.03 (m, 2F, F_b).

Analytical data was in accordance with literature.[78c]

4,4'-di(iodo)perfluoroazobenzene (I_2F_8)

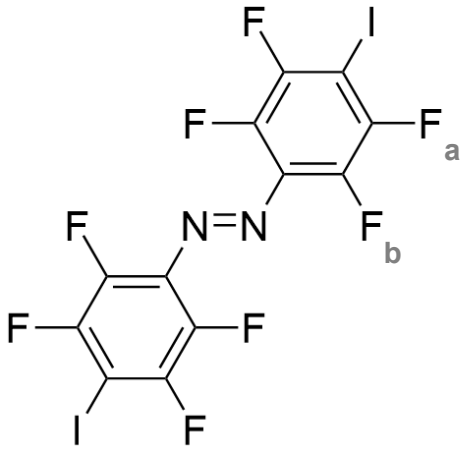

DBU (1.91 mL, 7.00 mmol, 2.00 eq.) and aniline **29** (1.02 g, 3.50 mmol, 1.00 eq.) were dissolved in CH_2Cl_2 (50 mL) and stirred at room temperature for 10 minutes. After cooling to -78 °C NCS (0.935 g, 7.00 mmol, 2.00 eq.) was added to the yellow solution which immediately

turned red. The mixture was stirred for 20 minutes before saturated aqueous sodium bicarbonate solution (20 mL) was added and the suspension was allowed to thaw. The organic phase was washed with water (3 x 50 mL), aqueous HCl solution (1 M, 3 x 50 mL) and was then dried over Na_2SO_4. The solvent was removed *in vacuo* and the crude product was purified *via* column chromatography using CyHex:EtOAc (95:5) yielding azobenzene **I_2F_8** (0.251 g, 0.434 mmol, 25%) as dark red needles.

^{19}F NMR (565 MHz, $CDCl_3$): δ = *E*: -119.11 – -119.266 (m, 2F, F_a), -147.50 – -147.66 (m, 2F, F_b).

Analytical data was in accordance with literature.[78c]

1,3,5-trifluoro-2,4,6-triiodobenzene (I_3F_3)

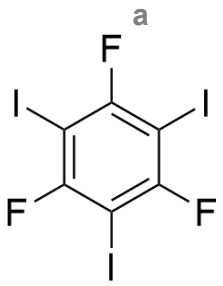

Potassium iodide (7.47 g, 45.0 mmol, 5.00 eq.) was added very slowly to a suspension of periodic acid (2.59 g, 13.5 mmol, 1.50 eq.) in concentrated H_2SO_4 (20 mL) at 0 °C. To the dark mixture, 1,2,4,5-tetrafluorobenzene (0.97 mL, 9.00 mmol, 1.00 eq.) was added dropwise. After finished addition, the suspension was heated to 70 °C overnight. The mixture was allowed to cool to room temperature and then poured onto ice. The aqueous solution was extracted with diethyl ether and the combined organic phases were washed with a saturated aqueous Na_2SO_3 solution and water. The solution was dried over $MgSO_4$ and concentrated under reduced pressure. The crude product was purified by recrystallization from CyHex to yield **I_3F_3** (3.33 g, 6.53 mmol, 73 %) as colourless needles.

^{19}F{^{1}H} NMR (282 MHz, $CDCl_3$): δ = -68.8 (s, 3F, F_a) ppm.

Analytical data was in accordance with literature.[77]

Association experiments

The constant component is referred to as “host” while the varied compound is called “guest”. 1,2,3,4,5-Pentafluoro-6-iodobenzene (**IF_5**) was used as the host and *N*-benzylideneaniline (**28**) was chosen as guests. ^{19}F NMR spectra were recorded on a 300 MHz Bruker Avance III at 298 K. Hexafluorobenzene in C_6D_6 was added as an internal standard.

The stock solution of the host (c = 11.51 mM) in cyclohexane was created using gravimetric analyses. This solution was then used to prepare the stock solution of the guest (*c* = 1.261 M). The guest was successively added to the host, keeping the total concentration of the host constant while the total concentration of the guest was varied. The titrations were carried out twice.

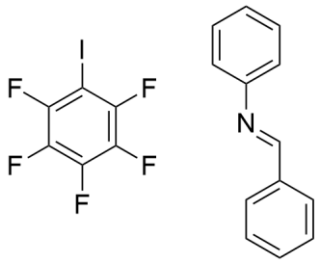

IF_5 **28**

Table S1: Concentration of guest, equivalents of guest added in comparison to host and resulting shift in the ^{19}F NMR for both titrations.

$[G]_0$ in M	$[G]_0/[H]_0$	|Δδ(F)| in ppm	
		1	2
0.000	0.0	0.000	0.000
0.006	0.5	0.010	0.006
0.011	1.0	0.025	0.016
0.023	2.0	0.031	0.020
0.044	3.9	0.038	0.033
0.065	5.7	0.050	0.044
0.086	7.4	0.068	0.063
0.105	9.1	0.074	0.071
0.151	13.1	0.103	0.091
0.194	16.8	0.119	0.107
0.269	23.4	0.145	0.141
0.334	29.0	0.164	0.160
0.391	33.9	0.185	0.176
0.441	38.3	0.200	0.196
0.485	42.1	0.208	0.210

Using OriginPro 2018b, the graphs of the change of the chemical shift ($\Delta\delta$) against the guest concentration $[G]_0$ were curve fitted using the orthogonal distance regression iteration algorithm. The following equation[130] was used for curve fitting:

$$\Delta\delta = \frac{\Delta\delta_{sat}}{2}\left[\left(\frac{[G]_0}{[H]_0} + 1 + \frac{1}{K_a[H]_0}\right) - \sqrt{\left(\frac{[G]_0}{[H]_0} + 1 + \frac{1}{K_a[H]_0}\right)^2 - 4\frac{[G]_0}{[H]_0}}\right] \quad (1)$$

The total concentration of the host $[H]_0$ is constant while the total concentration of the guest $[G]_0$ is varied. The association constant K_a and the change in chemical shift for a saturated system are obtained by curve fitting.

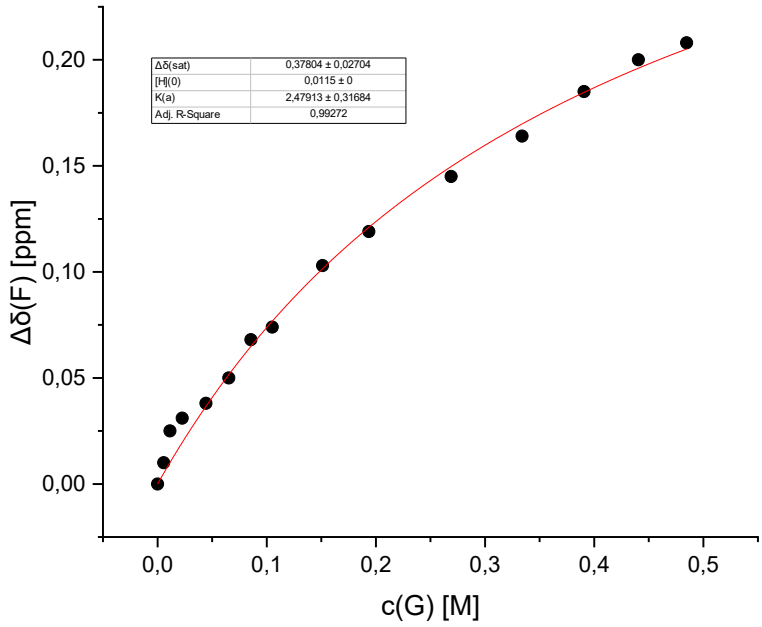

Figure S1: Binding titration 1.

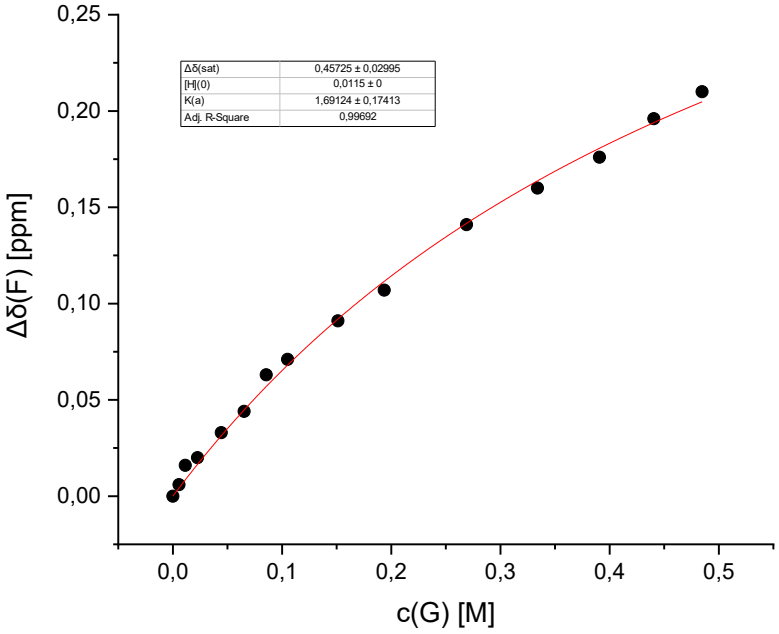

Figure S2: Binding titration 2.

The two determined binding constants for **28**···**IF_5** differ because of the very low association constant at room temperature. The shifts in the ^{19}F NMR spectra during the titration were very small, leading to the two values of K_a = 2.48 M^{-1} and K_a = 1.69 M^{-1}. Both values underline the weak binding of the model system in solution at room temperature and show the range of error.

Computational details

The DFT computations and QTAIM analyses in this section were performed by Dr. Oliver Weingart according to the method described in the general section.

28···IF_5 model system

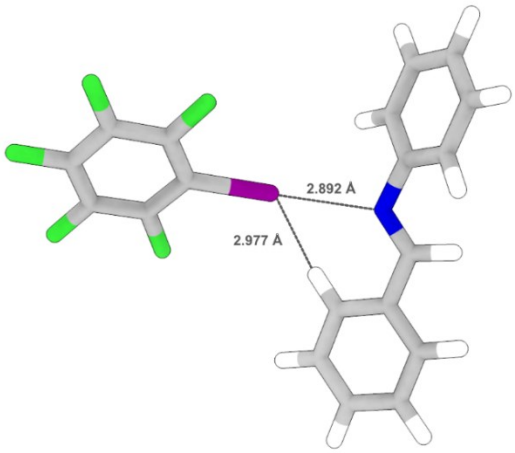

Figure S3: Binding mode of **28**···IF_5 model system.

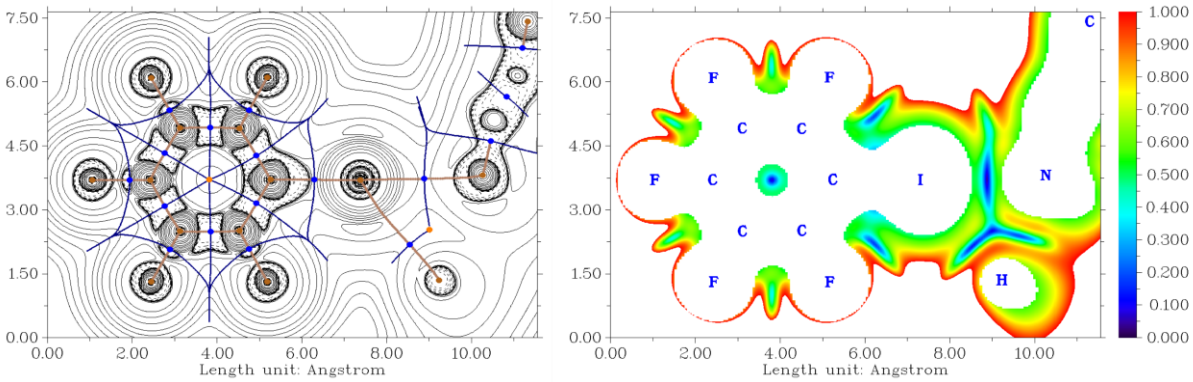

Figure S4: Left: Laplacian of electron density with critical points and bond paths. Bond critical (3,-1) points in blue, nuclear critical (3,-3) points in brown, ring critical (3,+1) points in orange, paths and zero-flux surfaces as brown and blue lines. Right: reduced density gradient map denoting halogen bonds in **28**···IF_5 model system.

Table S2: Distances and binding energies (kJ/mol) in **28**···IF_5.

Model	Bond	Distance [Å]	0.429·G(r)	-0.5·V(r)	0.67·G(r)	-0.68·V(r)
28···IF_5	I-N	2.89	18.62	20.15	29.07	27.41
	I-H	3.00	5.98	5.40	9.34	7.34

4.2.2 Experimental details for part 3.1.2

Synthesis

1,3,5-Tris(bromomethyl)-2,4,5-trimethylbenzene (30)

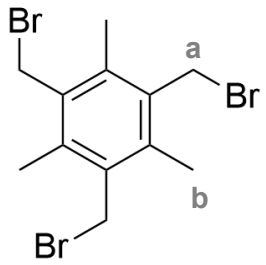

To a mixture of Zn (2.59 g, 39.6 mmol, 1.23 eq.) and AcOH (26 mL) was slowly added HBr in AcOH (25 mL, 33 wt%) while the mixture was vigorously stirred. After all Zn had dissolved the solution turned slightly orange. Mesitylene (4.50 ml, 32.3 mmol, 1.00 eq.), paraformaldehyde (5.83 g, 194 mmol, 6.01 eq.) and HBr in AcOH (74 ml, 33 wt%) were added to the orange solution. The mixture was then heated to 90 °C for 48 hours. The reaction was allowed to cool to room temperature and the precipitate was collected by vacuum filtration. The solid was washed thoroughly with water until the acetic acid and the remaining paraformaldehyde were removed completely and dried under reduced pressure at 110 °C for 24 hours yielding **30** as a white powder (11.8 g, 29.6 mmol, 75%).

^{1}H NMR (300 MHz, $CDCl_3$): δ = 4.58 (s, 6H, H_a), 2.47 (s, 9H, H_b).
Analytical data was in accordance with literature.[81]

1,3,5-Tris(azidomethyl)-2,4,5-trimethylbenzene (31)

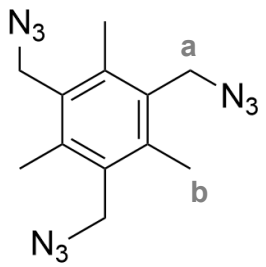

Tribromide (**1**) (11.8 g, 29.6 mmol, 1.00 eq.) was dissolved in DMF (166 mL). To this solution NaN_3 (11.6 g, 178 mmol, 6.01 eq.) was added and the mixture was stirred for 24 hours at room temperature. Afterwards the reaction mixture was diluted with EtOAc (560 mL), washed with

brine (3 x 500 mL) and water (3 x 500 mL). The organic phase was dried over $MgSO_4$ and the solvent was removed under reduced pressure. The product was obtained as a pale yellow crystalline solid (7.81 g, 27.4 mmol, 93%).

^{1}H NMR (300 MHz, $CDCl_3$): δ = 4.50 (s, 6H, H_a), 2.46 (s, 9H, H_b).
Analytical data was in accordance with literature.[81]

1,3,5-Tris(aminomethyl)-2,4,5-trimethylbenzene (Me)

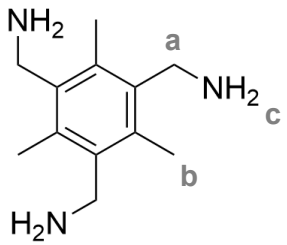

Triazide (**2**) (7.81 g, 27.4 mmol, 1.00 eq.) was dissolved in methanol (244 mL). To this solution 10 wt% Pd/C (0.157 g, 0.147 mmol, 0.538 mol%) was added. The Schlenk flask was first flushed trice, then filled with H_2 gas. The reaction mixture was stirred at room temperature overnight under an H_2 atmosphere. The mixture was filtered, and the solvent removed under reduced pressure. Since the ^{1}H NMR-spectrum showed in complete conversion, the product was redissolved in methanol (120 mL) and 10 wt% Pd/C (0.155 g, 0.146 mmol, 0.532 mol%) was again added. The Schlenk flask was again flushed and filled with hydrogen gas. The mixture was again stirred at room temperature for 92 hours. Afterwards the suspension was filtered, and the solvent removed under reduced pressure. Drying the obtained solid in a vacuum oven at 40 °C for 72 hours yielded amine **Me** (5.22 g, 25.2 mmol, 92 %) as an off-white solid.

^{1}H NMR (300 MHz, $CDCl_3$): δ = 3.92 (s, 6H, H_a), 2.45 (s, 9H, H_b), 1.26 (br, 6H, H_c)
Analytical data was in accordance with literature.[81]

Me²Iso³

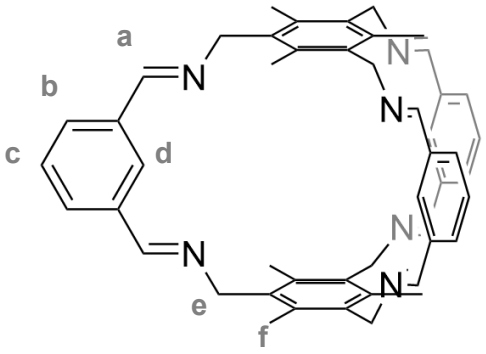

Iso (537 mg, 4.00 mmol, 1.00 eq.) and **Me** (829 mg, 4.00 mmol, 1.00 eq.) were dissolved in CH_2Cl_2 (865 mL) and heated to 40 °C for 5 days. The mixture was allowed to cool to room temperature and filtered to remove any precipitates that formed. CyHex (665 mL) was added and the CH_2Cl_2 was removed under reduced pressure at 30 °C. The precipitate that formed after removing the solvent was filtered off yielding the **Me²Iso³** (361 mg, 0.509 mmol, 38%) as an off-white solid.

¹H NMR (300 MHz, $CDCl_3$): δ = 8.15 (dd, *J* = 7.8 Hz, *J* = 1.7 Hz, 6H, H_b), 7.81 (t, *J* = 2.3 Hz, 6H, H_a), 7.50 (t, *J* = 7.8 Hz, 3H, H_c), 7.03 (br, 3H, H_d), 5.08 (d, *J* = 2.4 Hz, 12H, H_e), 2.11 (s, 18H, H_f); **MS** (MALDI) calc. for $[C_{48}H_{49}N_6]^+$: 709.401, meas.: 709.435.
Analytical data was in accordance with literature.[80]

Synthesis of Me²Iso³···IF₅

Slow evaporation of a solution of imine cage **Me²Iso³** (7.0 mg, 10 µmol, 1 eq.) and donor **IF₅** (1.3 µL, 10 µmol, 1.0 eq.) in a mixture of chloroform and methanol ($CHCl_3$:MeOH 10:1) led to the formation of crystalline **Me²Iso³···IF₅**.

Synthesis of Me²Iso³···2(*p*-I₂F₄)

Slow evaporation of a solution of imine cage **Me²Iso³** (7.0 mg, 10 µmol, 1 eq.) and donor ***p*-I₂F₄** (8.0 mg, 20 µmol, 2 eq.) in chloroform led to the formation of crystalline **Me²Iso³···2(*p*-I₂F₄)**.

Synthesis of Me²Iso³···4(I₃F₃)

Slow evaporation of a solution of imine cage **Me²Iso³** (7.0 mg, 10 µmol, 1 eq.) and donor **I₃F₃** (20 mg, 40 µmol, 4 eq.) in chloroform led to the formation of crystalline **Me²Iso³···4(I₃F₃)**.

Halogen-bonded complex synthesis by liquid assisted grinding

Samples prepared liquid assisted grinding were obtained by using a MM 400 Retsch ball-mill. The starting materials were mixed in targeted stoichiometry with a small amount of the corresponding solvent and then grinded using 5 mm zirconium dioxide balls at 25 Hz for 15 minutes.

Crystallographic details

$Me^2Iso^3\cdots IF_5$

Crystals of **$Me^2Iso^3\cdots IF_5$** were obtained by slow evaporation of a methanol/chloroform mixture at room temperature. A colourless block was mounted and data collection was performed at 153 K using Mo-K_α radiation. The structure was found to contain one well resolved methanol molecule enclosed into the centre of cage **Me^2Iso^3**. No other (disordered) solvent molecules were observed. However, the **IF_5** molecule displayed a minor rotational disorder (60°, 88:12 % occupancy) which was freely modelled and well resolved.

$Me^2Iso^3\cdots 2(p\text{-}I_2F_4)$

Crystals of **$Me^2Iso^3\cdots 2(p\text{-}I_2F_4)$** were grown by slow evaporation of a chloroform solution at room temperature. A colourless prism was mounted and data collection was performed at 100 K using Mo-K_α radiation. The cavities are filled with one partially disordered chloroform solvent molecule, which was modelled, and a second, heavily disordered chloroform molecule, that was ultimately removed using SQUEEZE.[131] The solvent accessible volume (SAV) found was 370 $Å^3$ with 118 electrons (per unit cell). Platon[132] suggested the presence of twinning and the structure was treated accordingly using the twinning routine.

$Me^2Iso^3\cdots 4(I_3F_3)$

Crystals of **$Me^2Iso^3\cdots 4(I_3F_3)$** were grown by slow evaporation of a saturated chloroform solution at room temperature. A colourless prism was mounted, and data collection was performed at 100 K using Mo-K_α radiation. The structure has three sites occupied by chloroform molecules each with three or more orientations. Modelling was attempted but all solvent molecules were ultimately removed using SQUEEZE.[131] The solvent accessible volume (SAV) found was 1341 $Å^3$ with 392 electrons (per unit cell). Checkcif produces one B-Alert for this structure: “PLAT910_ALERT_3_B Missing # of FCF Reflection(s) Below Theta(Min). 11 Note” this is likely due to the beam-stop, originating from using Mo radiation in combination with the geometry of our goniometer.

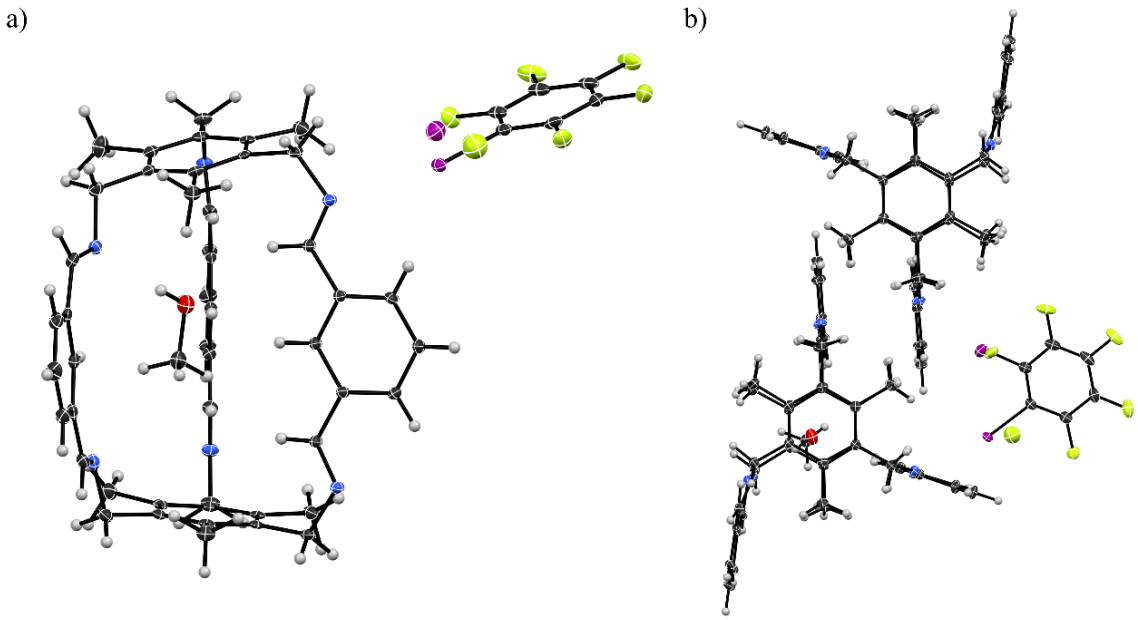

Figure S5: Data set of **Me²Iso³···IF₅** showing a), the asymmetric unit bearing one cage **Me²Iso³** and one **IF₅** molecule, together with an ordered methanol solvent molecule, thermal ellipsoids set at 50 % probability. The iodine atom shows positional disorder (88:12), which was treated accordingly, which is also visible in b), please see Table S5 for both possible halogen bonding interactions.

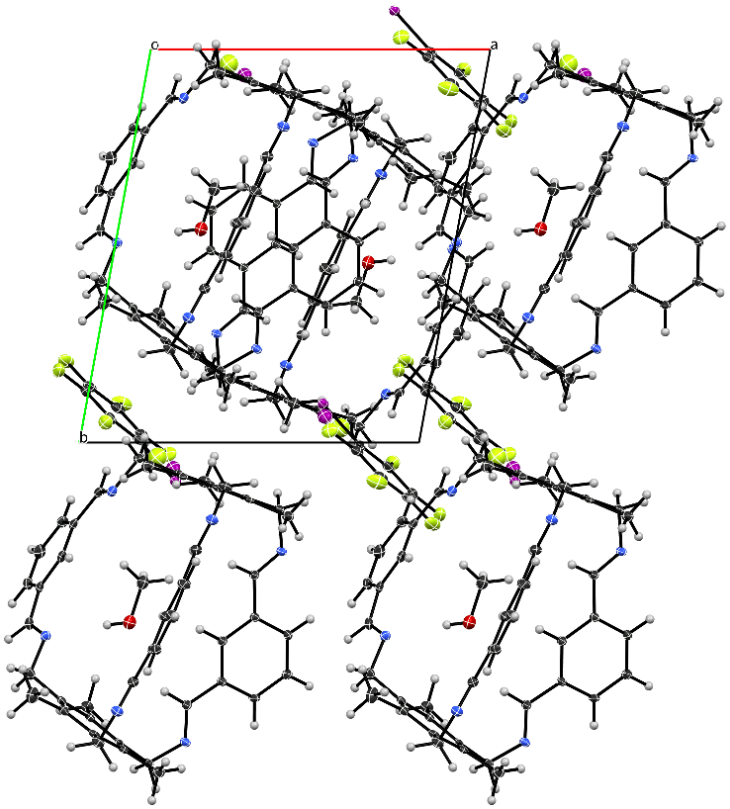

Figure S6: View of the extended unit cell of **Me²Iso³···IF₅** along the crystallographic *c* axis.

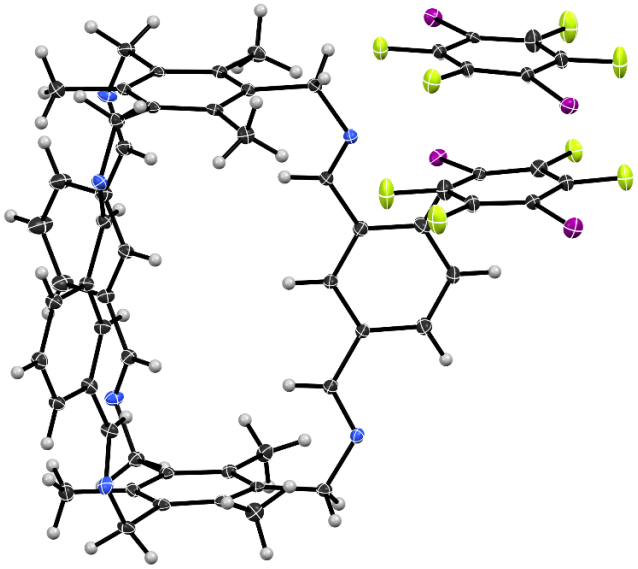

Figure S7: Data set of **Me²Iso³···2(*p*-I₂F₄)** showing the asymmetric unit bearing one cage **Me²Iso³** and two ***p*-I₂F₄** molecules, thermal ellipsoids set at 50 % probability, one disordered chloroform molecule was omitted for clarity.

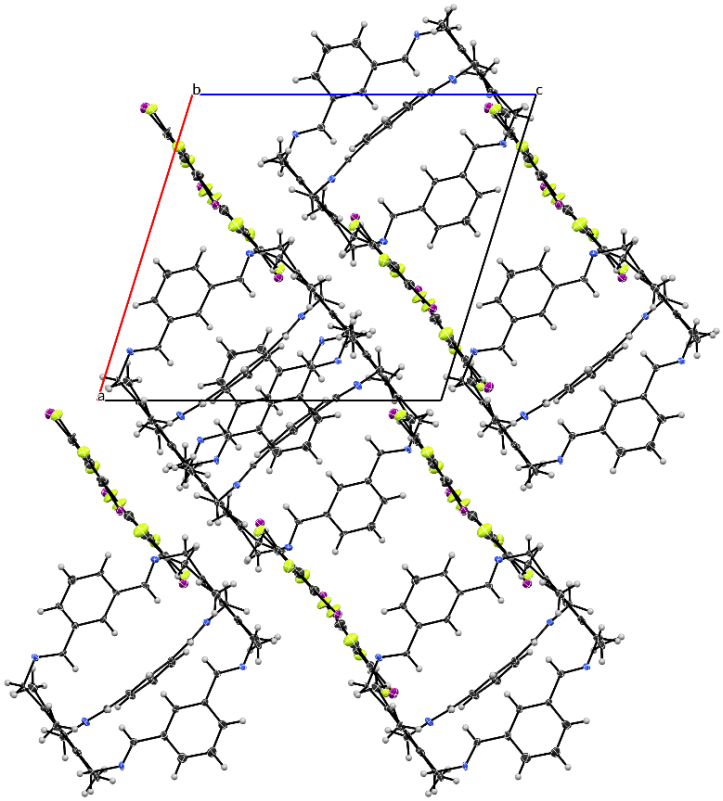

Figure S8: View of the extended unit cell of **Me²Iso³···2(*p*-I₂F₄)** along the crystallographic *b* axis, with solvent molecules omitted for clarity.

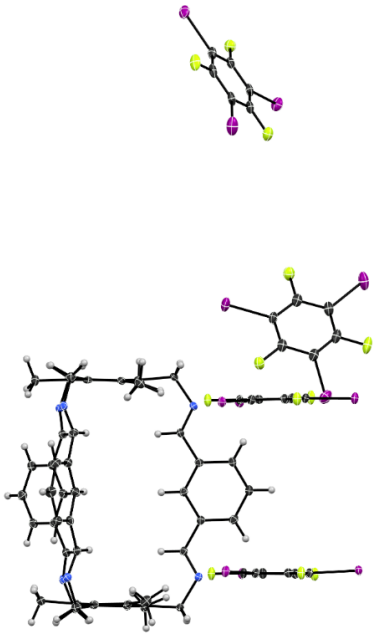

Figure S9: Data set of **Me²Iso³···4(I_3F_3)** showing the asymmetric unit bearing one cage **Me²Iso³** and four **I_3F_3** molecules, thermal ellipsoids set at 50 % probability.

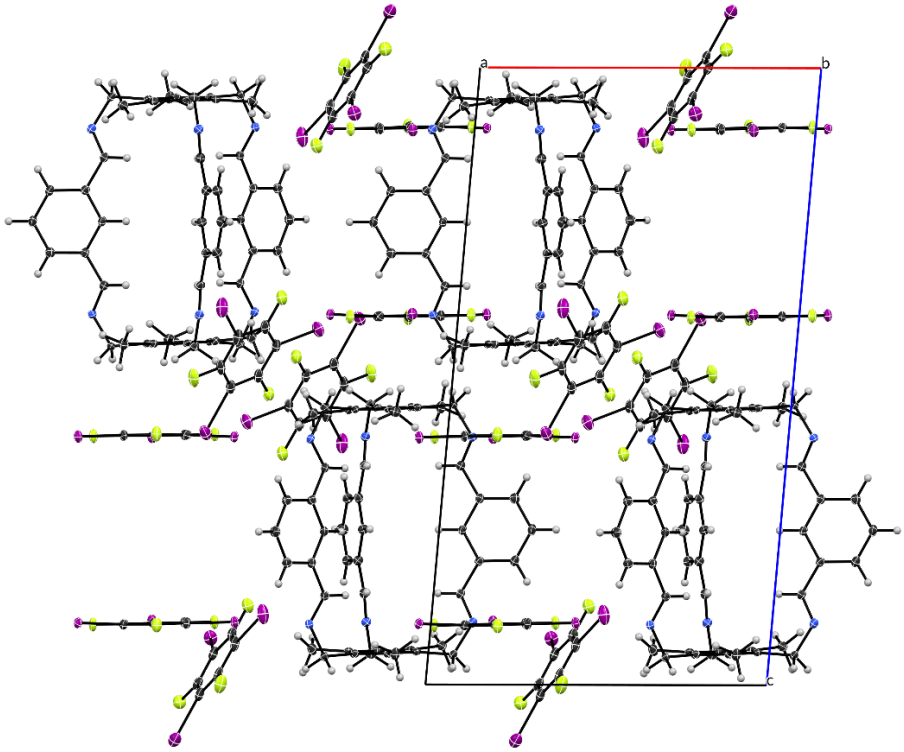

Figure S10: View of the extended unit cell of **Me²Iso³···4(I_3F_3)** along the crystallographic *b* axis.

Table S3: Crystal structure refinement details for **$Me^2Iso^3\cdots IF_5$** and **$Me^2Iso^3\cdots 2(p\text{-}I_2F_4)$**.

	$Me^2Iso^3\cdots IF_5$	**$Me^2Iso^3\cdots 2(p\text{-}I_2F_4)$**
Wavelength [Å]	Mo Kα	Mo Kα
Collection Temperature [K]	153	100
Formula	$C_{55}H_{52}F_5IN_6O$	$C_{61}H_{49}Cl_3F_8I_4N_6$
Formula weight	1034.92	1632.01
Crystal System	Triclinic	Triclinic
Space Group	P-1	P-1
a [Å]	12.0972(18)	14.6891(4)
b [Å]	15.049(3)	15.0515(2)
c [Å]	15.5995(18)	15.8495(4)
α [°]	116.465(5)	96.972(2)
β [°]	108.720(5)	106.882(2)
γ [°]	90.484(7)	91.054(2)
V [$Å^3$]	2369.1(6)	3323.09(14)
Z	2	2
μ [mm^{-1}]	0.74	2.06
Crystal size [mm]	0.15 x 0.14 x 0.11	0.46 x 0.24 x 0.18
Reflections collected	80779	17048
Independent reflections	9695	17048
Observed reflections [$I > 2\sigma(I)$]	7992	13997
R_{int}	0.089	-
Data/ parameters/restraints	9695/640/10	17048/786/267
$R[F^2>2\sigma(F^2)]$	0.037	0.056
$wR(F^2)$	0.079	0.167

Table S4: Crystal structure refinement details for **$Me^2Iso^3\cdots4(I_3F_3)$**.

	$Me^2Iso^3\cdots4(I_3F_3)$
Wavelength [Å]	Mo Kα
Collection Temperature [K]	100
Formula	$C_{72}H_{48}F_{12}I_{12}N_6$
Formula weight	2747.96
Crystal System	Triclinic
Space Group	P-1
a [Å]	15.1876(3)
b [Å]	15.3098(2)
c [Å]	23.9698(4)
α [°]	89.922(1)
β [°]	85.674(1)
γ [°]	60.309(2)
V [$Å^3$]	4823.73(16)
Z	2
μ [mm^{-1}]	3.91
Crystal size [mm]	0.33 x 0.27 x 0.19
Reflections collected	89851
Independent reflections	25176
Observed reflections [$I > 2\sigma(I)$]	20622
R_{int}	0.036
Data/ parameters/restraints	25176/925
$R[F^2>2\sigma(F^2)]$	0.039
$wR(F^2)$	0.088

Table S5: Bond lengths [Å] and angles [°] for **$Me^2Iso^3\cdots IF_5$**.

I(10)-N(11)	3.023(2)	N···I halogen bond
I(10A)-N(20)	3.043(4)	N···I halogen bond
N(31)-H(200)	2.234	hydrogen bonding
F(11)-H(19B)	2.968	H···F contact
F(12)-H(36)	2.646	H···F contact
F(12)-H(37)	2.629	H···F contact
F(13)-H(9AB)	2.662	H···F contact
F(13)-H(39A)	2.732	H···F contact
F(14)-H(8AA)	2.982	H···F contact
F(15)-H(31)	2.824	H···F contact
$Centroid_{(C1,2,3,4,5,6)}$-$Centroid_{(C1,2,3,4,5,6)}$	4.012	π-stacking (cage-cage)
$Centroid_{(C1A,2A,3A,4A,5A,6A)}$-$Centroid_{(C100,101,102,103,104,105)}$	3.653	π-stacking (cage-donor)
$Centroid_{(C12,13,14,15,16,17)}$- $Centroid_{(C12,13,14,15,16,17)}$	4.082	π-stacking (cage-cage)
$Centroid_{(C22,23,24,25,26,27)}$-$Centroid_{(C22,23,24,25,26,27)}$	3.729	π-stacking (cage-cage)
$Centroid_{(C100,101,102,103,104,105)}$-$Centroid_{(C100,101,102,103,104,105)}$	3.569	π-stacking (donor-donor)
C(100)-I(10)-N(11)	166.17(9)	N···I halogen bond
C(101)-I(10A)-N(20)	162.9(3)	N···I halogen bond
O(200)-H(200)-N(31)	173.6	hydrogen bonding
C(101)-F(11)-H(19B)	74.8	H···F contact
C(102)-F(12)-H(36)	127.6	H···F contact
C(102)-F(12)-H(37)	148.1	H···F contact
C(103)-F(13)-H(9AB)	82.6	H···F contact
C(103)-F(13)-H(39A)	97.4	H···F contact
C(104)-F(14)-H(8AA)	120.8	H···F contact
C(105)-F(15)-H(31)	149.8	H···F contact

Table S6: Bond lengths [Å] and angles [°] for **$Me^2Iso^3\cdots 2(p\text{-}I_2F_4)$**.

I(1)-N(6)	2.997(5)	N···I halogen bond
I(2)-N(1)	2.953(4)	N···I halogen bond
I(3)-N(5)	2.933(3)	N···I halogen bond
I(4)-N(3)	2.980(4)	N···I halogen bond
F(1)-H(23B)	3.047	H···F contact (inner layer)
F(1)-H(28)	2.634	H···F contact (inner layer)

F(1)-H(48C)	3.042	H···F contact (inner layer)
F(2)-H(23A)	2.882	H···F contact (inter layer)
F(2)-H(43)	3.063	H···F contact (inner layer)
F(2)-H(48C)	2.954	H···F contact (inner layer)
F(3)-H(19B)	3.011	H···F contact (inter layer)
F(4)-H(49C)	3.068	H···F contact (inter layer)
F(5)-H(11B)	3.085	H···F contact (inter layer)
F(6)-H(52B)	2.895	H···F contact (inter layer)
F(7)-H(7A)	3.120	H···F contact (inner layer)
F(7)-H(26)	2.616	H···F contact (inner layer)
F(7)-H(50B)	3.074	H···F contact (inner layer)
F(7)-H(50C)	2.682	H···F contact (inter layer)
F(8)-H(7A)	3.025	H···F contact (inter layer)
F(8)-H(45)	3.042	H···F contact (inner layer)
F(8)-H(50B)	2.992	H···F contact (inner layer)
$Centroid_{(C8,9,10,29,30,31)}$-$Centroid_{(C58,59,60,61,62,63)}$	3.731	π-stacking (donor-cage)
$Centroid_{(C14,15,16,53,54,55)}$- $Centroid_{(C14,15,16,53,54,55)}$	3.724	π-stacking (cage-cage)
$Centroid_{(C20,21,22,41,42,46)}$-$Centroid_{(C12,24,33,39,56,57)}$	3.844	π-stacking (donor-cage)
$Centroid_{(C35,36,37,43,44,45)}$- $Centroid_{(C35,36,37,43,44,45)}$	4.020	π-stacking (cage-cage)

C(12)-I(1)-N(6)	168.6(2)	N···I halogen bond
C(39)-I(2)-N(1)	165.0(2)	N···I halogen bond
C(58)-I(3)-N(5)	164.6(2)	N···I halogen bond
C(61)-I(4)-N(3)	171.6(2)	N···I halogen bond
C(56)-F(1)-H(23B)	151.4	H···F contact (inner layer)
C(56)-F(1)-H(28)	113.5	H···F contact (inner layer)
C(56)-F(1)-H(48C)	124.1	H···F contact (inner layer)
C(57)-F(2)-H(23A)	103.1	H···F contact (inter layer)
C(57)-F(2)-H(43)	128.7	H···F contact (inner layer)
C(57)-F(2)-H(48C)	127.0	H···F contact (inner layer)
C(24)-F(3)-H(19B)	71.9	H···F contact (inter layer)
C(33)-F(4)-H(49C)	98.6	H···F contact (inter layer)
C(62)-F(5)-H(11B)	99.4	H···F contact (inter layer)
C(63)-F(6)-H(H52B)	78.8	H···F contact (inter layer)
C(59)-F(7)-H(7A)	152.1	H···F contact (inner layer)
C(59)-F(7)-H(26)	113.0	H···F contact (inner layer)
C(59)-F(7)-H(50B)	124.2	H···F contact (inner layer)

C(59)-F(7)-H(50C)	104.2	H···F contact (inter layer)
C(60)-F(8)-H(7A)	122.9	H···F contact (inter layer)
C(60)-F(8)-H(45)	130.3	H···F contact (inner layer)
C(60)-F(8)-H(50B)	127.2	H···F contact (inner layer)

Table S7: Bond lengths [Å] and angles [°] for **Me^2Iso^3···4(I_3F_3)**.

I(1)-N(53)	2.972(5)	N···I halogen bond
I(2)-N(77)	3.016(4)	N···I halogen bond
I(3)-N(71)	2.967(5)	N···I halogen bond
I(19)-N(83)	2.994(4)	N···I halogen bond
I(20)-N(59)	2.978(5)	N···I halogen bond
I(21)-N(65)	3.004(4)	N···I halogen bond
I(3)-I(6)	3.8229(6)	I···I halogen bond
I(9)-I(20)	3.8433(5)	I···I halogen bond
F(10)-H(76B)	3.028	H···F contact
F(11)-H(98C)	2.946	H···F contact
F(12)-H(72A)	3.074	H···F contact
F(22)-H(95C)	2.942	H···F contact
F(23)-H(64A)	3.078	H···F contact
F(24)-H(60B)	3.066	H···F contact
F(46)-H(84A)	2.706	H···F contact
F(48)-H(60A)	2.671	H···F contact
$Centroid_{(C1,2,3,4,5,6)}$-$Centroid_{(C49,50,51,73,74,75)}$	3.785	π-stacking (cage-donor)
$Centroid_{(C13,14,15,16,17,18)}$-$Centroid_{(C61,62,63,85,86,93)}$	3.767	π-stacking (cage-donor)
$Centroid_{(C25,26,27,28,29,30)}$-$Centroid_{(C25,26,27,28,29,30)}$	3.657	π-stacking (donor-donor)
$Centroid_{(C37,38,39,40,41,42)}$-$Centroid_{(C37,38,39,40,41,42)}$	3.624	π-stacking (donor-donor)
C(3)-I(1)-N(53)	166.3(1)	N···I halogen bond
C(5)-I(2)-N(77)	164.7(1)	N···I halogen bond
C(1)-I(3)-N(71)	165.9(2)	N···I halogen bond
C(13)-I(19)-N(83)	165.5(1)	N···I halogen bond
C(15)-I(20)-N(59)	166.4(1)	N···I halogen bond
C(17)-I(21)-N(65)	163.5(1)	N···I halogen bond
C(29)-I(6)-I(3)	160.9(1)	I···I halogen bond
C(41)-I(9)-I(20)	159.3(1)	I···I halogen bond
C(6)-F(10)-H(76B)	108.6	H···F contact
C(4)-F(11)-H(98C)	91.3	H···F contact

C(2)-F(12)-H(72A)	76.7	H···F contact
C(18)-F(22)-H(95C)	91.4	H···F contact
C(16)-F(23)-H(64A)	108.1	H···F contact
C(14)-F(24)-H(60B)	77.4	H···F contact
C(42)-F(46)-H(84A)	82.5	H···F contact
C(38)-F(48)-H(60A)	138.7	H···F contact

Table S8: Bond lengths, sum of van der Waals Radii[133,134], and normalized bond lengths for the halogen bonds in the different networks.

	Contact	d_{XB} [Å]	ΣBvdW (Bondi) [Å]	d_{XB}/ ΣBvdW	ΣBvdW (Rowland) [Å]	d_{XB}/ ΣBvdW
$Me^2Iso^3\cdots IF_5$	N···I	3.023(2)	3.53	0.86	3.67	0.82
	N···I	3.043(4)	3.53	0.86	3.67	0.83
$Me^2Iso^3\cdots 2(p\text{-}I_2F_4)$	N···I	2.997(5)	3.53	0.85	3.67	0.82
	N···I	2.953(4)	3.53	0.84	3.67	0.80
	N···I	2.933(3)	3.53	0.83	3.67	0.80
	N···I	2.980(4)	3.53	0.84	3.67	0.81
$Me^2Iso^3\cdots 4(I_3F_3)$	N···I	2.972(5)	3.53	0.84	3.67	0.81
	N···I	3.016(4)	3.53	0.85	3.67	0.82
	N···I	2.967(5)	3.53	0.84	3.67	0.81
	N···I	2.994(4)	3.53	0.85	3.67	0.82
	N···I	2.978(5)	3.53	0.84	3.67	0.81
	N···I	3.004(4)	3.53	0.85	3.67	0.82
	I···I	3.8229(6)	3.96	0.97	4.06	0.94
	I···I	3.8433(5)	3.96	0.97	4.06	0.95

Computational details

The DFT computations and QTAIM analyses in this section were performed by Dr. Oliver Weingart according to the method described in the general section.

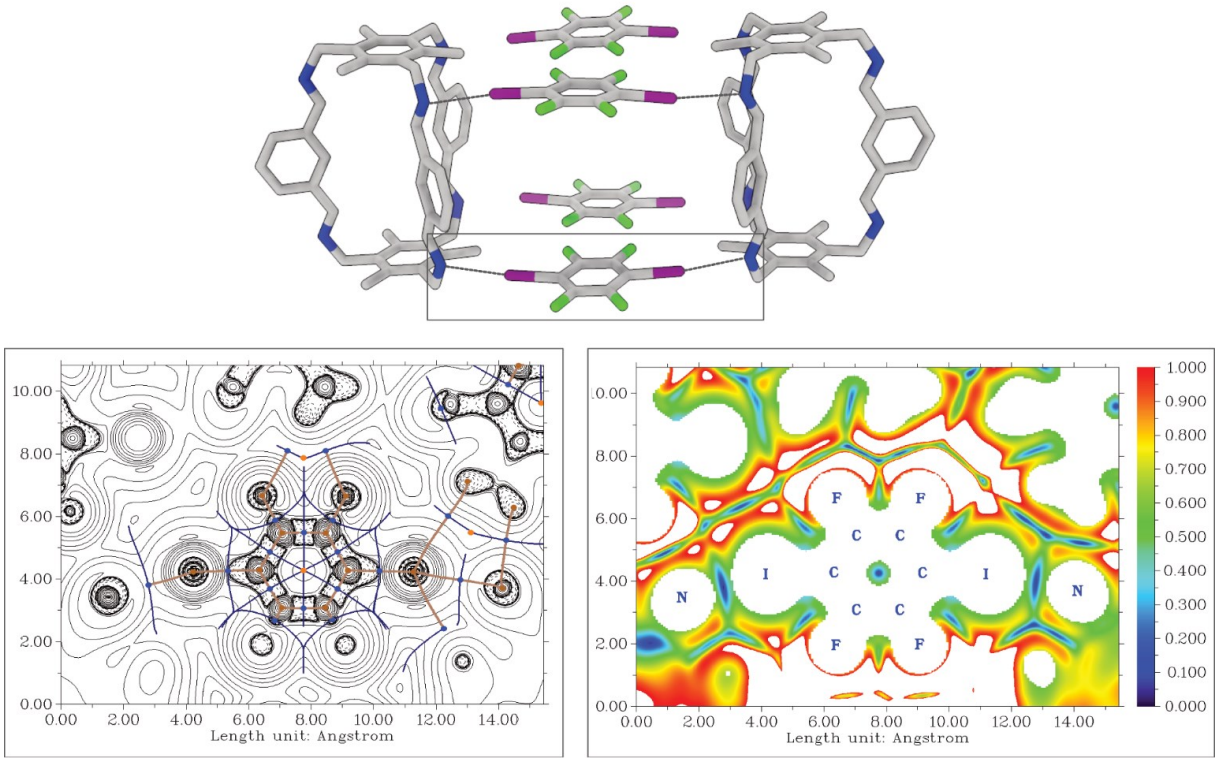

Figure S11: Structure of **Me^{2}Iso^3···2(*p*-I$_2$F$_4$)**. Laplacian map of the electron density (left) is depicted with critical points and bond paths. Bond critical (3,-1) points in blue, nuclear critical (3,-3) points in brown, ring critical (3,+1) points in orange, paths and zero-flux surfaces as brown and blue lines. The reduced density gradient map is shown on the right side.

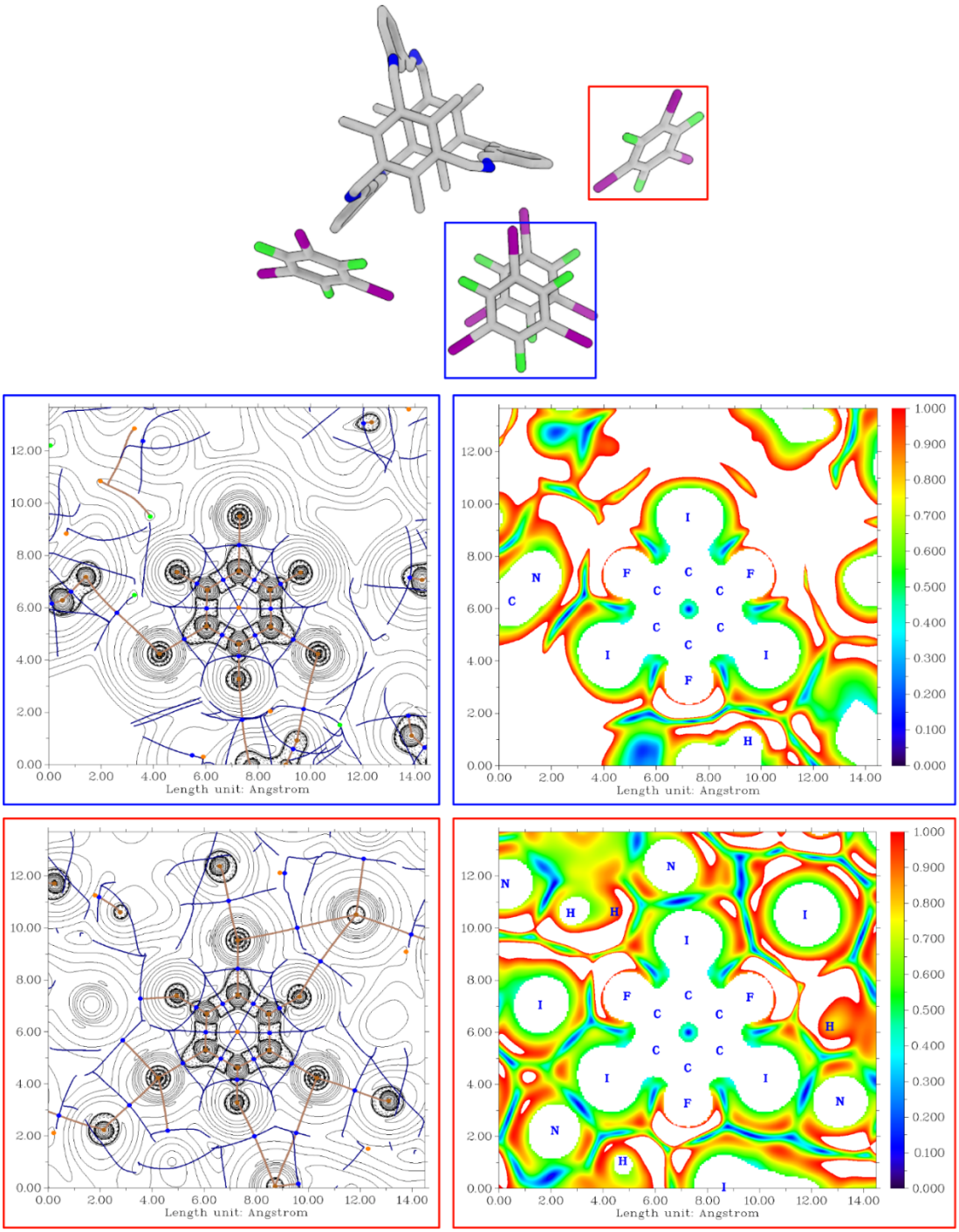

Figure S12: Structure of **$Me^2Iso^3\cdots4(I_3F_3)$** including the **I_3F_3** interconnecting the cages (blue outline) and the **I_3F_3** showing "solvent-like" behaviour (red outline). Laplacian maps of the electron density (left) are depicted with critical points and bond paths. Bond critical (3,-1) points in blue, nuclear critical (3,-3) points in brown, ring critical (3,+1) points in orange, paths and zero-flux surfaces as brown and blue lines. The reduced density gradient maps are shown on the right side.

Blue: Laplacian and reduced gradient maps for of **$Me^2Iso^3\cdots4(I_3F_3)$** with **I_3F_3** showing "solvent-like" behaviour.

Red: Laplacian and reduced gradient maps for of **$Me^2Iso^3\cdots4(I_3F_3)$** with **I_3F_3** interconnecting the cages.

Table S9: Distances and interaction energies (kJ/mol) in **Me^2Iso^3···2(*p*-I_2F_4)** and **Me^2Iso^3···4(I_3F_3)**.

Model	Bond	Distance [Å]	0.429·G(r)	-0.5·V(r)	0.67·G(r)	-0.68·V(r)
Me^2Iso^3···2(*p*-I_2F_4)$_{XB}$	I-N (1)	2.89	15.64	17.19	24.43	23.37
	I-N (2)	2.84	17.66	19.97	27.58	27.16
Me^2Iso^3···4(I_3F_3)$_{XB}$	I-N (1)	2.91	15.16	16.39	23.68	22.29
	I-N (2)	2.90	15.51	16.97	24.22	23.08
	I-N (3)	2.93	14.45	15.50	22.60	21.08
Me^2Iso^3···4(I_3F_3)$_{comp}$	I-N	4.07	2.02	1.66	3.16	2.26
	F-N	3.38	2.53	1.97	3.95	2.67
	I-H	3.39	2.53	2.12	3.96	2.89
	I-I (1)	3.86	4.74	4.40	7.39	5.98
	I-I (2)	4.48	2.12	1.76	3.31	2.40
	I-I (3)	4.67	1.46	1.13	2.28	1.54

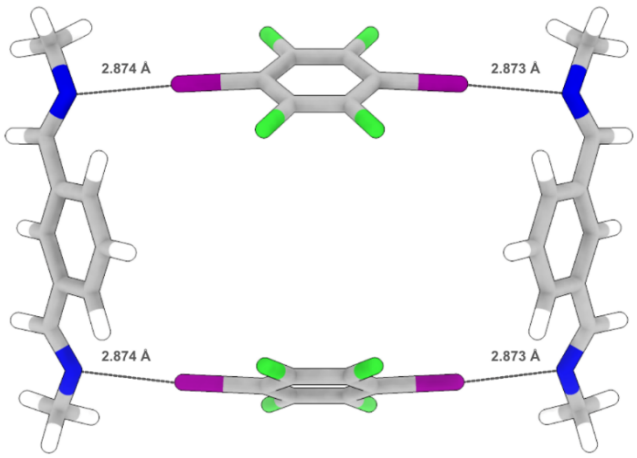

Figure S13: Simplified binding model of **Me^2Iso^3···2(*p*-I_2F_4)**.

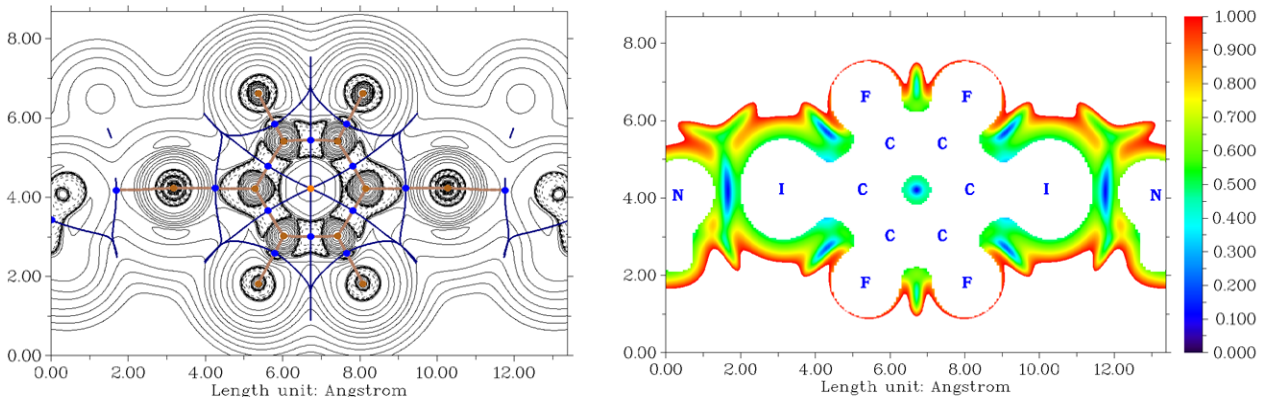

Figure S14: Left: Laplacian of electron density with critical points and bond paths. Bond critical (3,-1) points in blue, nuclear critical (3,-3) points in brown, ring critical (3,+1) points in orange, paths and zero-flux surfaces as brown and blue lines. Right: reduced density gradient map denoting halogen bonds in the simplified binding model of **Me^{2}Iso^3···2(*p*-I$_2$F$_4$)**.

Table S10: Distances and binding energies (kJ/mol) in the simplified binding model of **Me^{2}Iso^3···2(*p*-I$_2$F$_4$)**.

Model	Bond	Distance [Å]	0.429·G(r)	-0.5·V(r)	0.67·G(r)	-0.68·V(r)
model Me^{2}Iso^3···2(*p*-I$_2$F$_4$)	I-N	2.87	19.63	21.57	30.65	29.33

Powder X-ray diffraction measurements

Crystalline samples were prepared as mentioned above.

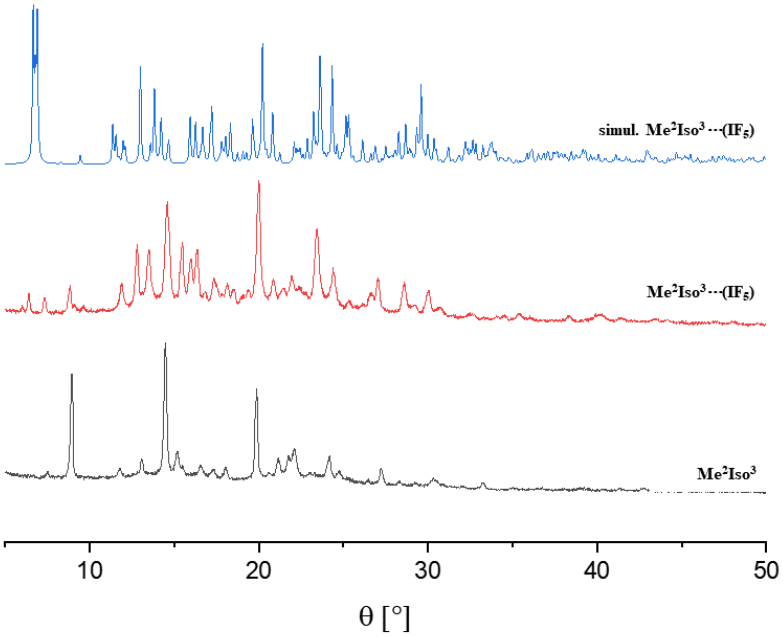

Figure S15: Simulated diffractogram of **Me²Iso³···IF₅** (blue) obtained by using the SXRD data and measured powder X-ray diffractograms of **Me²Iso³···IF₅** (red) and **Me²Iso³** (grey).

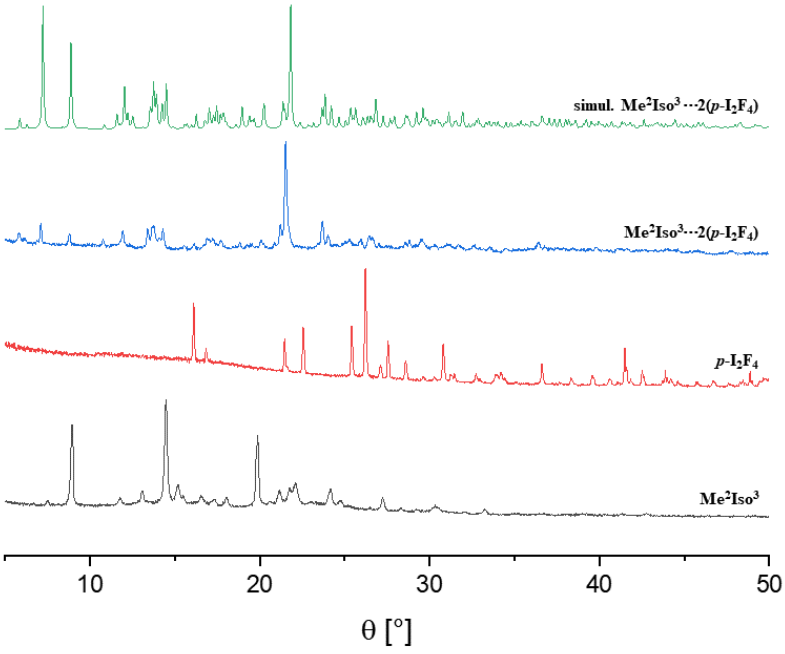

Figure S16: Simulated diffractogram of **Me²Iso³···2(*p*-I₂F₄)** (green) obtained by using the SXRD data and measured powder X-ray diffractograms of **Me²Iso³···2(*p*-I₂F₄)** (blue), ***p*-I₂F₄** (red) and **Me²Iso³** (grey).

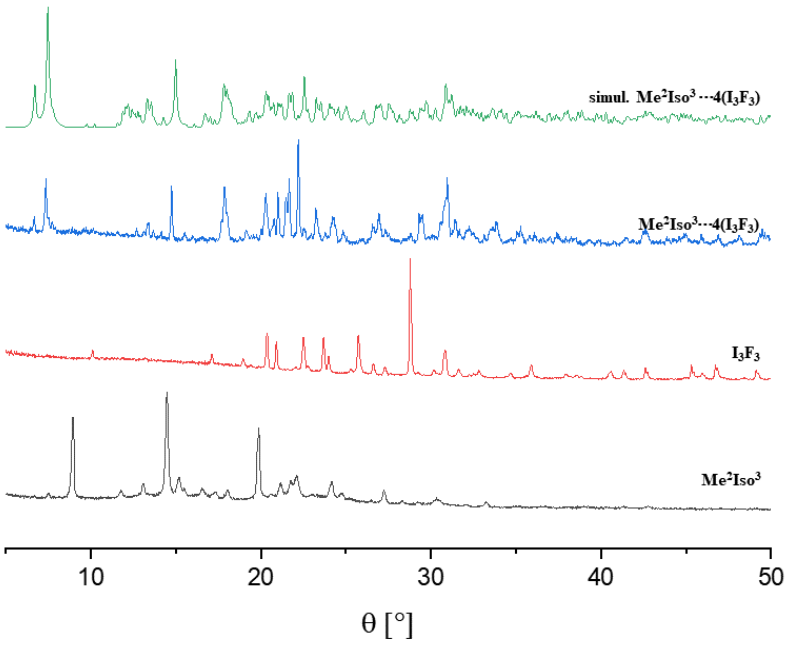

Figure S17: Simulated diffractogram of **Me²Iso³···4(I₃F₃)** (green) obtained by using the SXRD data and measured powder X-ray diffractograms of **Me²Iso³···4(I₃F₃)** (blue), **I₃F₃** (red) and **Me²Iso³** (grey).

IR analysis

Crystalline samples and samples obtained by liquid assisted grinding were prepared as mentioned above.

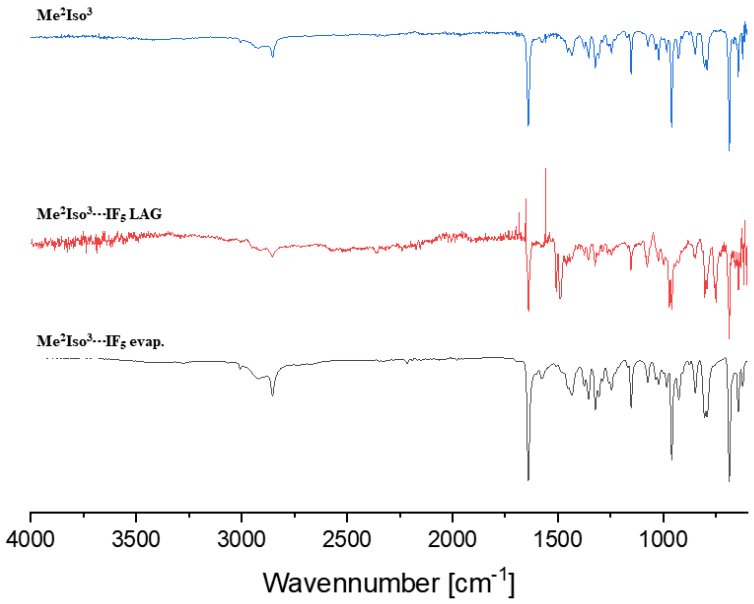

Figure S18: Measured IR-spectra of acceptor **Me²Iso³** (blue), **Me²Iso³···IF₅** synthesised by liquid assisted grinding (red) and **Me²Iso³ ···4(IF₅)** obtained by slow evaporation (grey).

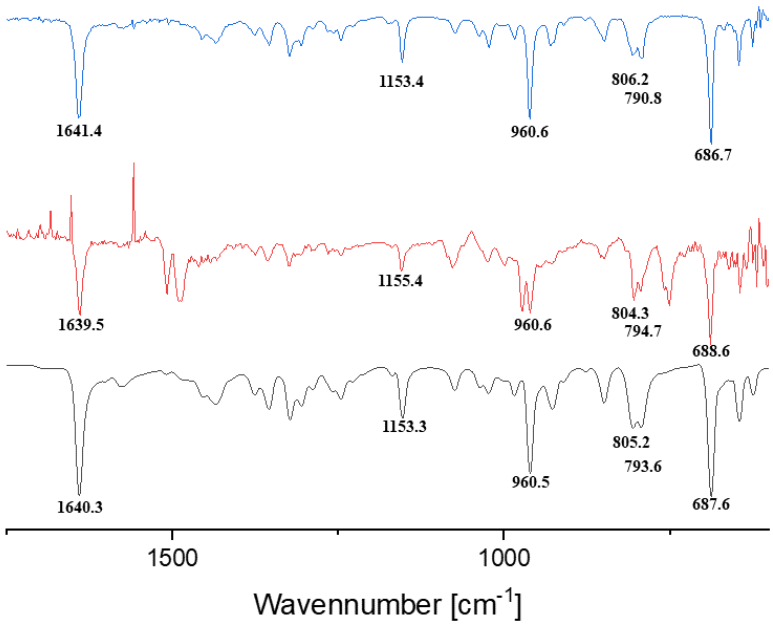

Figure S19: Enlarged detail of the measured IR-spectra of acceptor **Me²Iso³** (blue), **Me²Iso³···IF₅** synthesised by liquid assisted grinding (red) and **Me²Iso³···IF₅** obtained by slow evaporation (grey).

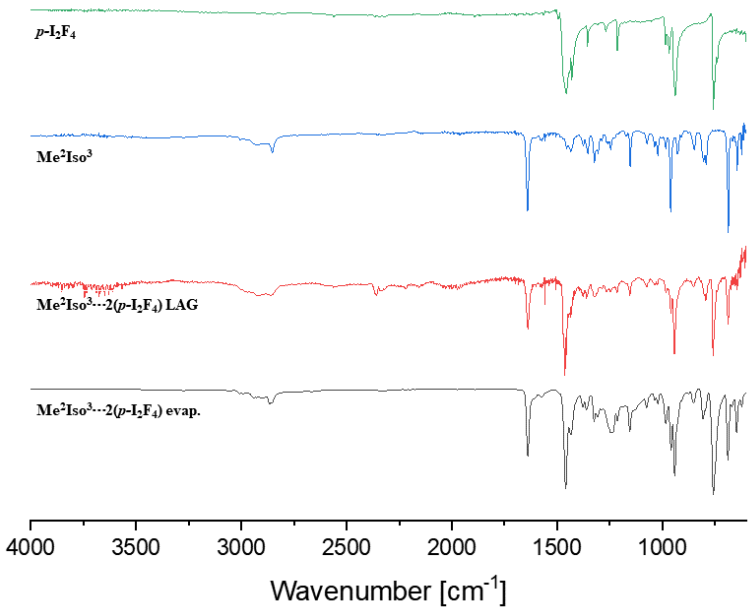

Figure S20: Measured IR-spectra of ***p*-I_2F_4** (green), acceptor **Me^2Iso^3** (blue), **Me^2Iso^3···2(*p*-I_2F_4)** synthesised by liquid assisted grinding (red) and **Me^2Iso^3···2(*p*-I_2F_4)** obtained by slow evaporation (grey).

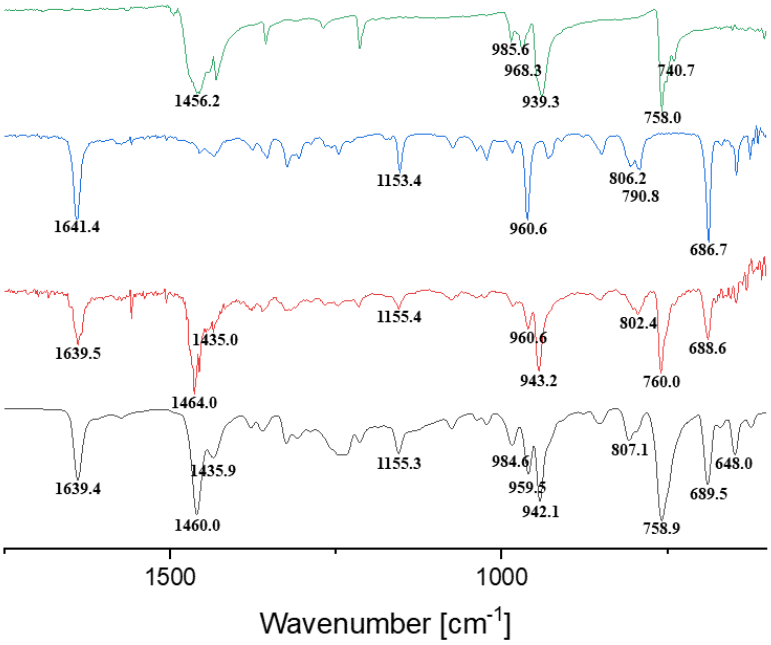

Figure S21: Enlarged detail of the measured IR-spectra of ***p*-I_2F_4** (green), acceptor **Me^2Iso^3** (blue) **Me^2Iso^3 ···2(*p*-I_2F_4)** synthesised by liquid assisted grinding (red) and **Me^2Iso^3 ···2(*p*-I_2F_4)** obtained by slow evaporation (grey).

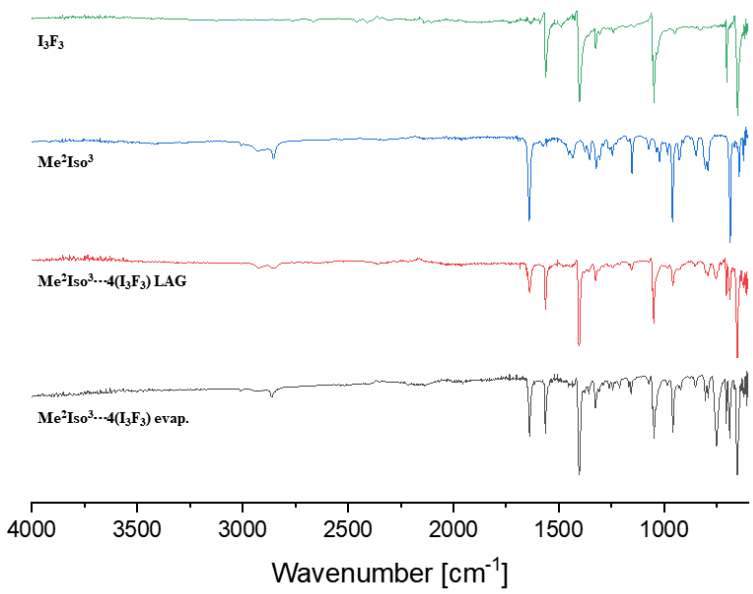

Figure S22: Measured IR-spectra of I_3F_3 (green), acceptor **Me²Iso³** (blue), **Me²Iso³···4(I_3F_3)** synthesised by liquid assisted grinding (red) and **Me²Iso³···4(I_3F_3)** obtained by slow evaporation (grey).

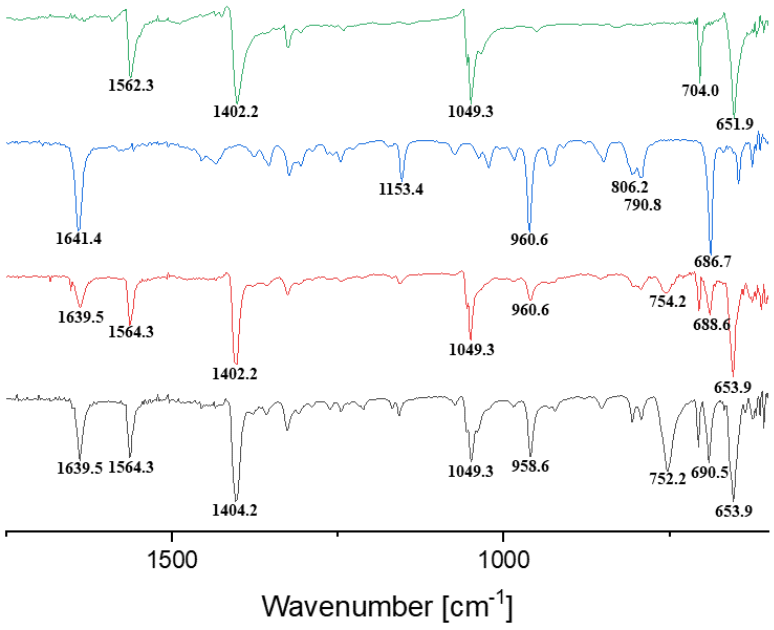

Figure S23: Enlarged detail of the measured IR-spectra of I_3F_3 (green), acceptor **Me²Iso³** (blue), **Me²Iso³···4(I_3F_3)** synthesised by liquid assisted grinding (red) and **Me²Iso³···4(I_3F_3)** obtained by slow evaporation (grey).

IRs Screening

Stock solution of imine cage **Me²Iso³** and the different donors were prepared in $CHCl_3$ and mixed in a ratio that would be needed to occupy all halogen bonding acceptor sites. The solutions were left to slowly evaporate at room temperature. IR spectra of the resulting solids were measured.

Table S11: Amounts of **Me²Iso³** and the corresponding donor, as well as the resulting cage-to-donor ratio.

Acceptor	Donor	Acceptor-to-donor ratio
Me²Iso³ (3.5 mg, 5.0 µmol)	***m*-I₂F₄** (6.0 mg, 15 µmol)	1:3
	***o*-I₂F₄** (6.0 mg, 15 µmol)	
	I₂F₄Et (5.3 mg, 15 µmol)	
	I₂F₈ (8.7 mg, 15 µmol)	

Table S12: Comparison of some bands, as observed in the IR spectrum, for **Me²Iso³** and the different combinations. Bands that show no shifts in comparison to the reference spectrum are highlighted in blue.

Me²Iso³	1641.4	1456.3	1435.0	1375.3	1354.0	1323.2	1246.0	1153.4	1074.4	983.7
Me²Iso³ + ***m*-I₂F₄**	1637.6	1469.8	1431.2	1377.2	1356.0	1325.1	1247.9	1155.4	1068.6	983.7
Me²Iso³ + **o-I₂F₄**	1637.6	1487.1	1437.0	1379.1	1356.0	1325.1	1249.9	1155.4	1074.4	983.7
Me²Iso³ + **I₂F₄Et**	1639.5	1469.8	1433.1	1379.1	1356.0	1325.1	1247.9	1153.4	1066.6	983.7
Me²Iso³ + **I₂F₈**	1639.5	1467.8	1431.2	1379.1	1354.0	1325.1	1247.9	1153.4	1074.4	976.0

Thermogravimetric analysis

Samples of **Me²Iso³···2**(***p*-I₂F₄**) and **Me²Iso³···4**(**I₃F₃**) were obtained by slow evaporation as described above.

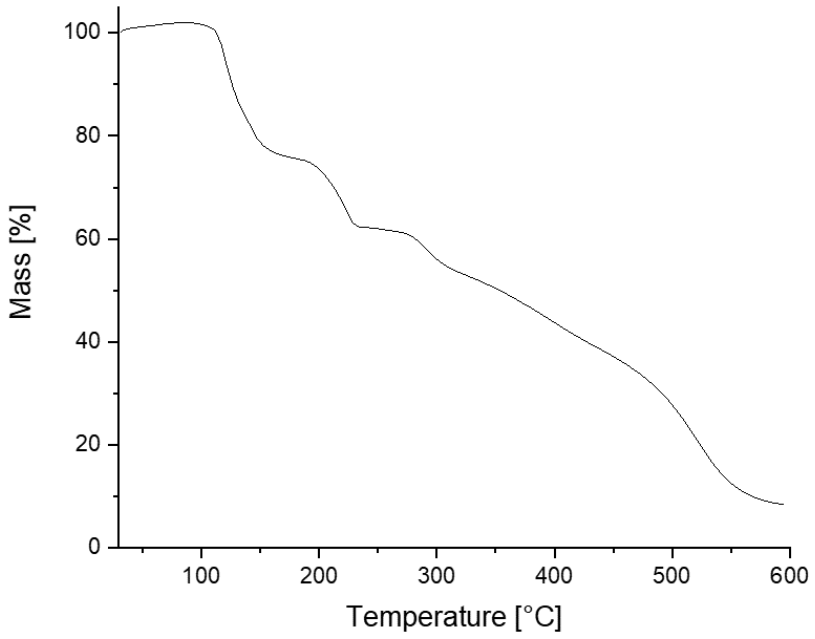

Figure S24: Measured TGA spectrum of **Me²Iso³···2**(***p*-I₂F₄**) obtained by slow evaporation. The determined onset temperature is 111.65 °C.

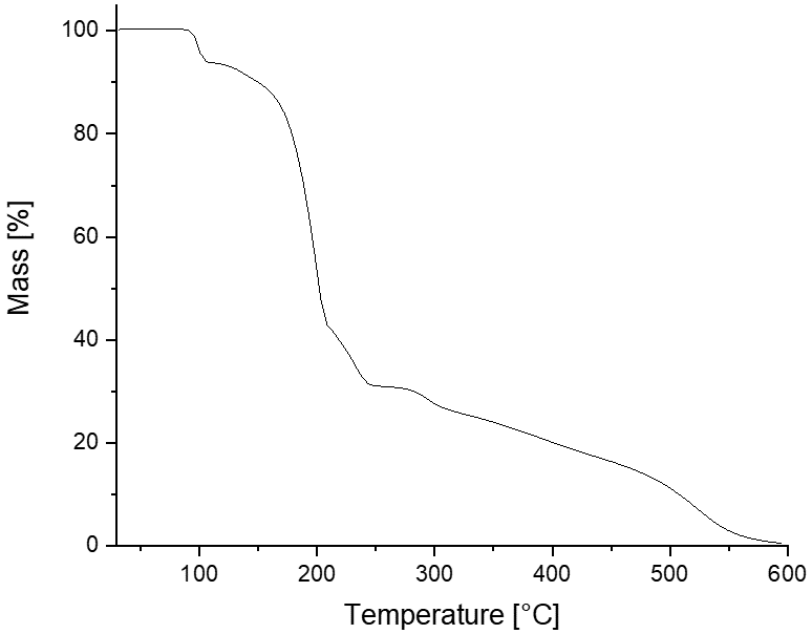

Figure S25: Measured TGA spectrum of **Me²Iso³···4**(**I₃F₃**) obtained by slow evaporation. The determined onset temperature is 91.33 °C.

Stability tests

Slow evaporation samples of **Me²Iso³···2(*p*-I₂F₄)** and **Me²Iso³···4(I₃F₃)**, were soaked in *n*-pentane. The solvent was carefully removed twice a day, and new solvent was added. After three days the solvent was allowed to slowly evaporate. For 10-16 hours, the solids were kept under high vacuum at 60 °C. Before and after heating, PXRD spectra were measured. The spectra were standardized for better comparability.

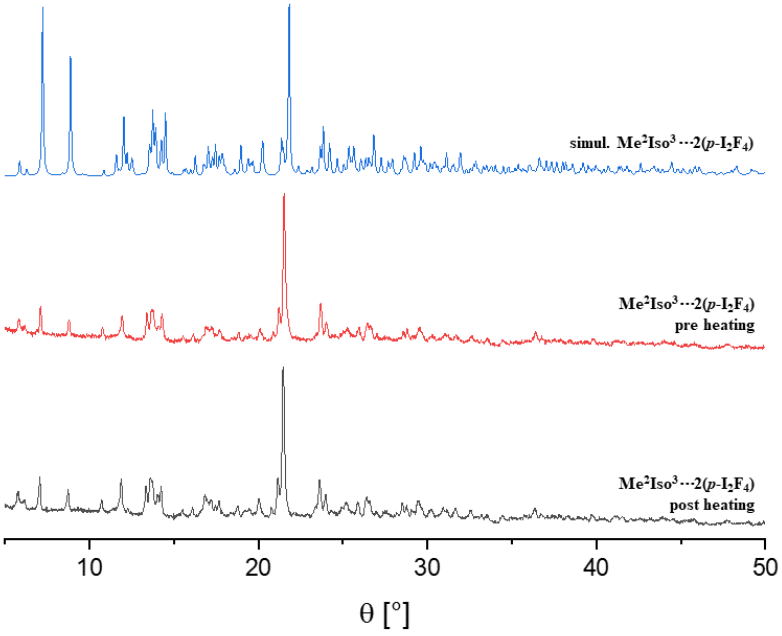

Figure S26: Simulated diffractogram of **Me²Iso³···2(*p*-I₂F₄)** (blue) obtained by using the SXRD data, measured PXRD spectra of **Me²Iso³···2(*p*-I₂F₄)** before (red) and after heating (black).

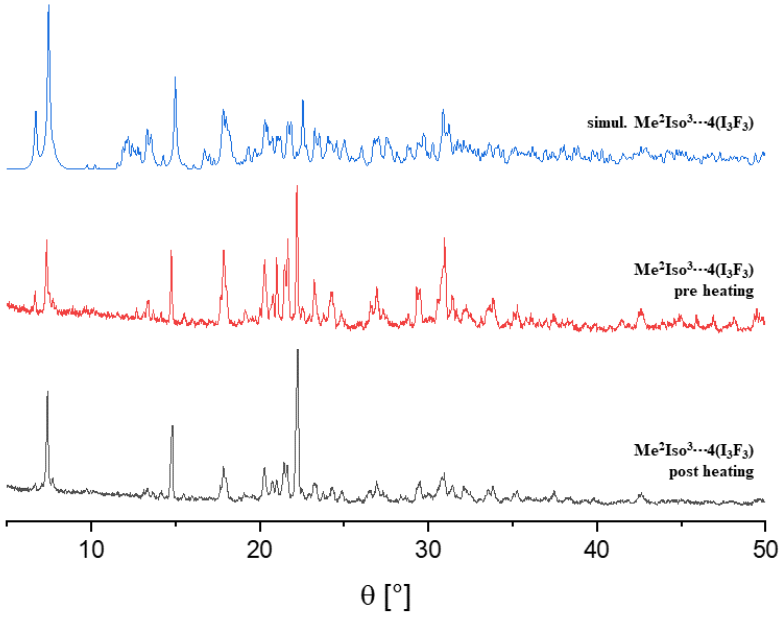

Figure S27: Simulated diffractogram of **Me²Iso³···4(I₃F₃)** (blue) obtained by using the SXRD data, measured PXRD spectra of **Me²Iso³···4(I₃F₃)** before (red) and after heating (black).

4.2.3 Experimental details for part 3.1.3

Synthesis

Me^4Ter^6

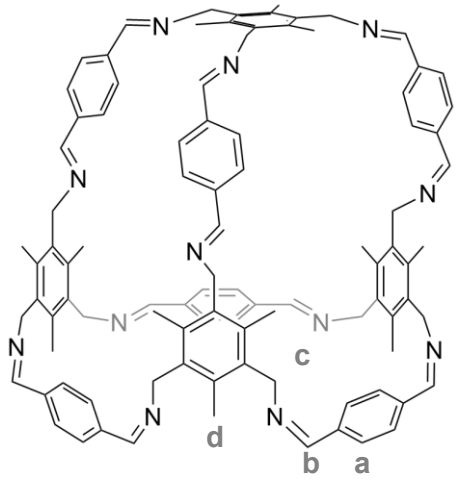

Ter (194 mg, 1.45 mmol, 1.20 eq.) and **Me** (251 mg, 1.21 mmol, 1.00 eq.) were dissolved in CH_2Cl_2 (260 mL) and heated to 40 °C for 5 days. The mixture was allowed to cool to room temperature and filtered to remove any precipitates that formed. CyHex (200 mL) was added and the CH_2Cl_2 was removed under reduced pressure at 30 °C. The precipitate that formed after removing the solvent was filtered off yielding the **Me^4Ter^6** (268 mg, 0.189 mmol, 63%) as an off-white solid.

^{1}H NMR (300 MHz, $CDCl_3$): δ = 8.30 (s, 12H, H_b), 7.75 (s, 24H, H_a), 4.93 (s, 24H, H_c), 2.37 (s, 36H, H_d); **MS** (MALDI) calc. for $[C_{96}H_{97}N_{12}]^+$: 1417.795, meas.: 1417.867.
Analytical data was in accordance with literature.[80]

Synthesis of $Me^4Ter^6\cdots2(p\text{-}I_2F_4)$

Slow evaporation of a solution of imine cage **Me^4Ter^6** (7.0 mg, 5.0 µmol, 1.0 eq.) and donor ***p*-F_4I_2** (4.0 mg, 10 µmol, 2.0 eq.) in a mixture of chloroform and acetonitrile ($CHCl_3$:MeCN 10:1) led to the formation of crystalline **$Me^4Ter^6\cdots2(p\text{-}I_2F_4)$**.

Halogen-bonded complex synthesis by liquid assisted grinding

Samples prepared liquid assisted grinding were obtained by using a MM 400 Retsch ball-mill. The starting materials were mixed in targeted stoichiometry with a small amount of the

corresponding solvent and then grinded using 5 mm zirconium dioxide balls at 25 Hz for 15 minutes.

Crystallographic details

$Me^4Ter^6\cdots2(p\text{-}I_2F_4)$

Crystals of **$Me^4Ter^6\cdots2(p\text{-}I_2F_4)$** were grown by slow evaporation of an acetonitrile/chloroform mixture at room temperature. A colourless plate was mounted and data collection was performed at 153 K using Mo-K_α radiation. The structure contained various sites of heavily disordered chloroform and acetonitrile molecules showing both, orientation and rotation disorder. Modelling was attempted but all solvent molecules were ultimately removed using SQUEEZE.[131] The solvent accessible volume (SAV) found was 5109.9 Å^3 with 1658.5 electrons (per unit cell). Various outlying reflections (ca. 90) needed to be omitted for stable refinements. These resulted from low crystal quality, long exposure times (60 s) or were affected by the beam-stop.

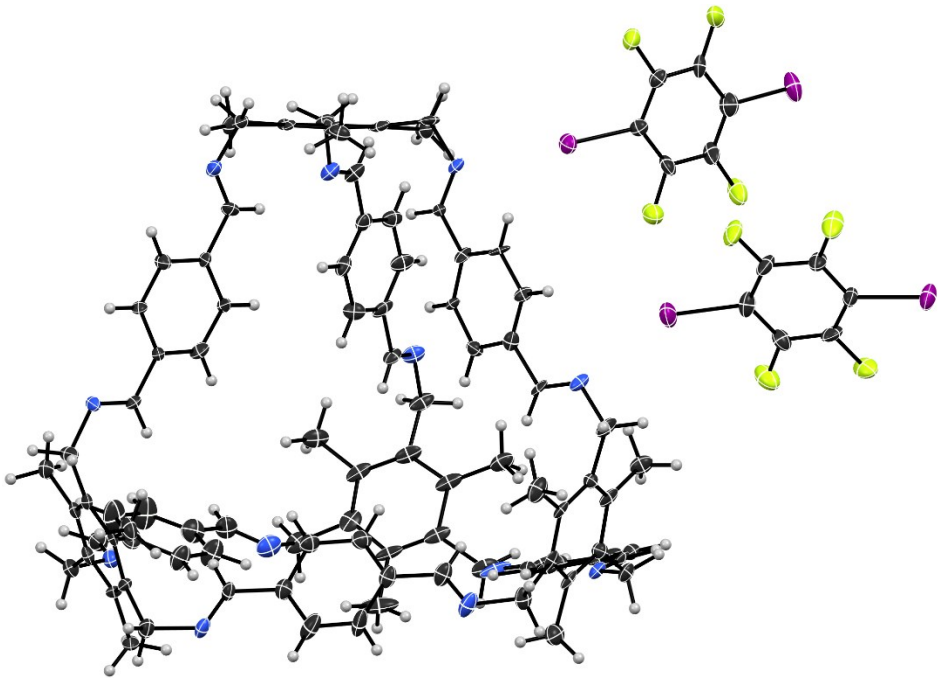

Figure S28: Data set of **$Me^4Ter^6\cdots2(p\text{-}I_2F_4)$** showing the asymmetric unit bearing one cage and two ***p*-I_2F_4** molecules, thermal ellipsoids set at 50 % probability.

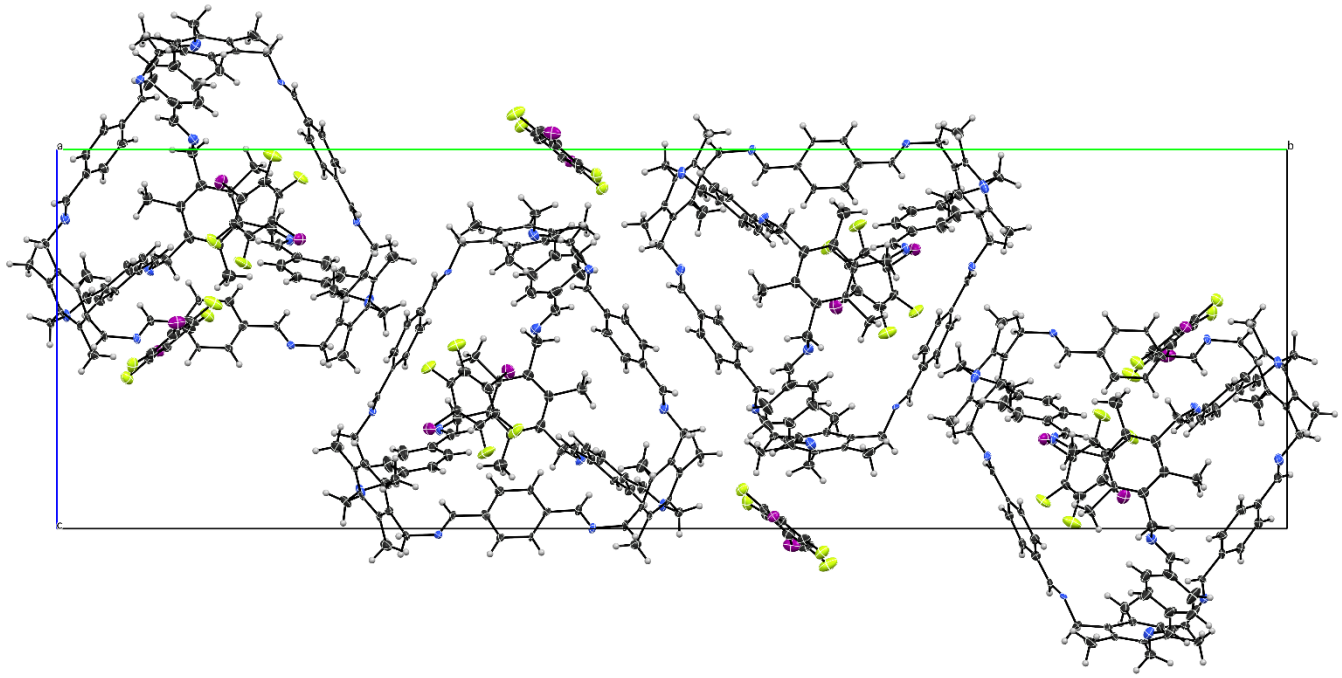

Figure S29: View of the unit cell of **Me^{4}Ter^6···2(*p*-I$_2$F$_4$)** along the crystallographic *a* axis.

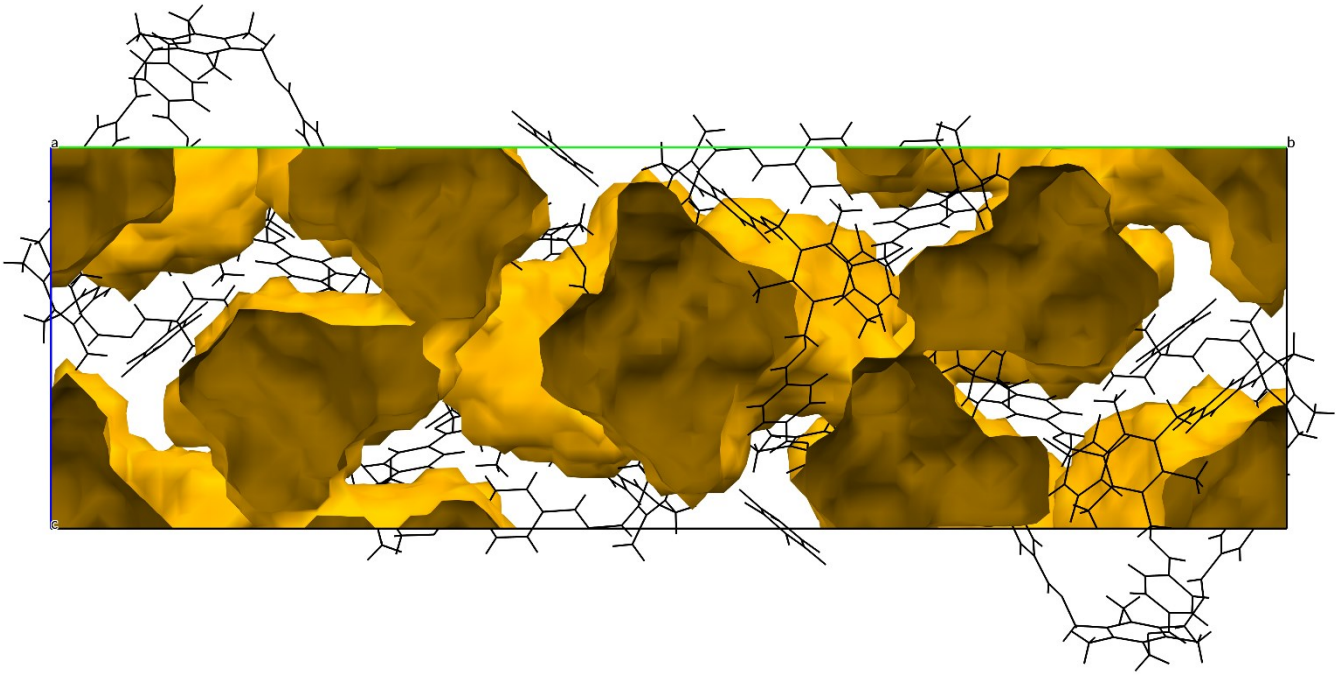

Figure S30: View of the unit cell of **Me^{4}Ter^6···2(*p*-I$_2$F$_4$)** along the crystallographic *a* axis, voids calculated using a probe of 1.2 Å and depicted in orange colour.

Table S13: Crystal structure refinement details for **$Me^2Iso^3\cdots4(I_3F_3)$** and **$Me^4Ter^6\cdots2(p\text{-}I_2F_4)$**.

	$Me^4Ter^6\cdots2(p\text{-}I_2F_4)$
Wavelength [Å]	Mo Kα
Collection Temperature [K]	153
Formula	$C_{108}H_{95}F_8I_4N_{12}$
Formula weight	2220.55
Crystal System	Monoclinic
Space Group	$P2_{1/c}$
a [Å]	13.882(1)
b [Å]	55.671(4)
c [Å]	17.1632(12)
α [°]	
β [°]	91.325(2)
γ [°]	
V [$Å^3$]	13260.5(17)
Z	4
μ [mm^{-1}]	0.99
Crystal size [mm]	0.19 x 0.17 x 0.04
Reflections collected	178104
Independent reflections	23276
Observed reflections [$I > 2\sigma(I)$]	15995
R_{int}	0.087
Data/ parameters/restraints	23276/1201/30
$R[F^2>2\sigma(F^2)]$	0.097
$wR(F^2)$	0.272

Table S14: Bond lengths [Å] and angles [°] for **Me^4Ter^6···2(*p*-I_2F_4)**.

I(200)-N(51)	2.978(7)	N···I halogen bond
I(203)-centroid$_{C54,55}$	3.281	π···I halogen bond[135]
I(300)-N(30)	3.251(9)	N···I halogen bond
I(303)-N(20)	3.448(7)	N···I contact
F(201)-H(49B)	2.550	H···F contact
F(205)-H(98B)	2.448	H···F contact
F(301)-H(43)	2.657	H···F contact
F(302)-H(53)	2.524	H···F contact
F(304)-H(69B)	2.520	H···F contact
Centroid$_{(C42,43,44,45,46,47)}$-Centroid$_{(200,201,202,203,204,205)}$	3.538	π-stacking (cage-donor)
C(200)-I(200)-N(51)	161.2(3)	N···I halogen bond
C(203)-I(203)-centroid$_{C54,55}$	171.32	π···I halogen bond
C(300)-I(300)-N(30)	164.6(3)	N···I halogen bond
C(303)-I(303)-N(20)	142.1(3)	N···I contact
C(201)-F(201)-H(49B)	122.0	H···F contact
C(205)-F(205)-H(98B)	152.0	H···F contact
C(301)-F(301)-H(43)	145.5	H···F contact
C(302)-F(302)-H(53)	132.6	H···F contact
C(304)-F(304)-H(69B)	140.9	H···F contact

Table S15: Bond lengths, sum of van der Waals Radii[133,134], and normalized bond lengths for the halogen bonds in the different networks.

	Contact	d_{XB} [Å]	ΣBvdW (Bondi) [Å]	d_{XB}/ ΣBvdW	ΣBvdW (Rowland) [Å]	d_{XB}/ ΣBvdW
Me^4Ter^6···2(*p*-I_2F_4)	N···I	2.978(7)	3.53	0.84	3.67	0.81
	N···I	3.251(9)	3.53	0.92	3.67	0.89
	N···I	3.448(7)	3.53	0.98	3.67	0.94

Computational details

The DFT computations and QTAIM analyses in this section were performed by Dr. Oliver Weingart according to the method described in the general section.

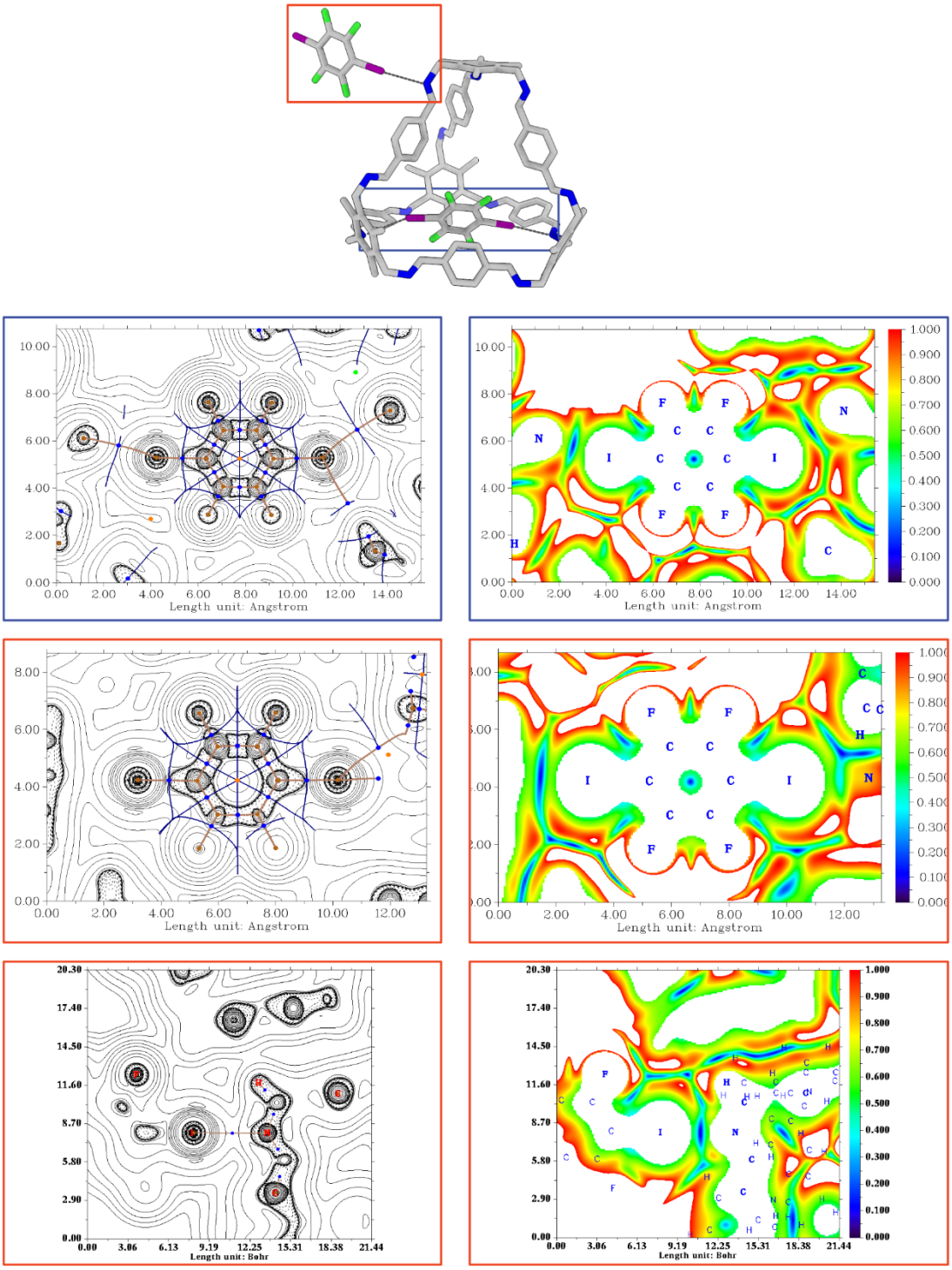

Figure S31: Structure of **Me^{4}Ter^6···2(*p*-I$_2$F$_4$)** including the ***p*-I$_2$F$_4$** located inside the cage (red outline) and the ***p*-I$_2$F$_4$** located on the outside (blue outline). Laplacian maps of the electron density (left) are depicted with critical points and bond paths. Bond critical (3,-1) points in blue, nuclear critical (3,-3)

points in brown, ring critical (3,+1) points in orange, paths and zero-flux surfaces as brown and blue lines. The reduced density gradient maps are shown on the right side.

Blue: Laplacian and reduced gradient maps for **Me⁴Ter⁶···2(*p*-I₂F₄)** with ***p*-I₂F₄** inside cage.

Red: Laplacian and reduced density gradient map of **Me⁴Ter⁶···2(*p*-I₂F₄)** with ***p*-I₂F₄** outside cage showing the whole donor (depicted along the ring plane, upper section) and the imine halogen bond (shown along the I···N bond axis, lower section). Zero-flux surfaces were omitted in the latter.

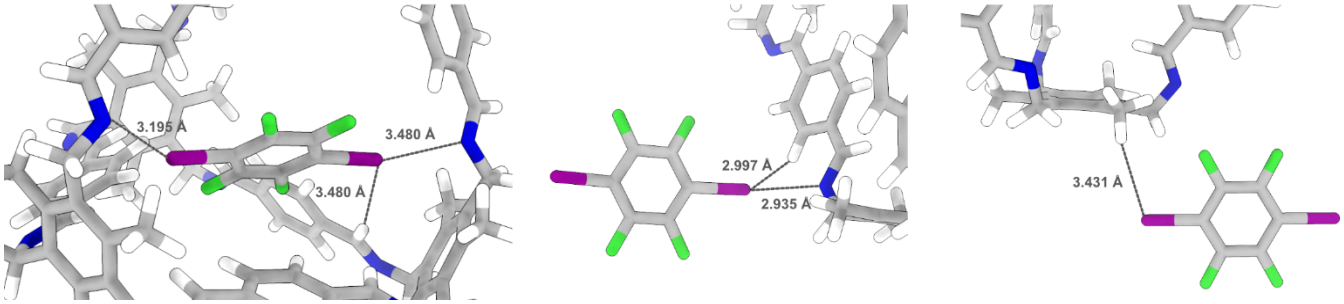

Figure S32: Binding modes of ***p*-I₂F₄** inside and outside cage.

Table S16: Distances and binding energies (kJ/mol) in **Me⁴Ter⁶···2(*p*-I₂F₄)**.

Model	Bond	Distance [Å]	0.429·G(r)	-0.5·V(r)	0.67·G(r)	-0.68·V(r)
$Me^4Ter^6\cdots2(p\text{-}I_2F_4)_{XB(ext)}$	I-N	2.94	14.59	15.78	22.78	21.45
	I-H	3.00	5.96	5.46	9.31	7.43
$Me^4Ter^6\cdots2(p\text{-}I_2F_4)_{external}$	I-H	3.43	2.58	2.17	4.02	2.95
$Me^4Ter^6\cdots2(p\text{-}I_2F_4)_{cage}$	I-N(1)	3.20	8.55	8.37	13.35	11.39
	I-N(2)	3.48	5.23	4.85	8.13	6.60
	I-H	3.48	2.11	1.76	3.30	2.39

Powder X-ray diffraction measurements

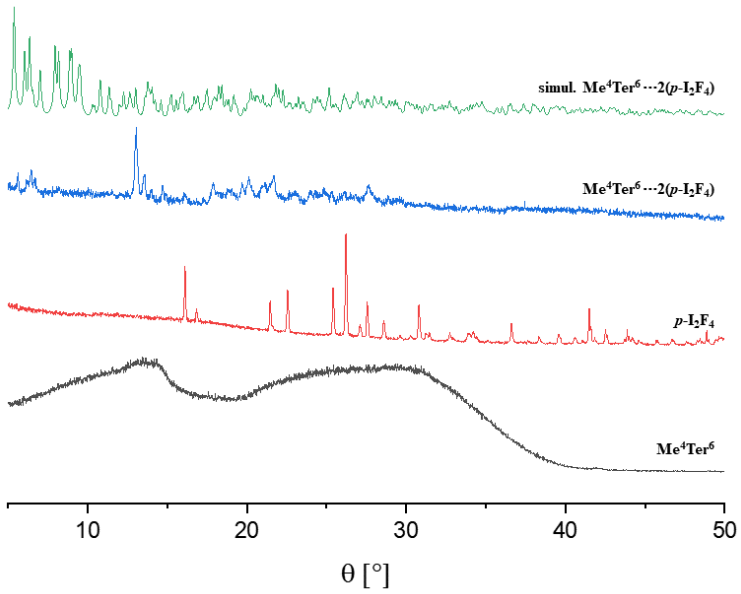

Figure S33: Simulated diffractogram of **Me⁴Ter⁶···2(*p*-I₂F₄)** (green) obtained by using the SXRD data and measured powder X-ray diffractograms of **Me⁴Ter⁶···2(*p*-I₂F₄)** (blue), ***p*-I₂F₄** (red) and **Me⁴Ter⁶** (grey).

IR analysis

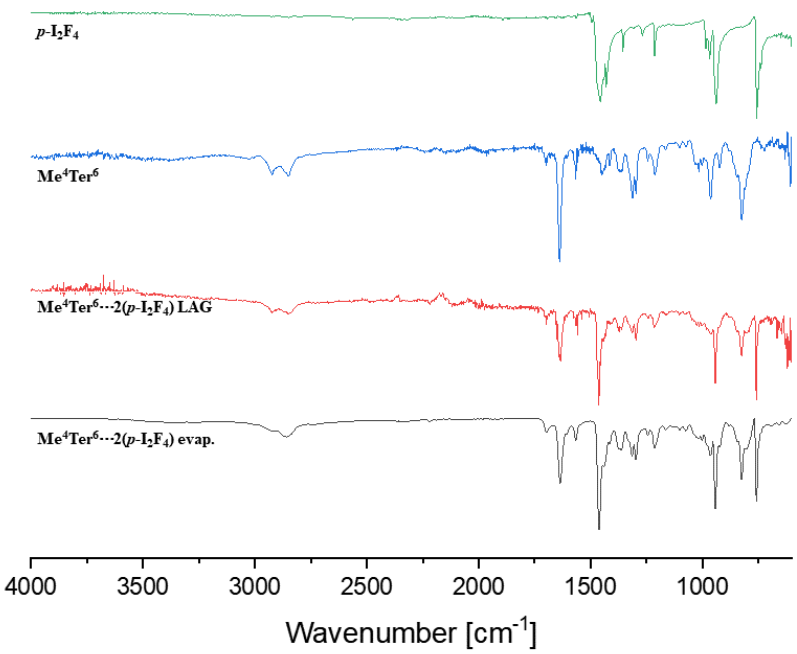

Figure S34: Measured IR-spectra of ***p*-I₂F₄** (green), acceptor **Me⁴Ter⁶** (blue), **Me⁴Ter⁶···2(*p*-I₂F₄)** synthesised by liquid assisted grinding (red) and **Me⁴Ter⁶···2(*p*-I₂F₄)** obtained by slow evaporation (grey).

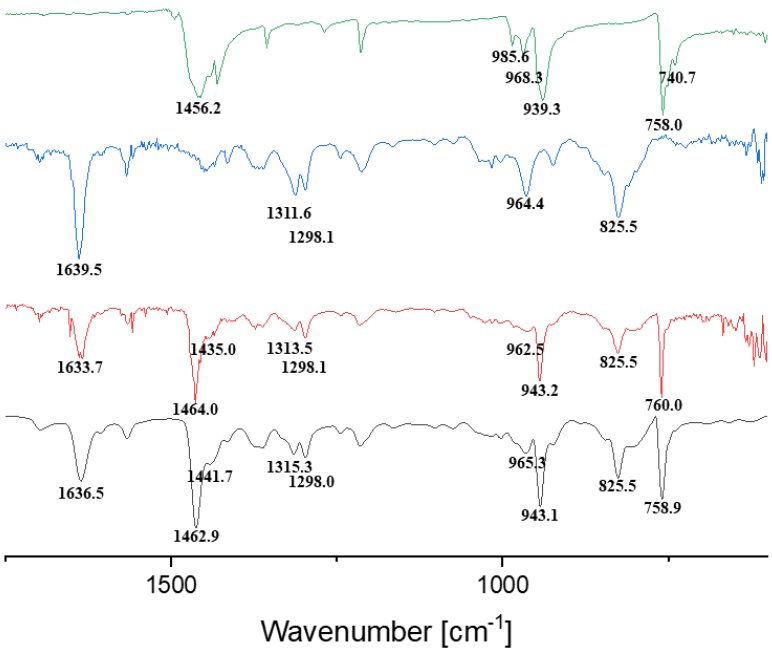

Figure S35: Enlarged detail of the measured IR-spectra of ***p*-I_2F_4** (green), acceptor **Me^4Ter^6** (blue), **Me^4Ter^6···2(*p*-I_2F_4)** synthesised by liquid assisted grinding (red) and **Me^4Ter^6···2(*p*-I_2F_4)** obtained by slow evaporation (grey).

Thermogravimetric analysis

A sample of **Me^4Ter^6···2(*p*-I_2F_4)** was obtained by slow evaporation and another sample of **Me^4Ter^6···2(*p*-I_2F_4)** was obtained by liquid assisted grinding.

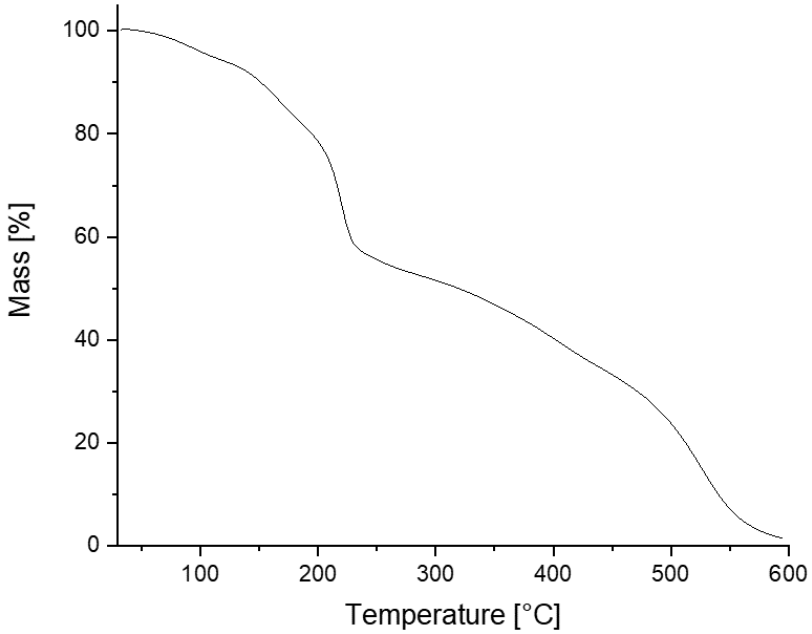

Figure S36: Measured TGA spectrum of **Me^4Ter^6···2(*p*-I_2F_4)** obtained by slow evaporation. The determined onset temperature is 108.67 °C. The initial dip is due to the evaporation of remaining solvent.

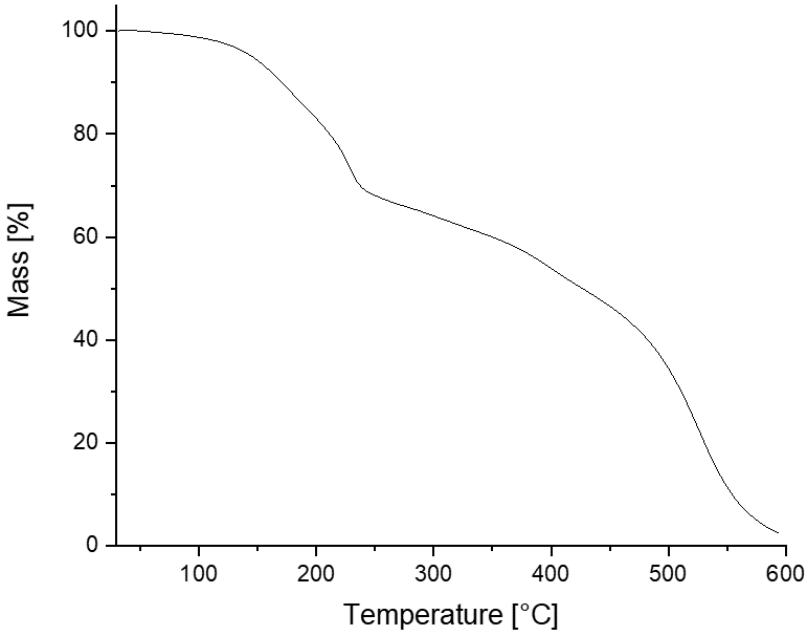

Figure S37: Measured TGA spectrum of **Me^{4}Ter^6···2(*p*-I$_2$F$_4$)** obtained by liquid assisted grinding. The determined onset temperature is 128.28 °C. The initial dip is due to the evaporation of remaining solvent.

As the processes of solvent loss and decomposition are overlapping at some temperatures, the determination of the onset decomposition temperatures for the samples of **Me^{4}Ter^6···2(*p*-I$_2$F$_4$)** is impeded, resulting in differing onset decomposition temperatures. Additionally, the amount of residual solvent in the **Me^{4}Ter^6···2(*p*-I$_2$F$_4$)** sample obtained by slow evaporation is significantly higher.

Stability tests

Slow evaporation samples of **Me^{4}Ter^6···2(*p*-I$_2$F$_4$)**, as well as **Me^{4}Ter^6···2(*p*-I$_2$F$_4$)** produced by liquid assisted grinding, were soaked in n-pentane. The solvent was carefully removed twice a day, and new solvent was added. After three days the solvent was allowed to slowly evaporate. For 10-16 hours, the solids were kept under high vacuum at 60 °C. Before and after heating, PXRD or IR spectra were measured. The spectra were standardized for better comparability.

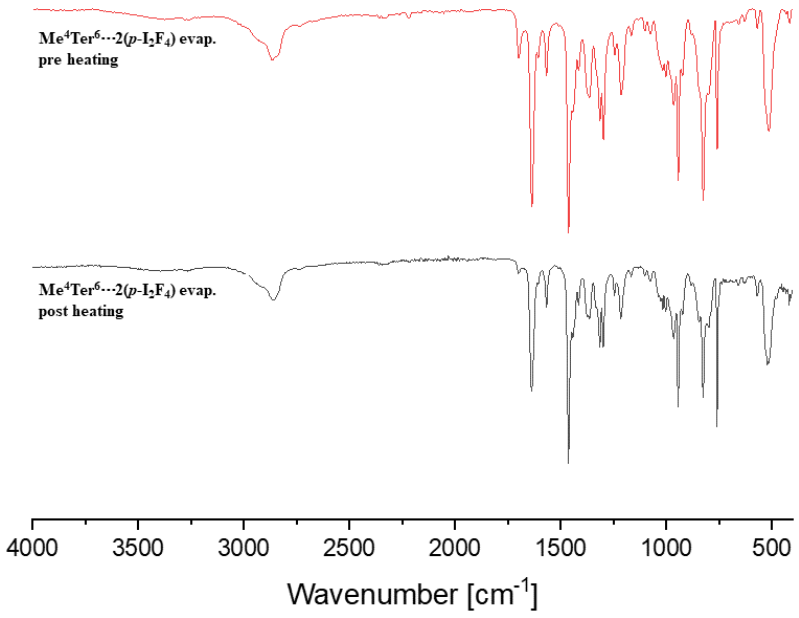

Figure S38: Measured IR-spectra of **Me^{4}Ter^6···2(*p*-I$_2$F$_4$)** synthesised by slow evaporation before (red) and after heating (black).

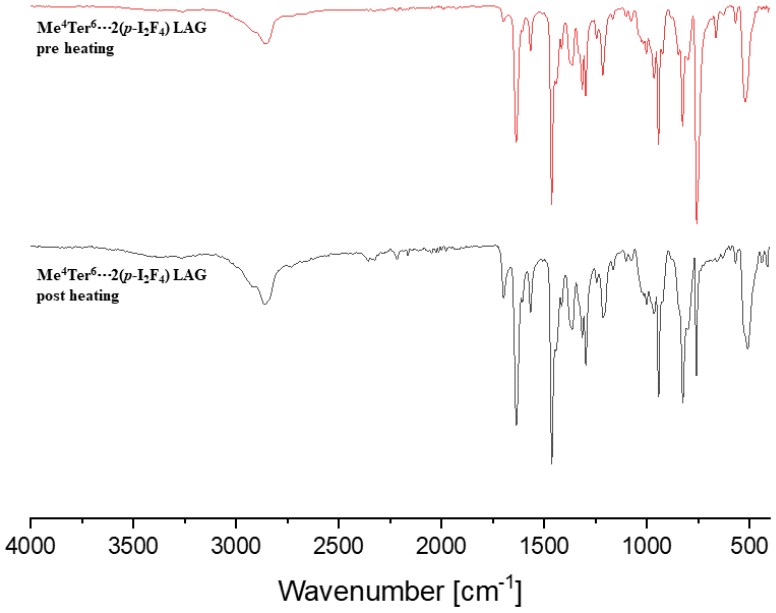

Figure S39: Measured IR-spectra of **Me^{4}Ter^6···2(*p*-I$_2$F$_4$)** synthesised by liquid assisted grinding before (red) and after heating (black).

Gas adsorption measurements

Sample preparation:

Samples of **Me^{4}Ter^6···2(*p*-I$_2$F$_4$)** obtained by slow evaporation and liquid assisted grinding were soaked in *n*-pentane for three days, the solvent was exchanged twice a day. After this time the solvent was allowed to evaporate in a fume hood and the sample was dried at 60 °C under high vacuum for 16 hours afterwards.

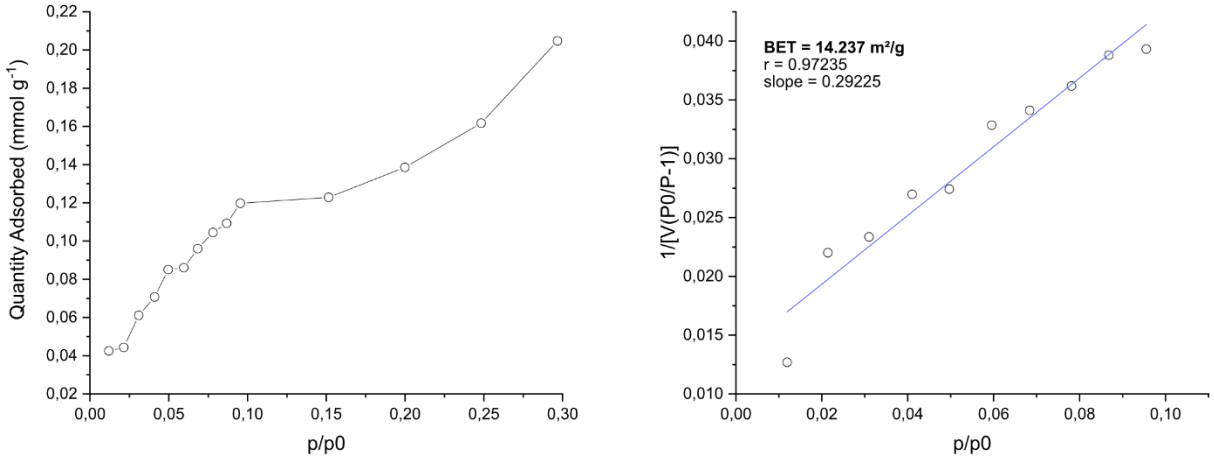

Figure S40: Left: Adsorption of nitrogen at 77 K of **Me^{4}Ter^6···2(*p*-I$_2$F$_4$)** obtained by slow evaporation. Right: BET plot of a sample of **Me^{4}Ter^6···2(*p*-I$_2$F$_4$)** obtained by slow evaporation in the range of p/p$_0$ 0.001 to 0.1. The BET surface area was calculated using a microporous assumption.

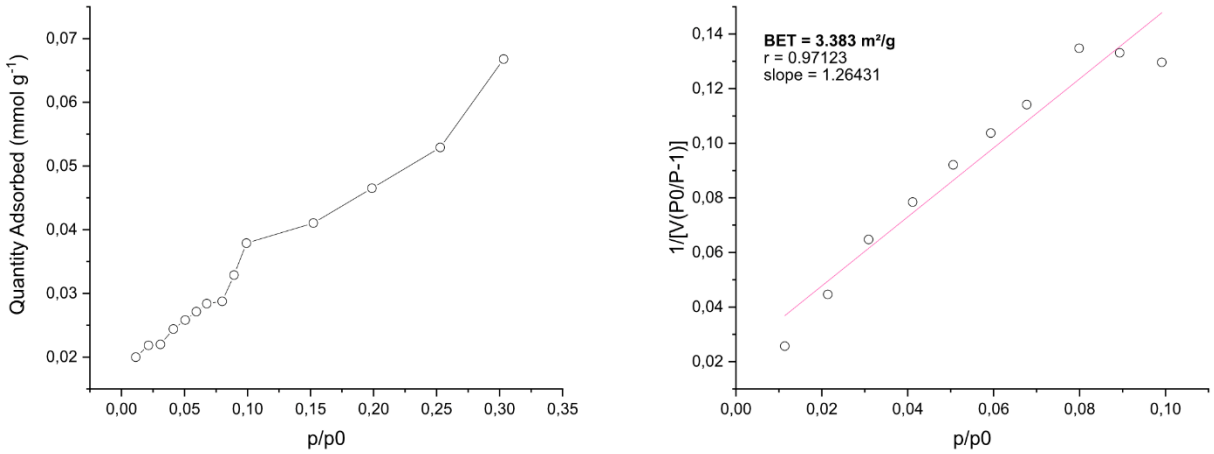

Figure S41: Left: Adsorption of nitrogen at 77 K of **Me^{4}Ter^6···2(*p*-I$_2$F$_4$)** obtained by liquid assisted grinding. Right: BET plot of a sample of **Me^{4}Ter^6···2(*p*-I$_2$F$_4$)** obtained by liquid assisted grinding in the range of p/p$_0$ 0.001 to 0.1. The BET surface area was calculated using a microporous assumption.

4.3 Experimental details for dissipative imine systems

4.3.1 Experimental Details for 3.2.1

Syntheses

4-Bromo-2,6-difluoroaniline (32)

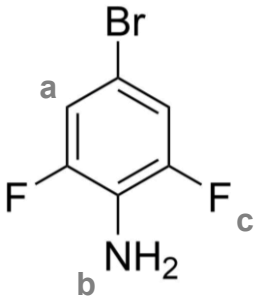

NBS (19.9 g, 111 mmol, 1.00 eq.) was added to a yellow solution of 2,6-difluoroaniline (12.0 mL, 111 mmol, 1.00 eq.) in MeCN (230 mL), whereas the solution quickly turned dark red and warmed up. The solution was stirred at room temperature for 20 hours before it was diluted with CH_2Cl_2 (200 mL) and H_2O (250 mL). Brine (50 mL) was added to facilitate the separation of the layers. The organic layer was washed with brine (2 x 75 mL), dried over $MgSO_4$, filtered and evaporated, yielding a dark brown solid. Column chromatography using CyHex:CH_2Cl_2 (1:1) yielded bromide **2** (22.2 g, 107 mmol, 96%) as slightly orange crystals.

***R*$_f$** (CyHex:CH_2Cl_2 (1:1)) = 0.50; **^{1}H NMR** (300 MHz, $CDCl_3$, 298 K): δ [ppm] = 7.05 – 6.94 (m, 2H, H_a), 3.63 (s, broad, 2H, H_b); **^{19}F{^{1}H} NMR** (282 MHz, $CDCl_3$, 298 K): δ [ppm] = -130.69 (s, 2F, F_c).
Analytical data was in accordance with literature.[39b]

4-Amino-3,5-difluorobenzonitrile (33)

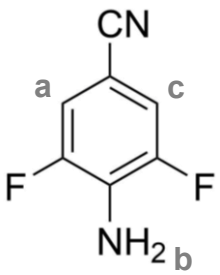

This reaction was performed under an N_2-atmosphere. A suspension of bromide **2** (21.2 g, 102 mmol, 1.00 eq.) and Cu(I)CN (10.9 g, 122 mmol, 1.20 eq.) in NMP (85 mL) was stirred for three hours at 185 °C and an additional 17 hours at 170 °C. After cooling the dark brown solution to rt, it was poured into an aqueous solution of NH_3 (12 wt%, 450 mL), whereas a precipitate formed. The suspension was filtered, the precipitate was washed with H_2O (50 mL), and the combined aqueous layers were extracted with EtOAc (2 x 400 mL, 2 x 200 mL). The combined organic layers were washed with brine (2 x 250 mL), dried over Na_2SO_4, filtered, and evaporated, resulting in a dark brown oily residue. With the addition of H_2O (50 mL), a dark brown precipitate formed, which was filtered off and washed with ice-cold H_2O (2 x 50 mL). Column chromatography (8 x 12 cm) using CyHex:CH_2Cl_2 (2:1) yielded nitrile **3** (10.6 g, 68.7 mmol, 67%) as colourless crystals.

R_f (CyHex:CH_2Cl_2 (2:1)) = 0.25; **^{1}H NMR** (300 MHz, $CDCl_3$, 298 K): δ [ppm] = 7.21 – 7.08 (m, 2H, H_a), 4.27 (s, broad, 2H, H_b); **^{19}F{^{1}H} NMR** (282 MHz, $CDCl_3$, 298 K): δ [ppm] = -130.77 (s, 2F, F_c).
Analytical data was in accordance with literature.[136]

4-Amino-3,5-difluorobenzoic acid (34) · n HCl

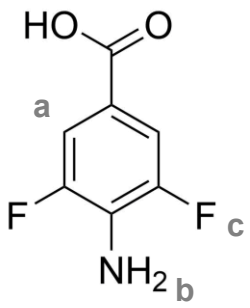

Nitrile **3** (10.6 g, 68.7 mmol, 1.00 eq.) was suspended in an aqueous NaOH solution (1 M, 350 mL) and stirred at 120 °C for one hour, resulting in a colourless solution, which was further stirred at room temperature for 19 hours. After which an aqueous HCl solution (2 M, 250 mL) was added until a pH value of 1 was reached, during which a colourless solid precipitated, which was removed by filtration and redissolved in EtOAc (100 mL). The filtrate was extracted with EtOAc (3 x 250 mL). The combined organic layers were dried over Na_2SO_4, filtered and evaporated to yield acid **4**, presumably as its HCl adduct (12.0 g, 57.3 mmol, 84% based on **4** · HCl).

^{1}H NMR (300 MHz, $CDCl_3$, 298 K): δ [ppm] = 7.69 – 7.51 (m, 2H, H_a), 4.27 (s, broad, 2H, H_b); **^{19}F{^{1}H} NMR** (282 MHz, $CDCl_3$, 298 K): δ [ppm] = -132.73 (s, 2F, F_c).

Analytical data was in accordance with literature.[136]

Methyl 4-amino-3,5-difluorobenzoate (35)

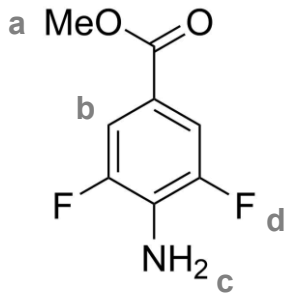

Acid **4** · n HCl (12.0 g, 57.3 mmol, 1.00 eq.) was dissolved in MeOH (300 mL) and concentrated aqueous H_2SO_4 (30 mL) was added in small portions. The solution was stirred at 60 °C for 22 hours and then allowed to cool to rt. Aqueous NaOH solution (3 M, 150 mL) was added until a pH value of 10 was reached, upon which two layers and a colourless precipitate formed. The colourless precipitate was removed by filtration and redissolved in EtOAc (150 mL) and H_2O (150 mL). The aqueous layer and the filtrate were combined and extracted with EtOAc (8 x 250 mL). The initial organic layer and the organic extracts were combined, dried over Na_2SO_4, filtered and evaporated, resulting in a colourless solid. Column chromatography using CyHex:EtOAc (9:1) yielded ester **5** (7.63 g, 40.8 mmol, 72%) as colourless crystals.

***R*$_f$** (CyHex:EtOAc (9:1)) = 0.20; **^{1}H NMR** (300 MHz, $CDCl_3$, 298 K): δ [ppm] = 7.61 – 7.45 (m, 2H, H_b), 4.14 (s, broad, 2H, H_c), 3.87 (s, 3H, H_a); **^{19}F{^{1}H} NMR** (282 MHz, $CDCl_3$, 298 K): δ [ppm] = -132.86 (s, 2F, H_d).

(4-Amino-3,5-difluorophenyl)methanol (36)

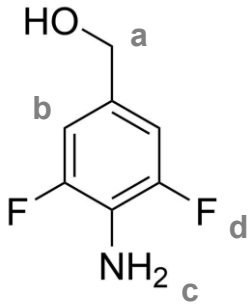

This reaction was performed under an N_2-atmosphere. A solution of ester **5** (7.61 g, 40.7 mmol, 1.00 eq.) in dry THF (30 mL) was added dropwise to a suspension of $LiAlH_4$

(2.31 g, 61.0 mmol, 1.50 eq.) in dry THF (55 mL) at 0 °C over the course of 90 minutes, during which the suspension gelled and could no longer be stirred. The mixture was kept at 0 °C for three hours, during which it was occasionally stirred using a glass rod. The suspension was diluted with dry THF (30 mL) and then stirred at room temperature for 66 hours. The suspension was cooled to 0 °C and H_2O (10 mL), an aqueous NaOH solution (15 wt%, 10 mL) and H_2O (15 mL) were added consecutively, resulting in a yellow solution, out of which a colourless solid quickly precipitated. After stirring for 15 minutes at rt, $MgSO_4$ (approx. 15 g) was added and the suspension was filtered. The solid was washed with EtOAc (5 x 50 mL). The combined organic layers were washed with brine (2 x 40 mL), dried over $MgSO_4$, filtered and evaporated, resulting in a colourless solid. Column chromatography using CyHex:EtOAc (7:3) yielded alcohol **6** (5.93 g, 37.3 mmol, 92%) as colourless crystals.

R_f (CyHex:EtOAc (7:3)) = 0.25; **^{1}H NMR** (300 MHz, $CDCl_3$, 298 K): δ [ppm] = 6.93 – 6.77 (m, 2H, H_b), 4.56 (s, 2H, H_a), 3.71 (s, 2H, H_c); **^{19}F{^{1}H} NMR** (282 MHz, $CDCl_3$, 298 K): δ [ppm] = -132.01 (s, 2F, F_d).

4-Amino-3,5-difluorobenzyl acetate (37)

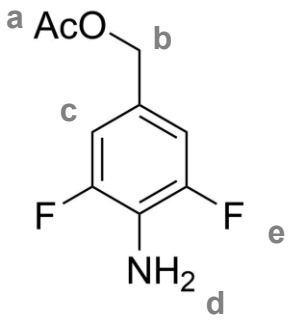

A solution of Ac_2O (3.40 mL, 36.0 mmol, 1.00 eq.) in pyridine (12 mL) was added dropwise to a solution of alcohol **6** (5.73 g, 36.0 mmol, 1.00 eq.) in pyridine (12 mL) at 0 °C over the course of 90 minutes. After stirring the yellow solution for six hours at 0 °C and 16 hours at rt, it was diluted with EtOAc (500 mL). The solution was washed with brine (5 x 80 mL), saturated aqueous $NaHCO_3$ solution (3 x 80 mL) and then dried over $MgSO_4$, filtered and evaporated, resulting in a yellow viscous oil. Column chromatography using CyHex:EtOAc (3:1) yielded acetate **7** (5.12 g, 25.5 mmol, 71%) as a yellow viscous oil. Then, by eluating with EtOAc, a colourless solid (1.97 g) was obtained that consisted mainly of alcohol **5**.

R_f (CyHex:EtOAc (3:1)) = 0.50; **^{1}H NMR** (300 MHz, $CDCl_3$, 298 K): δ [ppm] = 6.91 – 6.79 (m, 2H, H_c), 4.95 (s, 2H, H_b), 3.76 (s, 2H, H_d), 2.08 (s, 3H, H_a); **^{19}F{^{1}H} NMR** (282 MHz, $CDCl_3$, 298 K): δ [ppm] = -132.12 (s, 2F, F_e).

***E*-(Diazene-1,2-diylbis(3,5-difluoro-4,1-phenylene))bis(methylene) diacetate (38)**

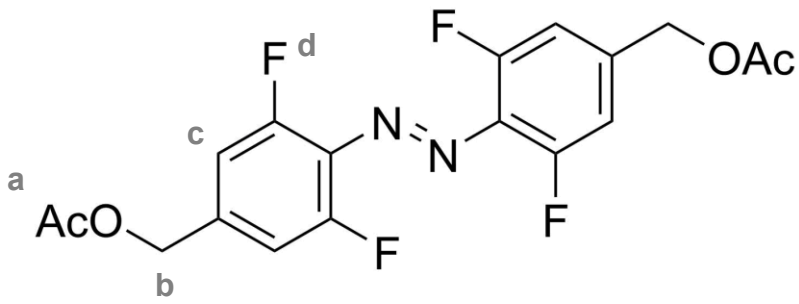

Acetate **7** (5.12 g, 25.5 mmol, 1.00 eq.) was dissolved in CH_2Cl_2 (380 mL), DBU (7.60 mL, 50.9 mmol, 2.00 eq.) was added and the yellowish solution was stirred at room temperature for five minutes before cooling to -78 °C. NCS (6.80 g, 50.9 mmol, 2.00 eq.) was added at -78 °C, resulting in immediate colour change to dark red. After stirring the solution for ten minutes at -78 °C, saturated aqueous $NaHCO_3$ solution (~ 100 mL) was added and the mixture was allowed to thaw. After phase separation, the aqueous layer was extracted with CH_2Cl_2 (2 x 75 mL). The combined organic layers were washed with H_2O (4 x 100 mL) and brine (2 x 100 mL), dried over $MgSO_4$, filtered and evaporated in the dark to obtain a dark red solid. Column chromatography using CH_2Cl_2:EtOAc (99:1) yielded red crystals containing a mixture of *E*- and *Z*-azobenzene **8** in molar ratio of 90:10 contaminated with 27 mol% succinimide (as integrated from ^{1}H NMR) (rectified yield: 3.31 g, 8.31 mmol, 65%). The product was not further purified as the contaminant can be more easily removed in the next step.

***R*$_f$** (CH_2Cl_2:EtOAc (99:1)) = 0.35; ***E*-8: ^{1}H NMR** (300 MHz, $CDCl_3$, 298 K): δ [ppm] = 7.11 – 7.01 (m, 4H, H_c), 5.12 (s, 4H, H_b), 2.17 (s, 6H, H_a); **^{19}F{^{1}H} NMR** (282 MHz, $CDCl_3$, 298 K): δ [ppm] = -119.99 (s, 4F, F_d); ***Z*-8: ^{1}H NMR** (300 MHz, $CDCl_3$, 298 K): δ [ppm] = 6.90 – 6.82 (m, 4H, H_c), 5.03 (s, 4H, H_b), 2.13 (s, 6H, CH_3); **^{19}F{^{1}H} NMR** (282 MHz, $CDCl_3$, 298 K): δ [ppm] = -118.52 (s, 4F, F_d).

The assignment of signal sets corresponding to the *E*- and *Z*-isomers is based on the literature[39b] and in comparison to known values for *E*- and *Z*-**A**.[43]

***E*-(Diazene-1,2-diylbis(2,6-difluoro-4,1-phenylene))dimethanol (39)**

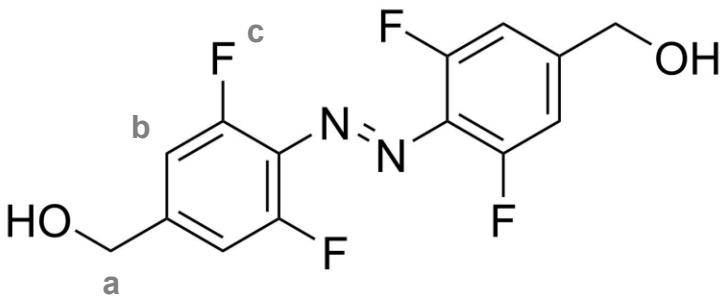

The mixture of products from the previous reaction was used without further purification. Diacetate **8** (3.30 g, 8.30 mmol, 1.00 eq.) was suspended in a mixture of MeOH (425 mL) and concentrated aqueous HCl solution (4.25 mL). The resulting red suspension was stirred at 40 °C for 22 hours, during which it became a solution. After the mixture was allowed to cool to rt, saturated aqueous $NaHCO_3$ solution (~ 100 mL) was added in small portions until a pH value of 8 was reached. Then, brine (150 mL), H_2O (200 mL) and EtOAc (400 mL) were added. The two resulting layers were separated, the aqueous layer was extracted with EtOAc (2 x 400 mL, 1 x 200 mL), the organic layers were combined, dried over $MgSO_4$, filtered and evaporated in the dark to obtain a red solid. Column chromatography using CyHex:EtOAc (3:2 to 100% EtOAc) yielded a red solid consisting of diol **39** contaminated with succinimide. To remove the succinimide, the crude product was dissolved in EtOAc (500 mL) and washed with aqueous HCl solution (1 M, 4 x 100 mL). The organic layer was dried over Na_2SO_4, filtered and evaporated to yield dialcohol *E*-**39** (2.44 g, 77.7 mmol, 94%).

***R*$_f$** (CyHex:EtOAc (3:2)) = 0.14 (*E*-**39**) and 0.03 (*Z*-**39**); ***R*$_f$** (CyHex:EtOAc (1:1)) = 0.30 (*E*-**39**) and 0.08 (*Z*-**39**); **^{1}H NMR** (300 MHz, $CDCl_3$, 298 K): δ [ppm] = 7.10 – 7.07 (m, 4H, H_b), 4.77 (s, 4H, H_a); **^{19}F{^{1}H} NMR** (282 MHz, $CDCl_3$, 298 K): δ [ppm] = -120.21 (s, 4F, F_c).

***E*-4,4'-(diazene-1,2-diyl)bis(3,5-difluorobenzaldehyde) *E*-A**

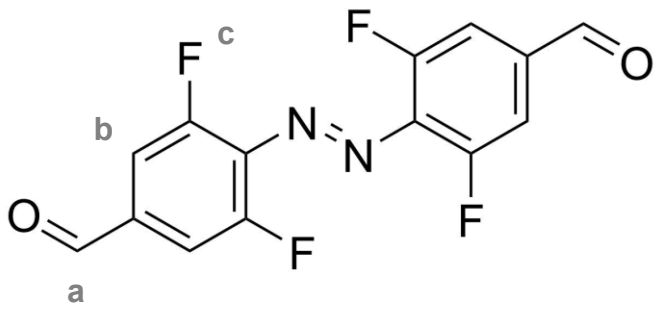

Dialcohol **9** (2.44 g, 7.77 mmol, 1.00 eq.) and Na_2SO_4 (50 g) were suspended in CH_2Cl_2 (210 mL) and the resulting orange suspension was stirred in the dark at room temperature for ten minutes. PCC (4.18 g, 19.4 mmol, 2.50 eq.) was added, resulting in a red suspension which was stirred in the dark at room temperature for 24 hours. The resulting brown suspension was filtered over a small silica plug and the residue was rinsed with CH_2Cl_2 until the filtrate remained colourless. The red filtrates were combined and evaporated in the dark to obtain a dark red solid. Flash column chromatography using CH_2Cl_2 yielded a first fraction containing azobenzene *E*-**A** (1.74 g) and a second fraction containing a mixture of **A** and other compounds (320 mg). The second fraction was again purified by flash column chromatography using CH_2Cl_2:CyHex (2:1) to obtain *E*-**A** (183 mg) and a mixture of **A** and the mono-oxidised substrate (58.0 mg). Azobenzene *E*-**A** (total yield: 1.92 g, 6.19 mmol, 80%) was obtained as a red solid.

R_f (CH_2Cl_2) = 0.66; ***E*-A: ^{1}H NMR** (300 MHz, $CDCl_3$, 298 K): δ [ppm] = 10.00 (t, *J* = 1.7 Hz, 2H, H_a), 7.65 – 7.60 (m, 4H, H_b); **^{1}H NMR** (300 MHz, CD_2Cl_2, 298 K): δ [ppm] = 10.00 (t, *J* = 1.7 Hz, 2H, H_a), 7.65 – 7.60 (m, 4H, H_b); **^{19}F{^{1}H} NMR** (282 MHz, $CDCl_3$, 298 K): δ [ppm] = -117.84 (s, 4F, F_c); **^{19}F{^{1}H} NMR** (300 MHz, CD_2Cl_2, 298 K): δ [ppm] = -118.93 (s, 4F, F_c); ***Z*-A: ^{1}H NMR** (300 MHz, CD_2Cl_2, 298 K): δ [ppm] = 9.86 (t, 2H, H_a), 7.44 – 7.40 (m, 4H, H_b); **^{19}F{^{1}H} NMR** (300 MHz, CD_2Cl_2, 298 K): δ [ppm] = -117.67 (s, 4F, F_c).

***E*-AC²**

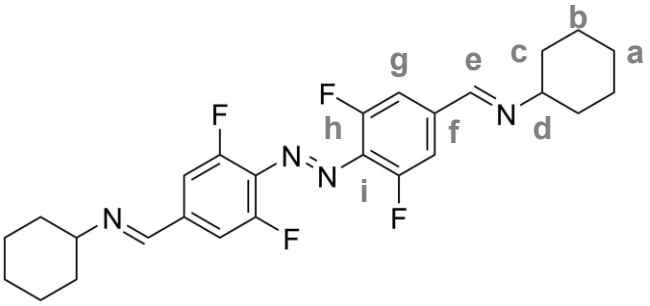

Azobenzene **A** (12 mg, 38 µmol, 1.0 eq.) was dissolved in a mixture of MeOH (5 mL) and CH_2Cl_2 (5 mL). $MgSO_4$ (excess) and amine **C** (26 µL, 0.23 mmol, 6.0 eq.) were added and the mixture was stirred at room temperature in the dark for 64 hours. The solvent was removed under reduced pressure and the precipitate was redissolved in CH_2Cl_2 (10 mL), filtered and concentrated under reduced pressure. Imine **AC²** was obtained as a dark red solid (17 mg, 36 µmol, 96 %).

^{1}H NMR (300 MHz, $CDCl_3$, 298 K): δ [ppm] = 8.25 (s, 2H, H_e), 7.45 – 7.43 (m, 4H, H_g), 3.34 – 3.21 (m, 2H, H_d), 1.77 – 1.27 (m, 10H, H_{a-c}); **^{1}H NMR** (300 MHz, CD_2Cl_2, 298 K): δ [ppm] = 8.26 (s, 2H, H_e), 7.50 – 7.40 (m, 4H, H_g), 3.35 – 3.23 (m, 2H, H_d), 1.90 – 1.32 (m, 20H, H_{a-c}); **^{19}F{^{1}H} NMR** (565 MHz, $CDCl_3$, 298 K): δ [ppm] = -119.84 (s, 4F, F_h); **^{19}F{^{1}H} NMR** (300 MHz, CD_2Cl_2, 298 K): δ [ppm] = -120.78 (s, 4F, F_h); **^{13}C{^{1}H} NMR** (75 MHz, $CDCl_3$, 298 K): δ [ppm] = 155.89 (dd, J = 262.2 Hz, J = 4.4 Hz, C_h), 155.50 (s, C_e), 140.38 (s, C_f), 132.58 (s, C_i), 111.95 (dd, J = 21.5 Hz, J = 3.3 Hz, C_g), 70.01 (s, C_d), 34.29 (s, C_c), 25.69 (s, C_a), 24.70 (s, C_b); **MS** HRMS (ESI) calc. for $[C_{26}H_{28}N_4F_4+H]^+$: 473.2323, meas.: 473.2331; **IR** $\tilde{\nu}$ [cm^{-1}]: 2928 (m), 2855 (m), 1639 (m), 1622 (m), 1574 (s), 1454 (m), 1445 (m), 1435 (s), 1383 (m), 1346 (s), 1335 (w), 1319 (w), 1300 (w), 1200 (m), 1153 (w), 1080 (m), 1070 (m), 1059 (m), 1042 (s), 999 (w), 962 (m), 887 (m), 864 (s), 847 (m), 814 (w), 750 (m), 707 (w), 631 (m).

UV/VIS spectroscopy

Table S17: Concentrations of the different compounds and the respective irradiation wavelength for the different measurements.

Compound	λ_{irr} / nm	c / µM
A	405	13.5
	470	13.5
	565	13.5
AC²	405	25.5
	565	25.5
	660	25.5

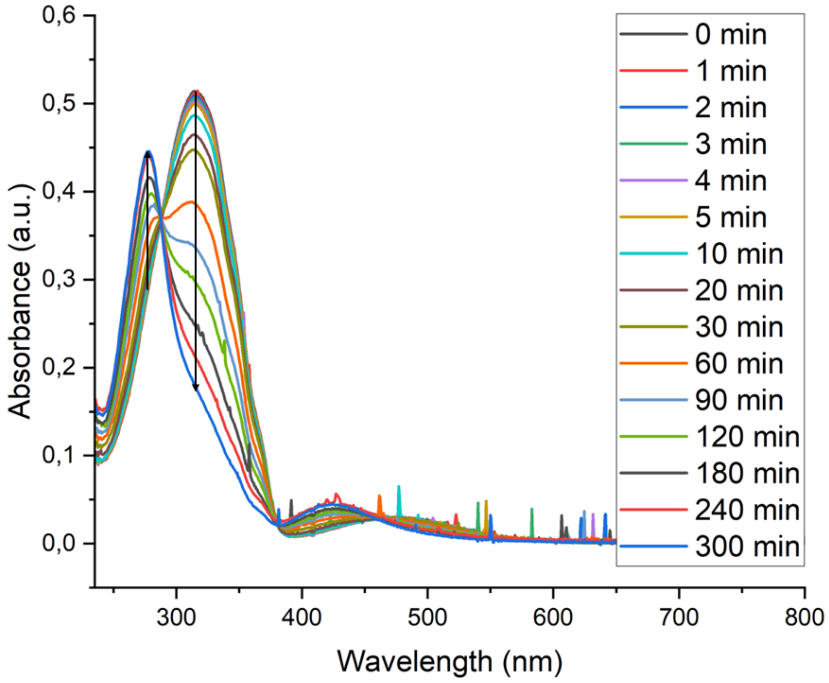

Figure S42: UV/VIS spectra of **A** after irradiation with red light (660 nm) in CH_2Cl_2.

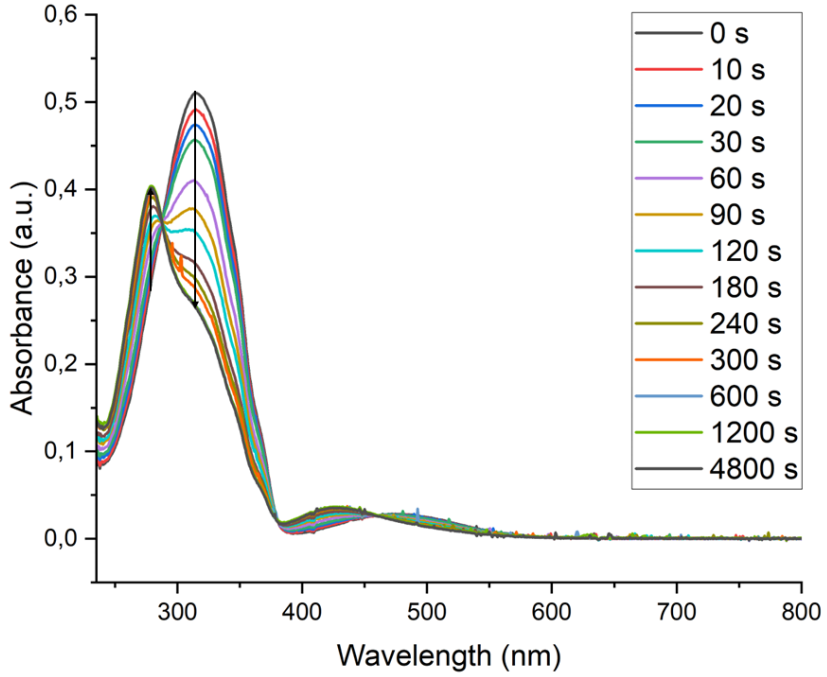

Figure S43: UV/VIS spectra of **A** after irradiation with green light (565 nm) in CH_2Cl_2.

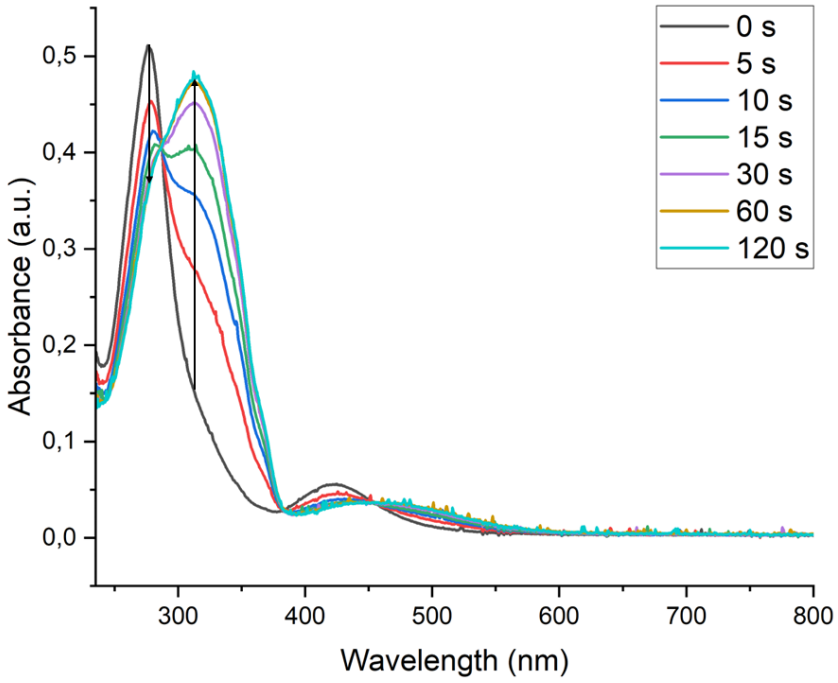

Figure S44: UV/VIS spectra of **A** in CH_2Cl_2. A solution that was *Z*-enriched by irradiation with red light (660 nm) was irradiated with light of the wavelength of 470 nm.

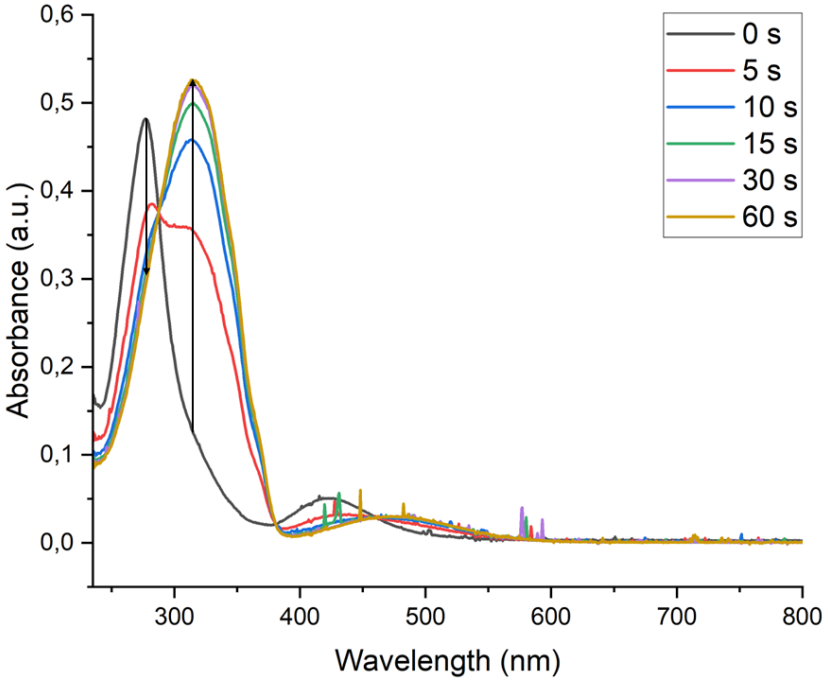

Figure S45: UV/VIS spectra of **A** in CH_2Cl_2. A solution that was *Z*-enriched by irradiation with red light (660 nm) was irradiated with light of the wavelength of 405 nm.

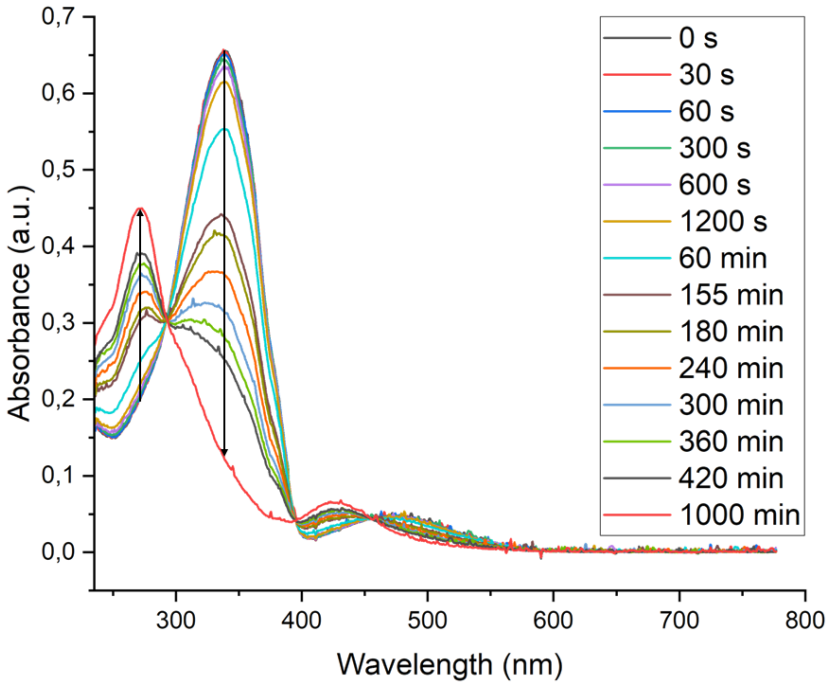

Figure S46: UV/VIS spectra of **AC²** after irradiation with red light (660 nm) in CH_2Cl_2.

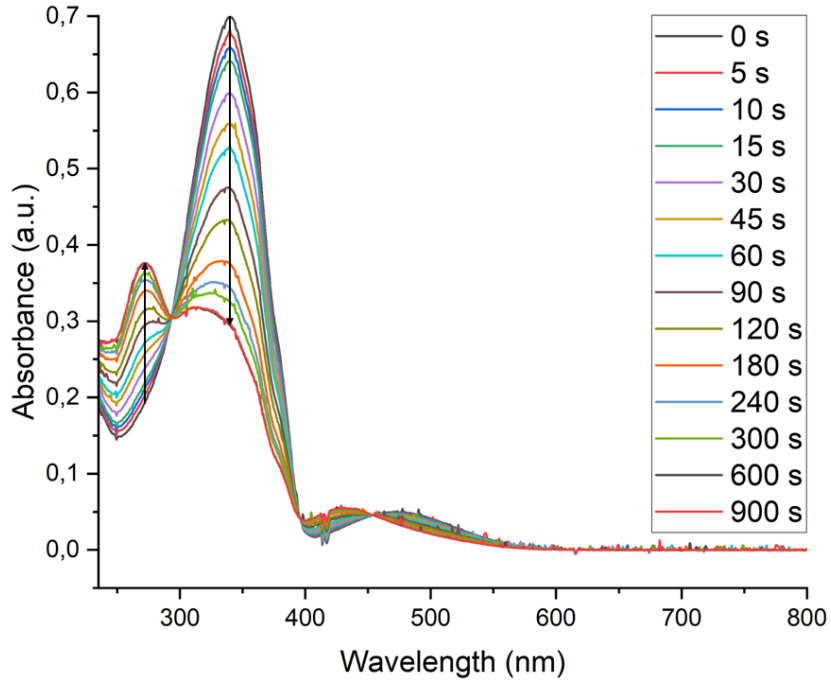

Figure S47: UV/VIS spectra of **AC²** after irradiation with green light (565 nm) in CH_2Cl_2.

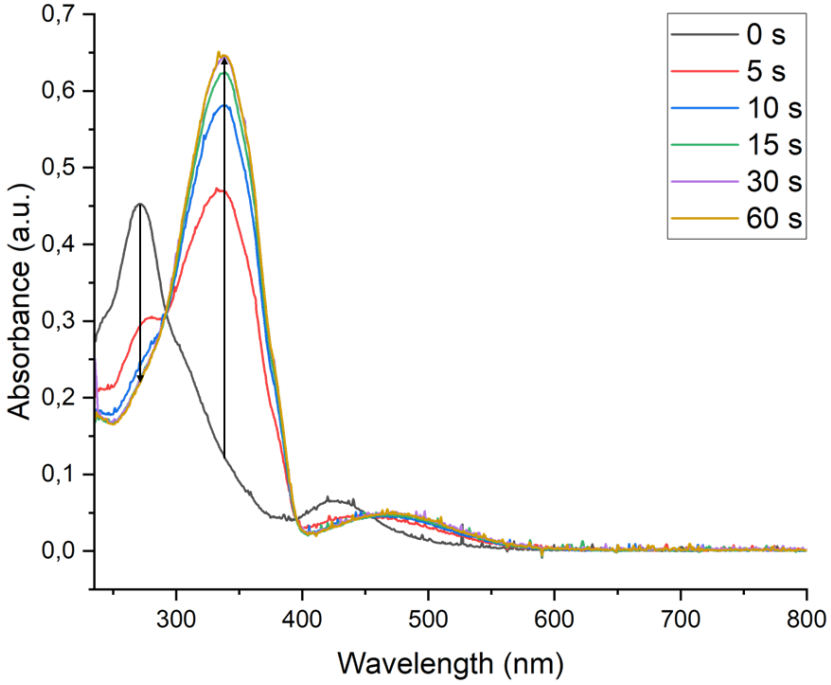

Figure S48: UV/VIS spectra of **AC²** in CH_2Cl_2. A solution that was *Z*-enriched by irradiation with red light (660 nm) was irradiated with light of the wavelength of 405 nm.

Table S18: Comparison of the wavelengths of absorption maxima λ_{max} and molar attenuation coefficients ε of the model system *E*-**AC²**, and the azobenzene *E*-**A**.

	E-**AC²**		*E*-**A**	
	π→π*	n→π*	π→π*	n→π*
λ_{max} / nm	340	475	314	475
ε / 10^3 L mol^{-1} cm^{-1}	26.0	1.84	37.8	2.11

PSS determination

Samples were dissolved in CD_2Cl_2 in concentrations of c = 8.59 mmol L^{-1} (**A**) and c = 6.49 mmol L^{-1} (**AC²**), respectively. The solutions were irradiated at room temperature while stirring for the times indicated. The *E* to *Z* ratio was determined using three different signals; those, as well as the integrals and the integral ranges, are listed in tables S19 and S20.

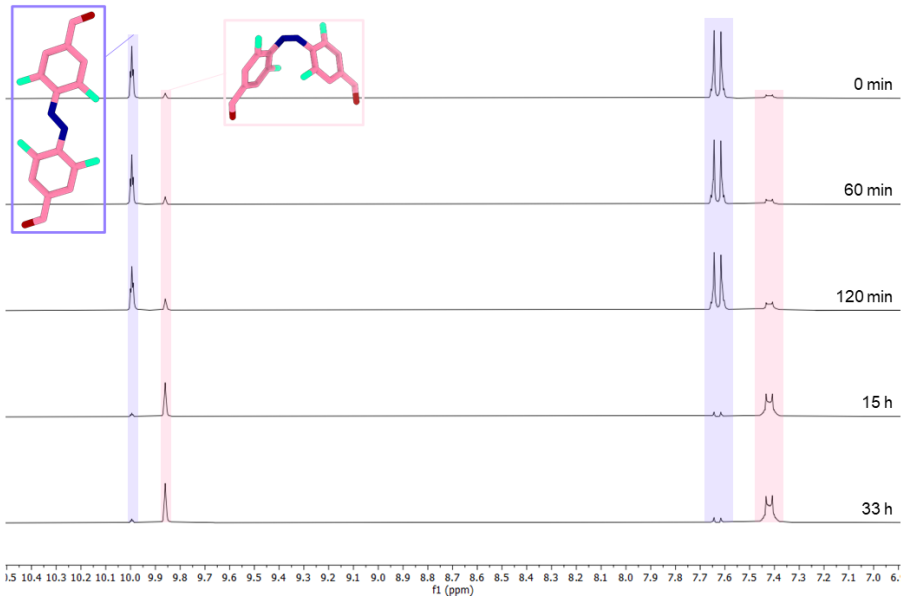

Figure S49: ^{1}H NMR spectra of **A** after irradiation with light of a wavelength of 660 nm. The signals of the *E*- and the *Z*-isomers are highlighted in blue and pink, respectively (CD_2Cl_2, 300 MHz).

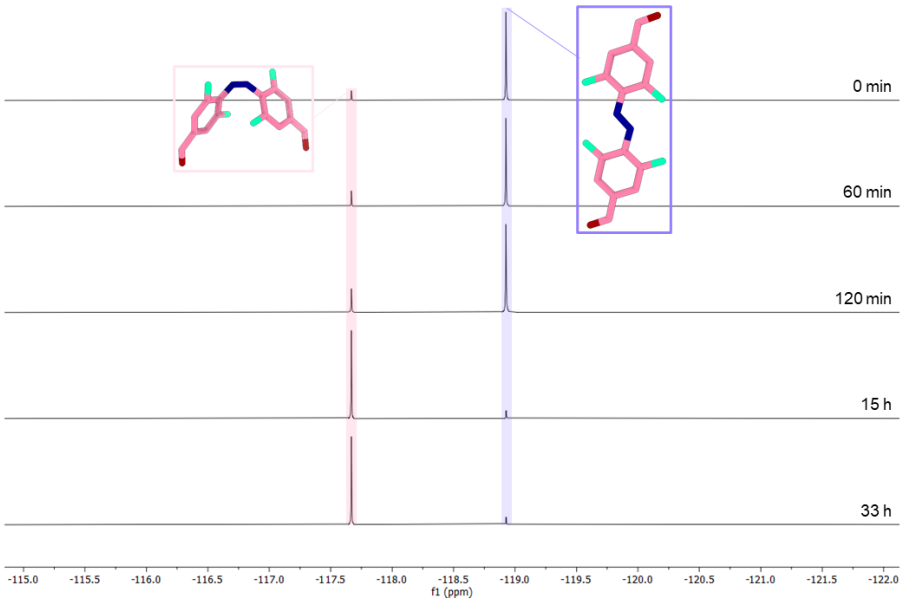

Figure S50: $^{19}F\{^{1}H\}$ NMR spectra of **A** after irradiation with light of a wavelength of 660 nm. The signals of the *E*- and the *Z*-isomers are highlighted in blue and pink, respectively (CD_2Cl_2, 282 MHz).

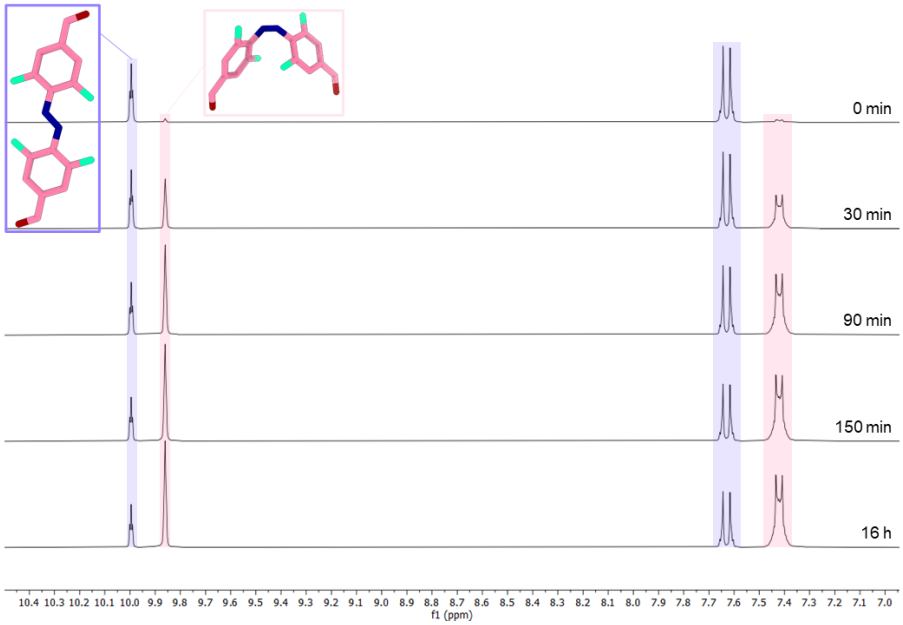

Figure S51: ^{1}H NMR spectra of **A** after irradiation with light of a wavelength of 565 nm. The signals of the *E*- and the *Z*-isomers are highlighted in blue and pink, respectively (CD_2Cl_2, 300 MHz).

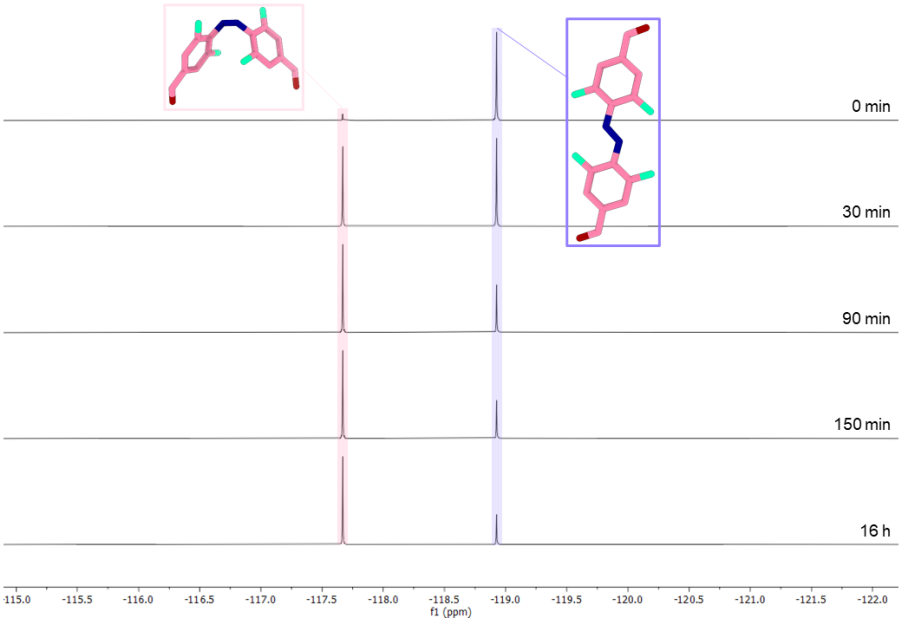

Figure S52: $^{19}F\{^{1}H\}$ NMR spectra of **A** after irradiation with light of a wavelength of 565 nm. The signals of the *E*- and the *Z*-isomers are highlighted in blue and pink, respectively (CD_2Cl_2, 282 MHz).

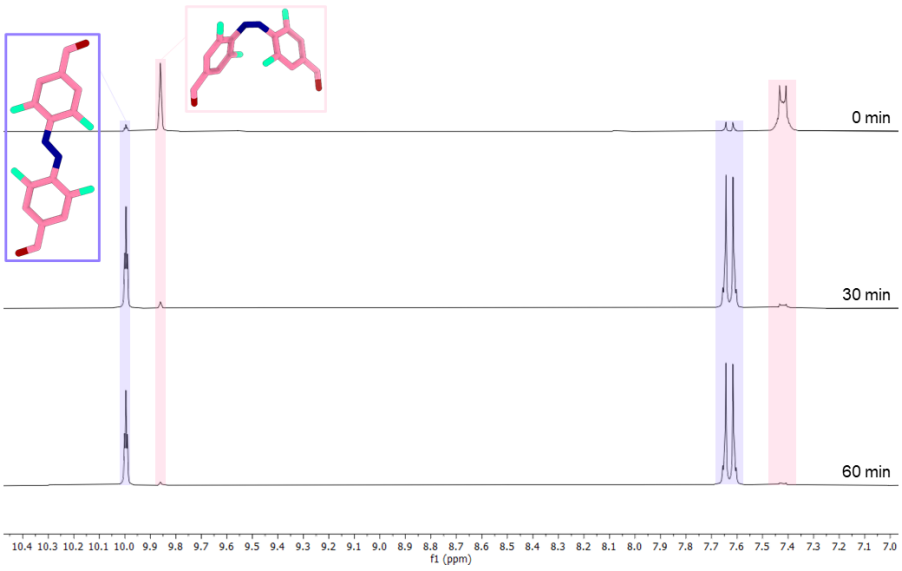

Figure S53: ^{1}H NMR spectra of **A** after irradiation with light of a wavelength of 405 nm. The signals of the *E*- and the *Z*-isomers are highlighted in blue and pink, respectively (CD_2Cl_2, 300 MHz). 0 minutes refers to a solution of **A**, that was previously irradiated with red light until the PSS_Z (660 nm) was reached.

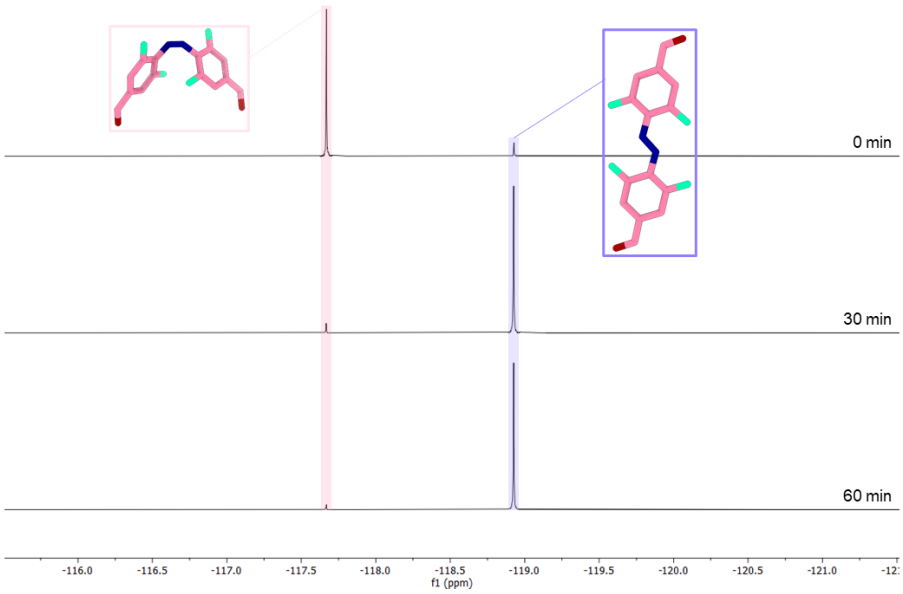

Figure S54: $^{19}F\{^{1}H\}$ NMR spectra of **A** after irradiation with light of a wavelength of 405 nm. The signals of the *E*- and the *Z*-isomers are highlighted in blue and pink, respectively (CD_2Cl_2, 282 MHz). 0 minutes refers to a solution of **A** that was previously irradiated with red light until the PSS_Z (660 nm) was reached.

Table S19: Determined integrals and resulting *E*:*Z* ratio after irradiation of **A** with different wavelengths.

Irradiation wavelength	Integral (^{1}H) 10.020 – 9.970	Integral (^{1}H) 9.875 – 9.845	*E*:*Z* ratio	Integral (^{1}H) 7.670 – 7.590	Integral (^{1}H) 7.450 – 7.390	*E*:*Z* ratio	Integral ($^{19}F\{^{1}H\}$) -117.600 - -117.750	Integral ($^{19}F\{^{1}H\}$) -118.900 - -118.950	*E*:*Z* ratio
660 nm ($E \rightarrow Z$)	0.22	2.00	10:90	0.46	4.02	10:90	4.00	0.38	9:91
565 nm ($E \rightarrow Z$)	0.82	2.00	29:71	1.67	3.99	30:70	4.00	1.64	29:71
405 nm ($Z \rightarrow E$)	2.00	0.10	95:5	4.13	0.23	95:5	0.14	4.00	97:3

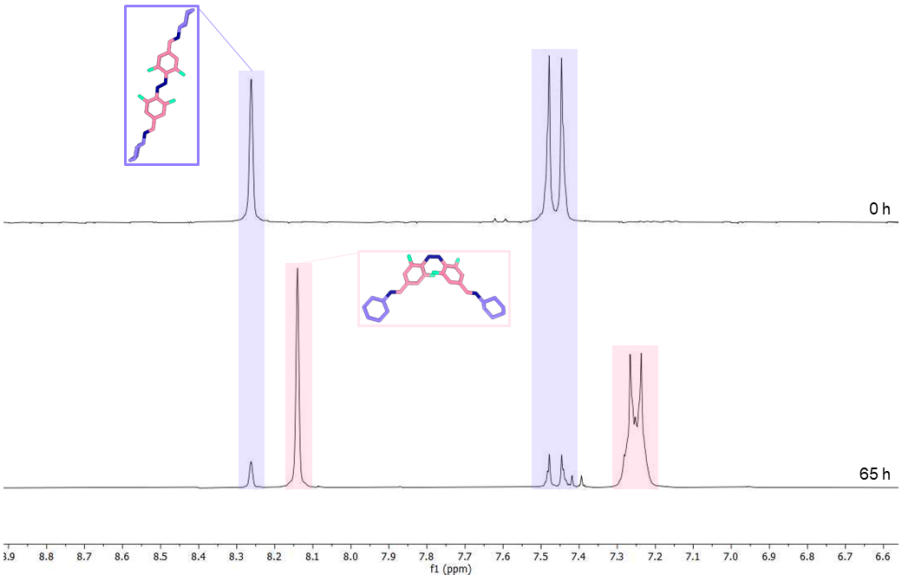

Figure S55: ^{1}H NMR spectra of **AC²** after irradiation with light of a wavelength of 660 nm. The signals of the *E*- and the *Z*-isomers are highlighted in blue and pink, respectively (CD_2Cl_2, 300 MHz). The small multiplet at δ = 7.40 ppm shows the formation of a small amount of monosubstituted **A**.

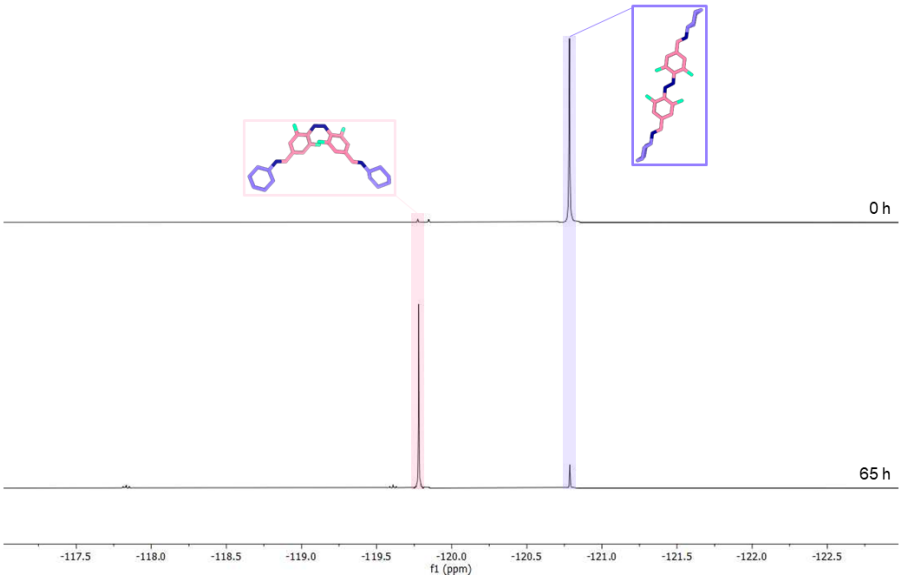

Figure S56: ^{19}F{^{1}H} NMR spectra of **AC²** after irradiation with light of a wavelength of 660 nm. The signals of the *E*- and the *Z*-isomers are highlighted in blue and pink, respectively (CD_2Cl_2, 282 MHz). The small multiplets at δ = - 117.84 and - 119.61 ppm show the formation of a small amount of monosubstituted **A**.

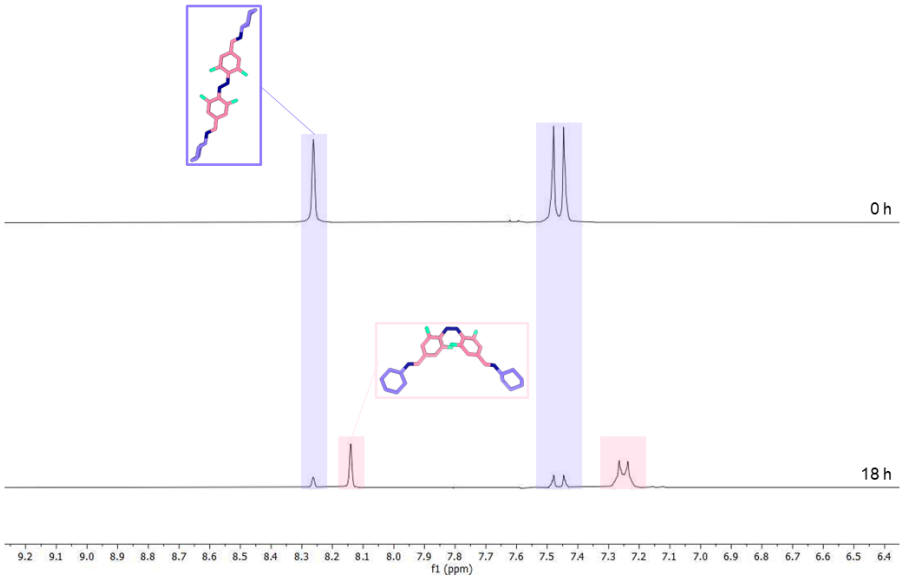

Figure S57: ^{1}H NMR spectra of **AC²** after irradiation with light of a wavelength of 565 nm. The signals of the *E*- and the *Z*-isomers are highlighted in blue and pink, respectively (CD_2Cl_2, 300 MHz).

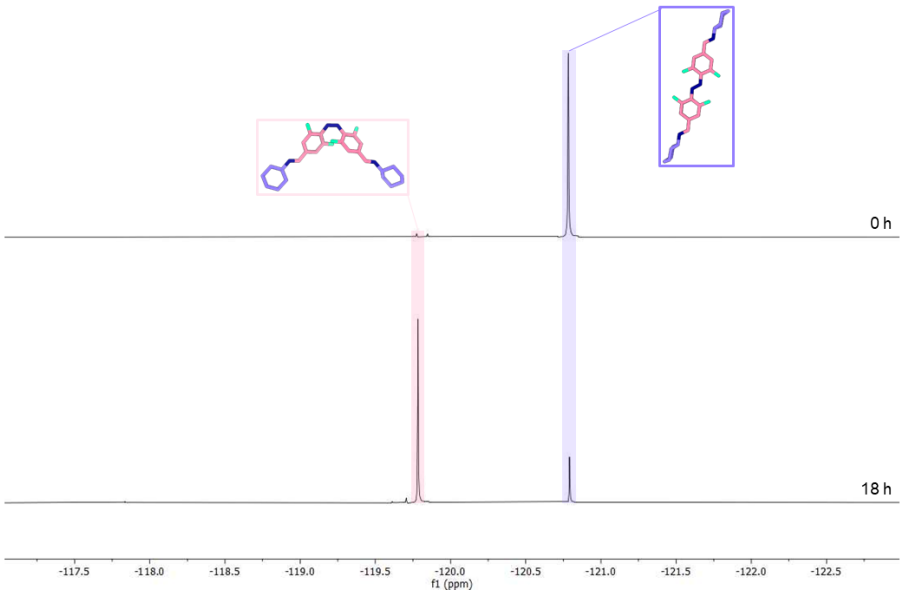

Figure S58: ^{19}F{^{1}H} NMR spectra of **AC²** after irradiation with light of a wavelength of 565 nm. The signals of the *E*- and the *Z*-isomers are highlighted in blue and pink, respectively (CD_2Cl_2, 282 MHz).

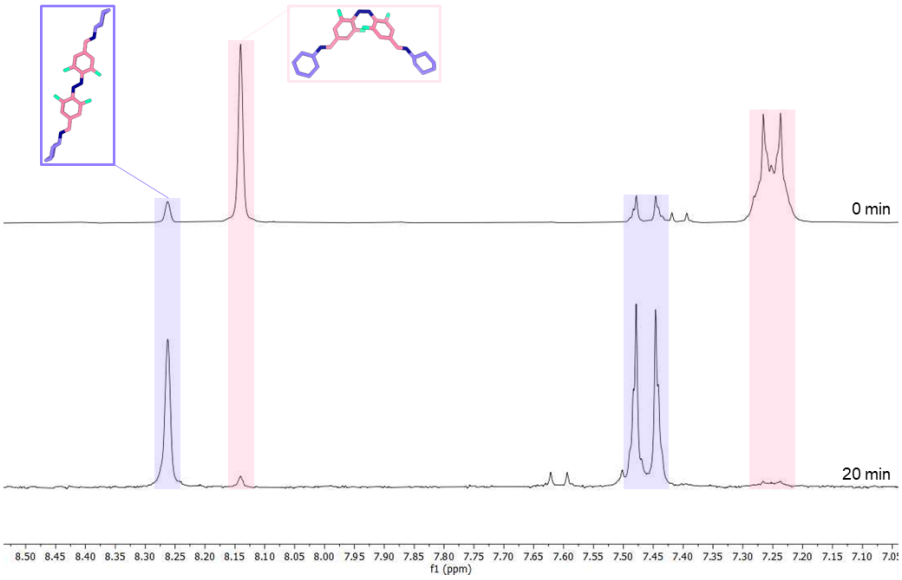

Figure S59: ^{1}H NMR spectra of **AC²** after irradiation with light of a wavelength of 405 nm. The signals of the *E*- and the *Z*-isomers are highlighted in blue and pink, respectively (CD_2Cl_2, 300 MHz). 0 minutes refers to a solution of **A** that was previously irradiated with red light until the PSS_Z (660 nm) was reached. The small multiplets at δ = 7.40 and 7.63 ppm show the presence of a small amount of monosubstituted *Z*- and *E*-**A**, respectively.

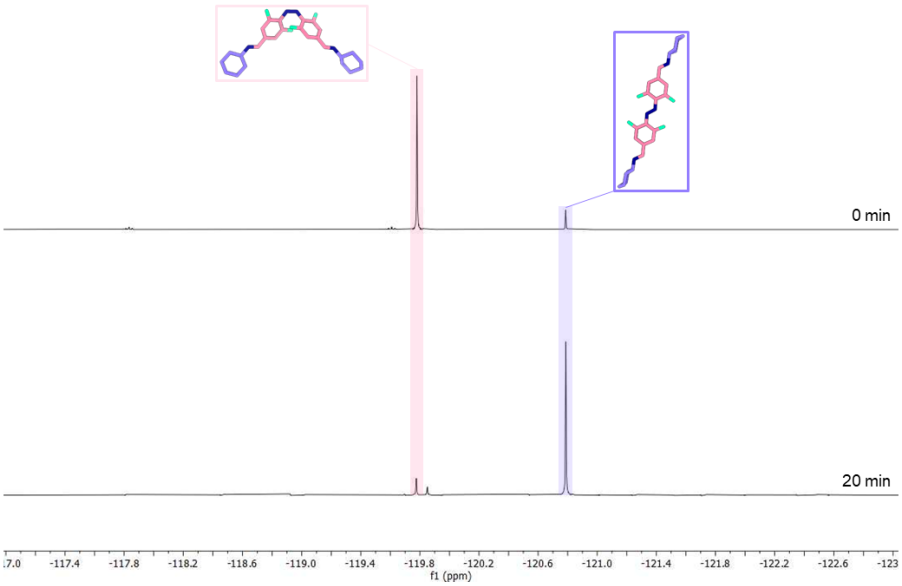

Figure S60: $^{19}F\{^{1}H\}$ NMR spectra of **AC²** after irradiation with light of a wavelength of 405 nm. The signals of the *E*- and the *Z*-isomers are highlighted in blue and pink, respectively (CD_2Cl_2, 282 MHz). 0 minutes refers to a solution of **A** that was previously irradiated with red light until the PSS_Z (660 nm) was reached. The small multiplets at δ = - 117.84 and - 119.82 ppm show the presence of a small amount of monosubstituted *Z*- and *E*-**A**, respectively.

Table S20: Determined integrals and resulting *E*:*Z* ratio after irradiation of **AC²** with different wavelengths.

Irradiation wavelength	Integral (^{1}H)		*E*:*Z* ratio	Integral (^{1}H)		*E*:*Z* ratio	Integral (^{19}F{^{1}H})		*E*:*Z* ratio
	8.300 – 8.215	8.175 – 8.110		7.515 – 7.400	7.305 – 7.190		-119.755 - -119.800	-120.750 - -120.825	
660 nm ($E \rightarrow Z$)	0.36	2.00	15:85	0.75	4.00	16:84	4.00	0.56	12:88
565 nm ($E \rightarrow Z$)	0.74	2.00	27:73	1.37	3.98	26:74	4.00	1.14	23:77
405 nm ($Z \rightarrow E$)	2.00	0.21	90:10	3.96	0.44	90:10	0.47	4.00	89:11

Imine formation kinetics

Azobenzene *E*-**A** (9.31 mg, 30 µmol) was dissolved in CD_2Cl_2 (3 mL). The solution was partitioned into four vials. Half of the vials were kept in the dark, while the other half was stirred under continuous irradiation with red light (660 nm) until ^{1}H and ^{19}F{^{1}H} NMR-spectra indicated, that the PSS was reached. A stock solution of cyclohexylamine (5.95 mg, 60 µmol) in CD_2Cl_2 (0.4 mL) was made and two equivalents of amine were added into each vial. ^{1}H and ^{19}F{^{1}H} NMR spectra were measured after the indicated times. Between the measurements all samples were kept in the dark.

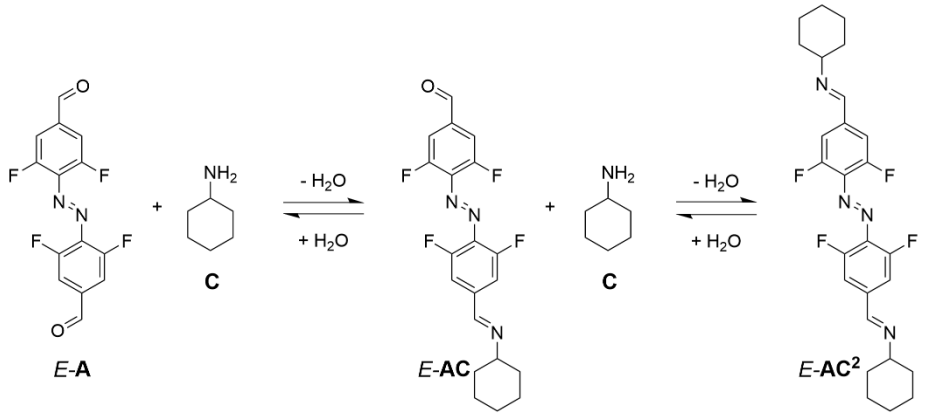

Figure S61: Formation of the **AC²** starting from **A** and cyclohexylamine (**C**).

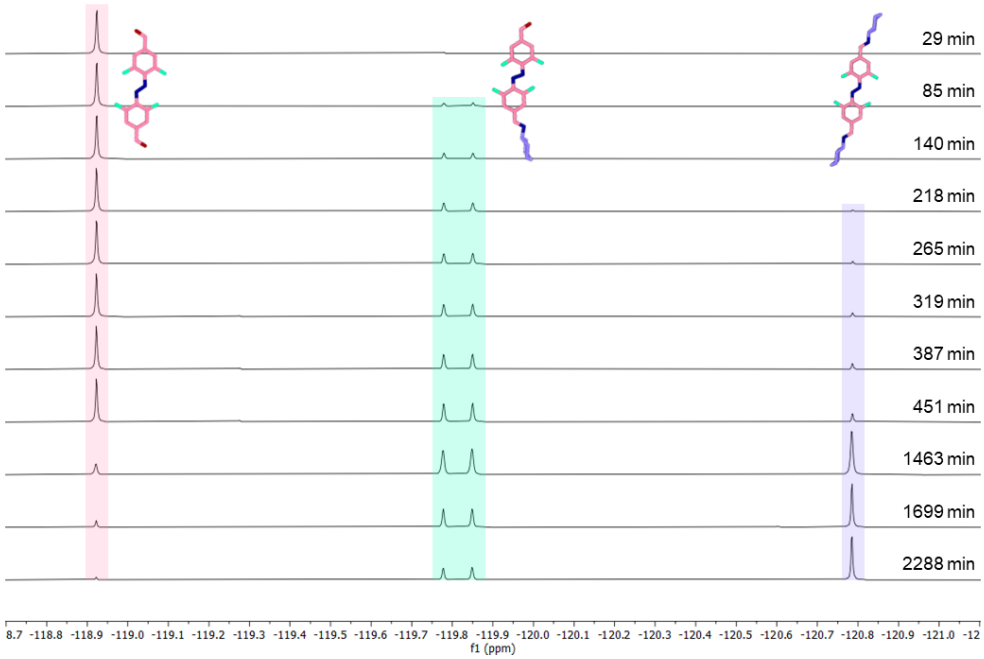

Figure S62: $^{19}F\{^{1}H\}$ NMR spectra of the reaction of azobenzene **A** (pink) with cyclohexylamine forming the monosubstituted azobenzene **AC** (turquoise) and following the bis-imine **AC²** (blue) (CD_2Cl_2, 282 MHz).

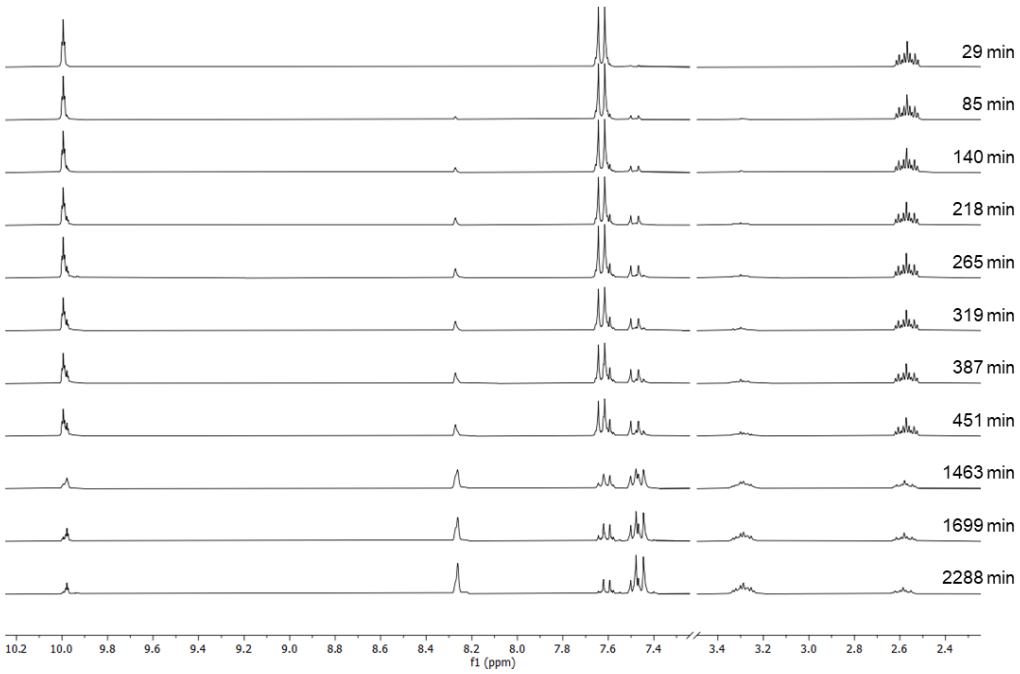

Figure S63: ^{1}H NMR spectra of the reaction of azobenzene **A** with cyclohexylamine (**C**) forming the monosubstituted azobenzene **AC** and following the bis-imine **AC²** (CD_2Cl_2, 300 MHz).

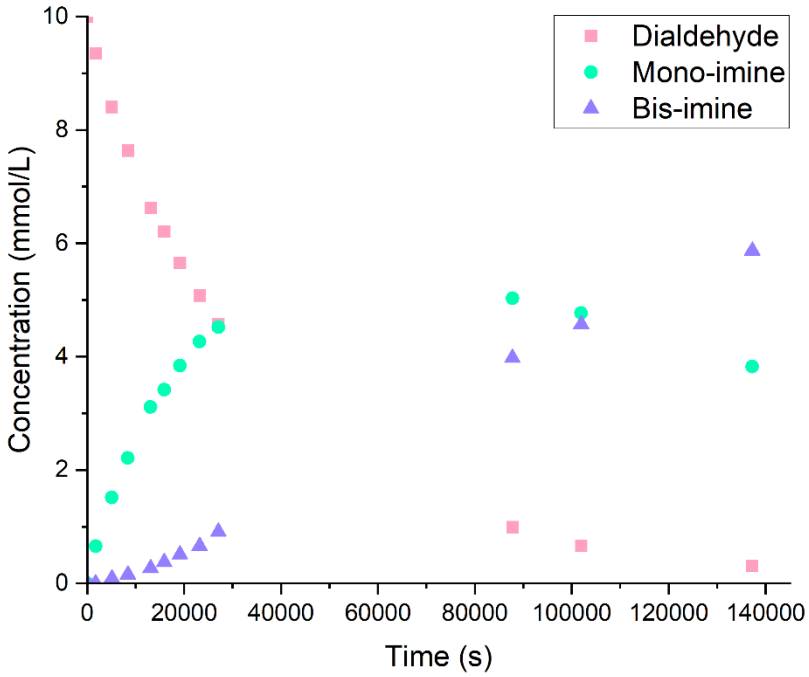

Figure S64: Observed concentrations of the dialdehyde **A** (pink), the mono-imine **AC** (turquoise) and the bis-imine **AC²** (blue) as determined from the $^{19}F\{^{1}H\}$ NMRs of the dark sample.

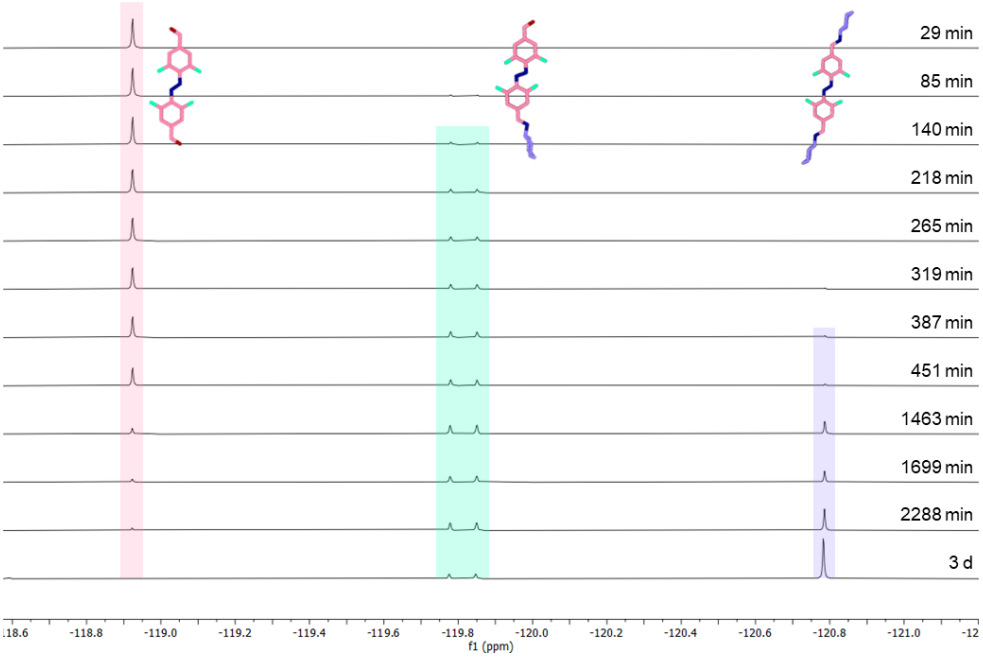

Figure S65: $^{19}F\{^{1}H\}$ NMR spectra of the reaction of azobenzene **A** (pink) with cyclohexylamine (**C**) forming the monosubstituted azobenzene **AC** (turquoise) and following the bis-imine **AC²** (blue) (CD_2Cl_2, 282 MHz).

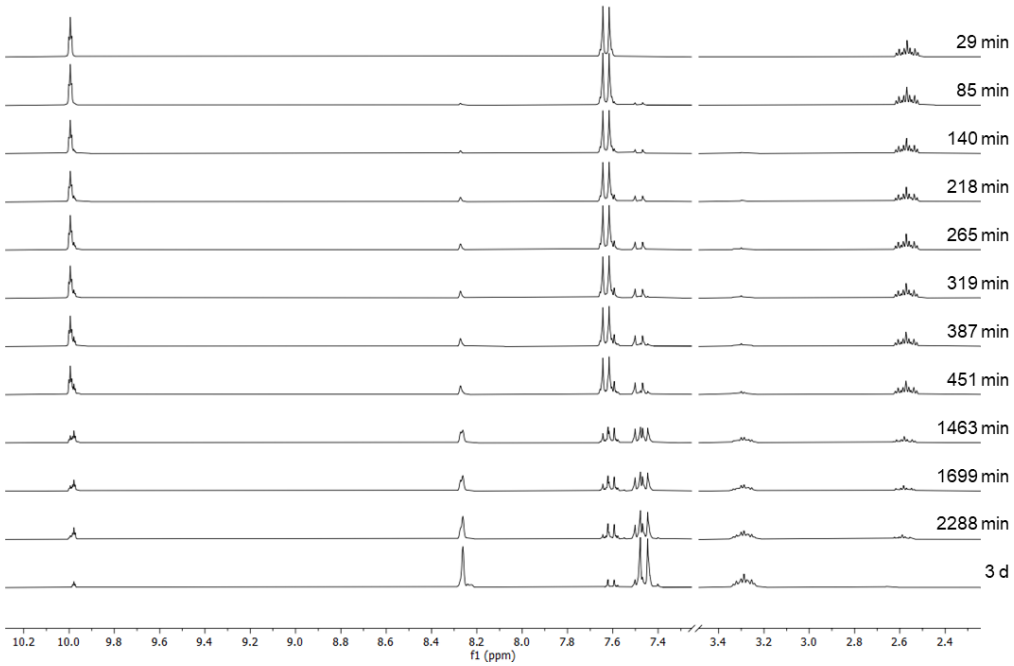

Figure S66: ^{1}H NMR spectra of the reaction of azobenzene **A** with cyclohexylamine (**C**) forming the monosubstituted azobenzene **AC** and following the bis-imine **AC²** (CD_2Cl_2, 300 MHz).

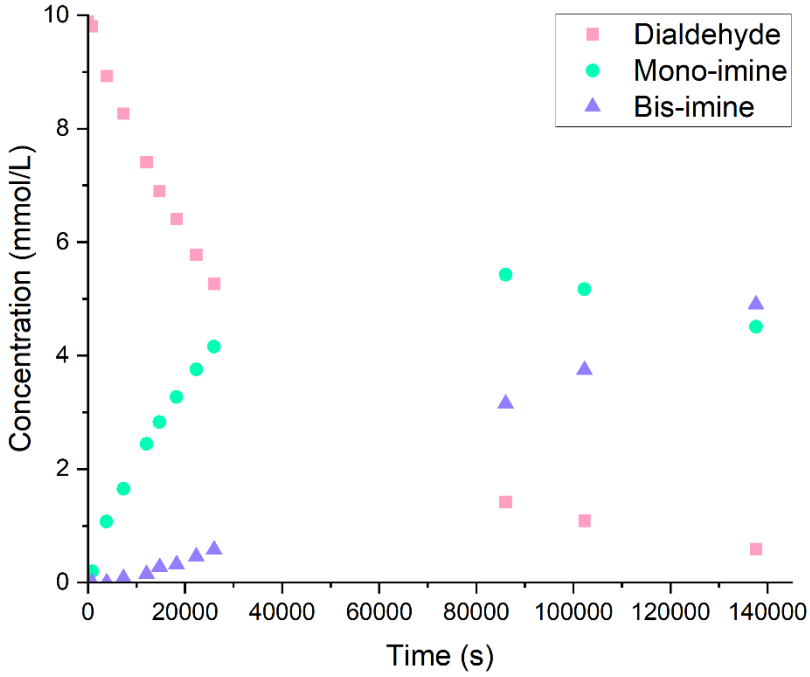

Figure S67: Observed concentrations of the dialdehyde **A** (pink), the mono-imine **AC** (turquoise) and the bis-imine **AC²** (blue) as determined from the $^{19}F\{^{1}H\}$ NMRs of the dark sample.

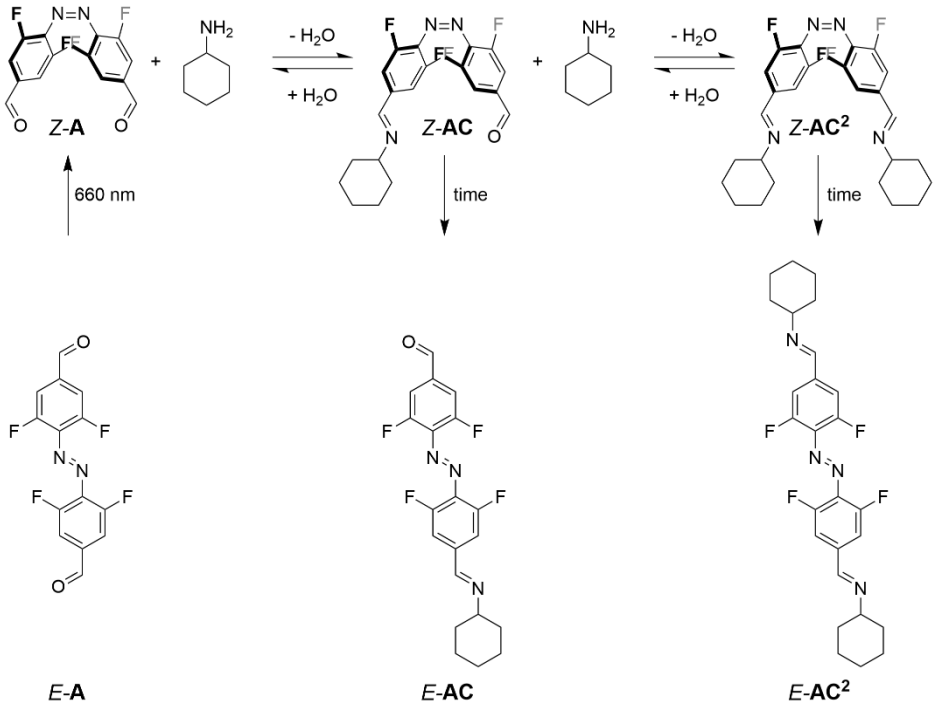

Figure S68: Formation of **AC²** starting from *Z*-enriched **A** and cyclohexylamine (**C**). As the mixture was not irradiated between the measurements a small amount of *E*- **AC²** and *E*-monosubstituted azobenzene **AC** are formed.

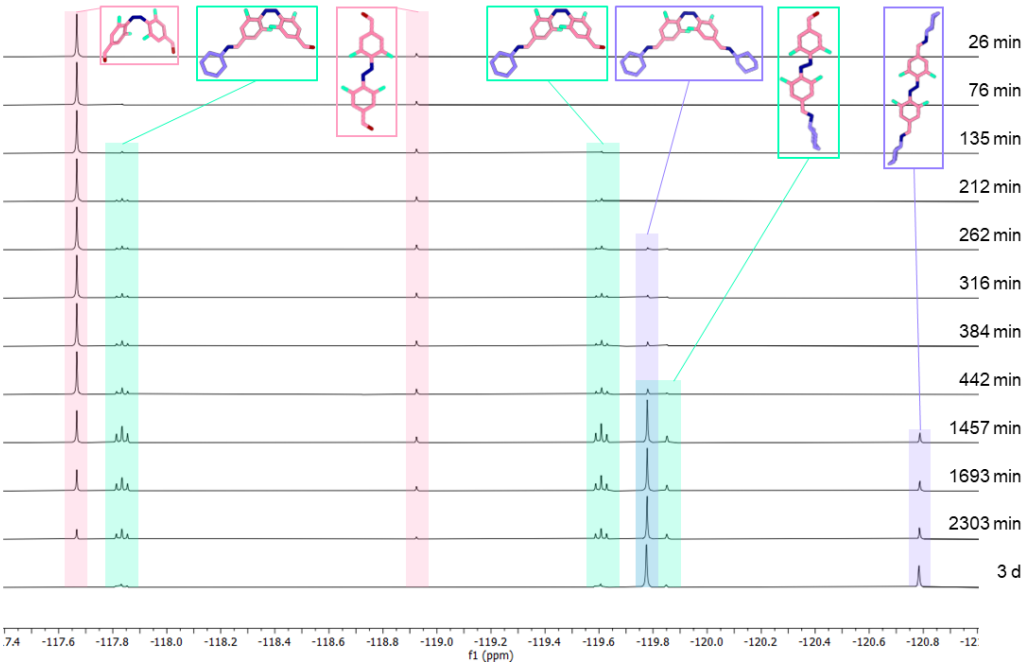

Figure S69: $^{19}F\{^{1}H\}$ NMR spectra of the reaction of a *Z*-enriched solution of azobenzene **A** (pink) with cyclohexylamine (**C**), forming the mono-imine **AC** (turquoise) and following the bis-imine **AC²** (blue) (CD_2Cl_2, 282 MHz). As the solution is not continuously irradiated, the corresponding *E*-compounds are also formed over time.

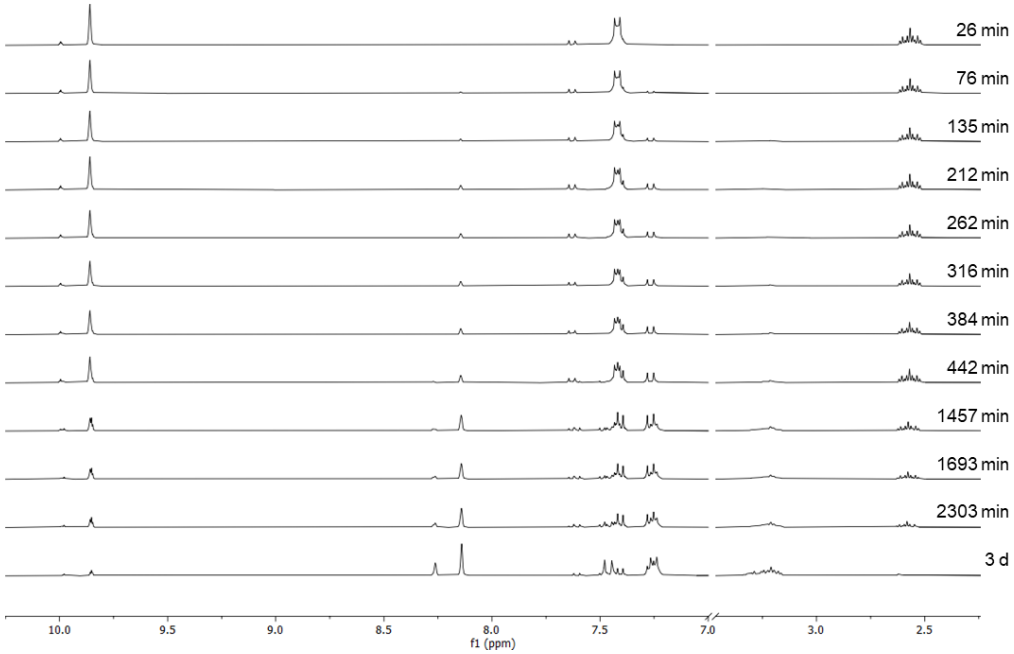

Figure S70: ^{1}H NMR spectra of the reaction of a *Z*-enriched solution of azobenzene **A** with cyclohexylamine (**C**), forming the mono-imine **AC** and following the bis-imine **AC²** (CD_2Cl_2, 300 MHz). As the solution is not continuously irradiated, the corresponding *E*-compounds are also formed over time.

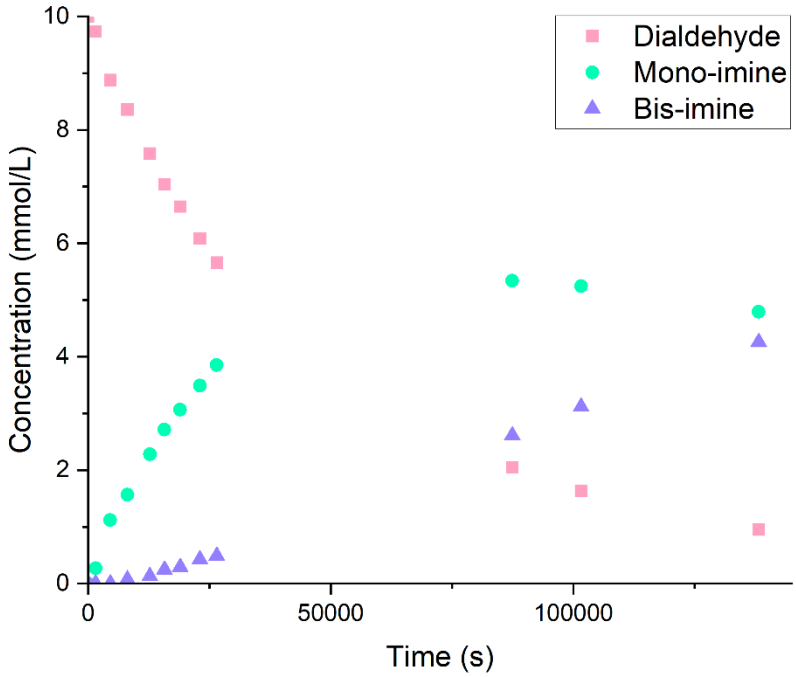

Figure S71: Observed concentrations of the dialdehyde **A** (pink), the mono-imine **AC** (turquoise) and the bis-imine **AC²** (blue) as determined from the ^{19}F{^{1}H} NMRs of the dark sample. As both isomers are formed over time, the concentration of each compound refers to both isomers.

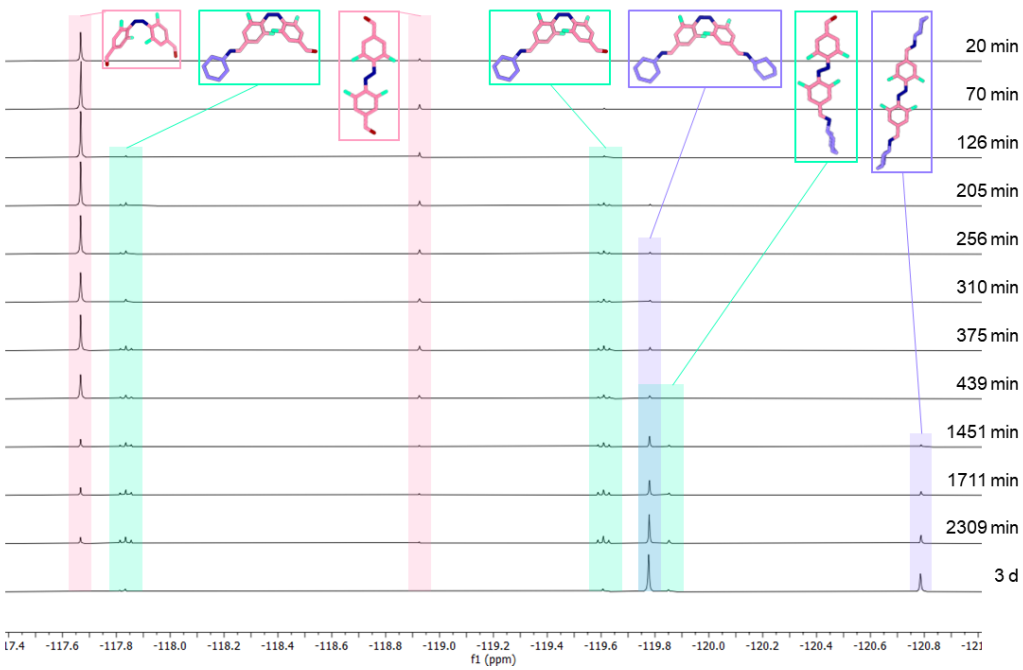

Figure S72: $^{19}F\{^{1}H\}$ NMR spectra of the reaction of a *Z*-enriched solution of azobenzene **A** (pink) with cyclohexylamine (**C**), forming the mono-imine **AC** (turquoise) and following the bis-imine **AC²** (blue) (CD_2Cl_2, 282 MHz). As the solution is not continuously irradiated, the corresponding *E*-compounds are also formed over time.

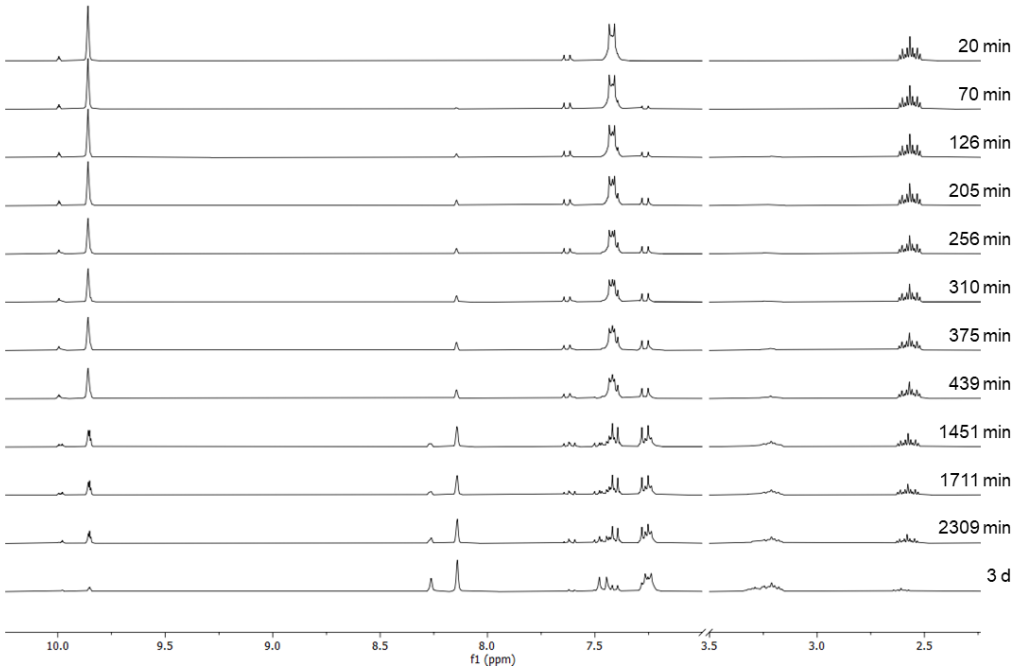

Figure S73: ^{1}H NMR spectra of the reaction of a *Z*-enriched solution of azobenzene **A** with cyclohexylamine (**C**), forming the mono-imine **AC** and following **AC²** (CD_2Cl_2, 300 MHz). As the solution is not continuously irradiated the corresponding *E*-compounds are also formed over time.

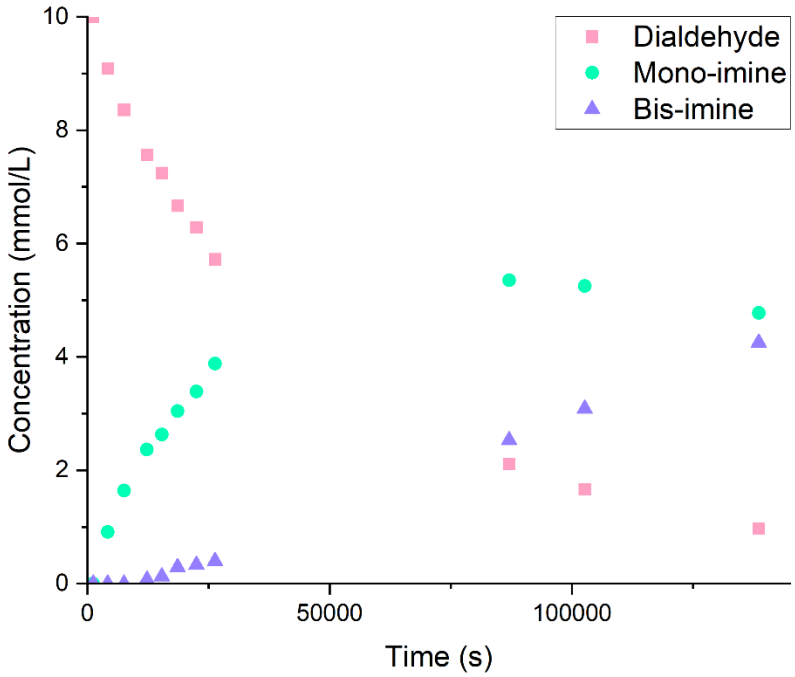

Figure S74: Observed concentrations of the dialdehyde **A** (pink), the mono-imine **AC** (turquoise) and the bis-imine **AC²** (blue) as determined from the $^{19}F\{^{1}H\}$ NMRs of the dark sample. As both isomers are formed over time the concentration of each compound refers to both isomers.

4.3.2 Experimental Details for 3.2.2

Syntheses

***E,E,E*-A^{3}D^3**

a) Evaluation of a reaction conditions

Reactions and work-up were carried out in the dark. A solution of diamine **D** (1.84 mg, 16.1 µmol, 1.00 eq.) in solvent **I** was added dropwise to a stirred suspension of **A** (5.00 mg, 16.1 µmol, 1.00 eq.) in solvent **II** at room temperature over a period of 30 minutes using a syringe pump. The resulting red solutions were stirred in the dark. After three and four days MALDI mass spectrometry measurements were conducted showing the formation of the targeted macrocycle. After 5 days solvent **III** (1 reaction volume) was added to each reaction mixture, before the solvent was evaporated under reduced pressure at 30 °C. The resulting red residues were examined by MALDI-mass spectrometry and ^{1}H and ^{19}F{^{1}H}-spectroscopy.

Table S21: Comparison of the reaction conditions with varying solvents I, II, III, solvent volumes V_I, and V_{II}, concentration of reactants after complete addition of the diamine *c*. Additionally a comment on the obtained product.

	I	**II**	**III**	V_I **/ mL**	V_{II} **/ mL**	***c*** **/ mM**	**comment**
#1	CH_2Cl_2	CH_2Cl_2	C_6H_{12}	1.1	0.5	10	oligomers, residues of **A**
#2	CH_2Cl_2	CH_2Cl_2	C_6H_{12}	2.2	1.0	5.1	oligomers, residues of **A**
#3	CH_2Cl_2	MeCN	$PhCH_3$	2.3	1.0	5.0	mainly **A**, oligomeric traces

b) Evaluation of work-up methods

The reaction and work-ups were carried out in the dark. A solution of diamine **D** (7.44 mg, 65.2 µmol, 1.00 eq.) in CH_2Cl_2 (8.0 mL) was added dropwise to a stirred suspension of azobenzene *E*-**A** (20.1 mg, 64.8 µmol, 1.00 eq.) in MeCN (3.5 mL) at room temperature over the course of 35 minutes *via* a syringe driver. After stirring the resulting red solution at room temperature for three days a sample of the reaction mixture was taken and a MALDI-MS measurement was conducted confirming the formation of the macrocycle. After a total of four days, two parts (2000 µL each) of the reaction solution were taken and diluted with either EtOH (2000 µL), or toluene (2000 µL). The solvents were removed under reduced pressure at 30 °C to yield red solids. These residues were examined by MALDI-mass spectrometry and ^{1}H and ^{19}F NMR spectroscopy.

The NMR-spectra of the crude products were comparable, but the MALDI-MS data of the crude product after work-up with toluene showed some traces of higher mass macrocycles, which are not present in the crude product after work-up with EtOH.

c) Optimised Synthesis

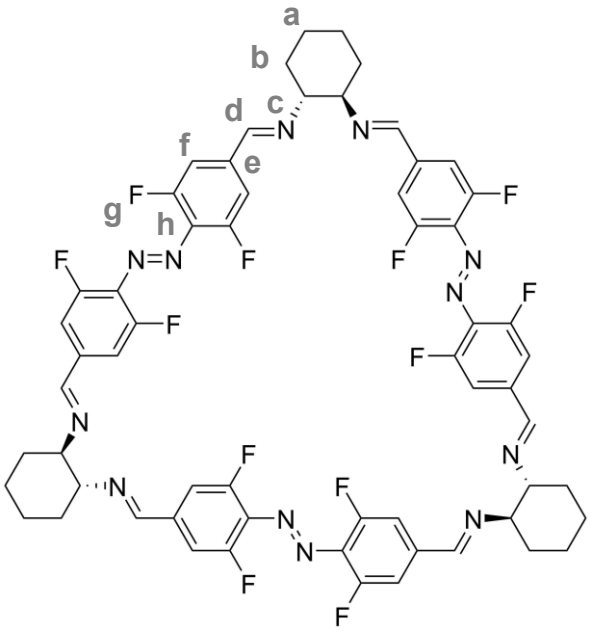

The reaction and work-up were carried out in the dark. A solution of diamine **D** (8.74 mg, 76.5 µmol, 1.20 eq.) in CH_2Cl_2 (8.0 mL) was added to a stirred red suspension of azobenzene *E*-**A** (19.8 mg, 63.8 µmol, 1.00 eq.) in MeCN (3.5 mL) at room temperature over a period of 30 minutes using a syringe pump. The resulting red solution was stirred at room temperature for three days. After the addition of EtOH (10 mL), the solution was evaporated at 30 °C to obtain a dark red powder. The solid was suspended in *n*-pentane (0.5 mL), and after the solid had settled, the supernatant pale orange solution was pipetted off. This procedure was repeated four times, then the residue was dried *in vacuo* to obtain *E*,*E*,*E*-$\mathbf{A^3D^3}$ (23.8 mg, 20.4 µmol, 96%) as a dark red powder. The NMR spectroscopic data indicated the presence of small traces of oligomeric residues or higher mass macrocycles, whereas the mass spectrum showed traces of $\mathbf{A^4D^4}$.

^{1}H NMR (600 MHz, $CDCl_3$, 298 K): δ [ppm] = 8.07 (s, 6H, H_d), 7.34 – 7.23 (m, 12H, H_f), 3.48 – 3.37 (m, 6H, H_c), 1.94 – 1.62 (set of m, 24H, H_{a-b}); **^{1}H NMR** (300 MHz, CD_2Cl_2, 298 K): δ [ppm] = 8.08 (s, 6H, H_d), 7.37 – 7.27 (m, 12H, H_f), 3.47 – 3.36 (m, 6H, H_c), 1.96 – 1.59 (set of m, 24H, H_{a-b}); **^{19}F{^{1}H} NMR** (282 MHz, $CDCl_3$, 298 K): δ [ppm] = -119.25 (s, 4F, F_g); **^{19}F{^{1}H} NMR** (282 MHz, CD_2Cl_2, 298 K): δ [ppm] = -120.37 (s, 4F, F_g); **^{19}F NMR** (564 MHz, CD_2Cl_2, 293 K): δ [ppm] = -120.35 (d, *J* = 10.3 Hz, 4F, F_g); **^{13}C{^{1}H} NMR** (151 MHz, $CDCl_3$, 298 K): δ [ppm] = 157.81 (s, C_d), 155.92 (dd, *J* = 263.2 Hz, *J* = 3.4 Hz, C_g), 139.61 (s, C_e), 132.60 (s, C_h), 111.88 (dd, *J* = 21.0 Hz, *J* = 3.6 Hz, C_f), 74.02 (s, C_c), 32.57 (s, C_b), 24.35 (s, C_a); **MS** HRMS (ESI) calcd. for $[C_{60}H_{48}N_{12}F_{12}+H]^+$: 1165.4006, meas.: 1165.4023; **IR** $\tilde{\nu}$ [cm^{-1}]: 2928 (m), 2859 (m),

1643 (s), 1622 (s), 1572 (s), 1433 (s), 1379 (w), 1344 (w), 1323 (w), 1302 (w), 1196 (m), 1146 (w), 1043 (s), 997 (m), 935 (m), 854 (s), 804 (w), 708 (w), 697 (w), 613 (m).

***E,E,E*-$\mathbf{A^3D^3}_{ss}$**

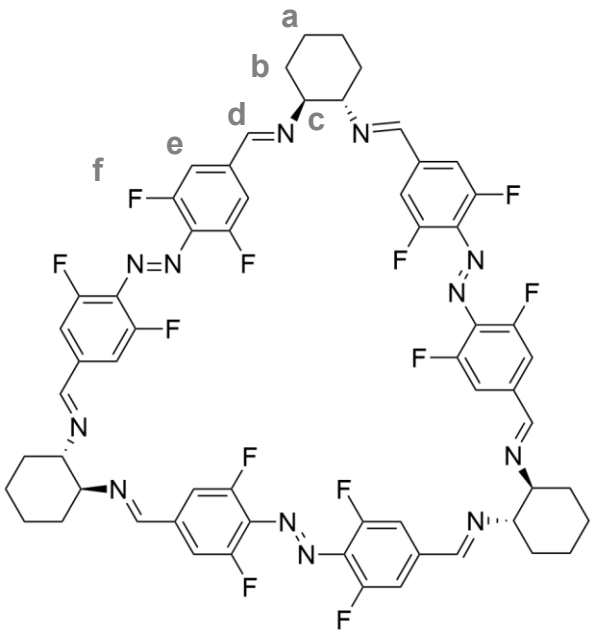

The reaction and work-up were carried out in the dark. A solution of diamine $\mathbf{D}_{ss}$ (5.43 mg, 39.6 µmol, 1.20 eq.) in CH_2Cl_2 (4.0 mL) was added to a stirred red suspension of azobenzene *E*-**A** (10.2 mg, 33.0 µmol, 1.00 eq.) in MeCN (2.0 mL) at room temperature over a period of 30 minutes using a syringe pump. The resulting red solution was stirred at room temperature for three days. After the addition of EtOH (5.0 mL), the solution was evaporated at 30 °C to obtain *E*,*E*,*E*-$\mathbf{A^3D^3}_{ss}$ (12.1 mg, 10.4 µmol, 94%) as a dark red powder. The NMR spectroscopic data indicated the presence of small traces of oligomeric residues or higher mass macrocycles, whereas the mass spectrum showed traces of $\mathbf{A^4D^4}$ and oligomeric residues.

^{1}H NMR (600 MHz, $CDCl_3$, 298 K): δ [ppm] = 8.07 (s, 6H, H_d), 7.34 – 7.23 (m, 12H, H_e), 3.50 – 3.35 (m, 6H, H_c), 1.94 – 1.62 (set of m, 24H, $H_{a\text{-}b}$); **^{19}F{^{1}H} NMR** (282 MHz, $CDCl_3$, 298 K): δ [ppm] = -119.26 (s, 4F, F_f); **MS** MALDI-ms calcd. for $[C_{60}H_{48}N_{12}F_{12}+H]^+$: 1165.401, meas.: 1165.334.

***E*,*E*,*E*-$\mathbf{A^3D^3_{red}}$**

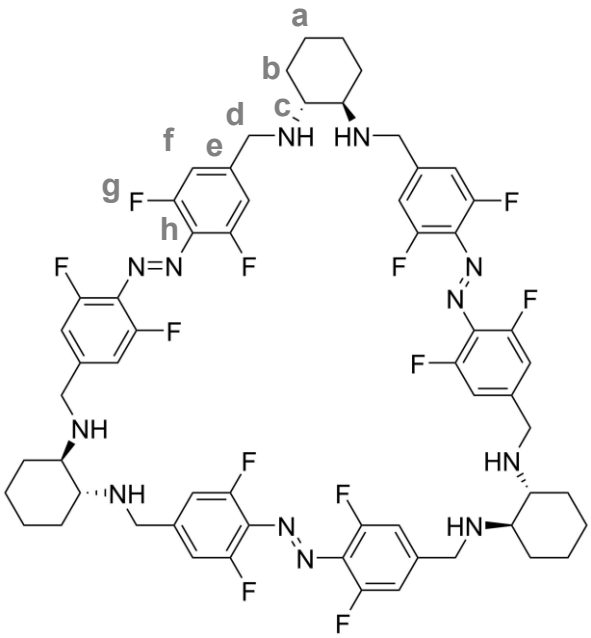

The reaction and work-up were carried out in the dark. $NaBH_4$ (16.1 mg, 425 µmol, 20.2 eq.) was added to a red solution of *E*,*E*,*E*-$\mathbf{A^3D^3}$ (24.5 mg, 21.0 µmol, 1.00 eq.) in a mixture of $CHCl_3$ (3.25 mL) and MeOH (3.25 mL) in one portion, resulting in a red suspension slowly evolving gas. After stirring at room temperature for three days, the mixture became an orange solution. The solvents were removed under reduced pressure, yielding an orange solid. This residue was suspended in saturated aqueous $NaHCO_3$ solution (3 mL) and $CHCl_3$ (3 mL) and stirred for approx. 30 minutes, whereupon a clear orange organic layer and a turbid aqueous layer precipitating colourless solid formed. After separation of the layers, the aqueous layer was extracted with $CHCl_3$ (3 x 3 mL). The combined organic layers were dried over $MgSO_4$, filtered and evaporated, yielding an orange solid. The solid was suspended in *n*-pentane (0.5 mL), and after the solid had settled, the supernatant pale orange solution was pipetted off. This procedure was repeated four times, then the residue was dried *in vacuo* to obtain *E*,*E*,*E*-$\mathbf{A^3D^3_{red}}$ (23.0 mg, 19.6 µmol, 93%) as an orange powder. NMR spectroscopic data indicated the presence of other macrocyclic residues in small traces, whereas the mass spectrum showed small traces of $\mathbf{A^2D^2_{red}}$.

^{1}H NMR (300 MHz, $CDCl_3$, 298 K) δ [ppm] = 7.09 – 6.97 (m, 12H, H_f), 4.00 – 3.63 (two m, 12H, H_d), 2.41 – 0.91 (set of m, 30H, $H_{a\text{-}c}$); **^{19}F{^{1}H} NMR** (282 MHz, $CDCl_3$, 298 K) δ [ppm] = -120.53 (s, F_g); **^{13}C{^{1}H} NMR** (75 MHz, $CDCl_3$, 298 K): δ [ppm] = 155.82 (dd, *J* = 261.5 Hz, *J* = 4.7 Hz, C_g), 146.34 (s, C_e), 130.48 (s, C_h), 111.73 (dd, *J* = 21.2, *J* = 2.6, C_f), 60.90 (s, C_c), 50.07 (s, C_d), 31.44 (s, C_b), 24.99 (s, C_a); **MS** HRMS (ESI) calcd. for $[C_{60}H_{60}N_{12}F_{12}+2H]^{2+}$: 589.2509, meas.: 589.2525; **IR** $\tilde{\nu}$ [cm^{-1}]: 2926 (m), 2855 (m), 1626 (s), 1574 (s), 1435 (s), 1312 (w), 1323

(w), 1225 (w), 1194 (w), 1126 (m), 1105 (m), 1074 (w), 1040 (s), 984 (m), 853 (s), 843 (s), 791 (w), 779 (w), 748 (m), 718 (w), 683 (w).

UV/VIS spectroscopy

Table S22: Concentrations of the different compounds and the respective irradiation wavelength for the different measurements

Compound	λ_{irr} / nm	c / µM
E,E,E-**A^{3}D^3**	405	5.92
	470	5.92
	565	3.45
	660	5.92
E,E,E-**A^{3}D$^3_{red}$**	405	6.03
	565	6.03
	660	6.03

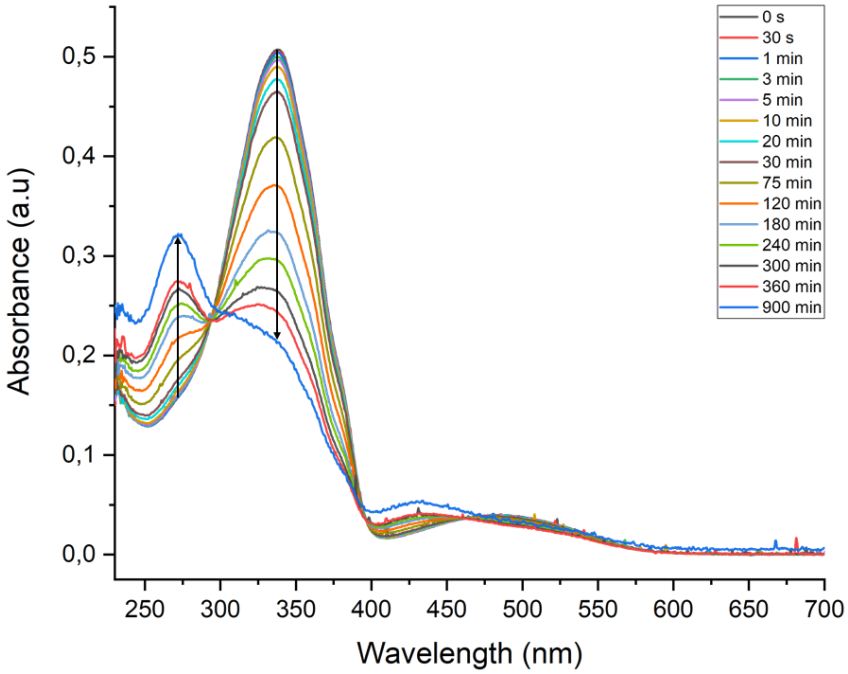

Figure S75: UV/VIS spectra of **A^{3}D^3** after irradiation with red light (660 nm) in CH_2Cl_2. Due to evaporation of the solvent while stirring overnight, the curve for 900 minutes is slightly shifted.

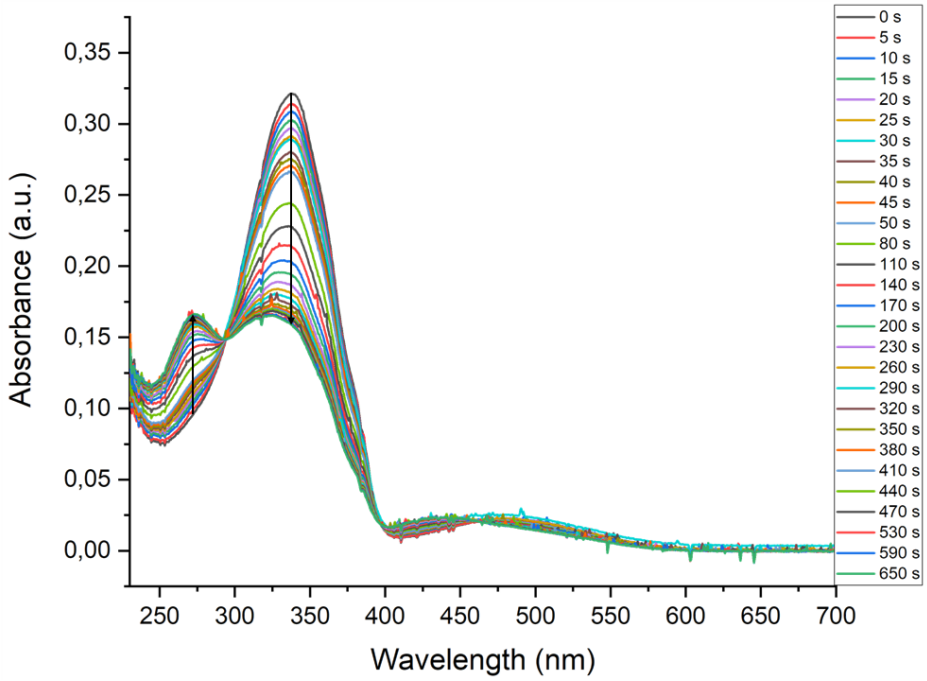

Figure S76: UV/VIS spectra of $\mathbf{A^3D^3}$ after irradiation with green light (565 nm) in CH_2Cl_2.

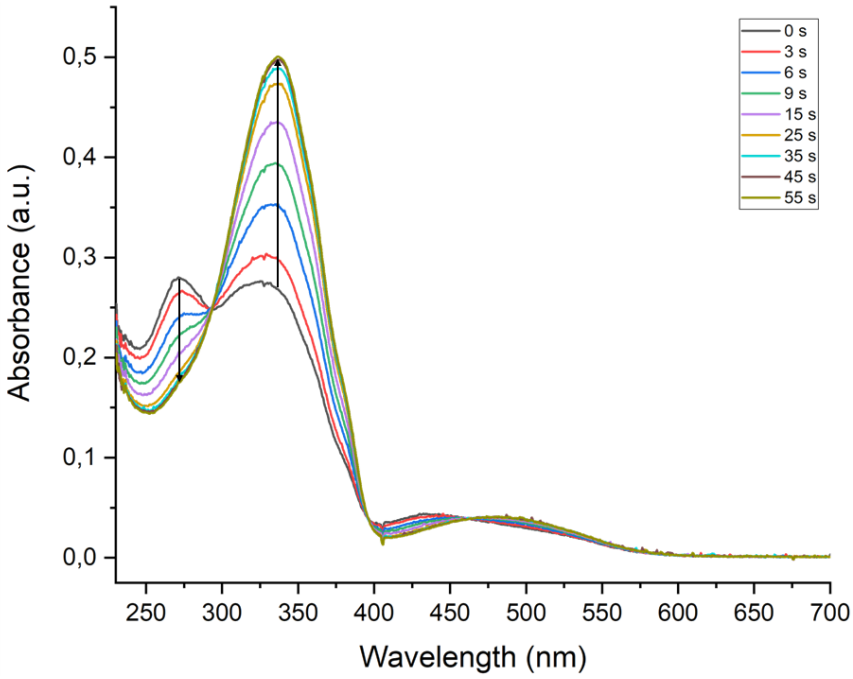

Figure S77: UV/VIS spectra of $\mathbf{A^3D^3}$. A solution that was *Z*-enriched by irradiation with green light was irradiated with light of the wavelength of 405 nm in CH_2Cl_2.

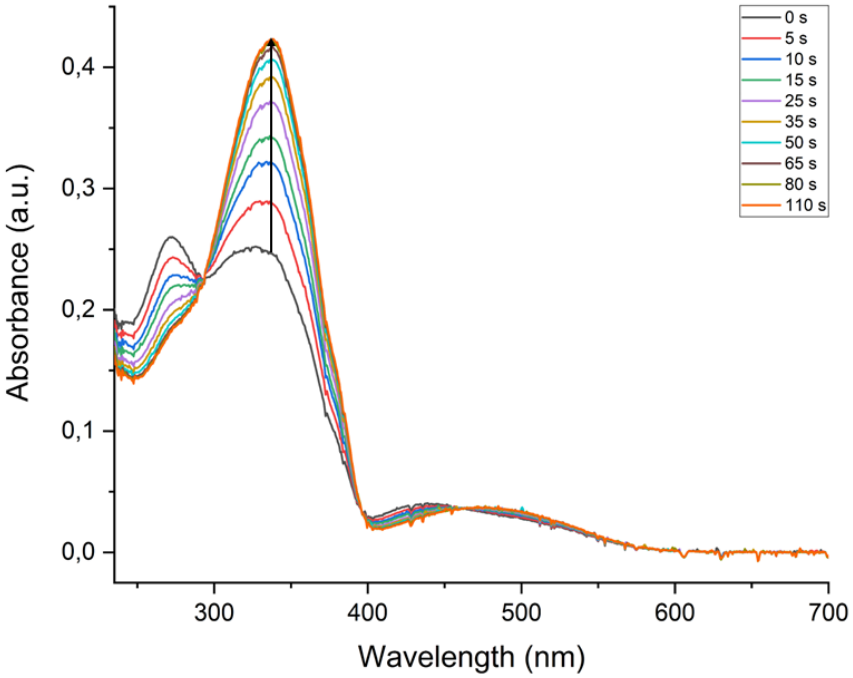

Figure S78: UV/VIS spectra of **A^{3}D^3**. A solution that was *Z*-enriched by irradiation with green light was irradiated with light of the wavelength of 470 nm in CH_2Cl_2.

The absorbance at 339 nm was plotted against the time and fitted to the following equation:

$$A(\lambda_{max}) = A_0 + k_0 * e^{-k*t_{irr}} \quad (3)$$

Table S23: Irradiation wavelength, and parameters obtained from fitting and R^2 values for the obtained curves.

Irradiation wavelength	k	R^2
660 nm (*E*→*Z*)	7.55 x 10^{-5}	0.99947
565 nm (*E*→*Z*)	7.75 x 10^{-3}	0.99968
405 nm (*Z* →*E*)	8.20 x10^{-2}	0.99407
470 nm (*Z* →*E*)	5.08 x10^{-2}	0.99905

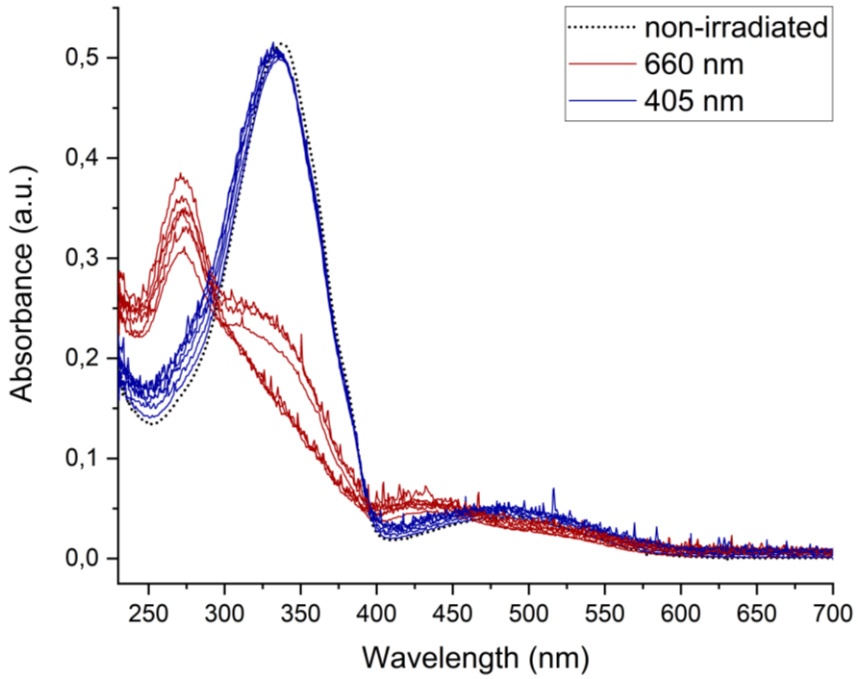

Figure S79: Absorption spectra of **A^{3}D^3** in CH_2Cl_2 after alternating irradiation with 660 nm (8-15 h) and 405 nm (5 min).

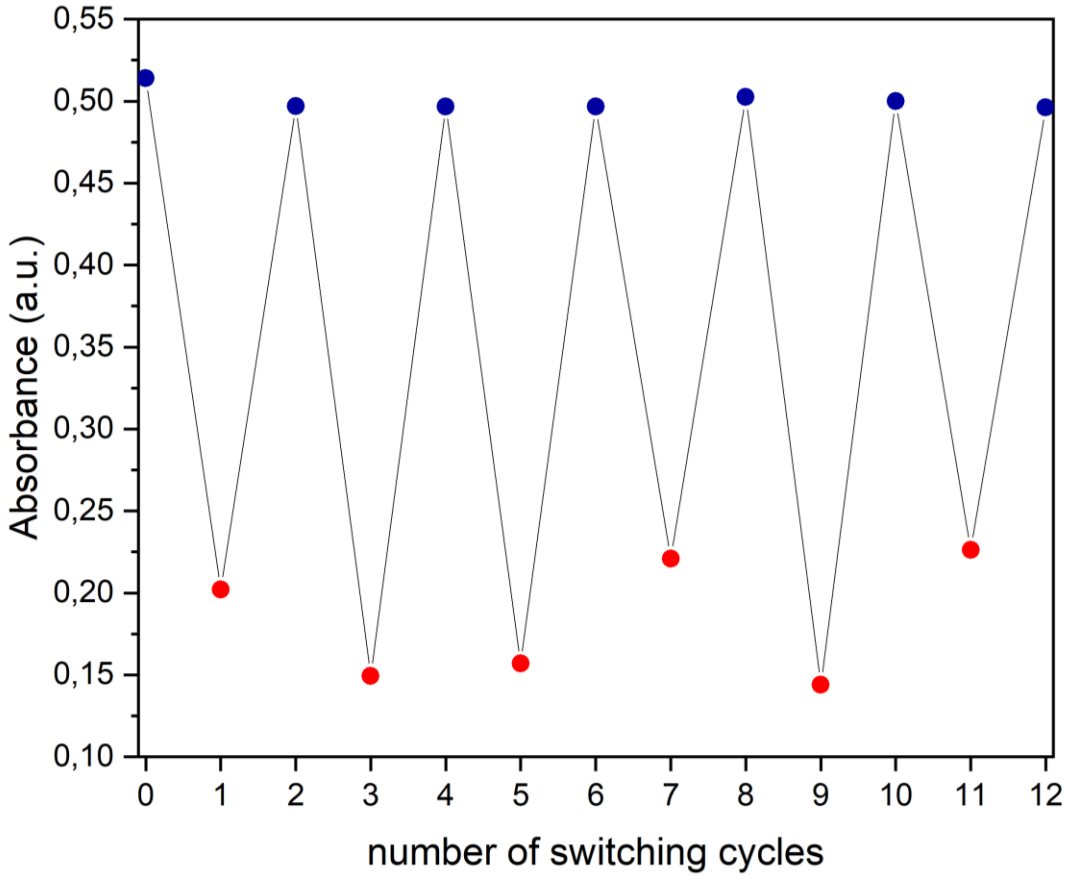

Figure S80: Absorbance at λ_{max} = 339 nm of **A^{3}D^3** in CH_2Cl_2 after alternating irradiation with 660 nm (8-15 h) and 405 nm (5 min). Incomplete *E* to *Z*-isomerisation after irradiation in some cycles is due to varying irradiation times as well as experimental inaccuracies such as the orientation of the sample to the light source.

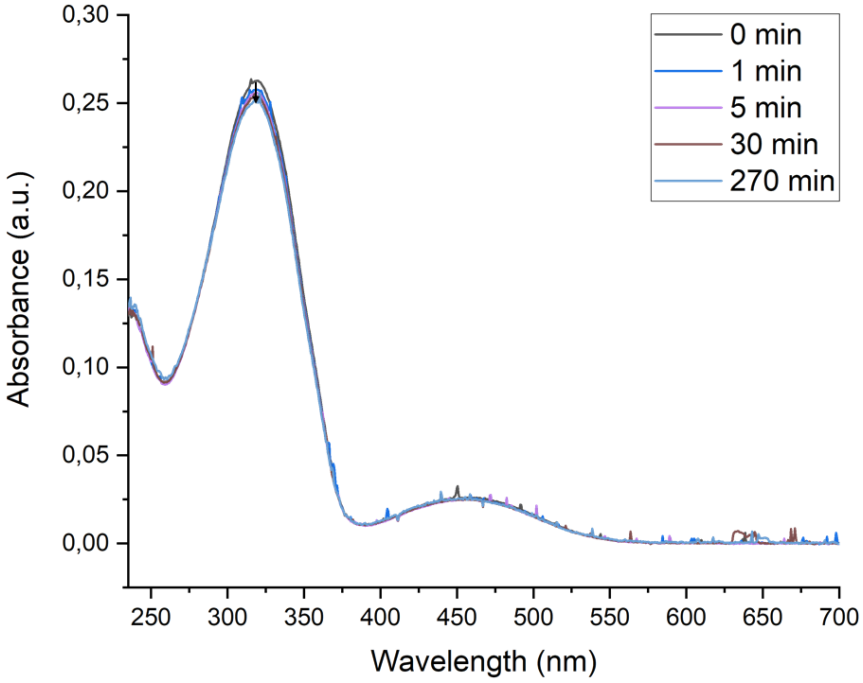

Figure S81: UV/VIS spectra of $\mathbf{A^3D^3_{red}}$ after irradiation with red light (660 nm) in CH_2Cl_2.

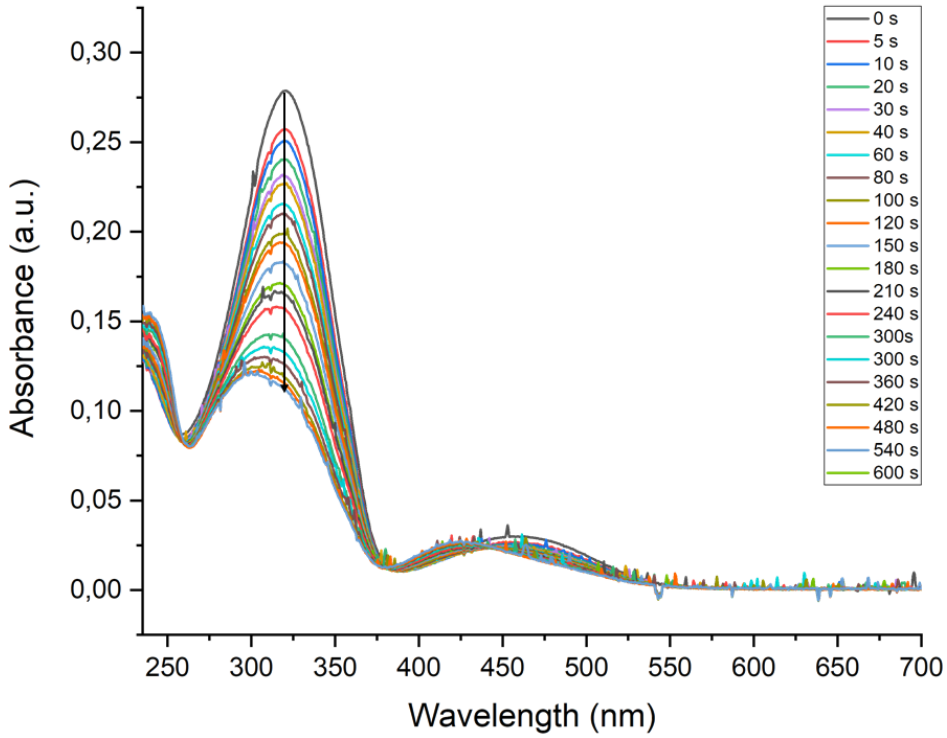

Figure S82: UV/VIS spectra of $\mathbf{A^3D^3_{red}}$ after irradiation with green light (565 nm) in CH_2Cl_2.

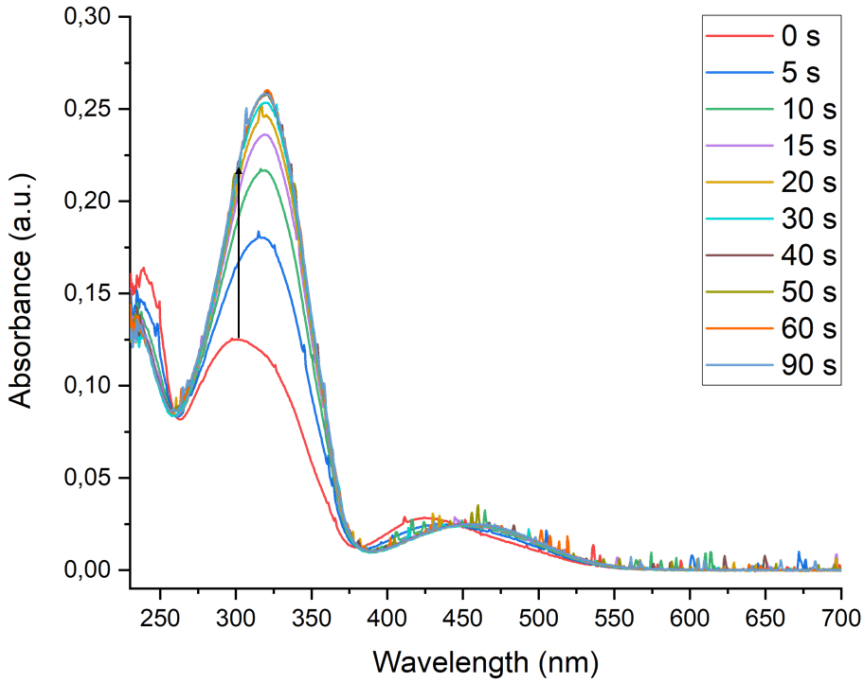

Figure S83: UV/VIS spectra of $\mathbf{A^3D^3_{red}}$. A solution that was *Z*-enriched by irradiation with green light, was irradiated with light of the wavelength of 405 nm in CH_2Cl_2.

Table S24: Comparison of the wavelengths of absorption maxima λ_{max} and molar attenuation coefficients ε of the macrocycles *E,E,E*-$\mathbf{A^3D^3}$, and *E,E,E*-$\mathbf{A^3D^3_{red}}$.

	E,E,E-$\mathbf{A^3D^3}$		*E,E,E*-$\mathbf{A^3D^3_{red}}$	
	π→π*	n→π*	π→π*	n→π*
λ_{max} / nm	339	495	322	461
ε / 10^3 L mol^{-1} cm^{-1}	86.8	7.52	45.4	4.65

Irradiation studies

In the following experiments, the volume of CD_2Cl_2 was adjusted to the initial volume after each reaction control to keep the reaction volume sufficiently high for NMR-analyses and to compensate for solvent losses due to evaporation. The entire reaction mixture was used for ^{1}H and ^{19}F{^{1}H} NMR analyses, while 50 µL aliquots of the reaction mixture were sampled for MALDI-MS measurements.

Assembly of $\mathbf{A^nD^n}$ macrocycles under irradiation

A solution of azobenzene *E*-**A** (2.0 mg, 6.5 µmol, 1.0 eq.) in CD_2Cl_2 (0.75 mL) was irradiated with red light (660 nm) until the ^{1}H NMR spectrum of the reaction mixture revealed *E*-**A** and *Z*-**A** in a molar ratio of approximately 13:87 (as integrated from ^{1}H NMR). A solution of diamine **D** (0.75 mg, 6.6 µmol, 1.0 eq.) in CD_2Cl_2 (0.40 mL) was added dropwise to the stirred solution of azobenzene **A** at room temperature over the course of approx. 40 min *via* a syringe pump.

The solution was continuously stirred at room temperature while being irradiated with red light (660 nm). During this reaction, controls *via* MALDI-MS, and ^{1}H and $^{19}F\{^{1}H\}$ NMR, were conducted at regular intervals. Since the NMR-, and MALDI-mass spectra showed no significant changes after a total irradiation time of 151 h, the solution was then continuously stirred in the dark and reaction controls were performed at regular intervals.

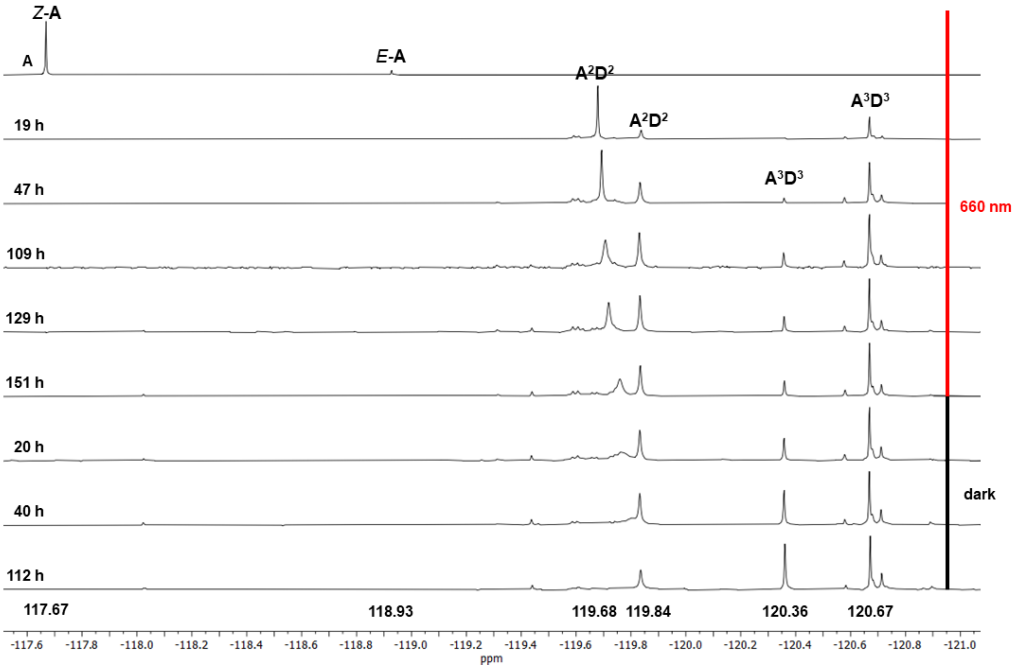

Figure S84: Comparison of $^{19}F\{^{1}H\}$ NMR spectra (CD_2Cl_2, 282 MHz) of the reaction between a *Z*-enriched solution of **A** and **D** under continuous irradiation with red light (660 nm) followed by a period in which the solution was allowed to stir in the dark.

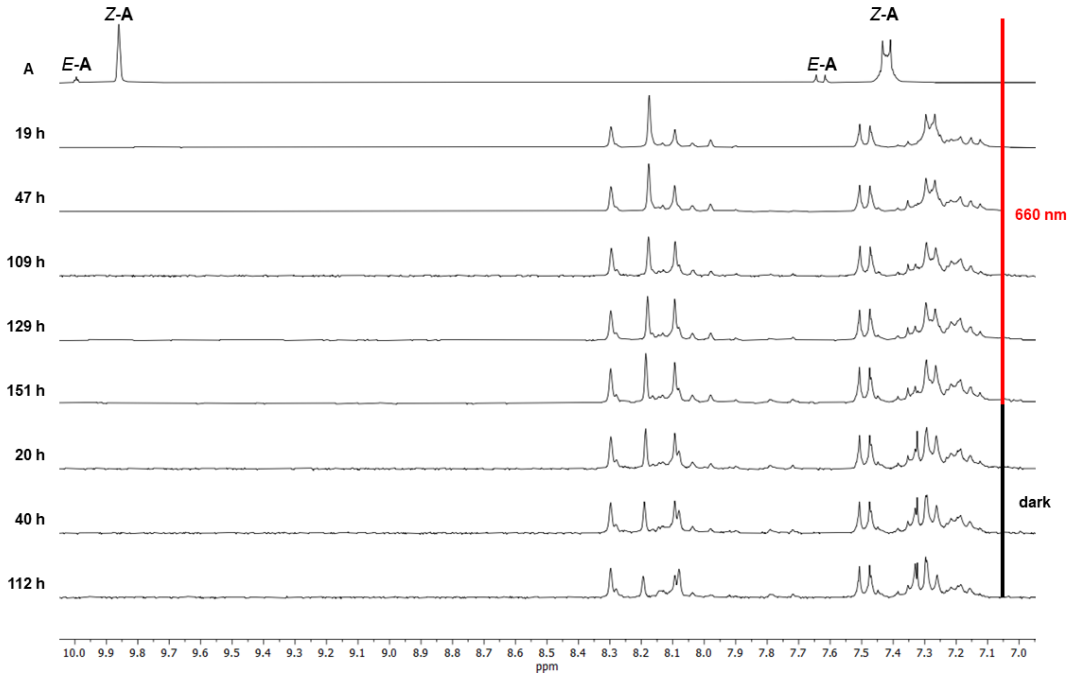

Figure S85: Comparison of ^{1}H NMR spectra (CD_2Cl_2, 300 MHz) of the reaction between a *Z*-enriched solution of **A** and **D** under continuous irradiation with red light (660 nm) followed by a period in which the solution was allowed to stir in the dark.

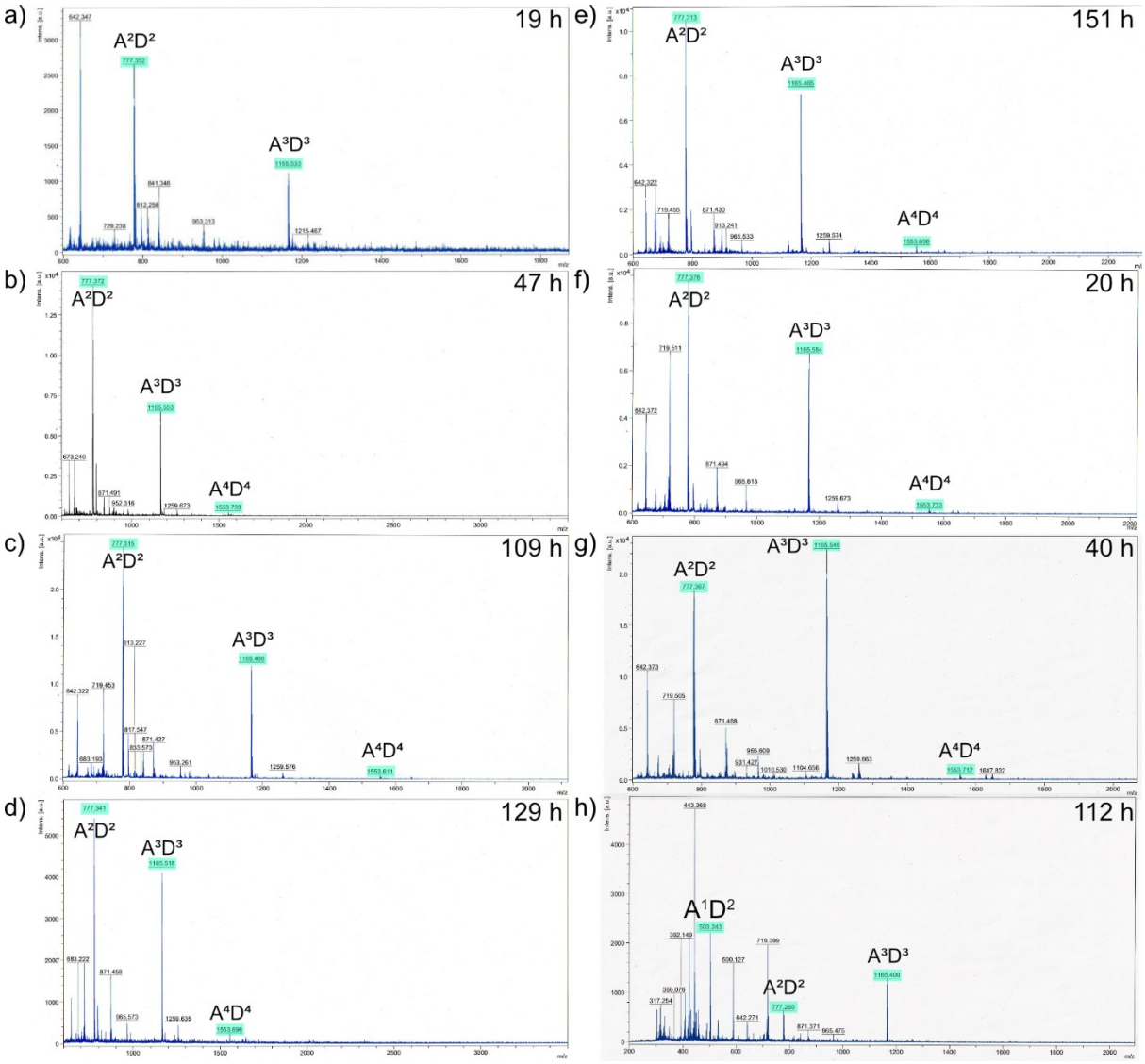

Figure S86: Comparison of MALDI-mass spectra of the formation of the reaction between a *Z*-enriched solution of **A** and **D** under continuous irradiation with red light (660 nm) (a-e) followed by a period in which the solution was allowed to stir in the dark (f-h). Peaks that can be attributed to $\mathbf{A^nD^n}$ compounds are highlighted in turquoise.

Isomerisation of $\mathbf{A^3D^3}$ under irradiation

A solution of *E,E,E*-$\mathbf{A^3D^3}$ (4.88 mg, 4.19 µmol) in CD_2Cl_2 (1.5 mL) was stirred at room temperature while being irradiated with 660 nm. During this reaction controls *via* MALDI-MS, and ^1H and $^{19}F\{^1H\}$ NMR, were conducted at regular intervals. Once the NMR spectra indicated a PSS, the solution was irradiated with light at a wavelength of 405 nm. Analyses were also performed after designated time intervals.

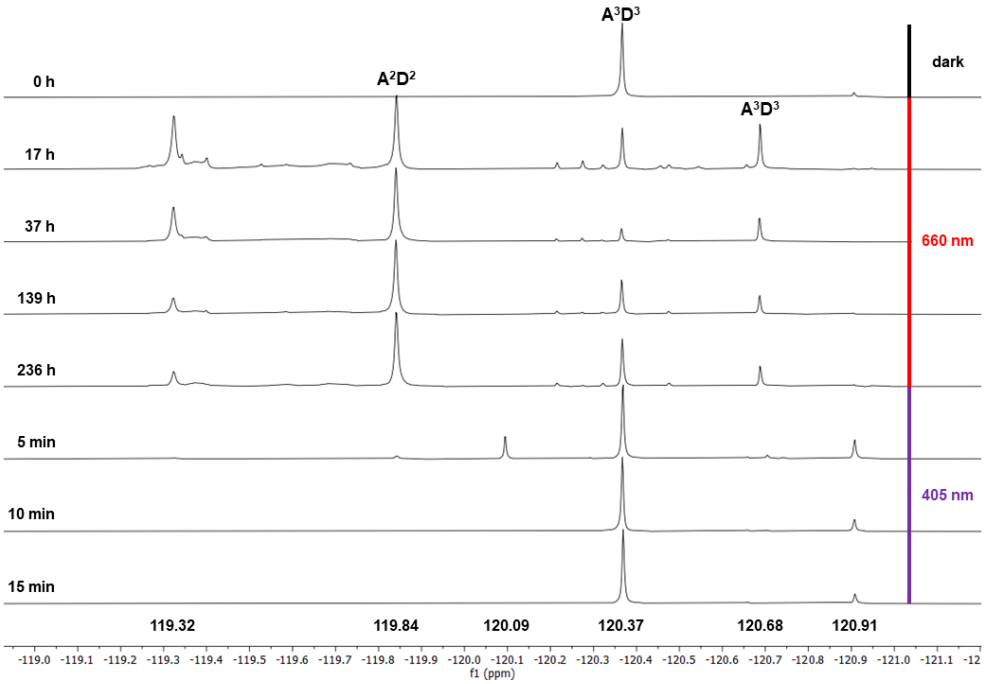

Figure S87: Comparison of $^{19}F\{^{1}H\}$ NMR spectra (CD_2Cl_2, 282 MHz) of **A^3D^3**, in the dark, after irradiation with red light (660 nm) followed by the irradiation with light at a wavelength of 405 nm for the indicated times, respectively.

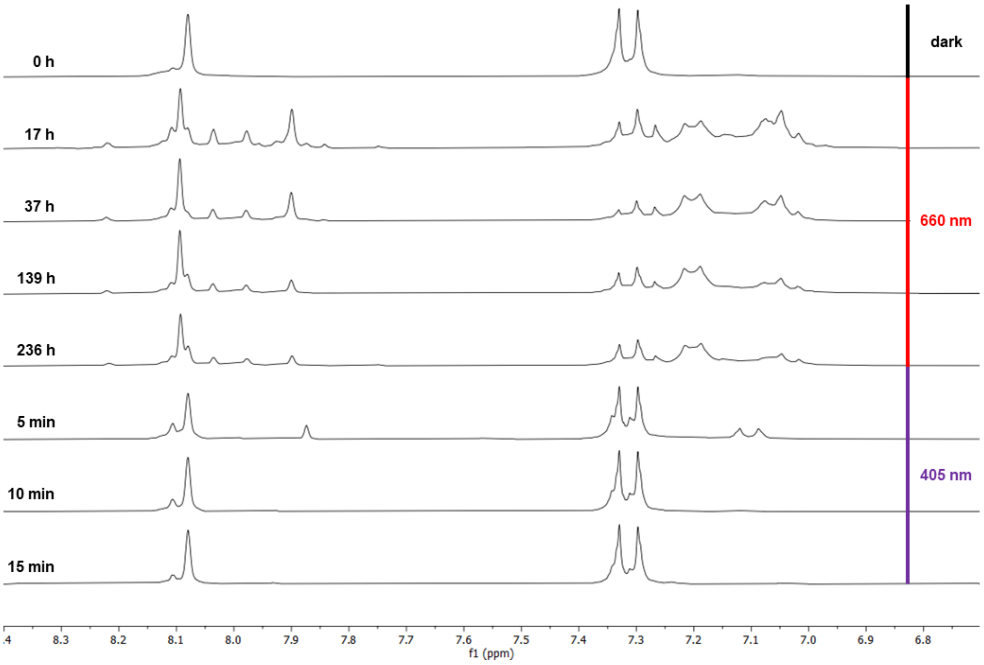

Figure S88: Comparison of ^{1}H NMR spectra (CD_2Cl_2, 300 MHz) of **A^3D^3**, in the dark, after irradiation with red light (660 nm) followed by the irradiation with light at a wavelength of 405 nm for the indicated times, respectively.

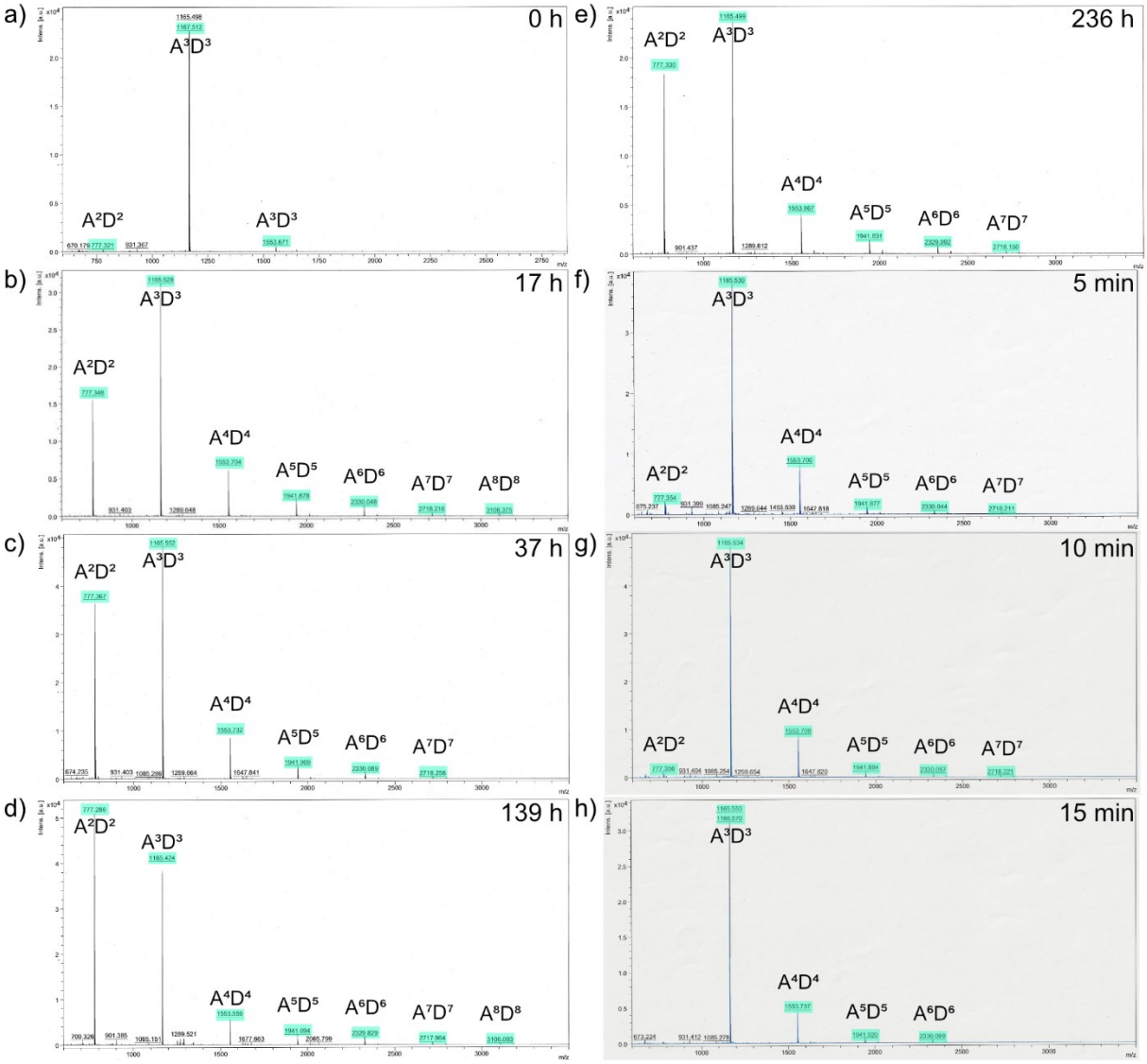

Figure S89: Comparison of MALDI spectra of the isomerisation of **A^{3}D^3** under continuous irradiation with red light (660 nm) (a-e) followed by the irradiation with light at a wavelength of 405 nm (f-h). Peaks that can be attributed to **A^{n}D^n** compounds, are highlighted in turquoise.

Assembly experiments using DPEN and mP

A stock solution of **A** in $CDCl_3$ was prepared and distributed into two parts. While one part was kept in the dark the other part was irradiated with red light (660 nm) until a percentage of 77% of *Z*-**A** was obtained. The different isomers were combined with a stock solution of either **DPEN** or **mP** in an aldehyde to amine ratio of 1 to 1.2. The resulting mixtures were diluted with $CDCl_3$ to a concentration of 5 mM in regard to **A**.

Table S25: Amount of starting materials employed in each reaction and reaction times.

Amine	Aldehyde	Reaction time
DPEN (1.3 mg, 6.0 µmol, 1.2 eq.)	*E*-**A** (1.6 mg, 5.0 µmol, 1.0 eq.)	3 days (dark), 3 days (660 nm)
	Z-***A*** (1.6 mg, 5.0 µmol, 1.0 eq.)	3 days
mP (0.82 mg, 6 µmol, 1.2 eq.)	*E*-**A** (1.6 mg, 5.0 µmol, 1.0 eq.)	3 days (dark), 3 days (660 nm)
	Z-***A*** (1.6 mg, 5.0 µmol, 1.0 eq.)	3 days

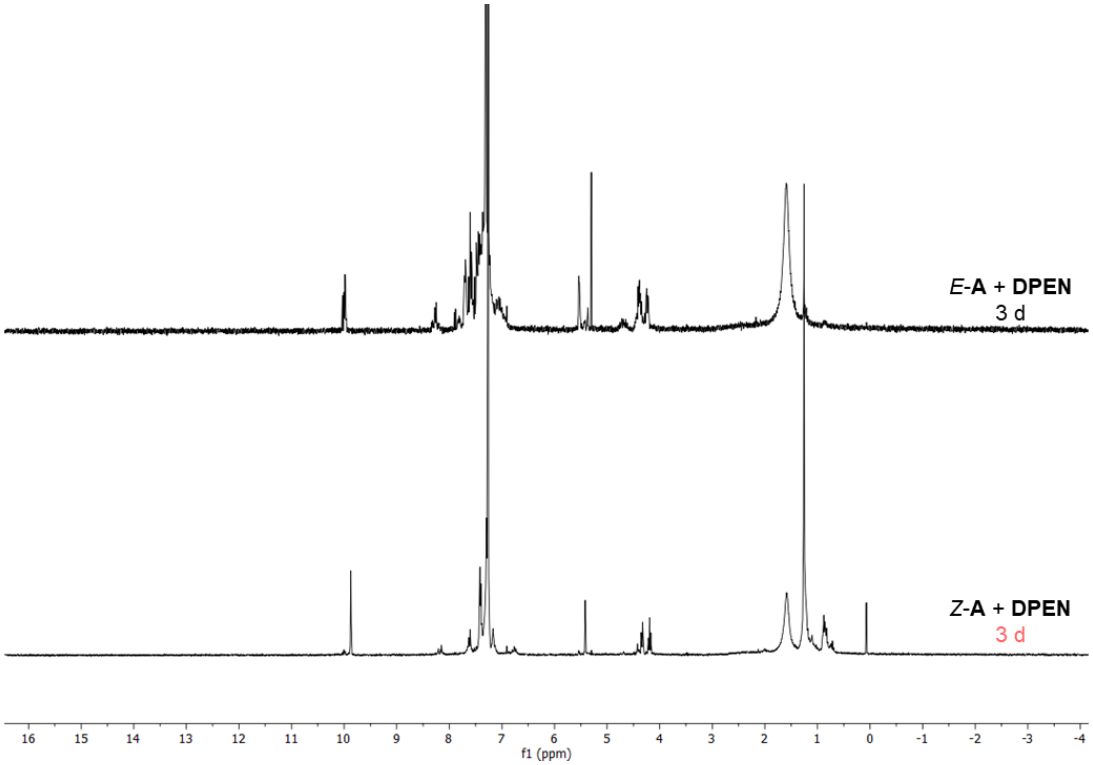

Figure S90: Comparison of ^{1}H NMR spectra ($CDCl_3$, 300 MHz) of *E*-**A** and **DPEN** in the dark, and of *Z*-**A** and **DPEN** after irradiation with red light.

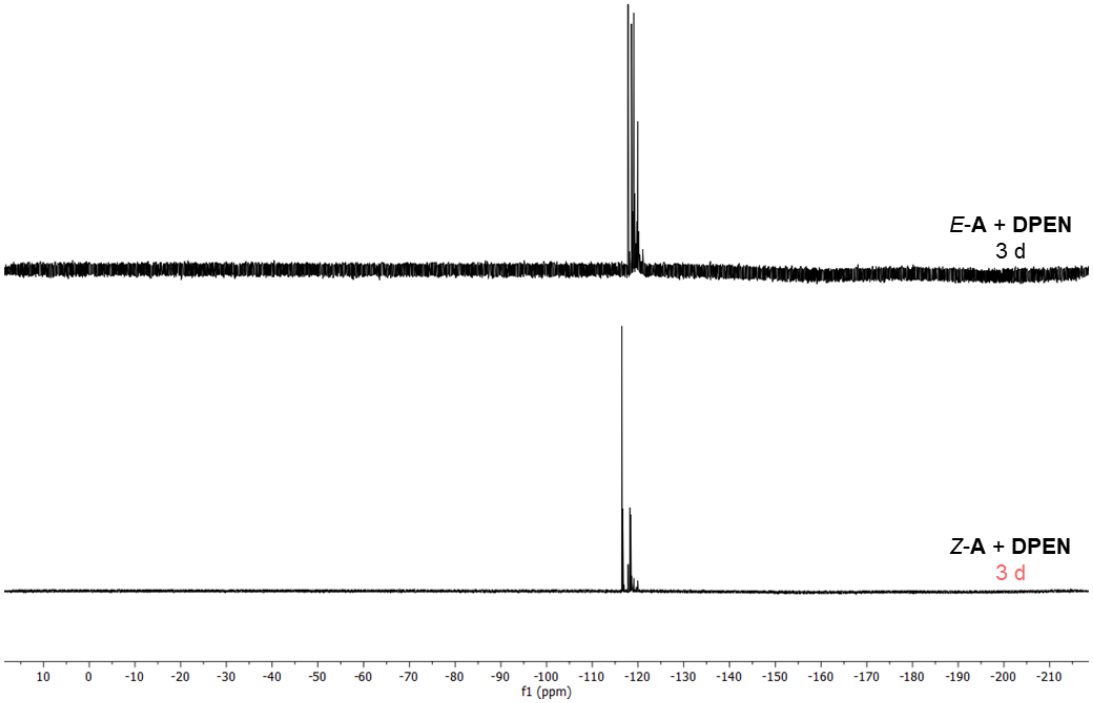

Figure S91: Comparison of $^{19}F\{^{1}H\}$ NMR spectra ($CDCl_3$, 282 MHz) of *E*-**A** and **DPEN** in the dark, and of *Z*-**A** and **DPEN** after irradiation with red light.

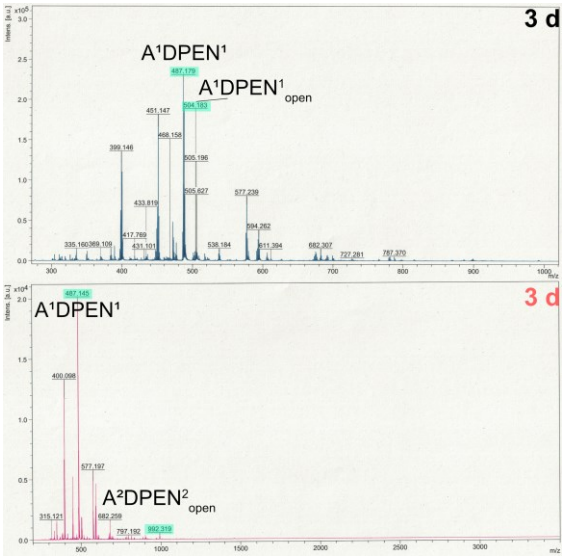

Figure S92: Comparison of MALDI-mass spectra of the reaction of *E*-**A** and **DPEN** in the dark, and of the reaction of *Z*-**A** and **DPEN** under continuous irradiation with red light. Peaks that can be attributed to **A^{n}DPEN^n** compounds are highlighted in turquoise.

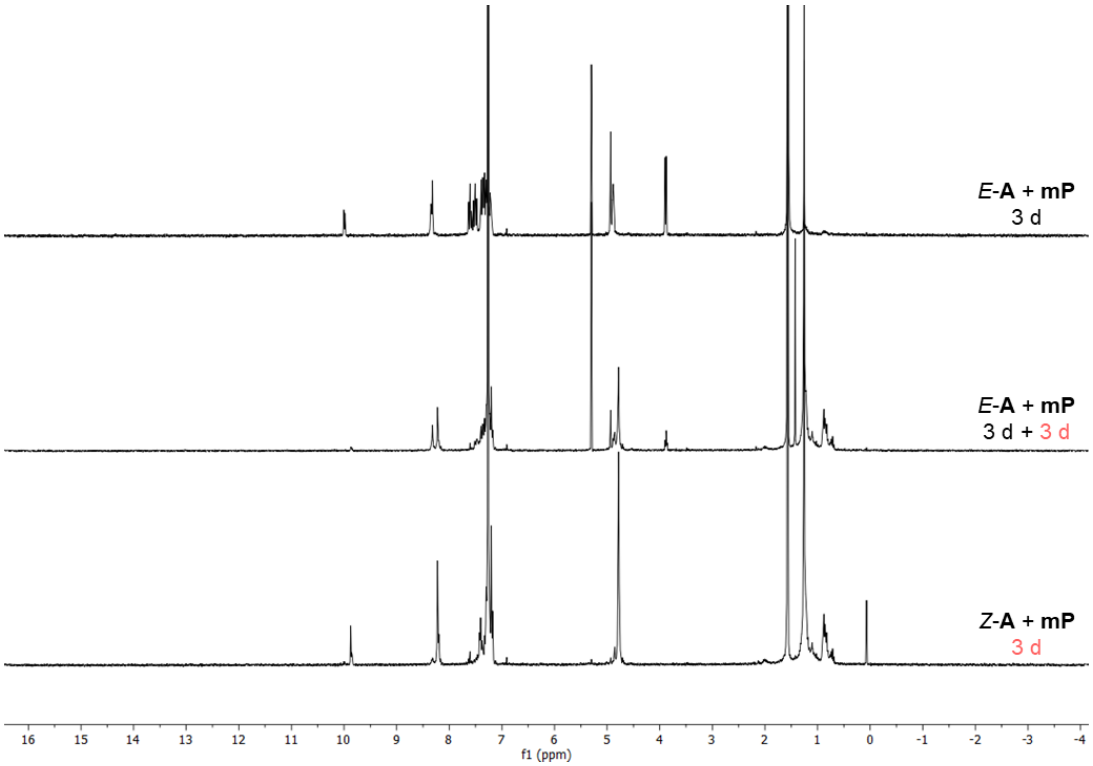

Figure S93: Comparison of ^{1}H NMR spectra ($CDCl_3$, 300 MHz) of *E*-**A** and **mP** in the dark, after irradiation with red light (660 nm), and of *Z*-**A** and **mP** after irradiation with red light.

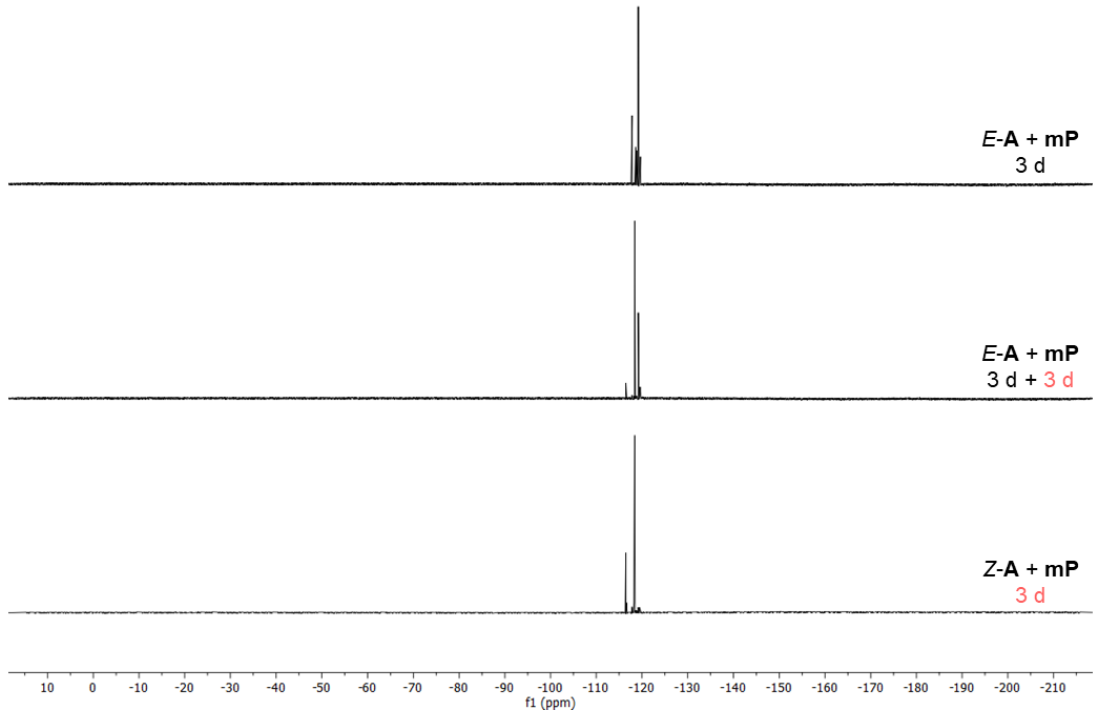

Figure S94: Comparison of $^{19}F\{^{1}H\}$ NMR spectra ($CDCl_3$, 282 MHz) of *E*-**A** and **mP** in the dark, after irradiation with red light (660 nm), and of *Z*-**A** and **mP** after irradiation with red light.

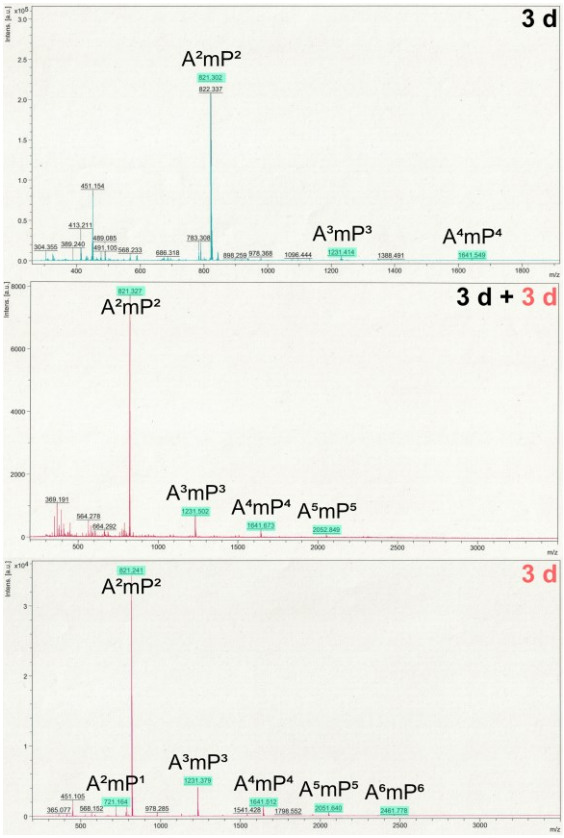

Figure S95: Comparison of MALDI-mass spectra of the reaction of *E*-**A** and **mP** in the dark and under irradiation with red light (660 nm) and of the reaction of *Z*-**A** and **mP** under continuous irradiation with red light. Peaks that can be attributed to **A^{n}mP^n** compounds are highlighted in turquoise.

DOSY measurements

The solvodynamic radii were estimated using the unmodified Stokes-Einstein-equation (equation (4)),[137] where D is the measured diffusion coefficient, $k_B = 1.381 \cdot 10^{-23}\ J \cdot \mathrm{K}^{-1}$ [138] is the Boltzmann constant, T is the absolute Temperature, $\eta_{CHCl_3}(298.15\ K) = 0.537 \cdot 10^{-3}\ Pa \cdot s$ [138], $\eta_{CH_2Cl_2}(293.15\ K) = 0.431 \cdot 10^{-3}\ Pa \cdot s$[138] and $\eta_{CH_2Cl_2}(298.15\ K) = 0.413 \cdot 10^{-3}\ Pa \cdot s$[138] are the viscosities of the solvent at temperature T, while r_s is the solvodynamic radius of the analyte.

$$D = \frac{k_B T}{6\pi\eta r_s} \tag{4}$$

^{1}H DOSY NMR

^{1}H DOSY NMR experiments were recorded on a Bruker Avance III 600 spectrometer at 25 °C. DOSY plots presenting the diffusion constants in F1 dimension have been prepared with MestReNova.

Sample preparation

A solution of **A**^{3}**D**^{3} in $CDCl_3$ was prepared in the dark and immediately measured to determine the diffusion coefficient. An additional sample was prepared by creating a saturated solution of **A** (8.35 mg, 26.9 µmol, 1.0 eq.) in CD_2Cl_2 (1.0 mL) that was stirred under red light (660 nm) until the PSS was reached as indicated by $^{19}F\{^{1}H\}$ NMR. A solution of diamine **D** (3.66 mg, 32.1 µmol, 1.2 eq.) in CD_2Cl_2 (0.4 mL) was added over the course of approx. 40 minutes. The mixture was stirred under continuous irradiation for 15 hours before a ^{1}H DOSY NMR spectrum was measured.

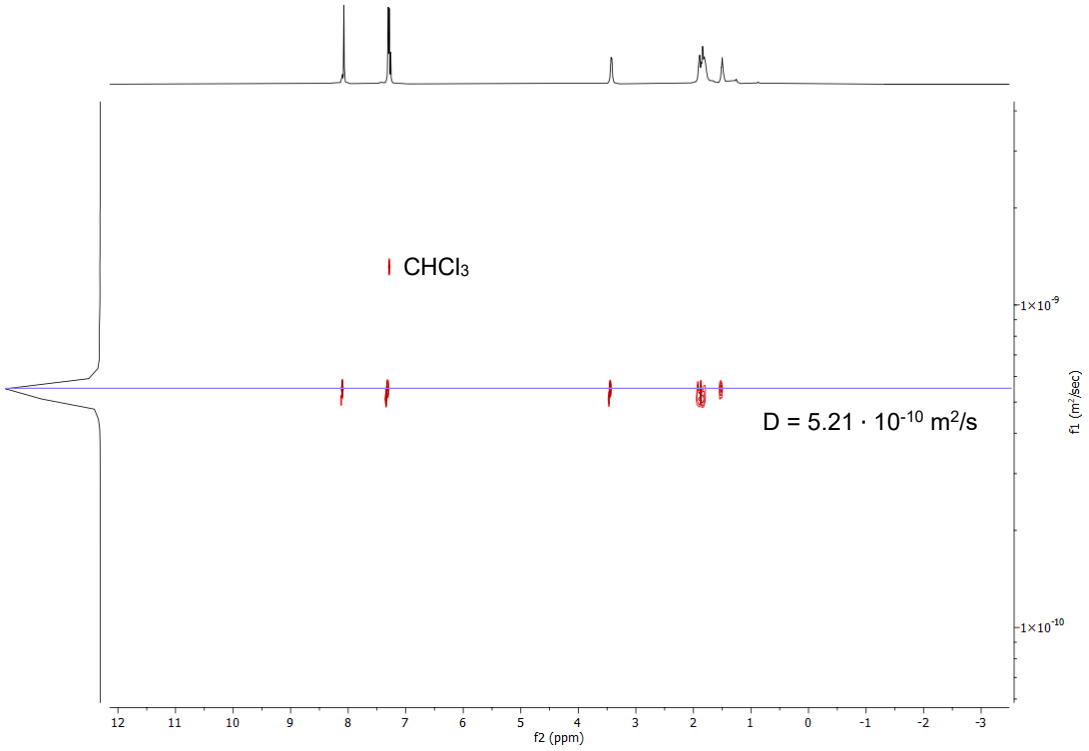

Figure S96: ^{1}H DOSY NMR spectrum of **A**^{3}**D**^{3} ($CDCl_3$, 600 MHz).

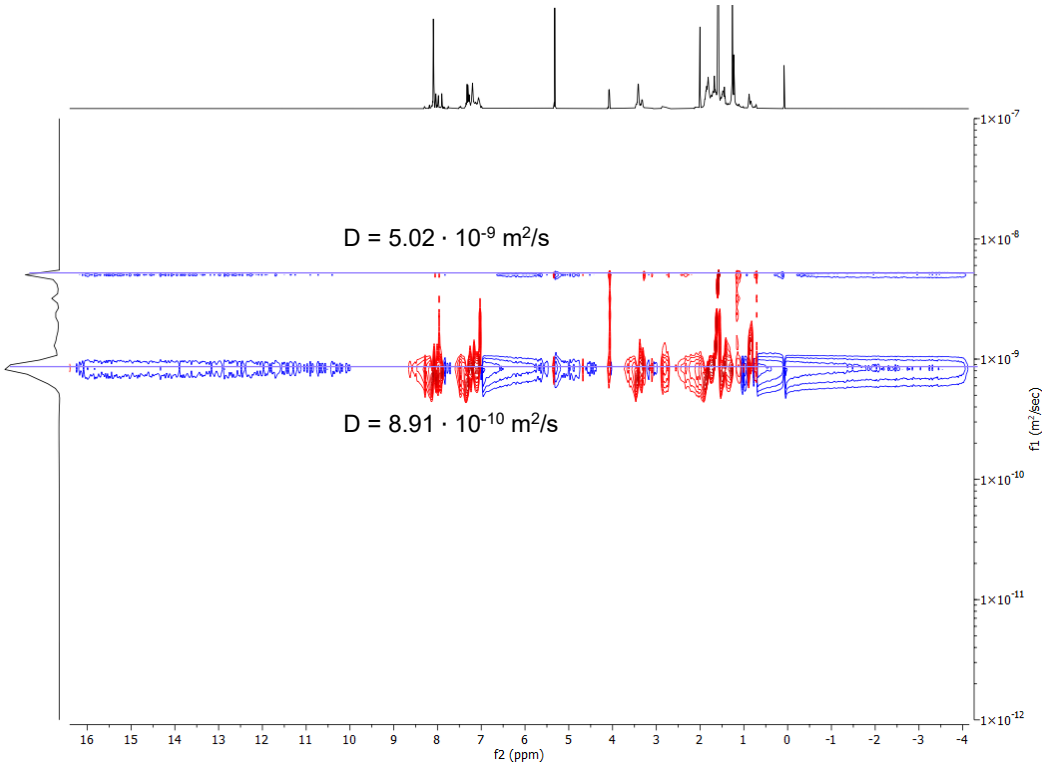

Figure S97: ^{1}H DOSY NMR spectrum of **A^{3}D^3** after irradiation with red light (660 nm) (CD_2Cl_2, 600 MHz).

Table S26: Measured diffusion coefficients and corresponding solvodynamic radii for a sample of **A^{3}D^3** that was kept in the dark and for a sample of the formation of **A^{3}D^3** under irradiation.

conditions	dark	660 nm	
compound	**A^{3}D^3**	**A^{3}D^3**	**A^{2}D^2**
Diffusion coefficient / m^2s^{-1}	$5.21 \cdot 10^{-10}$	$5.02 \cdot 10^{-10}$	$8.19 \cdot 10^{-10}$
Solvodynamic radius / Å	7.81	10.54	6.46

^{19}F DOSY NMR

^{19}F-diffusion NMR experiments have been performed on a BRUKER Avance *NEO* 600 FT NMR spectrometer, operating at a ^{1}H resonance frequency of 600.13 MHz. The instrument was equipped with a 5 mm BBO Prodigy cryoprobe exhibiting a *z*-gradient coil delivering a maximum gradient strength of 6.57 G mm^{-1} at 10 A. Diffusion data has been recorded using the *dstebpgp2s* pulse sequence delivered by the manufacturer. Diffusion coefficients have been corrected according to the diffusion coefficient of H_2O ($2.299 \cdot 10^{-9}$ m^2 s^{-1} at 298 K) reported in the literature.[139] The corresponding proportional factor $D_{H2O,lit.}/D_{H2O,est.}$ of 0.98 was determined on a sample of acetone-d_6 equipped with a capillary containing H_2O. The temperature unit of the instrument was calibrated according to the manual of the manufacturer of the instrument using the temperature dependence of the proton chemical shift difference of methanol. In order to obtain stable temperature conditions, the sample was kept within the magnet for at least one hour at the respective temperature prior to data collection. ^{19}F-diffusion data were recorded with 8k data points and a spectral width of 5556 Hz using a relaxation

delay of 10 s. The diffusion delay time (big Delta, Δ) was set to 80 ms. The gradient duration time (little delta, $\delta/2$) has been adjusted to values between 800 and 1000 μs. The gradient strength within the diffusion experiments was incremented linearly using 16 steps. The diffusion data have been analysed with the *T*1/*T*2 module which is part of the BRUKER TopSpin® software package. The standard deviation of the experimentally determined gradient strength dependent signal intensities to the fitted decay function was $\leq 5.2 \cdot 10^{-3}$. DOSY plots presenting uncorrected diffusion constants in the F1 dimension have been prepared with TopSpin. The solvodynamic radii have been calculated by the Stokes-Einstein equation (equation (4)) and the solvodynamic volume has been calculated by the equation for a spherical volume (equation (5)):

$$V_S = \frac{4}{3}\pi {r_s}^3 \quad (5)$$

Sample preparation of A^3D^3

A solution of $\mathbf{A^3D^3}$ in CD_2Cl_2 was prepared and distributed into 3 vials. The first sample was kept in the dark, while the other samples were irradiated with red light (660 nm) for 19 hours. One of those samples was then irradiated with light of the wavelength of 405 nm for 2 minutes.

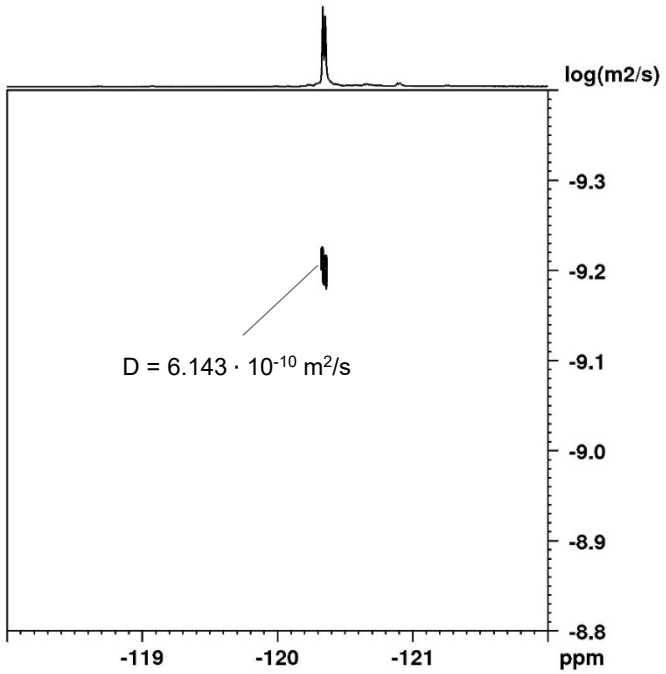

Figure S98: ^{19}F DOSY NMR spectrum of $\mathbf{A^3D^3}$ (CD_2Cl_2, 565 MHz) with uncorrected diffusion constants.

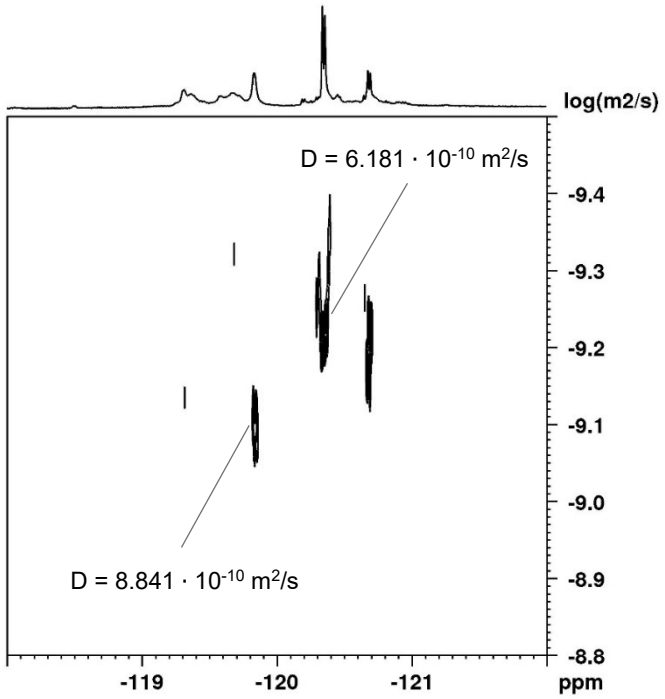

Figure S99: ^{19}F DOSY NMR spectrum of **A^{3}D^3** after irradiation with red light (660 nm) (CD_2Cl_2, 565 MHz).

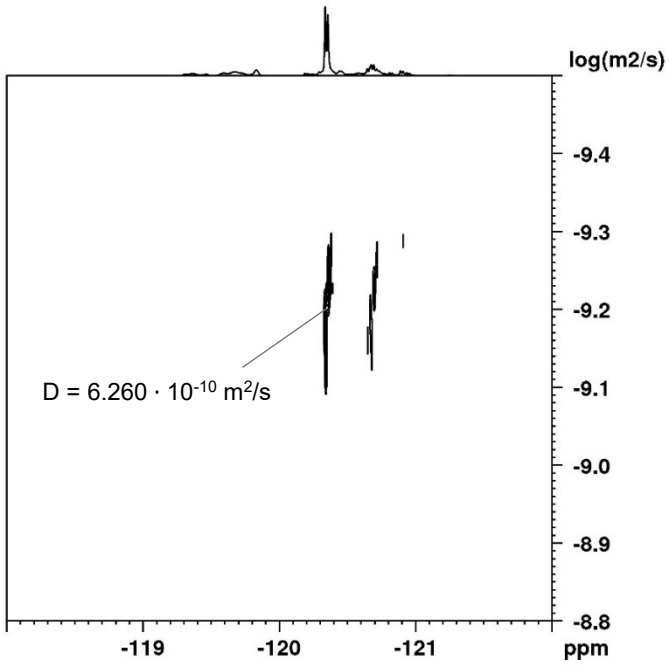

Figure S100: ^{19}F DOSY NMR spectrum of **A^{3}D^3** after irradiation with red light (660 nm) and light of the wavelength of 405 nm (CD_2Cl_2, 565 MHz).

Table S27: Integral range, uncorrected and corrected diffusion coefficient (D), solvodynamic radius (r_s) and solvodynamic volume (V_s) (both calculated based on the corrected diffusion coefficient) for the ^{19}F DOSY NMR spectra **A^3D^3** in the dark and after the irradiation with either red light (660 nm) or red light (660 nm) and with light of the wavelength of 405 nm.

	Integral range ppm	D $m^2\ s^{-1}$	$D_{corrected}$ $m^2\ s^{-1}$	r_s Å	V_s $Å^3$
dark	-120.3 – -120.4	$6.143 \cdot 10^{-10}$	$6.020 \cdot 10^{-10}$	8.29	2386.00
660 nm	-119.8 – -119.9	$8.841 \cdot 10^{-10}$	$8.664 \cdot 10^{-10}$	5.76	800.40
	-120.2 – -120.5	$6.181 \cdot 10^{-10}$	$6.057 \cdot 10^{-10}$	8.24	2342.26
660 nm+405 nm	-120.3 – -120.4	$6.260 \cdot 10^{-10}$	$6.130 \cdot 10^{-10}$	8.14	2555.78

Sample preparation of the formation of A^3D^3 under continuous irradiation

A solution of **A** in CD_2Cl_2 was prepared and distributed into 2 vials. Both solutions were irradiated with red light (660 nm) until the PSS was reached. A solution of DACH in CD_2Cl_2 was added over the course of 40 minutes, and the solution was continuously irradiated for either 19 h or 4 d before a ^{19}F DOSY NMR spectrum was measured.

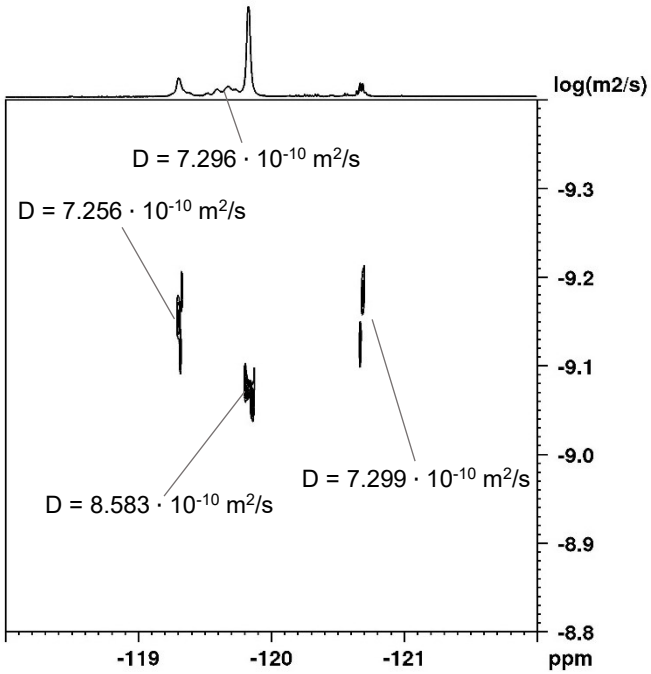

Figure S101: ^{19}F DOSY NMR spectrum of the formation **A^3D^3** under continuous irradiation with red light (660 nm) for 19 h (CD_2Cl_2, 565 MHz).

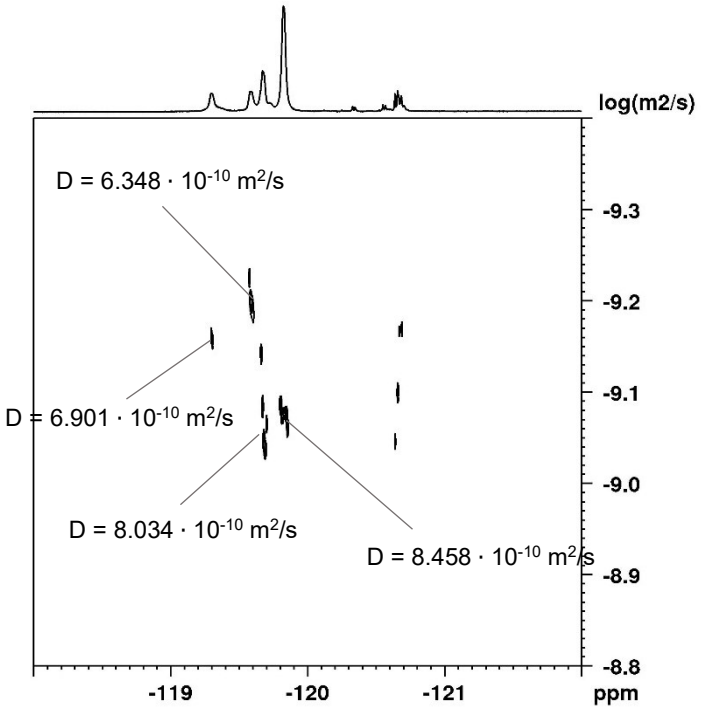

Figure S102: ^{19}F DOSY NMR spectrum of the formation **A^{3}D^3** under continuous irradiation with red light (660 nm) for 4 d (CD_2Cl_2, 565 MHz).

Table S28: Integral range, uncorrected and corrected diffusion coefficient (D), solvodynamic radius (r_s) and solvodynamic volume (both calculated based on the corrected diffusion coefficient) for the ^{19}F DOSY NMR spectra of the formation of **A^{3}D^3** under irradiation with red light (660 nm) after 19 h and 4 d.

	Integral range ppm	D $m^2\ s^{-1}$	$D_{corrected}$ $m^2\ s^{-1}$	r_s Å	V_s Å^3
19 h	-119.2 – -119.4	$7.256 \cdot 10^{-10}$	$7.111 \cdot 10^{-10}$	7.02	1447.84
	-119.5 – -119.8	$7.296 \cdot 10^{-10}$	$7.150 \cdot 10^{-10}$	6.98	1424.15
	-119.8 – -120.0	$8.583 \cdot 10^{-10}$	$8.411 \cdot 10^{-10}$	5.93	874.77
	-120.6 – -120.8	$7.299 \cdot 10^{-10}$	$7.153 \cdot 10^{-10}$	6.98	1422.40
4 d	-119.2 – -119.4	$6.901 \cdot 10^{-10}$	$6.763 \cdot 10^{-10}$	7.38	1682.96
	-119.5 – -119.6	$6.348 \cdot 10^{-10}$	$6.221 \cdot 10^{-10}$	8.02	2162.22
	-119.6 – -119.8	$8.034 \cdot 10^{-10}$	$7.873 \cdot 10^{-10}$	6.34	1066.63
	-119.8 – -119.9	$8.458 \cdot 10^{-10}$	$8.289 \cdot 10^{-10}$	6.02	914.13

4.3.3 Experimental Details for 3.2.3

Syntheses

***Z,Z*-A²E²**

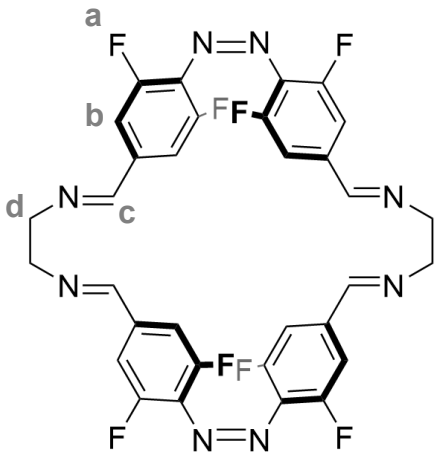

Method A

Dialdehyde **A** (40.3 mg, 130 µmol, 1.00 eq.) was dissolved in CH_2Cl_2 (15 mL) and irradiated with red light (660 nm) for 72 hours. A solution of diamine **E** (7.81 mg, 130 µmol, 1.00 eq.) in CH_2Cl_2 (8 mL) was added at room temperature in the dark over the course of 30 minutes *via* a syringe pump. After the addition was completed, the mixture was stirred for 15 hours at room temperature under continuous irradiation with red light (660 nm). The solution was layered under EtOH (45 mL) and kept in the fridge in the dark for one week, yielding red square-shaped crystals as well as some non-crystalline, red, presumably polymeric by-products. The crystals were carefully isolated and washed with EtOH and *n*-pentane before being dried at room temperature to obtain *Z,Z*-**A²E²** (21.5 mg, 32.1 µmol, 49%).

Method B

Dialdehyde **A** (10.1 mg, 32.5 µmol, 1.00 eq.) was dissolved in CH_2Cl_2 (3.25 mL) and irradiated with red light (660 nm) for 23 hours. A solution of diamine **E** (1.95 mg, 32.5 µmol, 1.00 eq.) in CH_2Cl_2 (3.25 mL) was added at room temperature in the dark over the course of 40 minutes *via* a syringe pump. After the addition was completed, the mixture was stirred for 19 hours at room temperature under continuous irradiation with red light (660 nm). EtOH (10 mL) was added, and the mixture was filtered before the solvent was removed under reduced pressure at rt. The dark red powder was washed with EtOH and *n*-pentane before being dried at room temperature to obtain *Z,Z*-**A²E²** (7.91 mg, 11.8 µmol, 73%).

^{1}H NMR (300 MHz, CD_2Cl_2, 298 K): δ [ppm] = 8.81 (s, 4H, H_c), 7.27 – 7.17 (m, 8H, H_b), 3.90 (s, 8H, H_d); **^{19}F{^{1}H} NMR** (300 MHz, CD_2Cl_2, 298 K): δ [ppm] = -119.49 (s, 8F, F_a); due to the low solubility of the compound and low stability in high concentrations, sufficient ^{13}C NMR data

could not be obtained; **MS** HRMS (ESI) calc. for $[C_{32}H_{21}N_8F_8]^+$: 669.1756, meas.: 669.1754; **IR** $\tilde{\nu}$ [cm^{-1}]: 1647 (m), 1618 (m), 1566 (s), 1504 (w), 1466 (w), 1425 (s), 1371 (m), 1337 (s), 1321 (s), 1294 (w), 1269 (w), 1192 (m), 1055 (w), 1034 (s), 995 (w), 961 (m), 901 (w), 889 (m), 874 (w), 860 (s), 851 (w), 739 (s), 702 (w), 687 (m), 668 (m), 646 (w), 629 (w), 615 (w).

***E*-A^{n}E^n**

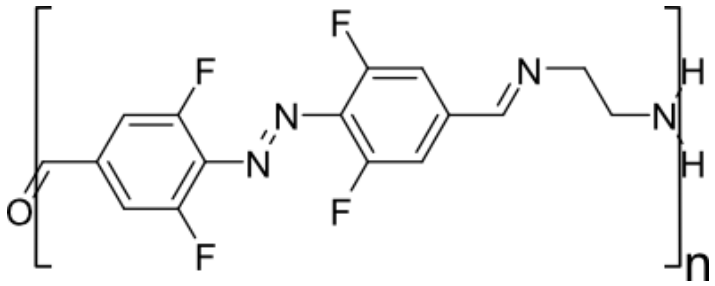

Azobenzene **A** (5.12 mg, 16.5 µmol, 1.00 eq.) was suspended in CH_2Cl_2 (0.5 mL). A solution of diamine **E** (0.991 mg, 16.5 µmol, 1.00 eq.) in CH_2Cl_2 (0.5 mL) was added over the course of 30 minutes *via* a syringe pump before the mixture was stirred in the dark. After 14 hours, the formation of a light red precipitate could be observed. After 3 days, the precipitate was filtered off and washed with CH_2Cl_2 and *n*-pentane before being dried under reduced pressure. The polymeric product was obtained as a light red solid (5.40 mg, 98%), which was insoluble in any solvent tested.

IR $\tilde{\nu}$ [cm^{-1}]: 1643 (m), 1620 (m), 1572 (s), 1435 (s), 1393 (w), 1371 (m), 1321 (w), 1225 (w), 1192 (m), 1173 (m), 1115 (m), 1047 (s), 995 (m), 962 (m), 860 (s), 629 (m).
Comparing those values to literature values for **A** the successful imine formation is confirmed as the former band at 1688 cm^{-1} shifts and significantly decreases in intensity.[72] Due to the insolubility of the compound no additional analytical data could be obtained.

General procedure for the attempted reduction of *Z,Z*-A^{2}Pr^2, *Z,Z*-A^{2}B^2 and *Z,Z*-A^{2}H^2

A solution of azobenzene **A** (10.3 mg, 33.3 µmol, 1.00 eq.) and the corresponding diamine in $CHCl_3$ (6 mL) was irradiated with red light (660 nm) for **5** days. MeOH (6 mL) and $NaBH_4$ were added, and the mixture was stirred for 18 hours. The solvent was removed under reduced pressure and saturated aqueous $NaHCO_3$ solution (5 mL) and $CHCl_3$ (5 mL) were added to the resulting solid and the mixture was stirred for approximately one hour. The layers were separated, and the aqueous phase was extracted with $CHCl_3$ (3 x 5 mL) until the organic phase stayed colourless. The combined organic layers were dried over $MgSO_4$ and concentrated under reduced pressure. Due to the low yields no purification was attempted. No percentages for the yields are given due to the fact that insoluble oligomeric and polymeric species are still present after work-up.

Table S29: Amount of starting materials used and corresponding yields of the different attempts to generate the amine macrocycles ***Z,Z*-A^{2}Pr$^2_{red}$, *Z,Z*-A^{2}B$^2_{red}$ and *Z,Z*-A^{2}H$^2_{red}$**. Calculations of yields and percentages are based on the assumption that the product contains only the reduced imine macrocycle, however as the solid is not completely soluble oligomeric and polymeric species are still present after work-up and NMR analysis shows the formation of by-products.

	amine	reducing agent	yield
***Z,Z*-A^{2}Pr$^2_{red}$**	2.47 mg, 33.3 µmol, 1.00 eq.	8.48 mg, 222 µmol, 6.73 eq. 12.9 mg, 340 µmol, 10.20 eq.	6.07 mg, 8.61 µmol, 52% 3.50 mg, 4.97 µmol, 30%
***Z,Z*-A^{2}B$^2_{red}$**	3.35 µL, 33.3 µmol, 1.00 eq.	8.48 mg, 222 µmol, 6.73 eq. 12.9 mg, 340 µmol, 10.20 eq.	4.21 mg, 5.74 µmol, 34% 2.25 mg, 3.07 µmol, 18%
***Z,Z*-A^{2}H$^2_{red}$**	3.87 mg, 33. 3 µmol, 1.00 eq.	8.48 mg, 222 µmol, 6.73 eq. 12.9 mg, 340 µmol, 10.20 eq.	3.82 mg, 4.84 µmol, 28% 12.5 mg, 47.6 µmol, 94%

Dietyhlene glycol ditosylate (43)

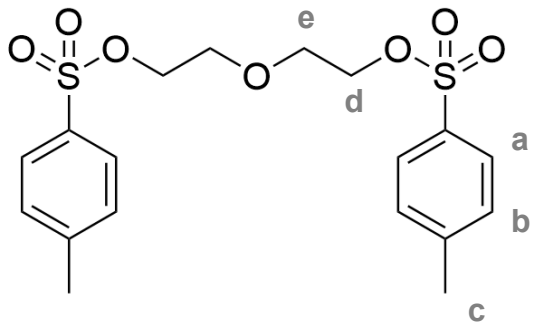

To a solution of diethylene glycol (5.7 mL, 60 mmol, 1.00 eq.) in CH_2Cl_2 (80 mL) were added tosyl chloride (34 g, 180 mmol, 3.00 eq.) and triethylamine (17 ml, 120 mmol, 2.00 eq.). The mixture turned green upon addition and while stirring the colour changed to black. The mixture was stirred for 19 hours at room temperature during which the reaction turned brown. Water (100 mL) was added, and the layers were separated. The aqueous phase was extracted with EtOAc (2 x 50 mL) and the combined organic layers were dried over Na_2SO_4. The solvent was removed under reduced pressure and the crude product was purified by column chromatography using CyHex and EtOAc (3:1). **43** (20 g, 49 mmol, 82%) was isolated as off white crystals.

^{1}H NMR (300 MHz, $CDCl_3$, 298 K): δ [ppm] = 7.80 – 7.76 (m, 4H, H_a), 7.37 – 7.32 (m, 4H, H_b), 4.11 – 4.08 (m, 4H, H_e), 3.62 – 3.59 (m, 4H, H_d), 2.45 (s, 6H, H_c).
The spectra are in accordance with literature.[110]

Dietyhlene glycol bisazide (44)

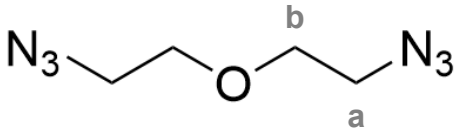

Tosylate **43** (20.35 g, 49.10 mmol, 1.00 eq.) was dissolved in DMF (164 mL) and NaN_3 (7.980 g, 122.8 mmol, 2.50 eq.) was added in small portions. The mixture was stirred for 62 hours during which a colourless solid precipitated. Water (200 ml) was added redissolving the solid and the mixture was extracted with EtOAc (2 x 200 ml). The combined organic layers were dried over Na_2SO_4 and the solvent was removed under reduced pressure. Column chromatography using CyHex:EtOAc yielded **44** (7.200 g, 46.11 mmol, 94%) as a light yellow oil.

^{1}H NMR (300 MHz, $CDCl_3$, 298 K): δ [ppm] = 3.70 – 3.66 (m, 4H, H_b), 3.42 – 3.39 (m, 4H, H_a).
The spectra are in accordance with literature.[110]

Dietyhlene glycol bisamine (O)

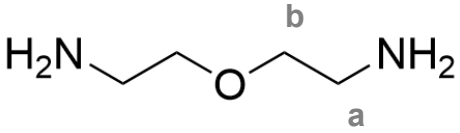

Azide **44** (2.03 g, 13.0 mmol, 1.00 eq.) was dissolved in MeOH (25 mL) and 10wt% Pd/C (138 mg, 0.130 mmol, 10 mol%). The mixture was stirred under an H_2-atmosphere for 24 hours. The precipitate was filtered off and the solvent was removed under reduced pressure. As the NMR indicated incomplete conversion the crude product was redissolved in EtOH (70 mL). 10wt% Pd/C (138 mg, 0.130 mmol, 10 mol%) was again added and the mixture was stirred under an H_2-atmosphere for 3 days. The suspension was filtered and concentrated under reduced pressure yielding diamine **O** (1.14, 11.0 mmol, 85%) as a light yellow oil. The obtained product was stored at -20 °C under an N_2-atmosphere.

^{1}H NMR (300 MHz, CD_3OD, 298 K): δ [ppm] = 3.59 (t, 4H, H_b), 2.95 (s, 4H, H_a).
The spectra are in accordance with literature.[110]

E,E-**A²O²**

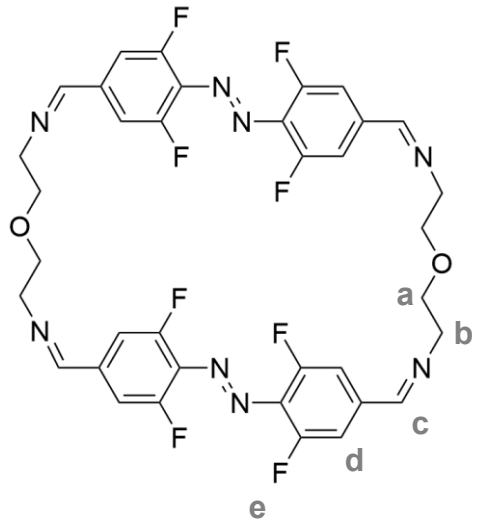

Azobenzene **A** (31.0 mg, 100 µmol, 1.00 eq.) was suspended in CH_2Cl_2 (5 mL) and a solution of **O** (12.0 mg, 120 µmol, 1.20 eq.) in EtOH (5 mL) was added in one portion. After 5 days the precipitate that had formed was collected by filtration and dried under reduced pressure. The crude product was recrystallised by vapor diffusion of Et_2O into a mixture of CH_2Cl_2 and EtOH yielding *E,E*-**A²O²** (8.40 mg, 11.1 µmol, 22%) as dark red crystals.

^{1}H NMR (300 MHz, $CDCl_3$, 298 K): δ [ppm] = 8.04 (s, 4H, H_c), 7.14 – 7.11 (m, 8H, H_d), 3.79 (s, 16H, H_{a-b}); **^{19}F{^{1}H} NMR** (282 MHz, $CDCl_3$, 298 K): δ [ppm] = -119.99 (s, 4F, F_d); due to the low solubility of the compound and low stability in high concentrations, sufficient ^{13}C NMR data could not be obtained; **MS** HRMS (ESI) calc. for $[C_{36}H_{29}N_8F_8O_2]^+$: 757.2280, meas.: 757.2277; calc. for $[C_{36}H_{29}N_8F_8O_2]^{2+}$: 379.1177, meas.: 379.1176; **IR** $\tilde{\nu}$ [cm^{-1}]: 3082 (w), 2935 (w), 2922 (m), 2852 (m), 2803 (w), 1705 (m), 1647 (m), 1618 (m), 1570 (s), 1543 (s), 1375 (m), 1325 (m), 1196 (m), 1118 (m), 1042 (s), 924 (m), 858 (s), 795 (w), 748 (w), 696 (w), 633 (m).

UV/VIS spectroscopy

UV/VIS spectroscopy was performed on a Cary 60 equipped with a Peltier thermostatted cell holder. Quartz cuvettes (d = 10 mm) and solvents of spectrophotometric grade were used. Irradiation times were determined using a stopwatch. UV vis spectra were recorded at 25 °C unless otherwise stated. The concentrations of the measured samples are listed in table S30.

Table S30: Concentrations of the different compounds and the respective irradiation wavelength for the different measurements.

Compound	λ_{irr} / nm	c / µM
Z,Z-**A²E²**	405	6.98
	470	6.98
	565	6.98
	660	6.98
E,E-**A²O²**	405	16.7
	565	16.7
	660	16.7

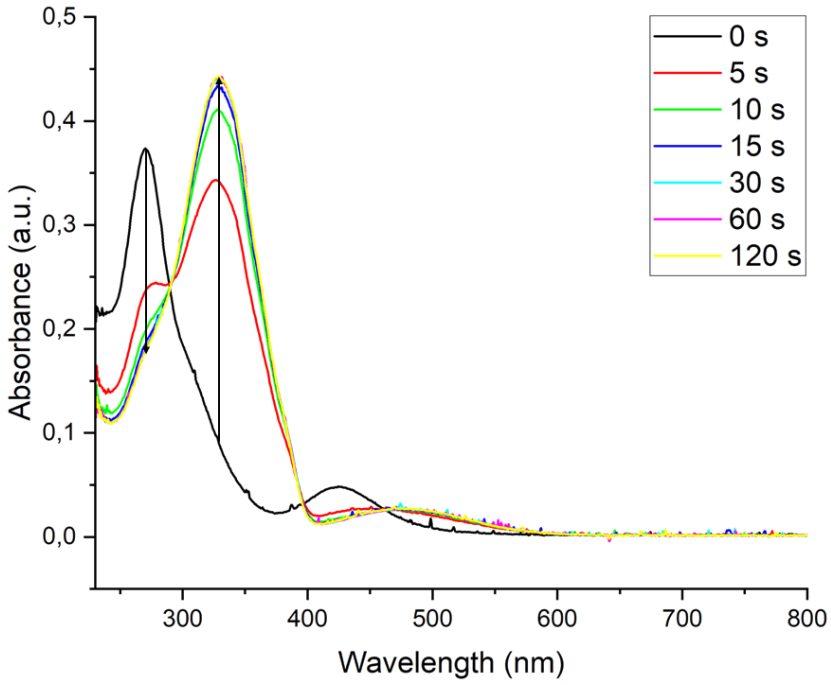

Figure S103: UV/VIS spectra of **A²E²** after irradiation with blue light (405 nm) in CH_2Cl_2.

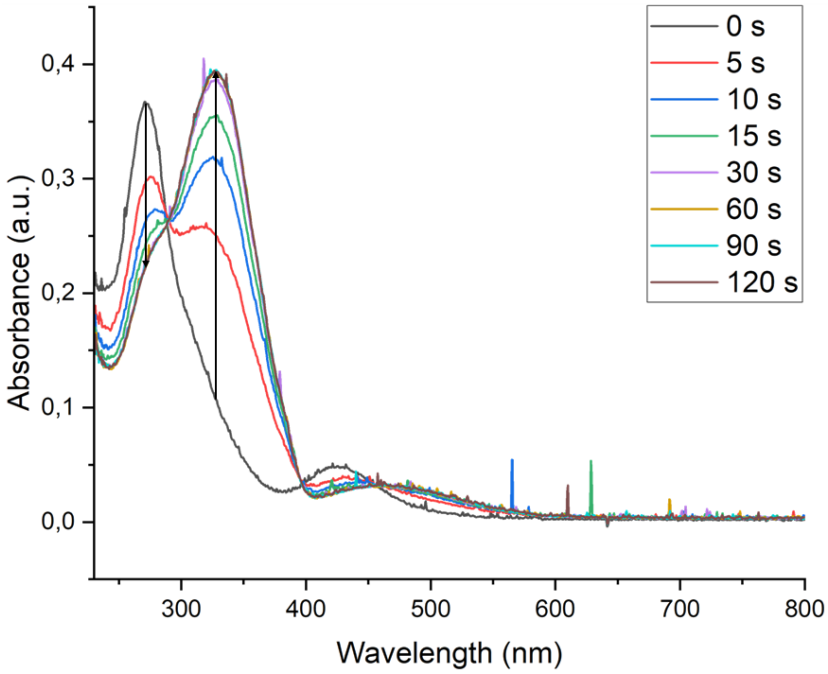

Figure S104: UV/VIS spectra of $\mathbf{A^2E^2}$ after irradiation with blue light (470 nm) in CH_2Cl_2.

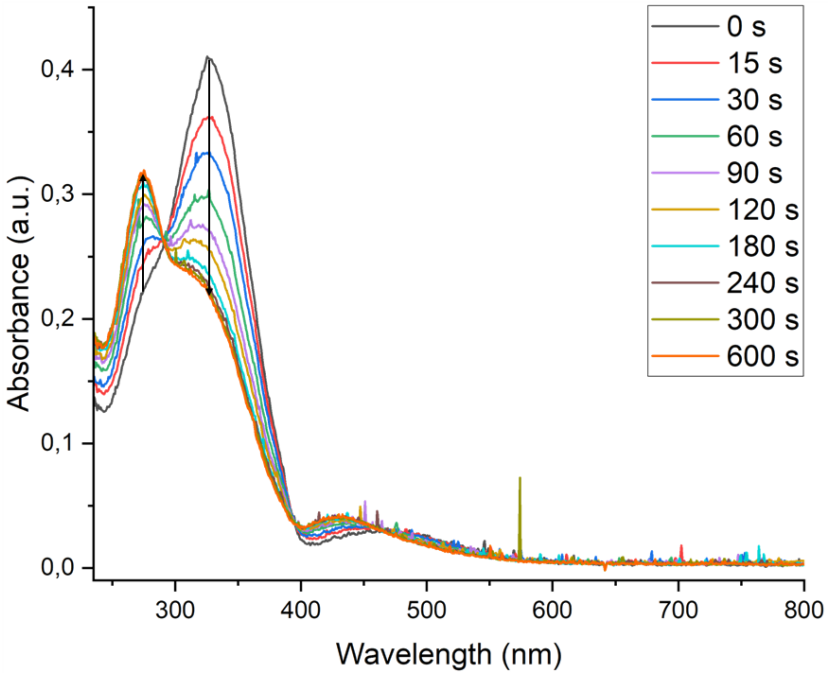

Figure S105: UV/VIS spectra of $\mathbf{A^2E^2}$. A solution that was *E*-enriched by irradiation with blue light (405 nm) was irradiated with green light (565 nm) in CH_2Cl_2.

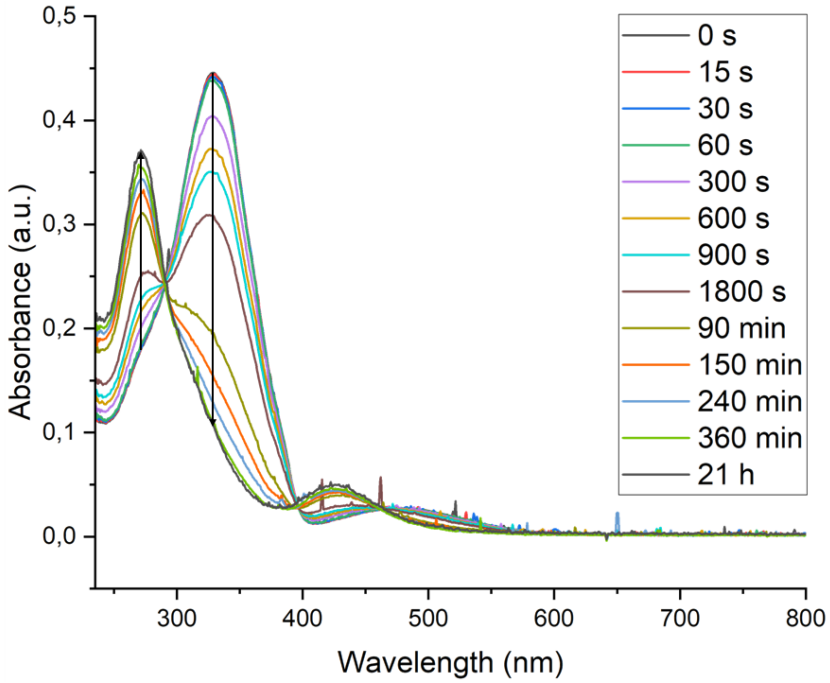

Figure S106: UV/VIS spectra of $\mathbf{A^2E^2}$. A solution that was *E*-enriched by irradiation with blue light (405 nm) was irradiated with red light (660 nm) in CH_2Cl_2.

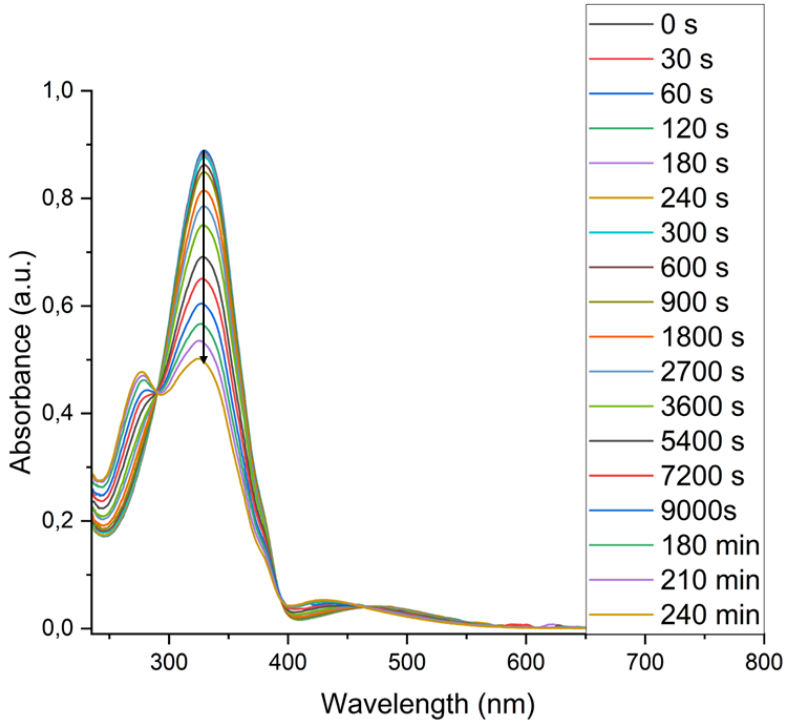

Figure S107: UV/VIS spectra of $\mathbf{A^2O^2}$ after irradiation with red light (660 nm) in CH_2Cl_2.

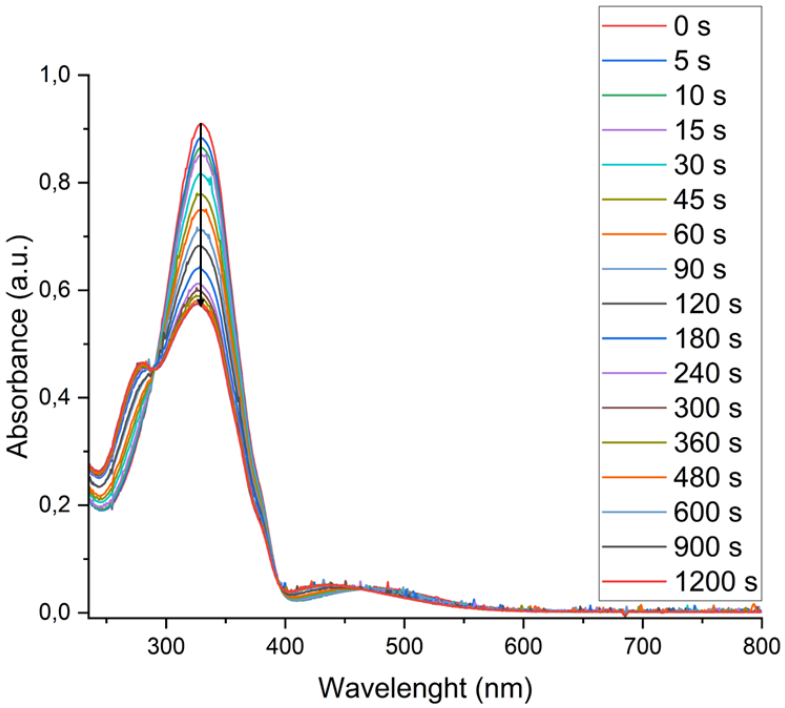

Figure S108: UV/VIS spectra of **A^2O^2** after irradiation with green light (565 nm) in CH_2Cl_2.

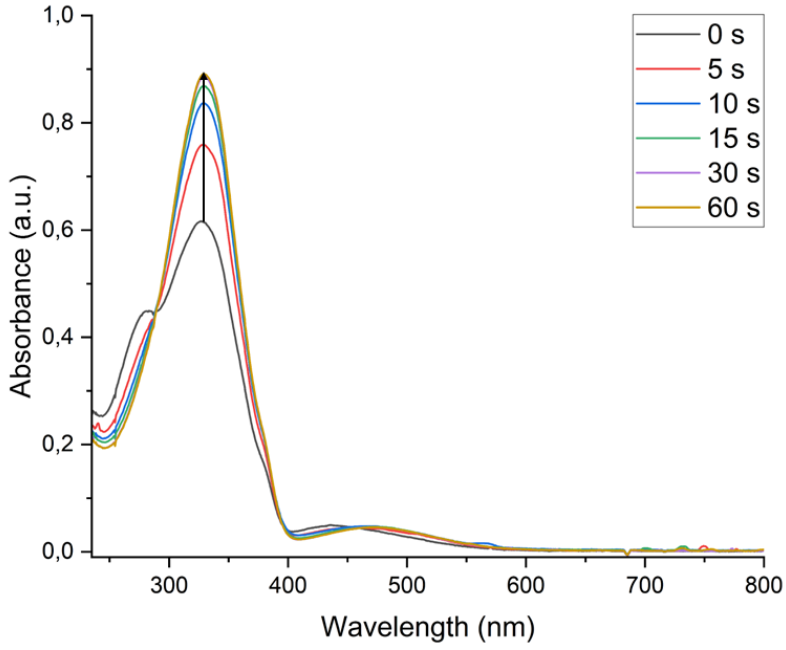

Figure S109: UV/VIS spectra of **A^2O^2** A solution that was *Z*-enriched by irradiation with green light was irradiated with light of the wavelength of 405 nm in CH_2Cl_2.

Table S31: Wavelengths of the absorption maxima λ_{max} and molar attenuation coefficients ε of the macrocycle *Z,Z*-**A²E²** and *E,E*-**A²O²**.

	Z,Z-**A²E²**		*E,E*-**A²O²**	
	π→π*	n→π*	π→π*	n→π*
λ_{max} / nm	270	424	330	486
ε / 10^3 L mol^{-1} cm^{-1}	53.5	6.97	54.4	3.44

Irradiation studies

Assembly of A²E² under irradiation

A solution of azobenzene *E*-**A** (2.02 mg, 6.51 µmol, 1.00 eq.) in CD_2Cl_2 (0.75 mL) was irradiated with red light (660 nm) for 70 h, after which the ^{1}H NMR spectrum of the reaction mixture revealed *E*-**A** and *Z*-**A** in a molar ratio of approximately 15:85 (as integrated from ^{1}H NMR). A solution of diamine **E** (0.43 mg, 6.50 µmol, 1.00 eq.) in CD_2Cl_2 (0.40 mL) was added dropwise to the stirred solution of azobenzene **A** at room temperature over the course of approx. 40 min *via* a syringe pump. The solution was continuously stirred at room temperature while being irradiated with red light (660 nm). After 19 h, a reaction control *via* MALDI-MS, and ^{1}H and ^{19}F{^{1}H} NMR, was conducted. Prolonged stirring under continuous irradiation led to the formation of a red insoluble precipitate.

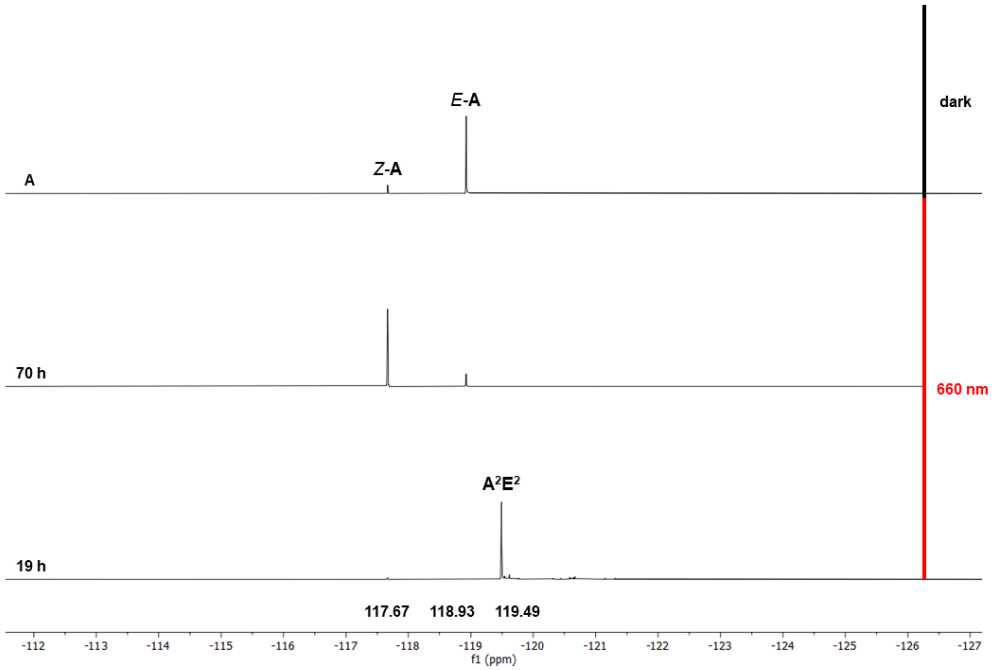

Figure S110: Comparison of ^{19}F{^{1}H} NMR spectra (CD_2Cl_2, 282 MHz) of **A** in the dark, after irradiation with red light, (660 nm) followed by the addition of **E** and stirring under continuous irradiation with red light for 19 h.

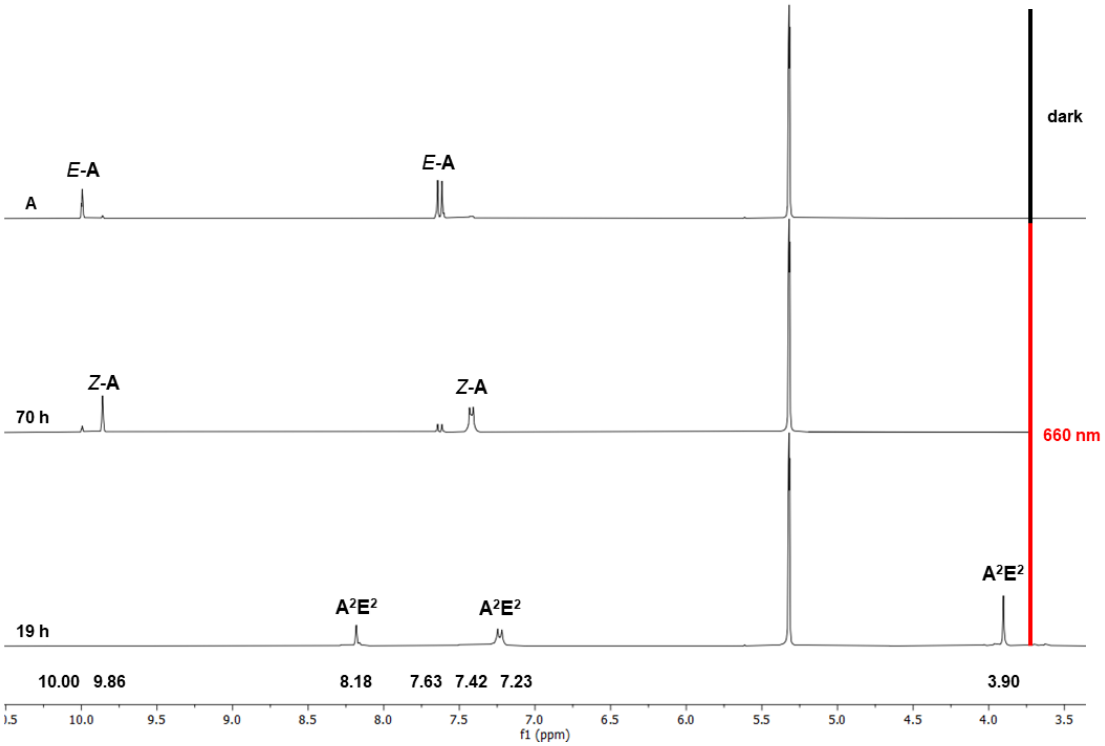

Figure S111: Comparison of ^{1}H NMR spectra (CD_2Cl_2, 300 MHz) of **A** in the dark, after irradiation with red light, (660 nm) followed by the addition of **E** and stirring under continuous irradiation with red light for 19 h.

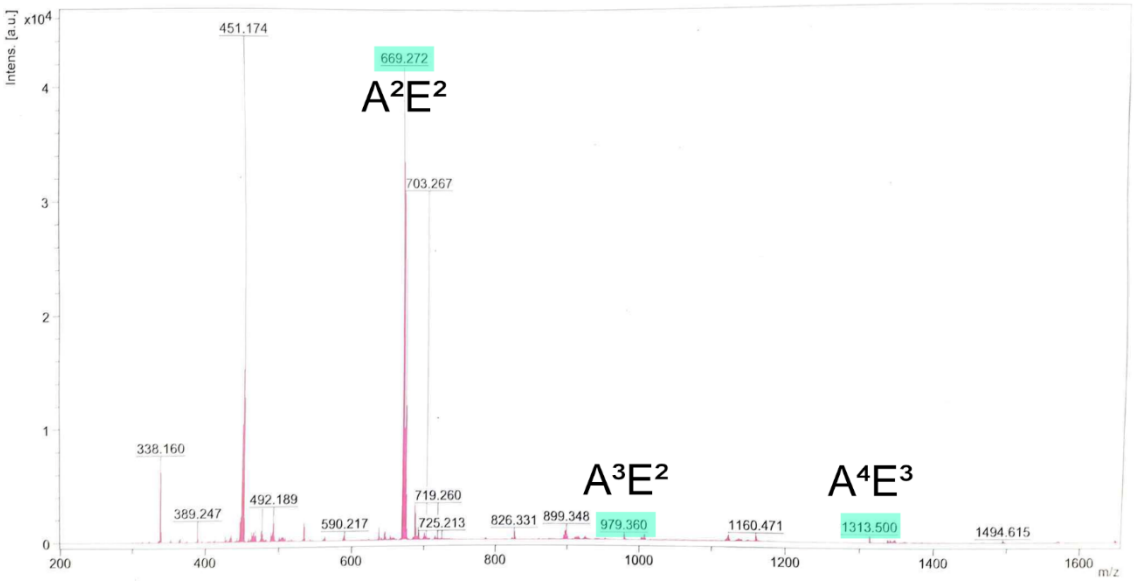

Figure S112: MALDI-mass spectrum of the formation $\mathbf{A^2E^2}$ under continuous irradiation with red light (660 nm) after 19 h. Peaks that can be attributed to $\mathbf{A^nE^n}$ compounds are highlighted in turquoise.

Reactions of A with longer aliphatic diamines

Stock solutions of the different diamines **Pr**, **B**, **Pe** and **H** were prepared in $CDCl_3$. A stock solution of **A** was prepared in $CDCl_3$ and distributed into two parts, one part was kept in the dark while the other part was irradiated with red light (660 nm) until the percentage of *Z*-isomer was approximately 77% as determined by $^{19}F\{^1H\}$ NMR. The stock solutions of *E*-**A** and *Z*-**A** were mixed in an aldehyde to amine ratio of 1.0 to 1.2 and the mixtures were diluted to a total concentration of 5.0 mM in regards to the aldehyde. The reactions containing *E*-**A** were stirred in the dark and then stirred under irradiation with red light. The vials containing *Z*-**A** were stirred under continuous irradiation. The reactions were monitored using ^1H and $^{19}F\{^1H\}$ NMR spectroscopy and MALDI-mass spectrometry. Reaction times and parameters are summarised in table S32.

Table S32: Amount of starting materials and solvents employed in each reaction and reaction times.

Amine	Aldehyde	V($CDCl_3$)	Reaction time
Pr (0.44 mg, 6.0 µmol, 1.2 eq.)	*E*-**A** (1.6 mg, 5.0 µmol, 1.0 eq.)	1.0 mL	3 days (dark), 3 days (660 nm)
	Z-***A*** (1.6 mg, 5.0 µmol, 1.0 eq.)	1.0 mL	3 days
B (0.53 mg, 6.0 µmol, 1.2 eq.)	*E*-**A** (1.6 mg, 5.0 µmol, 1.0 eq.)	1.0 mL	3 days (dark), 3 days (660 nm)
	Z-***A*** (1.6 mg, 5.0 µmol, 1.0 eq.)	1.0 mL	3 days
Pe (1.2 mg, 12 µmol, 1.2 eq.)	*E*-**A** (3.1 mg, 10 µmol, 1.0 eq.)	2.0 mL	4 days (dark), 3 days (660 nm)
	Z-***A*** (3.1 mg, 10 µmol, 1.0 eq.)	2.0 mL	4 days
H (0.70 mg, 6.0 µmol, 1.2 eq.)	*E*-**A** (1.6 mg, 5.0 µmol, 1.0 eq.)	1.0 mL	3 days (dark), 3 days (660 nm)
	Z-***A*** (1.6 mg, 5.0 µmol, 1.0 eq.)	1.0 mL	3 days

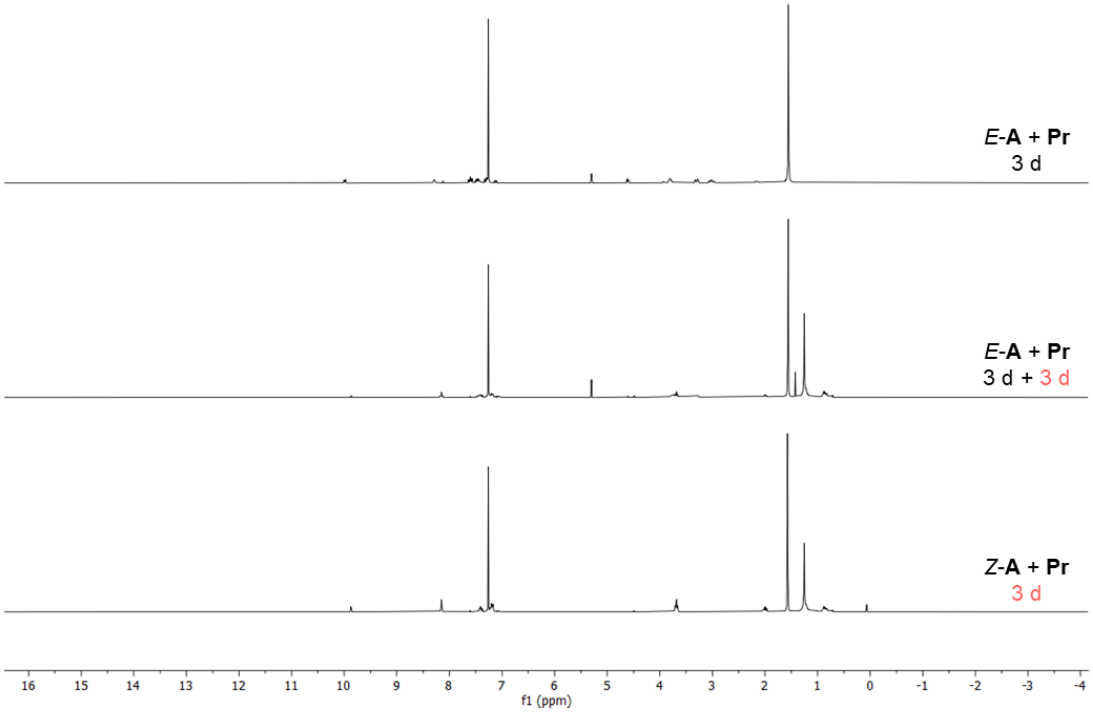

Figure S113: Comparison of ^{1}H NMR spectra ($CDCl_3$, 300 MHz) of *E*-**A** and **Pr** in the dark, after irradiation with red light (660 nm), and of *Z*-**A** and **Pr** after irradiation with red light.

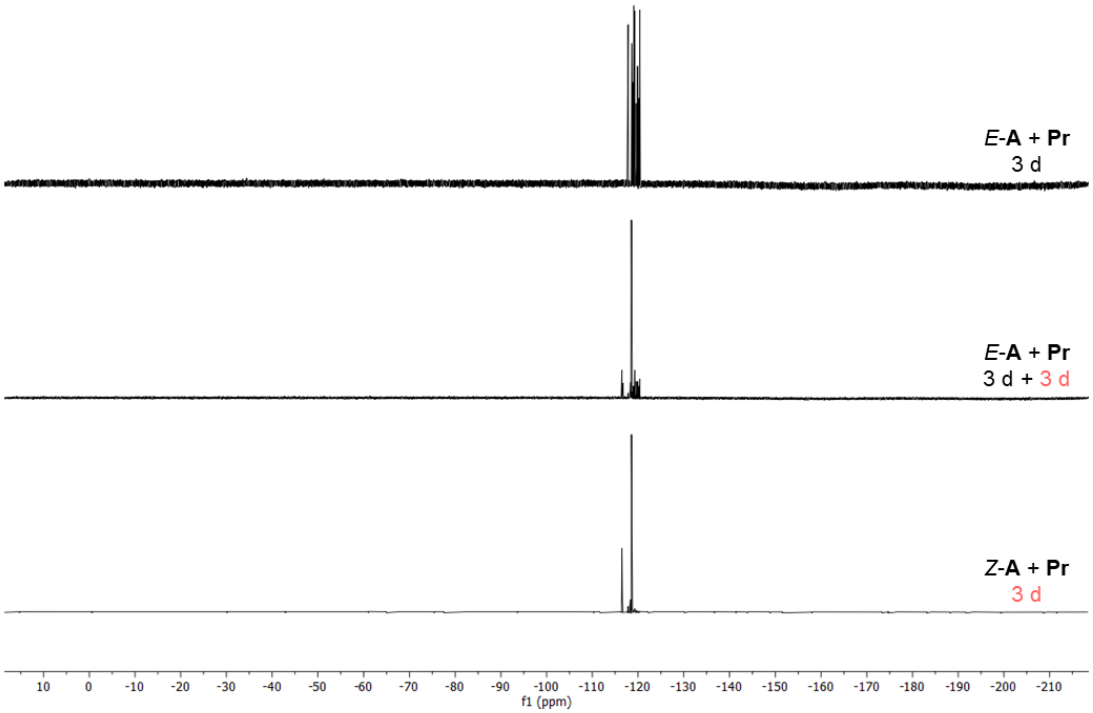

Figure S114: Comparison of $^{19}F\{^{1}H\}$ NMR spectra ($CDCl_3$, 282 MHz) of *E*-**A** and **Pr** in the dark, after irradiation with red light (660 nm), and of *Z*-**A** and **Pr** after irradiation with red light.

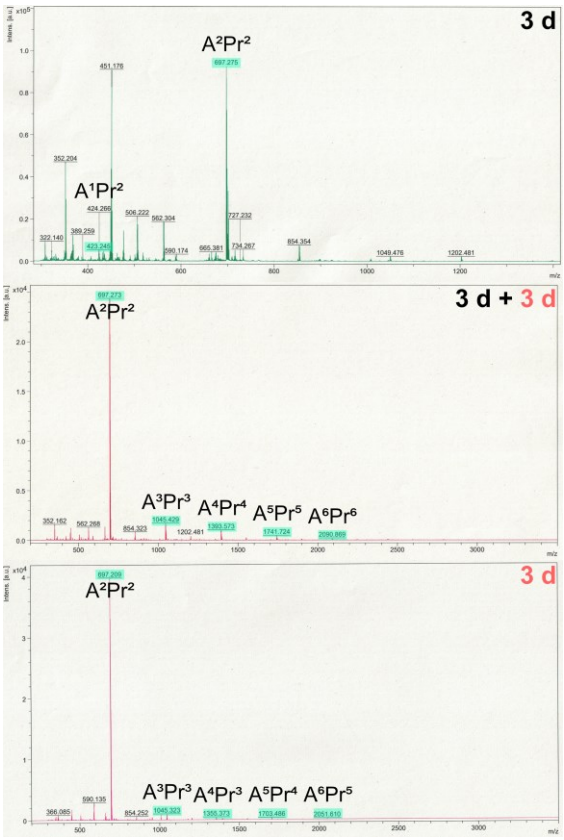

Figure S115: Comparison of MALDI-mass spectra of the reaction of *E*-**A** and **Pr** in the dark and under irradiation with red light (660 nm) and of the reaction of *Z*-**A** and **Pr** under continuous irradiation with red light. Peaks that can be attributed to $\mathbf{A^nPr^n}$ compounds are highlighted in turquoise.

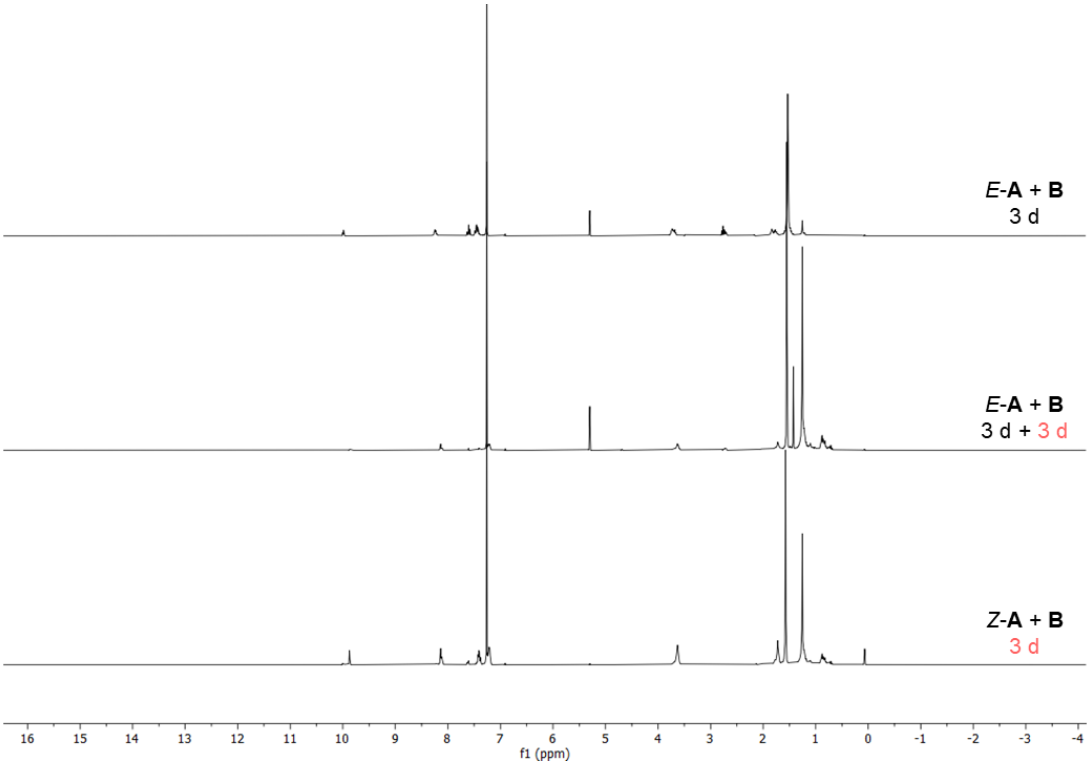

Figure S116: Comparison of ^{1}H NMR spectra ($CDCl_3$, 300 MHz) of *E*-**A** and **B** in the dark, after irradiation with red light (660 nm), and of *Z*-**A** and **B** after irradiation with red light.

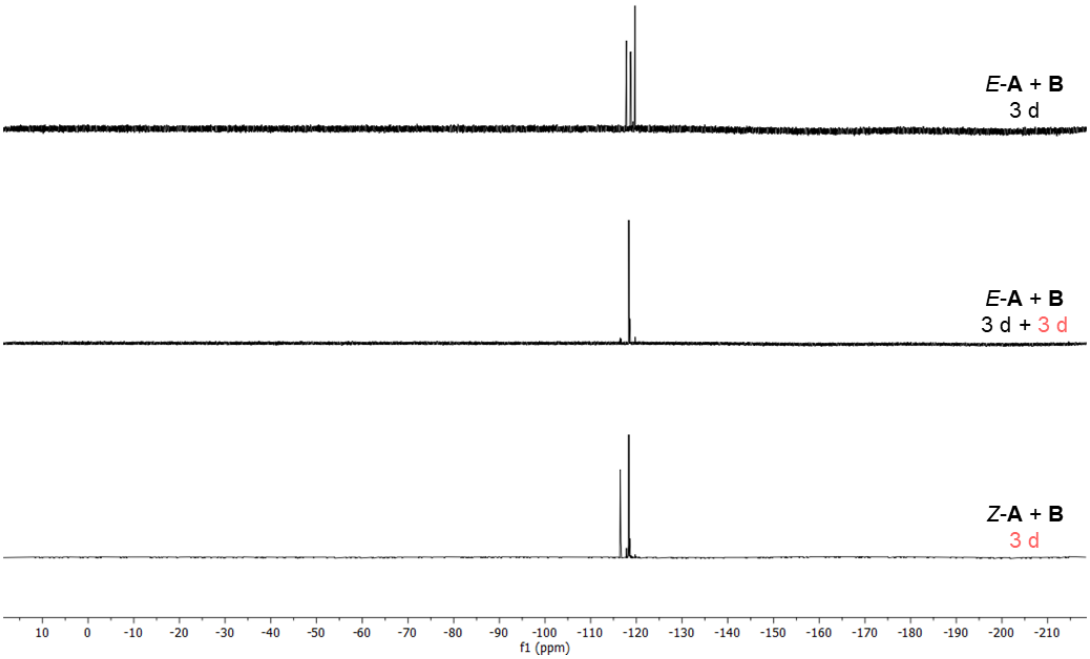

Figure S117: Comparison of $^{19}F\{^{1}H\}$ NMR spectra ($CDCl_3$, 282 MHz) of *E*-**A** and **B** in the dark, after irradiation with red light (660 nm), and of *Z*-**A** and **B** after irradiation with red light.

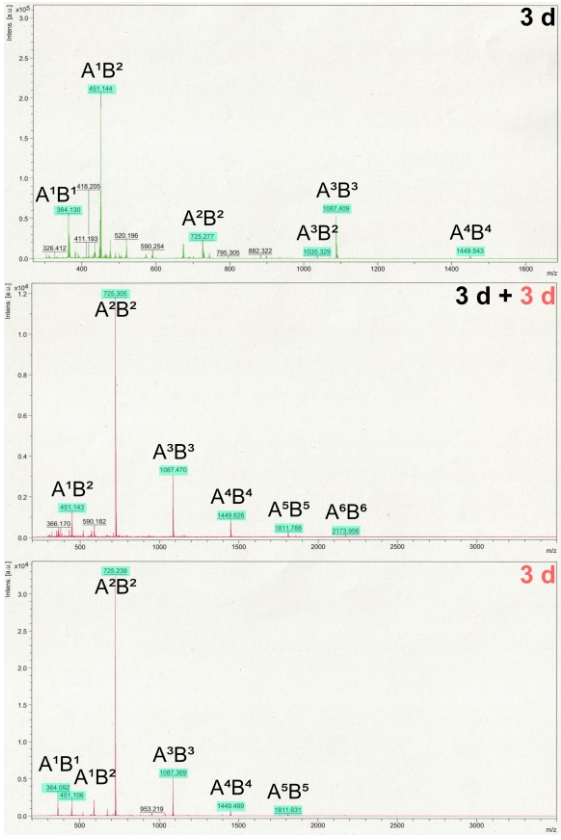

Figure S118: Comparison of MALDI-mass spectra of the reaction of *E*-**A** and **B** in the dark and under irradiation with red light (660 nm) and of the reaction of *Z*-**A** and **B** under continuous irradiation with red light. Peaks that can be attributed to $\mathbf{A^nB^n}$ compounds are highlighted in turquoise.

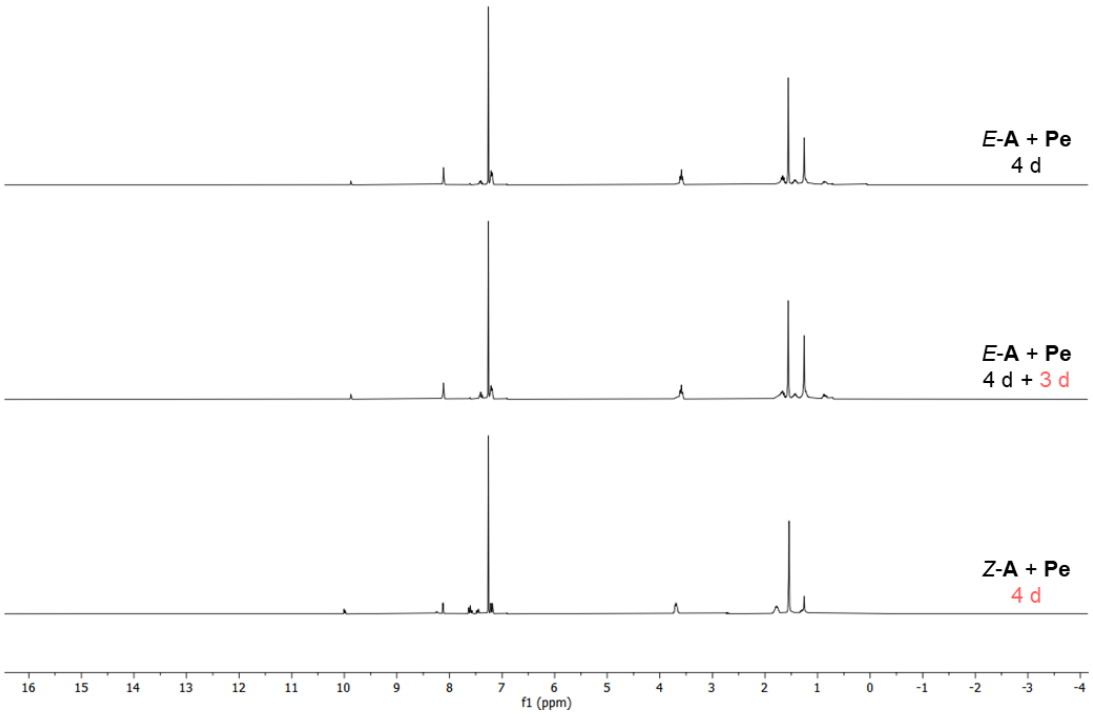

Figure S119: Comparison of ^{1}H NMR spectra ($CDCl_3$, 300 MHz) of *E*-**A** and **Pe** in the dark, after irradiation with red light (660 nm), and of *Z*-**A** and **Pe** after irradiation with red light.

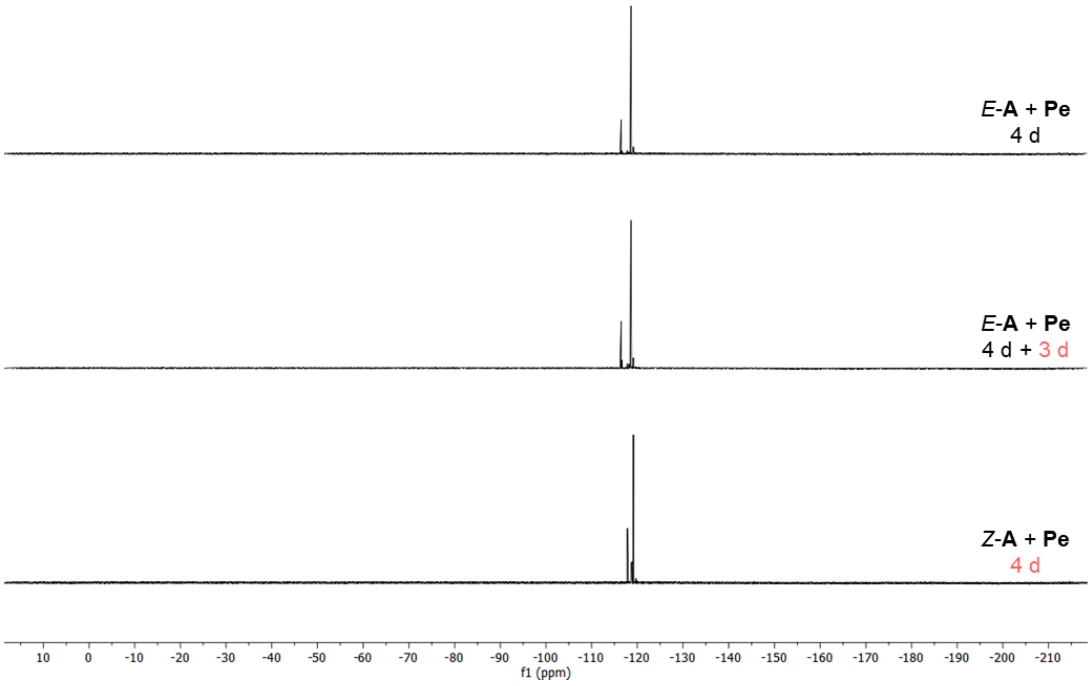

Figure S120: Comparison of $^{19}F\{^{1}H\}$ NMR spectra ($CDCl_3$, 282 MHz) of *E*-**A** and **Pe** in the dark, after irradiation with red light (660 nm), and of *Z*-**A** and **Pe** after irradiation with red light.

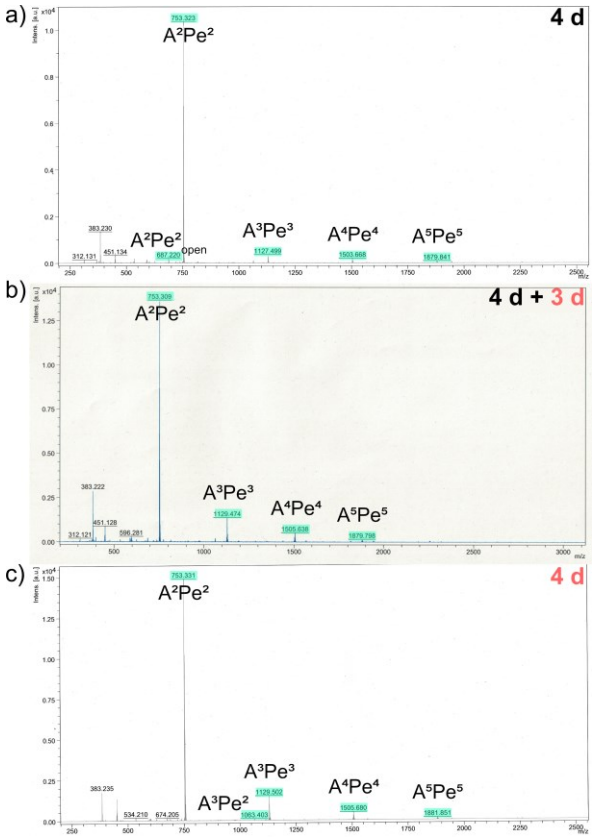

Figure S121: Comparison of MALDI-mass spectra of the reaction of *E*-**A** and **Pe** in the dark and under irradiation with red light (660 nm) and of the reaction of *Z*-**A** and **Pe** under continuous irradiation with red light. Peaks that can be attributed to $\mathbf{A^nPe^n}$ compounds are highlighted in turquoise.

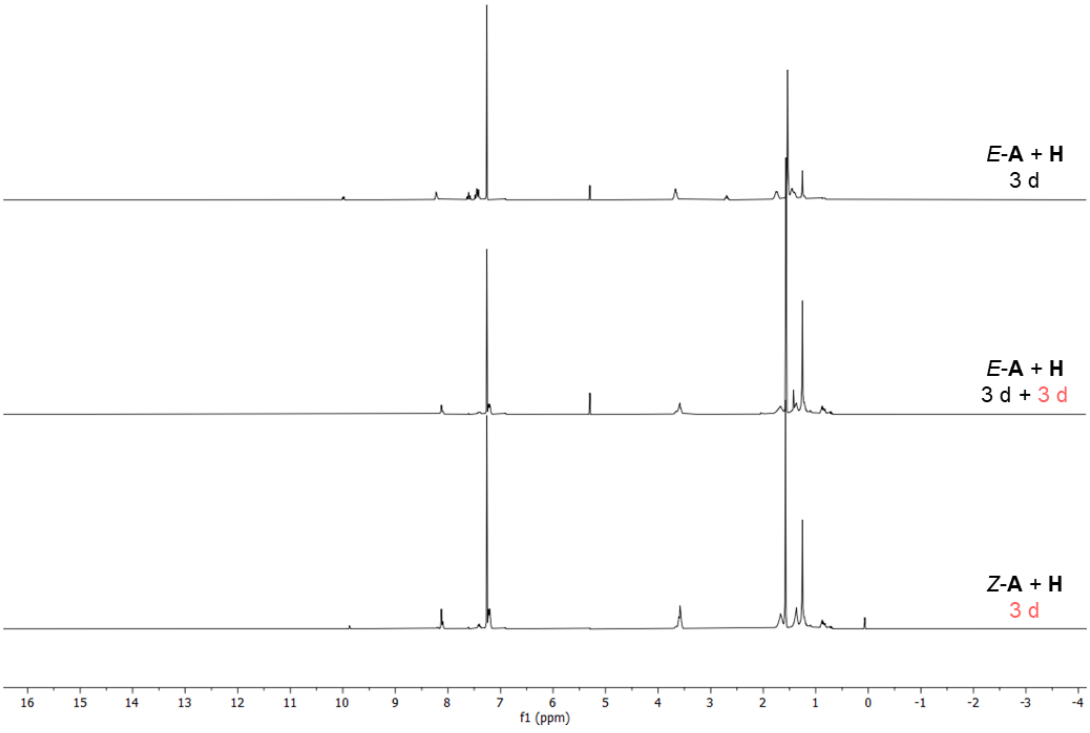

Figure S122: Comparison of ^{1}H NMR spectra ($CDCl_3$, 300 MHz) of *E*-**A** and **H** in the dark, after irradiation with red light (660 nm), and of *Z*-**A** and **H** after irradiation with red light.

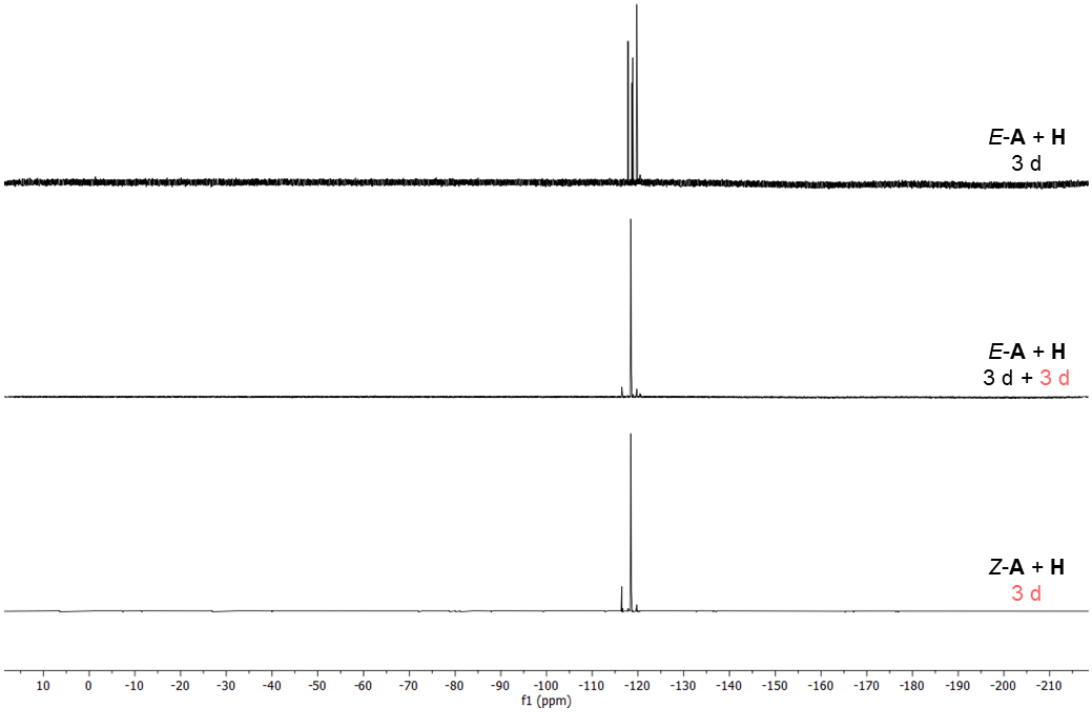

Figure S123: Comparison of $^{19}F\{^{1}H\}$ NMR spectra ($CDCl_3$, 282 MHz) of *E*-**A** and **H** in the dark, after irradiation with red light (660 nm), and of *Z*-**A** and **H** after irradiation with red light.

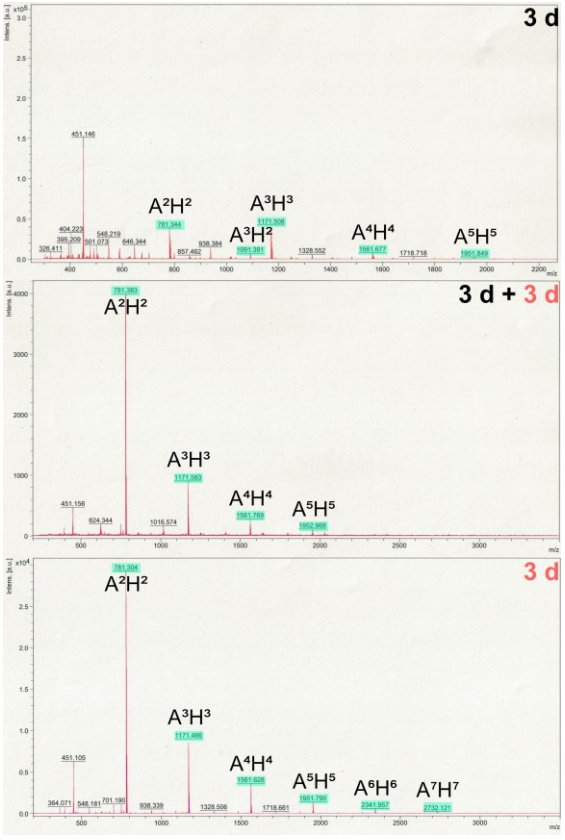

Figure S124: Comparison of MALDI-mass spectra of the reaction of *E*-**A** and **Pr** in the dark and under irradiation with red light (660 nm) and of the reaction of *Z*-**A** and **Pr** under continuous irradiation with red light. Peaks that can be attributed to $\mathbf{A^nPr^n}$ compounds are highlighted in turquoise.

Reaction of A with different aliphatic diamines at different concentrations

Stock solutions of the different diamines **Pr**, **B**, **Pe** and **H** were prepared in $CDCl_3$. A stock solution of **A** was prepared in $CDCl_3$ for the samples with concentrations between 1 and 5 mM and azobenzene **A** was weighed in for the samples with higher concentrations. Two samples of each combination and concentration were prepared according to the details listed in table S33. The first half of those samples was kept in the dark or while the other half was irradiated with red light. The reactions were monitored by ^{1}H and ^{19}F NMR spectroscopy and MALDI mass spectrometry.

Table S33: Amount of starting materials and solvents employed in each reaction and reaction times.

Concentration	Aldehyde	Amine	V($CDCl_3$)	Reaction time
1.0 mM	**A** (0.25 mg, 0.80 µmol, 1.0 equiv.)	**Pr** (0.059 mg, 0.80 µmol, 1.0 equiv.)	0.8 ml	3 days (dark)
				3 days (660 nm)
		B (0.071 mg, 0.80 µmol, 1.0 equiv.)		3 days (dark)
				3 days (660 nm)
		Pe (0.082 mg, 0.80 µmol, 1.0 equiv.)		3 days (dark)
				3 days (660 nm)
		H (0.093 mg, 0.80 µmol, 1.0 equiv.)		3 days (dark)
				3 days (660 nm)
2.5 mM	**A** (0.62 mg, 2.0 µmol, 1.0 equiv.)	**Pr** (0.15 mg, 2.0 µmol, 1.0 equiv.)	0.8 ml	3 days (dark)
				3 days (660 nm)
		B (0.18 mg, 2.0 µmol, 1.0 equiv.)		3 days (dark)
				3 days (660 nm)
		Pe (0.20 mg, 2.0 µmol, 1.0 equiv.)		3 days (dark)
				3 days (660 nm)
		H (0.23 mg, 2.0 µmol, 1.0 equiv.)		3 days (dark)
				3 days (660 nm)

5.0 mM	**A** (1.2 mg, 24.0 µmol, 1.0 equiv.)	**Pr** (0.30 mg, 4.0 µmol, 1.0 equiv.)	0.8 ml	3 days (dark)
				3 days (660 nm)
		B (0.35 mg, 4.0 µmol, 1.0 equiv.)		3 days (dark)
				3 days (660 nm)
		Pe (0.41 mg, 4.0 µmol, 1.0 equiv.)		3 days (dark)
				3 days (660 nm)
		H (0.46 mg, 4.0 µmol, 1.0 equiv.)		3 days (dark)
				3 days (660 nm)
10 mM	**A** (2.5 mg, 8.0 µmol, 1.0 equiv.)	**Pr** (0.59 mg, 8.0 µmol, 1.0 equiv.)	0.8 ml	3 days (dark)
				3 days (660 nm)
		B (0.71 mg, 8.0 µmol, 1.0 equiv.)		3 days (dark)
				3 days (660 nm)
		Pe (0.82 mg, 8.0 µmol, 1.0 equiv.)		3 days (dark)
				3 days (660 nm)
		H (0.93 mg, 8.0 µmol, 1.0 equiv.)		3 days (dark)
				3 days (660 nm)
20 mM	**A** (5.0 mg, 16 µmol, 1.0 equiv.)	**Pr** (1.2 mg, 16 µmol, 1.0 equiv.)	0.8 ml	3 days (dark)
				3 days (660 nm)
		B (1.4 mg, 16 µmol, 1.0 equiv.)		3 days (dark)
				3 days (660 nm)
		Pe (1.6 mg, 16 µmol, 1.0 equiv.)		3 days (dark)
				3 days (660 nm)
		H (1.9 mg, 16 µmol, 1.0 equiv.)		3 days (dark)
				3 days (660 nm)

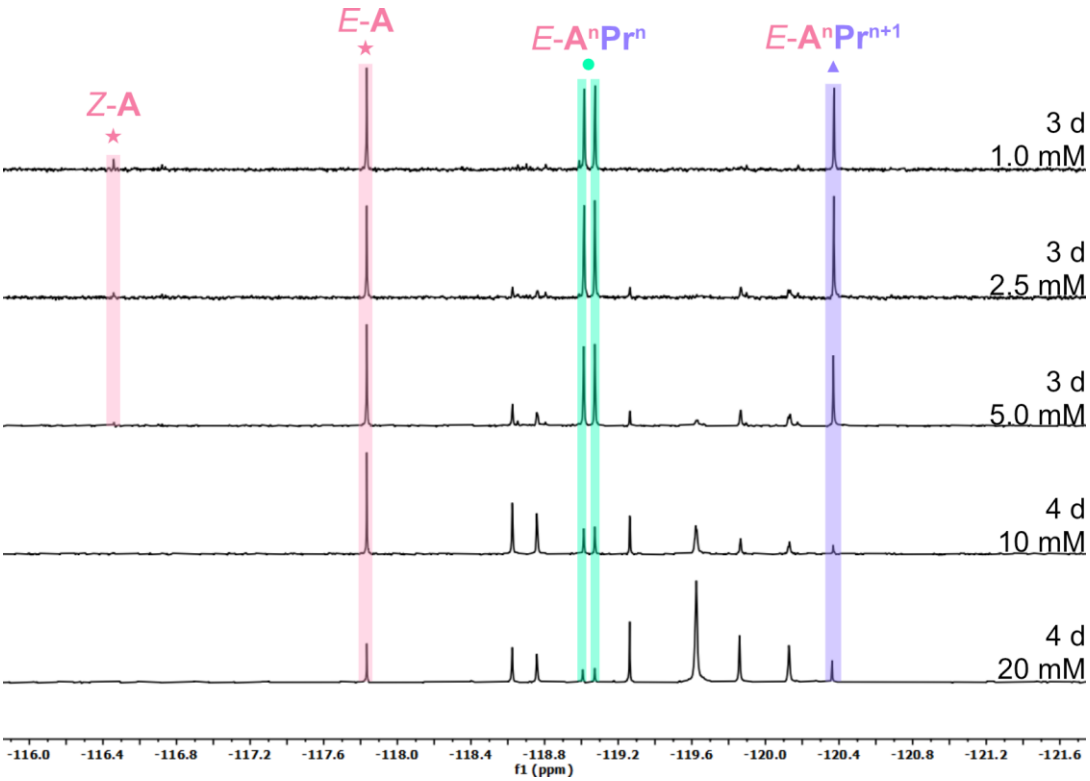

Figure S125: Comparison of $^{19}F\{^{1}H\}$ NMR spectra ($CDCl_3$, 282 MHz) of *E*-**A** and **H** at different concentrations after stirring in the dark.

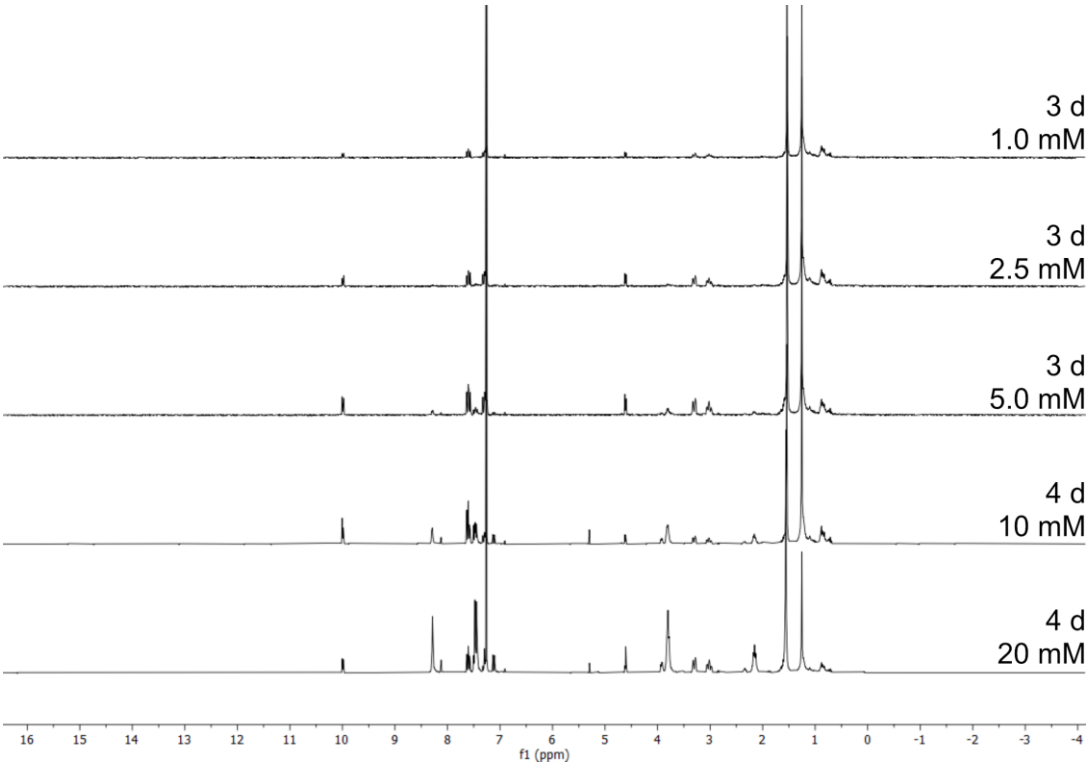

Figure S126: Comparison of ^{1}H NMR spectra ($CDCl_3$, 300 MHz) of *E*-**A** and **Pr** at different concentrations after stirring in the dark.

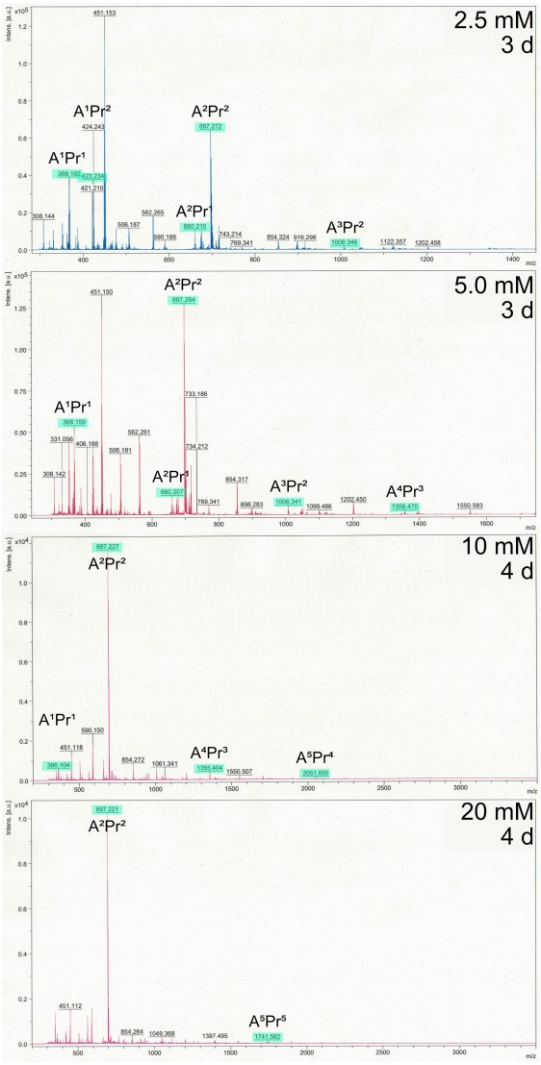

Figure S127: Comparison of MALDI-mass spectra of the reaction of *E*-**A** and **Pr** at different concentrations in the dark. Peaks that can be attributed to $\mathbf{A^nPr^n}$ compounds are highlighted in turquoise.

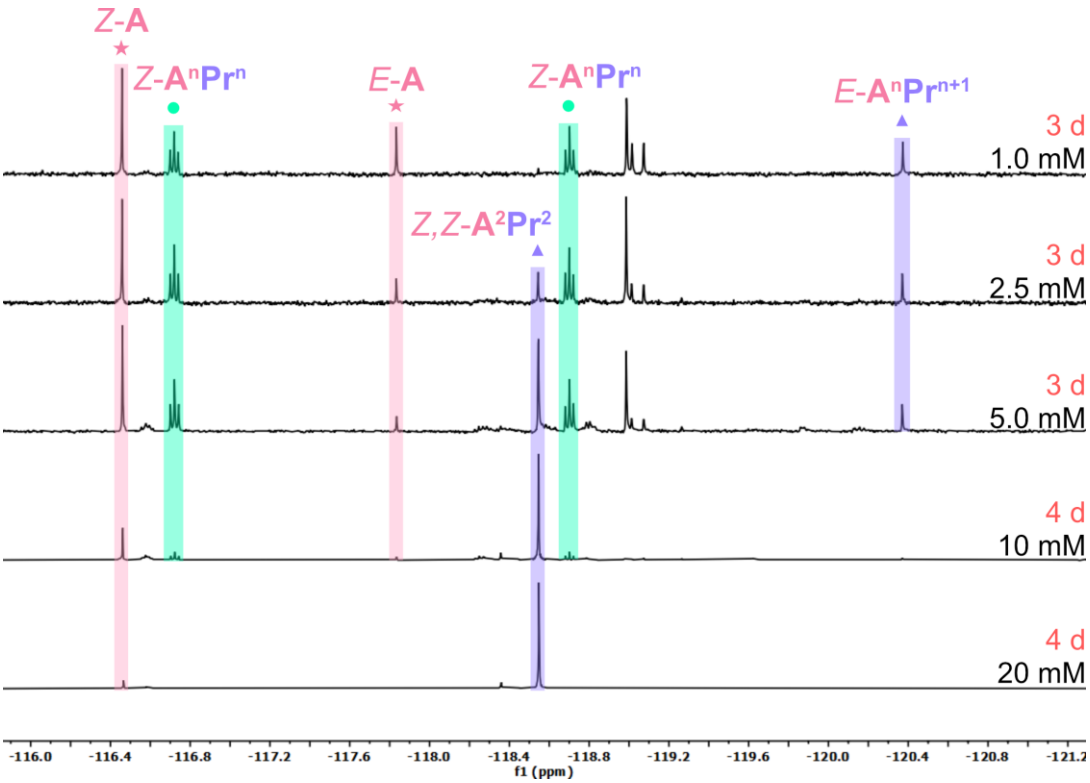

Figure S128: Comparison of $^{19}F\{^{1}H\}$ NMR spectra ($CDCl_3$, 282 MHz) of *E*-**A** and **Pr** at different concentrations after stirring under irradiation with red light.

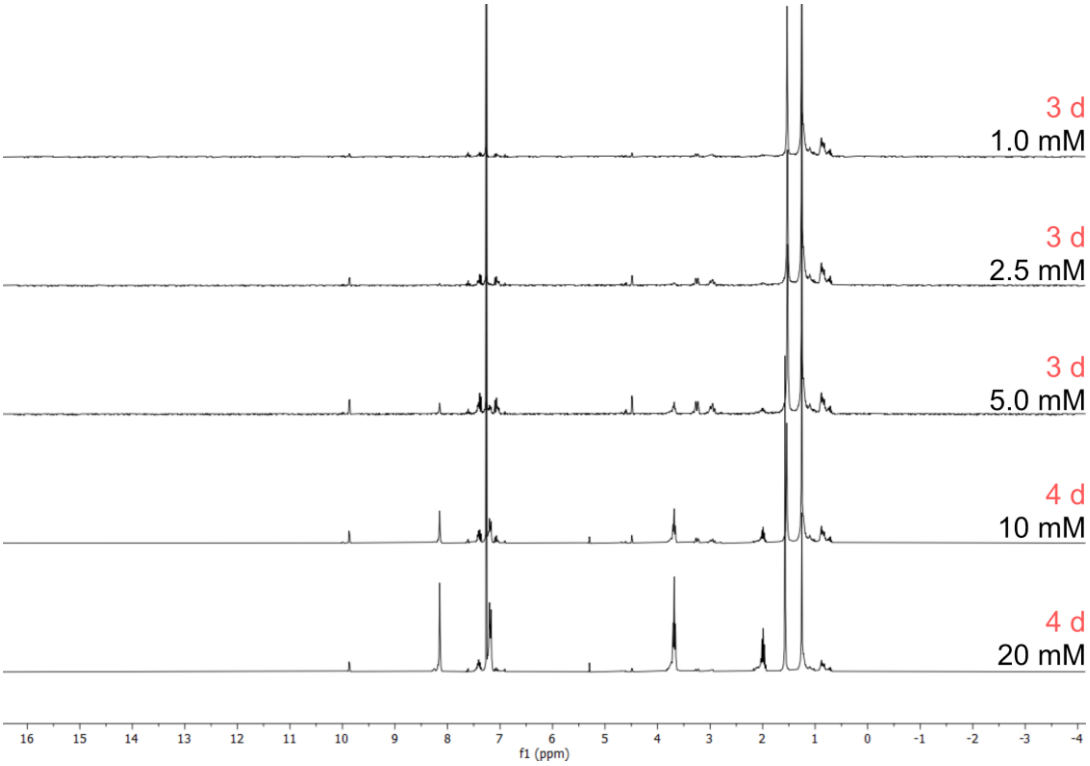

Figure S129: Comparison of ^{1}H NMR spectra ($CDCl_3$, 300 MHz) of *E*-**A** and **Pr** at different concentrations after stirring under irradiation with red light.

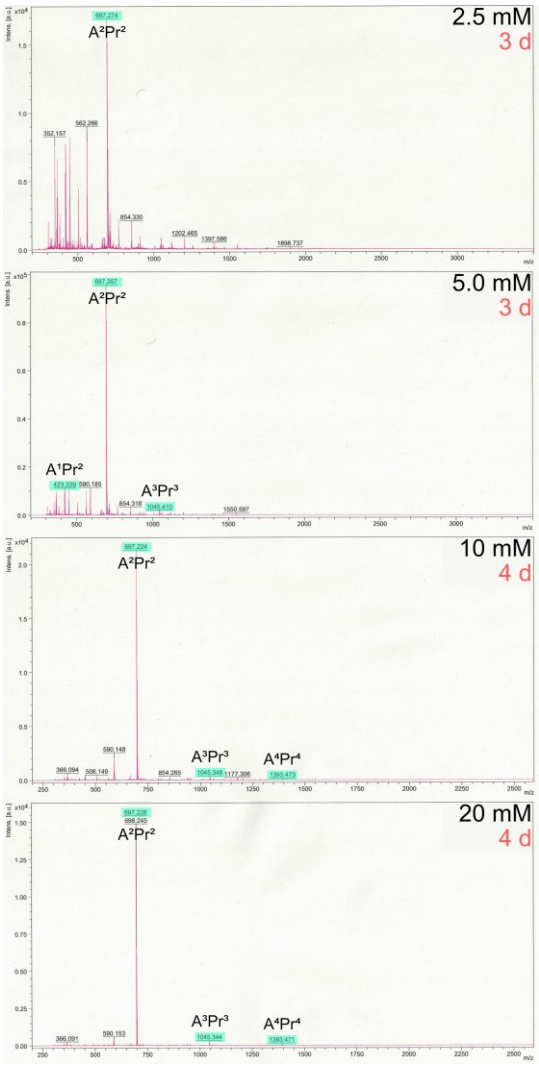

Figure S130: Comparison of MALDI-mass spectra of the reaction of *E*-**A** and **Pr** at different concentrations under irradiation with red light (660 nm). Peaks that can be attributed to $\mathbf{A^nPr^n}$ compounds are highlighted in turquoise.

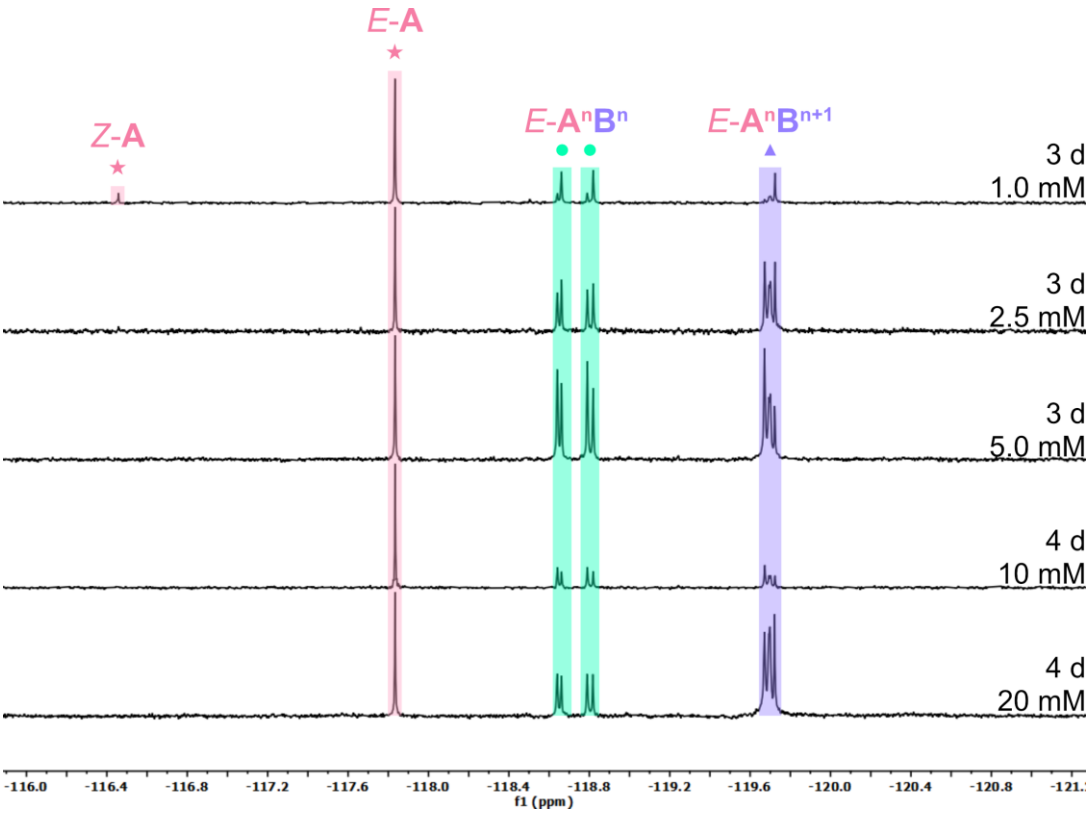

Figure S131: Comparison of $^{19}F\{^{1}H\}$ NMR spectra ($CDCl_3$, 282 MHz) of *E*-**A** and **B** at different concentrations after stirring in the dark.

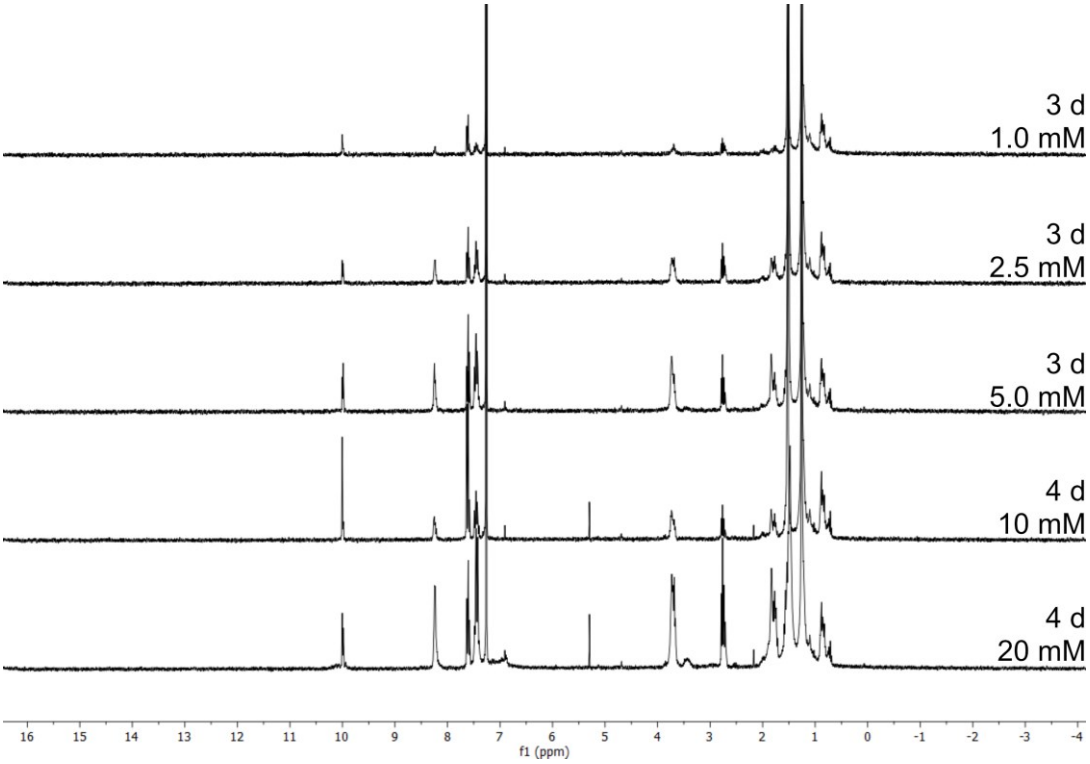

Figure S132: Comparison of ^{1}H NMR spectra ($CDCl_3$, 300 MHz) of *E*-**A** and **B** at different concentrations after stirring in the dark.

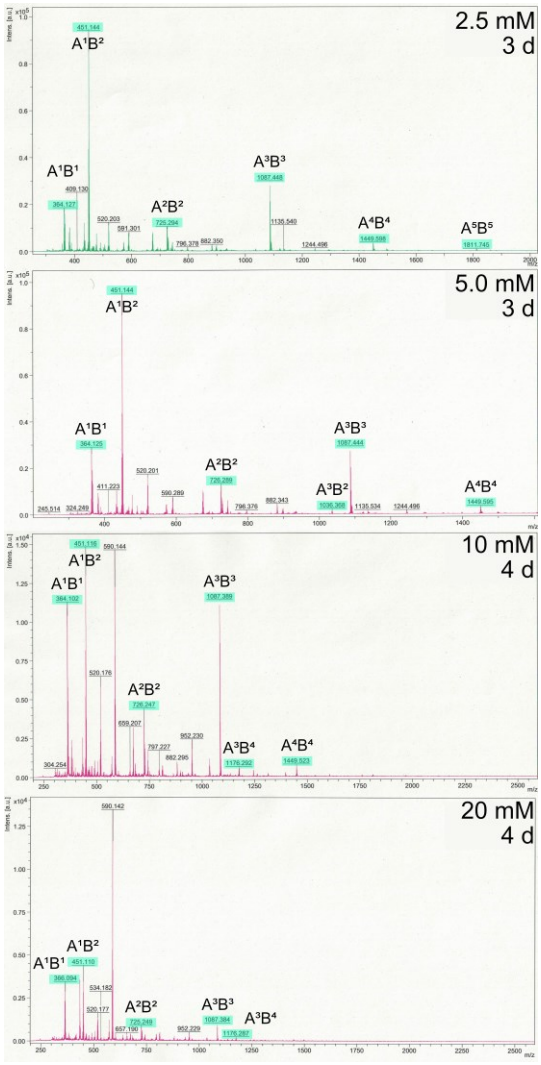

Figure S133: Comparison of MALDI-mass spectra of the reaction of *E*-**A** and **B** at different concentrations in the dark. Peaks that can be attributed to $\mathbf{A^nB^n}$ compounds are highlighted in turquoise.

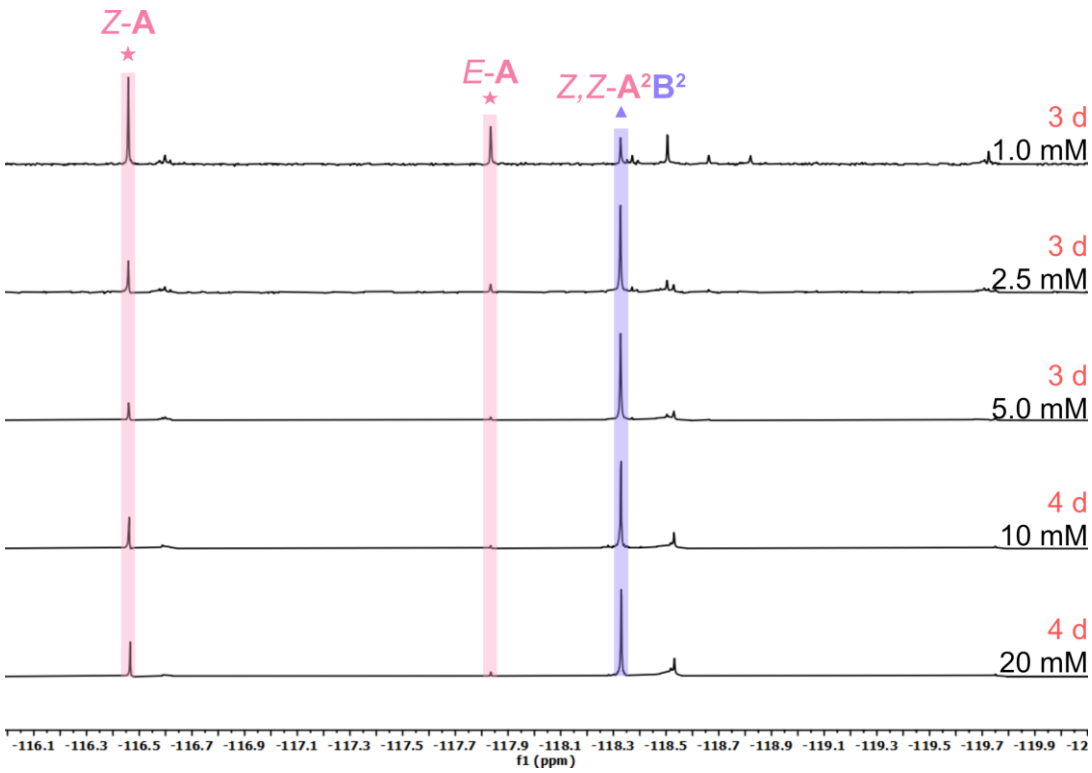

Figure S134: Comparison of $^{19}F\{^{1}H\}$ NMR spectra ($CDCl_3$, 282 MHz) of *E*-**A** and **B** at different concentrations after stirring under irradiation with red light.

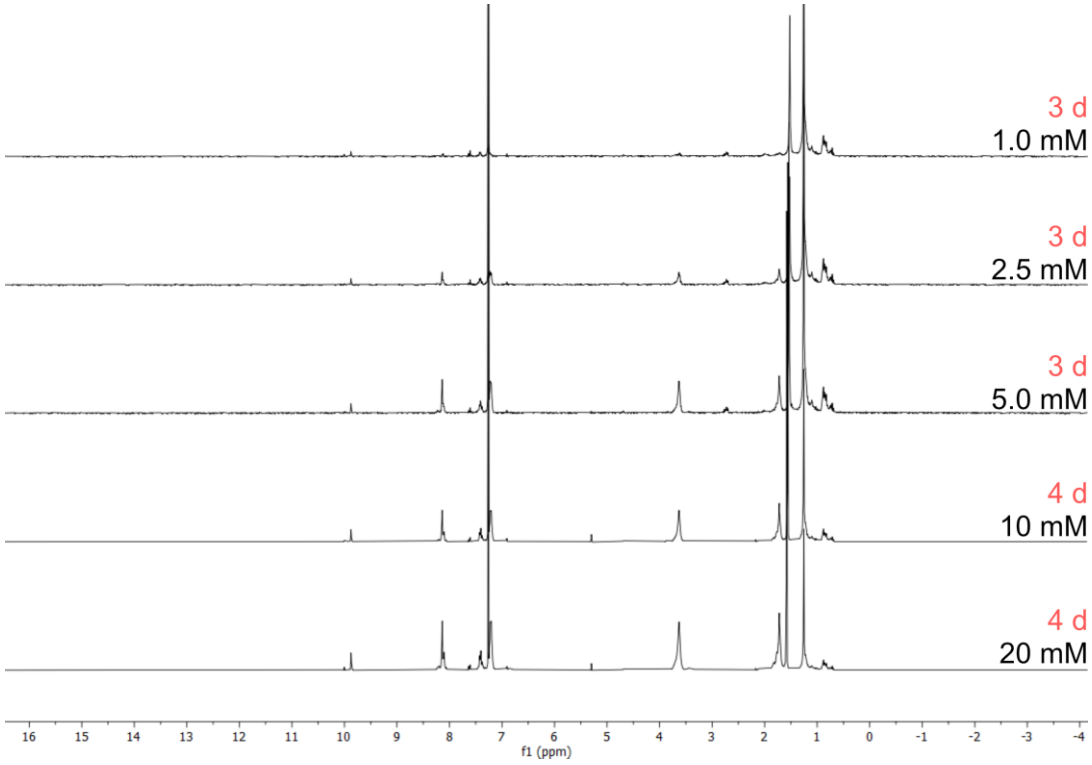

Figure S135: Comparison of ^{1}H NMR spectra ($CDCl_3$, 300 MHz) of *E*-**A** and **B** at different concentrations after stirring under irradiation with red light.

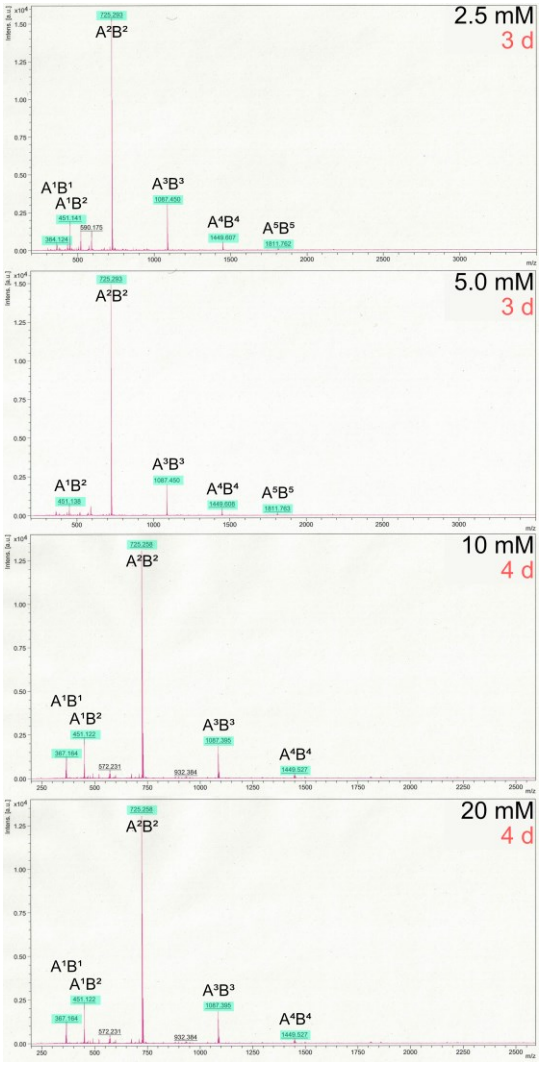

Figure S136: Comparison of MALDI-mass spectra of the reaction of *E*-**A** and **B** at different concentrations under irradiation with red light (660 nm). Peaks that can be attributed to $\mathbf{A^nB^n}$ compounds are highlighted in turquoise.

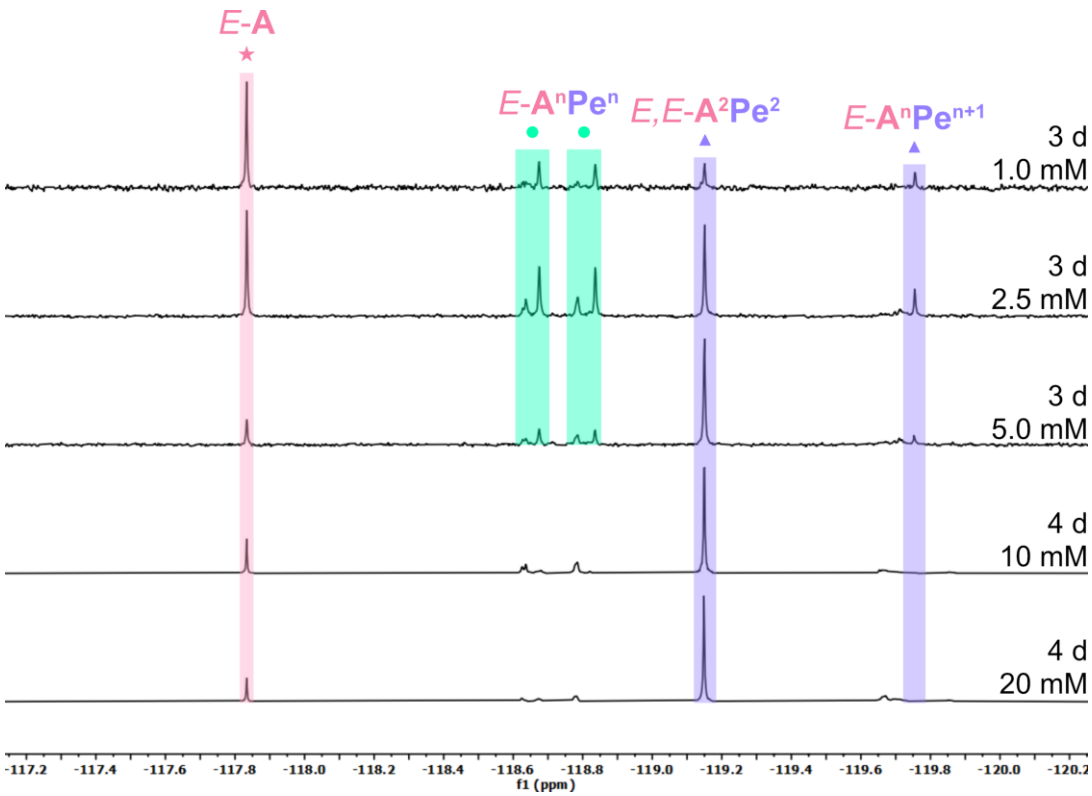

Figure S137: Comparison of $^{19}F\{^{1}H\}$ NMR spectra ($CDCl_3$, 282 MHz) of *E*-**A** and **Pe** at different concentrations after stirring in the dark.

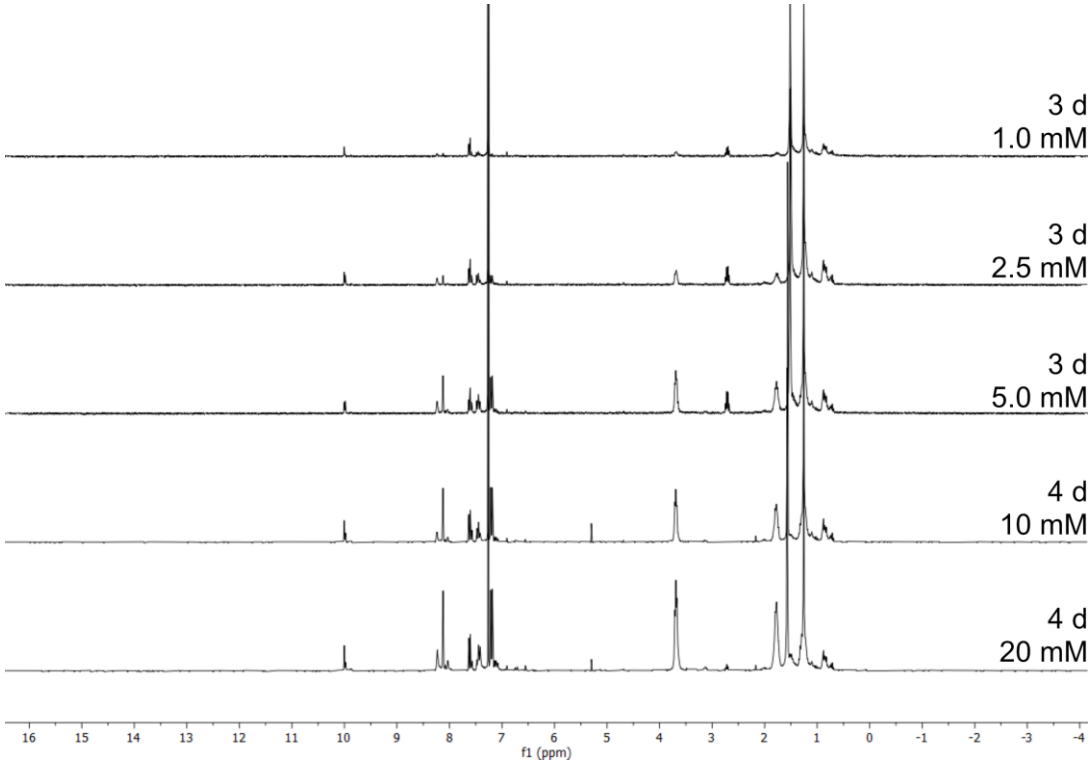

Figure S138: Comparison of ^{1}H NMR spectra ($CDCl_3$, 300 MHz) of *E*-**A** and **Pe** at different concentrations after stirring in the dark.

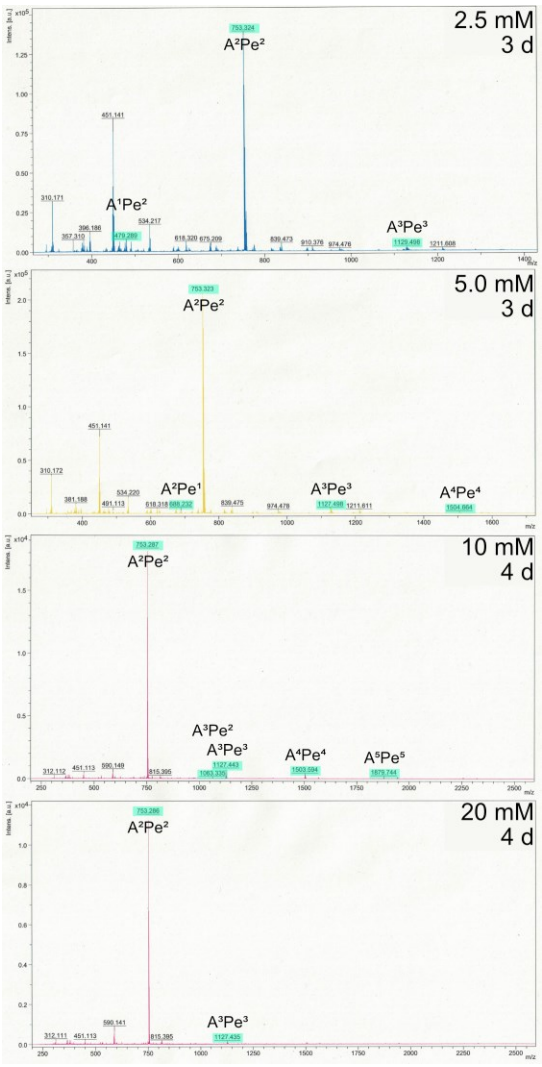

Figure S139: Comparison of MALDI-mass spectra of the reaction of *E*-**A** and **Pe** at different concentrations under irradiation in the dark. Peaks that can be attributed to $\mathbf{A^nPe^n}$ compounds are highlighted in turquoise.

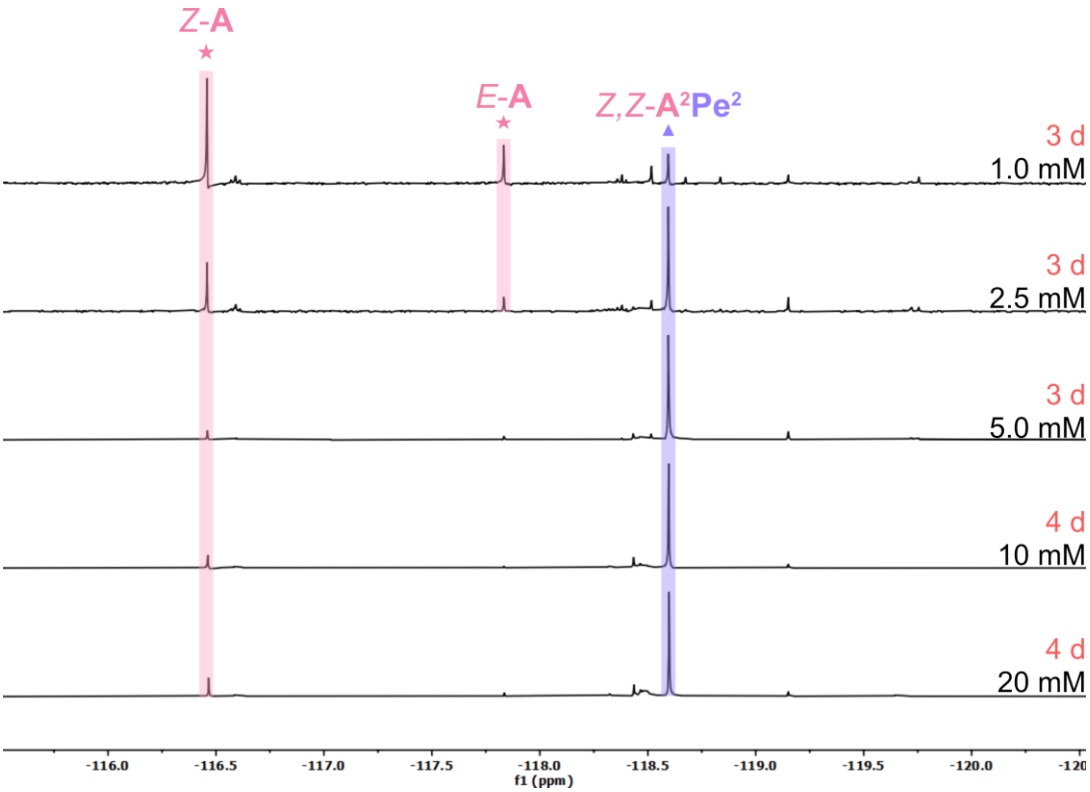

Figure S140: Comparison of $^{19}F\{^{1}H\}$ NMR spectra ($CDCl_3$, 282 MHz) of *E*-**A** and **Pe** at different concentrations after stirring under irradiation with red light.

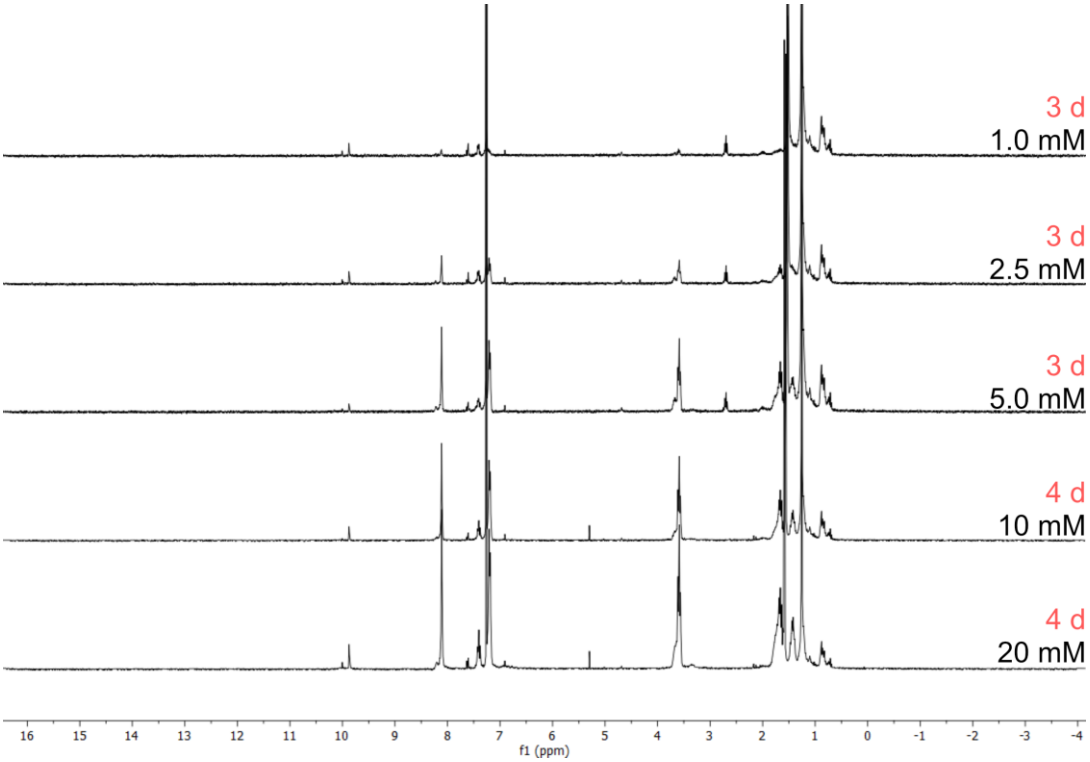

Figure S141: Comparison of ^{1}H NMR spectra ($CDCl_3$, 300 MHz) of *E*-**A** and **Pe** at different concentrations after stirring under irradiation with red light.

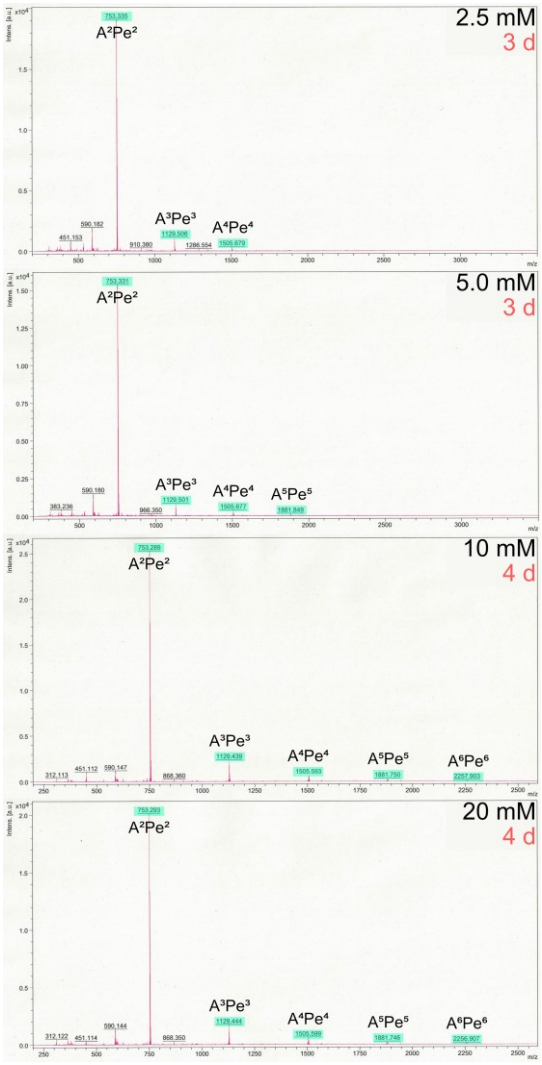

Figure S142: Comparison of MALDI-mass spectra of the reaction of *E*-**A** and **Pe** at different concentrations under irradiation with red light (660 nm). Peaks that can be attributed to $\mathbf{A^nPe^n}$ compounds are highlighted in turquoise.

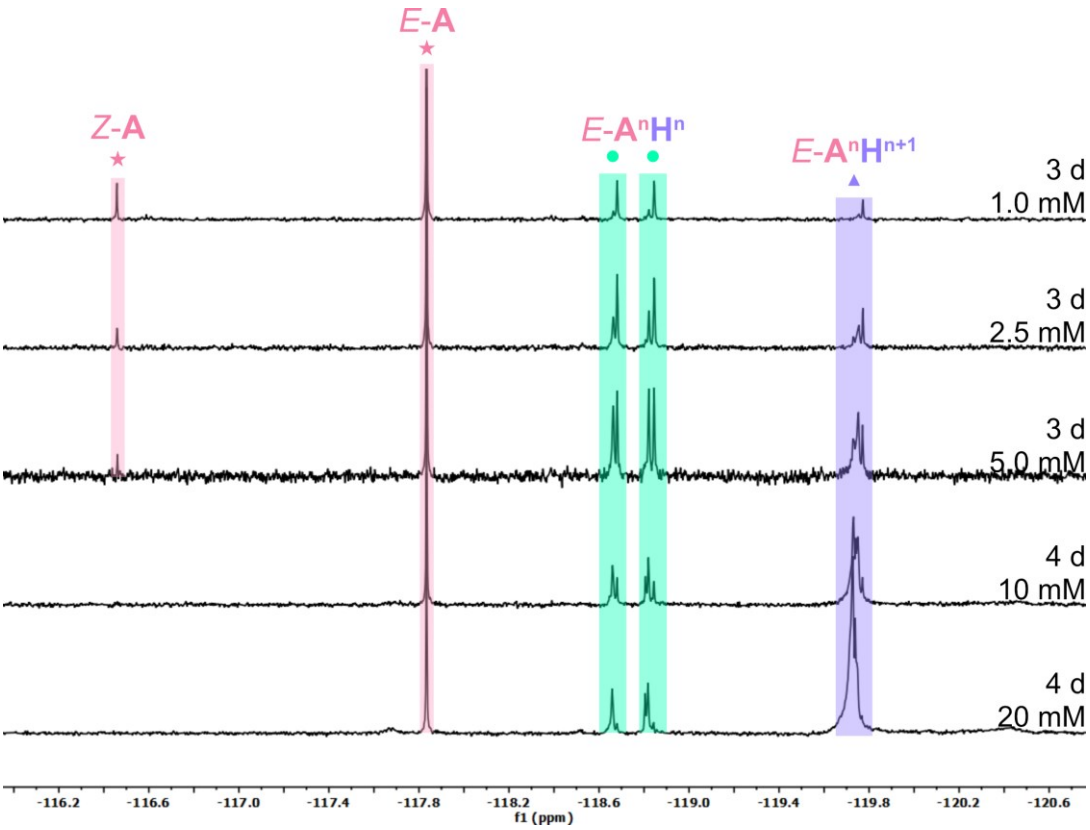

Figure S143: Comparison of $^{19}F\{^{1}H\}$ NMR spectra ($CDCl_3$, 282 MHz) of *E*-**A** and **H** at different concentrations after stirring in the dark.

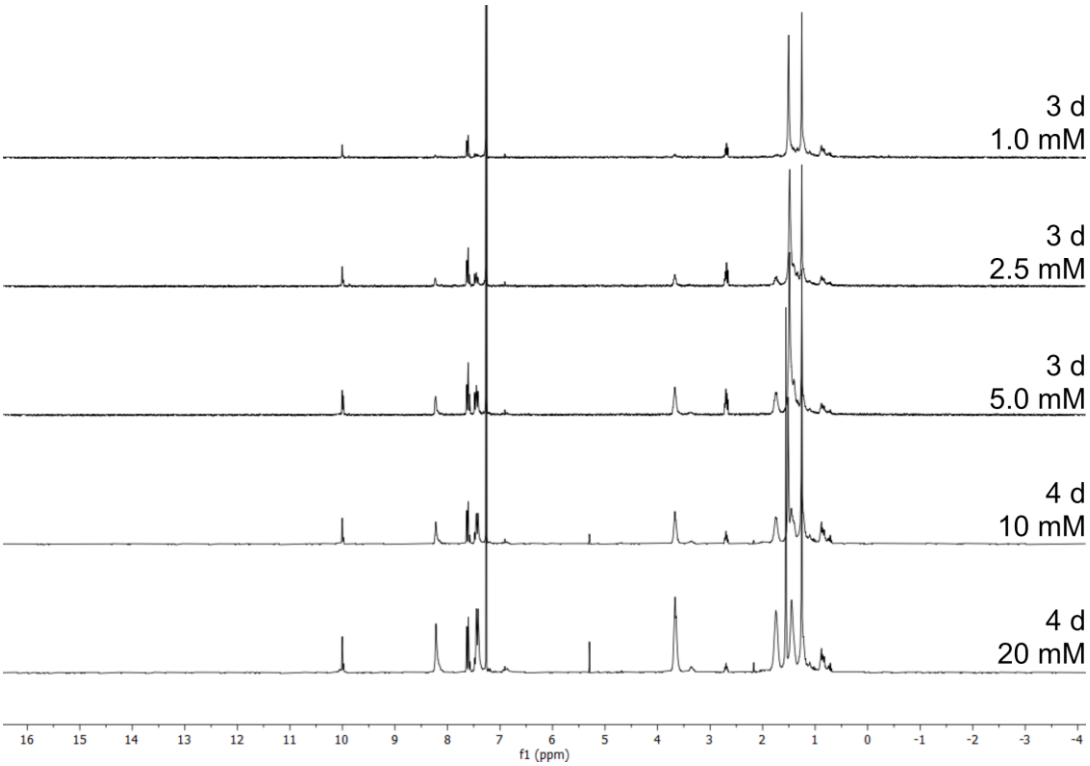

Figure S144: Comparison of ^{1}H NMR spectra ($CDCl_3$, 300 MHz) of *E*-**A** and **H** at different concentrations after stirring in the dark.

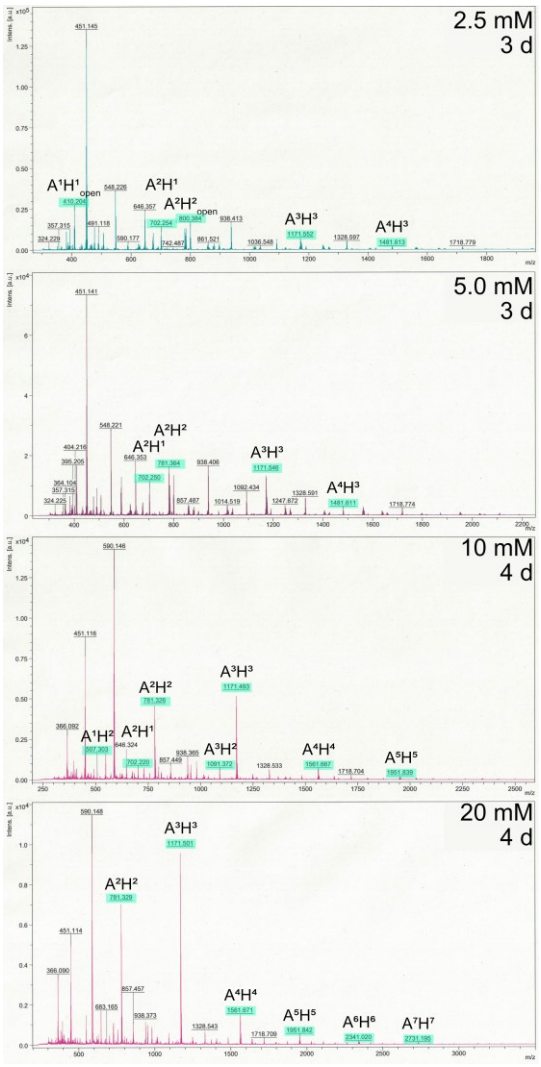

Figure S145: Comparison of MALDI-mass spectra of the reaction of *E*-**A** and **H** at different concentrations in the dark. Peaks that can be attributed to $\mathbf{A^nH^n}$ compounds are highlighted in turquoise.

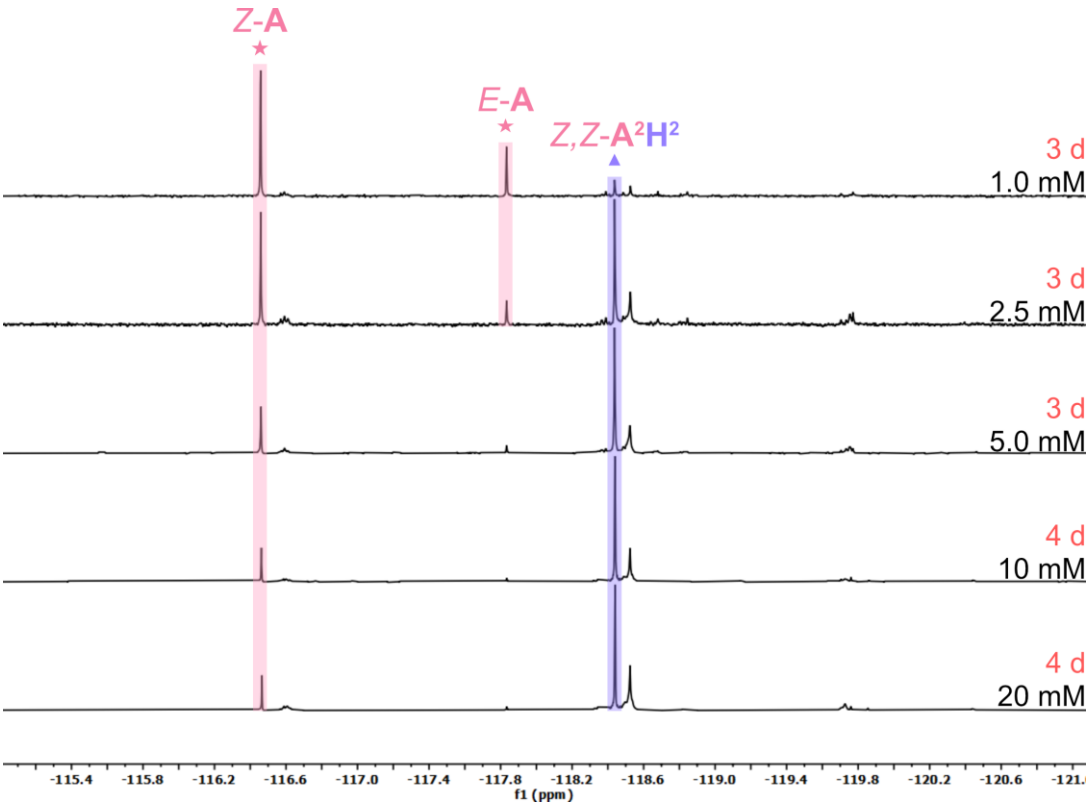

Figure S146: Comparison of $^{19}F\{^{1}H\}$ NMR spectra ($CDCl_3$, 282 MHz) of *E*-**A** and **H** at different concentrations after stirring under irradiation with red light.

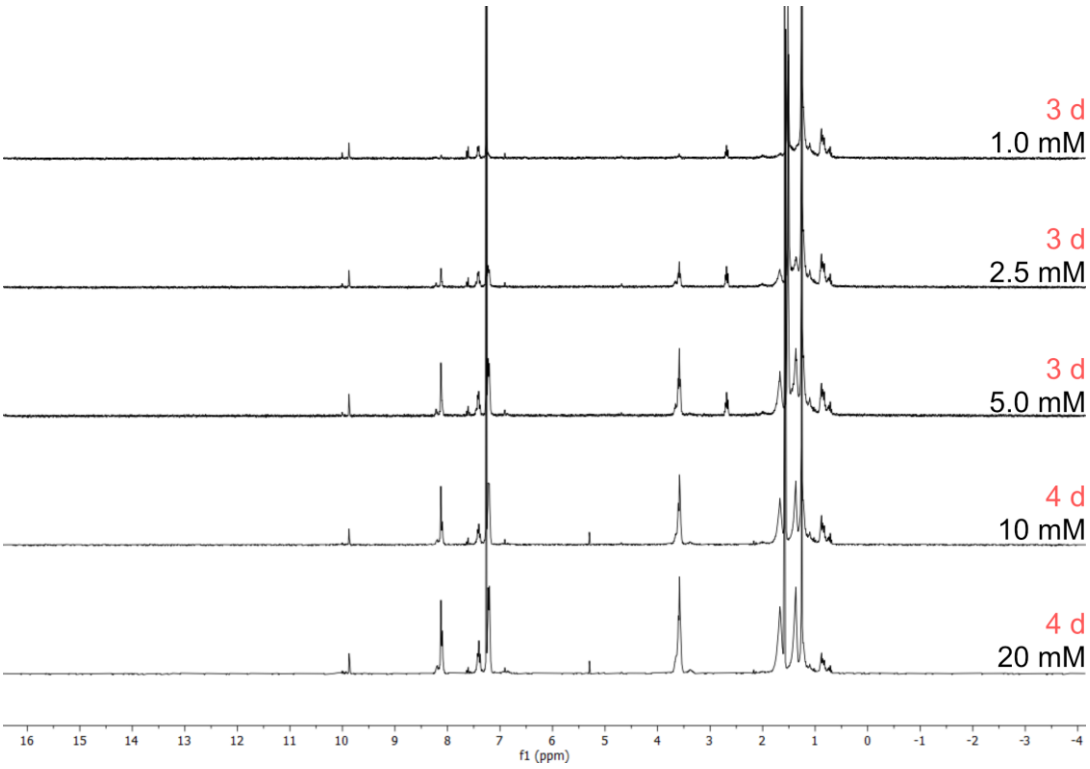

Figure S147: Comparison of ^{1}H NMR spectra ($CDCl_3$, 300 MHz) of *E*-**A** and **H** at different concentrations after stirring under irradiation with red light.

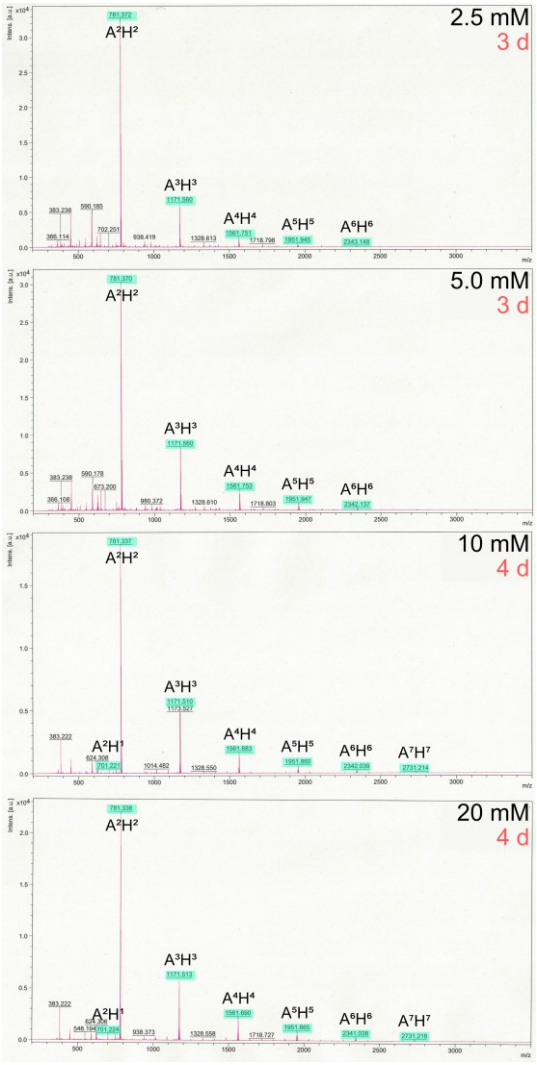

Figure S148: Comparison of MALDI-mass spectra of the reaction of *E*-**A** and **H** at different concentrations under irradiation with red light (660 nm). Peaks that can be attributed to $\mathbf{A^nH^n}$ compounds are highlighted in turquoise.

Crystallographic details

$\mathbf{A^2E^2}$

Crystals of $\mathbf{A^2E^2}$ were grown by slow liquid-liquid diffusion of EtOH into a CH_2Cl_2 solution of $\mathbf{A^2E^2}$. A dark red prism was mounted and the structure was obtained at 100 K using Cu-K_α radiation. Crystals of $\mathbf{A^2E^2}$ are heavily solvated and one dichloromethane molecule was modelled successfully (occupancy approximately 90 %). Two additional dichloromethane molecules showed rotational disorder and were ultimately removed using the SQUEEZE procedure implemented in Platon software.[121] The solvent accessible volume found (SAV) was 993 $Å^3$ with 324 electrons (per unit cell), which roughly corresponds to eight removed dichloromethane molecules per unit cell (336 electrons).

A^2O^2

Crystals of **A^2O^2** were grown by slow evaporation of a solution of **A^2O^2** in a solvent mixture of $CHCl_3$ and EtOH. A rectangular dark red prism was mounted and the structure was obtained at 100 K using Cu-K_α radiation. The slow vapor-liquid diffusion of Et_2O into a solution of **A^2O^2** in a solvent mixture of $CHCl_3$ and EtOH again yielded dark red rectangular prisms and in addition dark red platelets. SC-XRD measurements of the red platelets show a space group modification of **A^2O^2**.

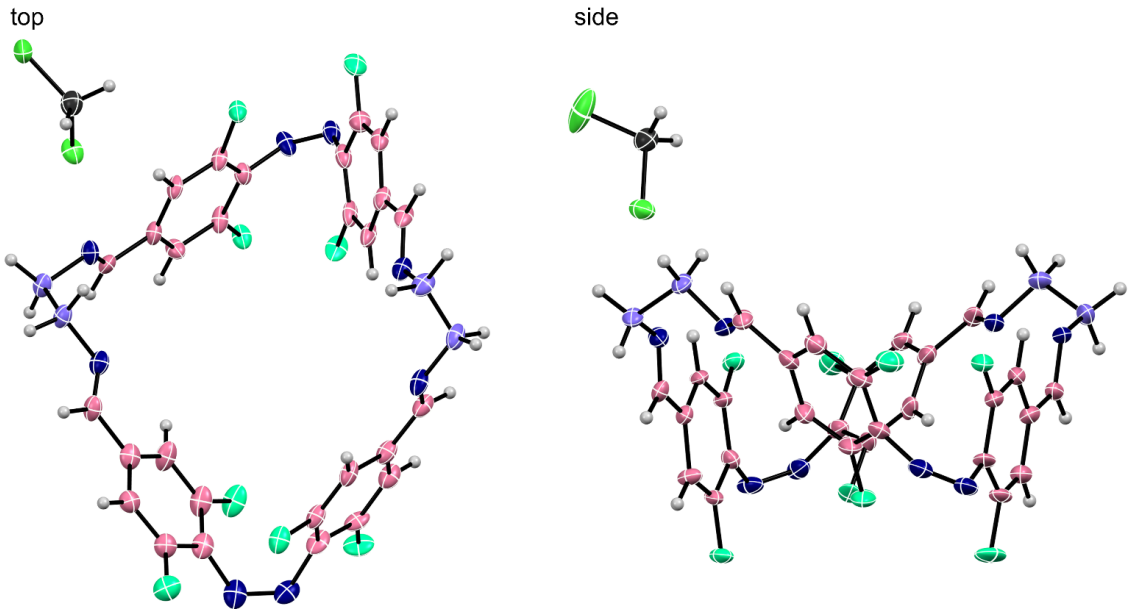

Figure S149: Data set of **A^2E^2** showing a part of the asymmetric unit bearing one unique **A^2E^2** molecule including a unique dichloromethane molecule with thermal ellipsoids set at 50% probability. The structure was measured at 100 K and solved in the monoclinic space group *Cc* with *R*int = 0.118, *R*1 = 0.087 and *wR*2 = 0.2631.

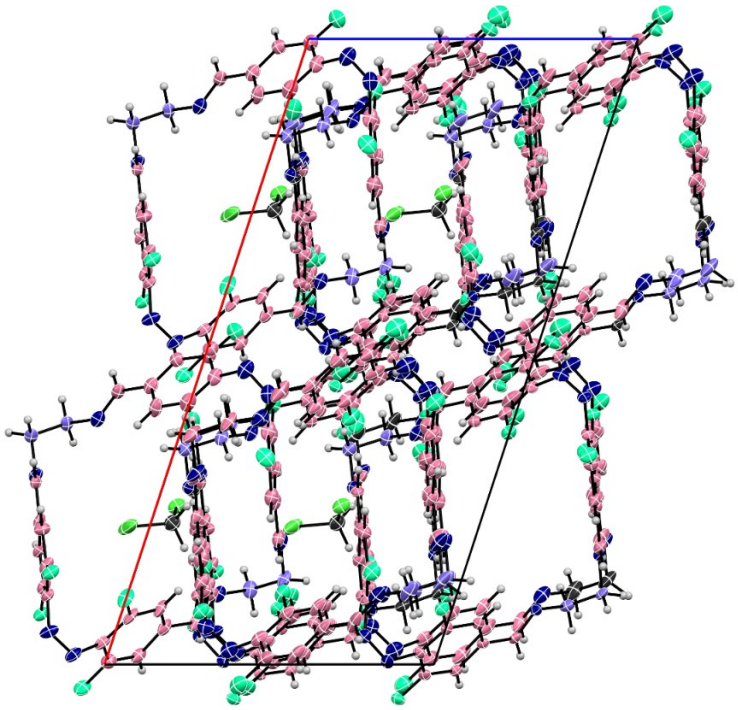

Figure S150: View of the unit cell of $\mathbf{A^2E^2}$ along the crystallographic *b* axis.

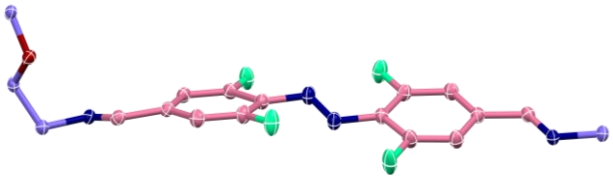

Figure S151: First data set of $\mathbf{A^2O^2}$ showing the asymmetric unit bearing half of an $\mathbf{A^2O^2}$ macrocycle with thermal ellipsoids set at 50% probability. The structure was measured at 100 K and solved in the triclinic space group *P-1*.

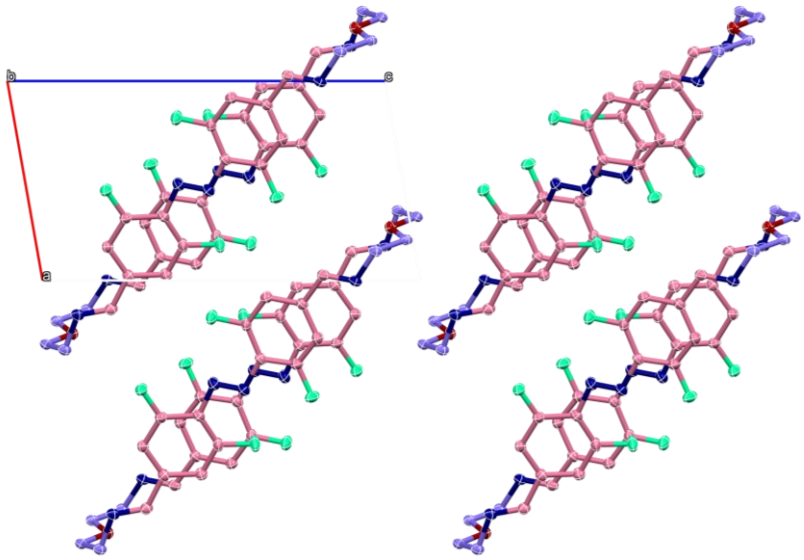

Figure S152: View of the unit cell of **A²O²** along the crystallographic *b* axis.

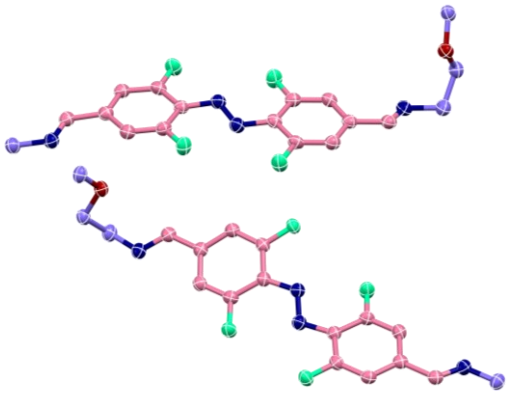

Figure S153: Second data set of **A²O²** showing the asymmetric unit bearing two half **A²O²** macrocycles with thermal ellipsoids set at 50% probability. The structure was measured at 100 K and solved in the triclinic space group *P-1*.

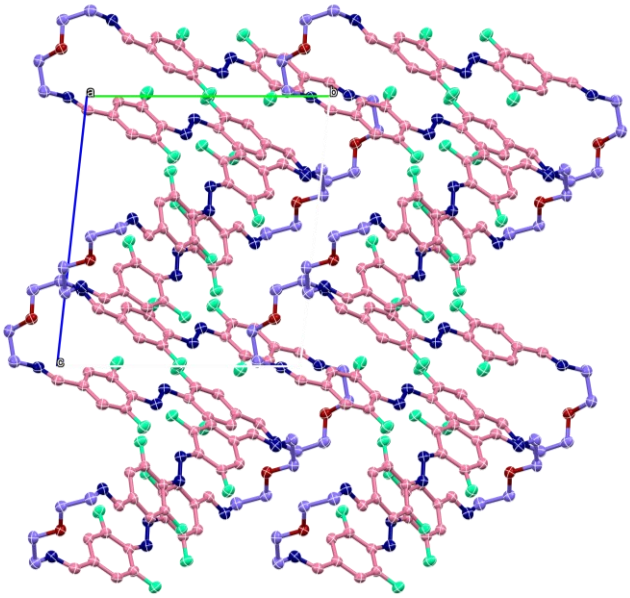

Figure S154: View of the unit cell of $\mathbf{A^2O^2}$ along the crystallographic *b* axis.

Stability of A^2E^2

Azobenzene **A** (7.44 mg, 24.0 µmol, 1.00 equiv.) was dissolved in CH_2Cl_2 (3 mL) and irradiated with red light (660 nm) for 22 hours. Diamine **E** (1.60 mg, 24.0 µmol, 1.00 equiv.) was dissolved in CH_2Cl_2 (1.5 mL) and added to the azobenzene solution over the course of 30 minutes *via* a syringe pump. After stirring for 19 hours under continuous irradiation, the mixture was distributed into three vials. The first one was kept under irradiation with red light, while one was stirred in the dark and one was stirred under irradiation with light of a wavelength of 405 nm.

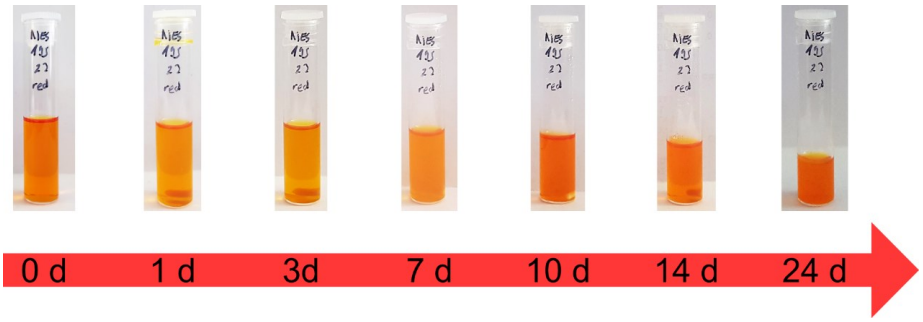

Figure S155: Sample of the $\mathbf{A^2E^2}$ reaction mixture over the course of 24 d during which it was stirred under continuous irradiation with red light (660 nm).

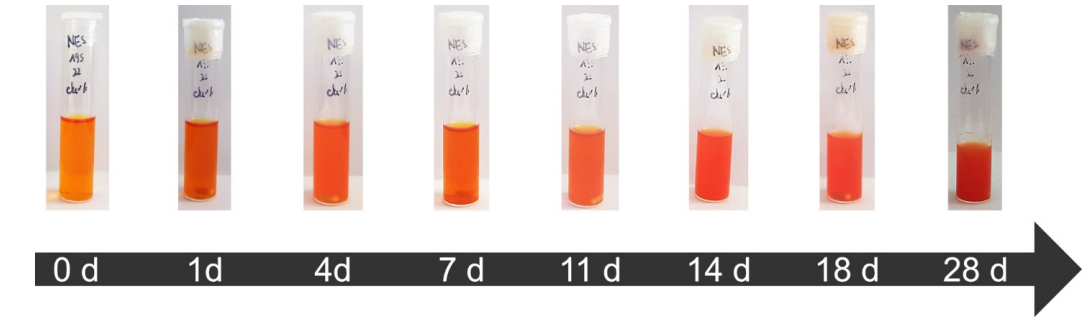

Figure S156: Sample of the **A²E²** reaction mixture over the course of 28 d, during which it was stirred in the dark.

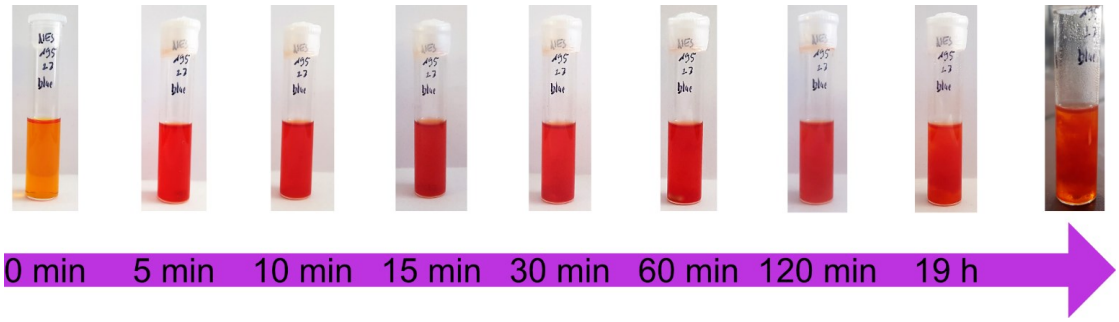

Figure S157: Sample of the **A²E²** reaction mixture over the course of 19 h during which it was stirred under continuous irradiation with light of a wavelength of 405 nm.

4.3.4 Experimental Details for 3.2.4

Synthesis

***E,E,E*-A^{3}Tren^2**

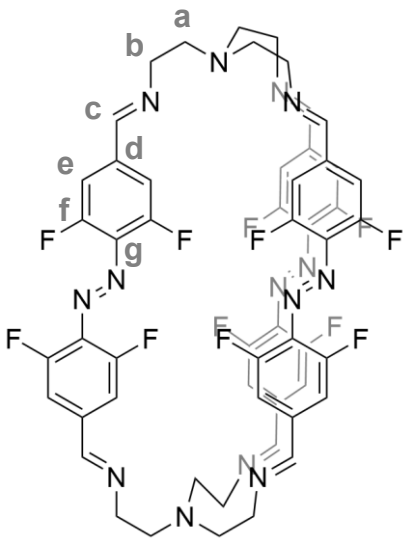

The reaction and work-up were carried out in the dark. A solution of **Tren** (9.88 µL, 66.0 µmol, 1.00 eq.) in EtOH (2 mL) was added to a stirred dark red suspension of azobenzene *E*-**A** (30.7 mg, 99.0 µmol, 1.50 eq.) in a mixture of EtOH (7 mL) and $CHCl_3$ (1 mL) over the course of 60 minutes using a syringe pump. The resulting dark red suspension was stirred for 18 hours at room temperature. During the reaction the dark red precipitate dissolved and a precipitate of a lighter red formed. The precipitate was filtered off, washed with EtOH (10 mL) and dried *in vacuo* to obtain *E,E,E*-**A^{3}Tren^2** (26.2 mg, 23.5 µmol, 71%) as a dark red powder.

^{1}H NMR (300 MHz, $CDCl_3$, 298 K): δ [ppm] = 8.04 (s, 6H, H_c), 7.01 – 6.89 (m, 12H, H_e), 3.78 (s (br), 12H, H_b), 2.81 (s (br), 12H H_a); **^{19}F{^{1}H} NMR** (282 MHz, $CDCl_3$, 298 K): δ [ppm] = -118.11 (s, 12F, F_f); **^{13}C{^{1}H} NMR** (151 MHz, $CDCl_3$, 298 K): δ [ppm] = 159.50 (s, C_c), 155.63 (d, J = 264.6 Hz, C_f), 139.14 (s, C_d), 132.49 (s, C_g), 111.32 (d, J = 22.8 Hz, C_e), 57.80 (s, C_b), 53.05 (s, C_a); **MS** HRMS (ESI) calcd. for $[C_{60}H_{50}N_{12}F_{12}]^{2+}$: 558.1835, meas.: 558.1842; **IR** $\tilde{\nu}$ [cm^{-1}]: 2957 (w), 2859 (w), 2789 (w), 1645 (m), 1620 (m), 1568 (s), 1433 (s), 1369 (m), 1342 (m), 1304 (w), 1196 (m), 1034 (s), 997 (m), 964 (w), 907 (m), 851 (s), 795 (w), 745 (w), 696 (w), 637 (w).

***E,E,E*-A^{3}Et^2**

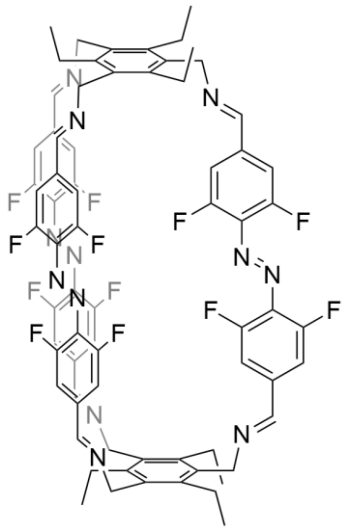

The reaction and work-up were carried out in the dark. *E*-**A** was suspended in a mixture of MeOH (1.5 mL) and CH_2Cl_2 (0.15 mL) and **Et** in MeOH (1.5 mL) was added over the course of 90 minutes using a syringe pump. After stirring overnight a red precipitate had formed which was isolated by filtration. The solid was washed with MeOH (2 x 2 mL) and dried under reduced pressure. The obtained red solid was insoluble in $CDCl_3$ and the isolation of a cage based on **A** and **Et** was unsuccessful.

UV/VIS spectroscopy

Table S34: Concentrations of the different compounds and the respective irradiation wavelength for the different measurements

Compound	λ_{irr} / nm	c / µM
E,E,E-A^{3}Tren^2	405	5.84
	565	5.84
	660	5.84

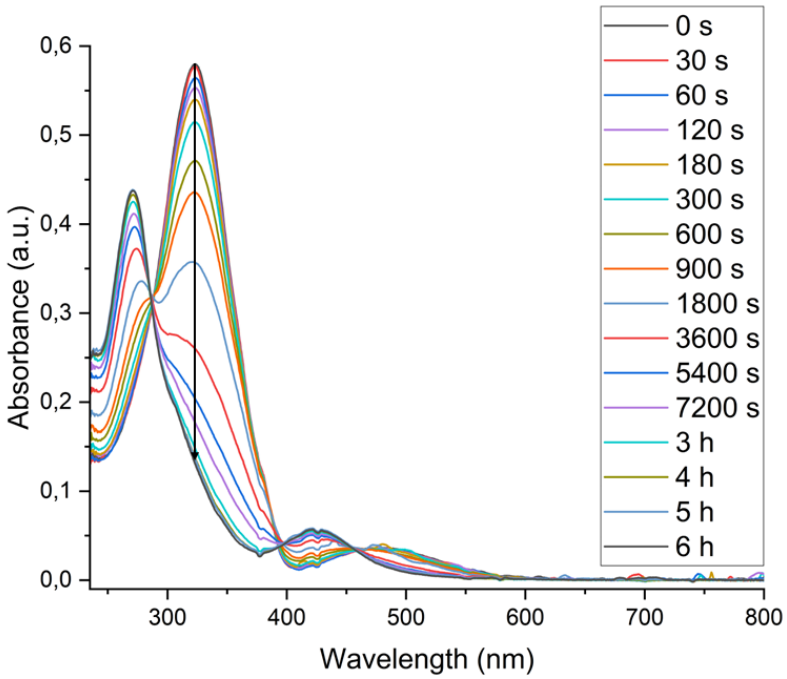

Figure S158: UV/VIS spectra of **A^3Tren^2** after irradiation with red light (660 nm) in CH_2Cl_2.

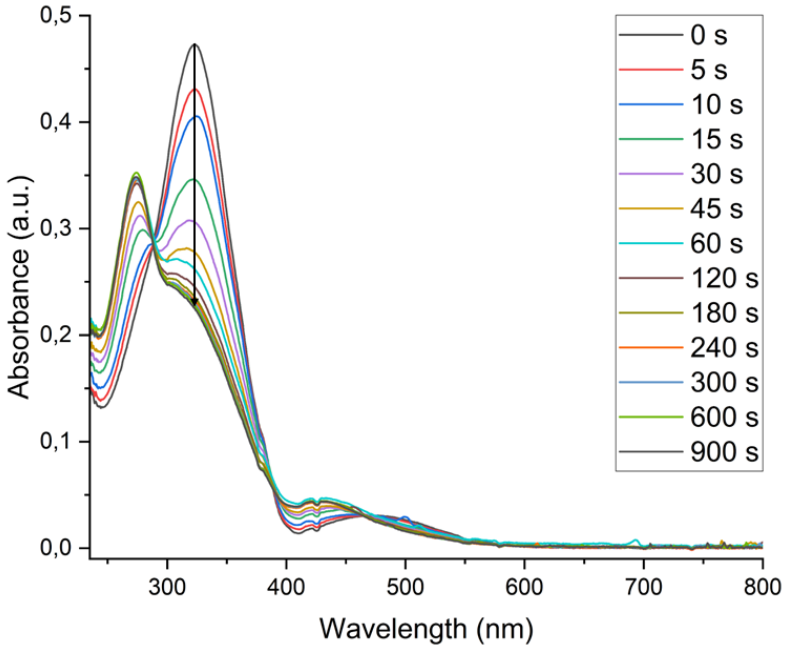

Figure S159: UV/VIS spectra of **A^3Tren^2** after irradiation with green light (565 nm) in CH_2Cl_2.

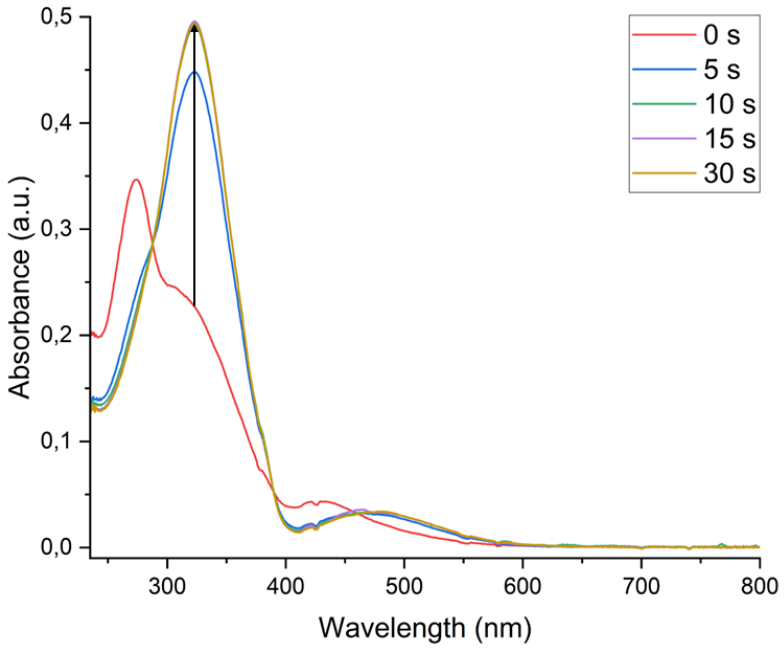

Figure S160: UV/VIS spectra of **A^{3}Tren^2** A solution that was *Z*-enriched by irradiation with green light was irradiated with light of the wavelength of 405 nm in CH_2Cl_2.

Table S35: Wavelengths of the absorption maxima λ_{max} and molar attenuation coefficients ε of the imine cage *E,E,E*-**A^{3}Tren^2**.

	E,E,E-**A^{3}Tren^2**	
	π→π*	n→π*
λ_{max} / nm	323	471
ε / 10^3 L mol^{-1} cm^{-1}	81.0	5.26

Crystallographic details

E,E,E-A^{3}Tren^2

Crystals of *E,E,E*-**A^{3}Tren^2** were grown by slow evaporation of a CHCl3 MeOH solution. A blood red prism was mounted, and the structure was obtained at 100 K using Cu-K_α radiation. Crystals of *E,E,E*-**A^{3}Tren^2** were solvated and the extrinsic pore was occupied by two heavily disordered chloroform solvent molecules (occupancy each around 30%) that could not be modelled. They were ultimately removed using the SQUEEZE procedure implemented in Platon software.[121] The solvent accessible volume (SAV) was 1016 Å^3 with 184 electrons (per unit cell).

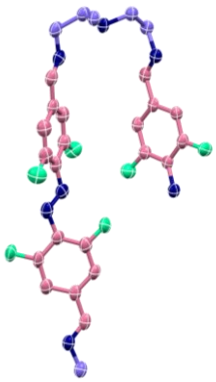

Figure S161: Data set of **A^{3}Tren^2** showing the asymmetric unit bearing half of an **A^{3}Tren^2** cage with thermal ellipsoids set at 50% probability. The structure was measured at 100 K and solved in the monoclinic space group *C2/c* with *R*int = 0.115.

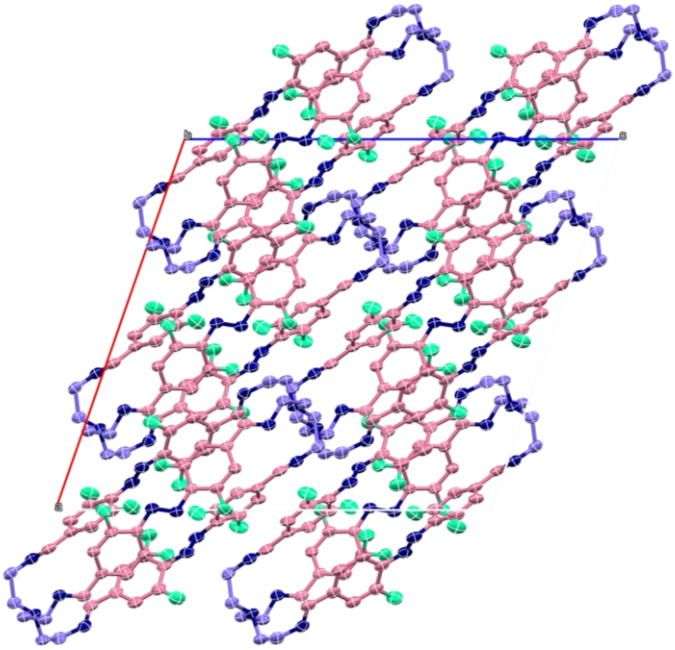

Figure S162: View of the unit cell of **A^{2}E^2** along the crystallographic *b* axis.

Irradiation studies

Irradiation of A^{3}Tren^2

A solution of *E,E,E*-**A^{3}Tren^2** (1.6 mg, 1.5 µmol) in CD_2Cl_2 (0.80 ml) was prepared. The solution wasa stirred under irradiation with red light (660 nm) for 5 days, followed by irradiation with UV light (405 nm) for 14 h, before the solution was again irradiated with red light for 5 days. The reaction was monitored by ^{1}H and ^{19}F{^{1}H} spectroscopy and a MALDI-mass spectrum was recorded after the first irradiation period.

4.3.5 Experimental Details for 3.2.5

Irradiation experiments

Competitive experiments using D

Stock solutions of **A** as well as of diamines **E**, **Pr**, **B**, **H**, **mP**, **DPEN**, and **D** in $CDCl_3$ were prepared. The stock solution of **A** was distributed into two parts, while one was kept in the dark the other part was irradiated with red light (660 nm) until a *E* to *Z* ration of approximately 77 to 23 as determined by $^{19}F\{^1H\}$ NMR was achieved. The stock solutions of *E*-**A** and *Z*-**A** were mixed with diamine **D** in an aldehyde to amine ratio of 1 to 1.2 and 1.2 equivalents of one of the other diamines were added before the mixture was diluted to 1.0 ml yielding a a total concentration of 5.0 mM in regards to the aldehyde. The reactions containing *E*-**A** were stirred in the dark and then stirred under irradiation with red light. The vials containing *Z*-**A** were stirred under continuous irradiation. The reactions were monitored using ^1H and $^{19}F\{^1H\}$ NMR spectroscopy and MALDI-mass spectrometry. Reaction times and parameters are summarised in Table S36.

Table S36: Amount of starting materials employed in each reaction and reaction times.

Aldehyde	Amine 1	Amine 2	Reaction time
A (1.6 mg, 5.0 µmol, 1.0 eq.)	**D** (0.69 mg, 6.0 µmol, 1.2 eq.)	**E** (0.36 mg, 6.0 µmol, 1.2 eq.)	3 days (dark), 3 days (660 nm)
			3 days
		Pr (0.44 mg, 6.0 µmol, 1.2 eq.)	3 days (dark), 3 days (660 nm)
			3 days
		B (0.53 mg, 6.0 µmol, 1.2 eq.)	3 days (dark), 3 days (660 nm)
			3 days
		H (0.70 mg, 6.0 µmol, 1.2 eq.)	3 days (dark), 3 days (660 nm)
			3 days
		mP (0.82 mg, 6.0 µmol, 1.2 eq.)	3 days (dark), 3 days (660 nm)
			3 days
		DPEN (1.3 mg, 6.0 µmol, 1.2 eq.)	3 days (dark), 3 days (660 nm)
			3 days

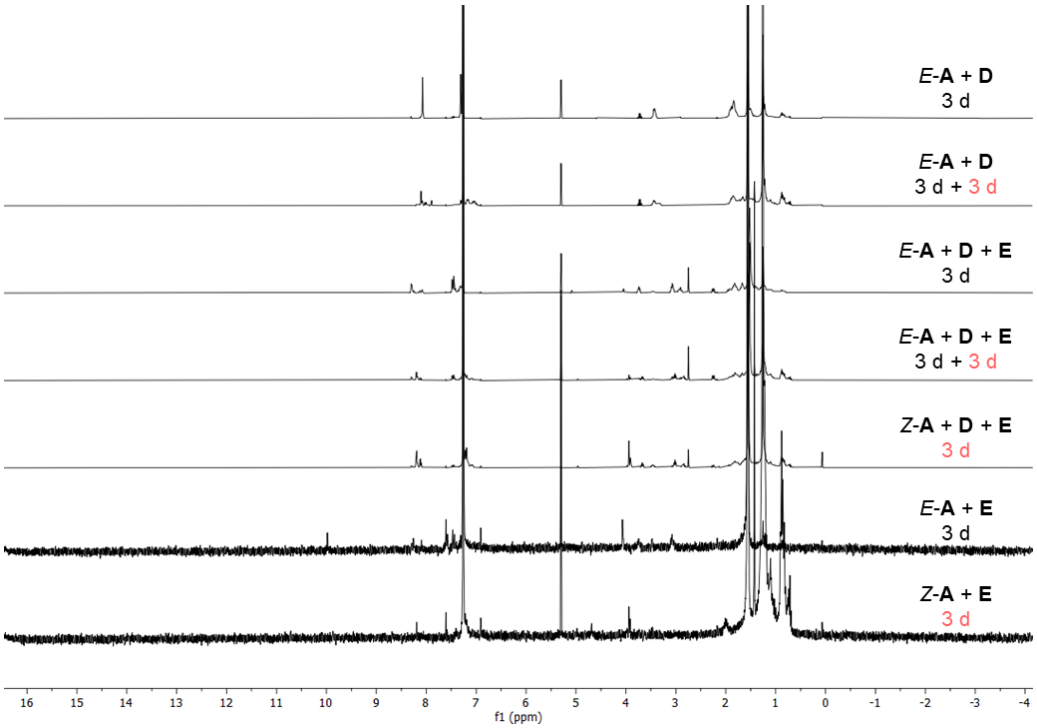

Figure S163: Comparison of ^{1}H NMR spectra ($CDCl_3$, 300 MHz) of the reaction of *E*-**A** and **D** in the dark and after irradiation with red light (660 nm), of the reaction mixture of *E*-**A**, **D**, and **E** in the dark and after irradiation with red light, of the reaction of *Z*-**A**, **D**, and **E** under continuous irradiation with red light and of the reaction of *E*-**A** with **E** in the dark and *Z*-**A** with **E** under continuous irradiation with red light.

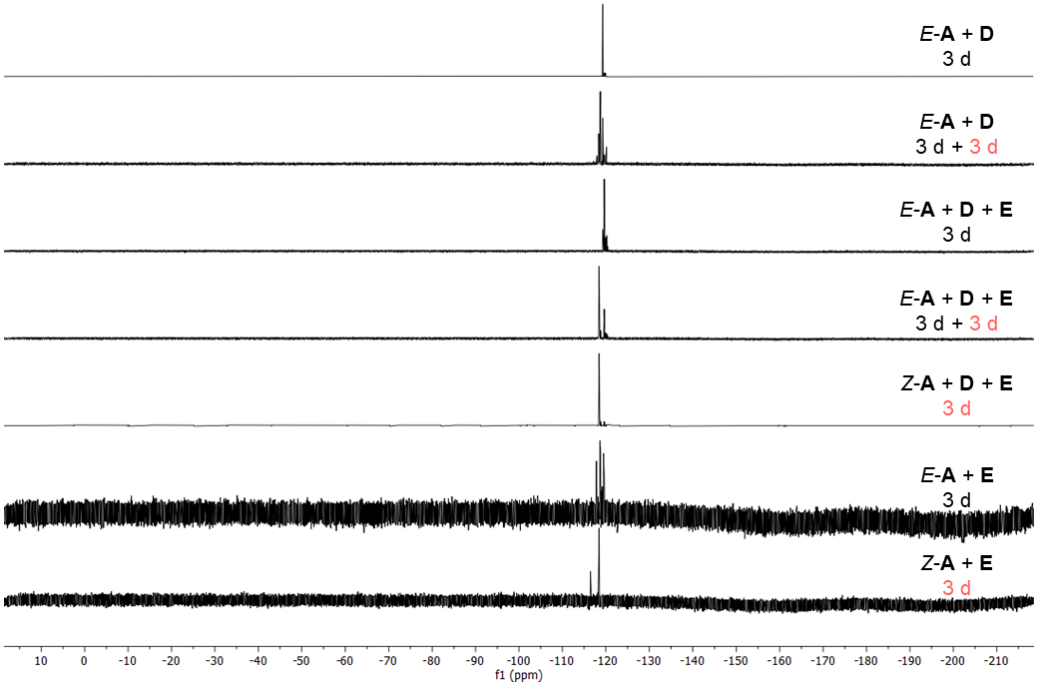

Figure S164: Comparison of ^{19}F{^{1}H} NMR spectra ($CDCl_3$, 282 MHz) of the reaction of *E*-**A** and **D** in the dark and after irradiation with red light (660 nm), of the reaction mixture of *E*-**A**, **D**, and **E** in the dark and after irradiation with red light, of the reaction of *Z*-**A**, **D**, and **E** under continuous irradiation with red light and of the reaction of *E*-**A** with **E** in the dark and *Z*-**A** with **E** under continuous irradiation with red light.

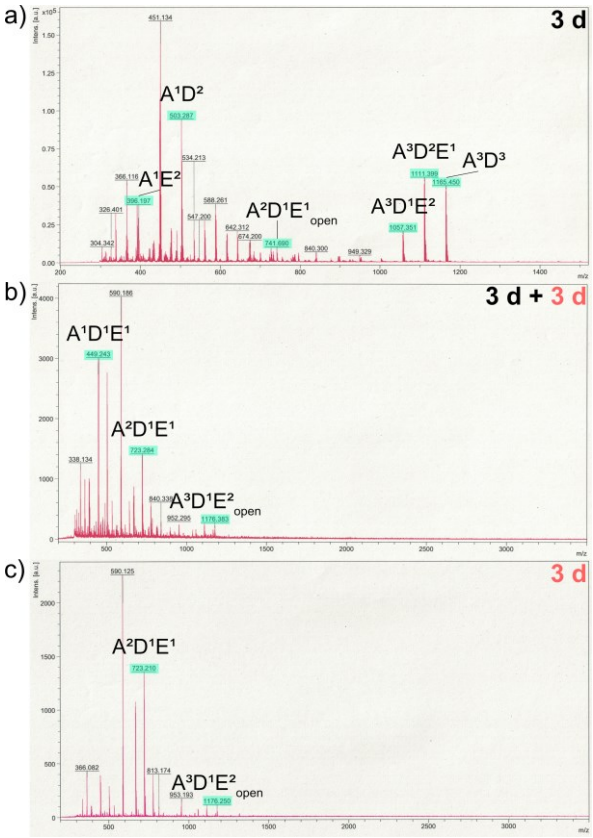

Figure S165: Comparison of MALDI-mass spectra of the reaction of *E*-**A**, **D**, and **E** a) in the dark and b) under irradiation with red light (660 nm) and c) of the reaction of *Z*-**A**, **D**, and **E** under continuous irradiation with red light. Peaks that can be attributed to $\mathbf{A^nD^n}$ or $\mathbf{A^nE^n}$ compounds or mixed $\mathbf{A^nD^nE^n}$ compounds are highlighted in turquoise.

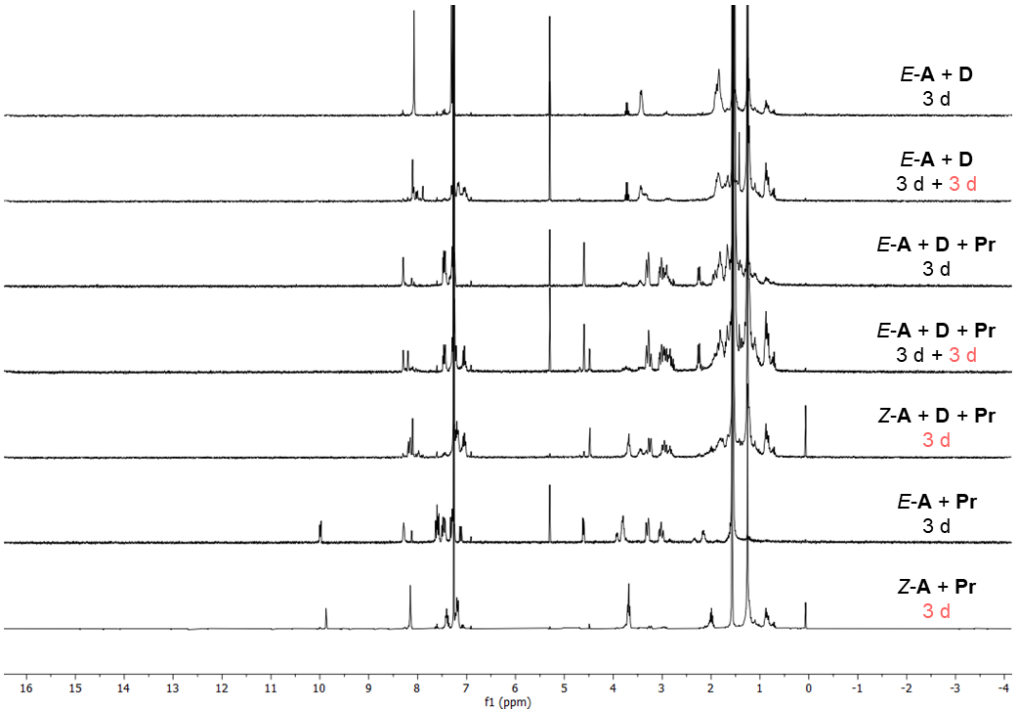

Figure S166: Comparison of ^{1}H NMR spectra ($CDCl_3$, 300 MHz) of the reaction of *E*-**A** and **D** in the dark and after irradiation with red light (660 nm), of the reaction mixture of *E*-**A**, **D**, and **Pr** in the dark and after irradiation with red light, of the reaction of *Z*-**A**, **D**, and **Pr** under continuous irradiation with red light and of the reaction of *E*-**A** with **Pr** in the dark and *Z*-**A** with **Pr** under continuous irradiation with red light.

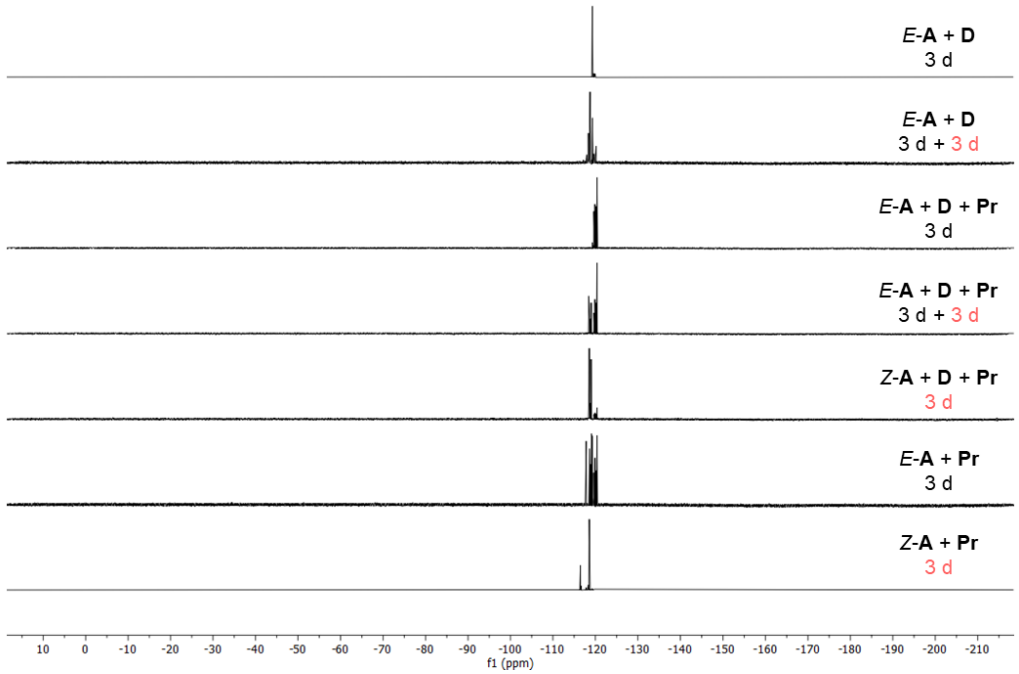

Figure S167: Comparison of ^{19}F{^{1}H} NMR spectra ($CDCl_3$, 282 MHz) of the reaction of *E*-**A** and **D** in the dark and after irradiation with red light (660 nm), of the reaction mixture of *E*-**A**, **D**, and **Pr** in the dark and after irradiation with red light, of the reaction of *Z*-**A**, **D**, and **Pr** under continuous irradiation with red light and of the reaction of *E*-**A** with **Pr** in the dark and *Z*-**A** with **Pr** under continuous irradiation with red light.

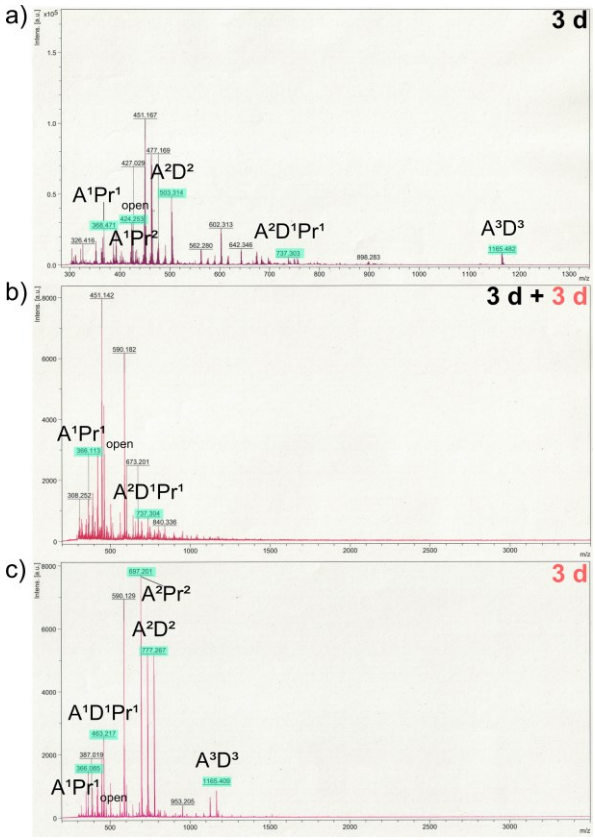

Figure S168: Comparison of MALDI-mass spectra of the reaction of *E*-**A**, **D**, and **Pr** a) in the dark and b) under irradiation with red light (660 nm) and c) of the reaction of *Z*-**A**, **D**, and **Pr** under continuous irradiation with red light. Peaks that can be attributed to $\mathbf{A^nD^n}$ or $\mathbf{A^nPr^n}$ compounds or mixed $\mathbf{A^nD^nPr^n}$ compounds are highlighted in turquoise.

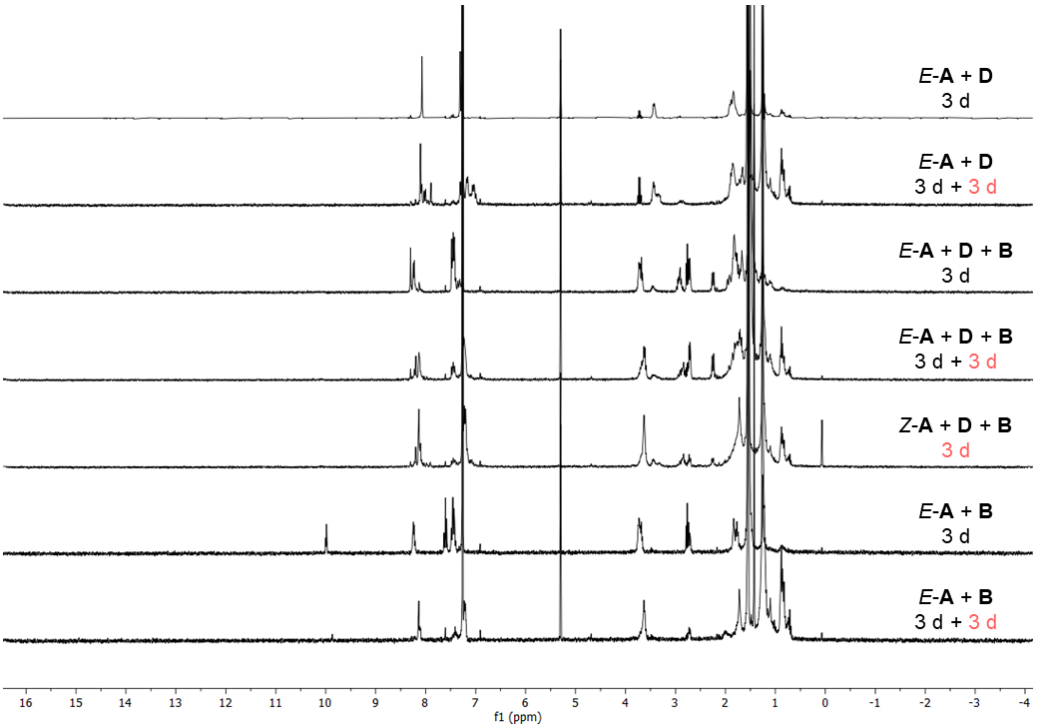

Figure S169: Comparison of ^{1}H NMR spectra ($CDCl_3$, 300 MHz) of the reaction of *E*-**A** and **D** in the dark and after irradiation with red light (660 nm), of the reaction mixture of *E*-**A**, **D**, and **B** in the dark and after irradiation with red light, of the reaction of *Z*-**A**, **D**, and **B** under continuous irradiation with red light and of the reaction of *E*-**A** with **B** in the dark and after irradiation with red light.

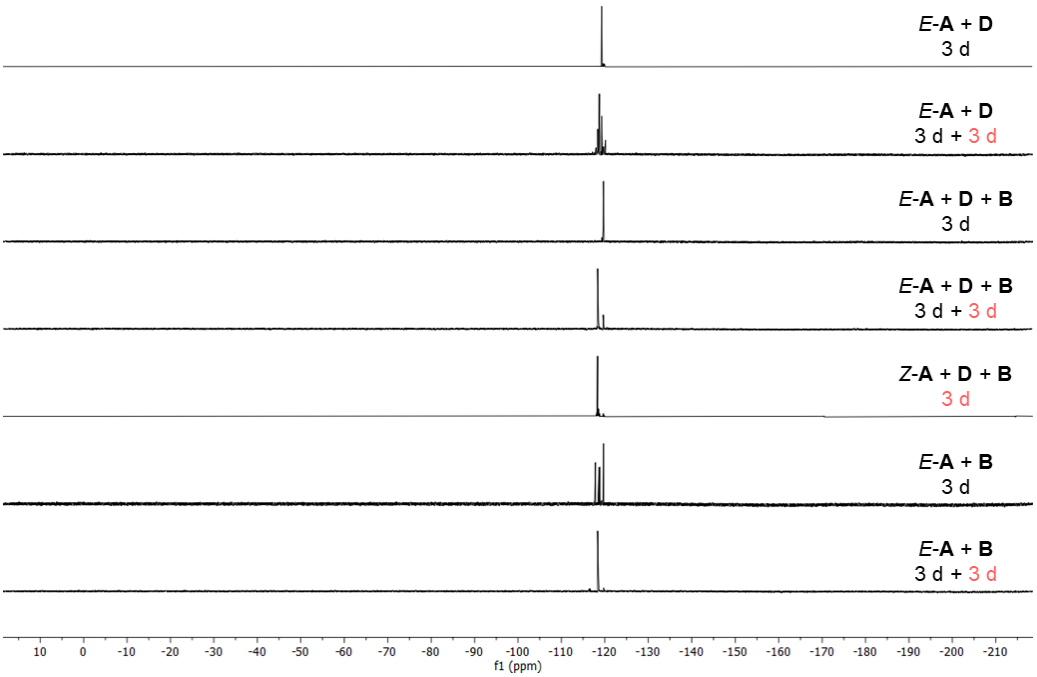

Figure S170: Comparison of $^{19}F\{^{1}H\}$ NMR spectra ($CDCl_3$, 282 MHz) of the reaction of *E*-**A** and **D** in the dark and after irradiation with red light (660 nm), of the reaction mixture of *E*-**A**, **D**, and **B** in the dark and after irradiation with red light, of the reaction of *Z*-**A**, **D**, and **B** under continuous irradiation with red light and of the reaction of *E*-**A** with **B** in the dark and after irradiation with red light.

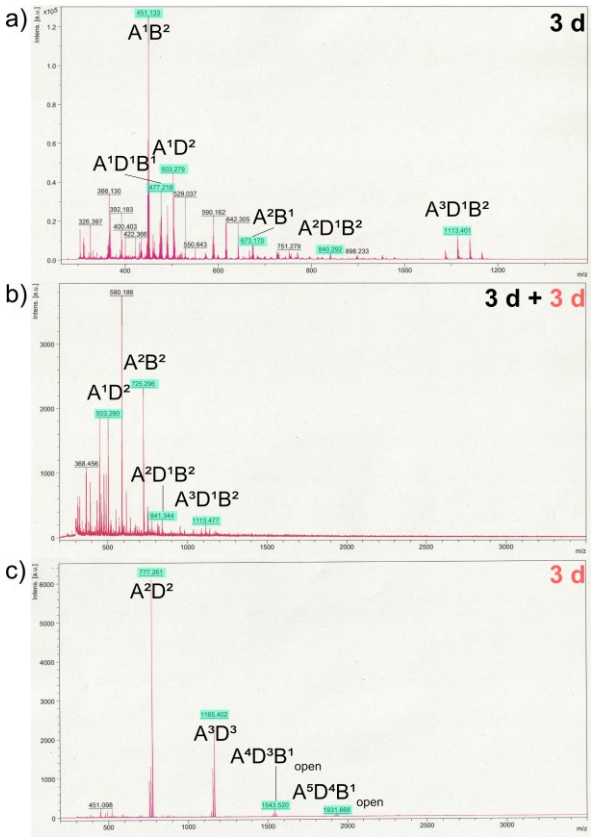

Figure S171: Comparison of MALDI-mass spectra of the reaction of *E*-**A**, **D**, and **B** a) in the dark and b) under irradiation with red light (660 nm) and c) of the reaction of *Z*-**A**, **D**, and **B** under continuous irradiation with red light. Peaks that can be attributed to $\mathbf{A^nD^n}$ or $\mathbf{A^nB^n}$ compounds or mixed $\mathbf{A^nD^nB^n}$ compounds are highlighted in turquoise.

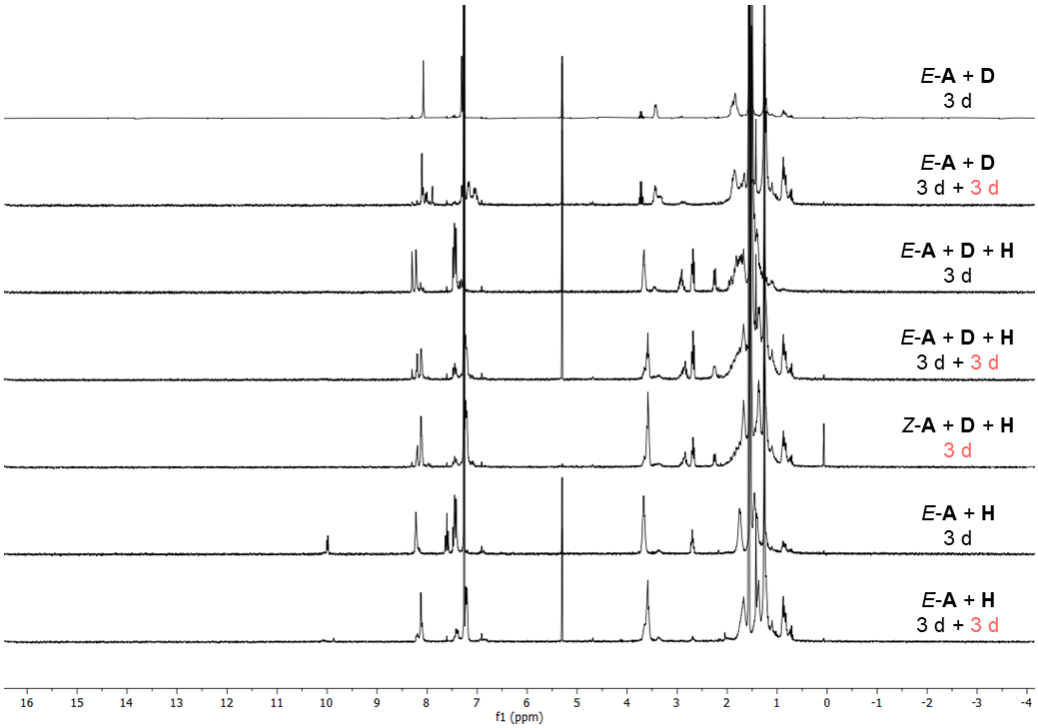

Figure S172: Comparison of ^{1}H NMR spectra ($CDCl_3$, 300 MHz) of the reaction of *E*-**A** and **D** in the dark and after irradiation with red light (660 nm), of the reaction mixture of *E*-**A**, **D**, and **H** in the dark and after irradiation with red light, of the reaction of *Z*-**A**, **D**, and **H** under continuous irradiation with red light and of the reaction of *E*-**A** with **H** in the dark and after irradiation with red light.

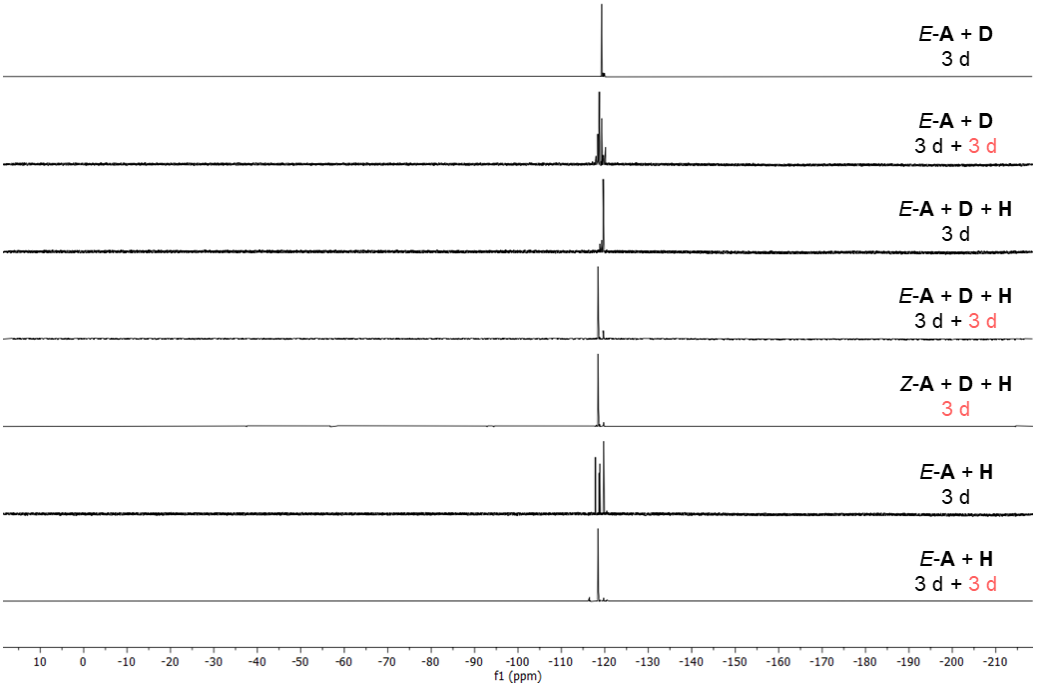

Figure S173: Comparison of ^{19}F{^{1}H} NMR spectra ($CDCl_3$, 282 MHz) of the reaction of *E*-**A** and **D** in the dark and after irradiation with red light (660 nm), of the reaction mixture of *E*-**A**, **D**, and **H** in the dark and after irradiation with red light, of the reaction of *Z*-**A**, **D**, and **H** under continuous irradiation with red light and of the reaction of *E*-**A** with **H** in the dark and after irradiation with red light.

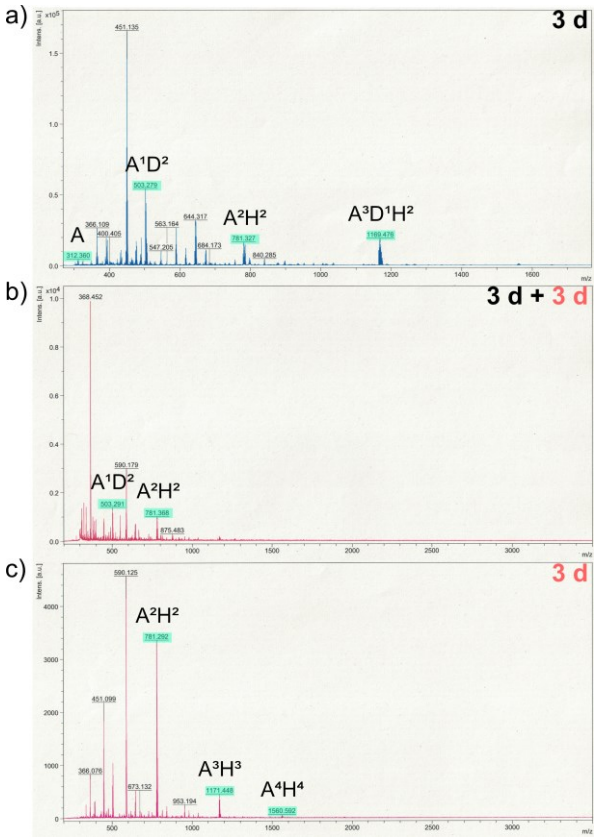

Figure S174: Comparison of MALDI-mass spectra of the reaction of *E*-**A**, **D**, and **H** a) in the dark and b) under irradiation with red light (660 nm) and c) of the reaction of *Z*-**A**, **D**, and **H** under continuous irradiation with red light. Peaks that can be attributed to $\mathbf{A^nD^n}$ or $\mathbf{A^nH^n}$ compounds or mixed $\mathbf{A^nD^nH^n}$ compounds are highlighted in turquoise.

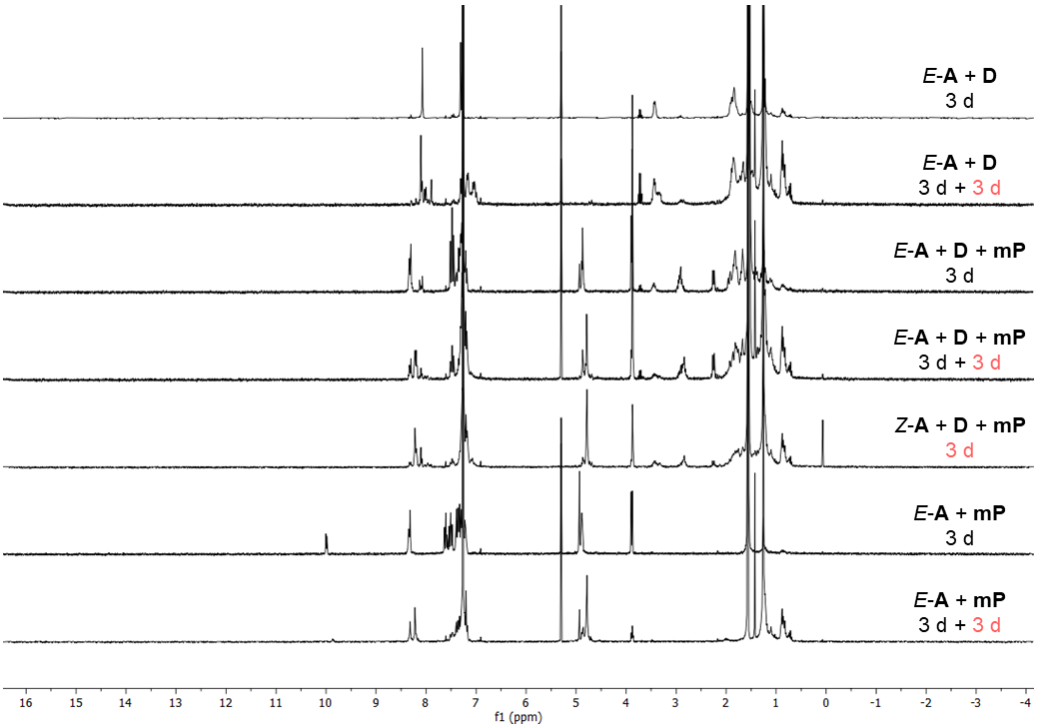

Figure S175: Comparison of ^{1}H NMR spectra ($CDCl_3$, 300 MHz) of the reaction of *E*-**A** and **D** in the dark and after irradiation with red light (660 nm), of the reaction mixture of *E*-**A**, **D**, and **mP** in the dark and after irradiation with red light, of the reaction of *Z*-**A**, **D**, and **mP** under continuous irradiation with red light and of the reaction of *E*-**A** with **mP** in the dark and after irradiation with red light.

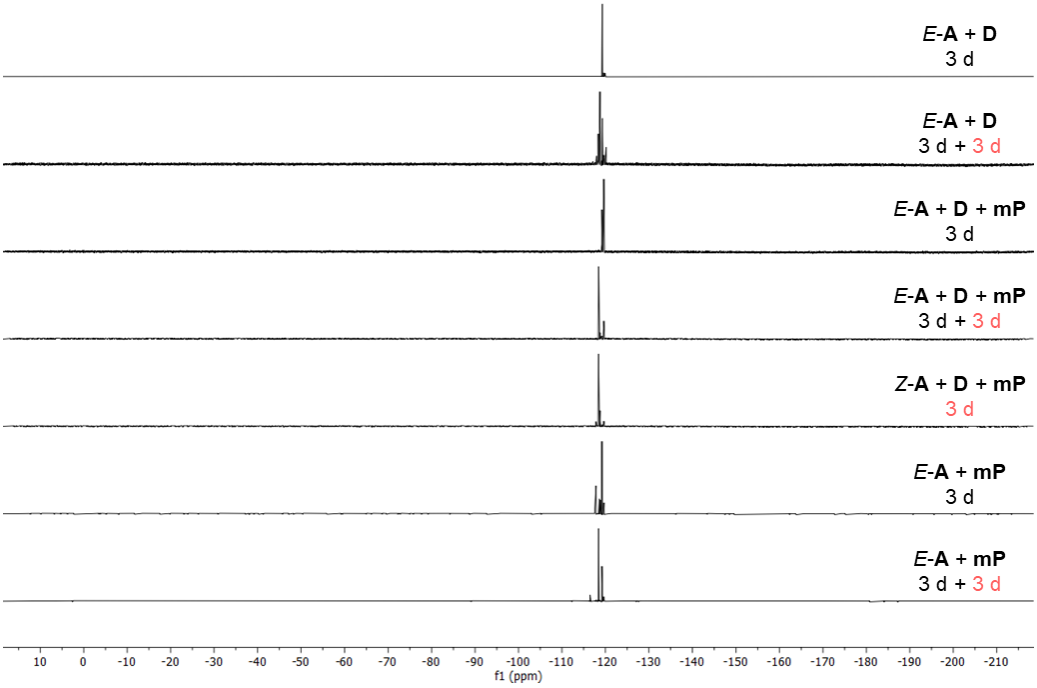

Figure S176: Comparison of ^{19}F{^{1}H} NMR spectra ($CDCl_3$, 282 MHz) of the reaction of *E*-**A** and **D** in the dark and after irradiation with red light (660 nm), of the reaction mixture of *E*-**A**, **D**, and **mP** in the dark and after irradiation with red light, of the reaction of *Z*-**A**, **D**, and **mP** under continuous irradiation with red light and of the reaction of *E*-**A** with **mP** in the dark and after irradiation with red light.

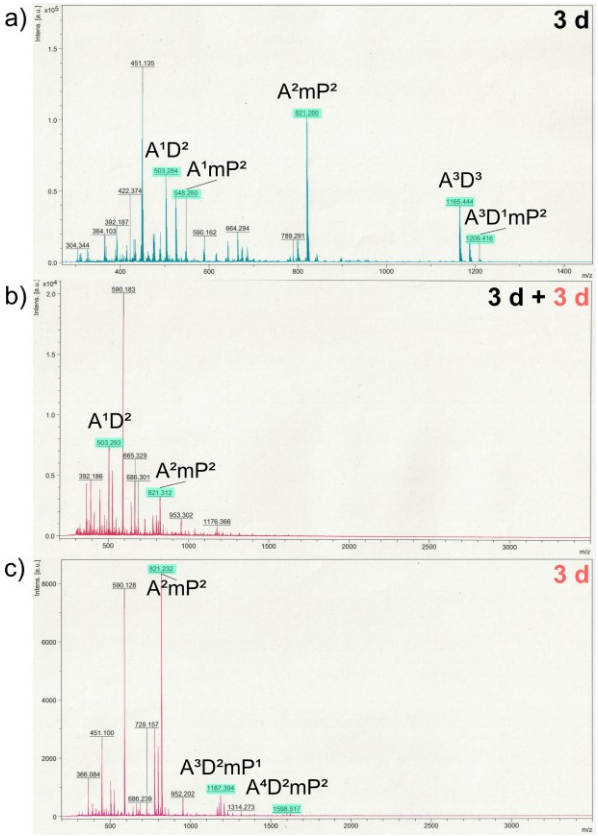

Figure S177: Comparison of MALDI-mass spectra of the reaction of *E*-**A**, **D**, and **mP** a) in the dark and b) under irradiation with red light (660 nm) and c) of the reaction of *Z*-**A**, **D**, and **mP** under continuous irradiation with red light. Peaks that can be attributed to $\mathbf{A^nD^n}$ or $\mathbf{A^nmP^n}$ compounds or mixed $\mathbf{A^nD^nmP^n}$ compounds are highlighted in turquoise.

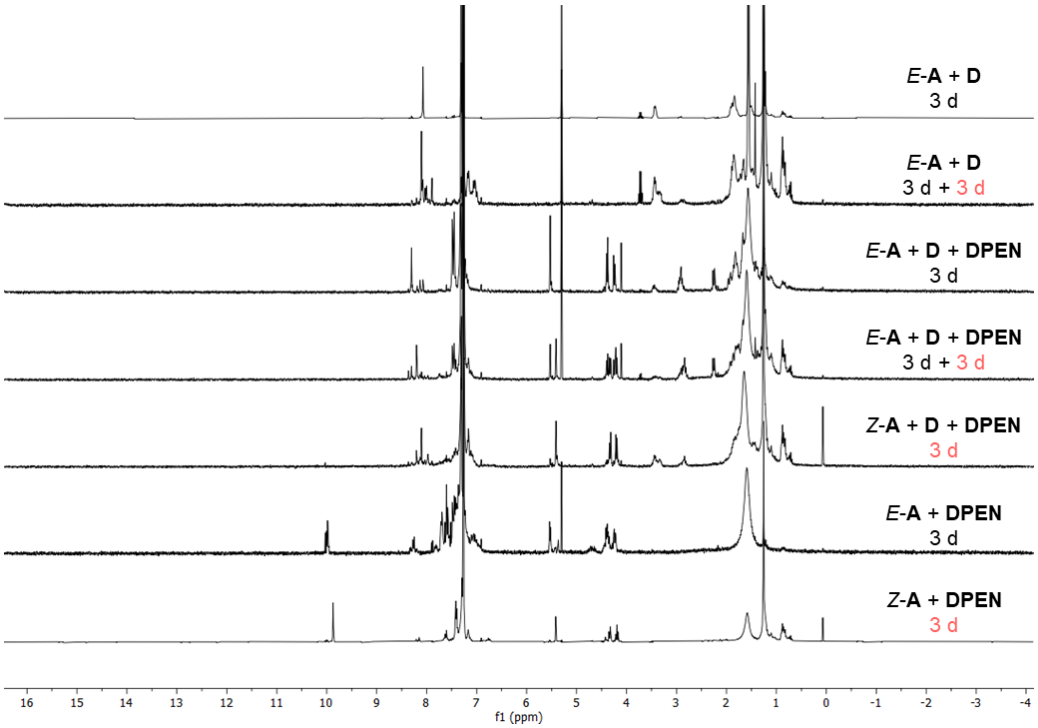

Figure S178: Comparison of ^{1}H NMR spectra ($CDCl_3$, 300 MHz) of the reaction of *E*-**A** and **D** in the dark and after irradiation with red light (660 nm), of the reaction mixture of *E*-**A**, **D**, and **DPEN** in the dark and after irradiation with red light, of the reaction of *Z*-**A**, **D**, and **DPEN** under continuous irradiation with red light and of the reaction of *E*-**A** with **DPEN** in the dark and after irradiation with red light.

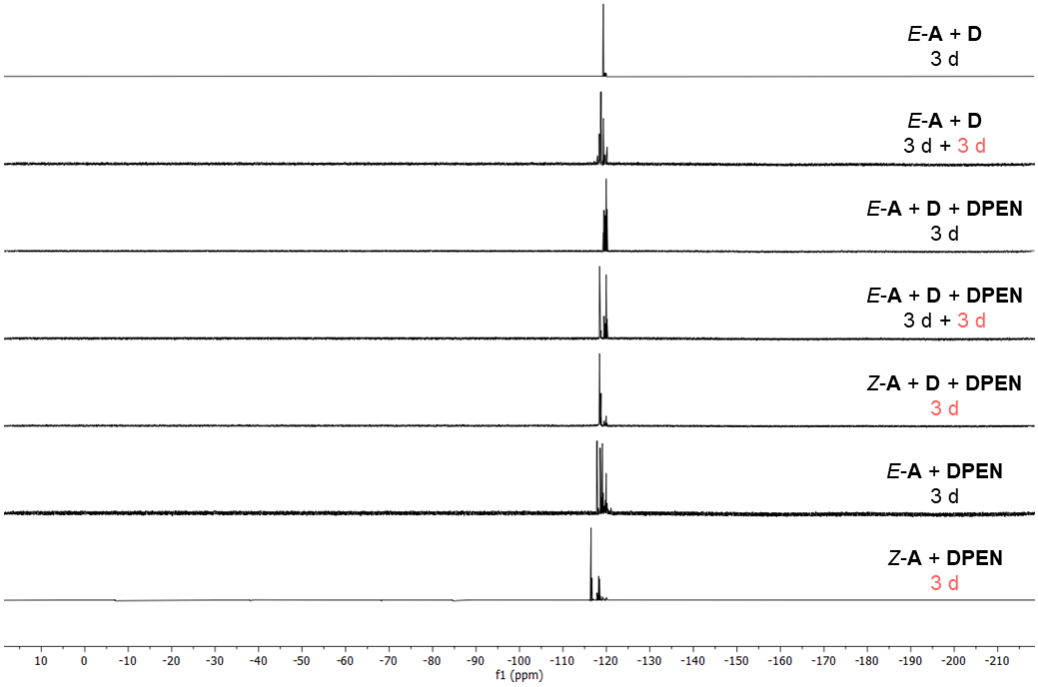

Figure S179: Comparison of $^{19}F\{^{1}H\}$ NMR spectra ($CDCl_3$, 282 MHz) of the reaction of *E*-**A** and **D** in the dark and after irradiation with red light (660 nm), of the reaction mixture of *E*-**A**, **D**, and **DPEN** in the dark and after irradiation with red light, of the reaction of *Z*-**A**, **D**, and **DPEN** under continuous irradiation with red light and of the reaction of *E*-**A** with **DPEN** in the dark and *Z*-**A** with **DPEN** under continuous irradiation with red light.

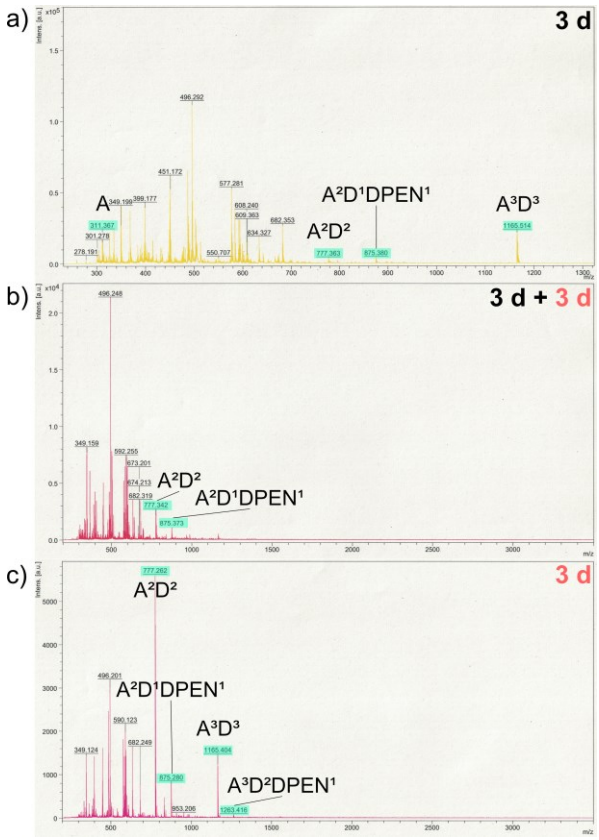

Figure S180: Comparison of MALDI-mass spectra of the reaction of *E*-**A**, **D**, and **DPEN** a) in the dark and b) under irradiation with red light (660 nm) and c) of the reaction of *Z*-**A**, **D**, and **DPEN** under continuous irradiation with red light. Peaks that can be attributed to $\mathbf{A^nD^n}$ or $\mathbf{A^nDPEN^n}$ compounds or mixed $\mathbf{A^nD^nDPEN^n}$ compounds are highlighted in turquoise.

Exchange experiments using *E,E,E*-$\mathbf{A^3D^3}$

Stock solutions of macrocycle *E,E,E*-$\mathbf{A^3D^3}$ as well as of diamines **E**, **Pr**, **B**, **H** and **mP** in $CDCl_3$ were prepared. The compounds were mixed in a cage to diamine ratio of 1 to 3 and diluted to 0.80 ml yielding a concentration of 1.78 mM. The mixtures were stirred under irradiation with red light (660 nm) for 5 days, followed by irradiation with UV light (405 nm) for 14 h, before the solutions were again irradiated with red light for 5 days and stirred in the dark at room temperature for 4 days and at 45 °C for 2 days. The reactions were monitored by ^1H and $^{19}F\{^1H\}$-spectroscopy and MALDI-mass spectra were recorded after the first irradiation period.

Table S37: Amounts of cage and diamine employed in the reactions.

E,E,E- $\mathbf{A^3D^3}$ (1.7 mg, 1.4 µmol, 1.0 eq.)	**E** (0.26 mg, 4.3 µmol, 3.0 eq.)
	Pr (0.32 mg, 4.3 µmol, 3.0 eq.)
	B (0.38 mg, 4.3 µmol, 3.0 eq.)
	H (0.50 mg, 4.3 µmol, 3.0 eq.)
	mP (0.58 mg, 4.3 µmol, 3.0 eq.)

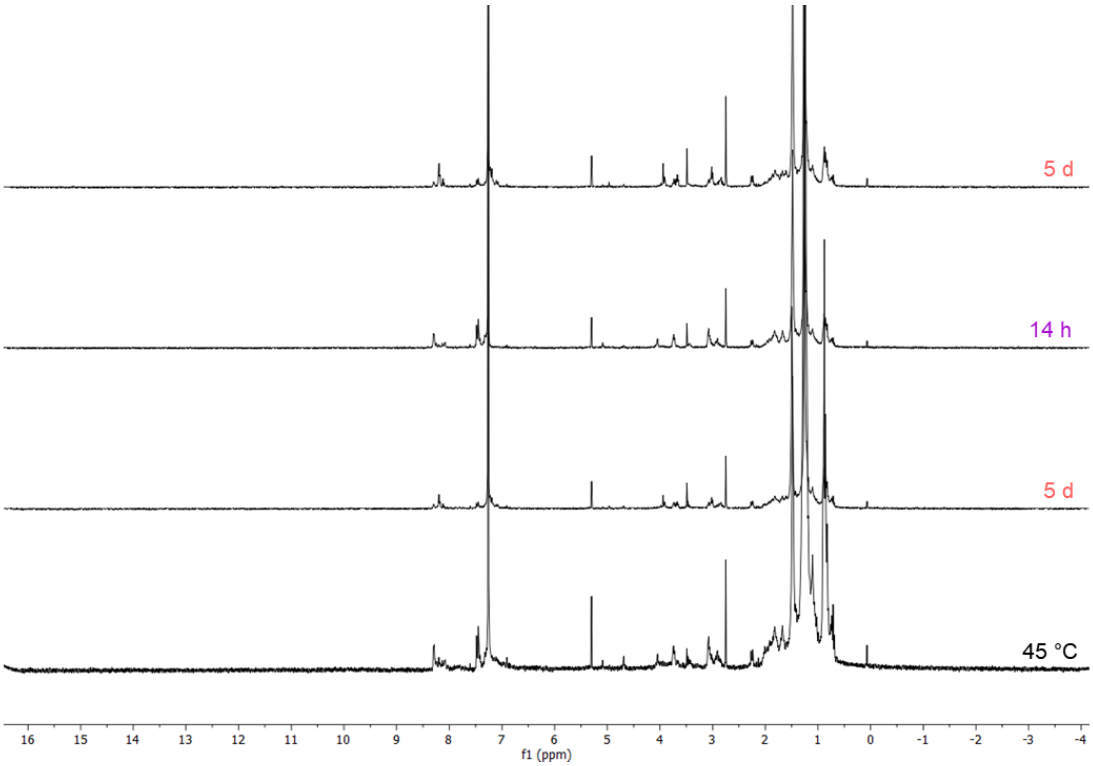

Figure S181: Comparison of ^{1}H NMR spectra ($CDCl_3$, 300 MHz) of *E,E,E*-**A^{3}D^3** and **E** after 5 days under irradiation with red light (660 nm), after 14 hours of irradiation with UV light (405 nm), followed by irradiation with red light for 5 days and stirring in the dark at room temperature for 4 days and for 2 days at 45 °C.

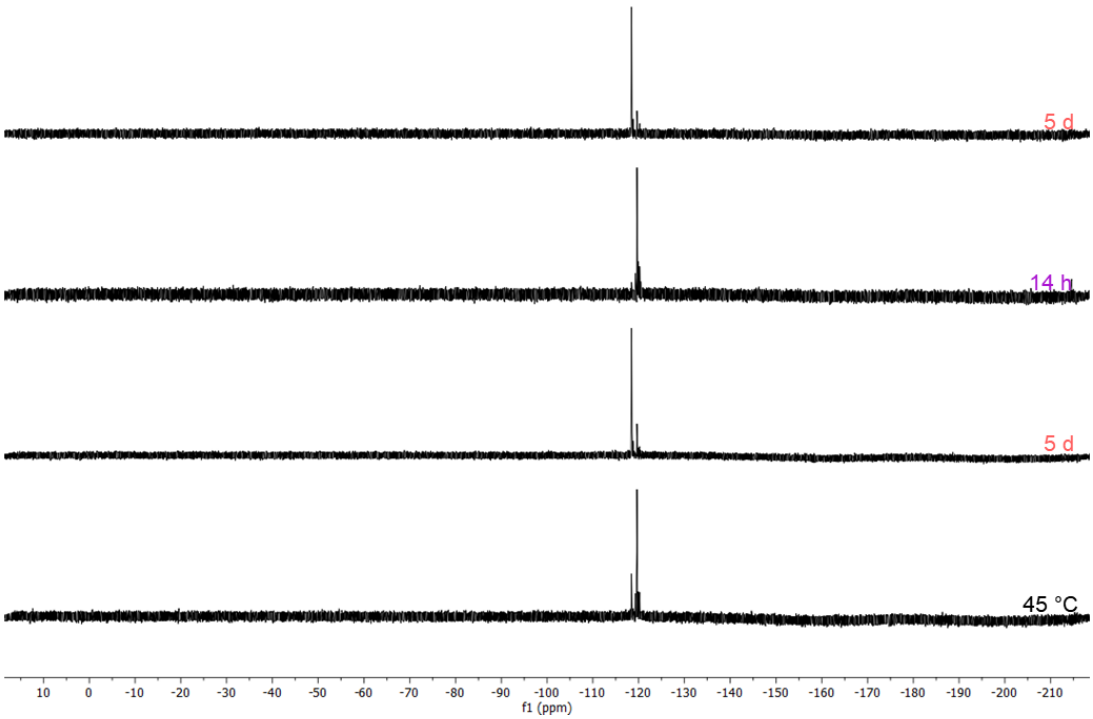

Figure S182: Comparison of ^{19}F{^{1}H} NMR spectra ($CDCl_3$, 282 MHz) of *E,E,E*-**A^{3}D^3** and **E** after 5 days under irradiation with red light (660 nm), after 14 hours of irradiation with UV light (405 nm), followed by irradiation with red light for 5 days and stirring in the dark at room temperature for 4 days and for 2 days at 45 °C.

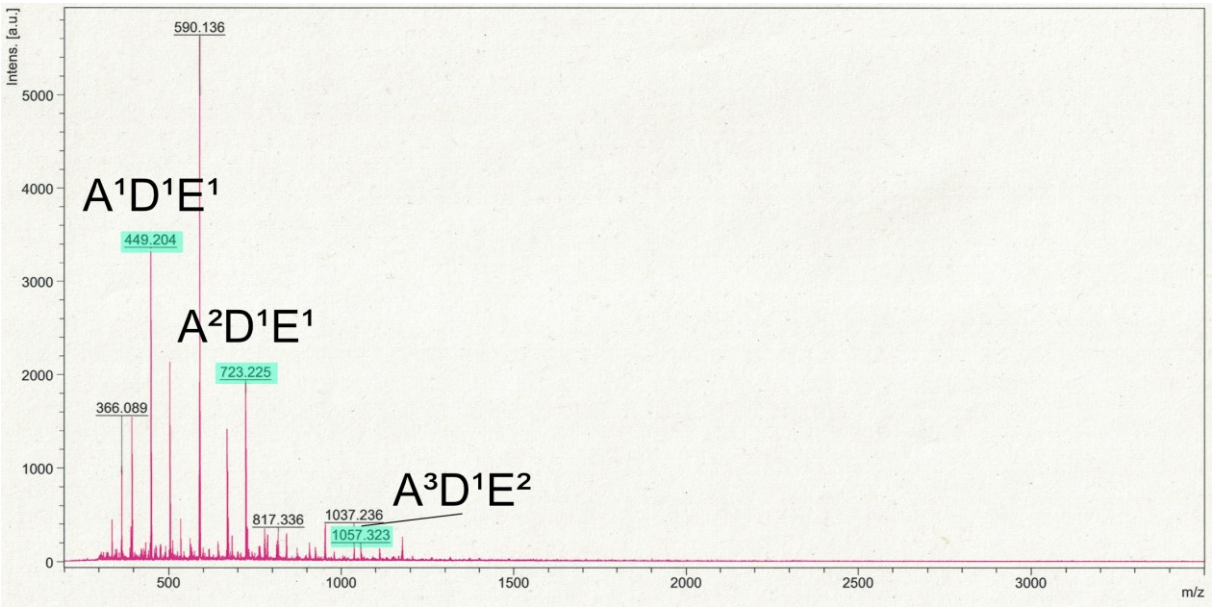

Figure S183: MALDI-mass spectrum of the reaction of *E,E,E*-**A³D³** and **E** after irradiation with red light (660 nm) for 5 days. Peaks that can be attributed to compounds are highlighted in turquoise.

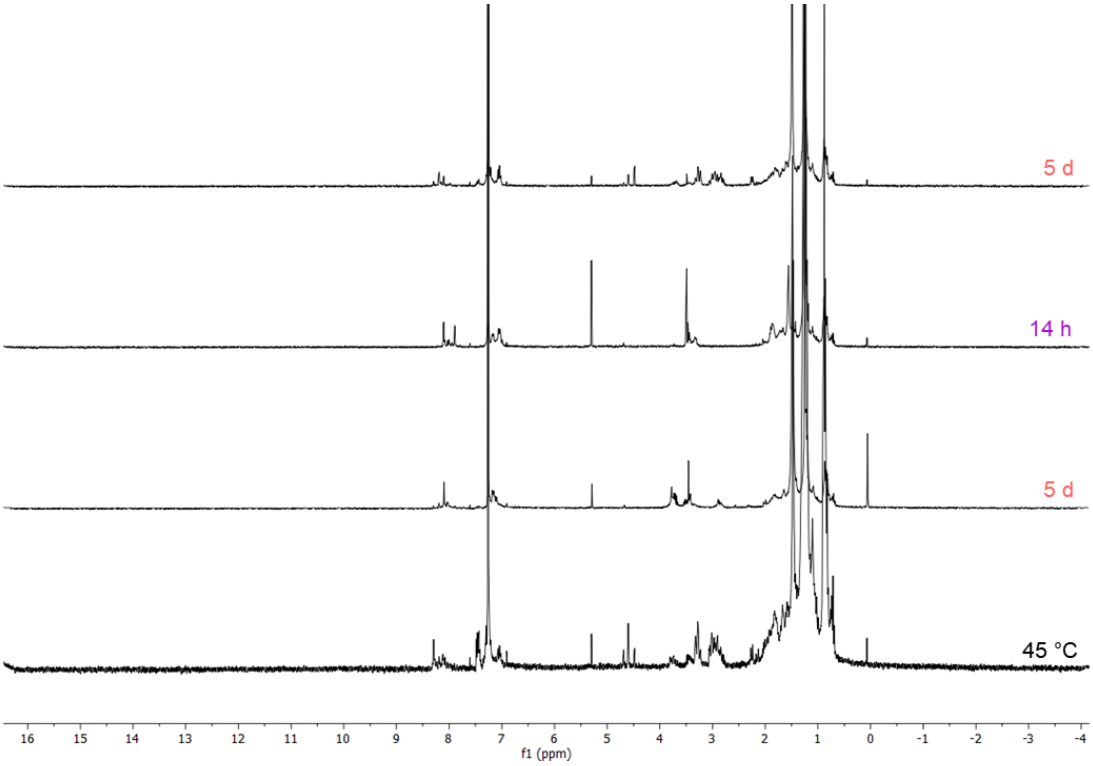

Figure S184: Comparison of ^{1}H NMR spectra ($CDCl_3$, 300 MHz) of *E,E,E*-**A³D³** and **Pr** after 5 days under irradiation with red light (660 nm), after 14 hours of irradiation with UV light (405 nm), followed by irradiation with red light for 5 days and stirring in the dark at room temperature for 4 days and for 2 days at 45 °C.

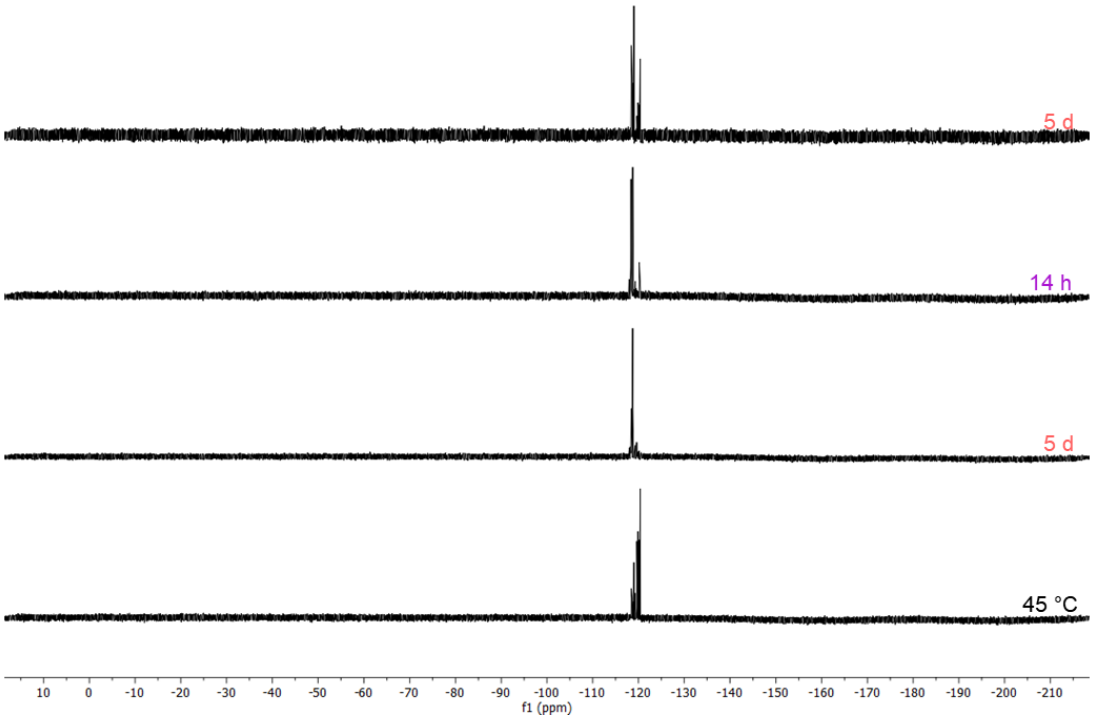

Figure S185: Comparison of $^{19}F\{^{1}H\}$ NMR spectra ($CDCl_3$, 282 MHz) of *E,E,E*-**A^{3}D^3** and **Pr** after 5 days under irradiation with red light (660 nm), after 14 hours of irradiation with UV light (405 nm), followed by irradiation with red light for 5 days and stirring in the dark at room temperature for 4 days and for 2 days at 45 °C.

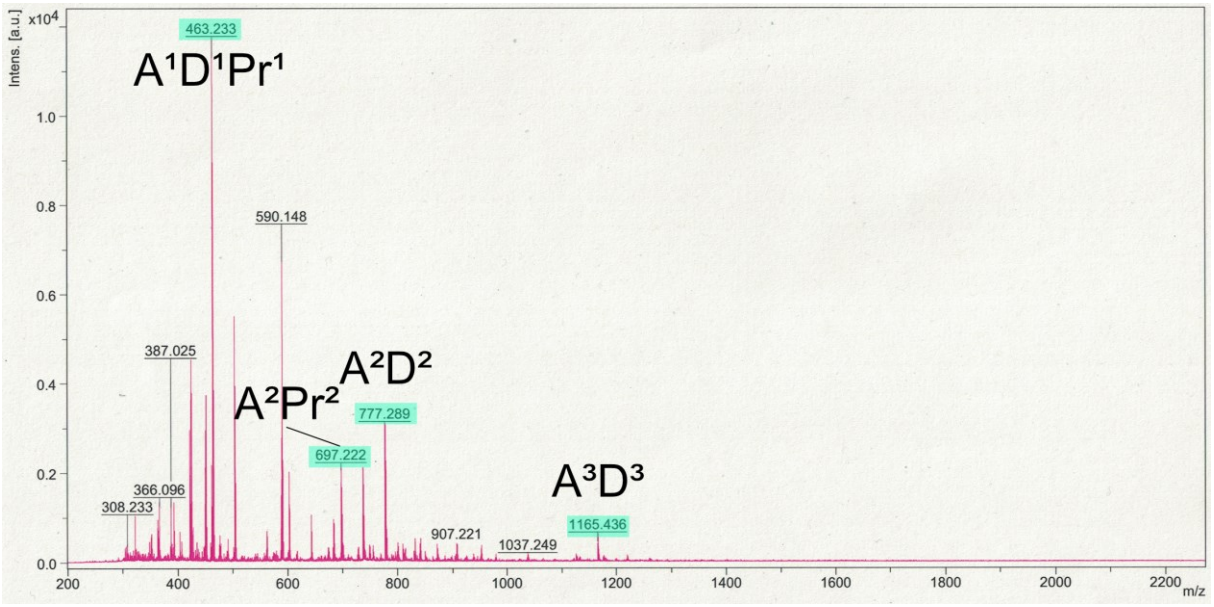

Figure S186: MALDI-mass spectrum of the reaction of *E,E,E*-**A^{3}D^3** and **Pr** after irradiation with red light (660 nm) for 5 days. Peaks that can be attributed to compounds are highlighted in turquoise.

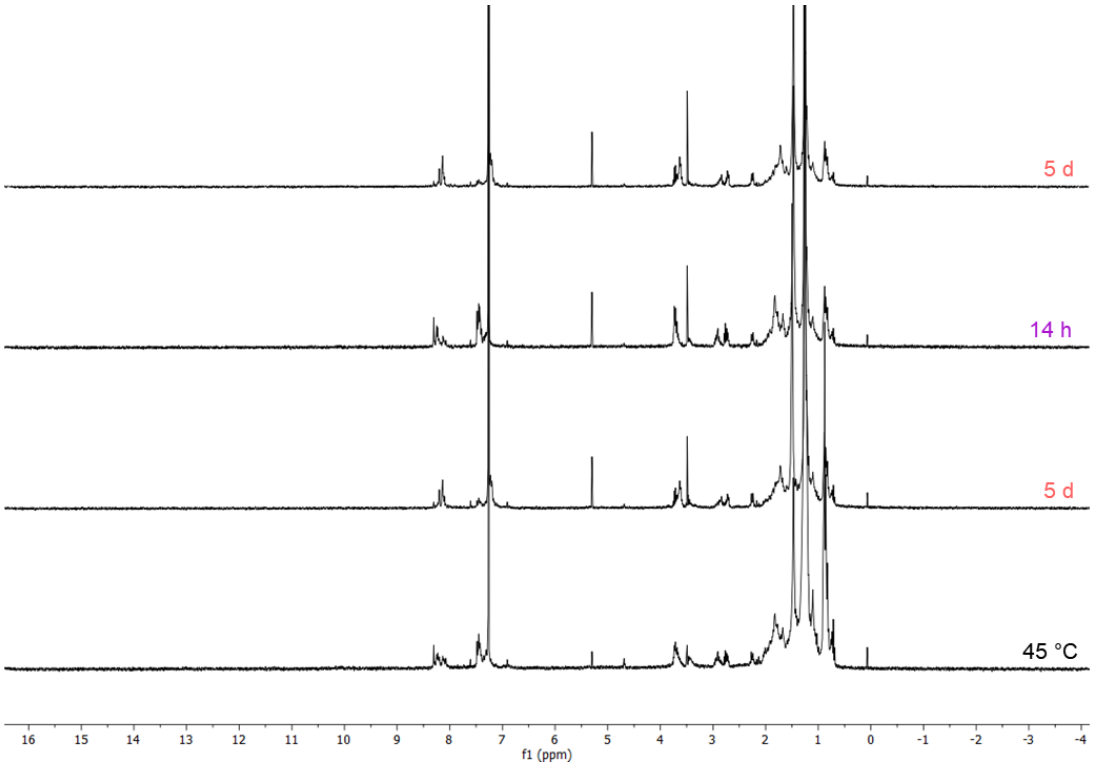

Figure S187: Comparison of ^{1}H NMR spectra ($CDCl_3$, 300 MHz) of *E,E,E*-**A^{3}D^3** and **B** after 5 days under irradiation with red light (660 nm), after 14 hours of irradiation with UV light (405 nm), followed by irradiation with red light for 5 days and stirring in the dark at room temperature for 4 days and for 2 days at 45 °C.

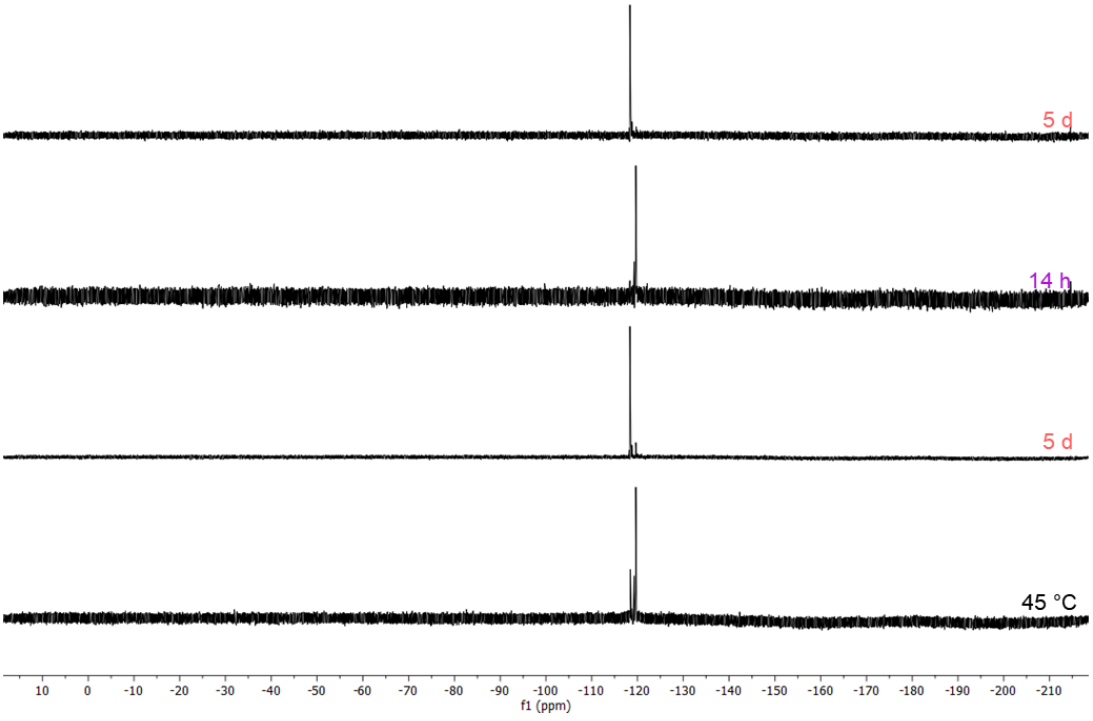

Figure S188: Comparison of ^{19}F{^{1}H} NMR spectra ($CDCl_3$, 282 MHz) of *E,E,E*-**A^{3}D^3** and **B** after 5 days under irradiation with red light (660 nm), after 14 hours of irradiation with UV light (405 nm), followed by irradiation with red light for 5 days and stirring in the dark at room temperature for 4 days and for 2 days at 45 °C.

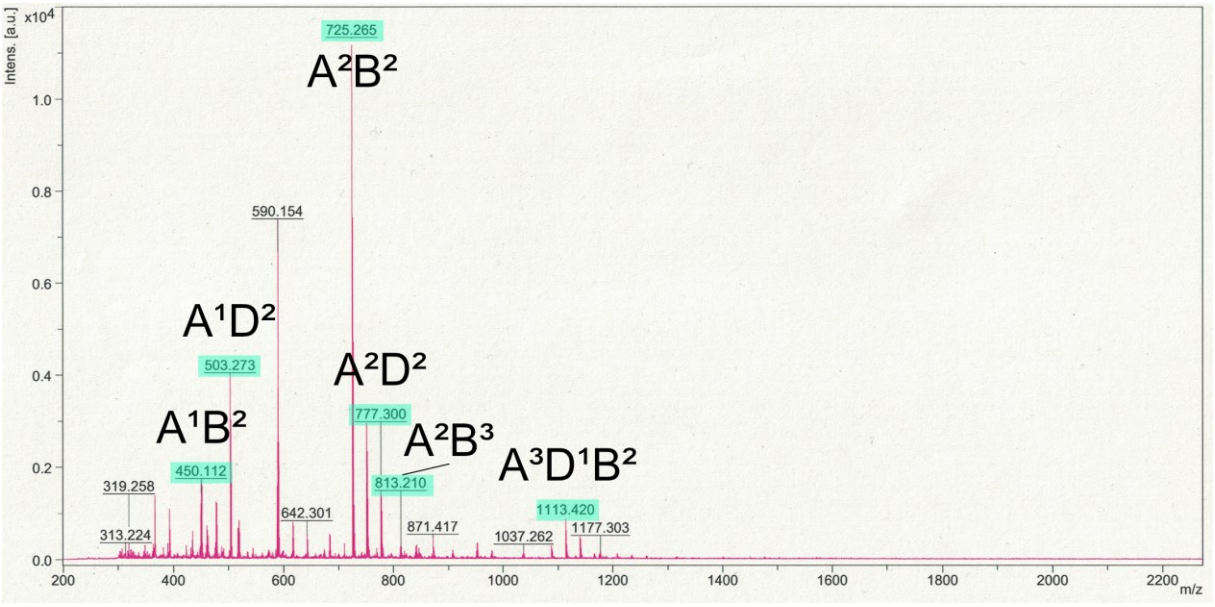

Figure S189: MALDI-mass spectrum of the reaction of *E,E,E*-**A³D³** and **B** after irradiation with red light (660 nm) for 5 days. Peaks that can be attributed to compounds are highlighted in turquoise.

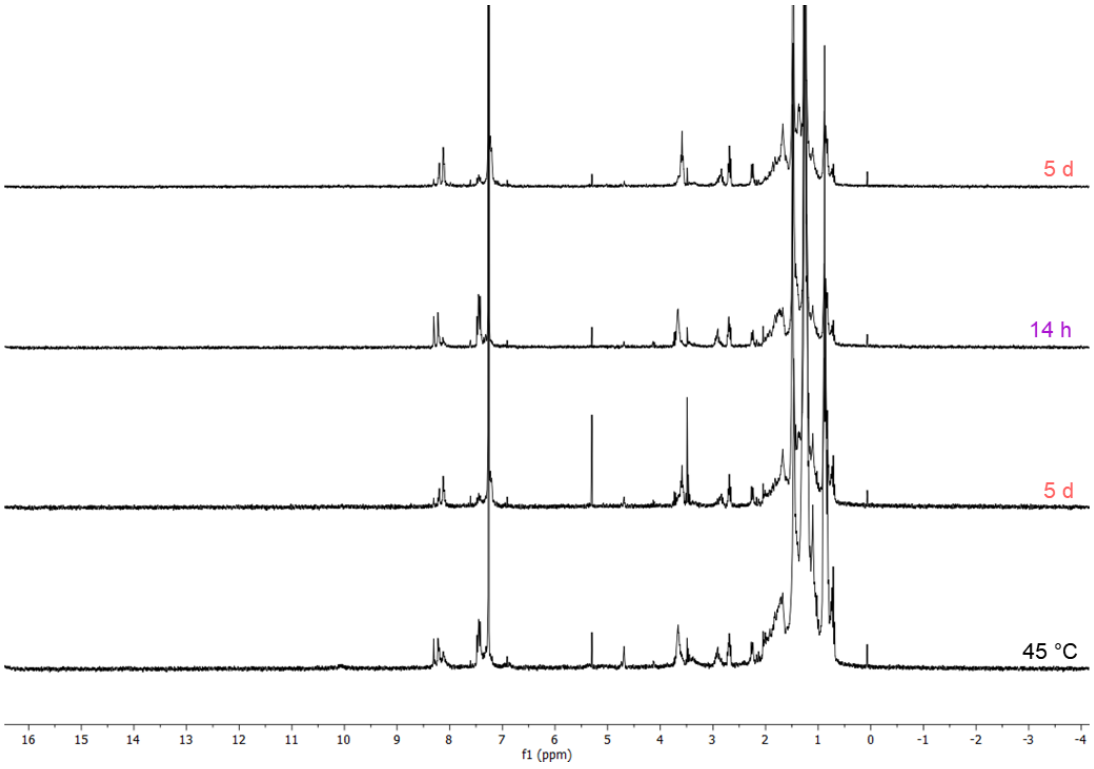

Figure S190: Comparison of ^{1}H NMR spectra ($CDCl_3$, 300 MHz) of *E,E,E*-**A³D³** and **H** after 5 days under irradiation with red light (660 nm), after 14 hours of irradiation with UV light (405 nm), followed by irradiation with red light for 5 days and stirring in the dark at room temperature for 4 days and for 2 days at 45 °C.

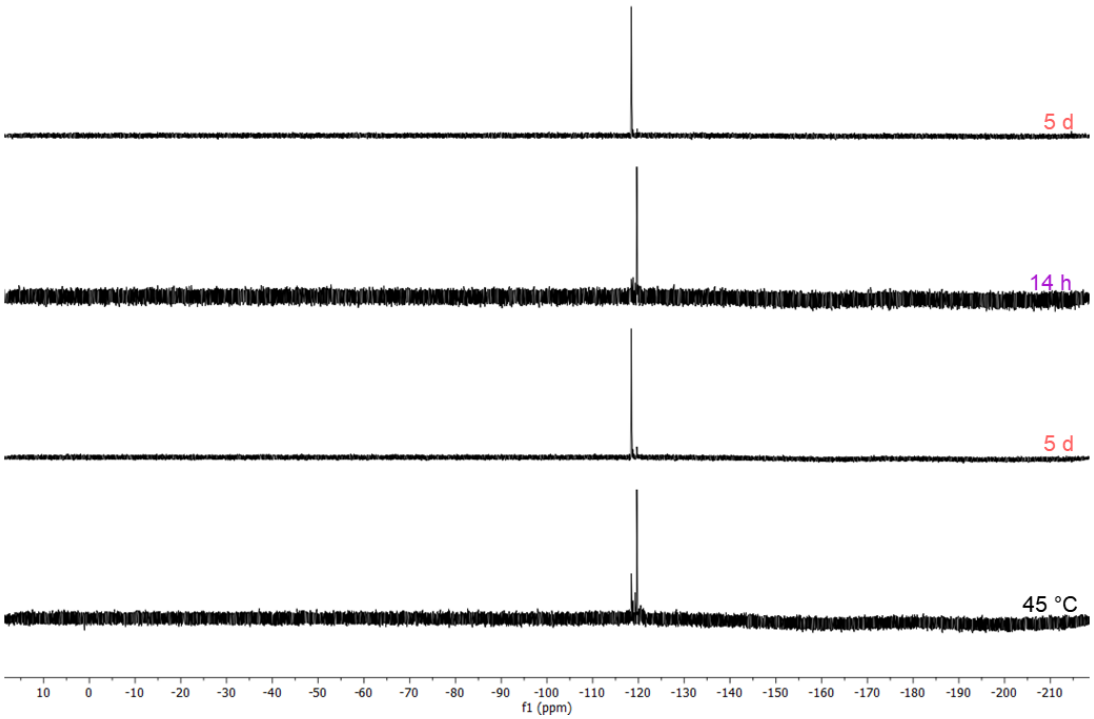

Figure S191: Comparison of $^{19}F\{^{1}H\}$ NMR spectra ($CDCl_3$, 282 MHz) of *E,E,E*-**A^{3}D^3** and **H** after 5 days under irradiation with red light (660 nm), after 14 hours of irradiation with UV light (405 nm), followed by irradiation with red light for 5 days and stirring in the dark at room temperature for 4 days and for 2 days at 45 °C.

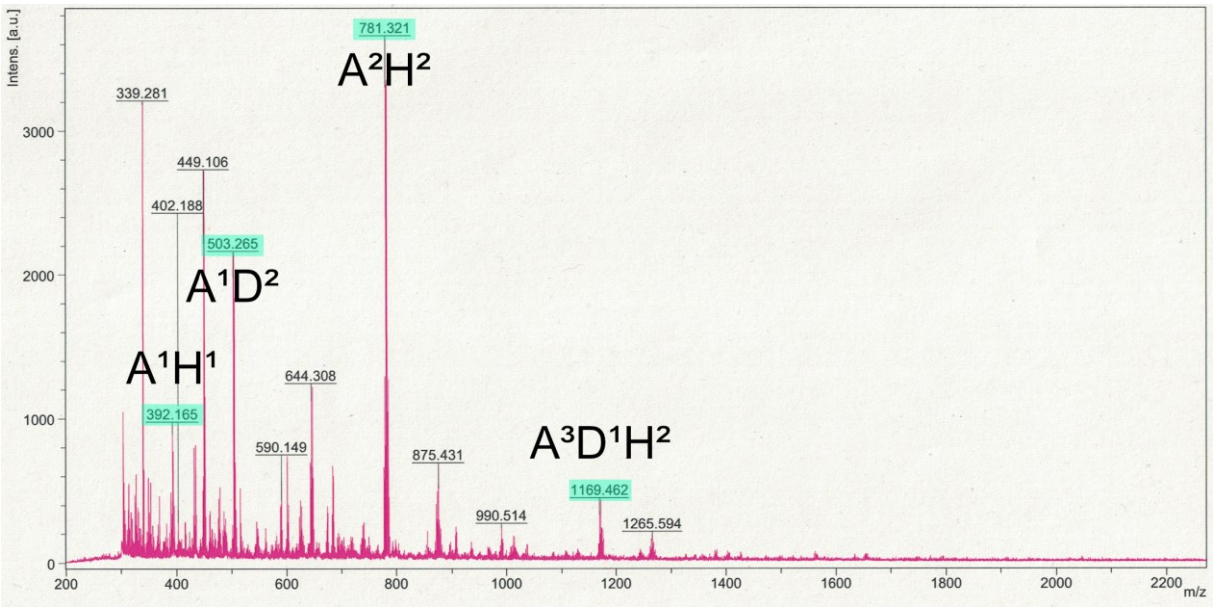

Figure S192: MALDI-mass spectrum of the reaction of *E,E,E*-**A^{3}D^3** and **H** after irradiation with red light (660 nm) for 5 days. Peaks that can be attributed to compounds are highlighted in turquoise.

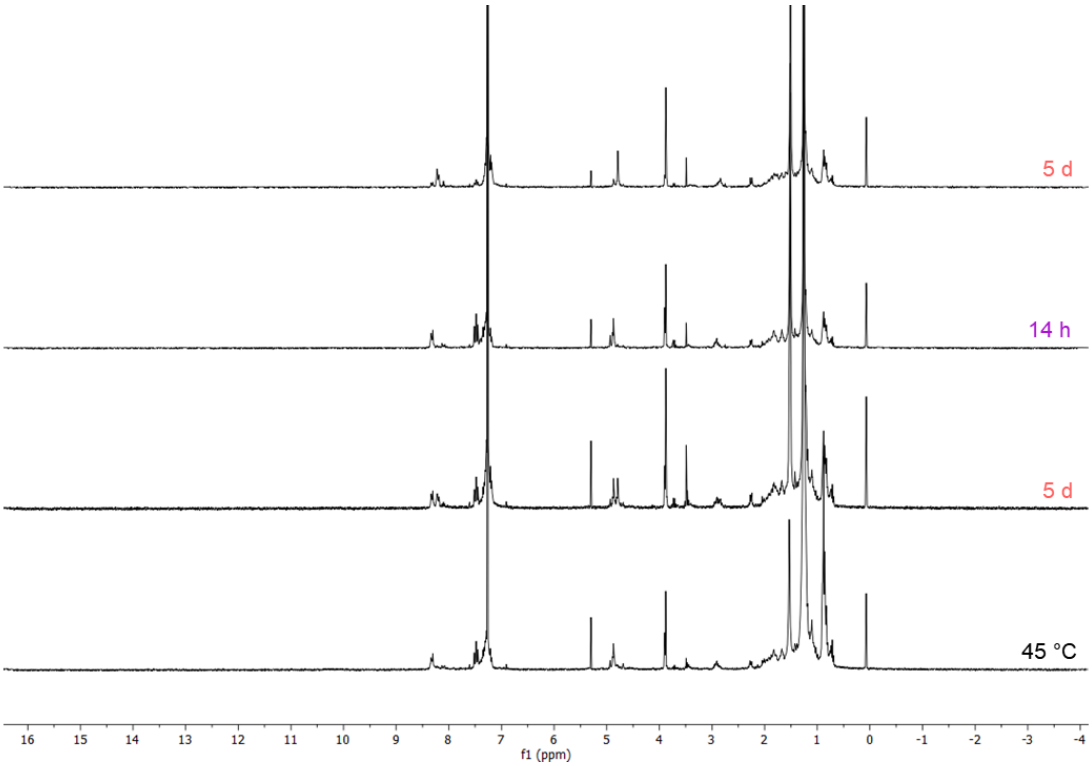

Figure S193: Comparison of ^{1}H NMR spectra ($CDCl_3$, 300 MHz) of *E,E,E*-**A^{3}D^3** and **mP** after 5 days under irradiation with red light (660 nm), after 14 hours of irradiation with UV light (405 nm), followed by irradiation with red light for 5 days and stirring in the dark at room temperature for 4 days and for 2 days at 45 °C.

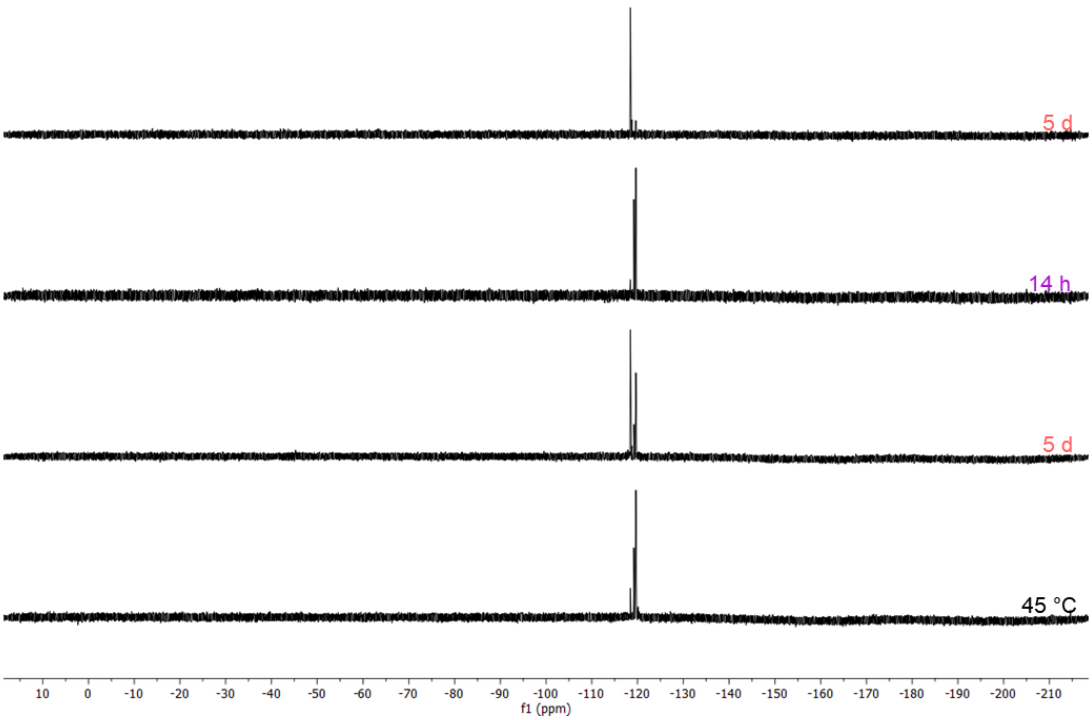

Figure S194: Comparison of ^{19}F{^{1}H} NMR spectra ($CDCl_3$, 282 MHz) of *E,E,E*-**A^{3}D^3** and **mP** after 5 days under irradiation with red light (660 nm), after 14 hours of irradiation with UV light (405 nm), followed by irradiation with red light for 5 days and stirring in the dark at room temperature for 4 days and for 2 days at 45 °C.

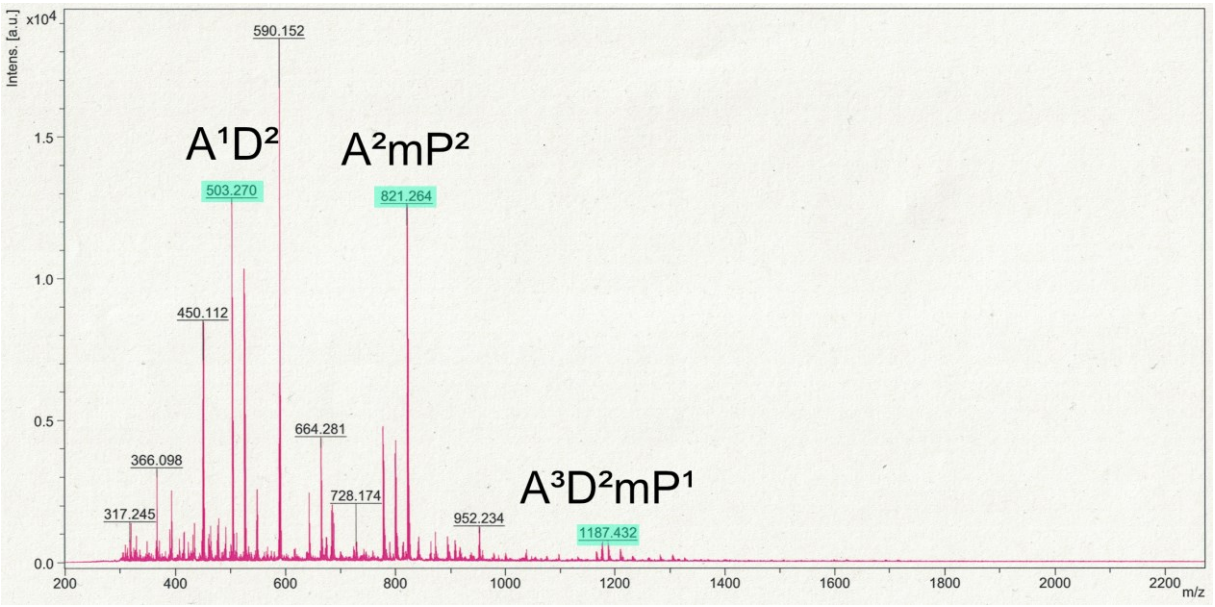

Figure S195: MALDI-mass spectrum of the reaction of *E,E,E*-**A^{3}D^3** and **mP** after irradiation with red light (660 nm) for 5 days. Peaks that can be attributed to compounds are highlighted in turquoise.

Reaction of A with H and an excess of D

Stock solutions of cage *E*-**A** as well as of diamines **H** and **D** in $CDCl_3$ were prepared. The compounds were mixed in varying ratios and diluted. The mixtures were stirred in the dark for 3 days and some of the mixtures were afterwards stirred under red light (660 nm) for approximately 2 days and stirred under irradiation with UV light (405 nm) for 1 hour. The reactions were monitored by ^{1}H and $^{19}F\{^{1}H\}$ NMR spectroscopy and MALDI-mass spectra were recorded after stirring in the dark.

Table S38: Amounts of cage and diamine employed in the reactions.

Aldehyde	Amine 1	Amine 2	Reaction time	Volume
E-**A** (1.3 mg, 4.0 µmol, 1.0 eq.)	**D** (0.92 mg, 8.1 µmol, 2.0 eq.)	-	3 days (dark)	0.8 ml
	D (2.8 mg, 24 µmol, 6.0 eq.)			
	D (5.5 mg, 48 µmol, 12 eq.)			
E-**A** (1.6 mg, 5.0 µmol, 1.0 eq.)	**D** (0.68 mg, 6.0 µmol, 1.2 eq.)	**H** (0.70 mg, 6.0 µmol, 1.2 eq.)	3 days (dark), 38 hours (660 nm), 1 hour (405 nm)	1 ml
	D (3.4 mg, 30 µmol, 6.0 eq.)			
	D (6.9 mg, 60 µmol, 12 eq.)			

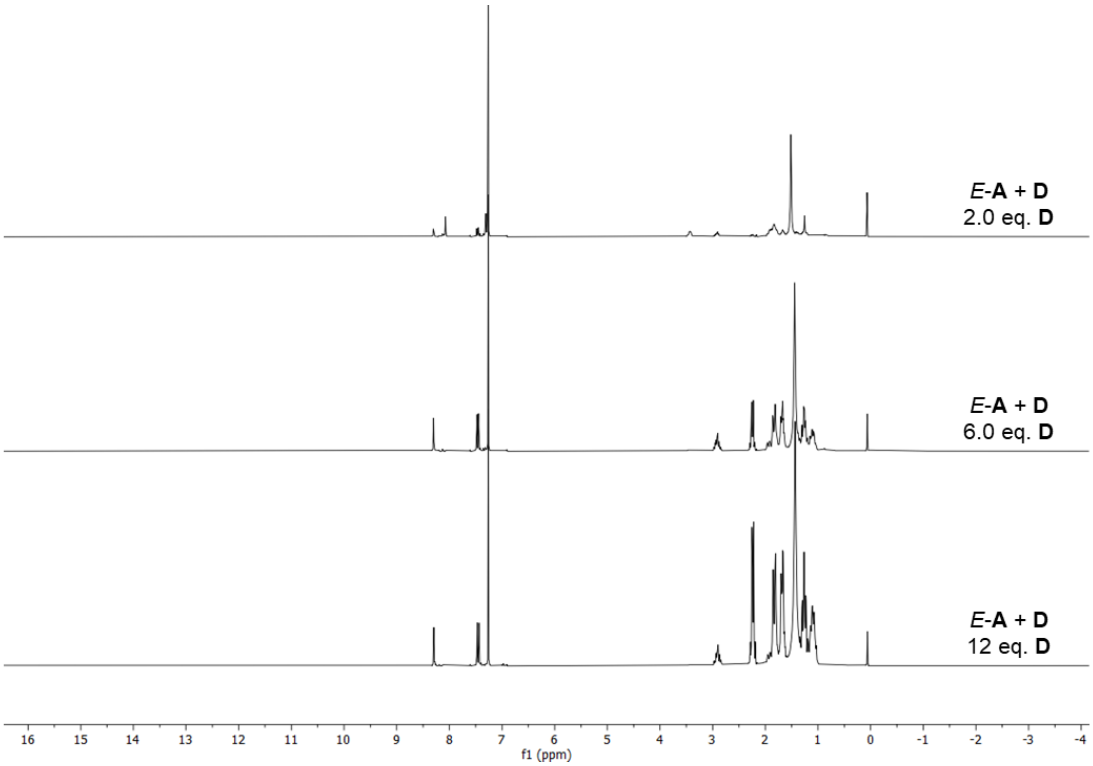

Figure S196: Comparison of ^{1}H NMR spectra ($CDCl_3$, 300 MHz) of *E*-**A** with varying amounts of **D** after 3 days of stirring in the dark.

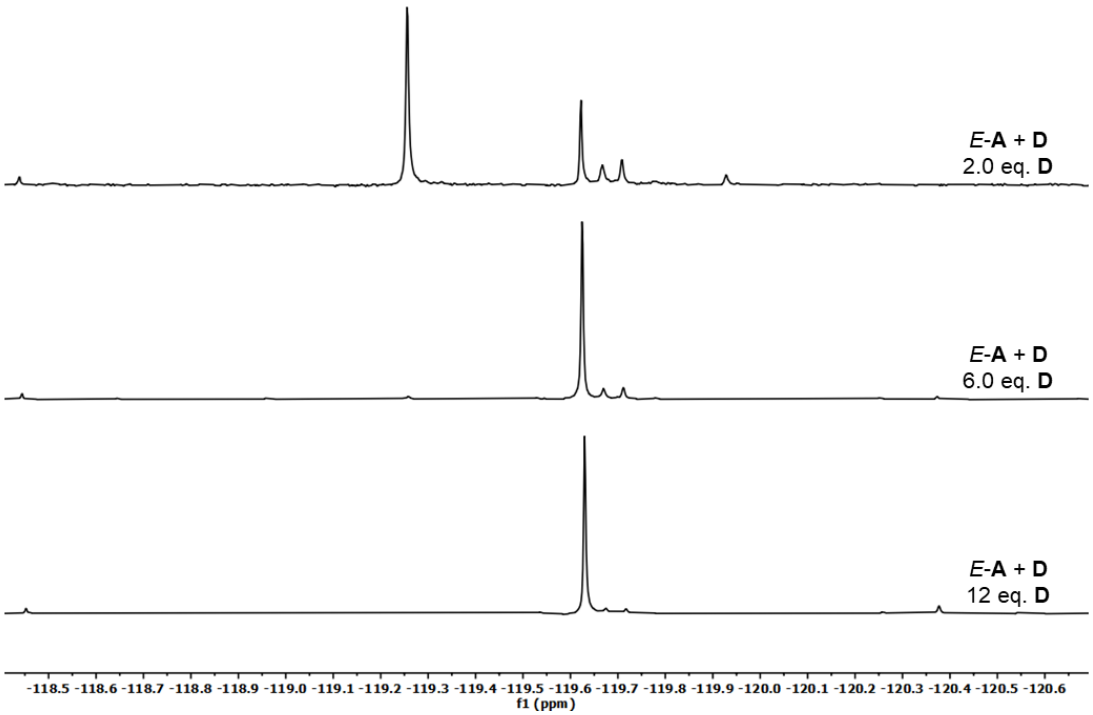

Figure S197: Comparison of $^{19}F\{^{1}H\}$ NMR spectra ($CDCl_3$, 282 MHz) of *E*-**A** with varying amounts of **D** after 3 days of stirring in the dark.

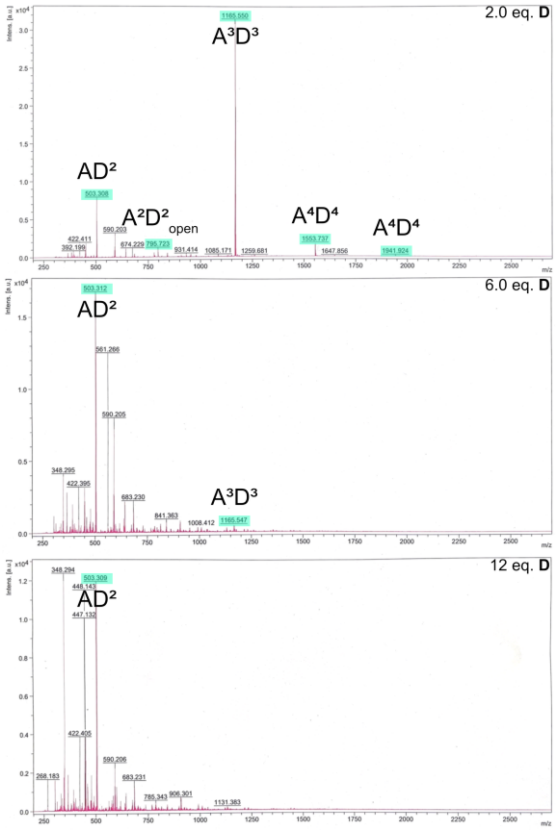

Figure S198: MALDI-mass spectra recorded after 3 days in the dark for the reaction of *E*-**A** with varying amounts of **D**. Peaks that can be attributed to compounds are highlighted in turquoise.

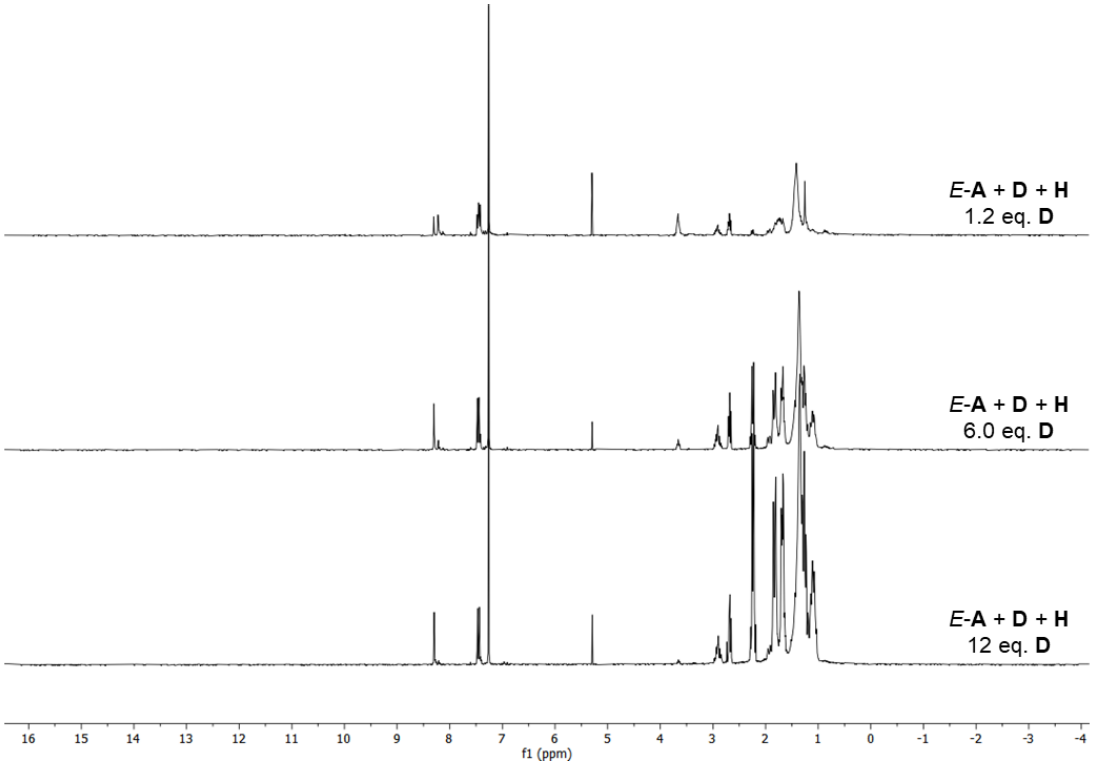

Figure S199: Comparison of ^{1}H NMR spectra ($CDCl_3$, 300 MHz) of *E*-**A** with **H** and varying amounts of **D** after 3 days of stirring in the dark.

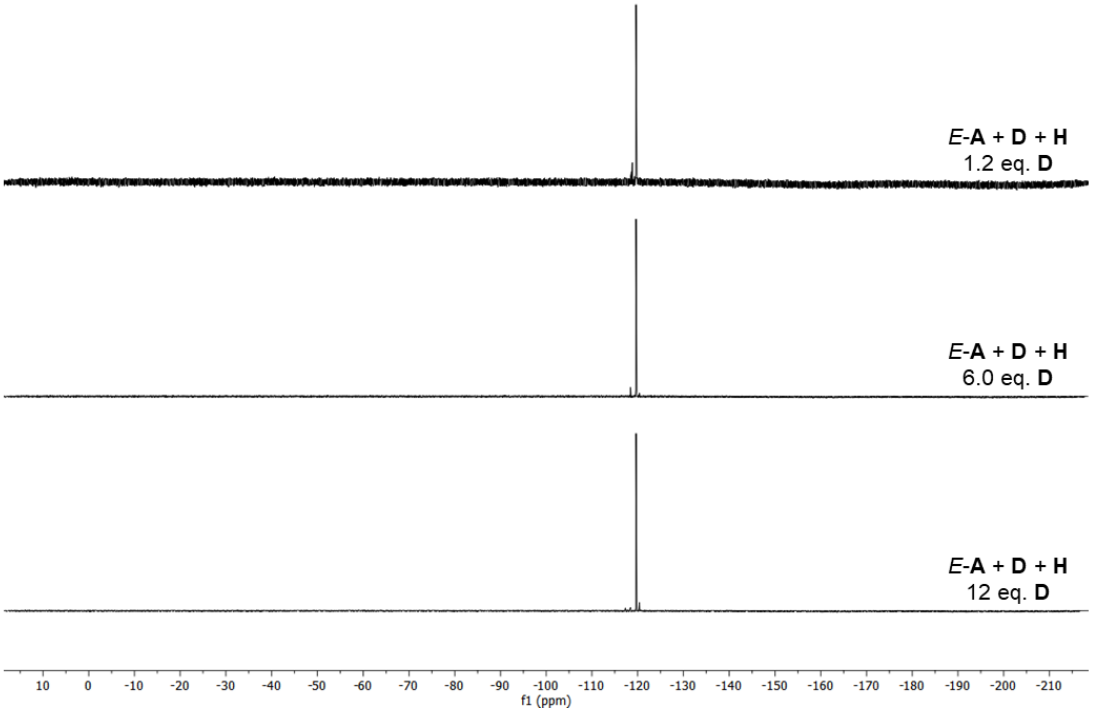

Figure S200: Comparison of $^{19}F\{^{1}H\}$ NMR spectra ($CDCl_3$, 282 MHz) of *E*-**A** with **H** and varying amounts of **D** after 3 days of stirring in the dark.

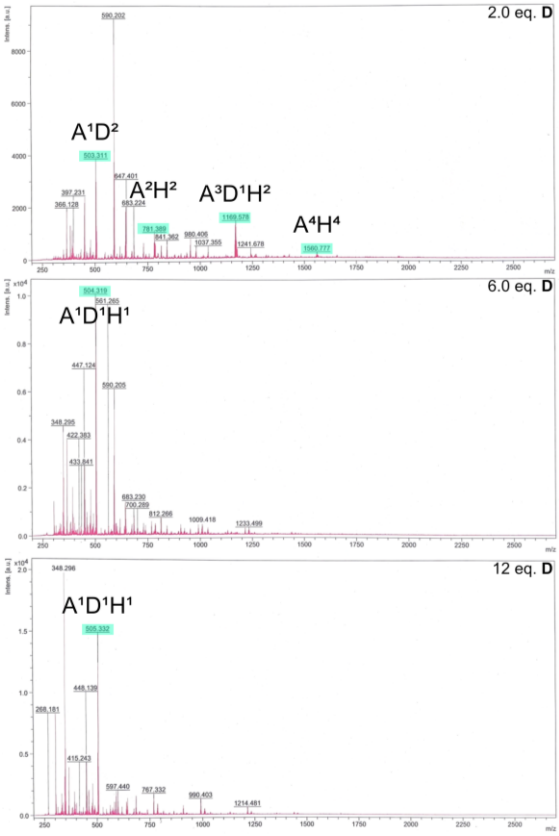

Figure S201: MALDI-mass spectra recorded after 3 days in the dark for the reaction of *E*-**A** with **H** and varying amounts of **D**. Peaks that can be attributed to compounds are highlighted in turquoise.

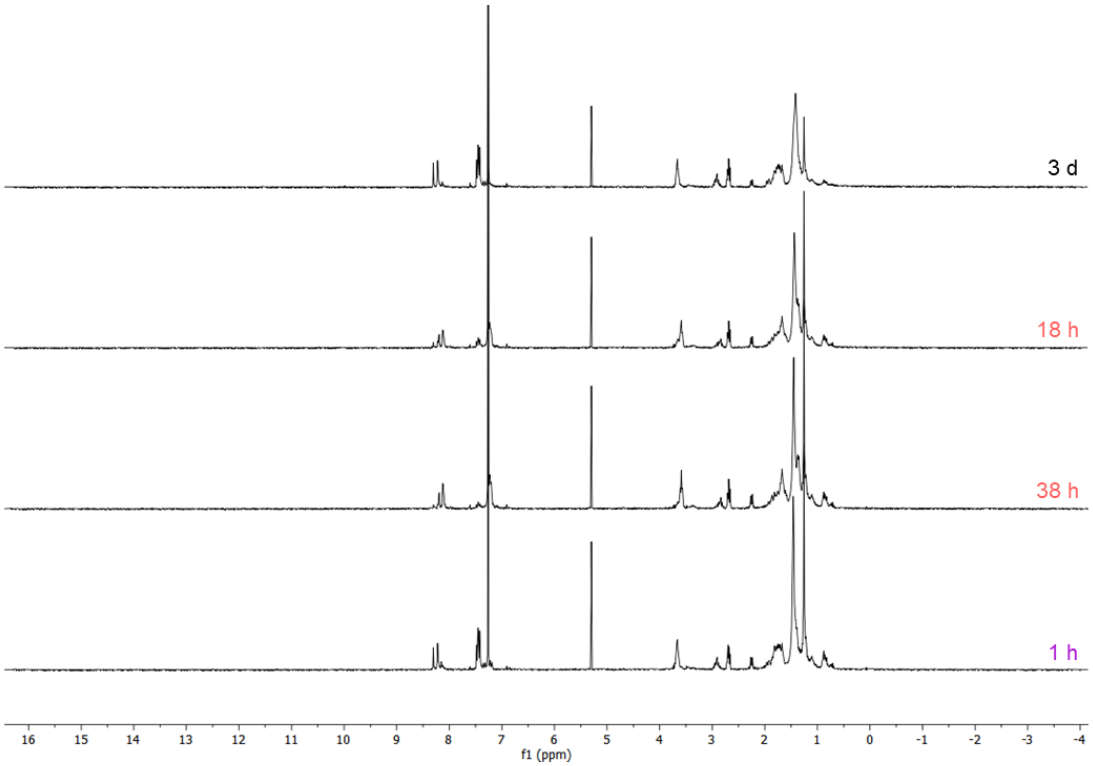

Figure S202: Comparison of ^{1}H NMR spectra ($CDCl_3$, 300 MHz) of *E*-**A** with **H** and 1.2 equivalents of **D** after 3 days of stirring in the dark, 18 hours and 38 hours under irradiation with red light (660 nm) and after irradiation with UV light (405 nm).

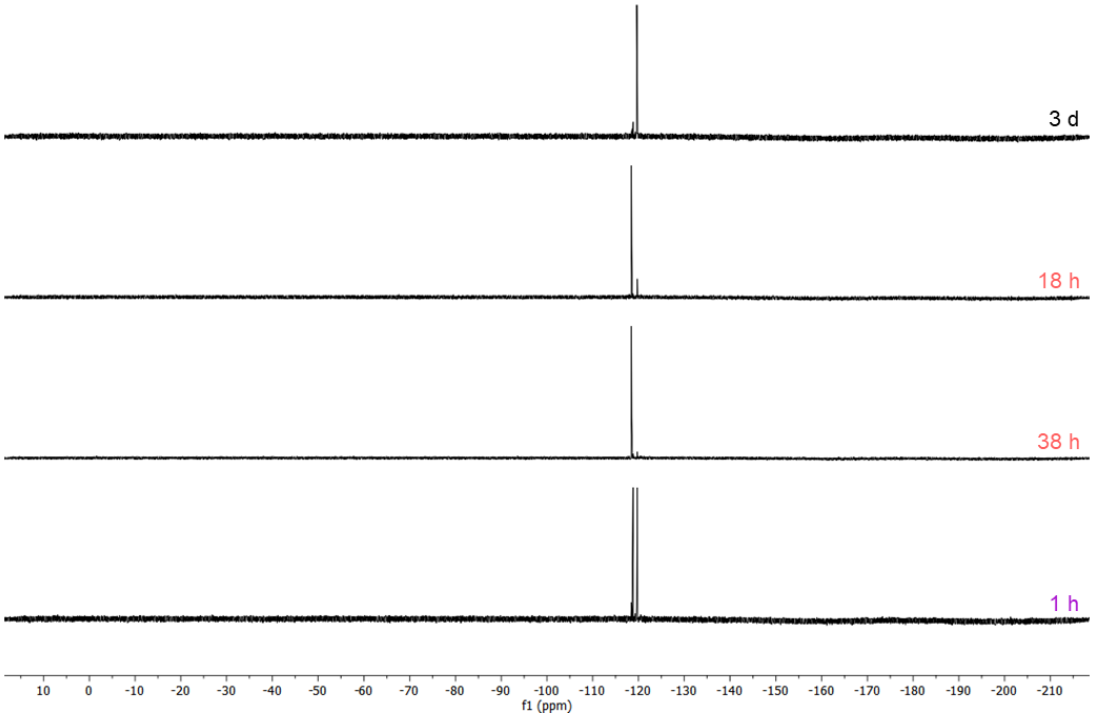

Figure S203: Comparison of $^{19}F\{^{1}H\}$ NMR spectra ($CDCl_3$, 282 MHz) of *E*-**A** with **H** and 1.2 equivalents of **D** after 3 days of stirring in the dark, 18 hours and 38 hours under irradiation with red light (660 nm) and after irradiation with UV light (405 nm).

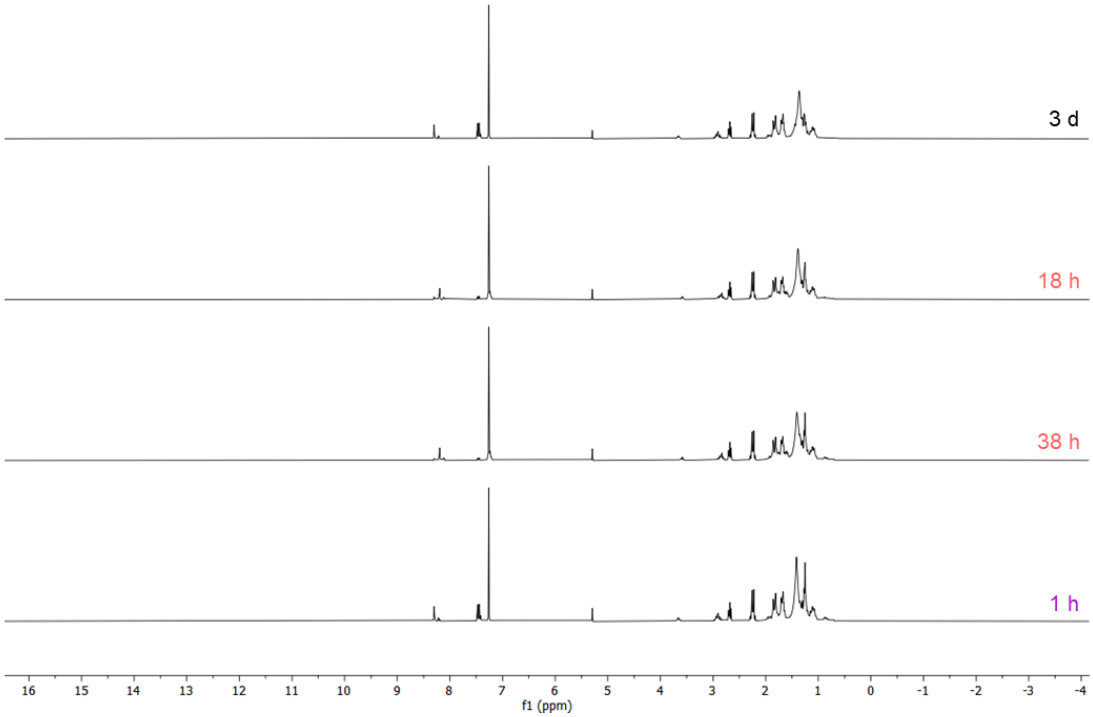

Figure S204: Comparison of ^{1}H NMR spectra ($CDCl_3$, 300 MHz) of *E*-**A** with **H** and 6.0 equivalents of **D** after 3 days of stirring in the dark, 18 hours and 38 hours under irradiation with red light (660 nm) and after irradiation with UV light (405 nm).

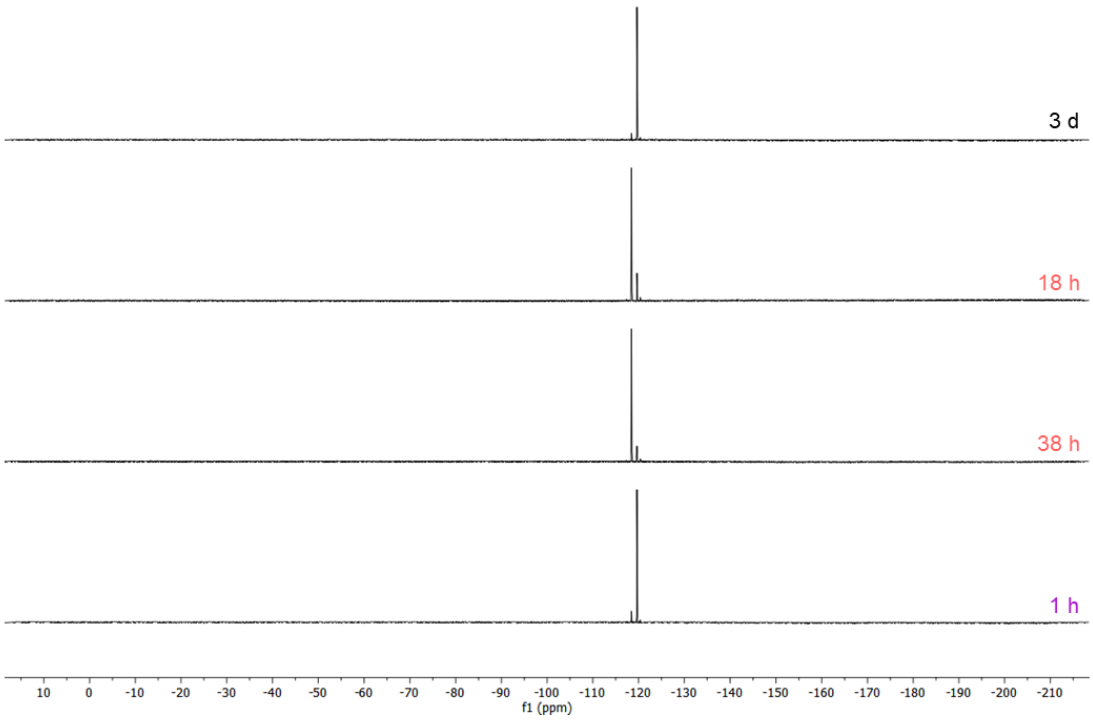

Figure S205: Comparison of $^{19}F\{^{1}H\}$ NMR spectra ($CDCl_3$, 282 MHz) of *E*-**A** with **H** and 6.0 equivalents of **D** after 3 days of stirring in the dark, 18 hours and 38 hours under irradiation with red light (660 nm) and after irradiation with UV light (405 nm).

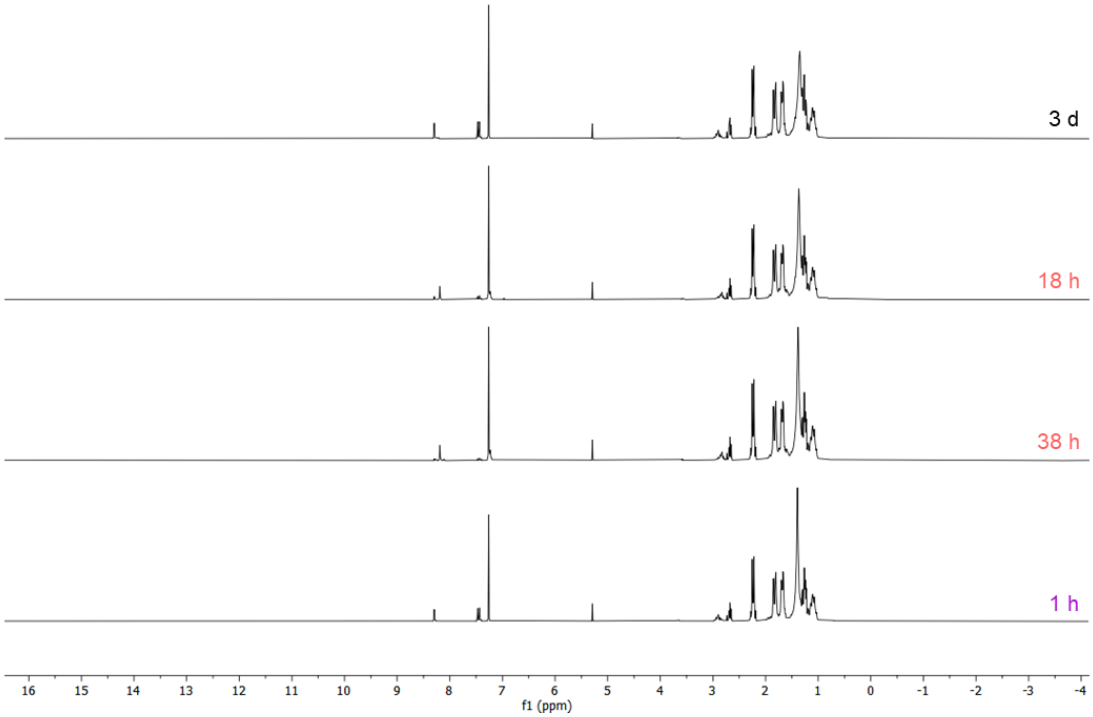

Figure S206: Comparison of ^{1}H NMR spectra ($CDCl_3$, 300 MHz) of *E*-**A** with **H** and 12 equivalents of **D** after 3 days of stirring in the dark, 18 hours and 38 hours under irradiation with red light (660 nm) and after irradiation with UV light (405 nm).

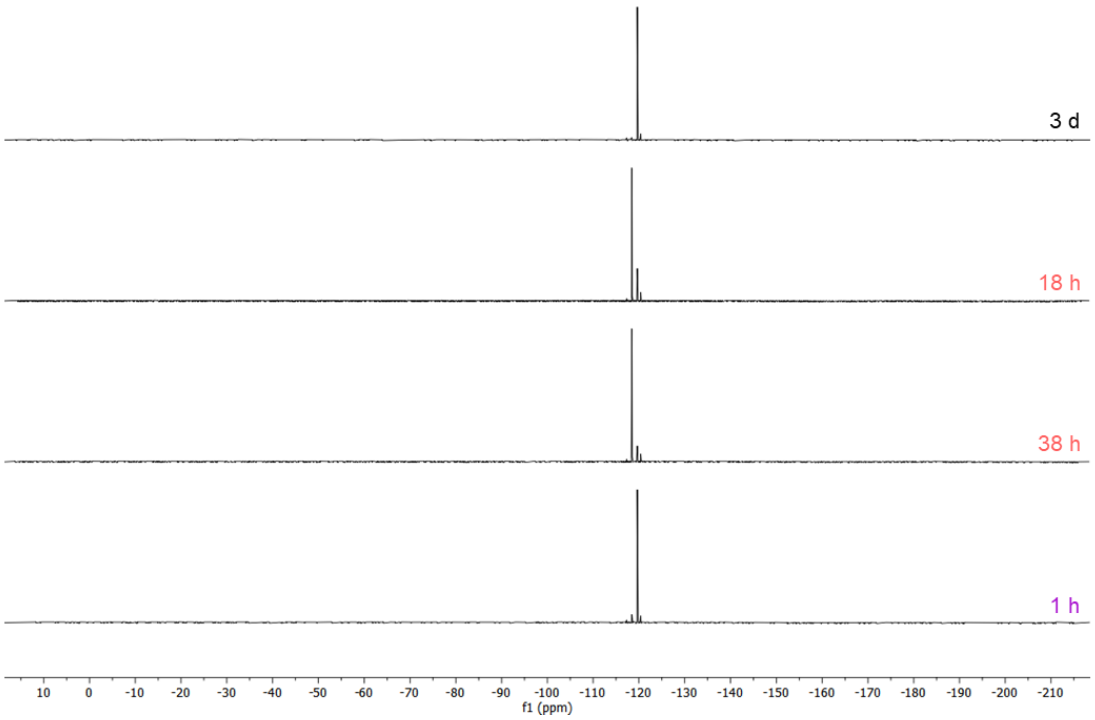

Figure S207: Comparison of $^{19}F\{^{1}H\}$ NMR spectra ($CDCl_3$, 282 MHz) of *E*-**A** with **H** and 6.0 equivalents of **D** after 3 days of stirring in the dark, 18 hours and 38 hours under irradiation with red light (660 nm) and after irradiation with UV light (405 nm).

Exchange experiments using *E,E,E*-A^{3}Tren^2

Stock solutions of cage *E,E,E*-**A^{3}Tren^2** as well as of diamines **E**, **Pr**, **B**, **H** and **D** in $CDCl_3$ were prepared. The compounds were mixed in a cage to diamine ratio of 1 to 3 and diluted to 0.80 ml yielding a concentration of 1.81 mM. The mixtures were stirred under irradiation with red light (660 nm) for 5 days, followed by irradiation with UV light (405 nm) for 14 h, before the solutions were again irradiated with red light for 5 days and stirred in the dark at room temperature for 4 days and at 45 °C for 2 days. The reactions were monitored by ^{1}H and ^{19}F{^{1}H} spectroscopy and MALDI-mass spectra were recorded after the first irradiation period.

Table S39: Amounts of cage and diamine employed in the reactions.

E,E,E-**A^{3}Tren^2** (1.6 mg, 1.5 µmol, 1.0 eq.)	**E** (0.26 mg, 4.4 µmol, 3.0 eq.)
	Pr (0.32 mg, 4.4 µmol, 3.0 eq.)
	B (0.38 mg, 4.4 µmol, 3.0 eq.)
	H (0.51 mg, 4.4 µmol, 3.0 eq.)
	D (0.50 mg, 4.4 µmol, 3.0 eq.)
	mP (0.74 mg, 4.4 µmol, 3.0 eq.)

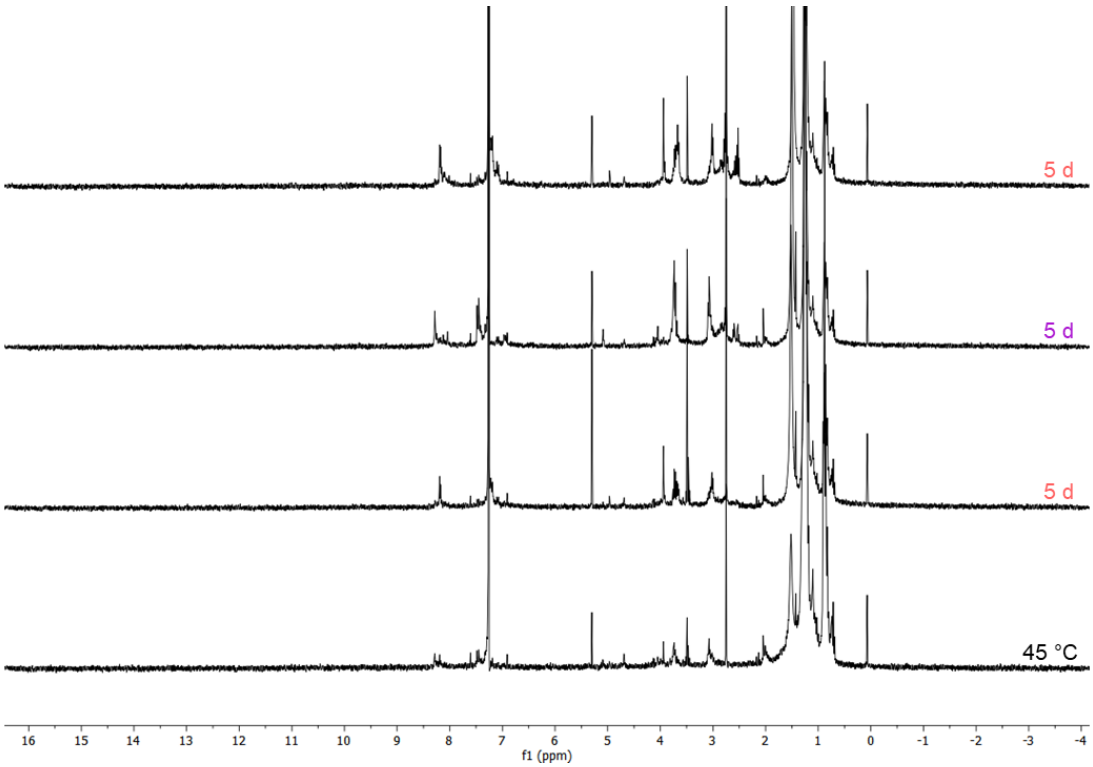

Figure S208: Comparison of ^{1}H NMR spectra ($CDCl_3$, 300 MHz) of *E,E,E*-**A^{3}Tren^2** and **E** after 5 days under irradiation with red light (660 nm), after 14 hours of irradiation with UV light (405 nm), followed by irradiation with red light for 5 days and stirring in the dark at room temperature for 4 days and for 2 days at 45 °C.

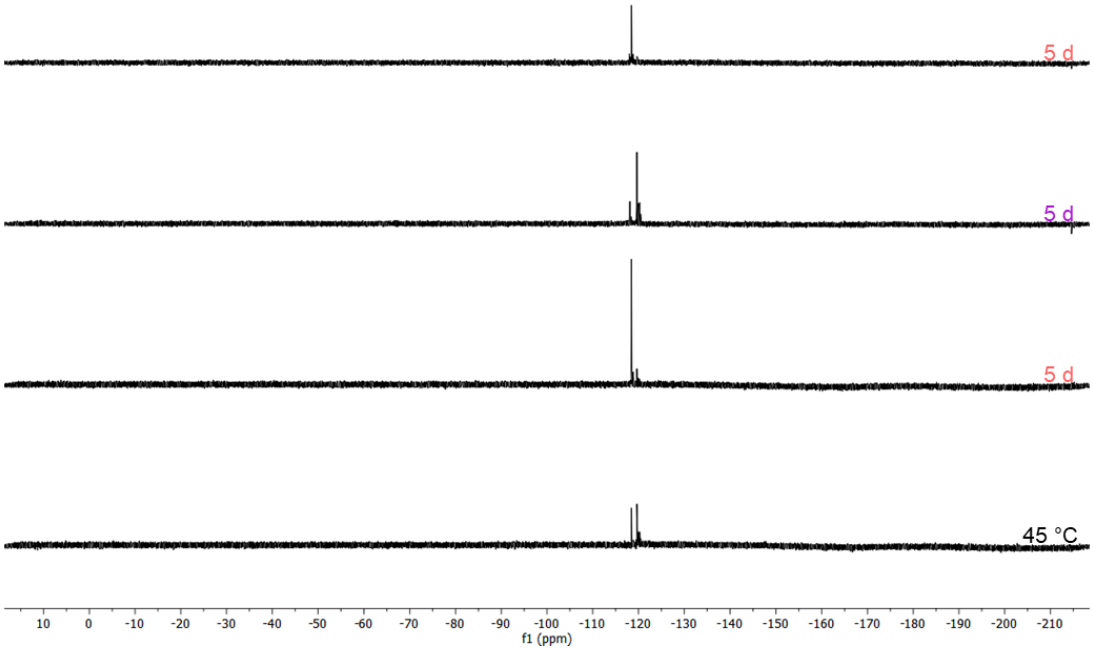

Figure S209: Comparison of $^{19}F\{^{1}H\}$ NMR spectra ($CDCl_3$, 282 MHz) of *E,E,E*-**A^{3}Tren^2** and **E** after 5 days under irradiation with red light (660 nm), after 14 hours of irradiation with UV light (405 nm), followed by irradiation with red light for 5 days and stirring in the dark at room temperature for 4 days and for 2 days at 45 °C.

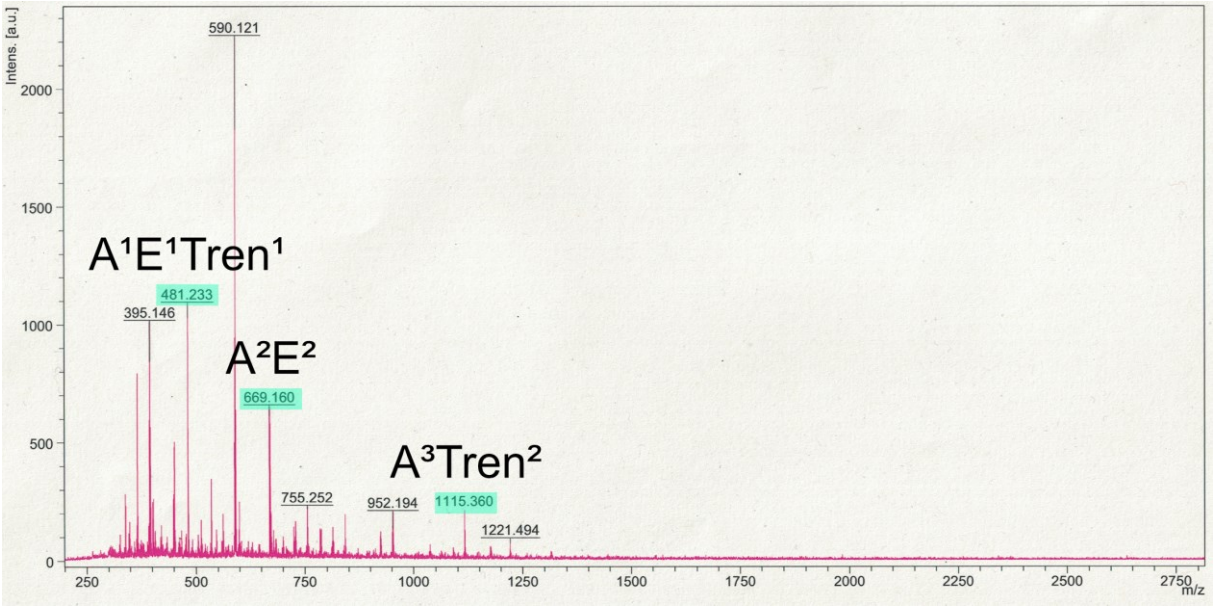

Figure S210: MALDI-mass spectrum of the reaction of *E,E,E*-**A^{3}Tren^2** and **E** after irradiation with red light (660 nm) for 5 days. Peaks that can be attributed to compounds are highlighted in turquoise.

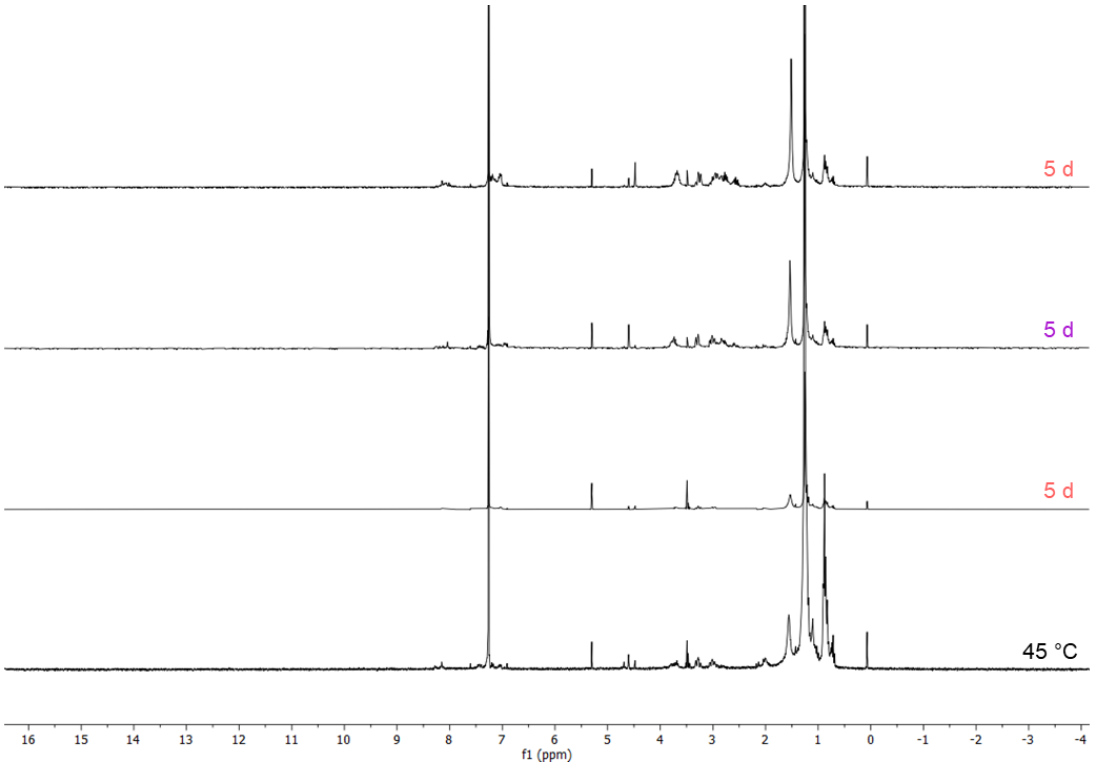

Figure S211: Comparison of ^{1}H NMR spectra ($CDCl_3$, 300 MHz) of *E,E,E*-**A^{3}Tren^{2}** and **Pr** after 5 days under irradiation with red light (660 nm), after 14 hours of irradiation with UV light (405 nm), followed by irradiation with red light for 5 days and stirring in the dark at room temperature for 4 days and for 2 days at 45 °C.

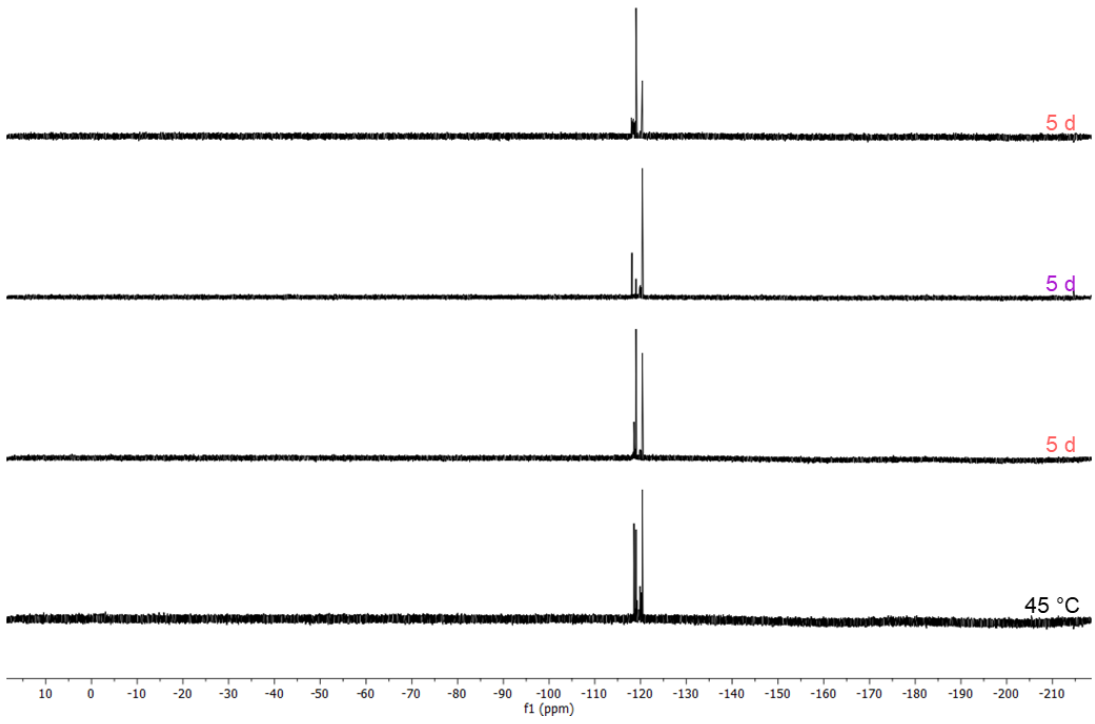

Figure S212: Comparison of ^{19}F{^{1}H} NMR spectra ($CDCl_3$, 282 MHz) of *E,E,E*-**A^{3}Tren^{2}** and **Pr** after 5 days under irradiation with red light (660 nm), after 14 hours of irradiation with UV light (405 nm), followed by irradiation with red light for 5 days and stirring in the dark at room temperature for 4 days and for 2 days at 45 °C.

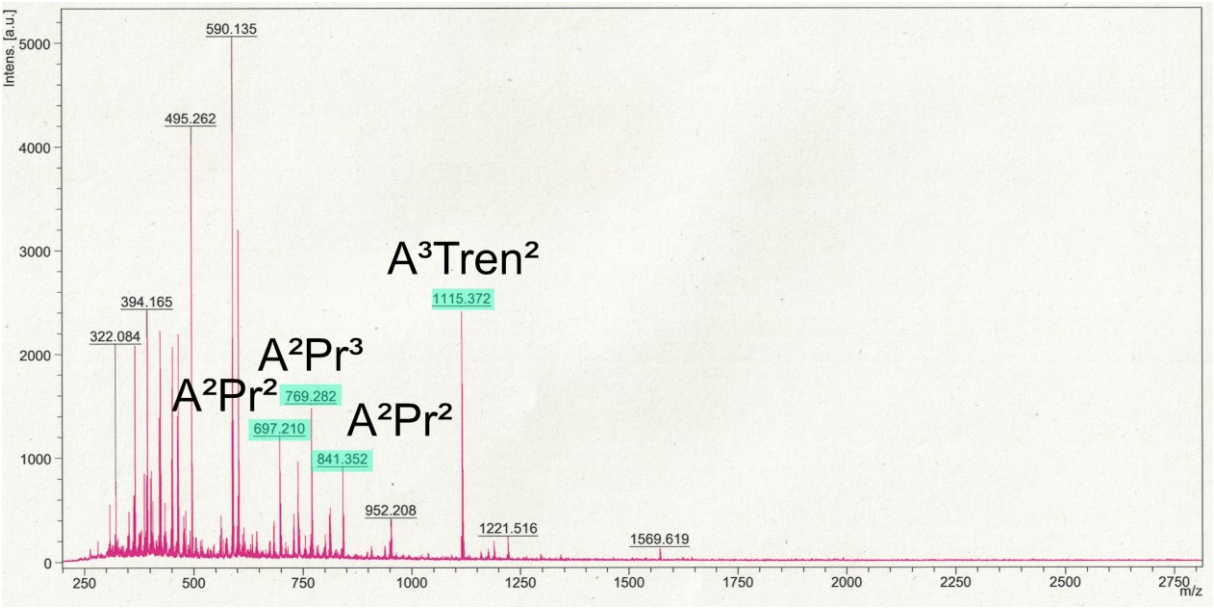

Figure S213: MALDI-mass spectrum of the reaction of *E,E,E*-**A³Tren²** and **Pr** after irradiation with red light (660 nm) for 5 days. Peaks that can be attributed to compounds are highlighted in turquoise.

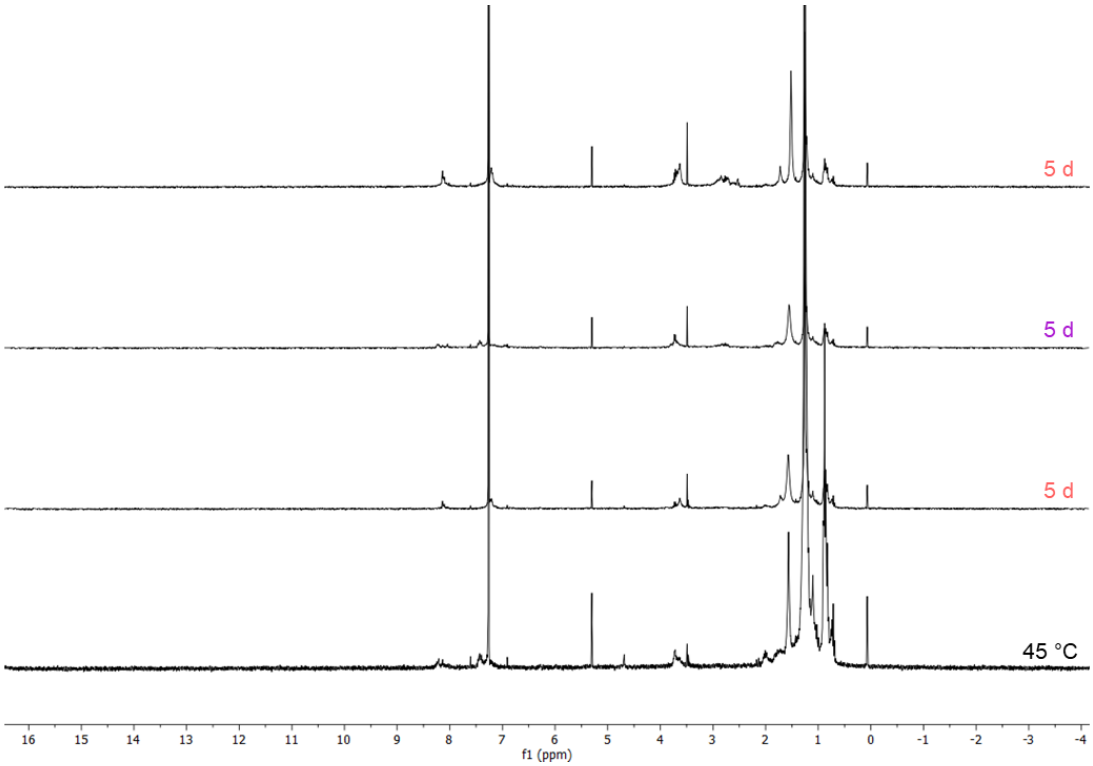

Figure S214: Comparison of ^{1}H NMR spectra ($CDCl_3$, 300 MHz) of *E,E,E*-**A³Tren²** and **B** after 5 days under irradiation with red light (660 nm), after 14 hours of irradiation with UV light (405 nm), followed by irradiation with red light for 5 days and stirring in the dark at room temperature for 4 days and for 2 days at 45 °C.

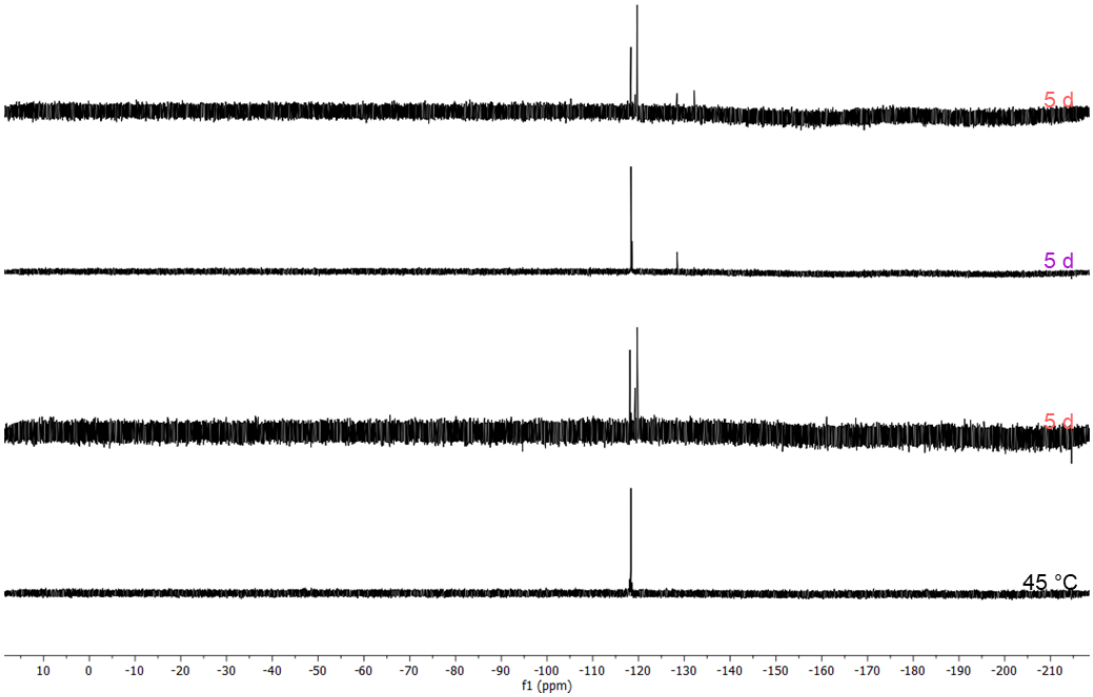

Figure S215: Comparison of $^{19}F\{^{1}H\}$ NMR spectra ($CDCl_3$, 282 MHz) of *E,E,E*-**A^{3}Tren^2** and **B** after 5 days under irradiation with red light (660 nm), after 14 hours of irradiation with UV light (405 nm), followed by irradiation with red light for 5 days and stirring in the dark at room temperature for 4 days and for 2 days at 45 °C.

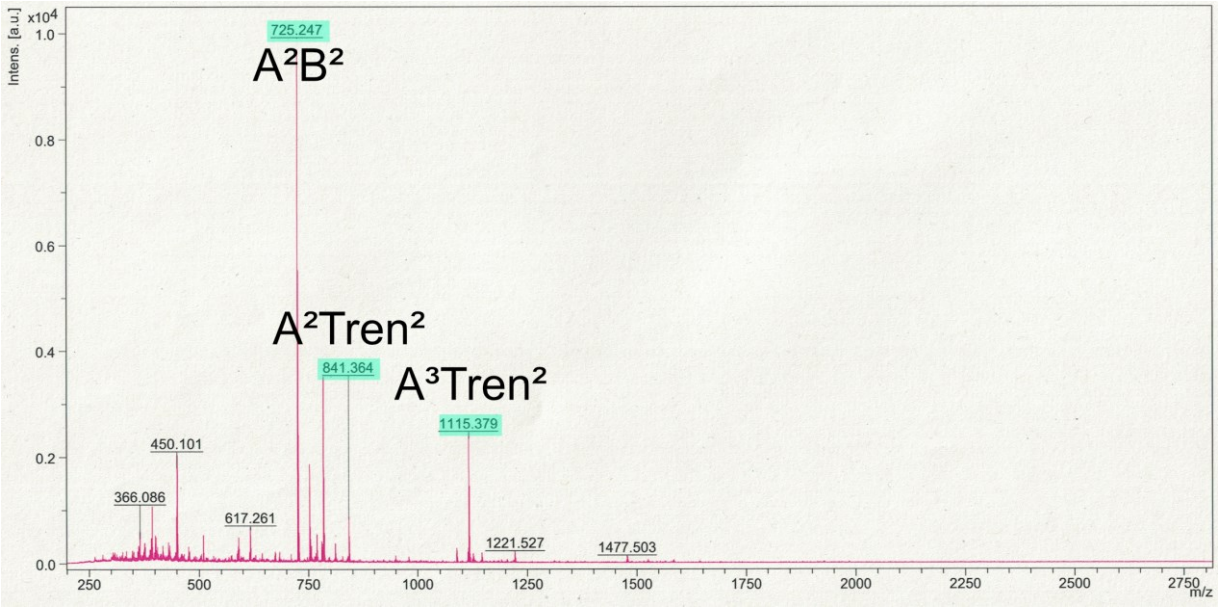

Figure S216: MALDI-mass spectrum of the reaction of *E,E,E*-**A^{3}Tren^2** and **B** after irradiation with red light (660 nm) for 5 days. Peaks that can be attributed to compounds are highlighted in turquoise.

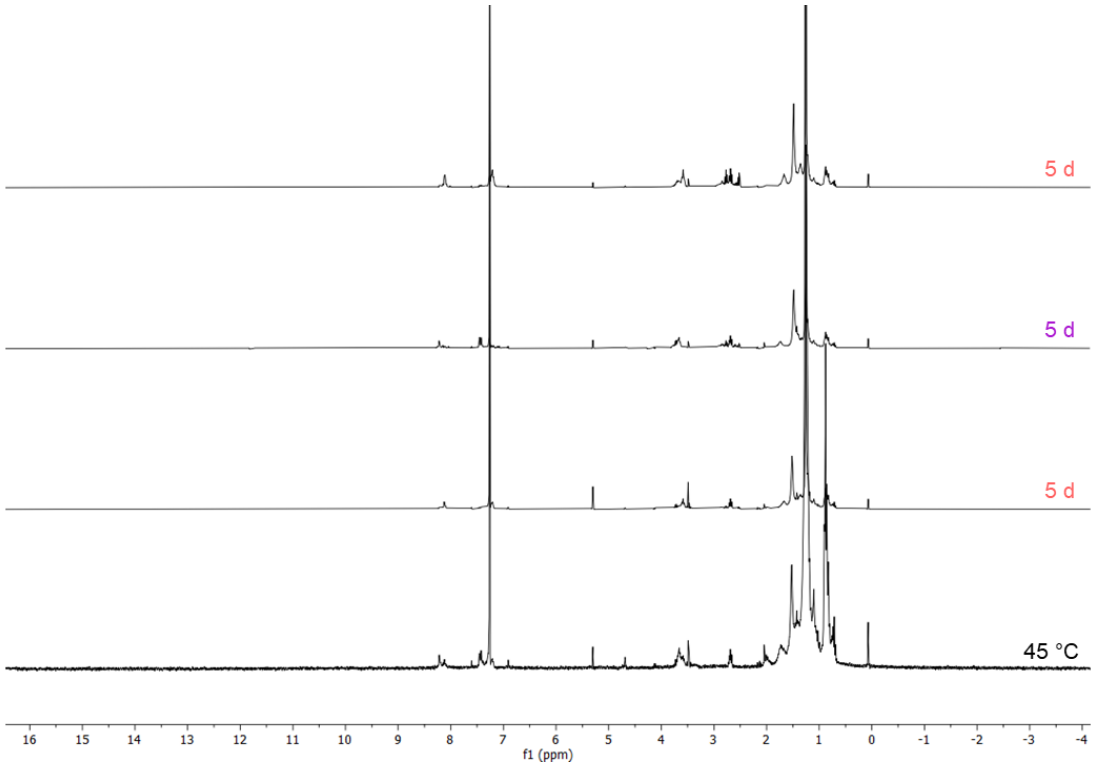

Figure S217: Comparison of ^{1}H NMR spectra ($CDCl_3$, 300 MHz) of *E,E,E*-**A^{3}Tren^{2}** and **H** after 5 days under irradiation with red light (660 nm), after 14 hours of irradiation with UV light (405 nm), followed by irradiation with red light for 5 days and stirring in the dark at room temperature for 4 days and for 2 days at 45 °C.

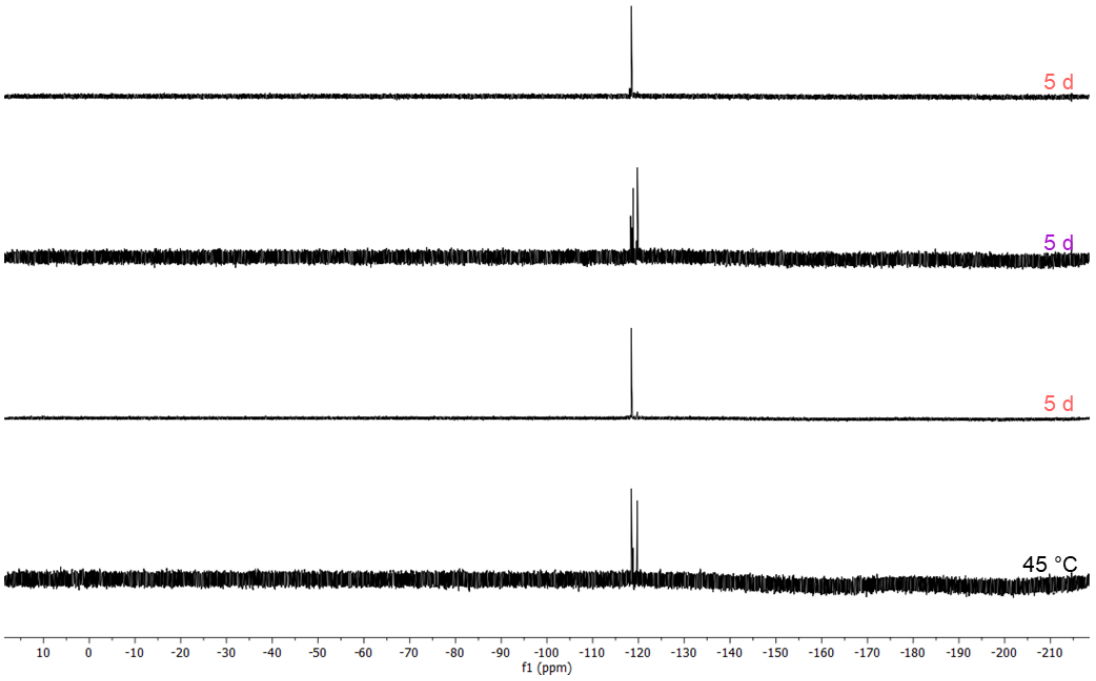

Figure S218: Comparison of ^{19}F{^{1}H} NMR spectra ($CDCl_3$, 282 MHz) of *E,E,E*-**A^{3}Tren^{2}** and **H** after 5 days under irradiation with red light (660 nm), after 14 hours of irradiation with UV light (405 nm), followed by irradiation with red light for 5 days and stirring in the dark at room temperature for 4 days and for 2 days at 45 °C.

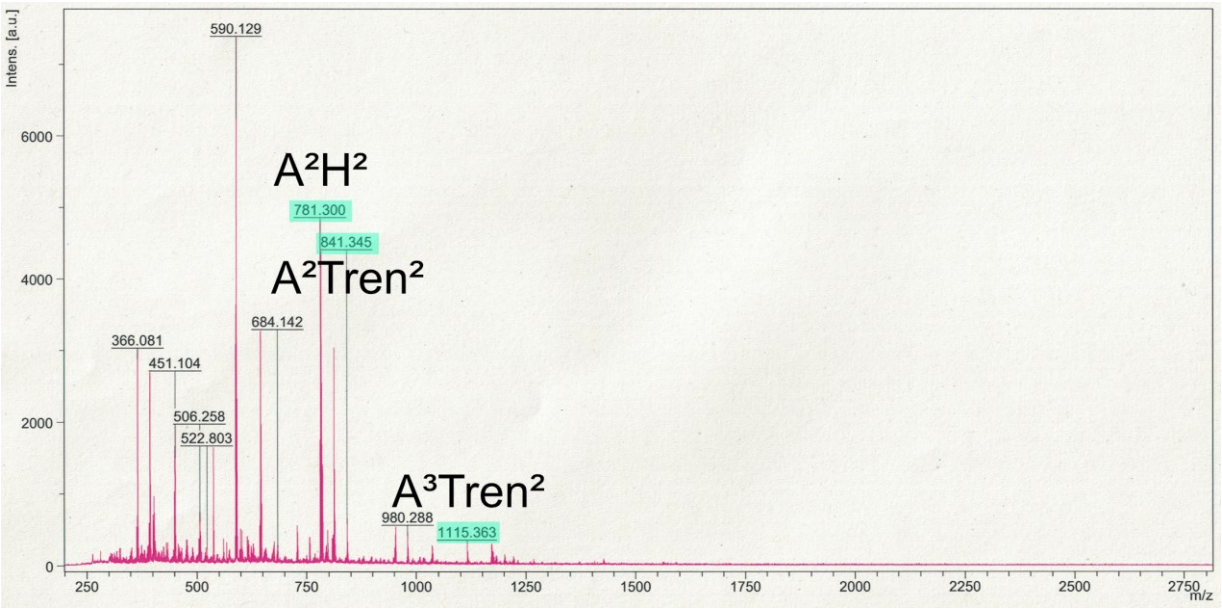

Figure S219: MALDI-mass spectrum of the reaction of *E,E,E*-**A³Tren²** and **H** after irradiation with red light (660 nm) for 5 days. Peaks that can be attributed to compounds are highlighted in turquoise.

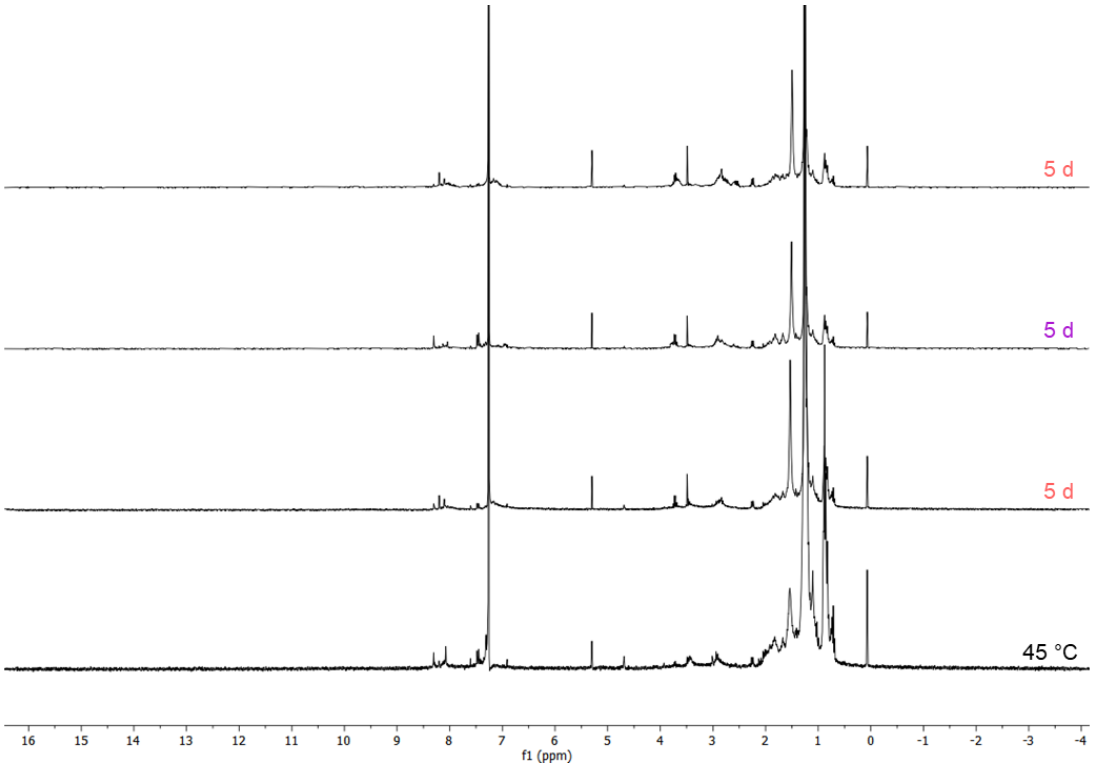

Figure S220: Comparison of ^{1}H NMR spectra ($CDCl_3$, 300 MHz) of *E,E,E*-**A³Tren²** and **D** after 5 days under irradiation with red light (660 nm), after 14 hours of irradiation with UV light (405 nm), followed by irradiation with red light for 5 days and stirring in the dark at room temperature for 4 days and for 2 days at 45 °C.

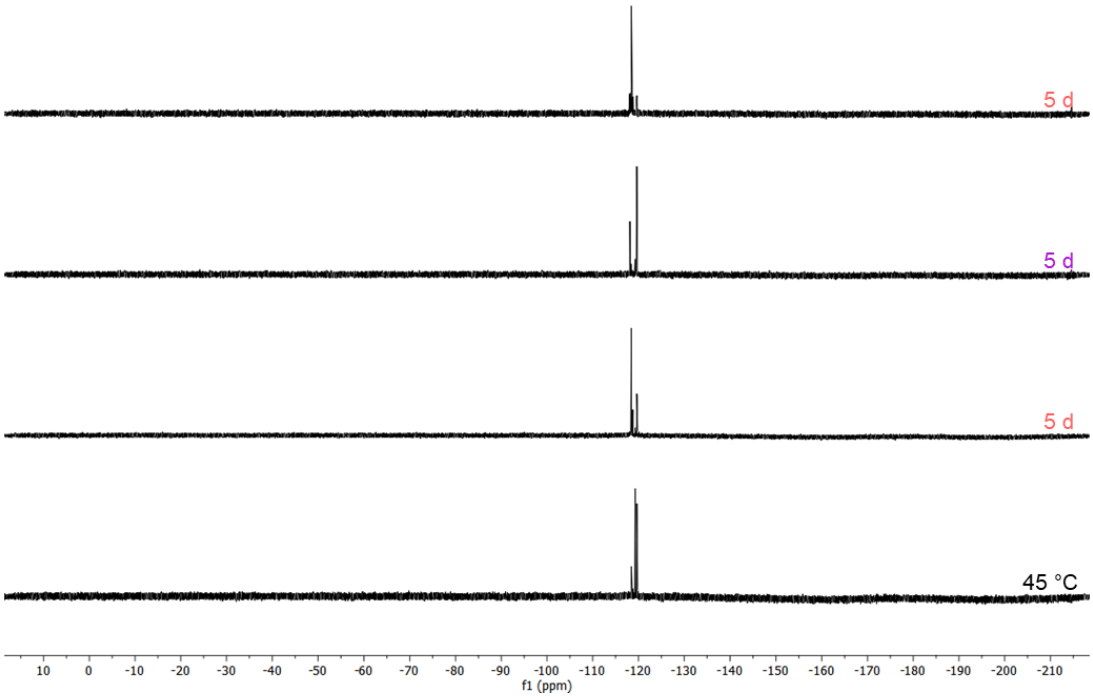

Figure S221: Comparison of $^{19}F\{^{1}H\}$ NMR spectra ($CDCl_3$, 282 MHz) of *E,E,E*-**A³Tren²** and **D** after 5 days under irradiation with red light (660 nm), after 14 hours of irradiation with UV light (405 nm), followed by irradiation with red light for 5 days and stirring in the dark at room temperature for 4 days and for 2 days at 45 °C.

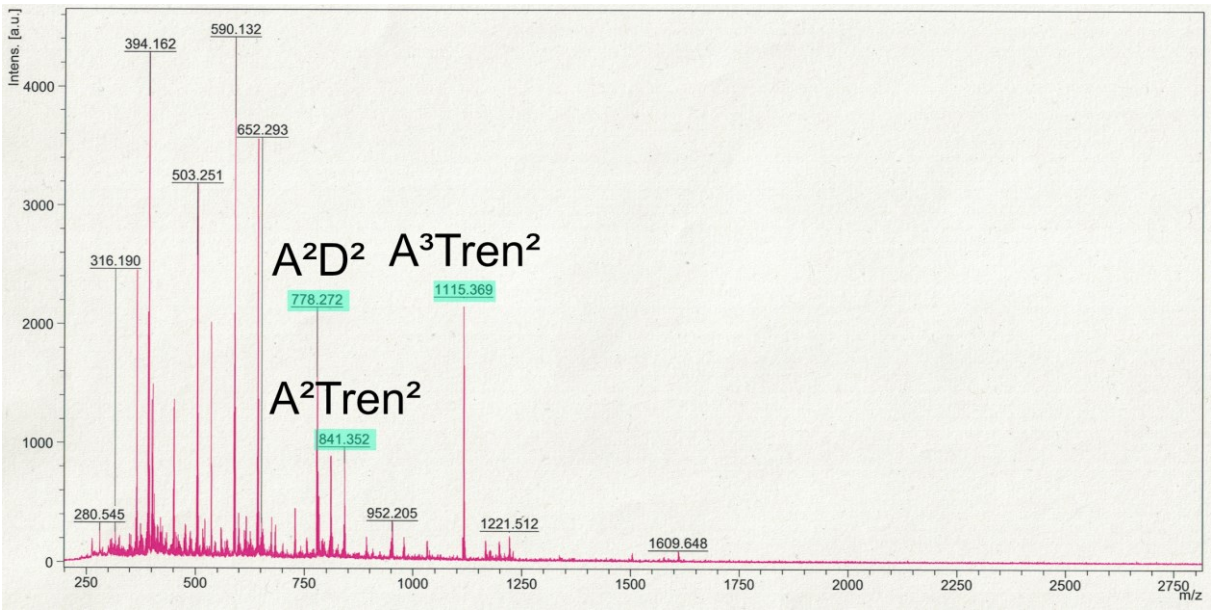

Figure S222: MALDI-mass spectrum of the reaction of *E,E,E*-**A³Tren²** and **D** after irradiation with red light (660 nm) for 5 days. Peaks that can be attributed to compounds are highlighted in turquoise.

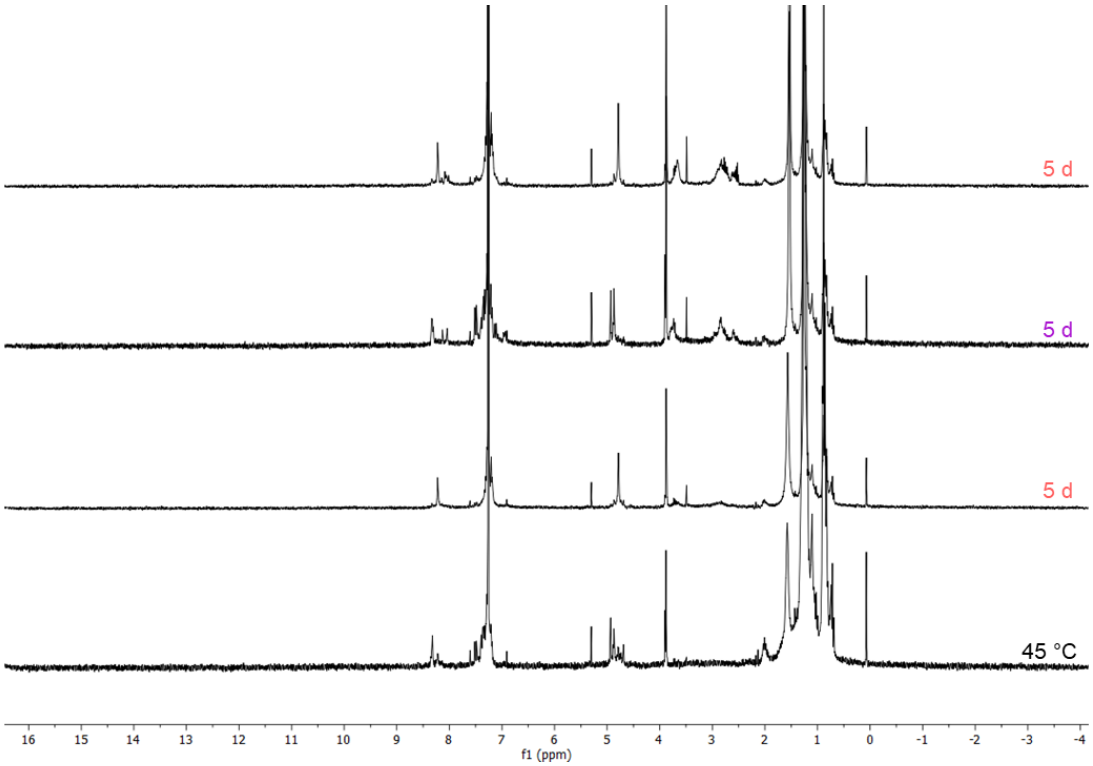

Figure S223: Comparison of ^{1}H NMR spectra ($CDCl_3$, 300 MHz) of *E,E,E*-**A^{3}Tren^{2}** and **mP** after 5 days under irradiation with red light (660 nm), after 14 hours of irradiation with UV light (405 nm), followed by irradiation with red light for 5 days and stirring in the dark at room temperature for 4 days and for 2 days at 45 °C.

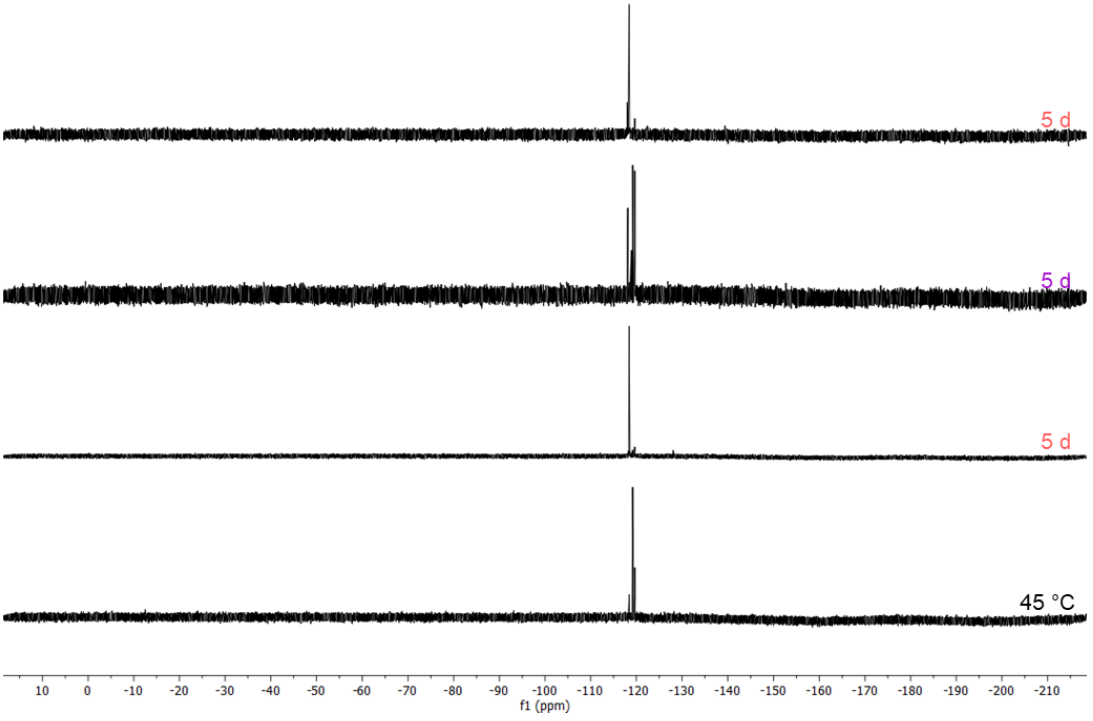

Figure S224: Comparison of ^{19}F{^{1}H} NMR spectra ($CDCl_3$, 282 MHz) of *E,E,E*-**A^{3}Tren^{2}** and **D** after 5 days under irradiation with red light (660 nm), after 14 hours of irradiation with UV light (405 nm), followed by irradiation with red light for 5 days and stirring in the dark at room temperature for 4 days and for 2 days at 45 °C.

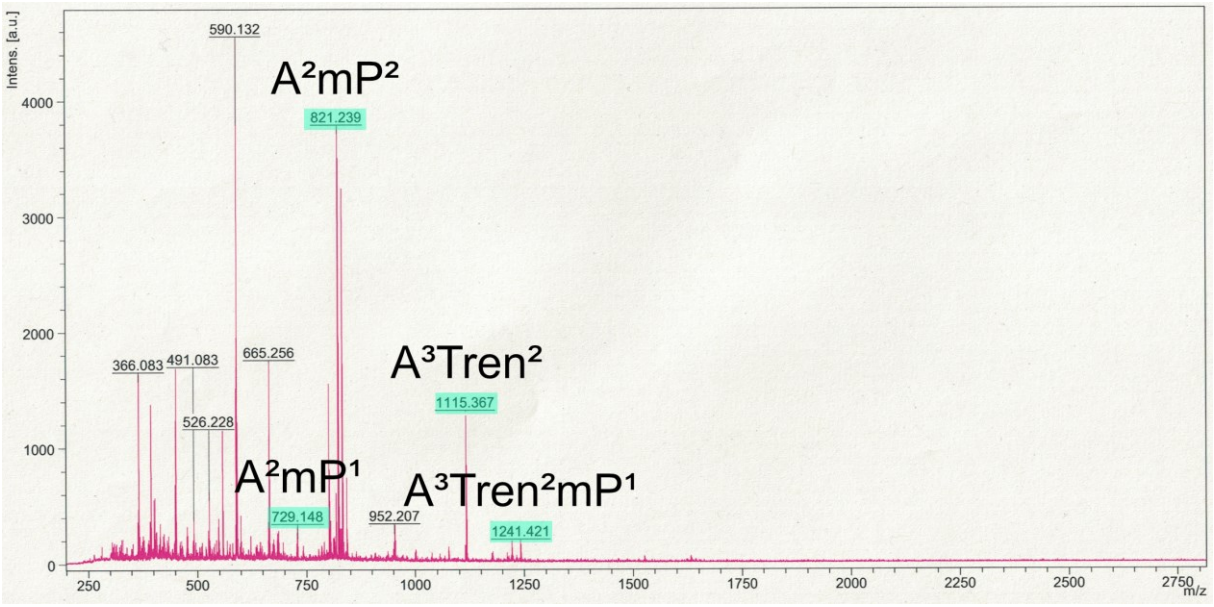

Figure S225: MALDI-mass spectrum of the reaction of *E,E,E*-**A^{3}Tren^2** and **E** after irradiation with red light (660 nm) for 5 days. Peaks that can be attributed to compounds are highlighted in turquoise.

5. References

[1] a) J.-M. Lehn, *Science*, **1993**, *260*, 1762–1763; b) J.-M. Lehn, *Science*, **1985**, *227*, 849–856.

[2] a) J.-M. Lehn, *Angew. Chem. Int. Ed.* **1988**, *27*, 89–112; b) D. J. Cram, *Angew. Chem. Int. Ed.* **1988**, *27*, 1009–1020; c) C. J. Pedersen, *Angew. Chem. Int. Ed.* **1988**, *27*, 1021–1027.

[3] a) G. R. Desiraju, *Nature,* **2001**, *412*, 397–400; b) M. C. T. Fyfe, J. F. Stoddart, *Acc. Chem. Res.* **1997**, *30*, 393–401.

[4] I. V. Kolesnichenko, E. V. Anslyn, *Chem. Soc. Rev.* **2017**, *46*, 2385–2390.

[5] a) E. Benchimol, B.-N. T. Nguyen, T. K. Ronson, J. R. Nitschke, *Chem. Soc. Rev.* **2022**, *51*, 5101–5135; b) R. Küng, R. Göstl, B. M. Schmidt, *Chem. Eur. J.* **2022**, *28*, e202103860; c) J. Yu, D. Qi, J. Li, *Commun. Chem.* **2020**, *3*, 189; d) L. Wang, Q. Li, *Chem. Soc. Rev.* **2018**, *47*, 1044–1097; e) A. J. McConnell, C. S. Wood, P. P. Neelakandan, J. R. Nitschke, *Chem. Rev.* **2015**, *115*, 7729–7793.

[6] a) M. Weißenfels, J. Gemen, R. Klajn, *Chem,* **2021**, *7*, 23–27; b) B. Rieß, R. K. Grötsch, J. Boekhoven, *Chem*, **2020**, *6*, 552–578; c) B. Rieß, J. Boekhoven, *ChemNanoMat,* **2018**, *4*, 710–719; d) G. Ragazzon, L. J. Prins, *Nat. Nanotechnol.* **2018**, *13*, 882–889; e) S. A. P. van Rossum, M. Tena-Solsona, J. H. van Esch, R. Eelkema, J. Boekhoven, *Chem. Soc. Rev.* **2017**, *46*, 5519–5535; f) F. della Sala, S. Neri, S. Maiti, Jack L.-Y. Chen, L. J. Prins, *Curr. Opin. Biotechnol.* **2017**, *46*, 27–33; g) M. Fialkowski, K. J. M. Bishop, R. Klajn, S. K. Smoukov, C. J. Campbell, B. A. Grzybowski, *J. Phys. Chem. B*, **2006**, *110*, 2482–2496.

[7] a) E. Nieland, O. Weingart, B. M. Schmidt, *Beilstein J. Org. Chem.* **2019**, *15*, 2013–2019; b) E. Nieland, T. Topornicki, T. Kunde, B. M. Schmidt, *Chem. Commun.* **2019**, *55*, 8768–8771.

[8] S. J. Rowan, S. J. Cantrill, G. R. L. Cousins, J. K. M. Sanders, J. F. Stoddart, *Angew. Chem. Int. Ed.* **2002**, *41*, 898–952.

[9] a) A. D. Buckingham, J. E. del Bene, S. A. C. McDowell, *Chem. Phys. Lett.* **2008**, *463*, 1–10; b) G. C. Pimentel, A. L. McClellan, *Annu. Rev. Phys. Chem.* **1971**, *22*, 347–385.

[10] a) F. Aparicio, M. J. Mayoral, C. Montoro-García, D. González-Rodríguez, *Chem. Commun.* **2019**, *55*, 7277–7299; b) M. J. Mayoral, N. Bilbao, D. González-Rodríguez, *ChemistryOpen* **2015**, *5*, 10–32; c) G. Armstrong, M. Buggy, *J. Mater. Sci.* **2005**, *40*, 547–559.

[11] Y. Liu, C. Hu, A. Comotti, M. D. Ward, *Science*, **2011**, *333*, 436–440.

[12] a) R. Kampes, S. Zechel, M. D. Hager, U. S. Schubert, *Chem. Sci.* **2021**, *12*, 9275–9286; b) Y.-J. Zhu, Y. Gao, M.-M. Tang, J. Rebek, Y. Yu, *Chem. Commun.* **2021**, *57*, 1543–1549; c) V. Nemec, K. Lisac, N. Bedeković, L. Fotović, V. Stilinović, D. Cinčić, *CrystEngComm*, **2021**, *23*, 3063–3083; d) D. von der Heiden, A. Vanderkooy, M. Erdélyi, *Coord. Chem. Rev.* **2020**, *407*, 213147; e) L. Turunen; M. Erdélyi, *Chem. Soc. Rev.* **2020**, *49*, 2688–2700; f) M. Saccone, L. Catalano, *J. Phys. Chem. B*, **2019**, *123*, 9281–9290; g) C. A. Gunawardana, C. B. Aakeröy, *Chem. Commun.* **2018**, *54*, 14047–14060; h) G. Cavallo, P. Metrangolo, R. Milani, T. Pilati, A. Priimagi, G. Resnati, G. Terraneo, *Chem. Rev.* **2016**, *116*, 2478–2601; i) L. C. Gilday, S. W. Robinson, T. A. Barendt, M. J. Langton, B. R. Mullaney, P. D. Beer, *Chem. Rev.* **2015**, *115*, 7118–7195; j) A. Priimagi, G. Cavallo, P. Metrangolo, G. Resnati, *Acc. Chem. Res.*, **2013**, *46*, 2686–2695; k) M. Erdélyi, *Chem. Soc. Rev.* **2012**, *41*, 3547–3557; l) M. G.

Sarwar, B. Dragisic, L. J. Salsberg, C. Gouliaras, M. S. Taylor, *J. Am. Chem. Soc.* **2010**, *132*, 1646–1653.

[13] a) E. Uran, L. Fotović, N. Bedeković, V. Stilinović, D. Cinčić, *Crystals*, **2021**, *11*, 529; b) A. J. Peloquin, J. M. McCollum, C. D. McMillen, W. T. Pennington, *Angew. Chem. Int. Ed.* **2021**, *60*, 22983–22989; c) L. Happonen, J. M. Rautiainen, A. Valkonen, *Cryst. Growth Des.* **2021**, *21*, 3409–3419; d) A. S. Mikherdov, A. S. Novikov, V. P. Boyarskiy, V. Y. Kukushkin, *Nat. Commun.* **2020**, *11*, 2921; e) Y. Xu, J. Huang, B. Gabidullin, D. L. Bryce, *Chem. Commun.* **2018**, *54*, 11041–11043; f) R. Núñez, P. Farràs, F. Teixidor, C. Viñas, R. Sillanpää, R. Kivekäs, *Angew. Chem. Int. Ed.* **2006**, *45*, 1270–1272.

[14] P. M. J. Szell, A. Siiskonen, L. Catalano, G. Cavallo, G. Terraneo, A. Priimagi, D. L. Bryce, P. Metrangolo, *New J. Chem.* **2018**, *42*, 10467–10471.

[15] a) T. K. Wijethunga, M. Đaković, J. Desper, C. B. Aakeröy, *Acta Crystallogr.* **2017**, *73*, 163–167; b) M. A. Sinnwell, L. R. MacGillivray, *Angew. Chem. Int. Ed.* **2016**, *55*, 3477–3480.

[16] a) U. Warzok, M. Marianski, W. Hoffmann, L. Turunen, K. Rissanen, K. Pagel, C. A. Schalley, *Chem. Sci.* **2018**, *9*, 8343–8351; b) O. Dumele, B. Schreib, U. Warzok, N. Trapp, C. A. Schalley, F. Diederich, *Angew. Chem. Int. Ed.* **2017**, *56*, 1152–1157; c) L. Turunen, U. Warzok, C. A. Schalley, K. Rissanen, *Chem*, **2017**, *3*, 861–869; d) L. Turunen, A. Peuronen, S. Forsblom, E. Kalenius, M. Lahtinen, K. Rissanen, *Chem. Eur. J.* **2017**, *23*, 11714–11718; e) L. Turunen, U. Warzok, R. Puttreddy, N. K. Beyeh, C. A. Schalley, K. Rissanen, *Angew. Chem. Int. Ed.* **2016**, *55*, 14033–14036; f) N. K. Beyeh, F. Pan, K. Rissanen, *Angew. Chem. Int. Ed.* **2015**, *54*, 7303–7307; g) O. Dumele, N. Trapp, F. Diederich, *Angew. Chem. Int. Ed.* **2015**, *54*, 12339–12344; h) C. B. Aakeröy, A. Rajbanshi, P. Metrangolo, G. Resnati, M. F. Parisi, J. Desper, T. Pilati, *CrystEngComm*, **2012**, *14*, 6366–6368.

[17] a) A. Vanderkooy, A. K. Gupta, T. Földes, S. Lindblad, A. Orthaber, I. Pápai, M. Erdélyi, *Angew. Chem. Int. Ed.* **2019**, *58*, 9012–9016; b) C. J. Massena, D. A. Decato, O. B. Berryman, *Angew. Chem. Int. Ed.* **2018**, *49*, 16109–16113; c) C. J. Massena, N. B. Wageling, D. A. Decato, E. M. Rodriguez, A. M. Rose, O. B. Berryman, *Angew. Chem. Int. Ed.* **2016**, *128*, 12586–12590.

[18] a) N. S. Soldatova, P. S. Postnikov, D. M. Ivanov, O. V. Semyonov, O. S. Kukurina, O. Guselnikova, Y. Yamauchi, T. Wirth, V. V. Zhdankin, M. S. Yusubov, R. M. Gomila, A. Frontera, G. Resnati, V. Y. Kukushkin, *Chem. Sci.* **2022**, *13*, 5650–5658; b) G. Gong, S. Lv, J. Han, F. Xie, Q. Li, N. Xia, W. Zeng, Y. Chen, L. Wang, J. Wang, S. Chen, *Angew. Chem. Int. Ed.* **2021**, *60*, 14831–14835; c) J. Zhou, L. Stojanović, A. A. Berezin, T. Battisti, A. Gill, B. M. Kariuki, D. Bonifazi, R. Crespo-Otero, M. R. Wasielewski, Y.-L. Wu, *Chem. Sci.* **2021**, *12*, 767–773; d) N. Chongboriboon, K. Samakun, T. Inprasit, F. Kielar, W. Dungkaew, L. W.-Y. Wong, H. H.-Y. Sung, D. B. Ninković, S. D. Zarić, K. Chainok, *CrystEngComm* **2020**, *22*, 24–34; e) I. G. Grosu, L. Pop, M. Miclăuş, N. D. Hădade, A. Terec, A. Bende, C. Socaci, M. Barboiu, I. Grosu, *Cryst. Growth Des.* **2020**, *20*, 3429–3441; f) V. I. Nikolayenko, D. C. Castell, D. P. van Heerden, L. J. Barbour, *Angew. Chem. Int. Ed.* **2018**, *57*, 12086–12091; g) M. C. Pfrunder, A. J. Brock, J. J. Brown, A. Grosjean, J. Ward, J. C. McMurtrie, J. K. Clegg, *Chem. Commun.* **2018**, *54*, 3974–3976; h) S. Shankar, O. Chovnik, L. J. W. Shimon, M. Lahav, M. E. van der Boom, *Cryst. Growth Des.* **2018**, *18*, 1967–1977.

[19] a) S. Lee, H. Jeong, D. Nam, M. S. Lah, W. Choe, *Chem. Soc. Rev.* **2021**, *50*, 528–555; b) S. Saha, I. Regeni, G. H. Clever, *Coord. Chem. Rev.* **2018**, *374*, 1–14; c) M. Han, D. M. Engelhard, *Chem. Soc. Rev.* **2014**, *43*, 1848–1860; d) M. M. J. Smulders, I. A. Riddell, C. Browne, J. R. Nitschke, *Chem. Soc.*

Rev. **2013**, *42*, 1728–1754; e) P. Jin, S. J. Dalgarno, J. L. Atwood, *Coord. Chem. Rev.* **2010**, *254*, 1760–1768; f) M. Yoshizawa, J. K. Klosterman, M. Fujita, *Angew. Chem. Int. Ed.* **2009**, *48*, 3418–3438; g) D. J. Tranchemontagne, Z. Ni, M. O'Keeffe, O. M. Yaghi, *Angew. Chem. Int. Ed.* **2008**, *47*, 5136–5147; h) M. Fujita, *Chem. Soc. Rev.* **1998**, *27*, 417–425.

[20] a) H.-C. Zhou, S. Kitagawa, *Chem. Soc. Rev.* **2014**, *43*, 5415–5418; b) H.-C. Zhou, J. R. Long, O. M. Yaghi, *Chem. Rev.* **2012**, *112*, 673–674; c) S. L. James, *Chem. Soc. Rev.* **2003**, *32*, 276–288.

[21] M. Fujita, D. Oguro, M. Miyazawa, H. Oka, K. Yamaguchi, K. Ogura, *Nature*, **1995**, *378*, 469–471.

[22] a) Y. Nishioka, T. Yamaguchi, M. Yoshizawa, M. Fujita, *J. Am. Chem. Soc.* **2007**, *129*, 7000–7001; b) K. Nakabayashi, M. Kawano, T. Kato, K. Furukawa, S. Ohkoshi, T. Hozumi, M. Fujita, *Chem. Asian J.* **2007**, *2*, 164–170; c) M. Yoshizawa, M. Tamura, M. Fujita, *Science*, **2006**, *312*, 251–254; d) M. Kawano, Y. Kobayashi, T. Ozeki, M. Fujita, *J. Am. Chem. Soc.* **2006**, *128*, 6558–6559; e) Y. Kobayashi, M. Kawano, M. Fujita, *Chem. Commun.* **2006**, 4377–4379; f) V. Maurizot, M. Yoshizawa, M. Kawano, M. Fujita, *Dalton Trans.* **2006**, 2750–2756.

[23] V. Santolini, M. Miklitz, E. Berardo, K. E. Jelfs, *Nanoscale*, **2017**, *9*, 5280–5298.

[24] a) M. A. Little, A. I. Cooper, *Adv. Funct. Mater.* **2020**, *30*, 1909842; b) F. Beuerle, B. Gole, *Angew. Chem. Int. Ed.* **2017**, *57*, 4850–4878; c) G. Zhang, M. Mastalerz, *Chem. Soc. Rev.* **2014**, *43*, 1934–1947; d) Y. Jin, Q. Wang, P. Taynton, W. Zhang, *Acc. Chem. Res.* **2014**, *47*, 1575–1586; e) M. E. Belowich, J. F. Stoddart, *Chem. Soc. Rev.* **2012**, *41*, 2003–2024; f) M. Mastalerz, *Angew. Chem. Int. Ed.* **2010**, *49*, 5042–5053.

[25] a) S. Klotzbach, F. Beuerle, *Angew. Chem. Int. Ed.* **2015**, *54*, 10356–10360; b) S. Klotzbach, T. Scherpf, F. Beuerle, *Chem. Commun.* **2014**, *50*, 12454–12457; c) G. Zhang, O. Presly, F. White, I. M. Oppel, *Angew. Chem. Int. Ed.* **2014**, *53*, 1516–1520; d) N. Nishimura, K. Kobayashi, *Angew. Chem. Int. Ed.* **2008**, *47*, 6255–6258.

[26] a) T. Tozawa, J. T. A. Jones, S. I. Swamy, S. Jiang, D. J. Adams, S. Shakespeare, R. Clowes, D. Bradshaw, T. Hasell, S. Y. Chong, C. Tang, S. Thompson, J. Parker, A. Trewin, J. Bacsa, A. M. Z. Slawin, A. Steiner, A. I. Cooper, *Nat. Mat.* **2009**, *8*, 973–978; b) P. Skowronek, J. Gawroński, *Org. Lett.* **2008**, *10*, 4755–4758.

[27] a) H. Bouas-Laurent, H. Dürr, *Pure Appl. Chem.* **2001**, *73*, 639–665; b) M. Irie, *Chem. Rev.* **2000**, *100*, 1683–1684.

[28] a) Z. Zhang, W. Wang, M. O'Hagan, J. Dai, J. Zhang, H. Tian, *Angew. Chem. Int. Ed.* **2022**, *61*, e202205758; b) A. Goulet-Hanssens, F. Eisenreich, S. Hecht, *Adv. Mater.* **2020**, *32*, 1905966; c) J. Zhang, Q. Zou, H. Tian, *Adv. Mater.* **2013**, *25*, 378–399; d) M.-M. Russew, S. Hecht, *Adv. Mater.* **2010**, *22*, 3348–3360.

[29] a) M. Irie, T. Fukaminato, K. Matsuda, S. Kobatake, *Chem. Rev.* **2014**, *114*, 12174–12277; b) M. Irie, *Chem. Rev.* **2000**, *100*, 1685–1716.

[30] a) A. S. Dvornikov, J. Malkin, P. M. Rentzepis, *J. Phys. Chem.* **1994**, *98*, 6746–6752; b) D. A. Parthenopoulos, P. M. Rentzepis, *Science,* **1989**, *245*, 843–845.

[31] a) D. Roke, S. J. Wezenberg, B. L. Feringa, *Proc. Natl. Acad. Sci. U.S.A.*, **2018**, *115*, 9423–9431; b) S. Kassem, T. V. Leeuwen, A. S. Lubbe, M. R. Wilson, B. L. Feringa, D. A. Leigh, *Chem. Soc. Rev.* **2017**, *46*, 2592–2621; c) B. L. Feringa, *Angew. Chem. Int. Ed.* **2017**, *56*, 11060–11078.

[32] C. Petermayer, H. Dube, *Acc. Chem. Res.* **2018**, *51*, 1153–1163.

[33] a) D. Villarón, S. J. Wezenberg, *Angew. Chem. Int. Ed.* **2020**, *132*, 13292–13302; b) D. H. Waldeck, *Chem. Rev.* **1991**, *91*, 415–436.
[34] H. M. D. Bandara, S. Burdette, *Chem. Soc. Rev.* **2012**, *41*, 1809–1825.
[35] a) S. Nakamura, M. Irie, *J. Org. Chem.* **1988**, *53*, 6136–6138; b) M. Irie, M. Mohri, *J. Org. Chem.* **1988**, *53*, 803–808.
[36] N. Koumura, R. W. J. Zijlstra, R. A. van Delden, N. Harada, B. L. Feringa, *Nature*, **1999**, *401*, 152–155.
[37] a) M. Gao, D. Kwaria, Y. Norikane, Y. Yue, *Nat. Sci.* **2023**, *3*, e20220020; b) D. Bléger, S. Hecht, *Angew. Chem. Int. Ed.* **2015**, *54*, 11338–11349.
[38] a) M. Dong, A. Babalhavaeji, C. V. Collins, K. Jarrah, O. Sadovski, Q. Dai, G. A. Woolley, *J. Am. Chem. Soc.* **2017**, *139*, 13483–13486; b) S. Samanta, A. A. Beharry, O. Sadovski, T. M. McCormick, A. Babalhavaeji, V. Tropepe, G. A. Woolley, *J. Am. Chem. Soc.* **2013**, *135*, 9777–9784; c) A. A. Beharry, O. Sadovski, G. A. Woolley, *J. Am. Chem. Soc.* **2011**, *133*, 19684–19687.
[39] a) C. Knie, M. Utecht, F. Zhao, H. Kulla, S. Kovalenko, A. M. Brouwer, P. Saalfrank, S. Hecht, D. Bléger, *Chem. Eur. J.* **2014**, *20*, 16492–16501; b) D. Bléger, J. Schwarz, A. M. Brouwer, S. Hecht, *J. Am. Chem. Soc.* **2012**, *134*, 20597–20600.
[40] S. Crespi, N. A. Simeth, B. König, *Nat. Rev. Chem.* **2019**, *3*, 133–146.
[41] a) J. L. Greenfield, M. A. Gerkman, R. S. L. Gibson, G. G. D. Han, M. J. Fuchter, *J. Am. Chem. Soc.* **2021**, *143*, 15250–15257; b) M. A. Gerkman, R. S. L. Gibson, J. Calbo, Y. Shi, M. J. Fuchter, G. G. D. Han, *J. Am. Chem. Soc.* **2020**, *142*, 8688–8695; c) J. Calbo, C. E. Weston, A. J. P. White, H. S. Rzepa, J. Contreras-Garcia, M. J. Fuchter, *J. Am. Chem. Soc.* **2017**, *139*, 1261–1274; d) C. E. Weston, R. D. Richardson, P. R. Haycock, A. J. P. White, M. J. Fuchter, *J. Am. Chem. Soc.* **2014**, *136*, 11878–11881.
[42] a) P. Lentes, E. Stadler, F. Röhricht, A. Brahms, J. Gröbner, F. D. Sönnichsen, G. Gescheidt, R. Herges, *J. Am. Chem. Soc.* **2019**, *141*, 13592–13600; b) M. Hammerich, C. Schütt, C. Stähler, P. Lentes, F. Röhricht, R. Höppner, R. Herges, *J. Am. Chem. Soc.* **2016**, *138*, 13111–13114; c) R. Siewertsen, H. Neumann, B. Buchheim-Stehn, R. Herges, C. Näther, F. Renth, F. Temps, *J. Am. Chem. Soc.* **2009**, *131*, 15594–15595.
[43] a) Z. L. Pianowski, *Chem. Eur. J.* **2019**, *25*, 5128–5144; b) M. Dong, A. Babalhavaeji, S. Samanta, A. A. Beharry, G. A. Woolley, *Acc. Chem. Res.* **2015**, *48*, 2662–2670; c) A. A. Beharry, G. A. Woolley, *Chem. Soc. Rev.* **2011**, *40*, 4422–4437.
[44] a) E. Pantuso, G. de Filpo, F. P. Nicoletta, *Adv. Opt. Mater.* **2019**, *7*, 1900252; b) O. Bertrand, J.-F. Gohy, *Polym. Chem.* **2017**, *8*, 52–73; c) M. Wei, Y. Gao, X. Li, M. J. Serpe; d) F. D. Jochum, P. Theato, *Chem. Soc. Rev.* **2013**, *42*, 7468–7483.
[45] a) W.-C. Geng, H. Sun, D.-S. Guo, *J. Incl. Phenom. Macrocycl. Chem.* **2018**, *92*, 1–79; b) Z. Li, J. Liang, W. Xue, G. Liu, S. H. Liu, J. Yin, *Supramol. Chem.* **2014**, *26*, 54–65.
[46] a) S. J. Wezenberg, *Chem. Lett.* **2020**, *49*, 609–615; b) A. Díaz-Moscoso, P. Ballester, *Chem. Commun.* **2017**, *53*, 4653–4652; c) D.-H. Qu, Q.-C. Wang, Q.-W. Zhang, X. Ma, H. Tian, *Chem. Rev.* **2015**, *115*, 7543–7588.
[47] a) A. I. Hanopolskyi, S. De, M. J. Białek, Y. Diskin-Posner, L. Avram, M. Feller, R. Klajn, *Beilstein J. Org. Chem.* **2019**, *15*, 2398–2407; b) D. Samanta, J. Gemen, Z. Chu, Y. Diskin-Posner, L. J. W. Shimon, R. Klajn, *Proc. Natl. Acad. Sci. U.S.A.* **2018**, *115*, 9379–9384; c) G. H. Clever, S. Tashiro, M.

Shionoya, *J. Am. Chem. Soc.* **2010**, *132*, 9973–9975; d) H. Dube, D. Ajami, J. Rebek, *Angw. Chem. Int. Ed.* **2010**, *49*, 3192–3195; e) T. Kusukawa, M. Fujita, *J. Am. Chem. Soc.* **1999**, *121*, 1397–1398.

[48] a) T. Murase, S. Sato, M. Fujita, *Angew. Chem. Int. Ed.* **2007**, *46*, 5133–5136; b) M. Tominaga, K. Suzuki, T. Murase, M. Fujita, *J. Am. Chem. Soc.* **2005**, *127*, 11950–11951.

[49] a) Y. Jang, J. Park, P. Tan, L. Feng, X.-Q. Liu, L.-B. Sun, H.-C. Zhou, *J. Am. Chem. Soc.* **2019**, *141*, 8221–8227; b) J. Park, L.-B. Sun, Y.-P. Chen, Z. Perry, H.-C. Zhou, *Angew. Chem. Int. Ed.* **2014**, *53*, 5842–5846.

[50] Y. Liu, W. Yang, H. Liu, *Chem. Eur. J.* **2015**, *21*, 4731–4738.

[51] a) S. Ghosh, C. Eschen, N. Eleya, A. Staubitz, *J. Org. Chem.* **2023**, *88*, 3372–3377; b) S. Xiong, Q. He, *Chem. Commun.* **2021**, *57*, 13514–13517; c) N. N. Mafy, Y. Kim, R. Thomas, T. Akasaka, N. Tamaoki, *ACS Appl. Mater. Interfaces,* **2019**, *11*, 15097–15102; d) G. Despras, J. Hain, S. O. Jaeschke, *Chem. Eur. J.* **2017**, *23*, 10838–10847; e) C. Lin, S. Maisonneuve, R. Métivier, J. Xie, *Chem. Eur. J.* **2017**, *23*, 14996–15001.

[52] a) Y. Liu, H. Wang, P. Liu, H. Zhu, B. Shi, X. Hong, F. Huang, *Angew. Chem. Int. Ed.* **2021**, *60*, 5766–5770; b) J. Wei, T.-T. Jin, J.X. Yang, X.-M. Jiang, L.-J. Liu, T.-G. Zhan, K.-D. Zhang, *Tet. Lett.* **2020**, *61*, 151389; c) X. Chi, W. Cen, J. A. Queenan, L. Long, V. Lynch, N. M. Khashab, J. L. Sessler, *J. Am. Chem. Soc.* **2019**, *141*, 6468–6472; d) A. H. Heindl, J. Becker, H. A. Wegner, *Chem. Sci.* **2019**, *10*, 7418–7425; e) C. Slavov, C. Yang, A. H. Heindl, T. Stauch, H. A. Wegner, A. Dreuw, J. Wachtveitl, *J. Phys. Chem. Lett.* **2018**, *9*, 4776–4781; f) L. Schweighauser, D. Häussinger, M. Neuburger, H. A. Wegner, *Org. Biomol. Chem.* **2014**, *12*, 3371–3379; g) R. Reuter, H. A. Wegner, *Chem. Commun.* **2013**, *49*, 146–148; h) R. Reuter, H. A. Wegner, *Chem. Eur. J.* **2011**, *17*, 2987–2995; i) Y. Norikane, Y. Hirai, M. Yoshida, *Chem. Commun.* **2011**, *47*, 1770–1772; j) M. Müri, K. C. Scheuermann, L. de Cola, M. Mayor, *Chem. Eur. J.* **2009**, 2562–2575; k) Y. Norikane, N. Tamaoki, *Org. Lett.* **2004**, *6*, 2595–2598; l) Y. Norikane, K. Kitamoto, N. Tamaoki, *Org. Lett.* **2002**, *4*, 3907–3910; m) J. Huuskonen, J. Schulz, E. Kolehmainen, K. Rissanen, *Chem. Eur. J.* **1994**, *127*, 2267–2272; n) N. Tamaoki, K. Koseki, T. Yamaoka, *Tet. Lett.* **1990**, *31*, 3309–3312; o) D. Gräf, H. Nitsch, D. Ufermann, G. Sawitzki, H. Patzelt, H. Rau, *Angew. Chem. Int. Ed.* **1982**, *21*, 373–374.

[53] a) H. Roithmeyer, M. Uudsemaa, A. Trummal, M.-L. Brük, S. Krämer, I. Reile, V. Rjabovs, K. Palmi, M. Rammo, R. Aav, E. Kalenius, J. Adamson, **2023**, *Research Square preprint*, DOI:10.21203/rs.3.rs-2621025/v1; b) M. Li, L.-J. Chen, Z. Zhang, Q. Luo, H.-B. Yang, H. Tian, W.-H. Zhu, *Chem. Sci.* **2019**, *10*, 4896–4904.

[54] a) K. Artmann, R.-J. Li, S. Juber, E. Benchimol, L. V. Schäfer, G. H. Clever, P. Nuernberger, *Angew. Chem. Int. Ed.* **2022**, *61*, e202212112; b) K. Artmann, R.-J. Li, S. Juber, E. Benchimol R.-J. Li, J. Tessarolo, H. Lee, G. H. Clever, *J. Am. Chem. Soc.* **2021,** *143*, 3865–3873; c) S. Juber, S. Wingbermühle, P. Nuernberger, G. H. Clever, L. V. Schäfer, *Phys. Chem. Chem. Phys.* **2021**, *23*, 7321–7332, d) R.-J. Li, M. Han, J. Tessarolo, J. J. Holstein, J. Lübben, B. Dittrich, C. Volkmann, M. Finze, C. Jenne, G. H. Clever, *ChemPhotoChem* **2019**, *3*, 378–383; e) R.-J. Li, J. J. Holstein, W. G. Hiller, J. Andréasson, G. H. Clever, *J. Am. Chem. Soc.* **2019**, *141*, 2097–2103; f) M. Han, R. Michel, B. He, Y.-S. Chen, D. Stalke, M. John, G. H. Clever, *Angew. Chem. Int. Ed.* **2013**, *52*, 1319–1323.

[55] a) C. Stuckhardt, D. Roke, W. Danowski, E. Otten, S. J. Wezenberg, B. L. Feringa, *Beilstein J. Org. Chem.* **2019**, *15*, 2767–2773; b) S. Oldknow, D. Rota Martir, V. E. Pritchard, M. A. Blitz, C. W. G.

Fishwick, E. Zysman-Colman, M. J. Hardie, *Chem. Sci.* **2018**, *42*, 8150–8159; c) H. Tang, N. Zhu, V. Wing-Wah Yam, *Organometallics,* **2007**, *26*, 22–25.
[56] S.-S. Sun, A. J. Lees, *J. Am. Chem. Soc.* **2000**, *122*, 8956–8967.
[57] S. Fu, Q. Luo, M. Zang, J. Tian, Z. Zhang, M. Zeng, Y. Ji, J. Xu, J. Liu, *Mater. Chem. Front.* **2019**, *3*, 1238–1243.
[58] A. Ghosh, L. Slappendel, B.-N. T. Nguyen, L. K. S. von Krbek, T. K. Ronson, A. M. Castilla, J. R. Nitschke, *J. Am. Chem. Soc.* **2023**, *145*, 3828–3862.
[59] E. Nieland, J. Voss, B. M. Schmidt, *Synlett*, **2023**, *34*, 975–982.
[60] D. Hugenbusch, M. Lehr, J.-S. von Glasenapp, A. J. McConnell, R. Herges, *Angew. Chem. Int. Ed.* **2023**, *62*, e202212571.
[61] S. Goldup, I. Aprahamian, **2022**, *ChemRxiv preprint*, DOI:10.26434/chemrxiv-2022-49s4d-v2.
[62] a) M. Mosharraf Hossain, I. M. Jayalath, R. Baral, C. S. Hartley, *ChemSystemsChem* **2022**, *4*, e202200016; b) C. S. Wood, C. Browne, D. M. Wood, J. R. Nitschke, *ACS Cent. Sci.* **2015**, *1*, 504–509; c) H. Fanlo-Virgós, A.-N. R. Alba, S. Hamieh, M. Colomb-Delsuc, S. Otto, *Angew. Chem. Int. Ed.* **2014**, *53*, 11346–11350.
[63] a) J.-F. Ayme, B. Bruchmann, L. Karmazin, N. Kyitsakas, *Chem. Sci.* **2023**, *14*, 1244–1251; b) V. W. Liyana Gunawardana, T. J. Finnegan, C. E. Ward, C. E. Moore, J. D. Badjić, *Angew. Chem. Int. Ed.* **2022**, *61*, e202207418; c) D. del Giudice, M. Valentini, G. Melchiorre, E. Spatola, S. di Stefano, *Chem. Eur. J.* **2022**, *28*, e202200685; d) F. Rispoli, E. Spatola, D. del Giudice, R. Cacciapaglia, A. Casnati, L. Baldini, S. di Stefano, *J. Org. Chem.* **2022**, *87*, 36233629.
[64] S. M. Jansze, G. Cecot, K. Severin, *Chem. Sci.* **2018**, *9*, 4253–4257.
[65] F. Rakotondradany, M. A. Whitehead, A.-M. Lebuis, H. F. Sleiman, *Chem. Eur. J.* **2003**, *9*, 4771–4780.
[66] M. Han, Y. Luo, B. Damaschke, L. Gómez, X. Ribas, A. Jose, P. Peretzki, M. Seibt, G. H. Clever, *Angew. Chem. Int. Ed.* **2016**, *55*, 445–449.
[67] a) R. G. DiNardi, A. O. Douglas, R. Tian, J. R. Price, M. Tajik, W. A. Donald, J. E. Beves, *Angew. Chem. Int. Ed.* **2022**, *61*, e202205701; b) A. D. W. Kennedy, R. G. DiNardi, L. L. Fillbrook, W. A. Donald, J. E. Beves, *Chem. Eur. J.* **2022**, *28*, e202104461.
[68] H. Lee, J. Tessarolo, D. Langbehn, A. Baksi, R. Herges, G. H. Clever, *J. Am. Chem. Soc.* **2022**, *144*, 3099–3105.
[69] J. Zhu, X. Chen, X. Jin, Q. Wang, *Chin. Chem. Lett.* **2023**, *34*, 108002.
[70] M. Bauer, F. Vögtle, *Chem. Ber.* **1992**, *125*, 1675–1686.
[71] M. Ovalle, M. Kathan, R. Toyoda, C. N. Stindt, S. Crespi, B. L. Feringa, *Angew. Chem. Int. Ed.* **2023**, *62*, e202214495.
[72] A.-L. Leistner, S. Kirchner, J. Karcher, T. Bantle, M. L. Schulte, P. Gödtel, C. Fengler, Z. Pianowski, *Chem. Eur. J.* **2021**, *27*, 8094–8099.
[73] a) X. Liu, P. H. Toy, *Adv. Synth. Catal.* **2020**, *362*, 3437–3441; b) T. Suzuki, S. Kuwano, T. Arai, *Adv. Synth. Catal.* **2020**, *362*, 3208–3212; c) M. Kaasik, A. Metsala, S. Kaabel, K. Kriis, I. Järving, T. Kanger, *J. Org. Chem.* **2019**, *84*, 4294–4303; d) R. Haraguchi, S. Hoshino, M. Sakai, S. Tanazawa, Y. Morita, T. Komatsu, S. Fukuzawa, *Chem. Commun.* **2018**, *54*, 10320–10323; e) Y. Takeda, D. Hisakuni, C.-H. Lin, S. Minakata, *Org. Lett.* **2015**, *17*, 318–321.

[74] J.-L. Syssa Magalé, K. Boubekeur, P. Palvadeau, A. Meerschaut, B. Schöllhorn, *J. Mol. Struct.* **2004**, *691*, 79–84.

[75] E. Nieland, D. Komisarek, S. Hohloch, K. Wurst, V. Vasylyeva, O. Weingart, B. M. Schmidt, *Chem. Commun.* **2022**, *58*, 5233–5236.

[76] a) M. Müller, M. Albrecht, V. Gossen, T. Peters, A. Hoffmann, G. Raabe, A. Valkonen, K. Rissanen, *Chem. Eur. J.* **2010**, *16*, 12446–12453; b) K. Xu, D. M. Ho, R. A. Pascal, *J. Am. Chem. Soc.* **1994**, *116*, 105–110.

[77] M. Servalli, N. Trapp, A. D. Schlüter, *Chem. Eur. J.* **2018**, *24*, 15003–15012.

[78] a) D. Hermann, H. A. Schwartz, U. Ruschewitz, *ChemistrySelect*, **2017**, *2*, 11846–11852; b) O. S. Bushuyev, A. Tomberg, J. R. Vinden, N. Moitessier, C. J. Barrett, T. Friščić, *Chem. Commun.* **2016**, *52*, 2103–2106; c) O. S. Bushuyev, A. Tomberg, T. Friščić, C. J. Barrett, *J. Am. Chem. Soc.* **2013**, *135*, 12556–12559.

[79] A. A. John, Q. Lin, *J. Org. Chem.* **2017**, *82*, 9873–9876.

[80] R. L. Greenaway, V. Santolini, M. J. Bennison, B. M. Alston, C. J. Pugh, M. A. Little, M. Miklitz, E. G. B. Eden-Rump, R. Clowes, A. Shakil, H. J. Cuthbertson, H. Armstrong, M. E. Briggs, K. E. Jelfs, A. I. Cooper, *Nat. Commun.* **2018**, *9*, 2849.

[81] J. N. Moorthy, S. Saha, *Eur. J. Org. Chem.* **2010**, *33*, 6359–6365.

[82] a) Z. X. Ng, D. Tan, W. L. Teo, F. León, X. Shi, Y. Sim, Y. Li, R. Ganguly, Y. Zhao, S. Mohamed, F. García, *Angew. Chem. Int. Ed.* **2021**, *60*, 2–12; b) M. Arhangelskis, F. Topić, P. Hindle, R. Tran, A. J. Morris, D. Cinčić, T. Friščić, *Chem. Commun.* **2020**, *56*, 8293–8296; c) J. Mavračić, D. Cinčić, B. Kaitner, *CrystEngComm*, **2016**, *18* 3343–3346; d) C. Aakeröy, M. Baldrighi, J. Desper, P. Metrangolo, G. Resnati, *Chem. Eur. J.* **2013**, *19*, 16240–16247; e) G. Lapadula, N. Judaš, T. Friščić, W. Jones, *Chem. Eur. J.* **2010**, *16*, 7400–7403; f) D. Cinčić, T. Friščić, W. Jones, *J. Am. Chem. Soc.* **2008**, *130*, 7524–7525; g) D. Cinčić, T. Friščić, W. Jones, *Chem. Eur. J.* **2008**, *14*, 747–753; h) T. Friščić, A. V. Trask, W. Jones, W. D. S. Motherwell, *Angew. Chem. Int. Ed.* **2006**, *45*, 7546–7550.

[83] a) T. Friščić, *Chem. Soc. Rev.* **2012**, *41*, 3496–3510; b) S. L. James, C. J. Adams, C. Bolm, D. Braga, P. Collier, T. Friščić, F. Grepioni, K. D. M. Harris, G. Hyett, W. Jones, A. Krebs, J. Mack, L. Maini, A. G. Orpen, I. P. Parkin, W. C. Shearouse, J. W. Steed, D. C. Waddell, *Chem. Soc. Rev.* **2012**, *41*, 413–447; c) T. Friščić, W. Jones, *Cryst. Growth Des.* **2009**, *9*, 1621–1637; d) D. Braga, F. Grepioni, *Angew. Chem. Int. Ed.* **2004**, *43*, 4002–4011.

[84] a) T. D. Kühne, M. Iannuzzi, M. Del Ben, V. V. Rybkin, P. Seewald, F. Stein, T. Laino, R. Z. Khaliullin, O. Schütt, F. Schiffmann, D. Golze, J. Wilhelm, S. Chulkov, M. H. Bani-Hashemian, V. Weber, U. Borštnik, M. Taillefumier, A. S. Jakobovits and A. Lazzaro, *et al.*, *J. Chem. Phys.* **2020**, *152*, 194103; b) P. Giannozzi, S. Baroni, N. Bonini, M. Calandra, R. Car, C. Cavazzoni, D. Ceresoli, G. L. Chiarotti, M. Cococcioni, I. Dabo, A. Dal Corso, S. de Gironcoli, S. Fabris, G. Fratesi, R. Gebauer, U. Gerstmann, C. Gougoussis, A. Kokalj, M. Lazzeri, L. Martin-Samos, N. Marzari, F. Mauri, R. Mazzarello, S. Paolini, A. Pasquarello, L. Paulatto, C. Sbraccia, S. Scandolo, G. Sclauzero, A. P. Seitsonen, A. Smogunov, P. Umari and R. M. Wentzcovitch, *J. Phys.: Condens. Matter*, **2009**, *21*, 395502.

[85] T. Lu and F. Chen, *J. Comput. Chem.* **2012**, *33*, 580–592.

[86] G. R. Desiraju, R. Parthasarathy, *J. Am. Chem. Soc.* **1989**, *111*, 8725–8726.

[87] G. R. Desiraju, P. S. Ho, L. Kloo, A. C. Legon, R. Marquardt, P. Metrangolo, P. Politzer, G. Resnati, K. Rissanen, *Pure Appl. Chem.* **2013**, *85*, 1711–1713.
[88] a) T. Kunde, T. Pausch, B. M. Schmidt, *Eur. J. Org. Chem.* **2021**, *43*, 5844–5856; b) T. Hasell, A. I. Cooper, *Nat. Rev. Mater.* **2016**, *1*, 16053.
[89] T. Yuan, Z.-Q. Wang, X.-Q. Gong, Q. Wang, *Tetrahedron Lett.* **2020**, *61*, 152626–152629.
[90] M. Yamamura, Y. Okazaki, T. Nabeshima, *Chem. Commun.* **2012**, *48*, 5724–5726.
[91] J. Tani, Y. Mushika, T. Yamaguchi, *Chem. Pharm. Bull.* **1982**, *30*, 3530–3543.
[92] X.-M. Liu, X.-Y. Jin, Z.-X. Zhang, J. Wang, F.-Q. Bai, *RSC Adv.* **2018**, *8*, 11580–11588.
[93] a) M. Kathan, P. Kovaříček, C. Jurissek, A. Senf, A. Dallmann, A. F. Thünemann, S. Hecht, *Angew. Chem. Int. Ed.* **2016**, *55*, 13882–13886; b) A. Ciesielski, M. El Garah, S. Haar, P. Kovaříček, J.-M. Lehn, P. Samorì, *Nat. Chem.* **2014**, *6*, 1017–1023.
[94] M. Kwit, J. Grajewski, P. Skowronek, M. Zgorzelak, J. Gawroński, *Chem. Rec.* **2019**, *19*, 213–237.
[95] a) J. Lisowski, *Molecules*, **2022**, *27*, 4097; b) J. Grajewski, *Molecules*, **2022**, *27*, 1004; c) N. E. Borisova, M. D. Reshetova, Y. A. Ustynyuk, *Chem. Rev.*, **2007**, *107*, 46–79.
[96] a) T. Kunde, T. Pausch, G. J. Reiss, B. M. Schmidt, *Synlett*, **2022**, *33*, 161–165; b) D. He, C. Zhao, L. Chen, M. A. Little, S. Y. Chong, R. Clowes, K. McKie, M. G. Roper, G. M. Day, M. Liu, A. I. Cooper, *Chem. Eur. J.* **2021**, *27*, 10589–10594; c) K. Tanaka, S. Fukuoka, H. Miyanishi, H. Takahashi, *Tetrahedron Lett.* **2010**, *51*, 2693–2696; d) J. Gawroński, H. Kołbon, M. Kwit, A. Katrusiak, *J. Org. Chem.* **2000**, *65*, 5768–5773.
[97] E. Nieland, J. Voss, A. Mix, B. M. Schmidt, *Angew. Chem. Int. Ed.* **2022**, *61*, e202212745.
[98] N. Kuhnert, A. M. Lopez-Periago, *Tetrahedron Lett.* **2002**, *43*, 3329–3332.
[99] a) J. Szymkowiak, M. Kwit, *Chirality*, **2017**, *30*, 117–130; b) J. Gao, J. H. Reibenspies, R. A. Zingaro, A. Pappalardo, M. E. Amato, F. P. Ballistreri, A. Notti, G. A. Tomaselli, R. M. Toscano, G. T. Sfrazzetto, *Tetrahedron Lett.* **2012**, *53*, 7150–7153; c) F. R. Woolley, A. E. Martell, A. Clearfield, *Inorg. Chem.* **2005**, *44*, 232–241; d) G.-J. Kim, D.-W. Park, Y.-S. Tak, *Catalysis*, **2000**, *65*, 127–133.
[100] M. J. Bojdys, M. E. Briggs, J. T. A. Jones, D. J. Adams, S. Y. Chong, M. Schmidtmann, A. I. Cooper, *J. Am. Chem. Soc.* **2011**, *133*, 16566–16571.
[101] a) J. Sun, R. Warmuth, *Chem. Commun.* **2011**, *47*, 9351–9353; b) X. Liu, Y. Liu, R. Warmuth, *Supramol. Chem.* **2008**, *20*, 41–50; c) X. Liu, R. Warmuth, *J. Am. Chem. Soc.* **2006**, 128*, 14120*–14127; d) X. Liu, Y. Liu, G. Li, R. Warmuth, *Angew. Chem. Int. Ed.* **2006**, *45*, 901–904.
[102] a) F. Begato, R. Penasa, G. Licini, C. Zonta, *Chem. Commun.* **2021**, *57*, 10019–10022; b) C. Bravin, E. Badetti, F. A. Scaramuzzo, G. Licini, C. Zonta, *J. Am. Chem. Soc.* **2017**, *139*, 6456–6460.
[103] M. E. Briggs, A. I. Cooper, *Chem. Mater.* **2017**, *29*, 149–157.
[104] K. E. Jelfs, E. G. B. Eden, J. L. Culshaw, S. Shakespeare, E. O. Pyzer-Knapp, Hugh P. G. Thompson, J. Bacsa, G. M. Day, D. J. Adams, A. I. Cooper, *J. Am. Chem. Soc.* **2013**, *135*, 9307–9310.
[105] a) Y. Wang, H. Fang, W. Zhang, Y. Zhuang, Z. Tian, X. Cao, *Chem. Commun.* **2017**, *53*, 8956–8959; b) X. Wang, Y. Wang, H. Yang, H. Fang, R. Chen, Y. Sun, N. Zheng, K. Tan, X. Lu, Z. Tian, X. Cao, *Nat. Commun.* **2016**, *7*, 12469.
[106] M. Tominaga, E. Takahashi, H. Ukai, K. Ohara, T. Itoh, K. Yamaguchi, *Org. Lett.* **2017**, *19*, 1508–1511.

[107] T. Xiao, X. Feng, S. Ye, Y. Guan, S.-L. Li, Q. Wang, Y. Ji, D. Zhu, X. Hu, C. Lin, Y. Pan, L. Wang, *Macromolecules* **2012**, *45*, 9585–9594; b) T. F. A. de Greef, M. M. J. Smulders, M. Wolffs, A. P. H. J. Schenning, R. P. Sijbesma, E. W. Meijer, *Chem. Rev.* **2009**, *109*, 5687–5754; c) C.-C. Chen, E. E. Dormidontova, *Macromolecules* **2004**, *37*, 3905–3917.

[108] a) A. H. Heindl, L. Schweighauser, C. Logemann, H. A. Wegner, *Synthesis*, **2017**, *49*, 2632–2639; b) E. Durgun, J. C. Grossman, *J. Phys. Chem. Lett.* **2013**, *4*, 854–860; c) Y. Norikane, N. Tamaoki, *Eur. J. Org. Chem.* **2006**, *5*, 1296–1302; d) Y. Norikane, K. Kitamoto, N. Tamaoki, *J. Org. Chem.* **2003**, *68*, 8291–8304.

[109] E. Merino, *Chem. Soc. Rev.* **2011**, *40*, 3835–3853.

[110] K. Chiba, M. Asanuma, M. Ishikawa, Y. Hashimoto, K. Dodo, M. Sodeoka, T. Yamaguchi, *Chem. Commun.* **2017**, *53*, 8751–8754.

[111] a) N. C. Craig, A. Chen, K. H. Suh, S. Klee, G. C. Mellau, B. P. Winnewisser, M. Winnewisser, *J. Am. Chem. Soc.* **1997**, *119*, 4789–4790; b) T. M. Connor, K. A. McLauchlan, *J. Phys. Chem.* **1965**, *69*, 1888–1893.

[112] a) Z. Yang, J.-M. Lehn, *J. Am. Chem. Soc.* **2020**, *142*, 15137–15145; b) J. Jazwinski, J.-M. Lehn, R. Méric, J.-P. Vigneron, M. Cesario, J. Guilhem, C. Pascard, *Tetrahedron. Lett.* **1987**, *28*, 3489–3492.

[113] B. Moosa, L. O. Alimi, A. Shkurenko, A. Fakim, P. M. Bhatt, G. Zhang, M. Eddaoudi, N. M. Khashab, *Angew. Chem. Int. Ed.* **2020**, *59*, 21367–21371.

[114] F. García, M. M. J. Smulders, *J. Polym. Sci.* **2016**, *54*, 3551–3577.

[115] J. C. Lauer, W.-S. Zhang, F. Rominger, R. R. Schröder, M. Mastalerz, *Chem. Eur. J.* **2018**, *24*, 1816–1820.

[116] a) K. Acharyya, P. S. Mukherjee, *Angew. Chem. Int. Ed.* **2019**, *58*, 8640–8653; b) Z. He, W. Jiang, C. A. Schalley, *Chem. Soc. Rev.* **2015**, *44*, 779–789; c) M. L. Saha, M. Schmittel, *Org. Biomol. Chem.* **2012**, *10*, 4651–4684; d) M. M. Safont-Sempere, G. Fernández, F. Würthner, *Chem. Rev.* **2011**, *111*, 5784–5814; e) K. Osowka, O. Š. Miljanić, *Synlett* **2011**, *12*, 1643–1648.

[117] V. Abet, F. T. Szczypiński, M. A. Little, V. Santolini, C. D. Jones, R. Evans, C. Wilson, X. Wu, M. F. Thorne, M. J. Bennison, P. Cui, A. I. Cooper, K. E. Jelfs, A. G. Slater, *Angew. Chem. Int. Ed.* **2020**, *59*, 16755–16763.

[118] a) K. Acharyya, P. S. Mukherjee, *Chem. Commun.* **2015**, b) K. Acharyya, P. S. Mukherjee, *Chem. Eur. J.* **2014**, *20*, 1646–1657; c) *51*, 4241–4244; K. Acharyya, S. Mukherjee, P. S. Mukherjee, *J. Am. Chem. Soc.* **2013**, *135*, 554–557.

[119] G. R. Fulmer, A. J. M. Miller, N. H. Sherden, H. E. Gottlieb, A. Nudelman, B. M. Stoltz, J. E. Bercaw. K. I. Goldberg, *Organometallics* **2010**, *29*, 2176–2179.

[120] G. M. Sheldrick, SHELXL-2014, Program for Crystal Structure Refinement, University of Göttingen, Göttingen, **2014**.

[121] G. M. Sheldrick, *Acta Crystallogr. Sect. C* **2015**, *71*, 3–8.

[122] M. J. Frisch, G. W. Trucks, H. B. Schlegel, G. E. Scuseria, M. A. Robb, J. R. Cheeseman, G. Scalmani, V. Barone, G. A. Petersson, H. Nakatsuji, X. Li, M. Caricato, A. V. Marenich, J. Bloino, B. G. Janesko, R. Gomperts, B. Mennucci, H. P. Hratchian, J. V. Ortiz, A. F. Izmaylov, J. L. Sonnenberg, D. Williams-Young, F. Ding, F. Lipparini, F. Egidi, J. Goings, B. Peng, A. Petrone, T. Henderson, D. Ranasinghe, V. G. Zakrzewski, J. Gao, N. Rega, G. Zheng, W. Liang, M. Hada, M. Ehara, K. Toyota, R.

Fukuda, J. Hasegawa, M. Ishida, T. Nakajima, Y. Honda, O. Kitao, H. Nakai, T. Vreven, K. Throssell, J. A., Jr. Montgomery, J. E. Peralta, F. Ogliaro, M. J. Bearpark, J. J. Heyd, E. N. Brothers, K. N. Kudin, V. N. Staroverov, T. A. Keith, R. Kobayashi, J. Normand, K. Raghavachari, A. P. Rendell, J. C. Burant, S. S. Iyengar, J. Tomasi, M. Cossi, J. M. Millam, M. Klene, C. Adamo, R. Cammi, J. W. Ochterski, R. L. Martin, K. Morokuma, O. Farkas, J. B. Foresman, D. J. Fox, Gaussian 16, Revision C.01, Gaussian, Inc., Wallingford CT, **2016**.

[123] S. Grimme, Semiempirical GGA-Type Density Functional Constructed with a Long-Range Dispersion Correction. *J. Comput. Chem.* **2006**, *27*, 1787–1799.

[124] Y. Zhao, D.G. Truhlar, *Theor. Chem. Acc.* **2008**, *120***,** 215–241.

[125] E. Espinosa, E. Molins, C. Lecomte, *Chem. Phys. Lett.* **1998**, *285*, 170–173.

[126] I. Mata, I. Alkorta, E. Espinosa, E. Molins, *Chem. Phys. Lett.* **2011**, *507*, 185–189.

[127] E. V. Bartashevich, V. G. Tsirelson, *Russ. Chem. Rev.* **2014**, *83*, 1181–1203.

[128] A. Schwartzen, J.-H. Weddeling, J. Langosch, B. Neumann, H.-G. Stammler, N. W. Mitzel, *Chem. Eur. J.* **2021**, *27*, 1821–1828.

[129] L. C. H. Maddock, T. Nixon, A. R. Kennedy, M. R. Probert, W. Clegg, E. Hevia, *Angew. Chem. Int. Ed.* **2017**, *130*, 193-197.

[130] K. Hirose, Quantitative Analysis of Binding Properties in *Analytical Methods in Supramolecular Chemistry* (Ed.: C. A. Schalley), Wiley-VCH, Weinheim, **2012**, 27-66.

[131] A. L. Spek, *Acta Cryst.* **2015**, *C71*, 9–18.

[132] A. L. Spek, *J. Appl. Cryst*. **2003**, *36*, 7–11.

[133] A. Bondi, *J. Phys. Chem.* **1964**, *68*, 441–451.

[134] R. S. Rowland, R. Taylor, *J. Phys. Chem.* **1996**, *100*, 7384–7391.

[135] a) S. Muniappan, S. Lipstman, I. Goldberg*, Chem. Commun.* **2008**, *15*, 1777–1779; b) P. Smart, G. Mínguez Espallargas, L. Brammer, *CrystEngComm*, **2008**, *10*, 1335–1344; c) R. K. R. Jetti, A. Nangia, F. Xue, T. C. W. Mak, *Chem. Commun.* **2001**, *10*, 919–920.

[136] S. Schultzke, M. Walther, A. Staubitz, *Molecules* **2021**, *26*, 3916–3929.

[137] P. W. Atkins, J. de Paula, J. J. Keeler, *Physikalische Chemie*, Wiley-VCH, Weinheim, **2022**.

[138] “Physical Constants of Organic Compounds” in *CRC Handbook of Chemistry and Physics*, Internet Version **2005**, D. R. Lide (Ed.).

[139] a) R. Mills, *J. Phys. Chem.* **1973**, *77*, 685–688, b) W. S. Price, H. Ide, Y. Arata, *J. Phys. Chem. A.* **1999**, *103*, 448–450.

6. Spectra

6.1 Spectra for 4.2.1

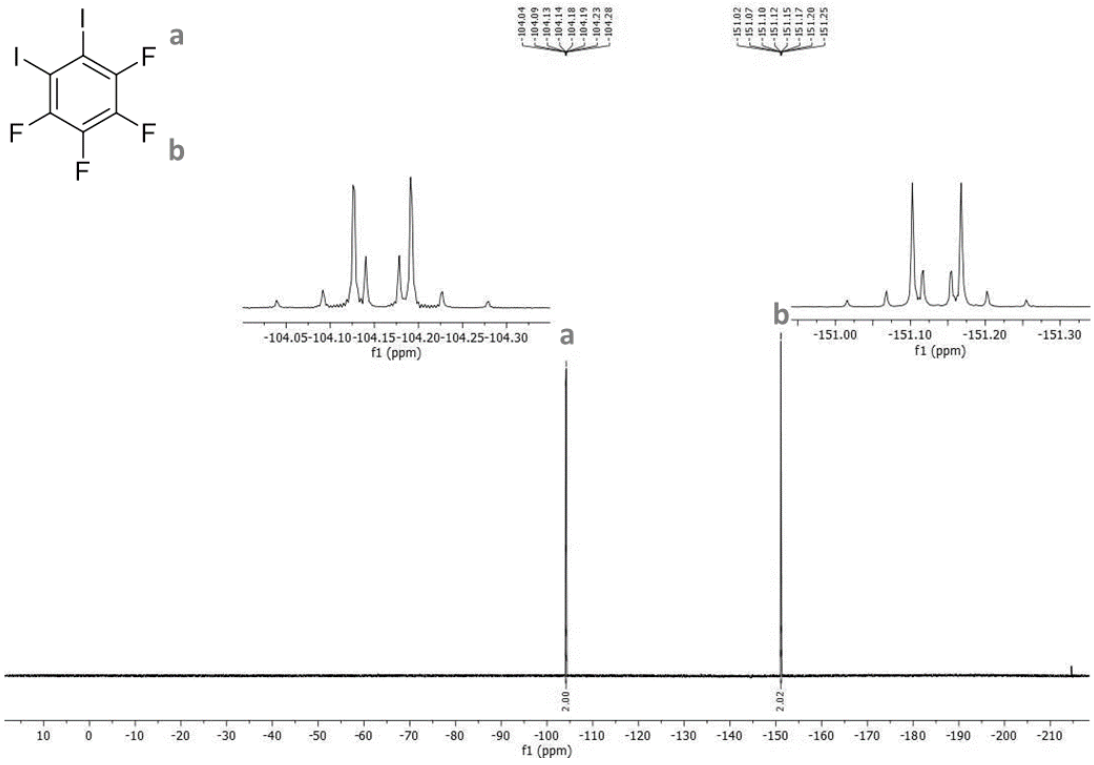

Figure S226: $^{19}F\{^{1}H\}$ NMR spectrum of ***o*-I_2F_4** ($CDCl_3$, 282 MHz).

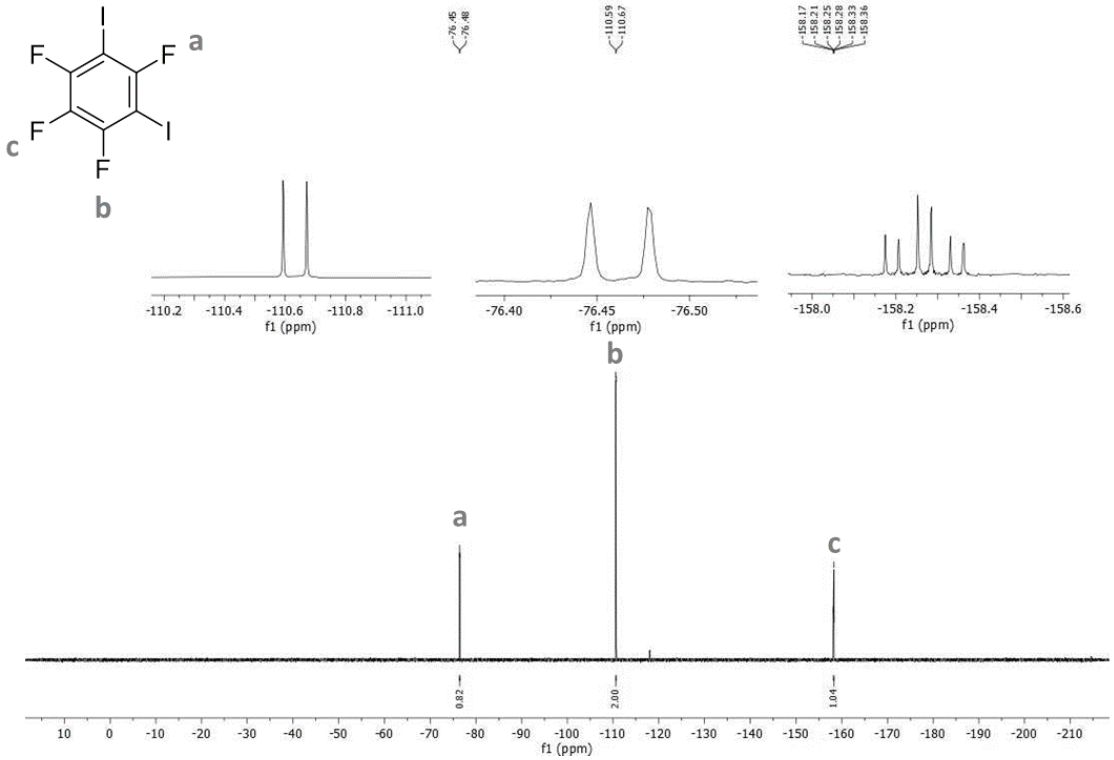

Figure S227: $^{19}F\{^{1}H\}$ NMR spectrum of ***m*-I_2F_4** ($CDCl_3$, 282 MHz).

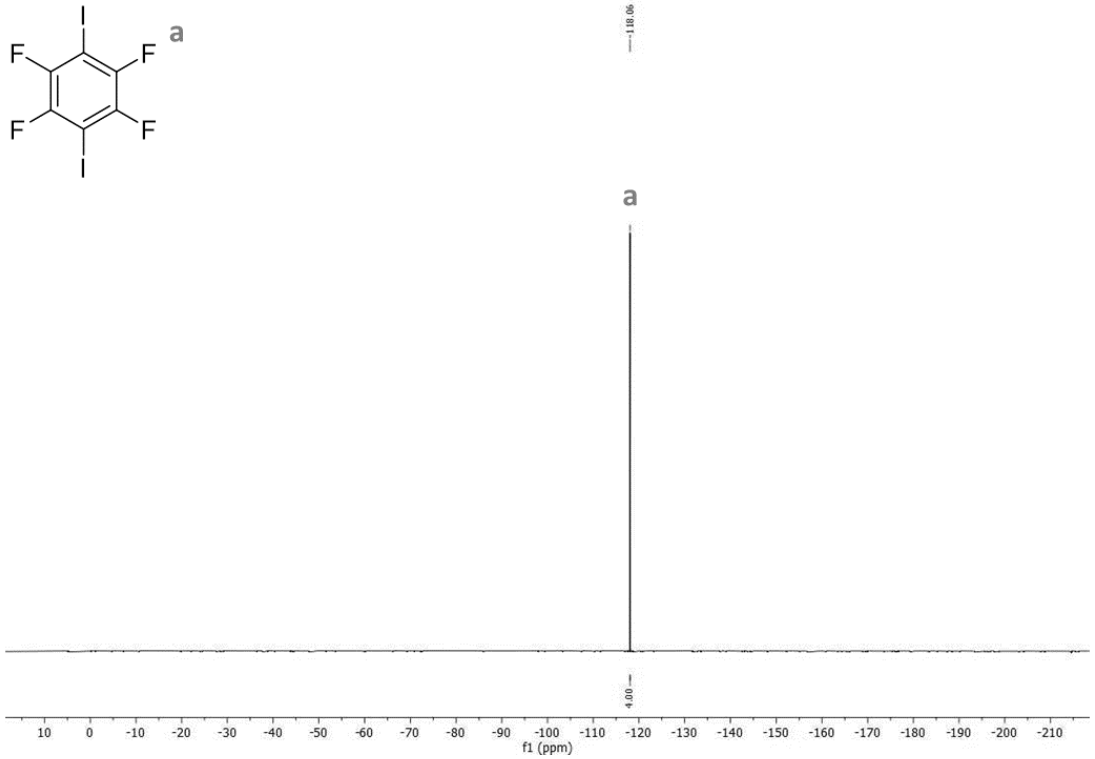

Figure S228: $^{19}F\{^{1}H\}$ NMR spectrum of ***p*-I_2F_4** ($CDCl_3$, 282 MHz).

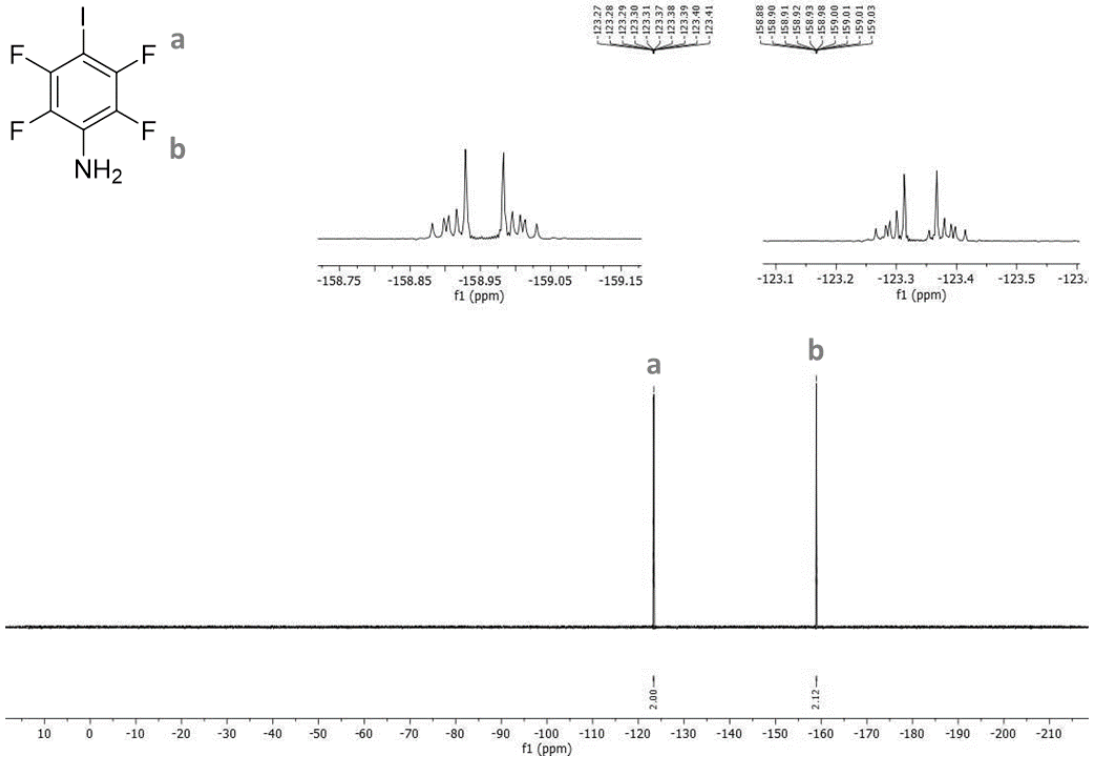

Figure S229: $^{19}F\{^{1}H\}$ NMR spectrum of **29** ($CDCl_3$, 282 MHz).

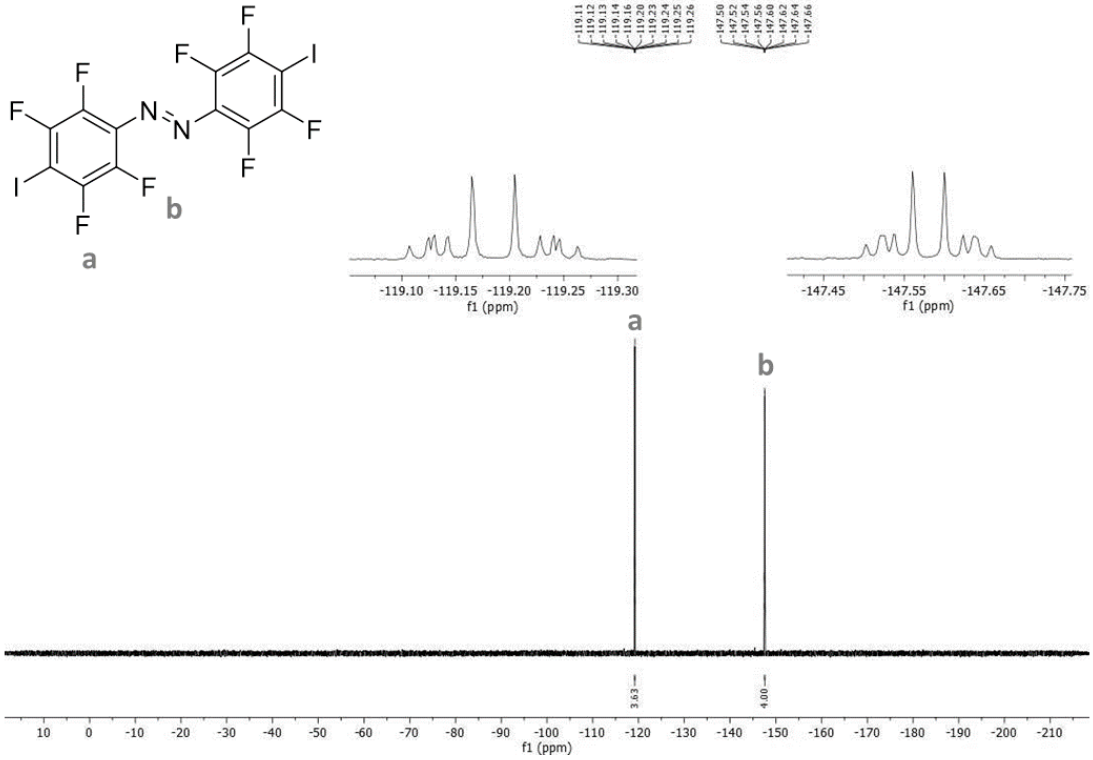

Figure S230: $^{19}F\{^{1}H\}$ NMR spectrum of **I_2F_8** ($CDCl_3$, 282 MHz).

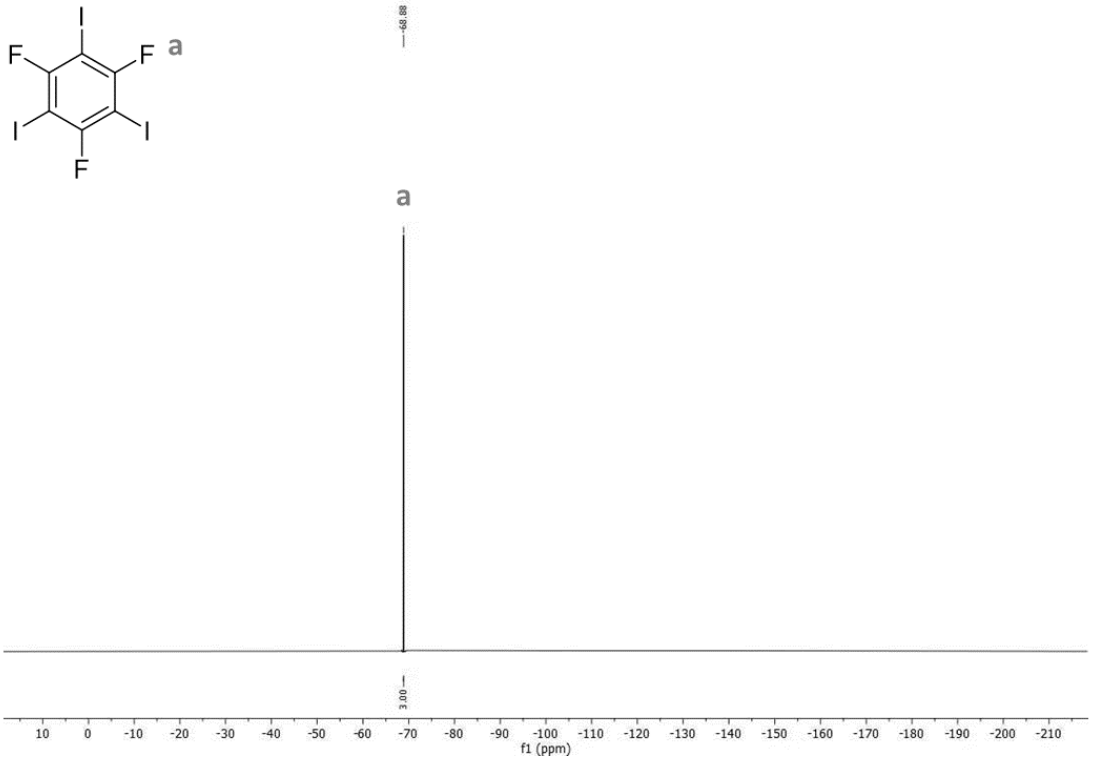

Figure S231: $^{19}F\{^{1}H\}$ NMR spectrum of $\mathbf{I_3F_3}$ ($CDCl_3$, 282 MHz).

6.2 Spectra for 4.2.2

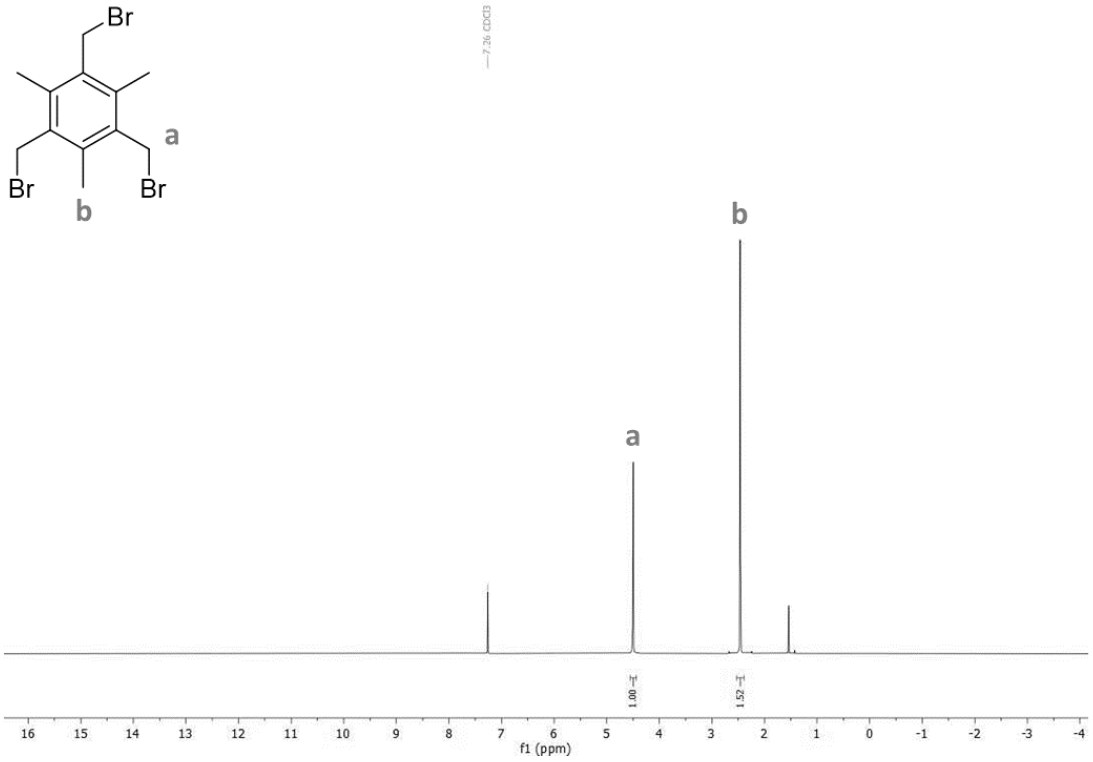

Figure S232: $^{19}F\{^{1}H\}$ NMR spectrum of **30** ($CDCl_3$, 282 MHz).

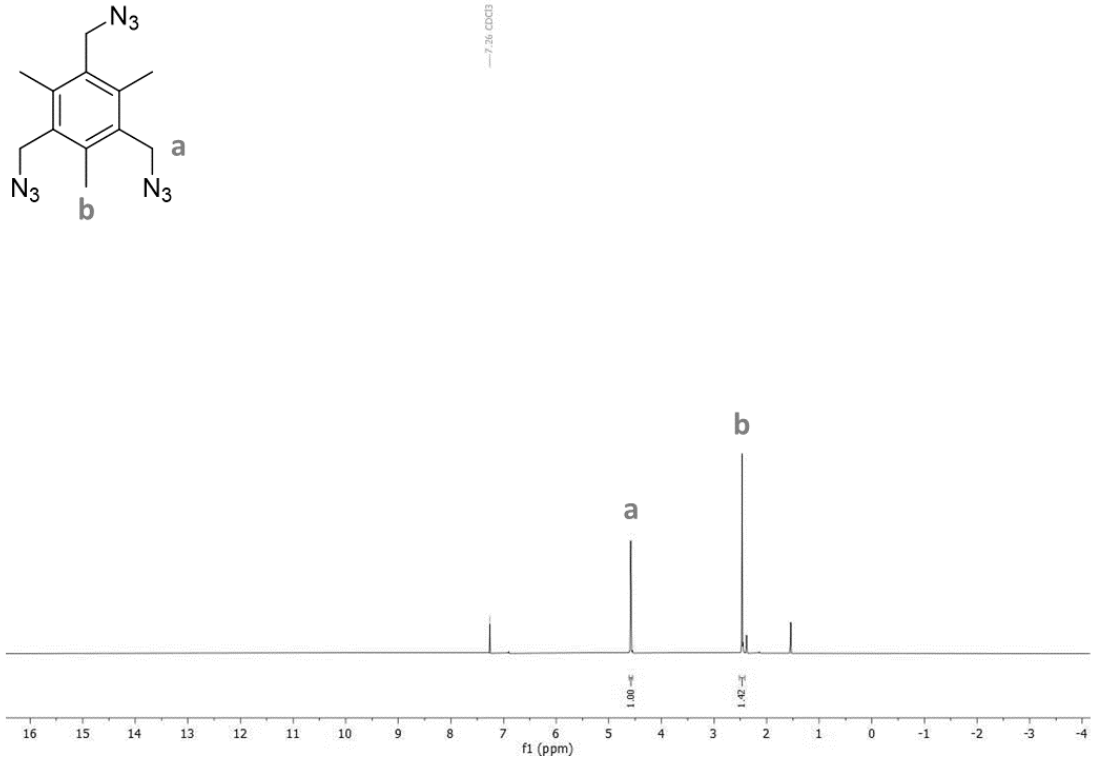

Figure S233: $^{19}F\{^{1}H\}$ NMR spectrum of **31** ($CDCl_3$, 282 MHz).

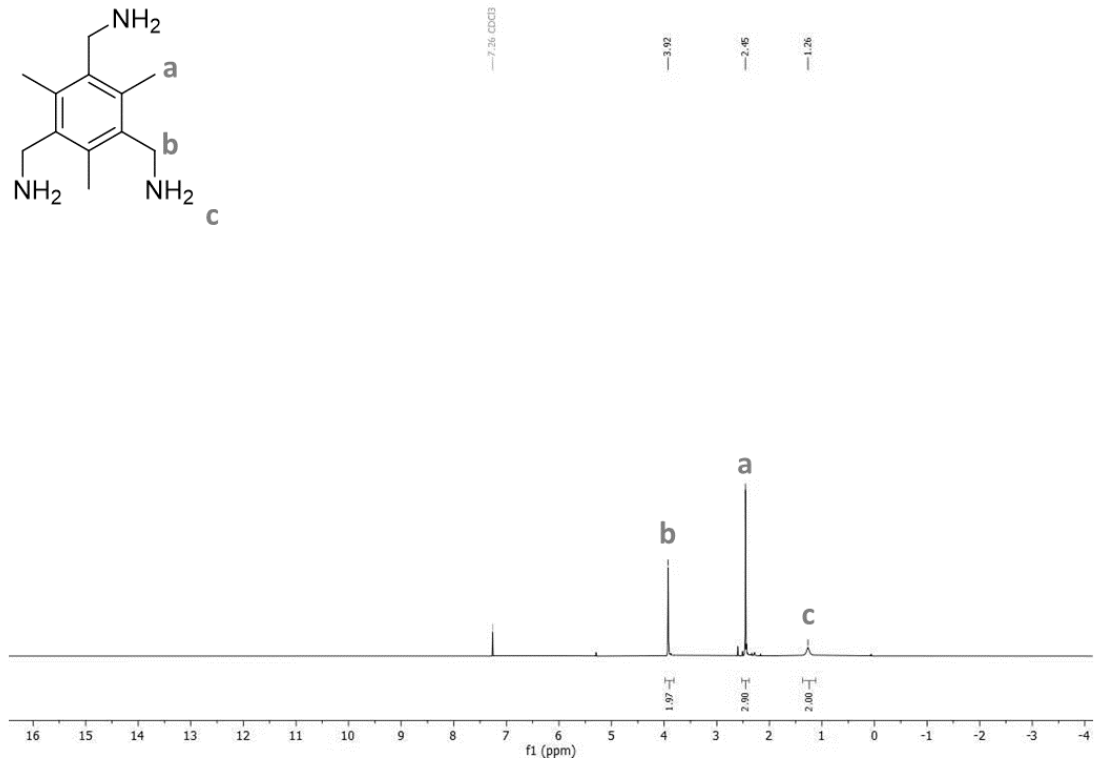

Figure S234: $^{19}F\{^{1}H\}$ NMR spectrum of **Me** ($CDCl_3$, 282 MHz).

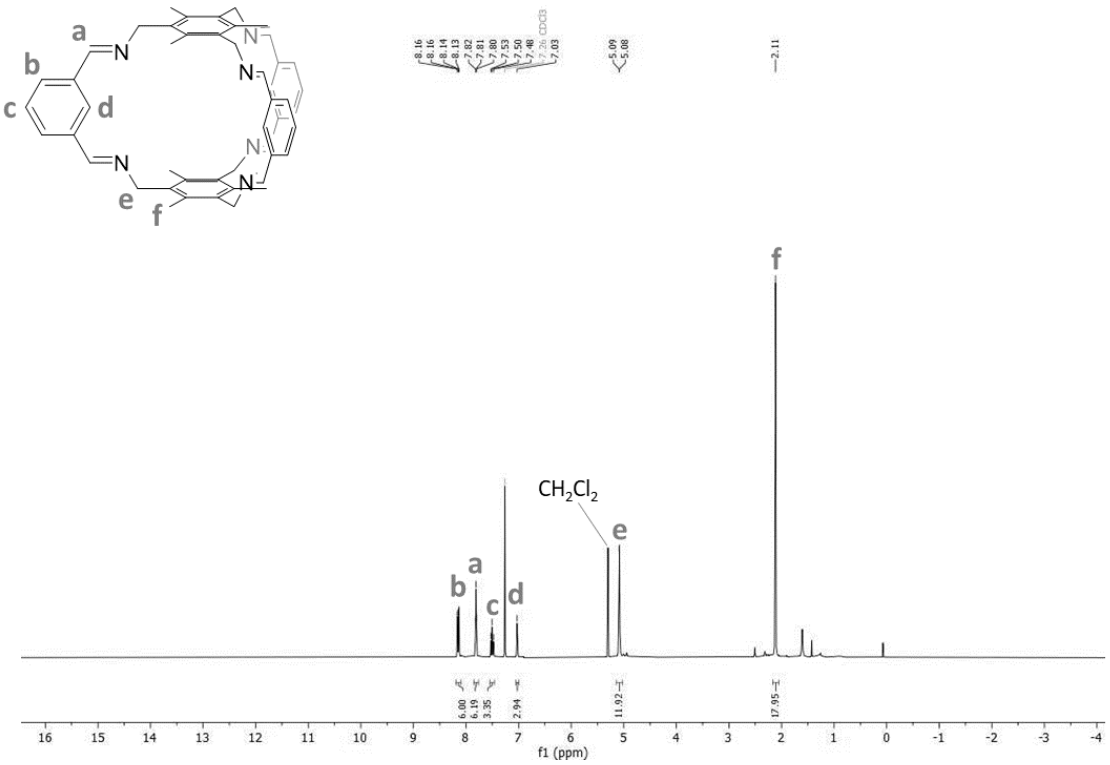

Figure S235: $^{19}F\{^{1}H\}$ NMR spectrum of **Me^{2}Iso^{3}** ($CDCl_3$, 282 MHz).

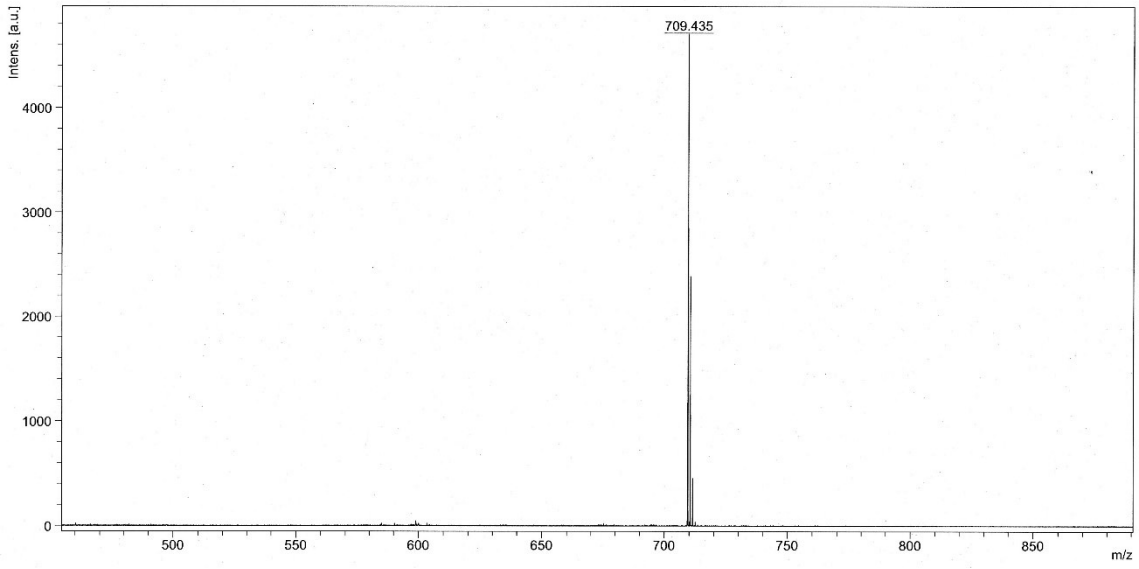

Figure S236: MALDI-mass spectrum of **Me²Iso³**.

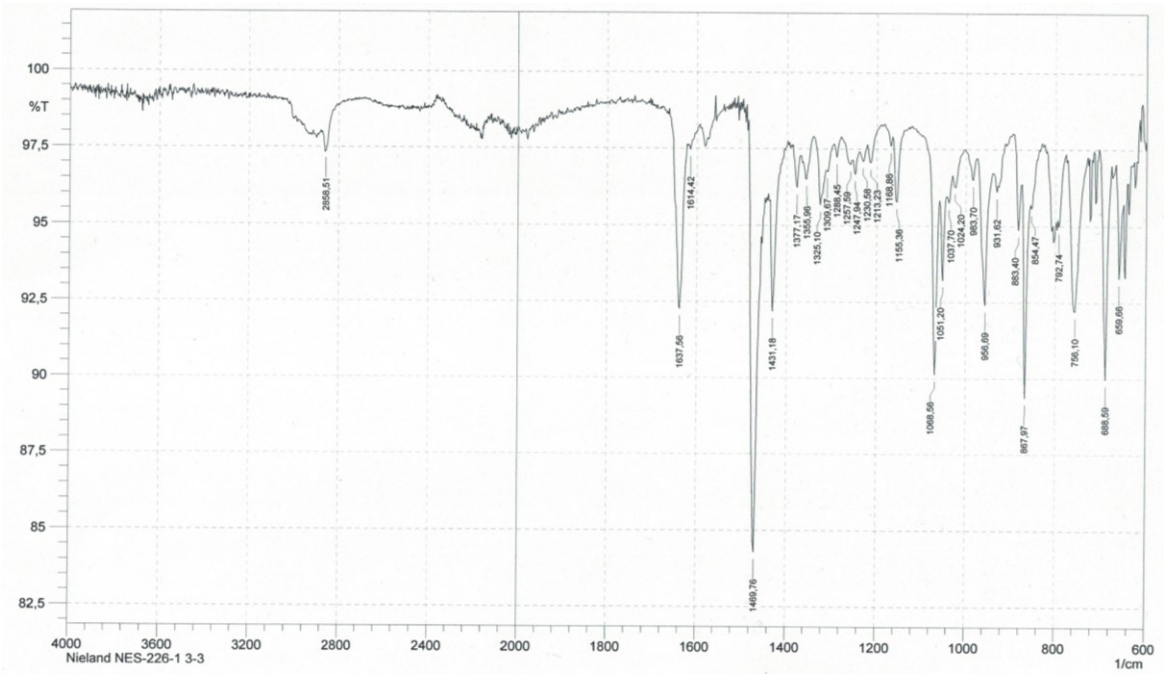

Figure S237: IR-spectrum of **Me²Iso³** + ***m*-I₂F₄**.

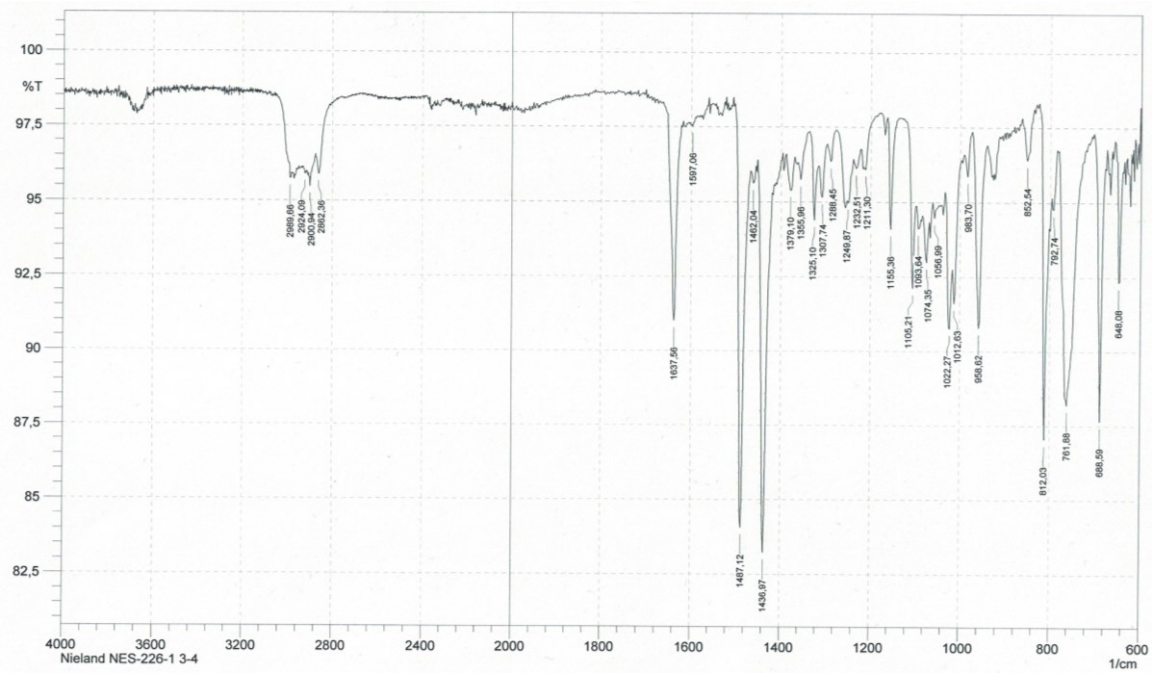

Figure S238: IR-spectrum of **Me²Iso³** + ***o*-I_2F_4**.

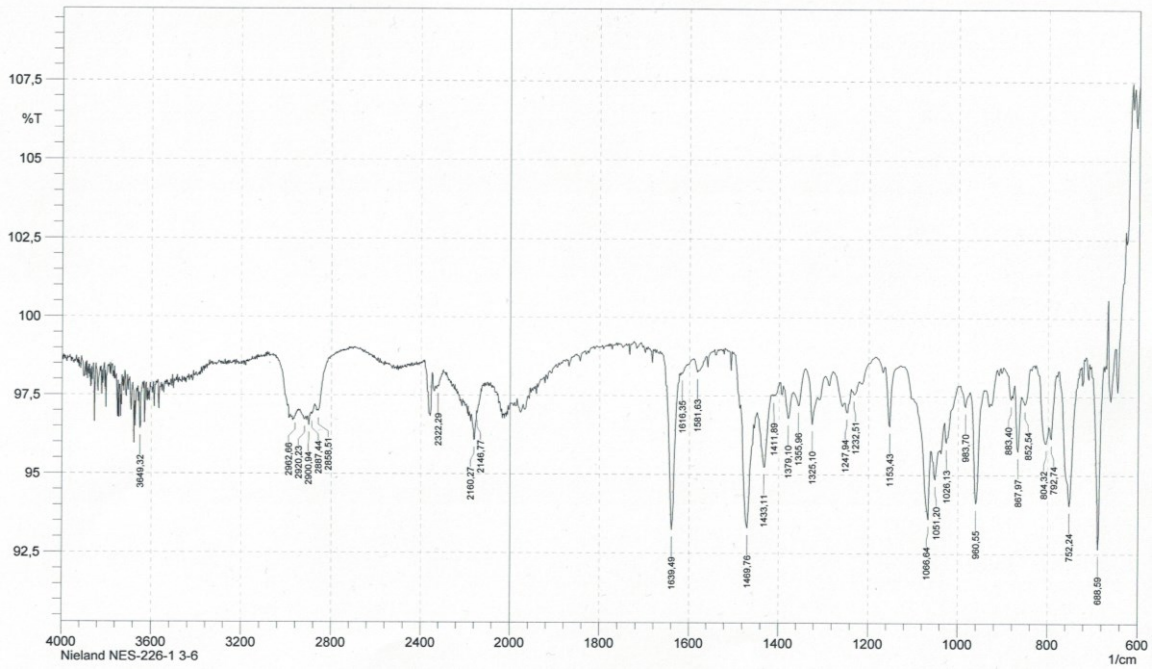

Figure S239: IR-spectrum of **Me²Iso³** + **I_2F_4Et**.

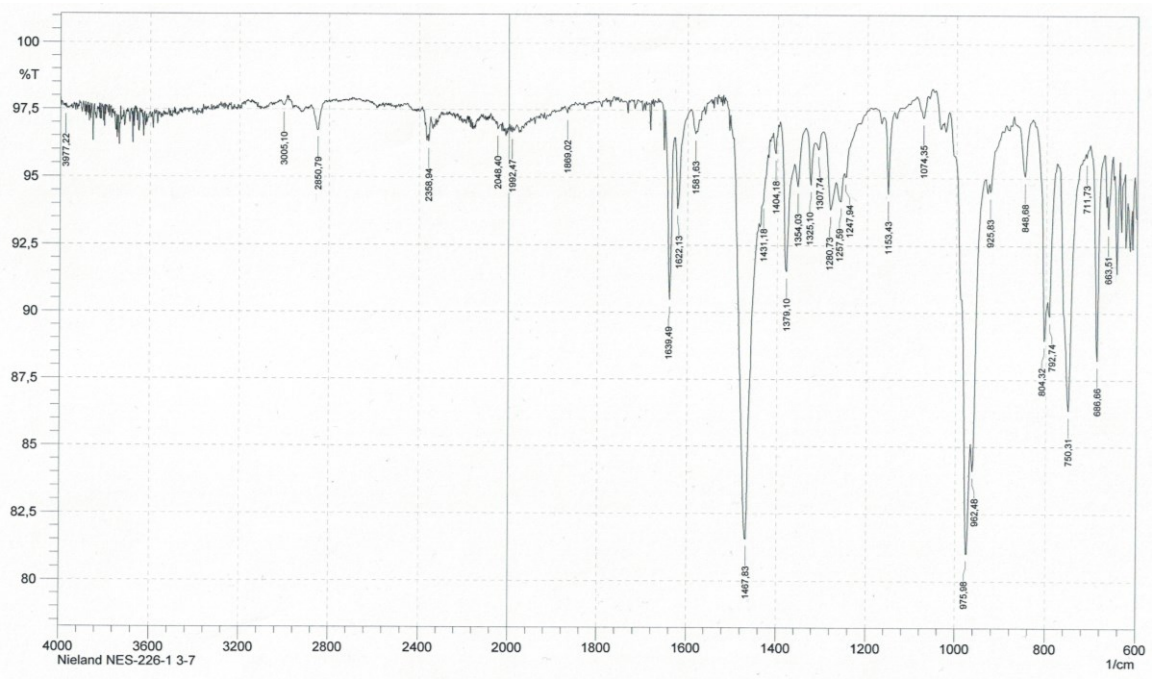

Figure S240: IR-spectrum of **Me^2Iso^3 + I_2F_8**.

6.3 Spectra for 4.2.3

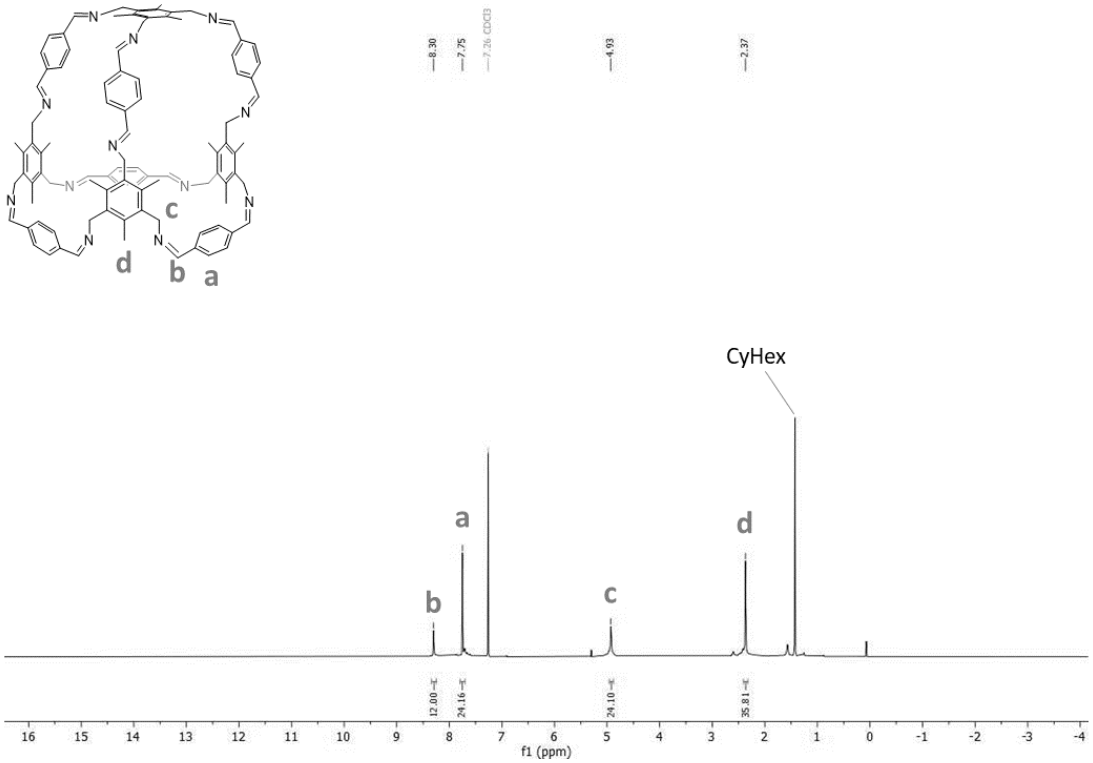

Figure S241: $^{19}F\{^{1}H\}$ NMR spectrum of **Me^{4}Ter^{6}** ($CDCl_3$, 282 MHz).

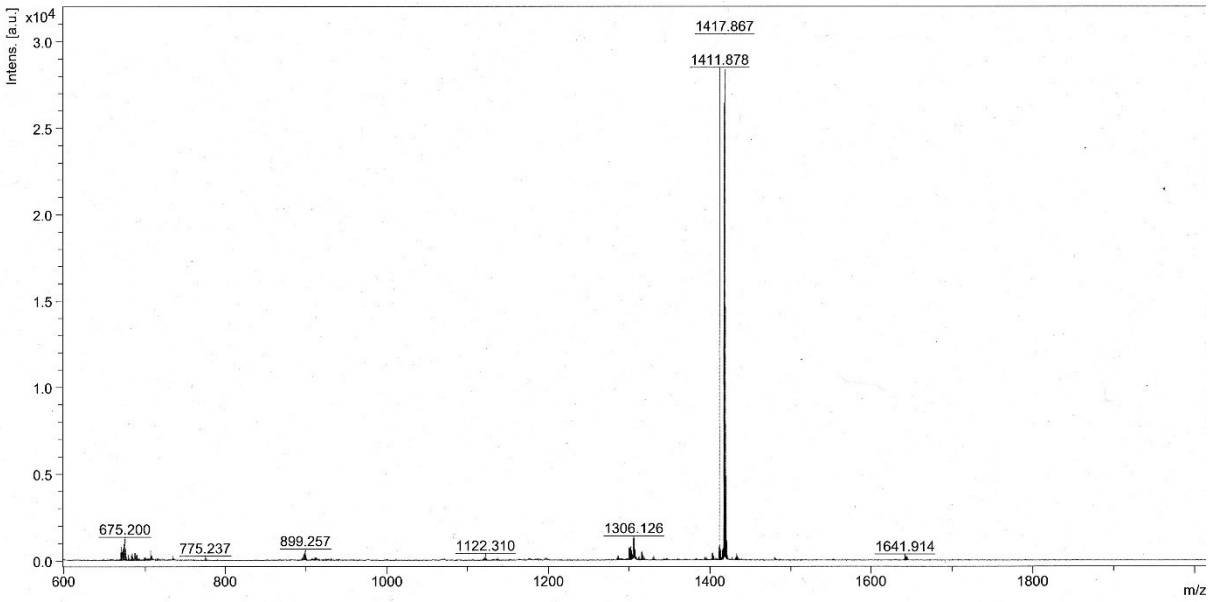

Figure S242: MALDI-mass spectrum of **Me^{4}Ter^{6}**.

6.4 Spectra for 4.3.1

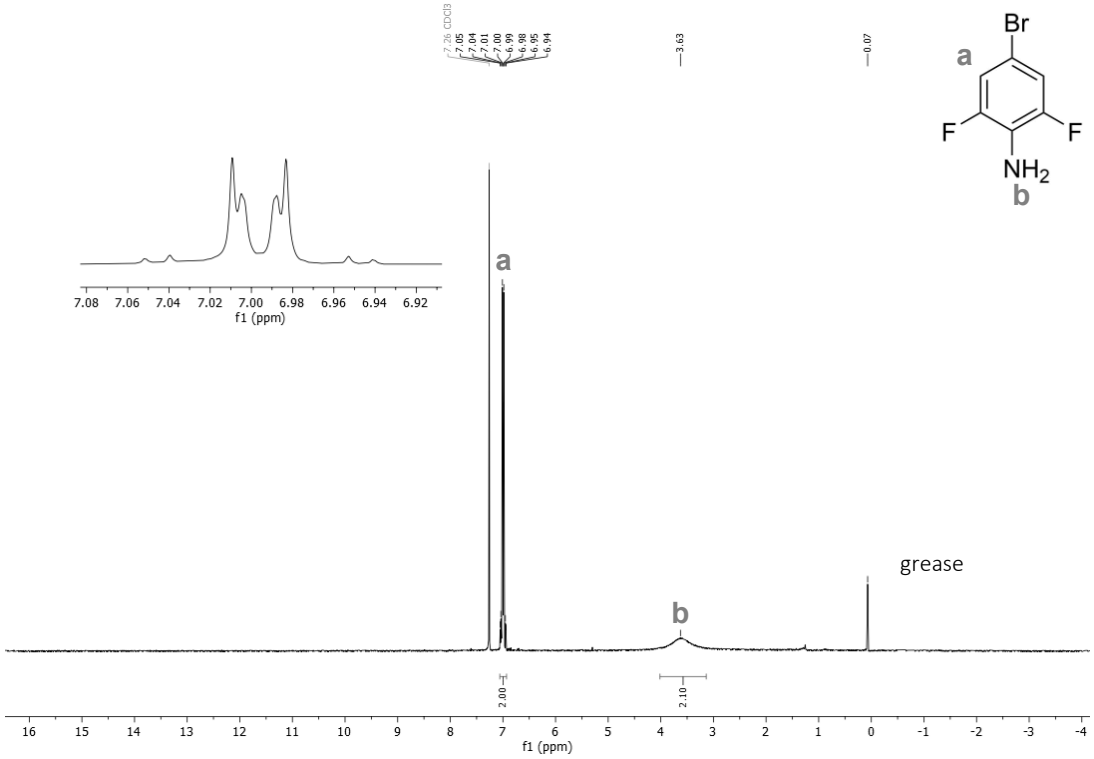

Figure S243: ^{1}H NMR spectrum of 4-bromo-2,6-difluoroaniline (**32**) ($CDCl_3$, 300 MHz).

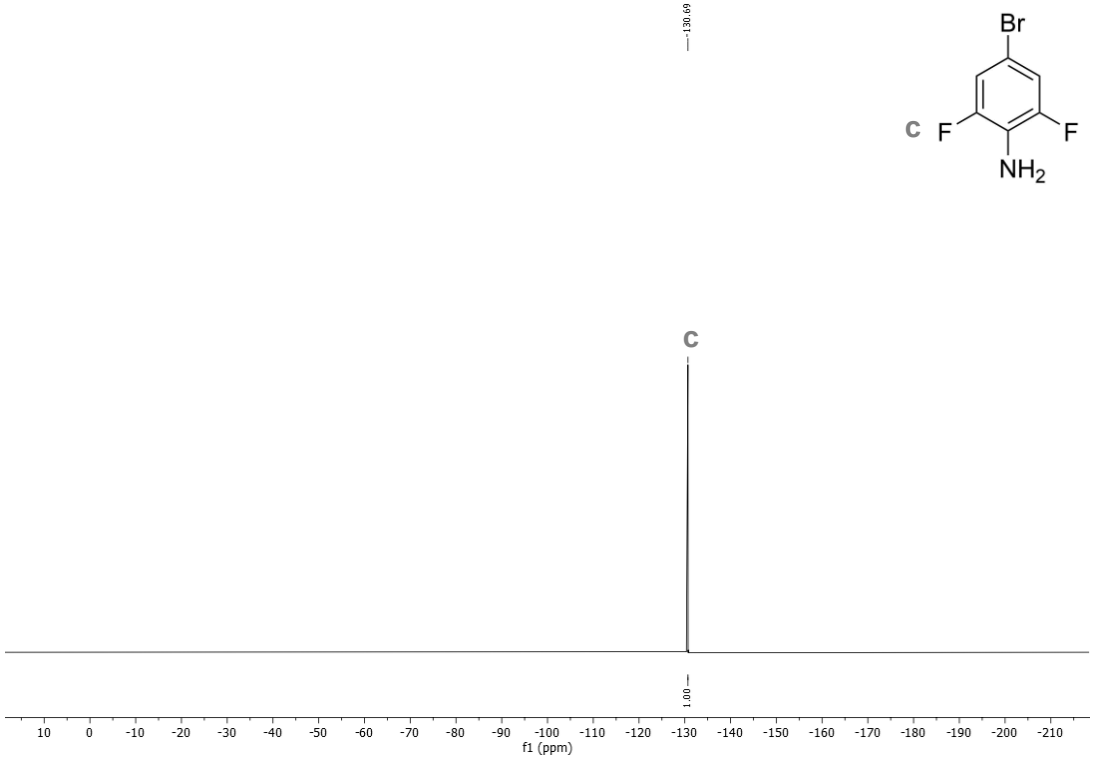

Figure S244: $^{19}F\{^{1}H\}$ NMR spectrum of 4-bromo-2,6-difluoroaniline (**32**) ($CDCl_3$, 282 MHz).

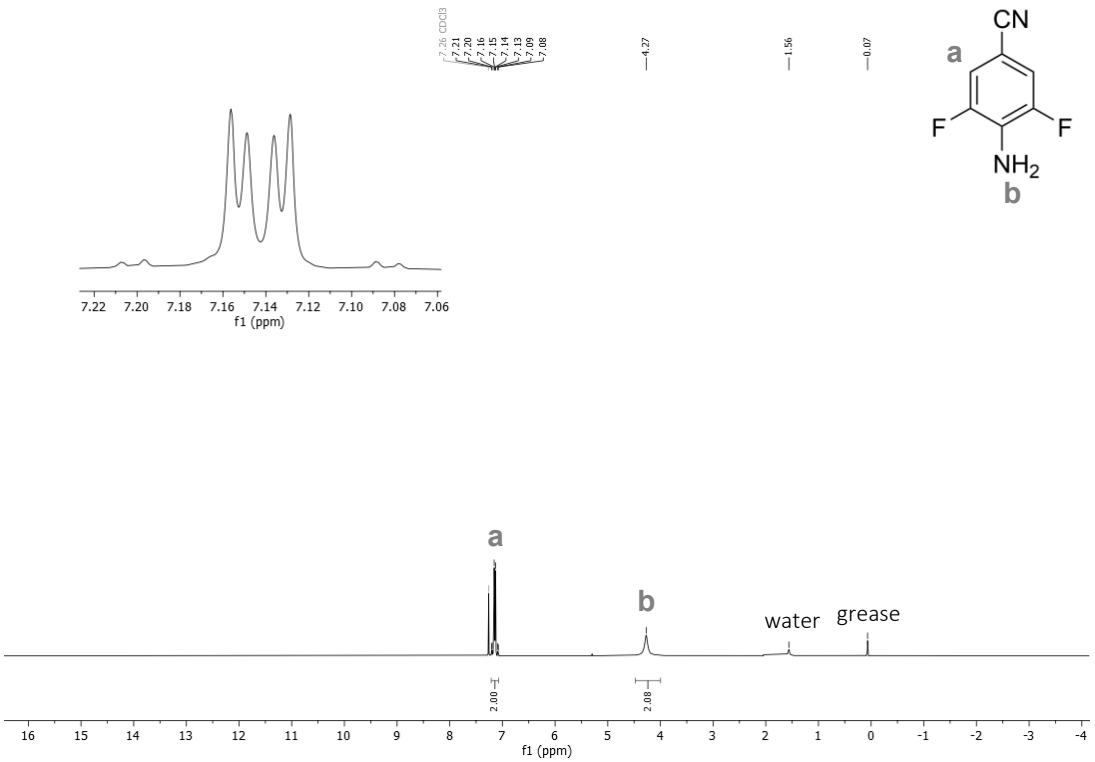

Figure S245: ^{1}H NMR spectrum of 4-amino-3,5-difluorobenzonitrile (**33**) ($CDCl_3$, 300 MHz).

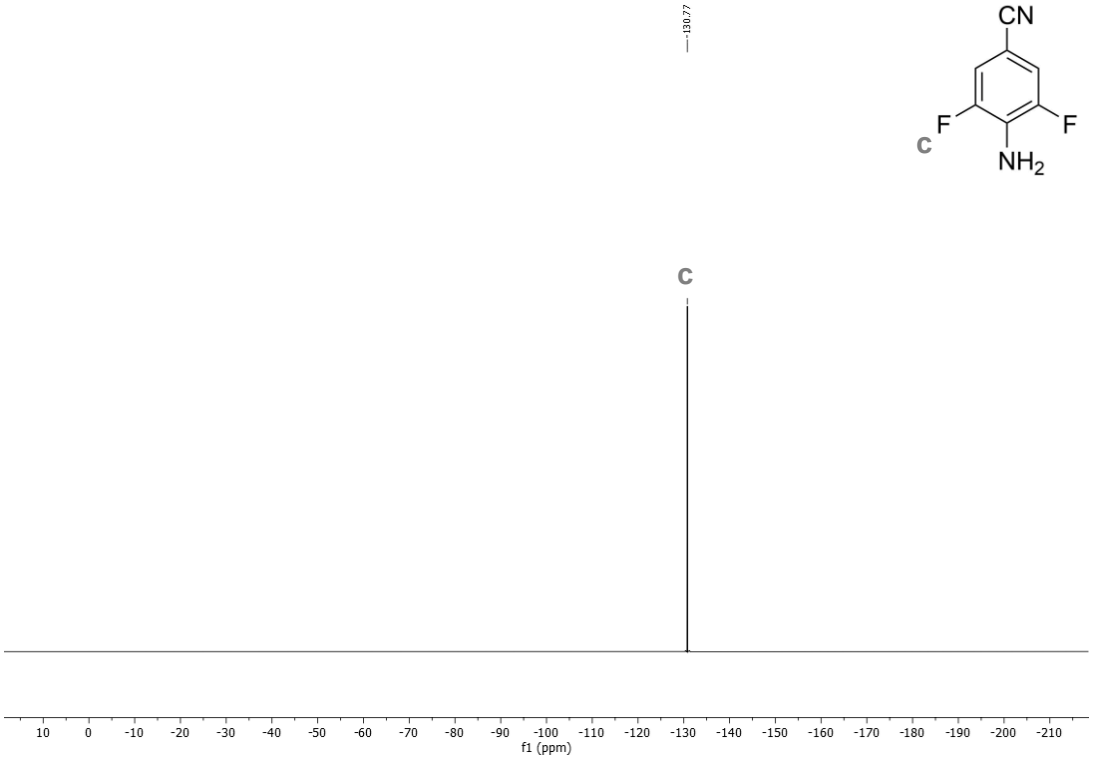

Figure S246: $^{19}F\{^{1}H\}$ NMR spectrum of 4-amino-3,5-difluorobenzonitrile (**33**) ($CDCl_3$, 282 MHz).

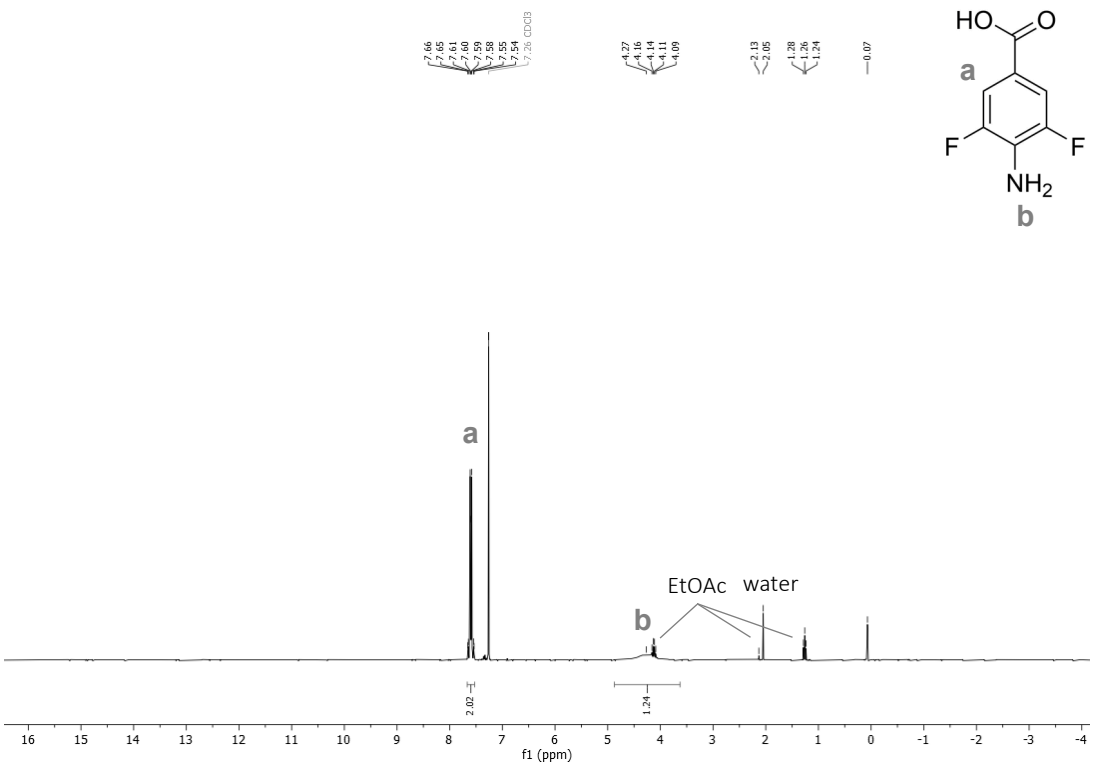

Figure S247: ^{1}H NMR spectrum of 4-amino-3,5-difluorobenzoic acid (**34**) · n HCl ($CDCl_3$, 300 MHz).

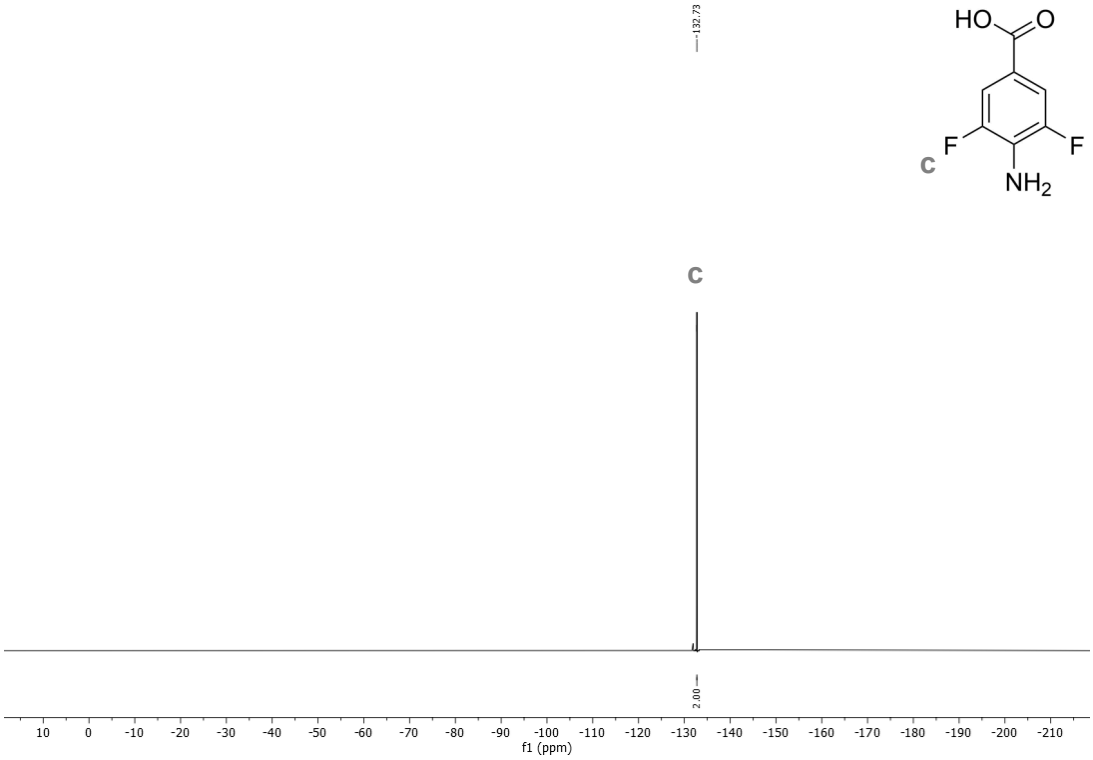

Figure S248: $^{19}F\{^{1}H\}$ NMR spectrum of 4-amino-3,5-difluorobenzoic acid (**34**) · n HCl ($CDCl_3$, 282 MHz).

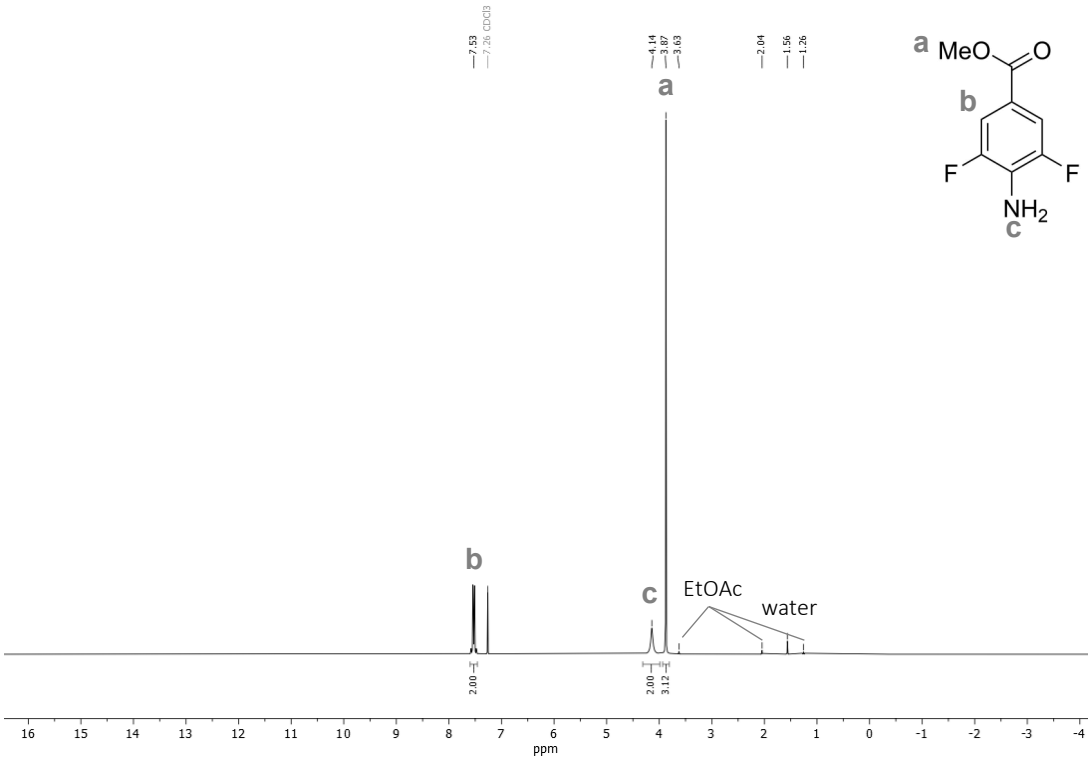

Figure S249: ^{1}H NMR spectrum of methyl 4-amino-3,5-difluorobenzoate (**35**) ($CDCl_3$, 300 MHz).

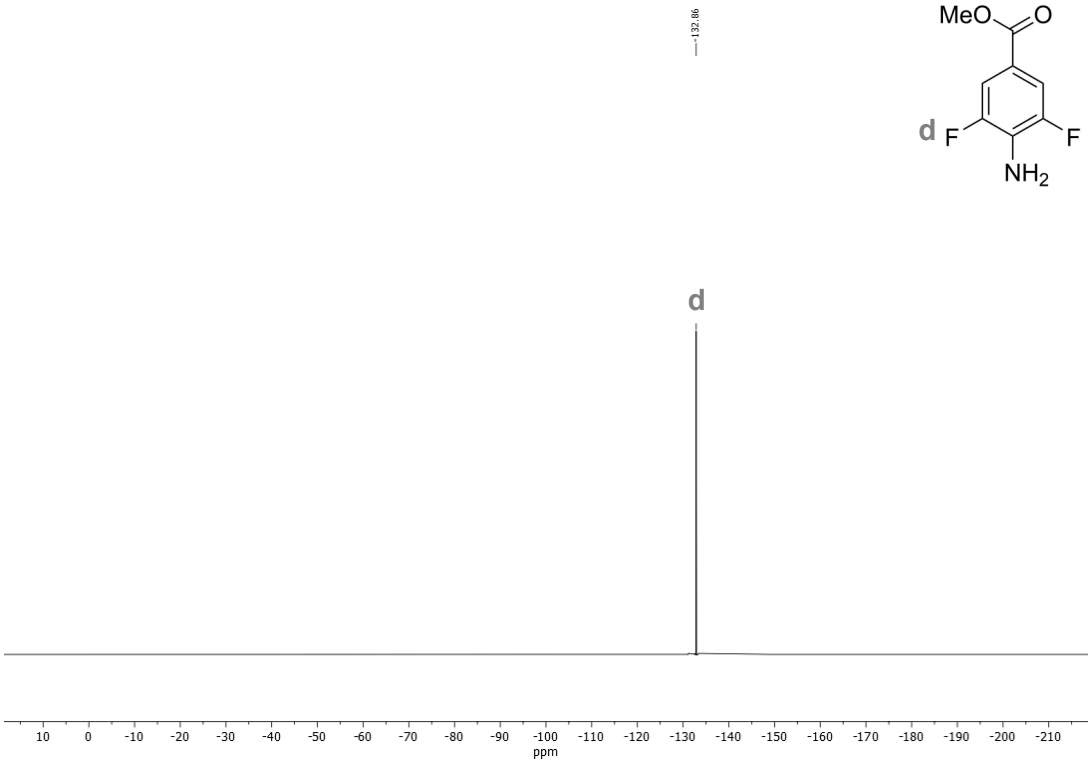

Figure S250: $^{19}F\{^{1}H\}$ NMR spectrum of methyl 4-amino-3,5-difluorobenzoate (**35**) ($CDCl_3$, 282 MHz).

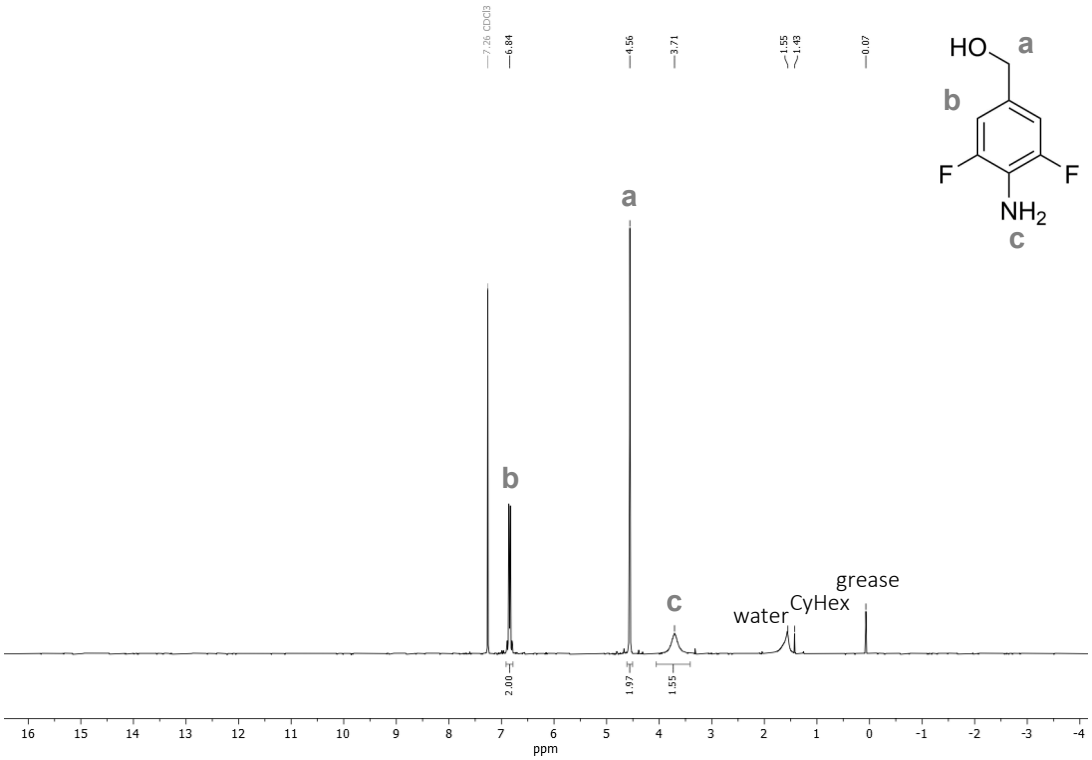

Figure S251: ^{1}H NMR spectrum of methyl (4-amino-3,5-difluorophenyl)methanol (**36**) ($CDCl_3$, 300 MHz).

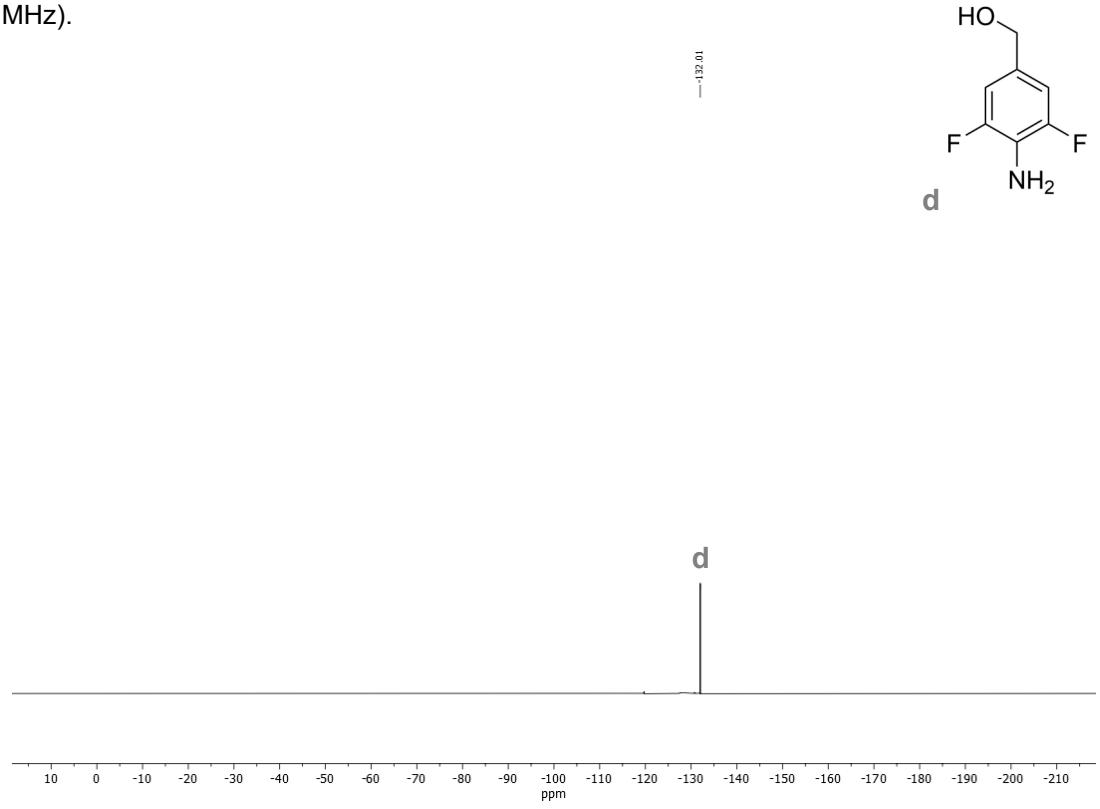

Figure S252: $^{19}F\{^{1}H\}$ NMR spectrum of methyl(4-amino-3,5-difluorophenyl)methanol (**36**) ($CDCl_3$, 282 MHz).

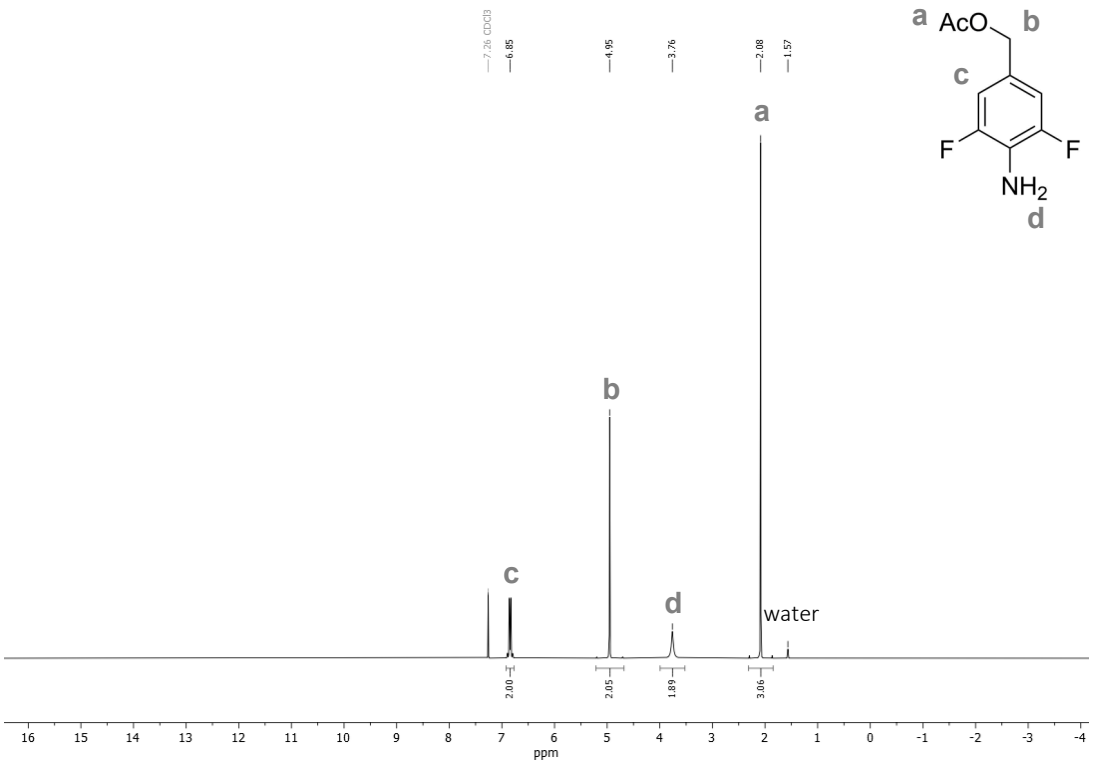

Figure S253: ^{1}H NMR spectrum of methyl-amino-3,5-difluorobenzyl acetate (**37**) ($CDCl_3$, 300 MHz).

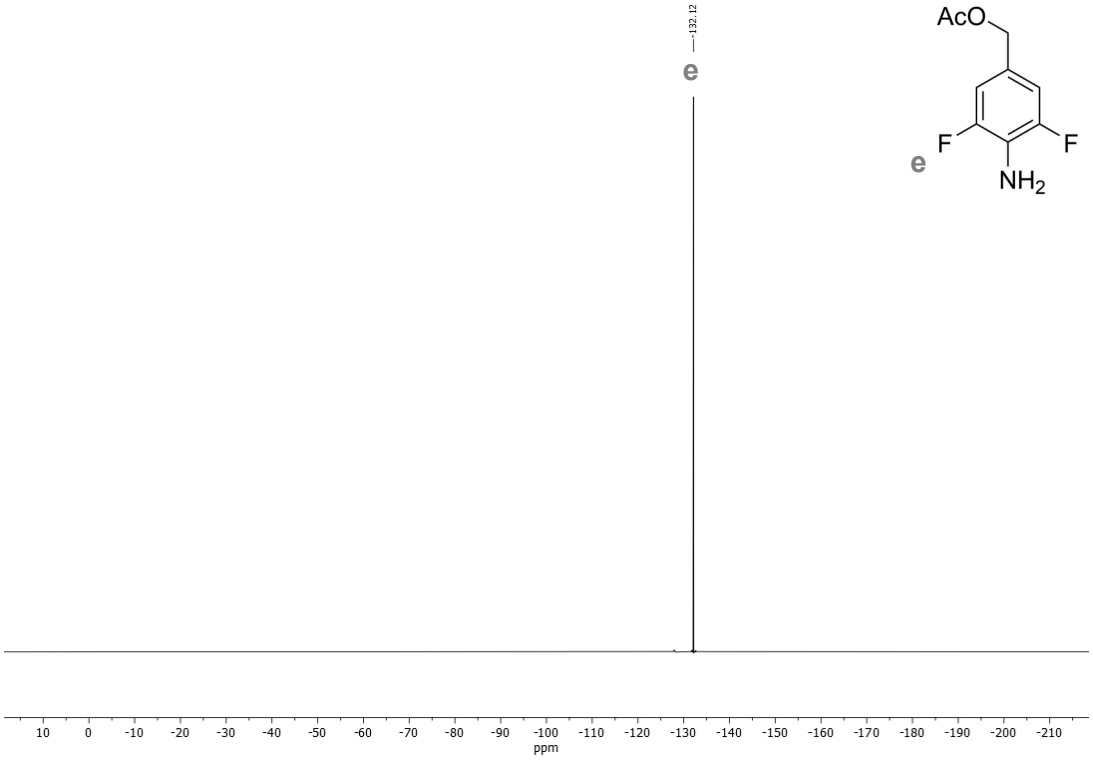

Figure S254: $^{19}F\{^{1}H\}$ NMR spectrum of methyl-amino-3,5-difluorobenzyl acetate (**37**) ($CDCl_3$, 282 MHz).

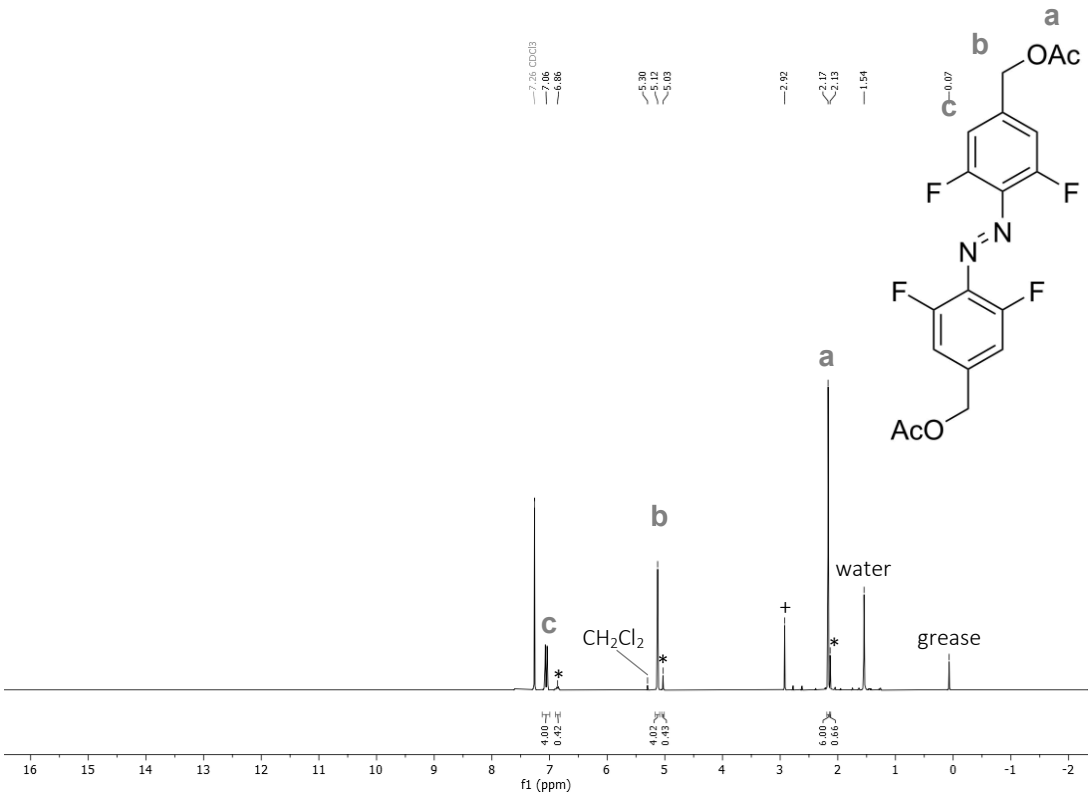

Figure S255: ^{1}H NMR spectrum of *E*-(diazene-1,2-diylbis(3,5-difluoro-4,1-phenylene))bis(methylene) diacetate (**38**) ($CDCl_3$, 300 MHz), signals of the *Z*-Isomer are marked with *, other impurities with +.

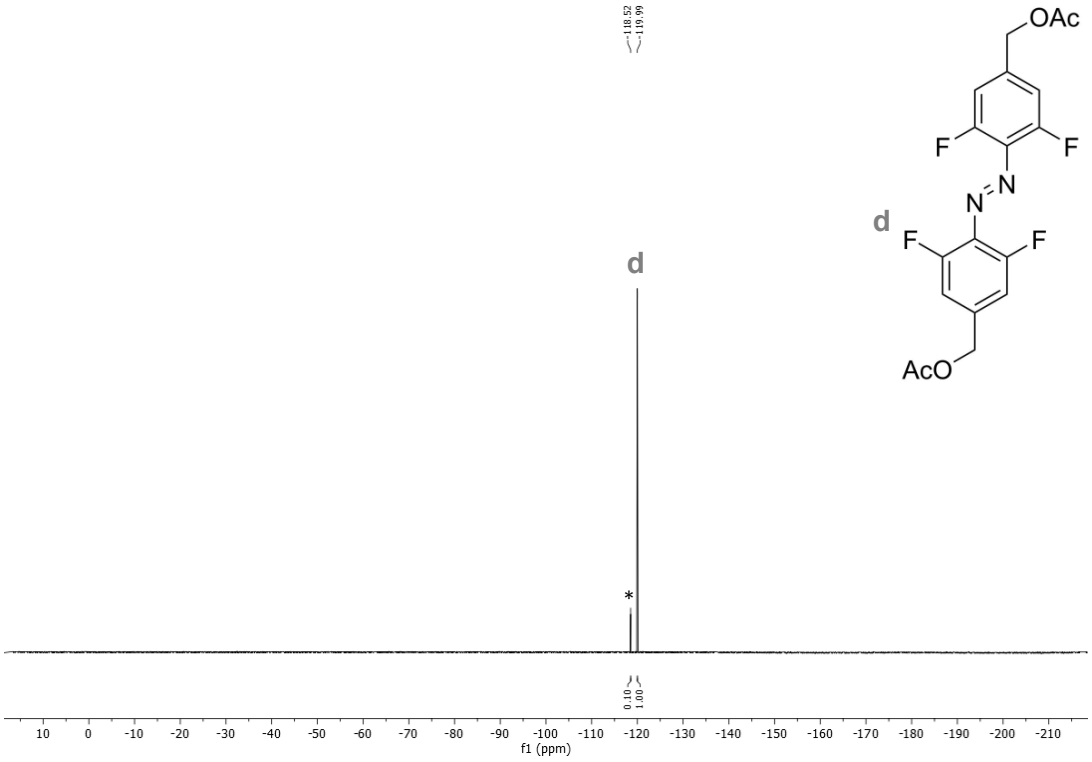

Figure S256: $^{19}F\{^{1}H\}$ NMR spectrum of *E*-(diazene-1,2-diylbis(3,5-difluoro-4,1-phenylene)) bis(methylene) diacetate (**38**) ($CDCl_3$, 282 MHz), signals of the *Z*-Isomer are marked with *.

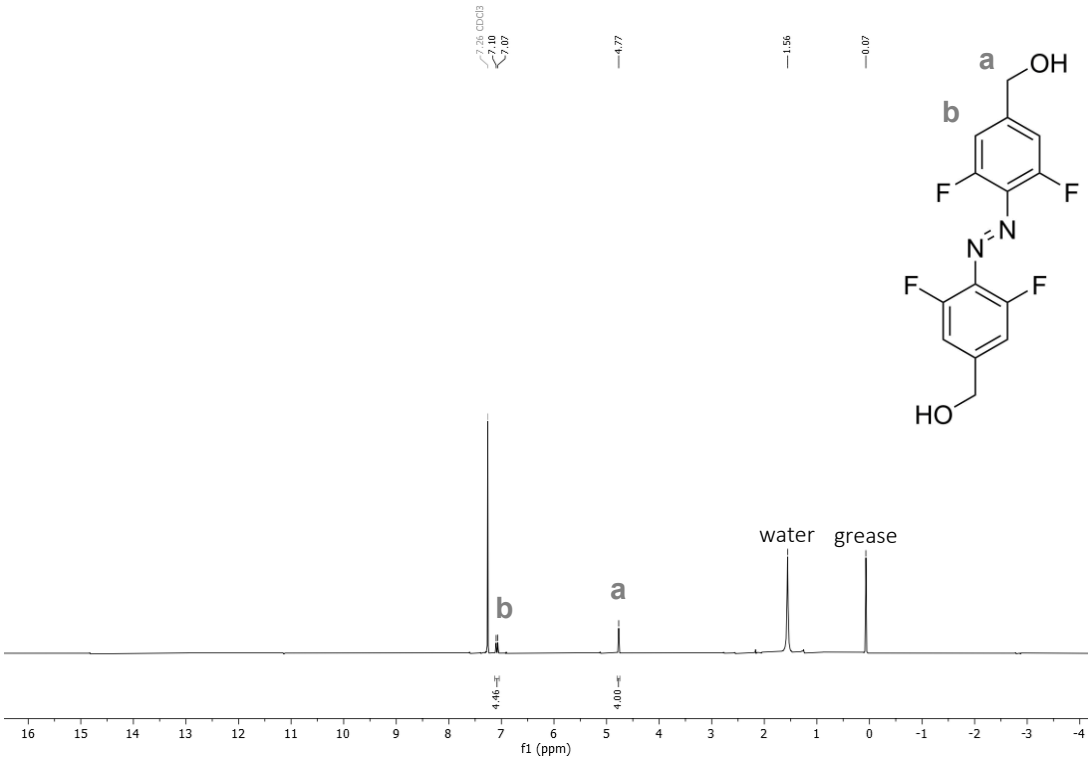

Figure S257: ^{1}H NMR spectrum of *E*-(diazene-1,2-diylbis(2,6-difluoro-4,1-phenylene))dimethanol (**39**) ($CDCl_3$, 300 MHz).

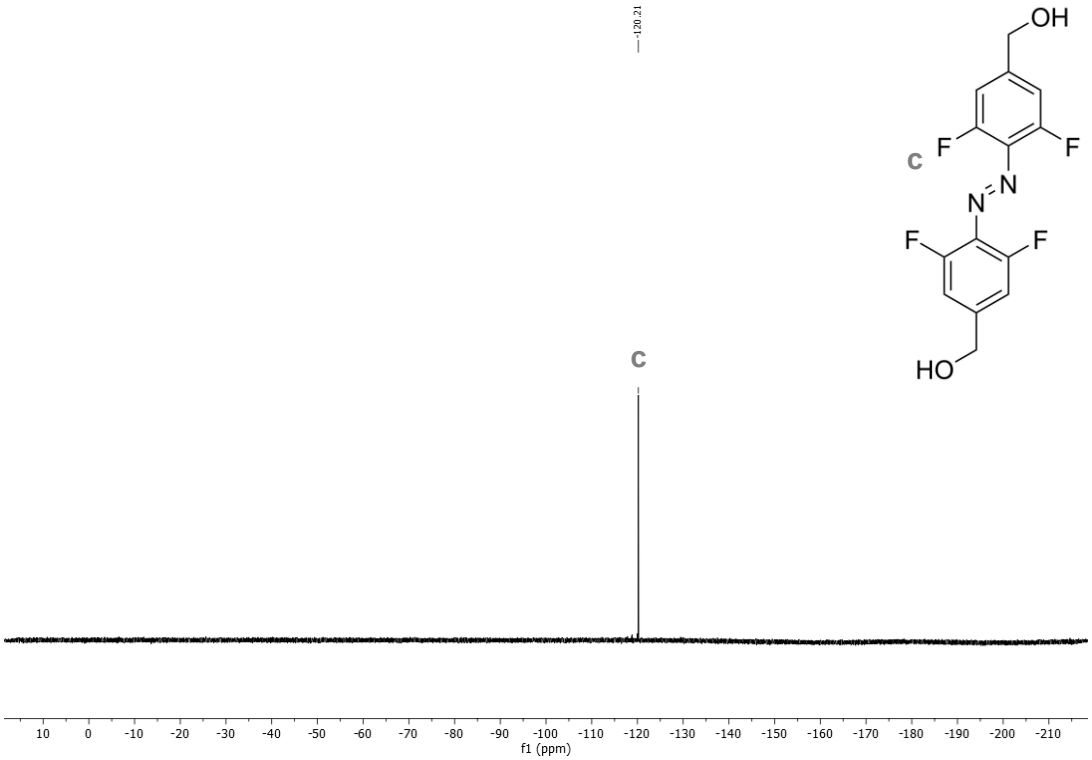

Figure S258: $^{19}F\{^{1}H\}$ NMR spectrum of *E*-(diazene-1,2-diylbis(2,6-difluoro-4,1-phenylene))dimethanol (**39**) ($CDCl_3$, 282 MHz).

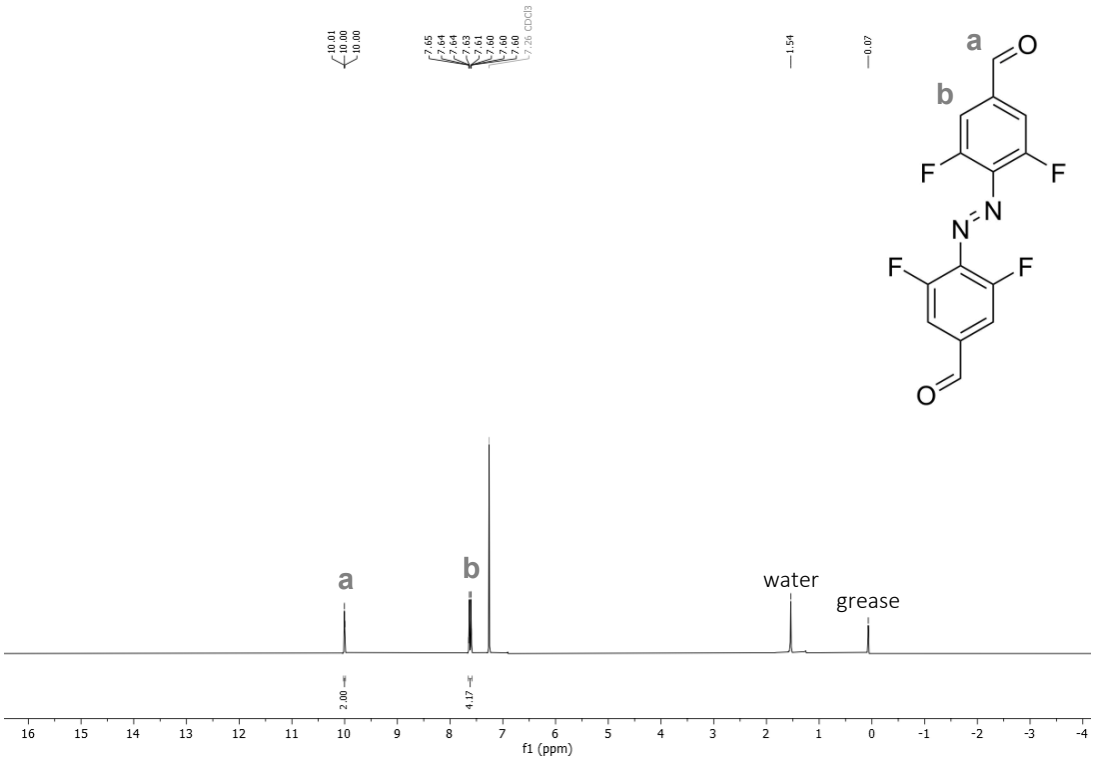

Figure S259: ^{1}H NMR spectrum of *E*-4,4'-(diazene-1,2-diyl)bis(3,5-difluorobenzaldehyde) (*E*-**A**) ($CDCl_3$, 300 MHz).

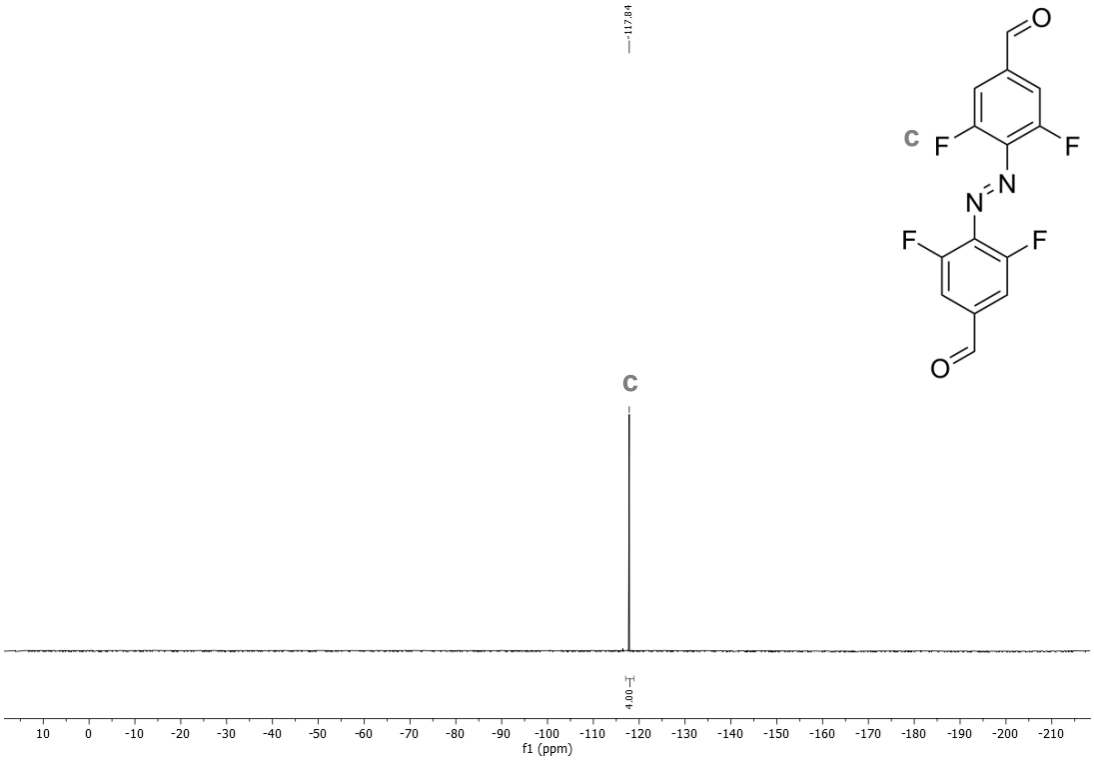

Figure S260: ^{19}F{^{1}H} NMR spectrum of *E*-4,4'-(diazene-1,2-diyl)bis(3,5-difluorobenzaldehyde) (*E*-**A**) ($CDCl_3$, 282 MHz).

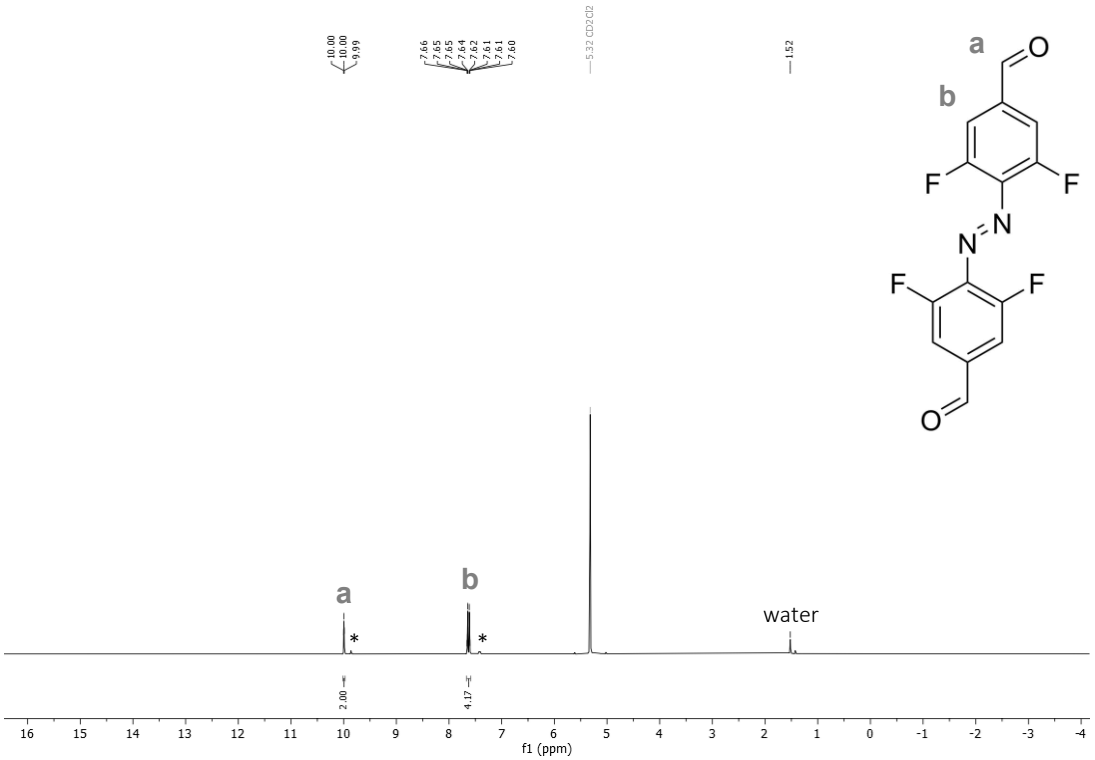

Figure S261: ^{1}H NMR spectrum of *E*-4,4'-(diazene-1,2-diyl)bis(3,5-difluorobenzaldehyde) (*E*-**A**) (CD_2Cl_2, 300 MHz), signals of the *Z*-Isomer are marked with *.

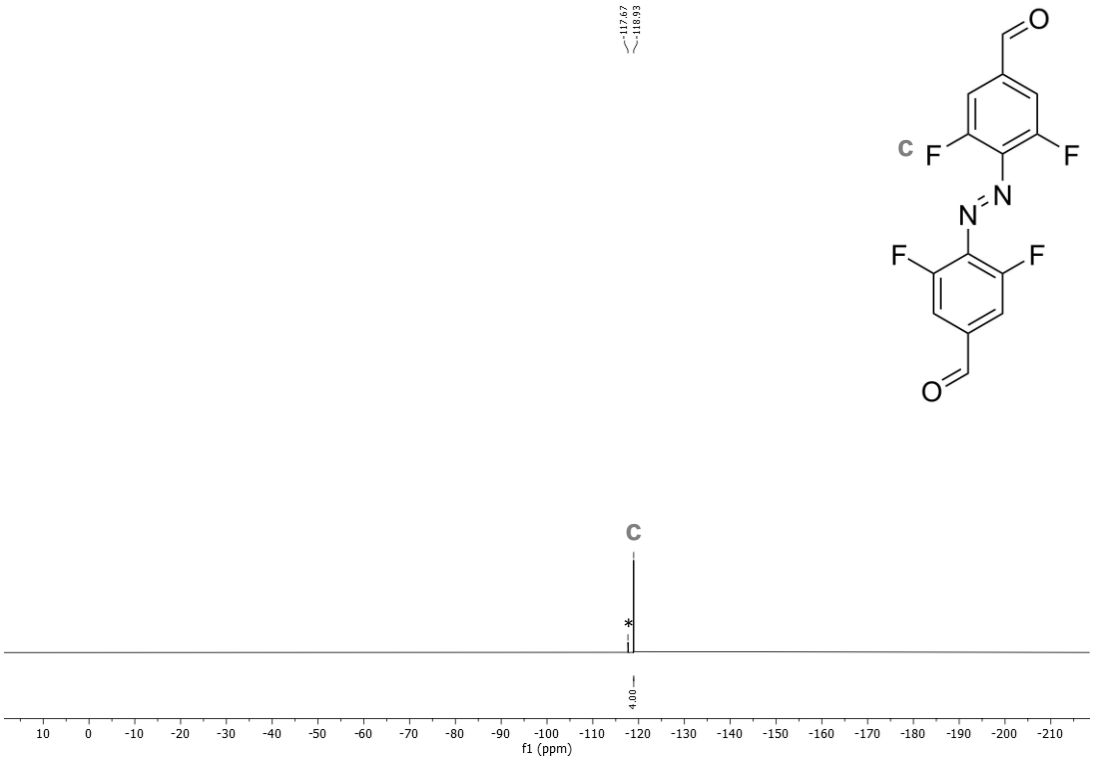

Figure S262: $^{19}F\{^{1}H\}$ NMR spectrum of *E*-4,4'-(diazene-1,2-diyl)bis(3,5-difluorobenzaldehyde) (*E*-**A**) (CD_2Cl_2, 282 MHz), signals of the *Z*-Isomer are marked with *.

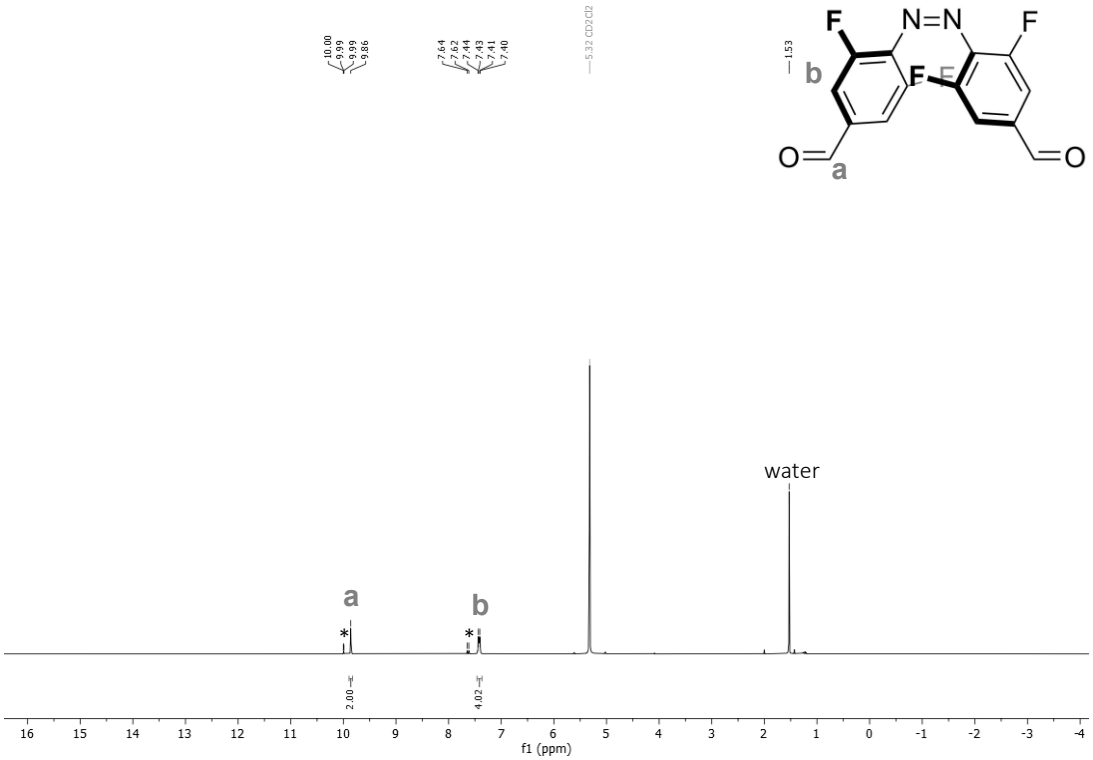

Figure S263: ^{1}H NMR spectrum of *Z*-4,4'-(diazene-1,2-diyl)bis(3,5-difluorobenzaldehyde) (*Z*-**A**) (CD_2Cl_2, 300 MHz), signals of the *E*-Isomer are marked with *.

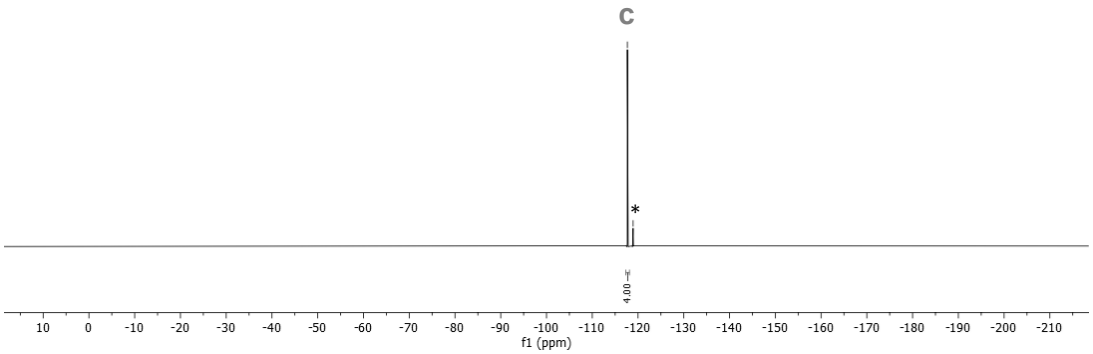

Figure S264: $^{19}F\{^{1}H\}$ NMR spectrum of *Z*-4,4'-(diazene-1,2-diyl)bis(3,5-difluorobenzaldehyde) (*Z*-**A**) (CD_2Cl_2, 282 MHz), signals of the *E*-Isomer are marked with *.

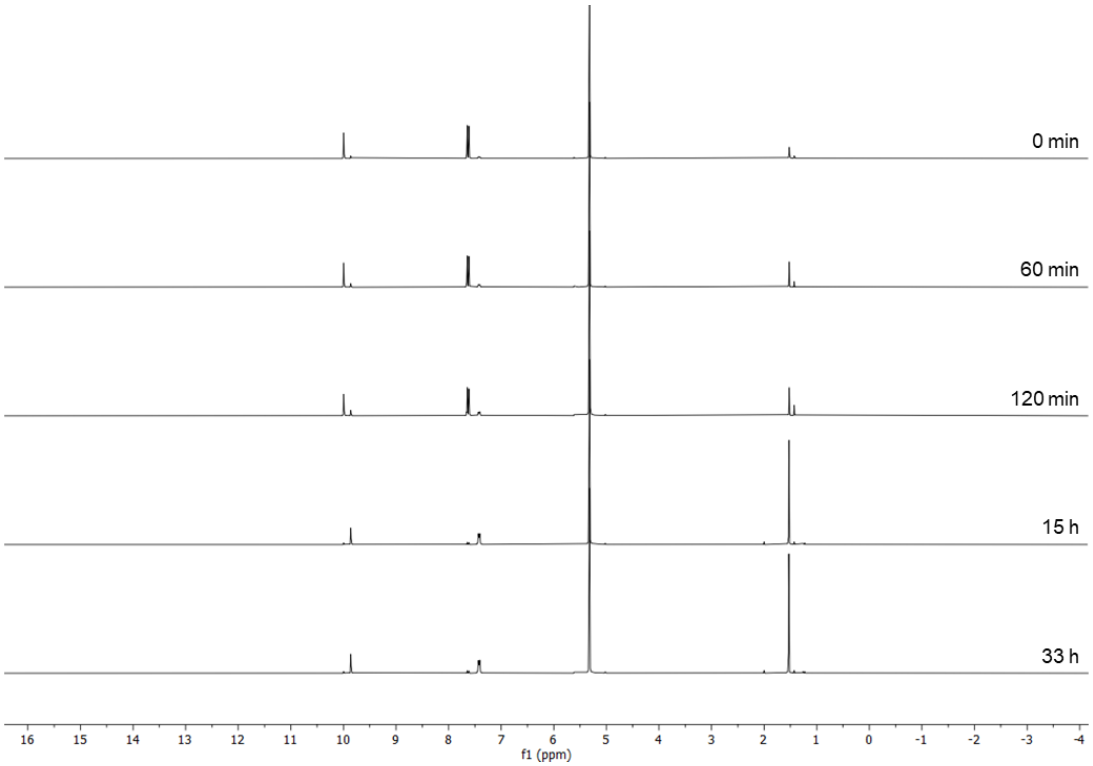

Figure S265: ^{1}H NMR spectra of **A** after irradiation with light of a wavelength of 660 nm (CD_2Cl_2, 300 MHz).

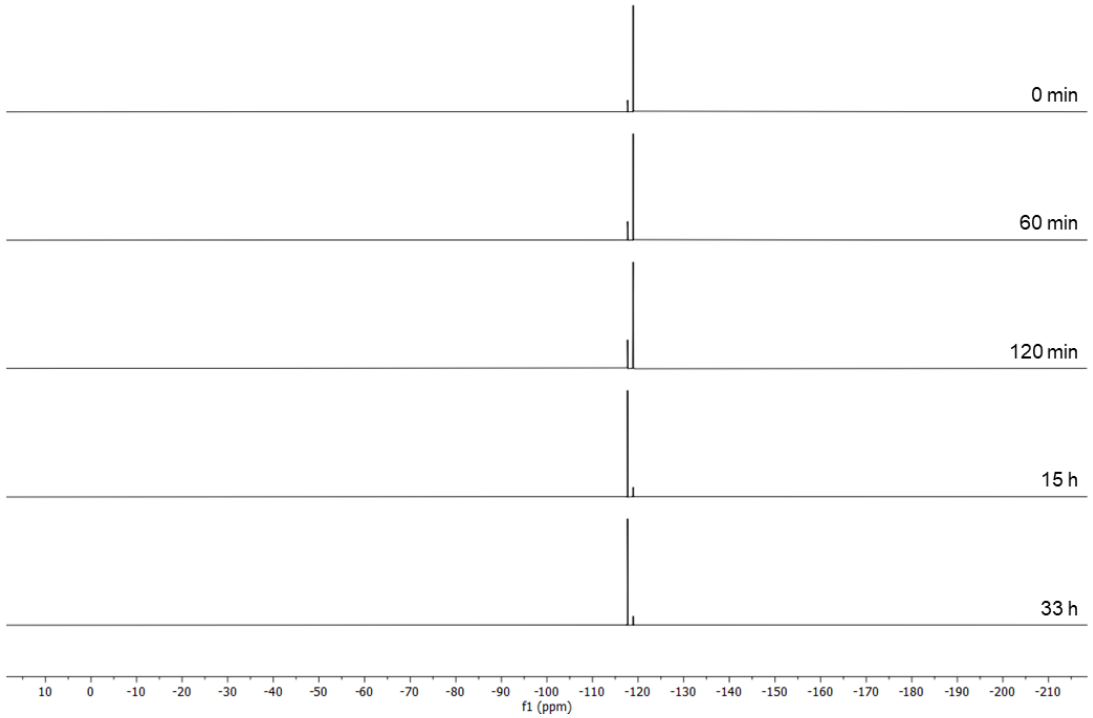

Figure S266: $^{19}F\{^{1}H\}$ NMR spectra of **A** after irradiation with light of a wavelength of 660 nm (CD_2Cl_2, 282 MHz).

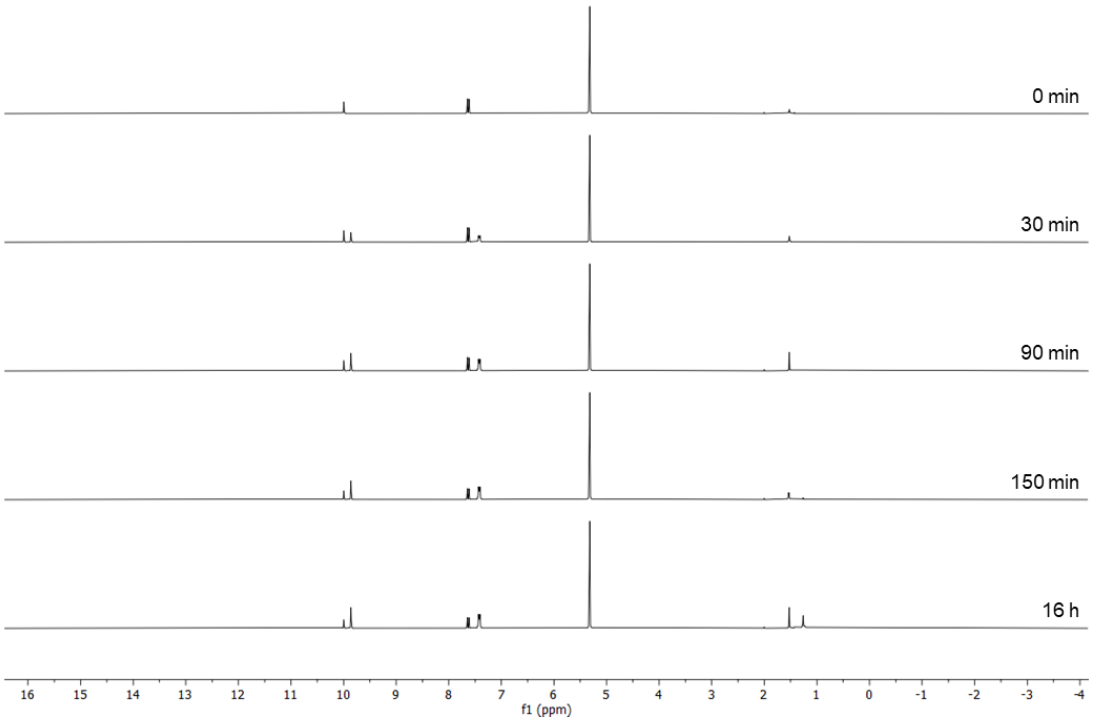

Figure S267: ^{1}H NMR spectra of **A** after irradiation with light of a wavelength of 565 nm (CD_2Cl_2, 300 MHz).

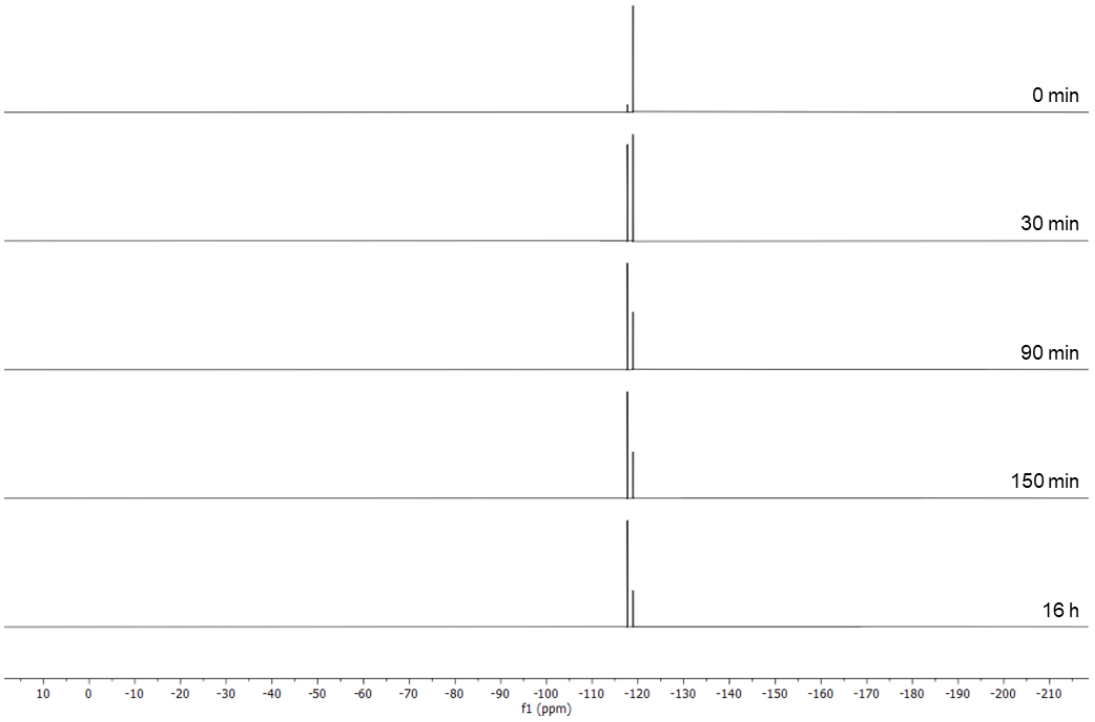

Figure S268: $^{19}F\{^{1}H\}$ NMR spectra of **A** after irradiation with light of a wavelength of 565 nm (CD_2Cl_2, 282 MHz).

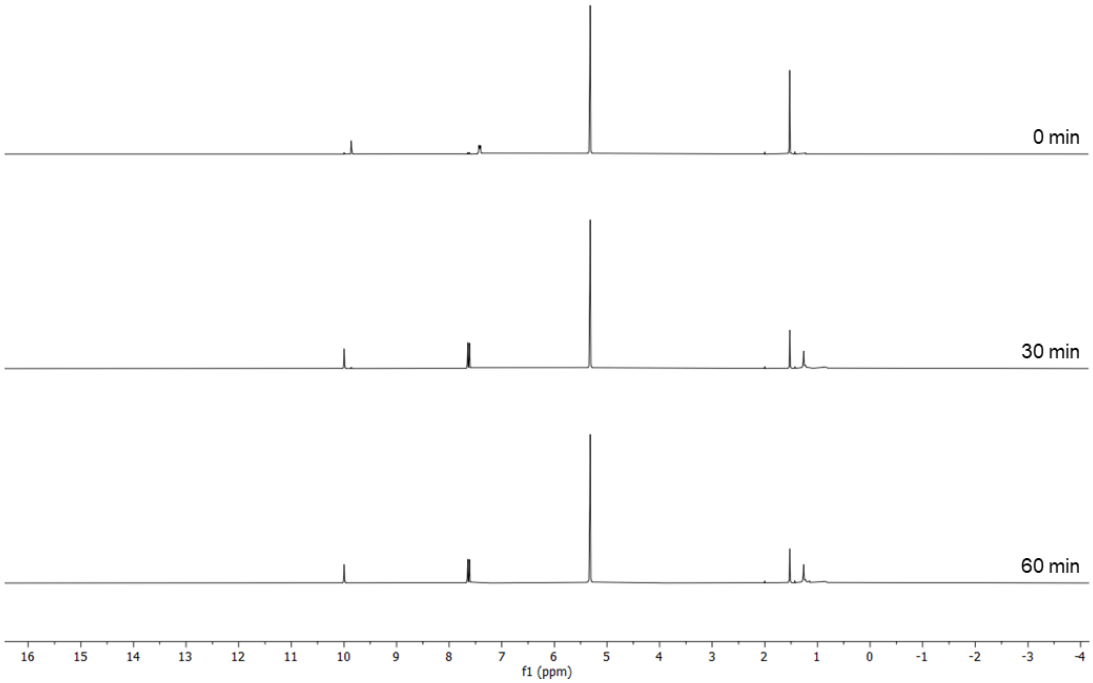

Figure S269: ^{1}H NMR spectra of **A** after irradiation with light of a wavelength of 405 nm (CD_2Cl_2, 300 MHz).

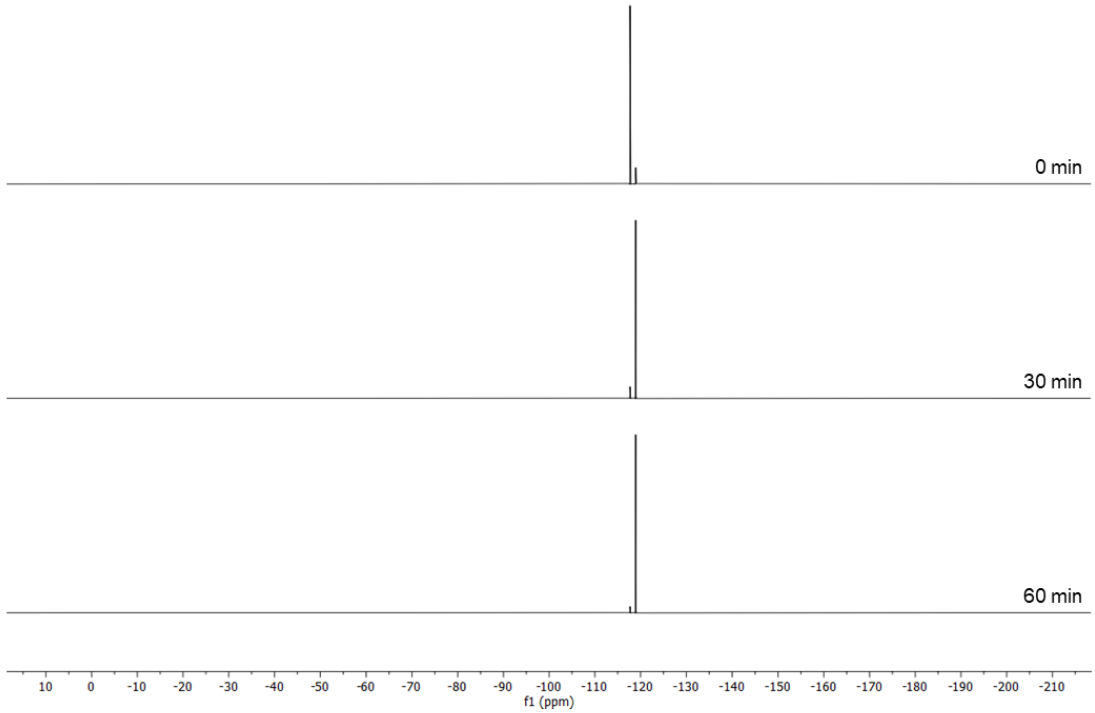

Figure S270: $^{19}F\{^{1}H\}$ NMR spectra of **A** after irradiation with light of a wavelength of 405 nm (CD_2Cl_2, 282 MHz).

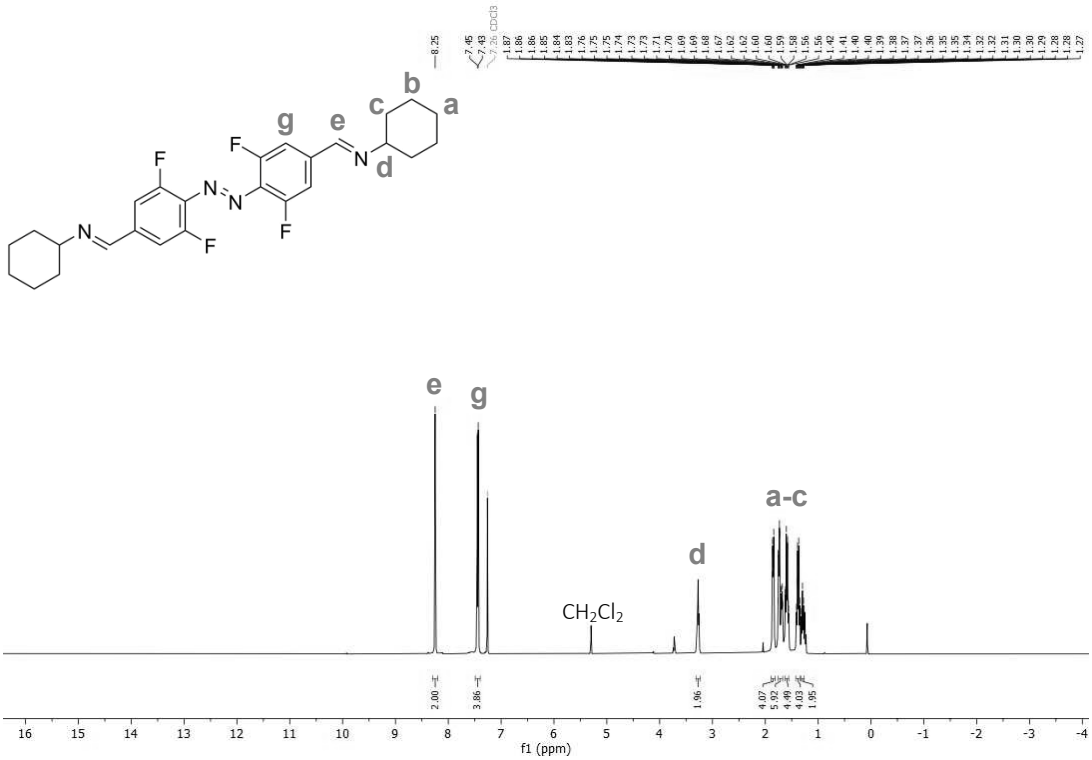

Figure S271: ^{1}H NMR spectrum of **AC²** ($CDCl_3$, 600 MHz).

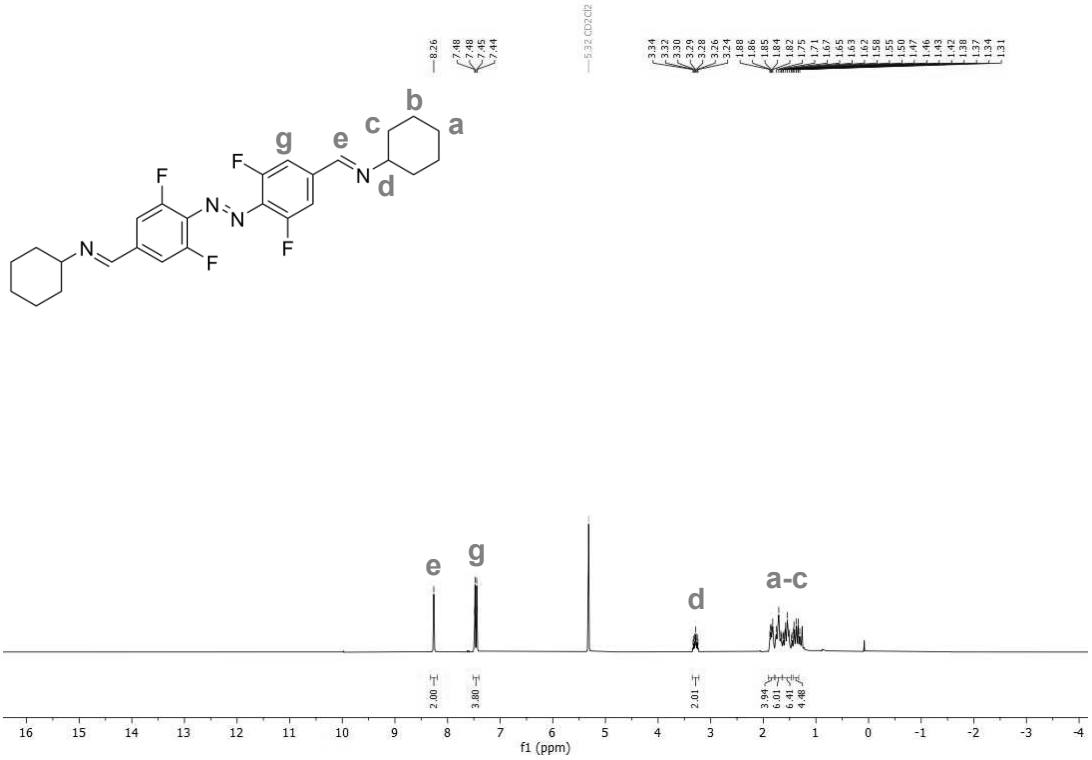

Figure S272: ^{1}H NMR spectrum of **AC²** (CD_2Cl_2, 300 MHz).

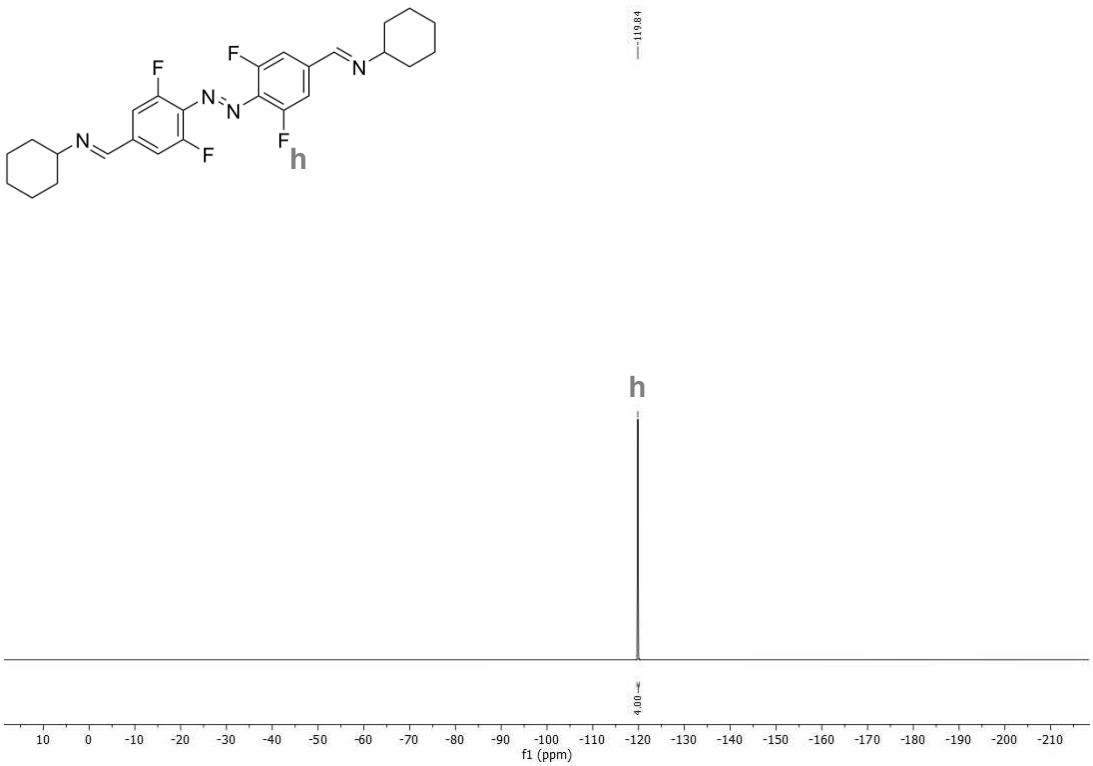

Figure S273: $^{19}F\{^{1}H\}$ NMR spectrum of **AC²** ($CDCl_3$, 565 MHz).

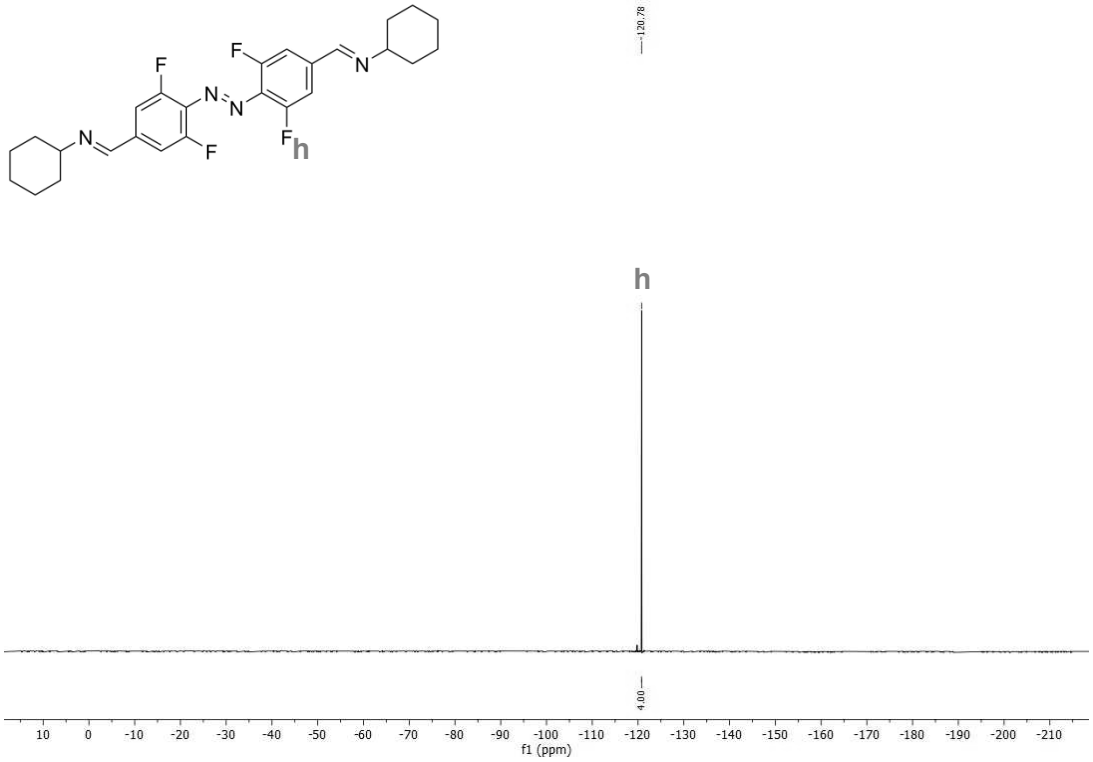

Figure S274: $^{19}F\{^{1}H\}$ NMR spectrum of **AC²** (CD_2Cl_2, 282 MHz).

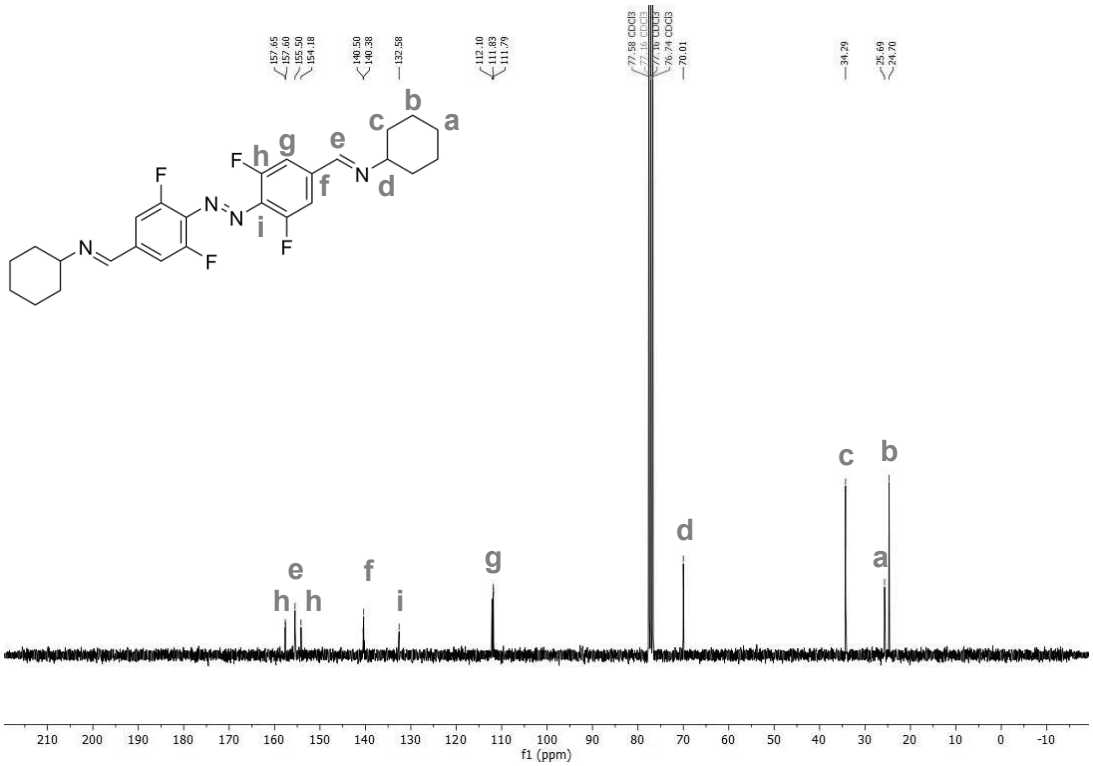

Figure S275: $^{13}C\{^{1}H\}$ NMR spectrum of **AC²** ($CDCl_3$, 75 MHz).

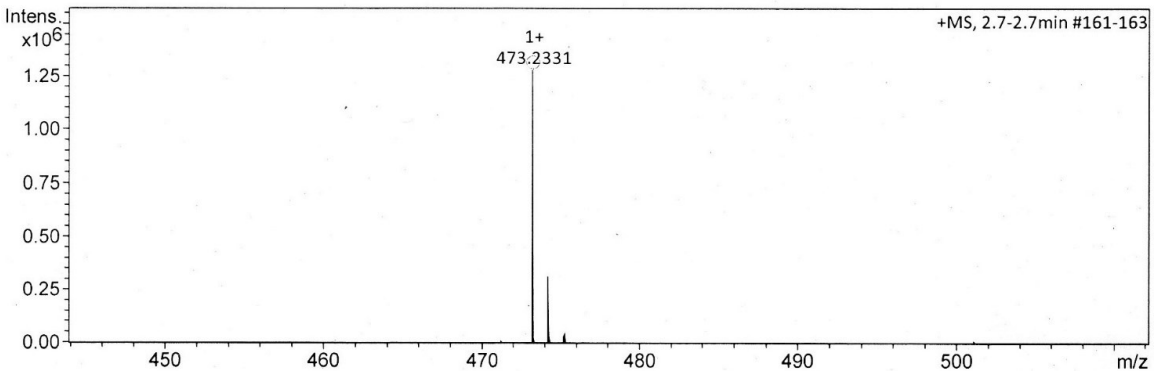

Figure S276: ESI-HR-mass spectrum of **AC²**.

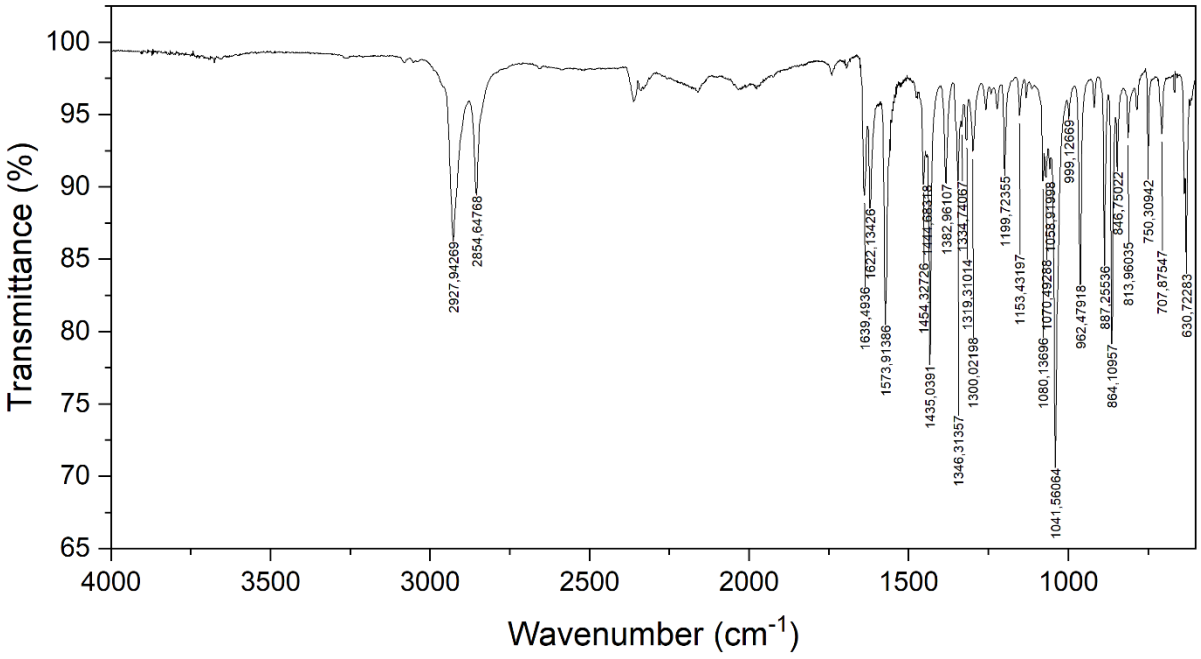

Figure S277: IR spectrum of **AC²**.

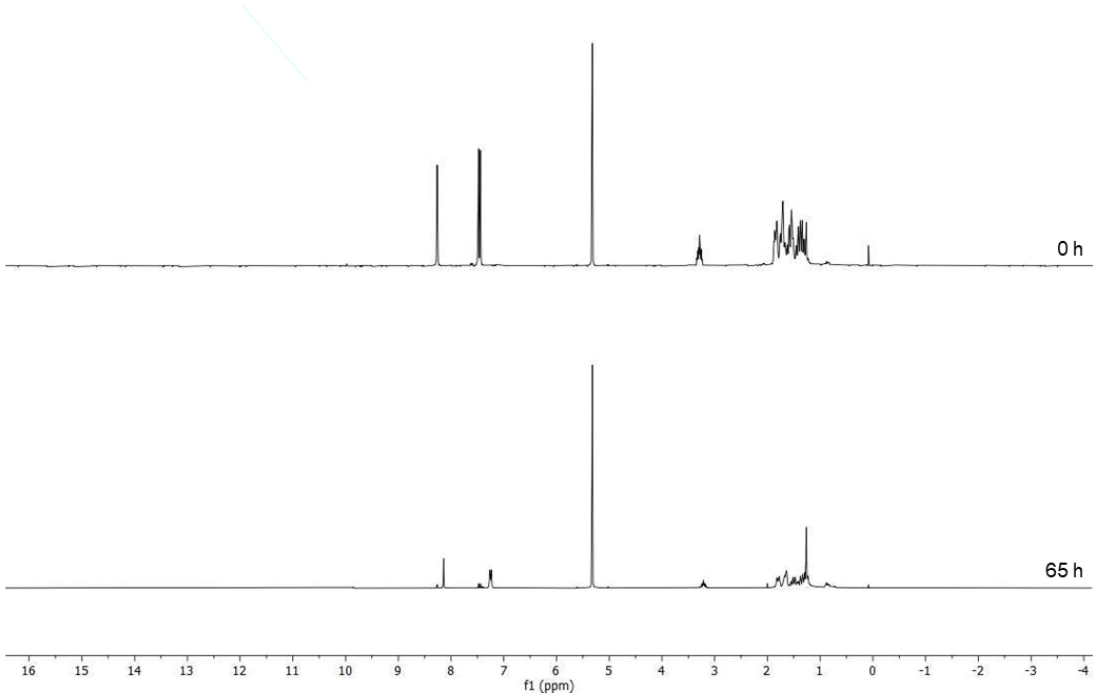

Figure S278: ^{1}H NMR spectra of **AC²** after irradiation with light of a wavelength of 660 nm (CD_2Cl_2, 300 MHz).

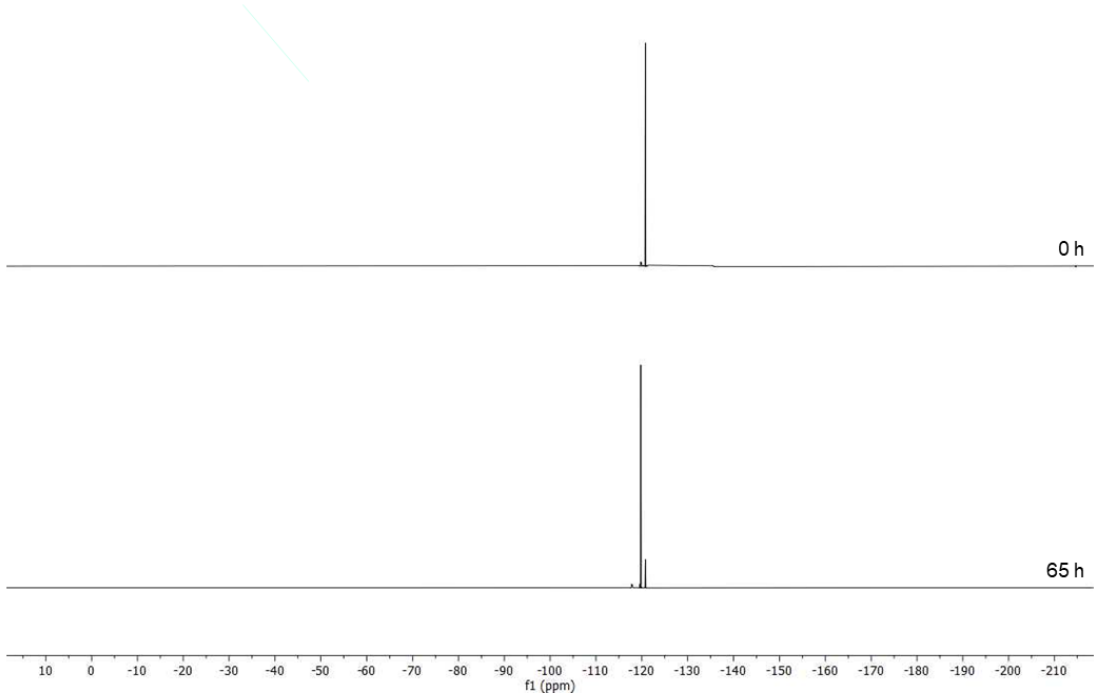

Figure S279: $^{19}F\{^{1}H\}$ NMR spectra of **AC²** after irradiation with light of a wavelength of 660 nm (CD_2Cl_2, 282 MHz).

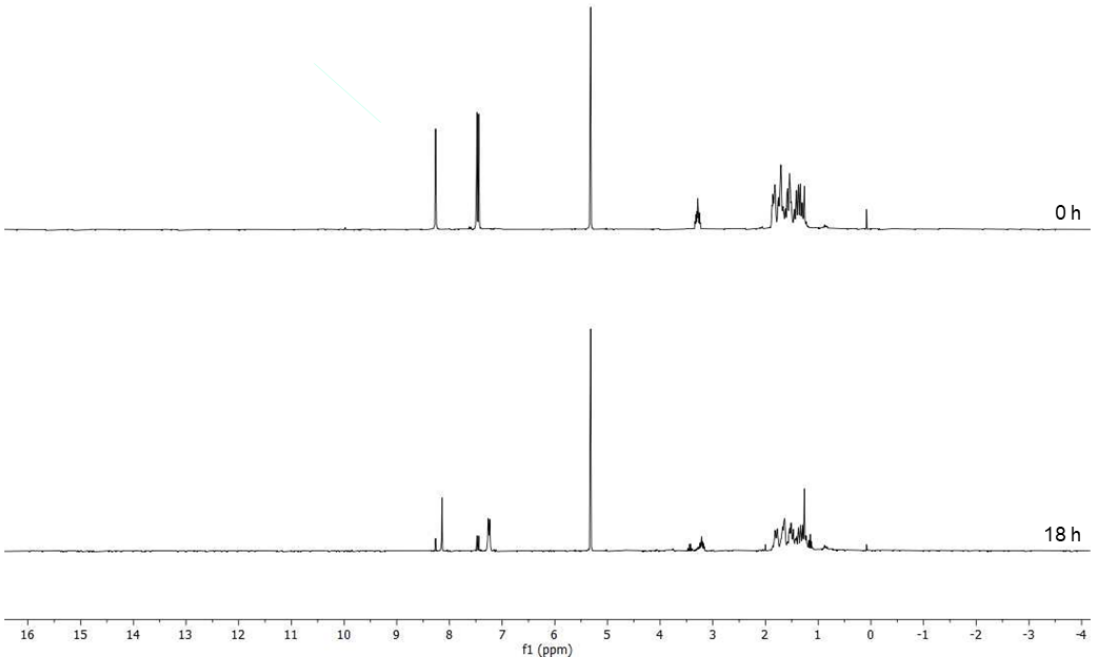

Figure S280: ^{1}H NMR spectra of **AC²** after irradiation with light of a wavelength of 565 nm (CD_2Cl_2, 300 MHz).

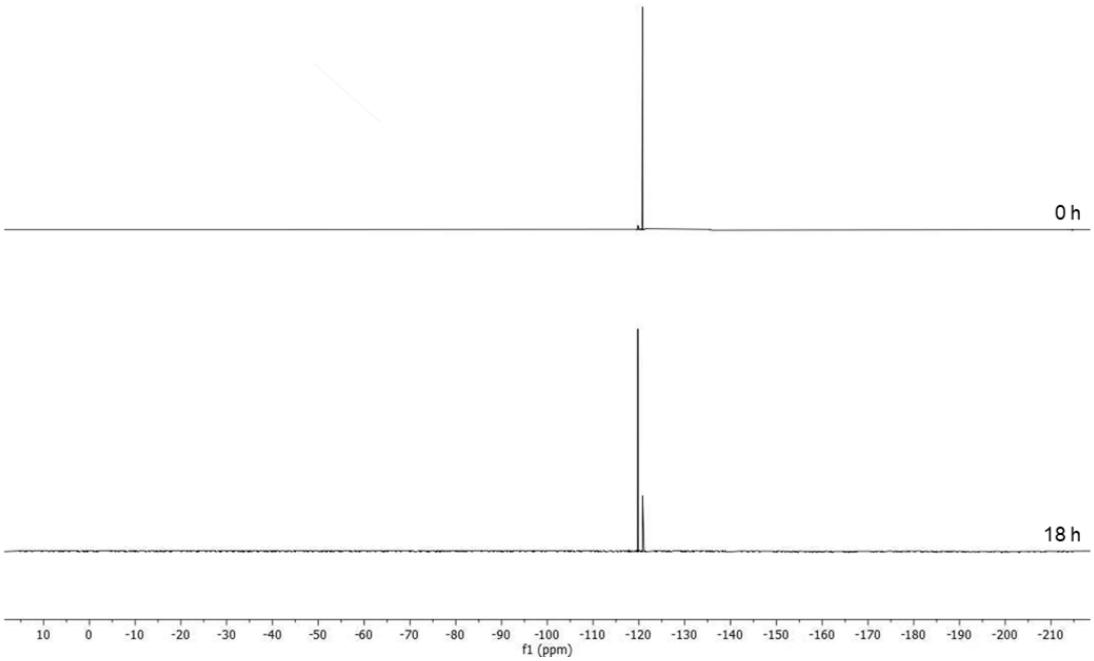

Figure S281: $^{19}F\{^{1}H\}$ NMR spectra of **AC²** after irradiation with light of a wavelength of 565 nm (CD_2Cl_2, 282 MHz).

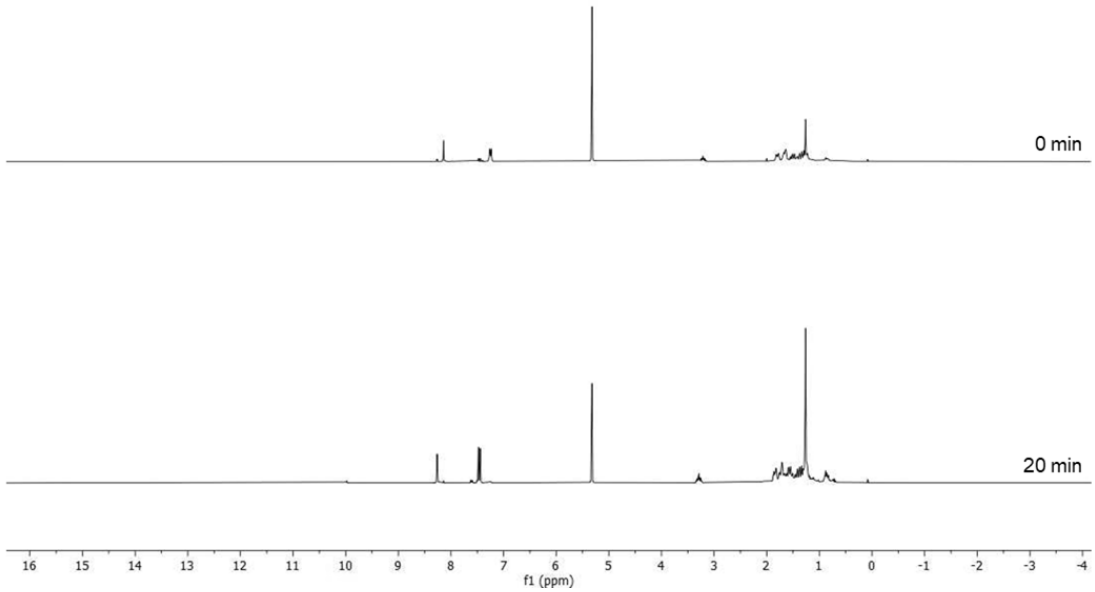

Figure S282: ^{1}H NMR spectra of **AC²** after irradiation with light of a wavelength of 405 nm (CD_2Cl_2, 300 MHz).

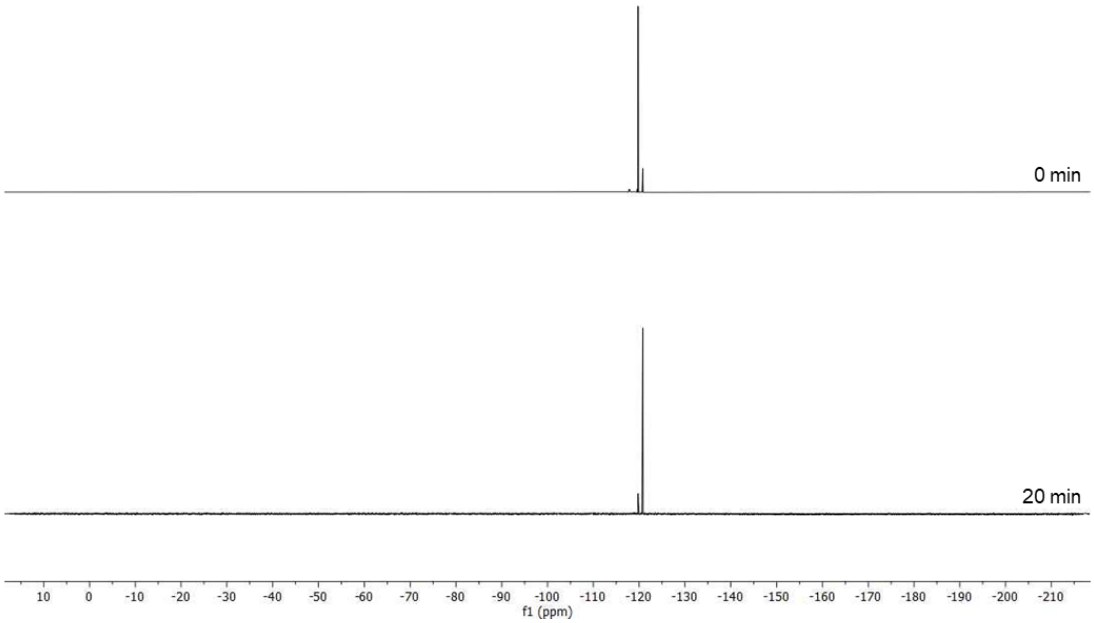

Figure S283: $^{19}F\{^{1}H\}$ NMR spectra of **AC²** after irradiation with light of a wavelength of 405 nm (CD_2Cl_2, 282 MHz).

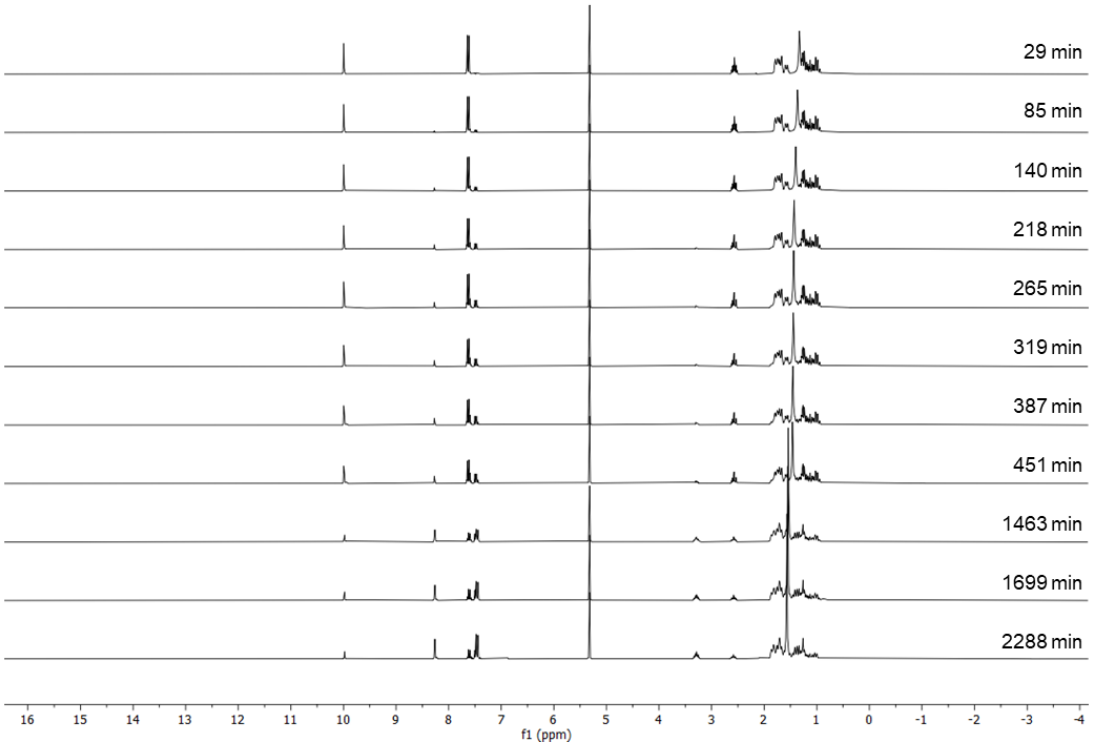

Figure S284: ^{1}H NMR spectra of the formation of **AC²** in the dark (CD_2Cl_2, 300 MHz).

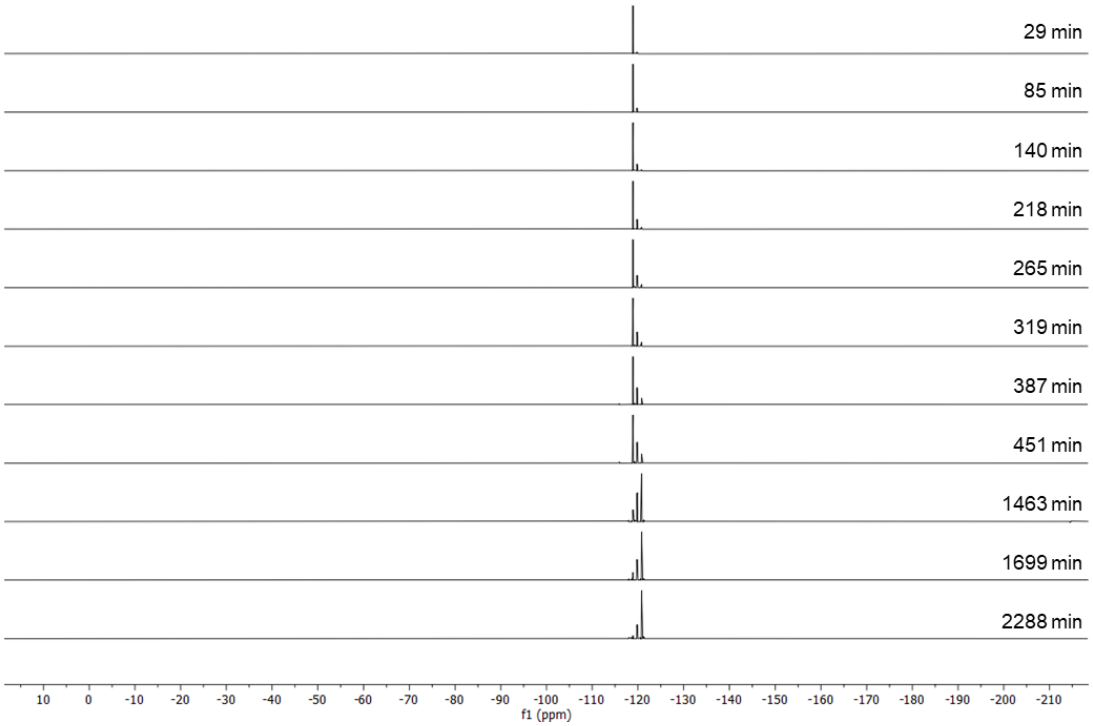

Figure S285: $^{19}F\{^{1}H\}$ NMR spectra of the formation of **AC²** in the dark (CD_2Cl_2, 282 MHz).

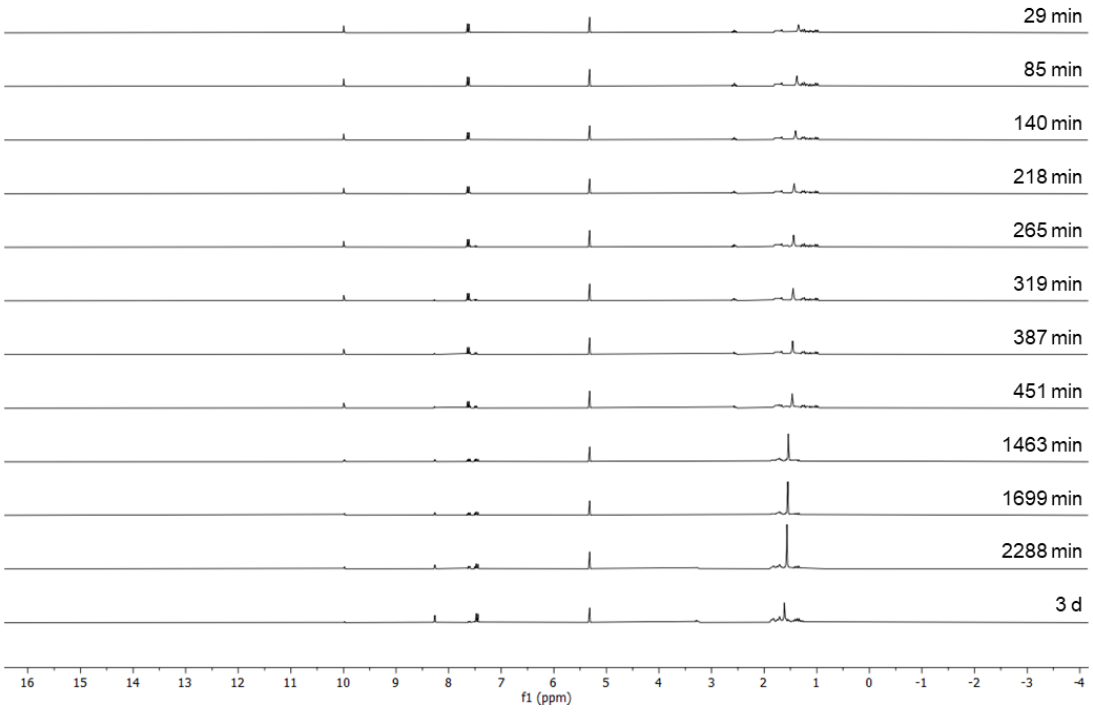

Figure S286: ^{1}H NMR spectra of the formation of **AC²** in the dark (CD_2Cl_2, 300 MHz).

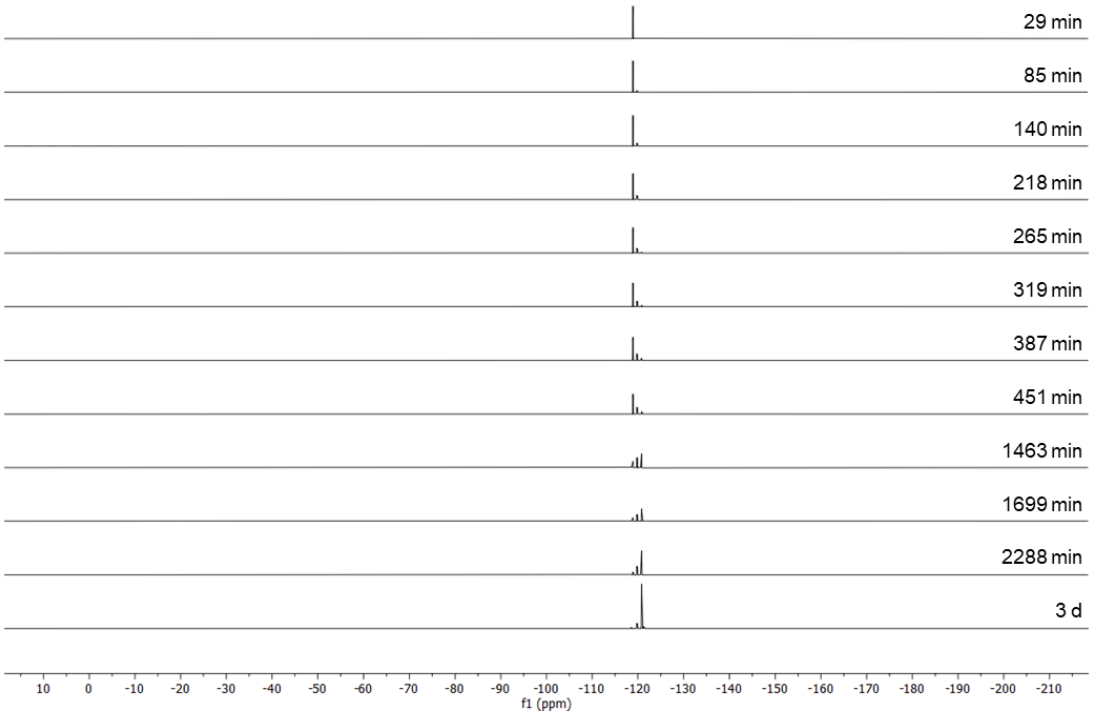

Figure S287: $^{19}F\{^{1}H\}$ NMR spectra of the formation of **AC²** in the dark (CD_2Cl_2, 282 MHz).

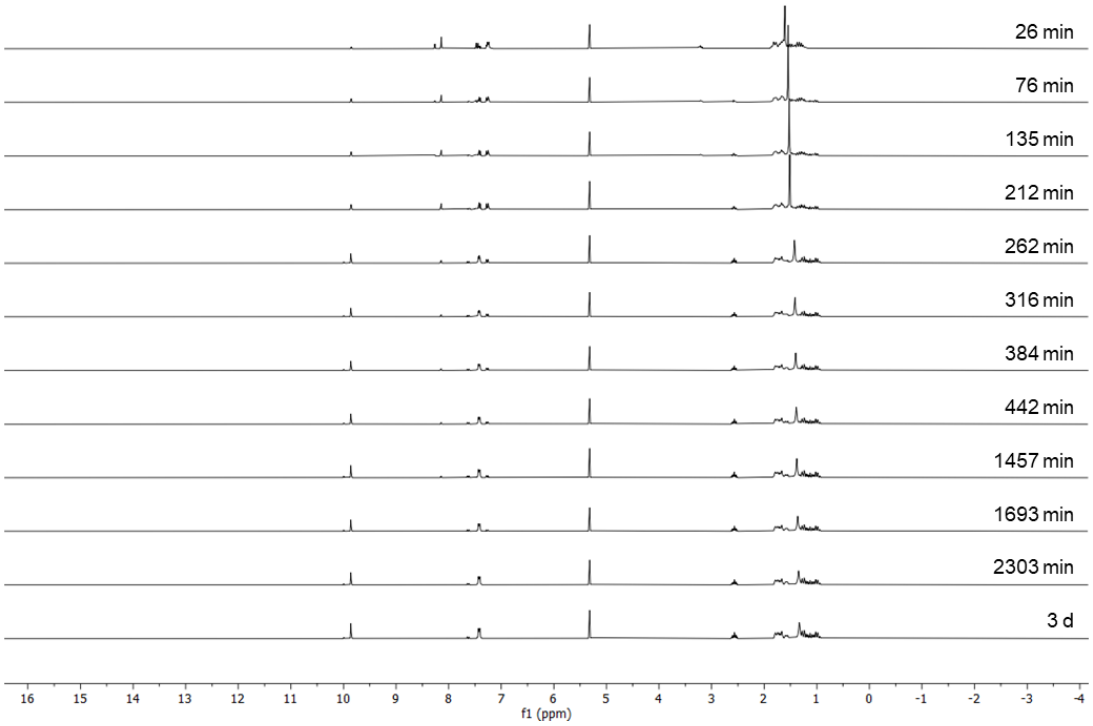

Figure S288: ^{1}H NMR spectra of the formation of **AC²** after initial irradiation of the azobenzene compound with red light (660 nm) (CD_2Cl_2, 300 MHz).

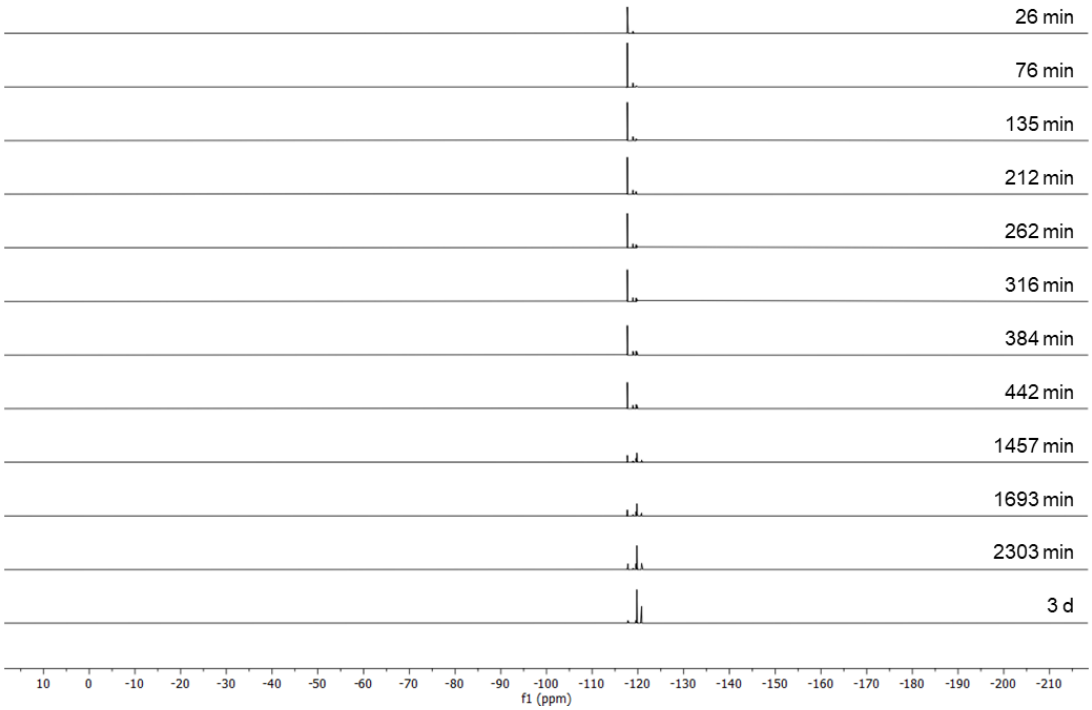

Figure S289: $^{19}F\{^{1}H\}$ NMR spectra of the formation of **AC²** after initial irradiation of the azobenzene compound with red light (660 nm) (CD_2Cl_2, 282 MHz).

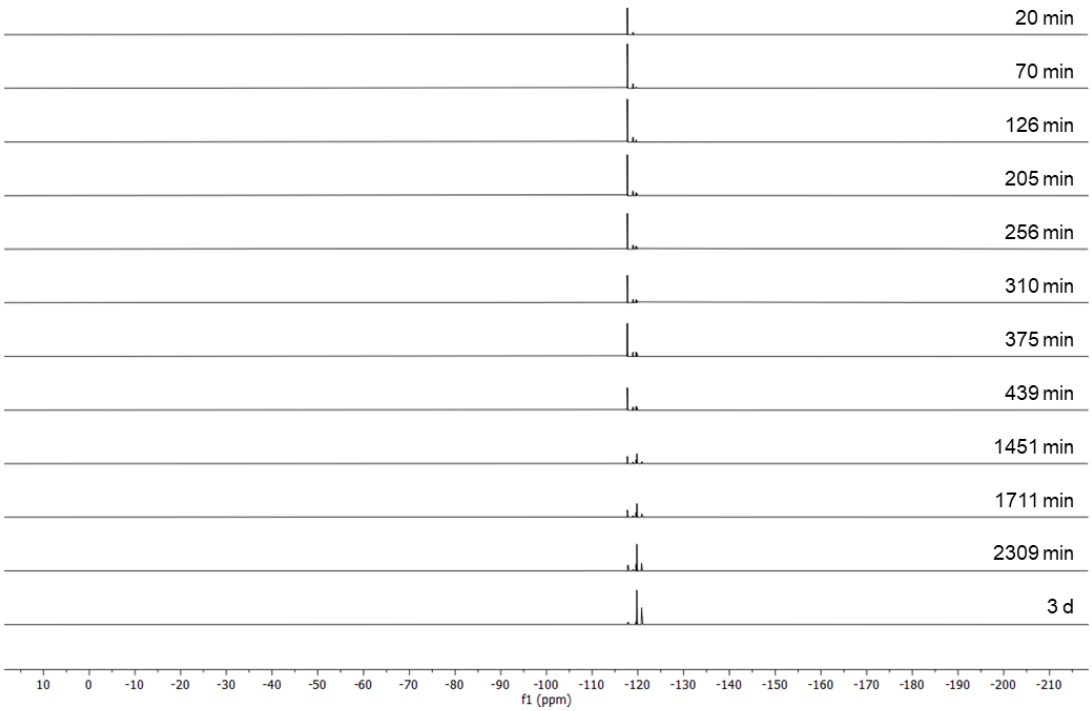

Figure S290: ^{1}H NMR spectra of the formation of **AC²** after initial irradiation of the azobenzene compound with red light (660 nm) (CD_2Cl_2, 300 MHz).

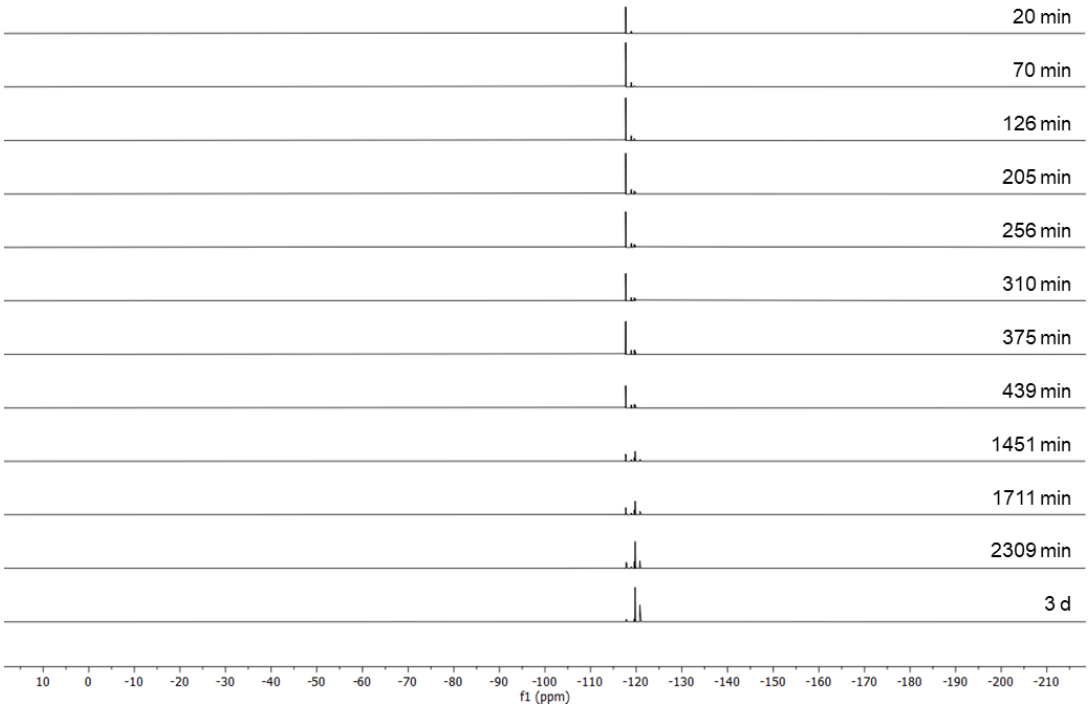

Figure S291: $^{19}F\{^{1}H\}$ NMR spectra of the formation of **AC²** after initial irradiation of the azobenzene compound with red light (660 nm) (CD_2Cl_2, 282 MHz).

6.5 Spectra for 4.3.2

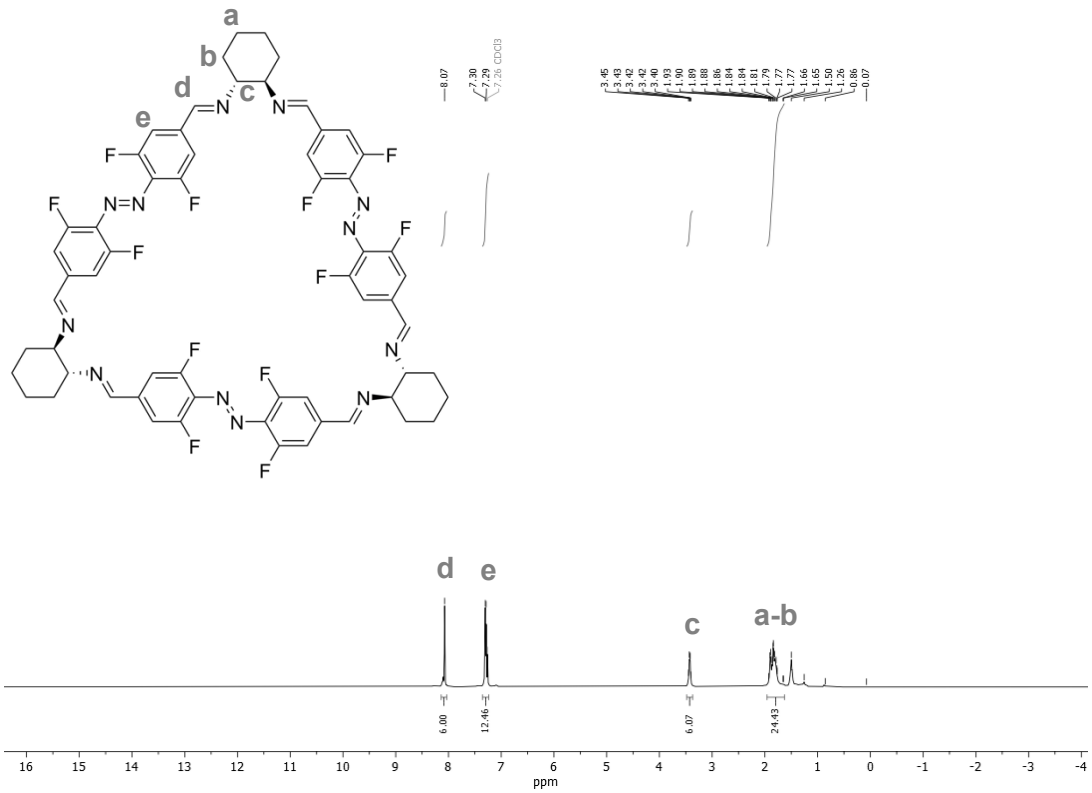

Figure S292: ^{1}H NMR spectrum of *E,E,E*-**A^{3}D^{3}** ($CDCl_3$, 600 MHz).

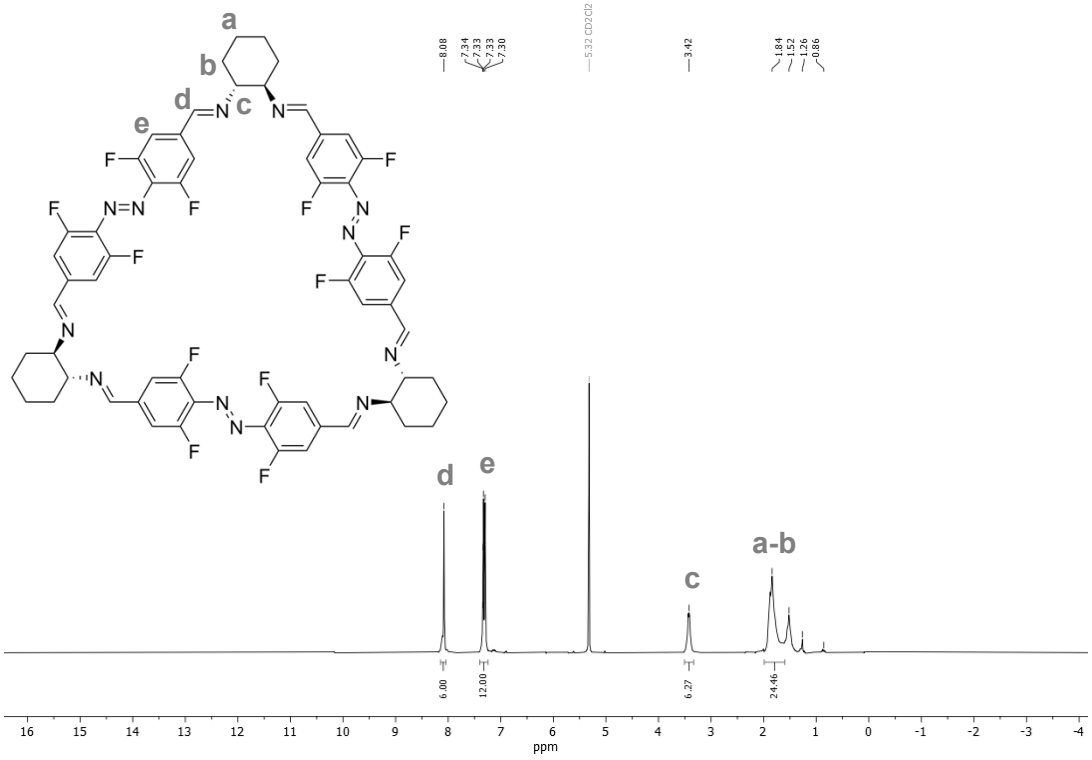

Figure S293: ^{1}H NMR spectrum of *E,E,E*-**A^{3}D^{3}** (CD_2Cl_2, 300 MHz).

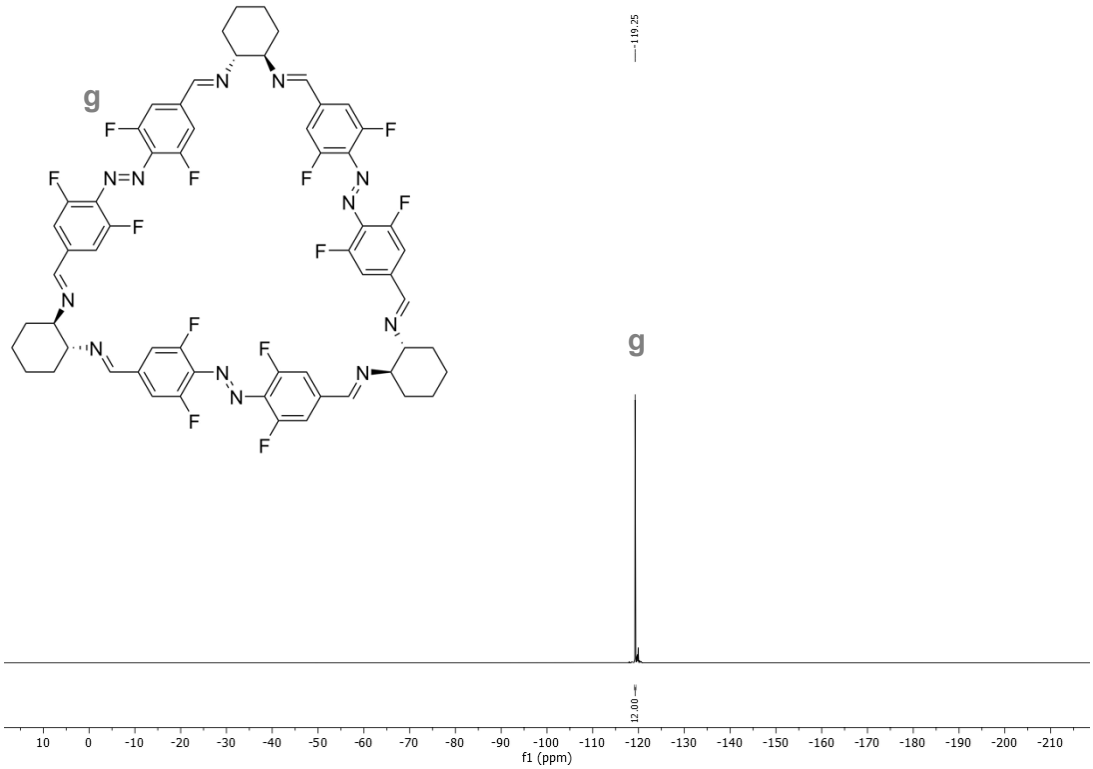

Figure S294: $^{19}F\{^{1}H\}$ NMR spectrum of *E*,*E*,*E*-**A^{3}D^3** ($CDCl_3$, 565 MHz).

Figure S295: $^{19}F\{^{1}H\}$ NMR spectrum of *E*,*E*,*E*-**A^{3}D^3** (CD_2Cl_2, 282 MHz).

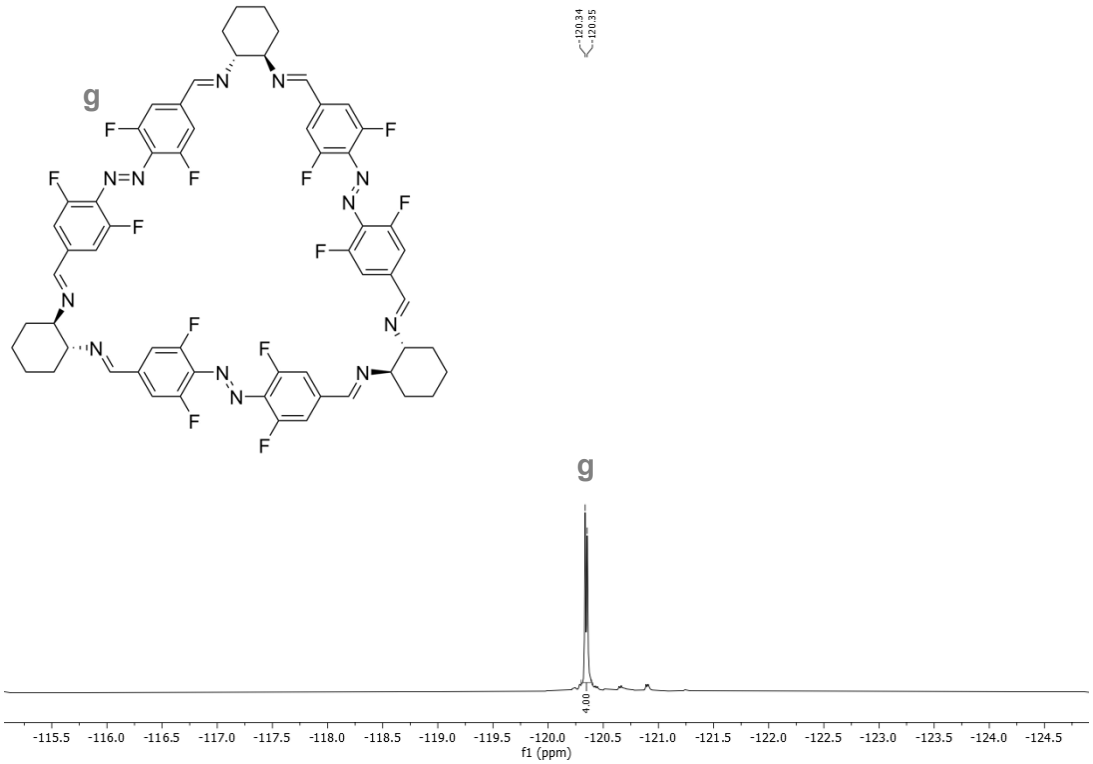

Figure S296: ^{19}F NMR spectrum of *E*,*E*,*E*-**A^{3}D^3** (CD_2Cl_2, 564 MHz).

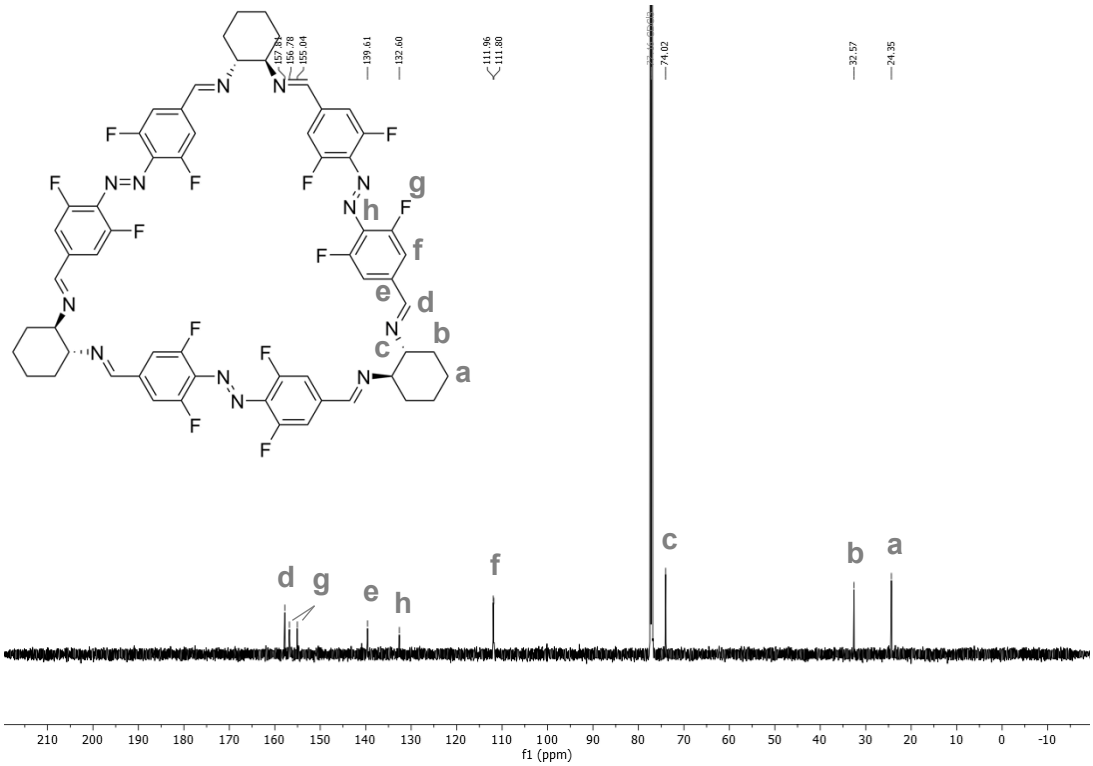

Figure S297: $^{13}C\{^1H\}$ NMR spectrum of *E*,*E*,*E*-**A^{3}D^3** ($CDCl_3$, 151 MHz).

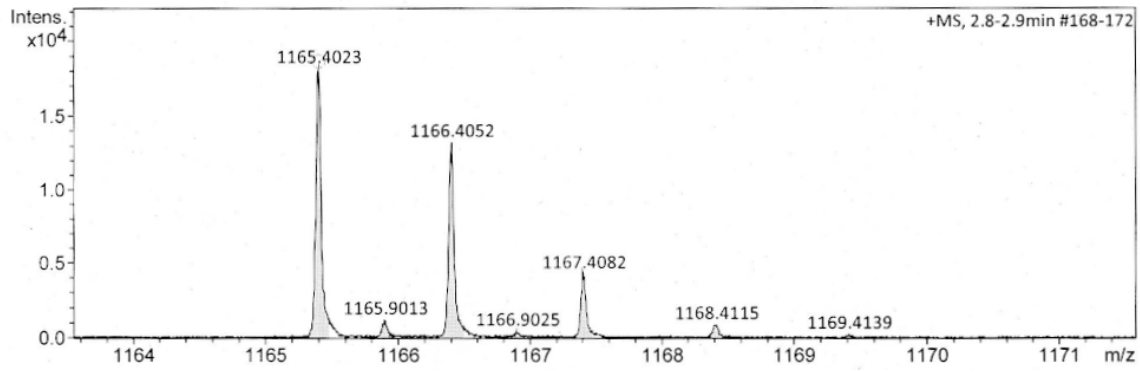

Figure S298: ESI-HR-mass spectrum of *E,E,E*-**A^{3}D^3**.

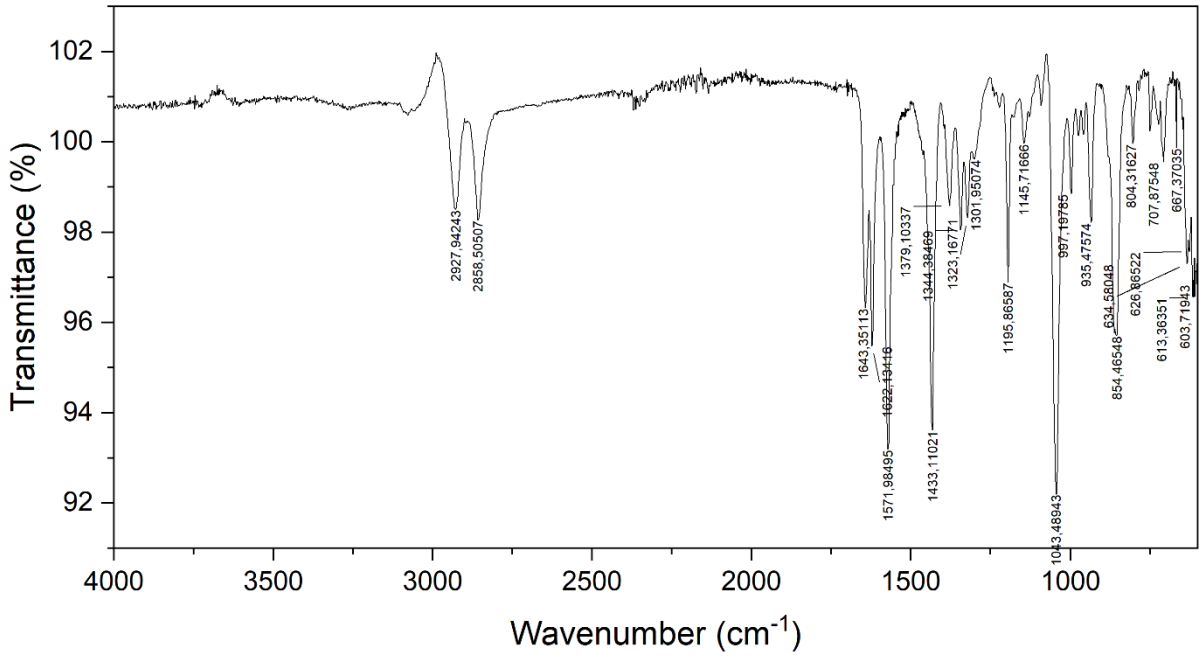

Figure S299: IR spectrum of *E,E,E*-**A^{3}D^3**.

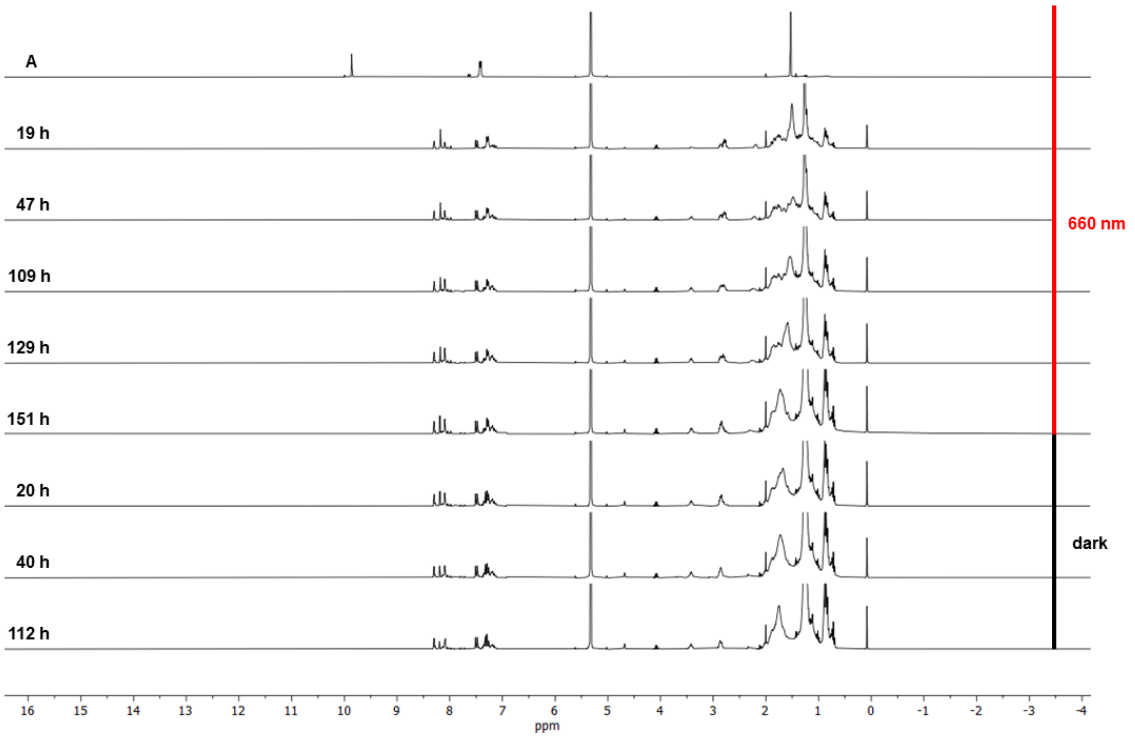

Figure S300: ^{1}H NMR spectra of the macrocycle formation of a *Z*-enriched solution of **A** and diamine **D** under continuous irradiation with red light (660 nm) and in the dark (CD_2Cl_2, 300 MHz).

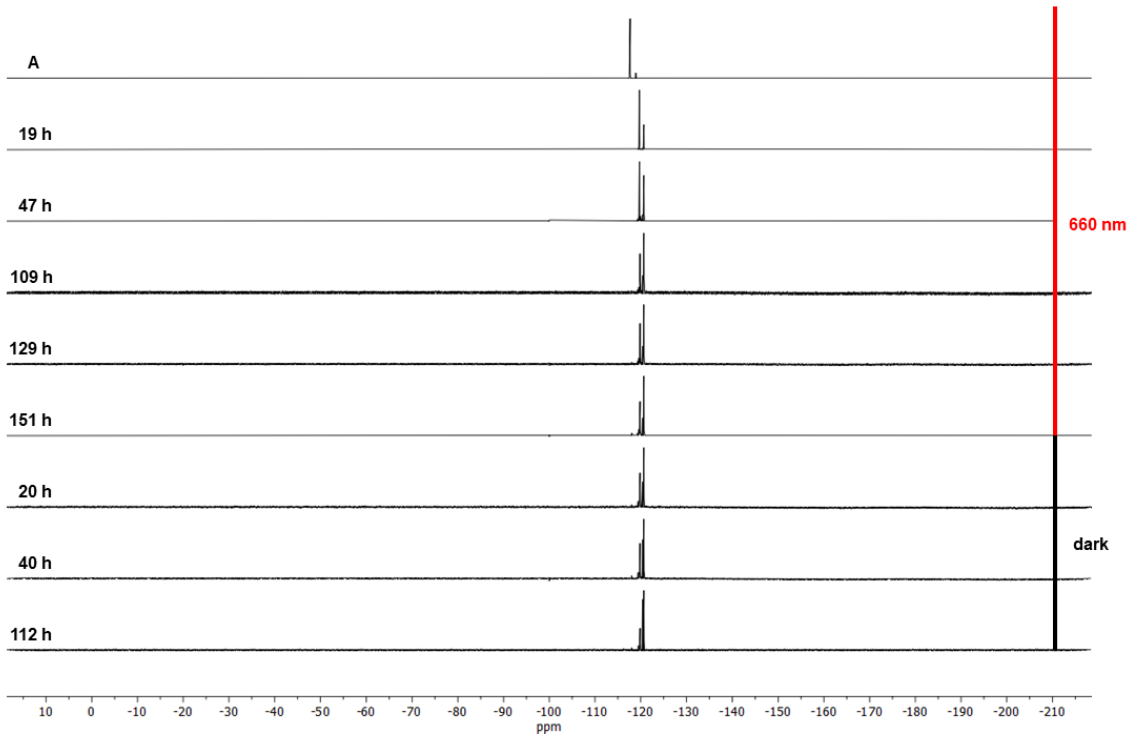

Figure S301: ^{19}F{^{1}H} NMR spectra of the macrocycle formation of a *Z*-enriched solution of **A** and diamine **D** under continuous irradiation with red light (660 nm) and in the dark (CD_2Cl_2, 282 MHz).

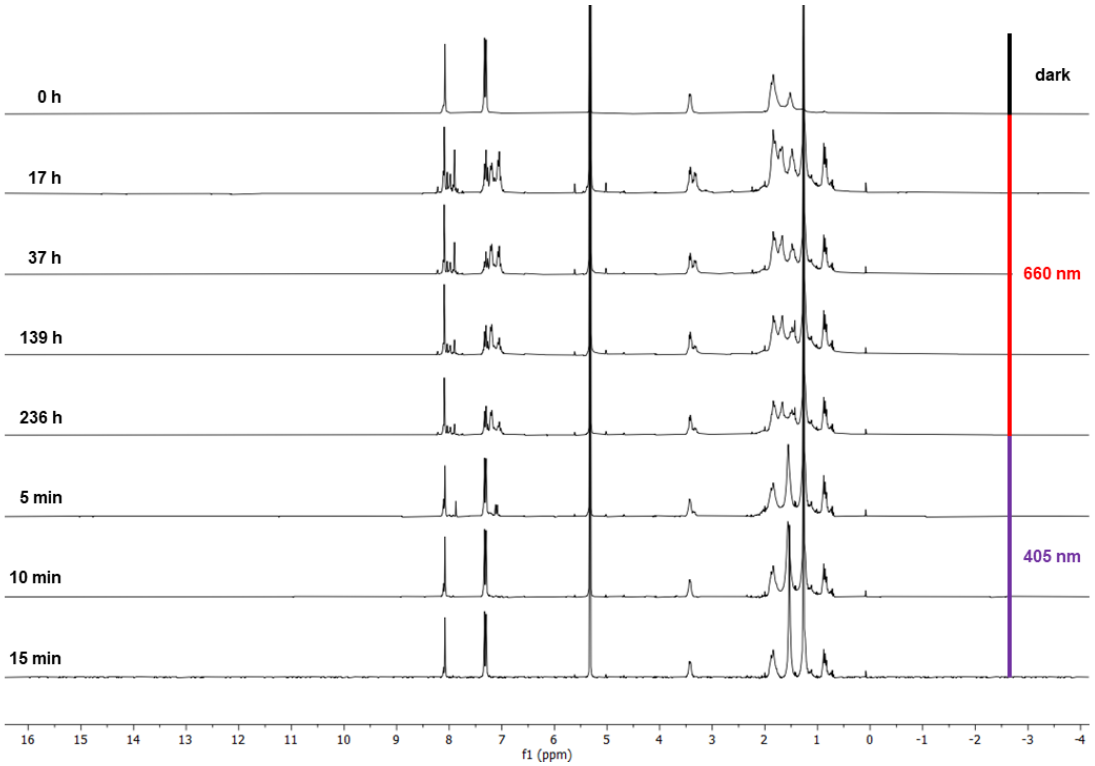

Figure S302: ^{1}H NMR spectra of the **A^{3}D^{3}** under continuous irradiation with red light (660 nm) followed by irradiation with light of a wavelength of 405 nm (CD_2Cl_2, 300 MHz).

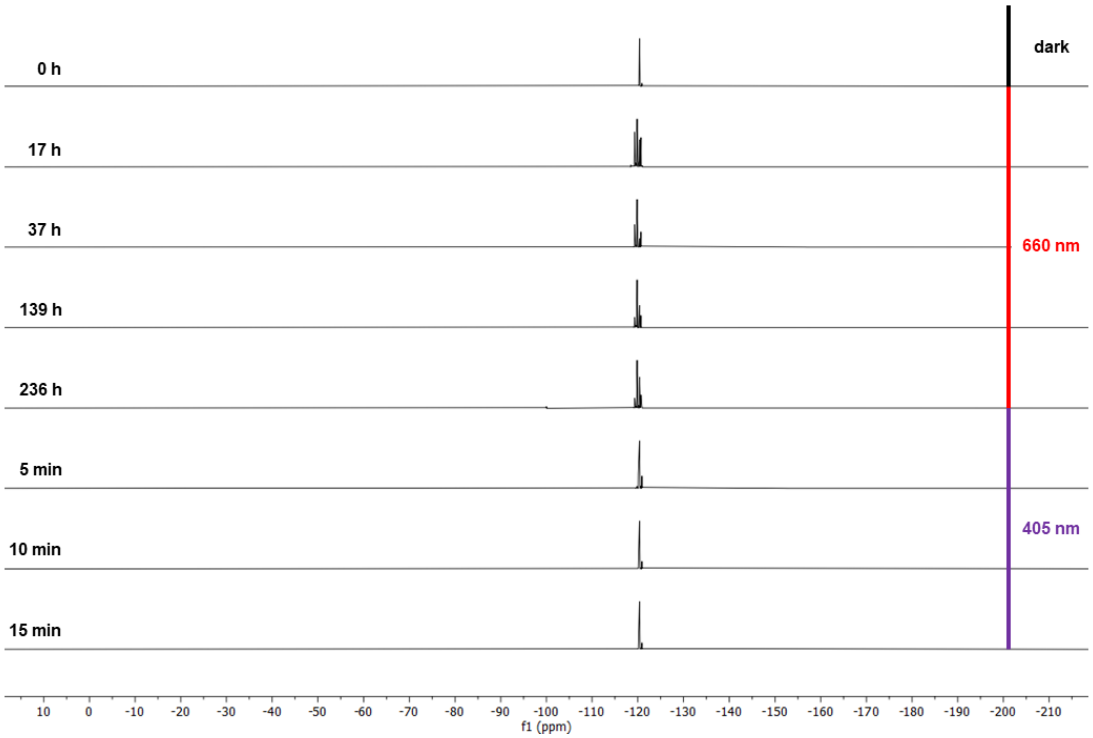

Figure S303: ^{19}F{^{1}H} NMR spectra of the **A^{3}D^{3}** under continuous irradiation with red light (660 nm) followed by irradiation with light of a wavelength of 405 nm (CD_2Cl_2, 282 MHz).

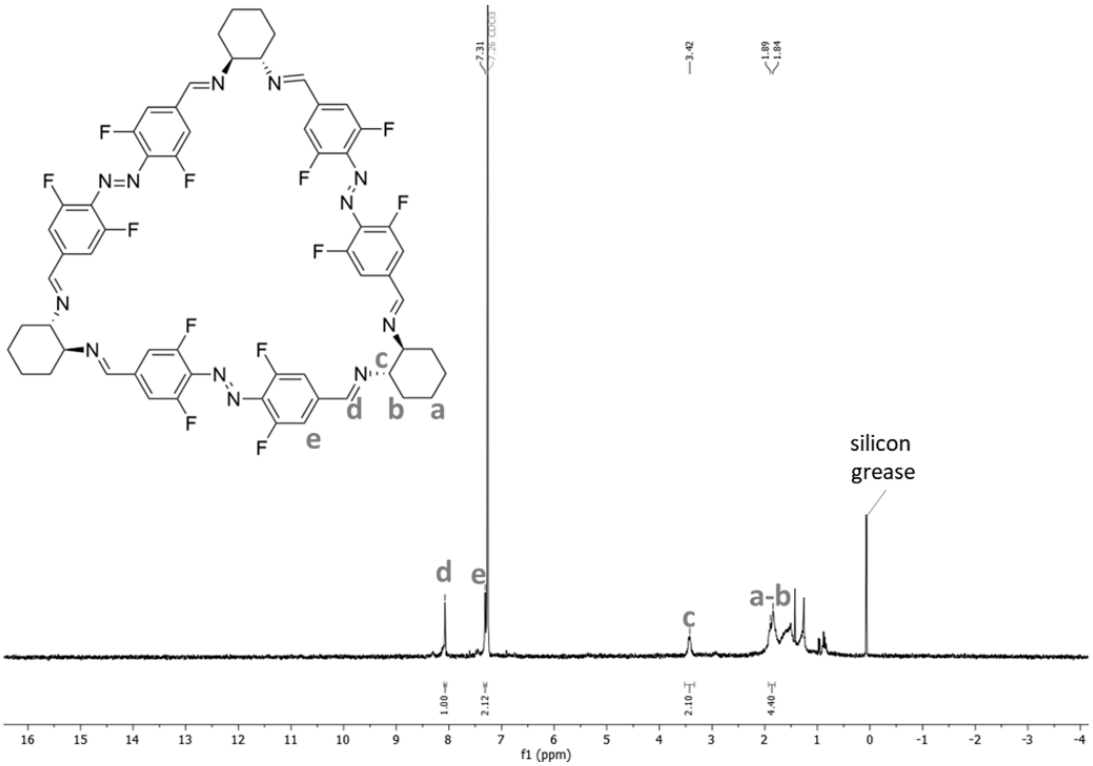

Figure S304: ^{1}H NMR spectrum of *E*,*E*,*E*-**A^{3}D^{3}*ss*** ($CDCl_3$, 300 MHz).

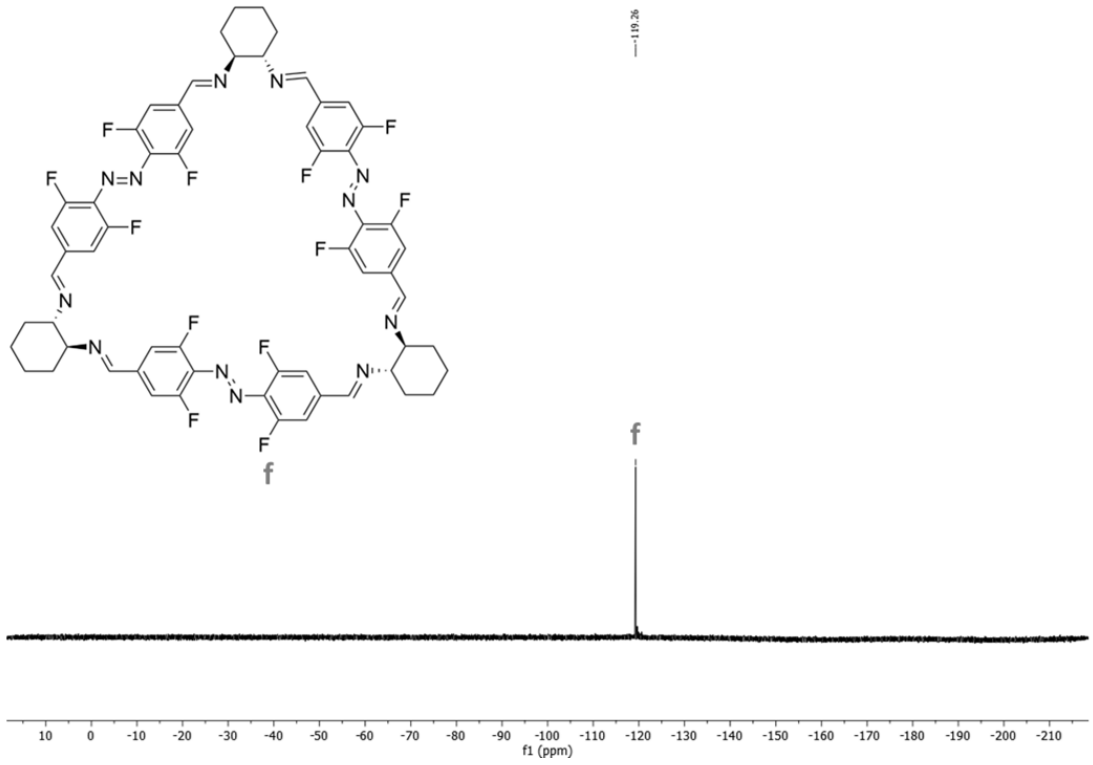

Figure S305: ^{19}F{^{1}H} NMR spectrum of *E*,*E*,*E*-**A^{3}D^{3}*ss*** ($CDCl_3$, 300 MHz).

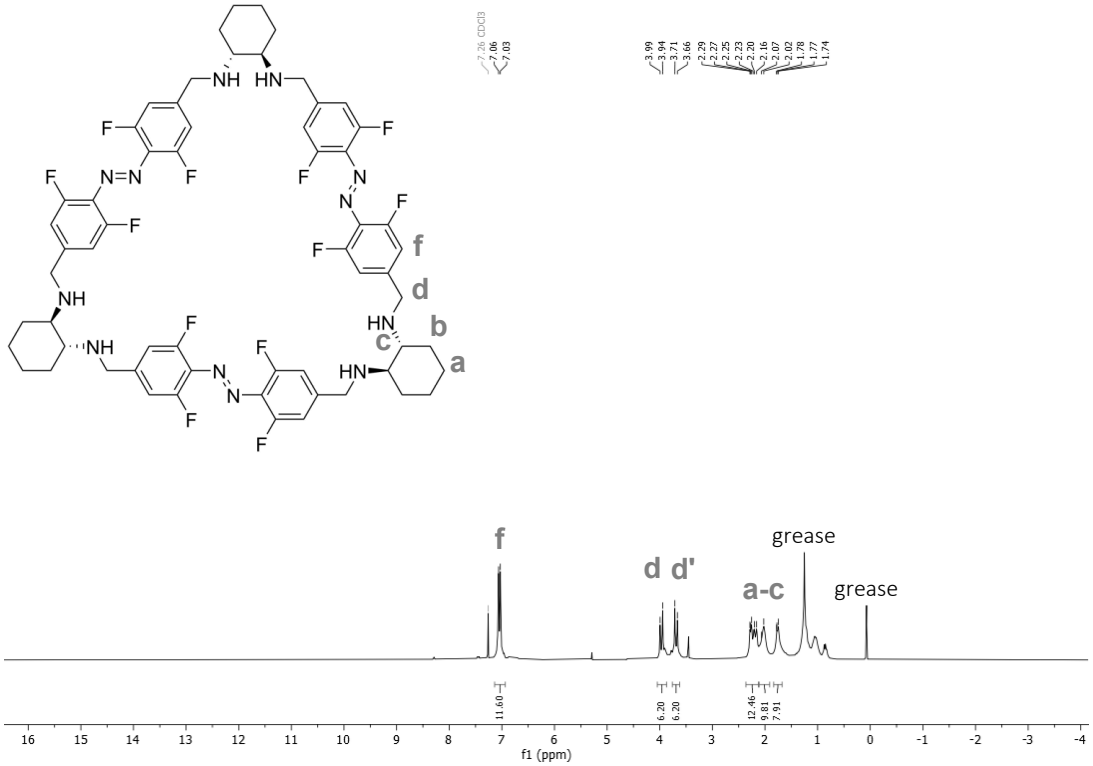

Figure S306: ^{1}H NMR spectrum of *E*,*E*,*E*-**A^{3}D^{3}$_{red}$** ($CDCl_3$, 300 MHz).

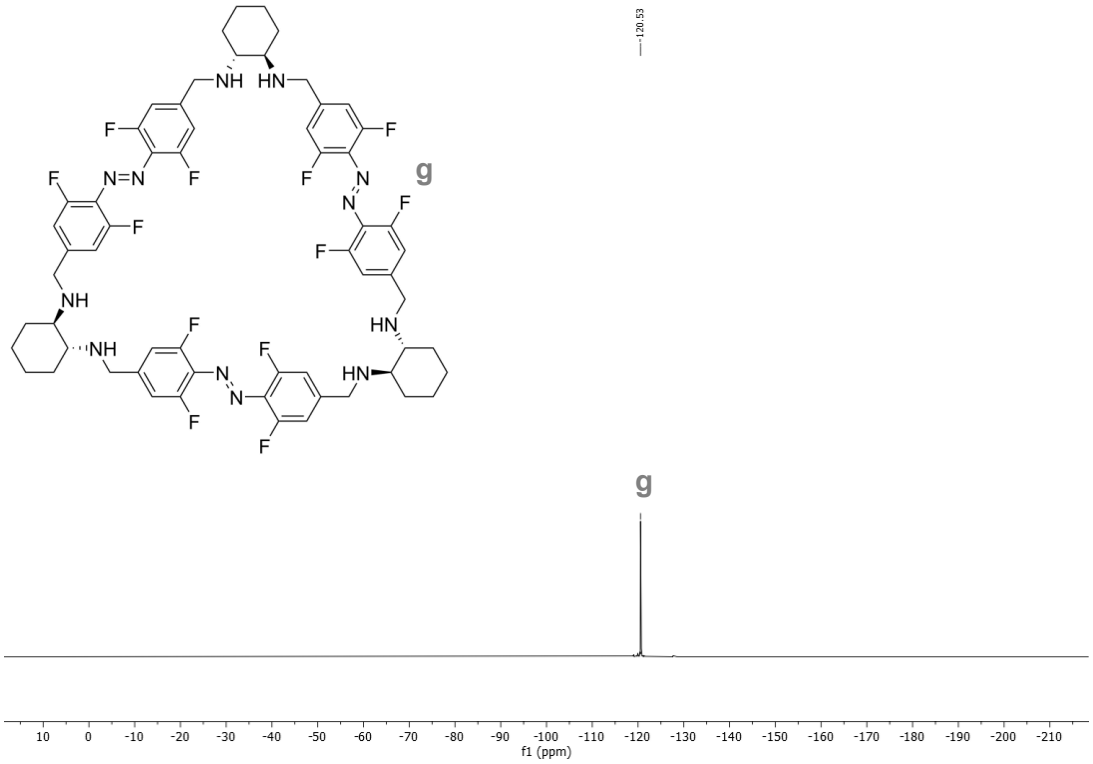

Figure S307: ^{19}F{^{1}H} NMR spectrum of *E*,*E*,*E*-**A^{3}D^{3}$_{red}$** ($CDCl_3$, 282 MHz).

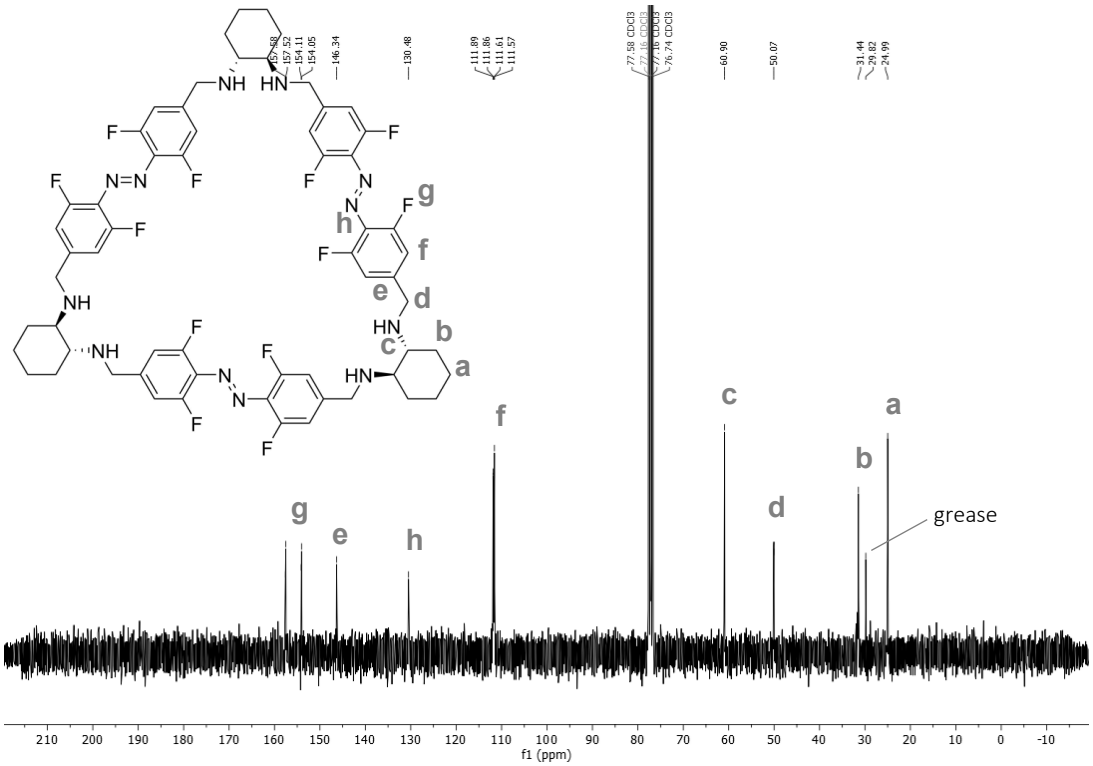

Figure S308: $^{13}C\{^{1}H\}$ NMR spectrum of *E,E,E*-$\mathbf{A^3D^3_{red}}$ ($CDCl_3$, 75 MHz).

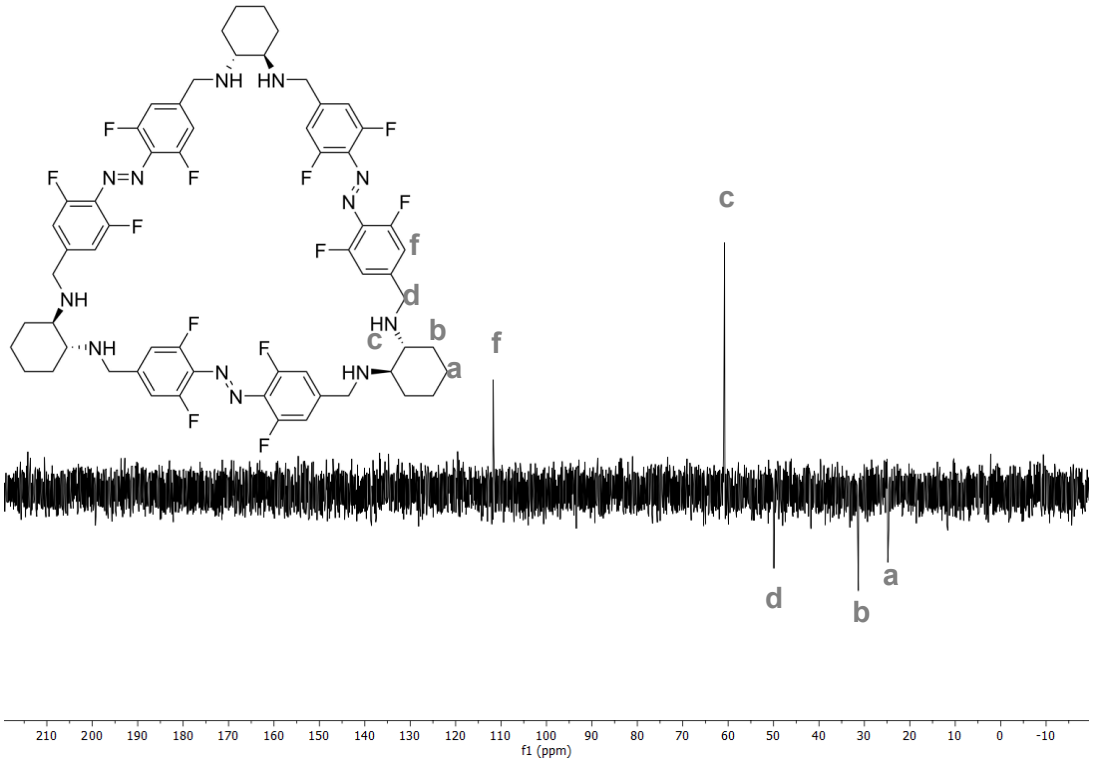

Figure S309: ^{13}C DEPT 135 NMR spectrum of *E,E,E*-$\mathbf{A^3D^3_{red}}$ ($CDCl_3$, 75 MHz).

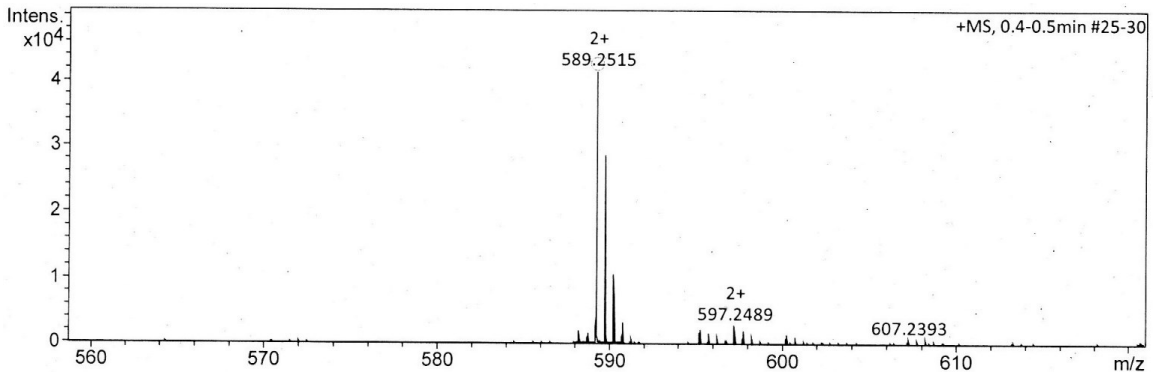

Figure S310: ESI-HR-mass spectrum of *E,E,E*-$\mathbf{A^3D^3_{red}}$.

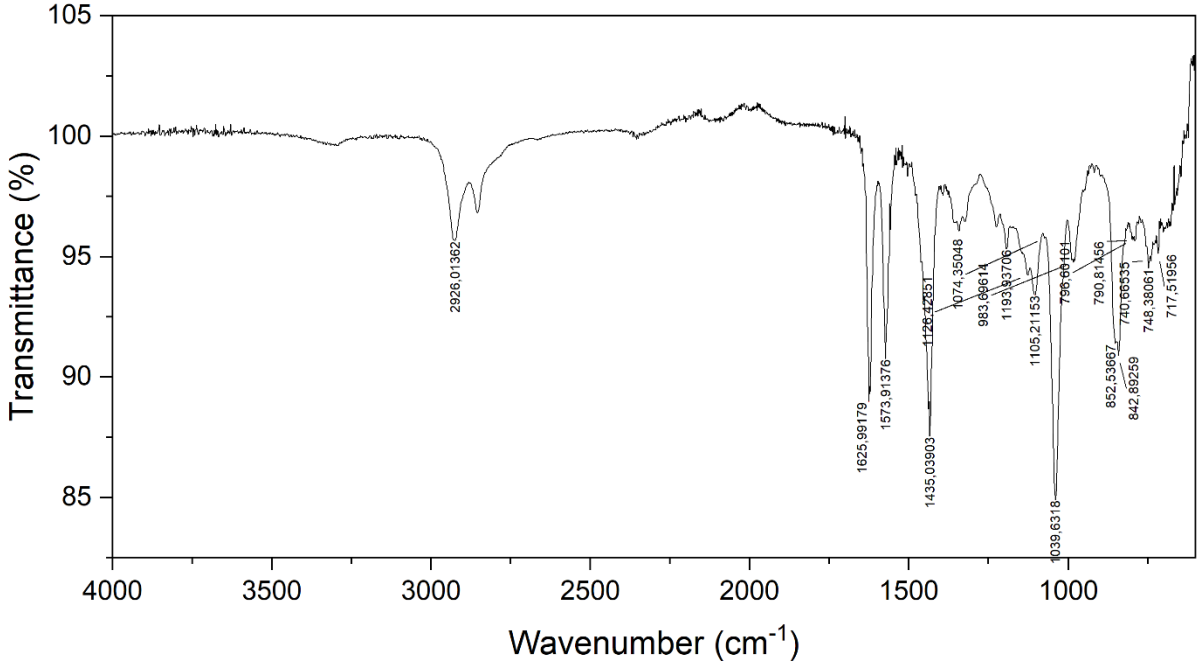

Figure S311: IR spectrum of *E,E,E*-$\mathbf{A^3D^3_{red}}$.

6.6 Spectra for 4.3.3

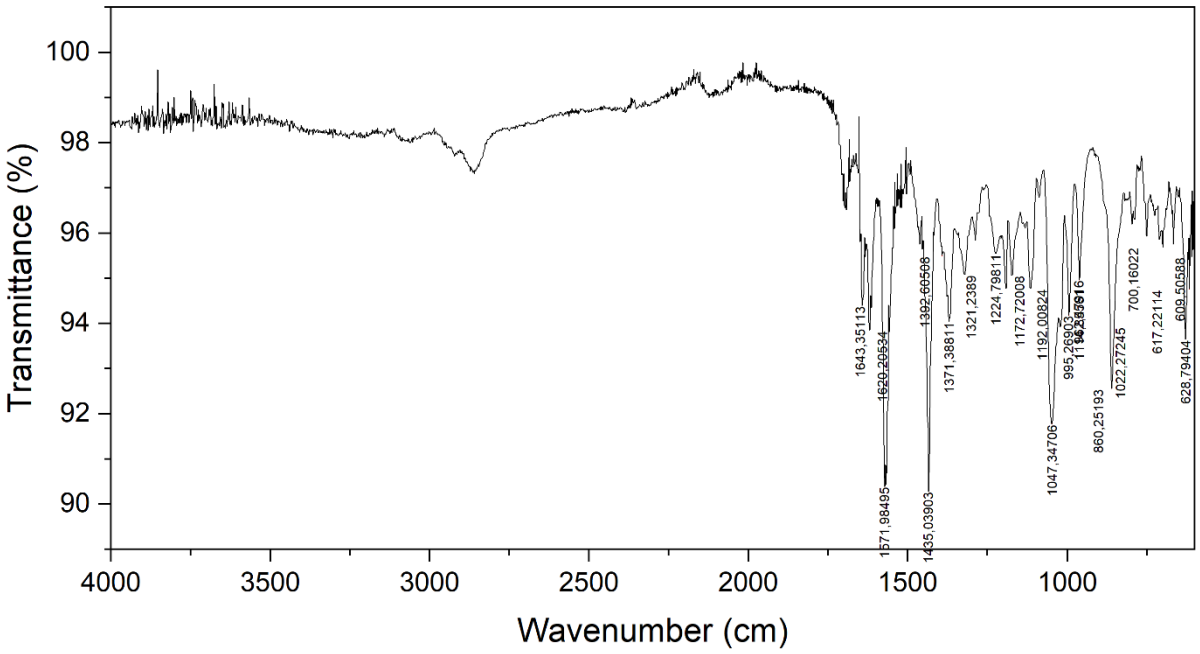

Figure S312: IR spectrum of $\mathbf{A^nD^n}$.

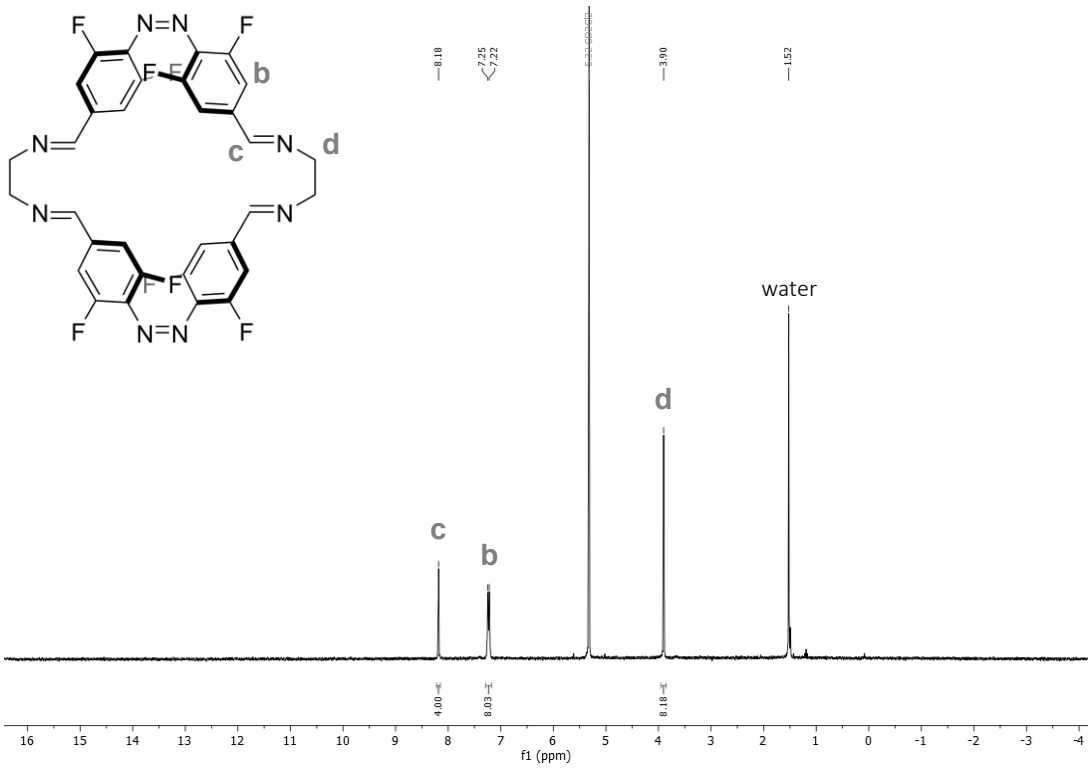

Figure S313: ^{1}H NMR spectrum of *Z*,*Z*-$\mathbf{A^2E^2}$ (CD_2Cl_2, 300 MHz).

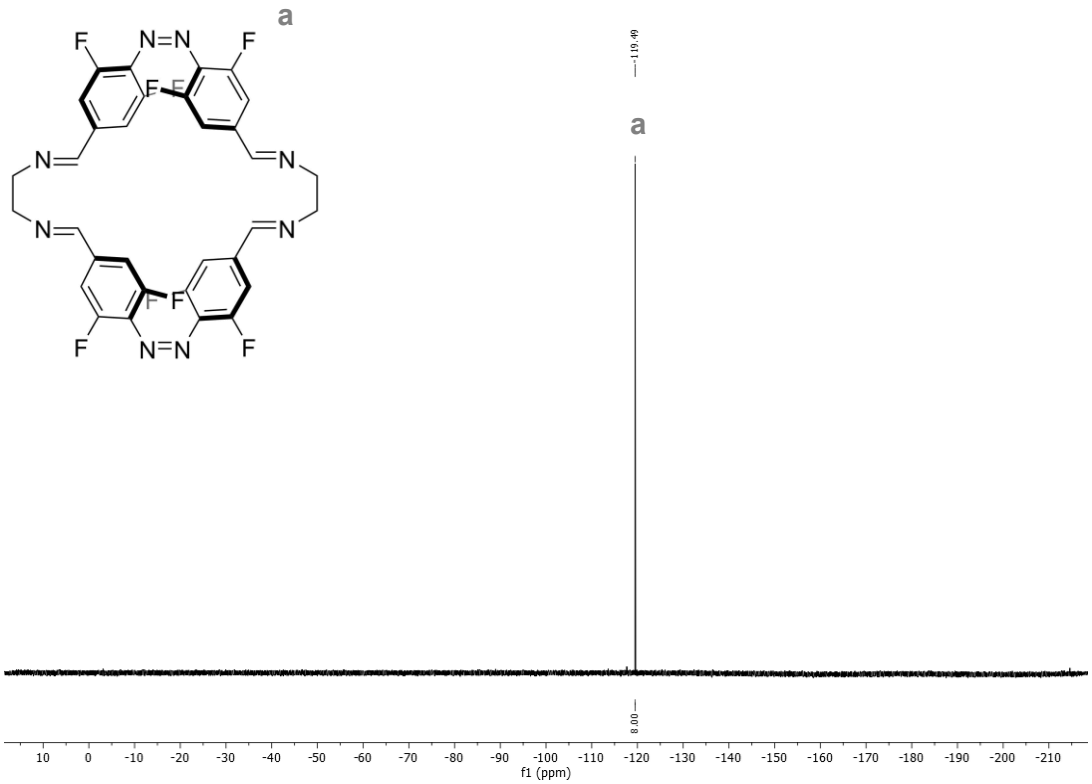

Figure S314: $^{19}F\{^{1}H\}$ NMR spectrum of *Z*,*Z*-**A²E²** (CD_2Cl_2, 282 MHz).

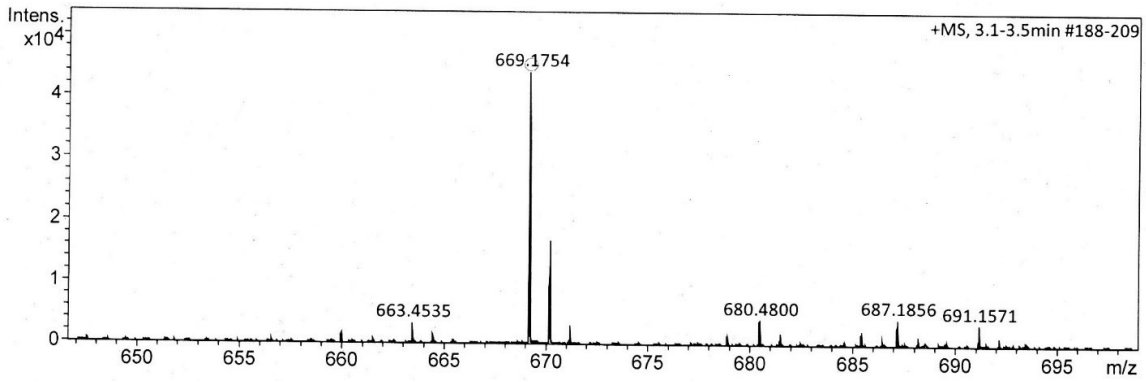

Figure S315: ESI-HR-mass spectrum of *Z*,*Z*-**A²E²**.

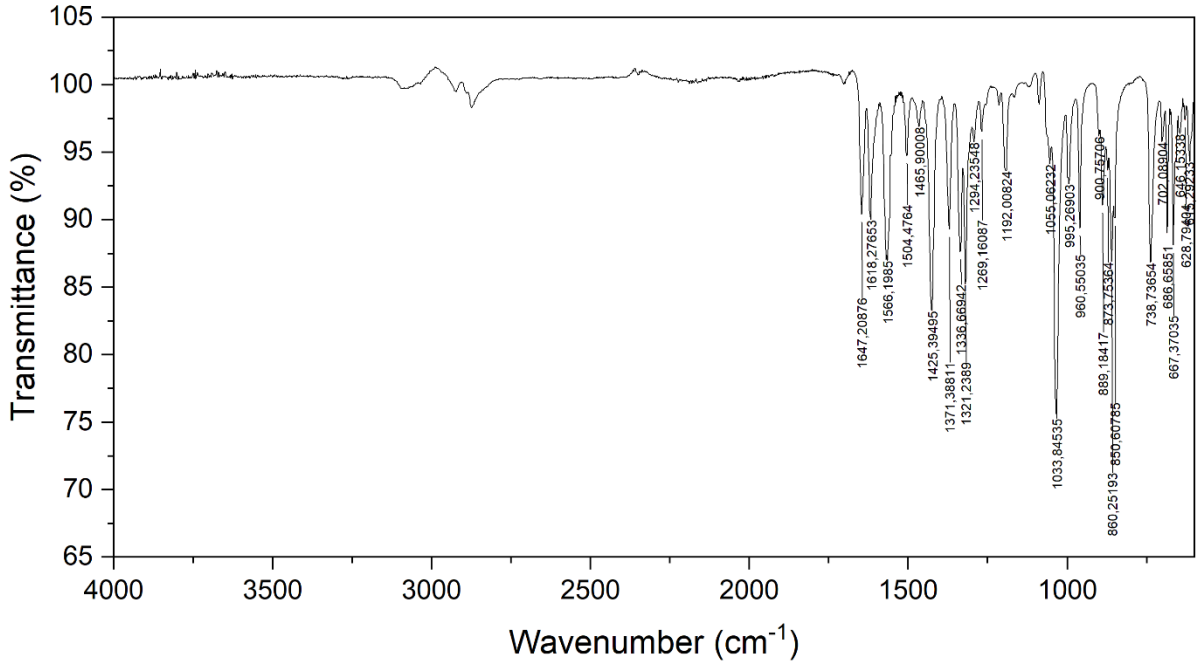

Figure S316: IR spectrum of *Z*,*Z*-**A²E²**.

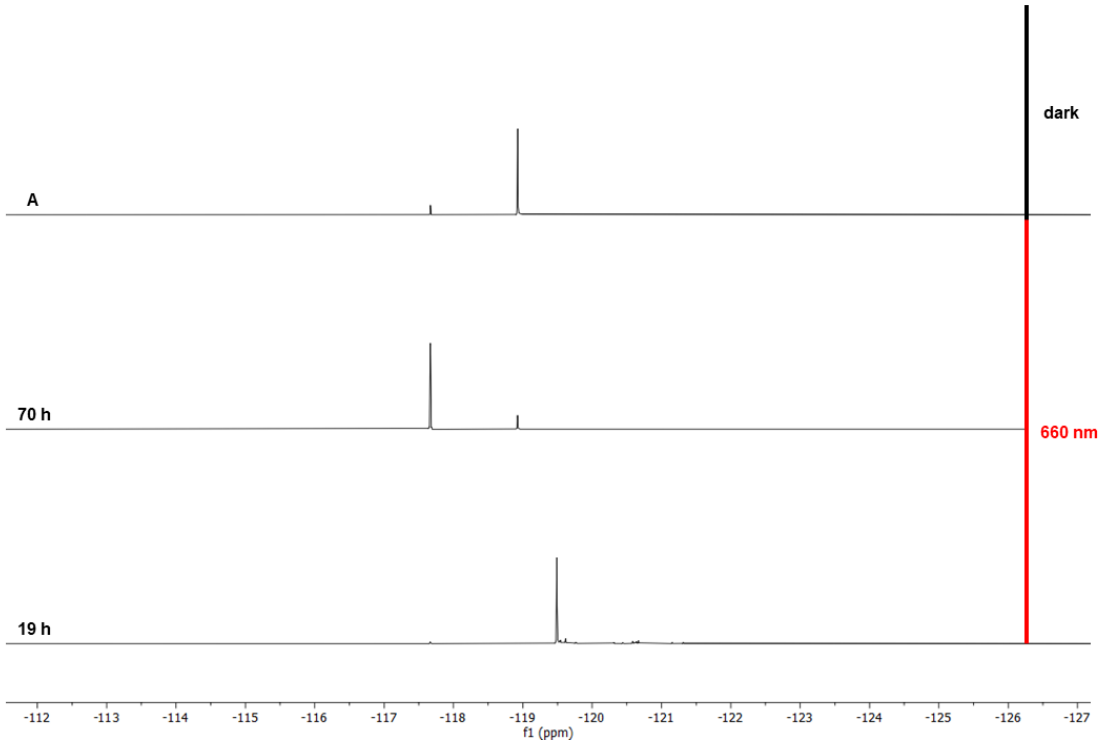

Figure S317: ^{1}H NMR spectra of the **A** in the dark, after irradiation with red light (660 nm) and after the addition of **E** and continuous irradiation with red light (660 nm).

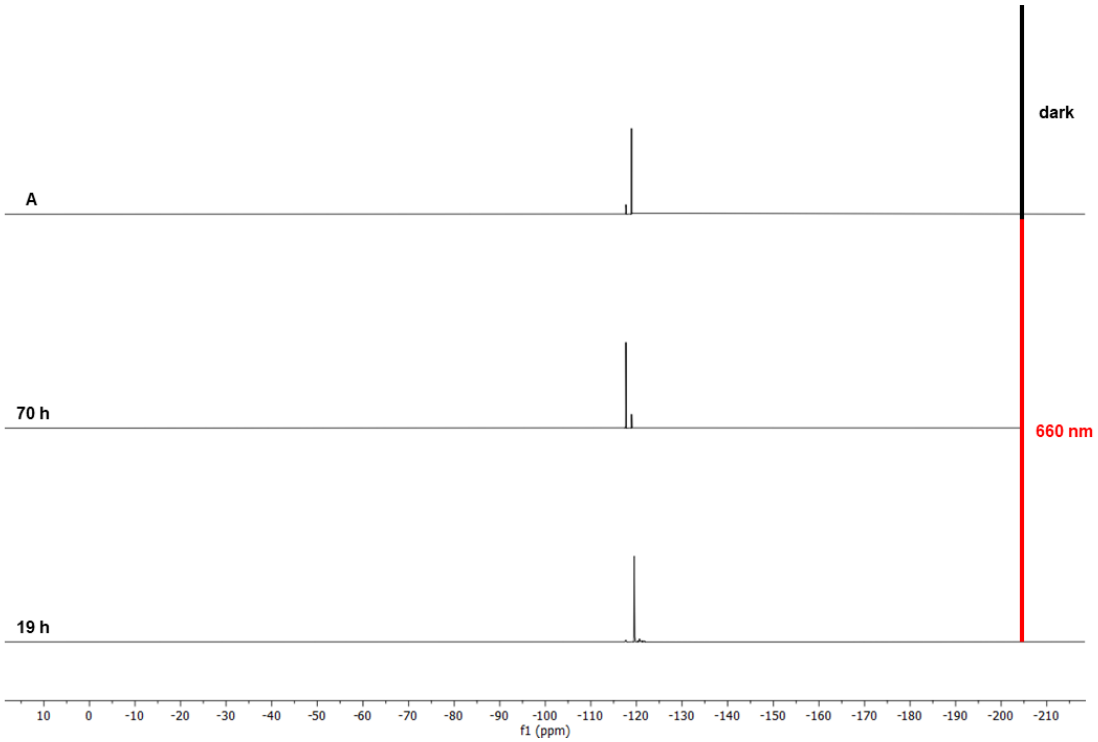

Figure S318: $^{19}F\{^{1}H\}$ NMR spectra of the **A** in the dark, after irradiation with red light (660 nm) and after the addition of **E** and continuous irradiation with red light (660 nm).

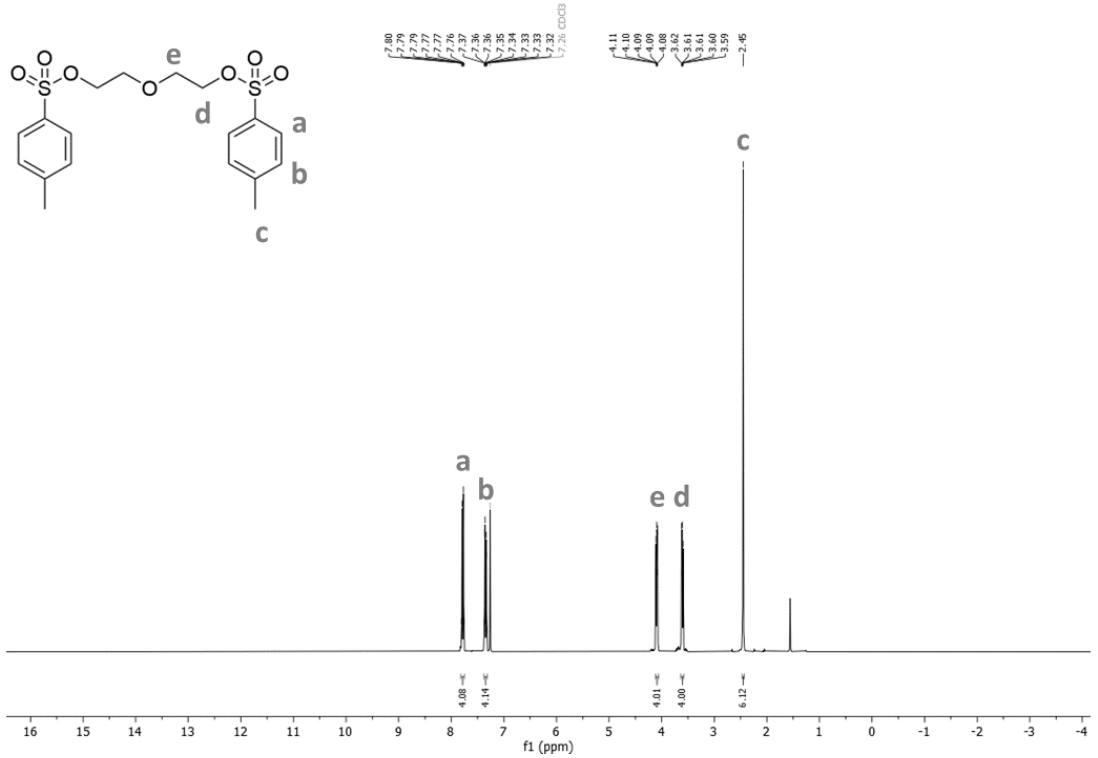

Figure S319: ^{1}H NMR spectrum of **43** ($CDCl_3$, 300 MHz).

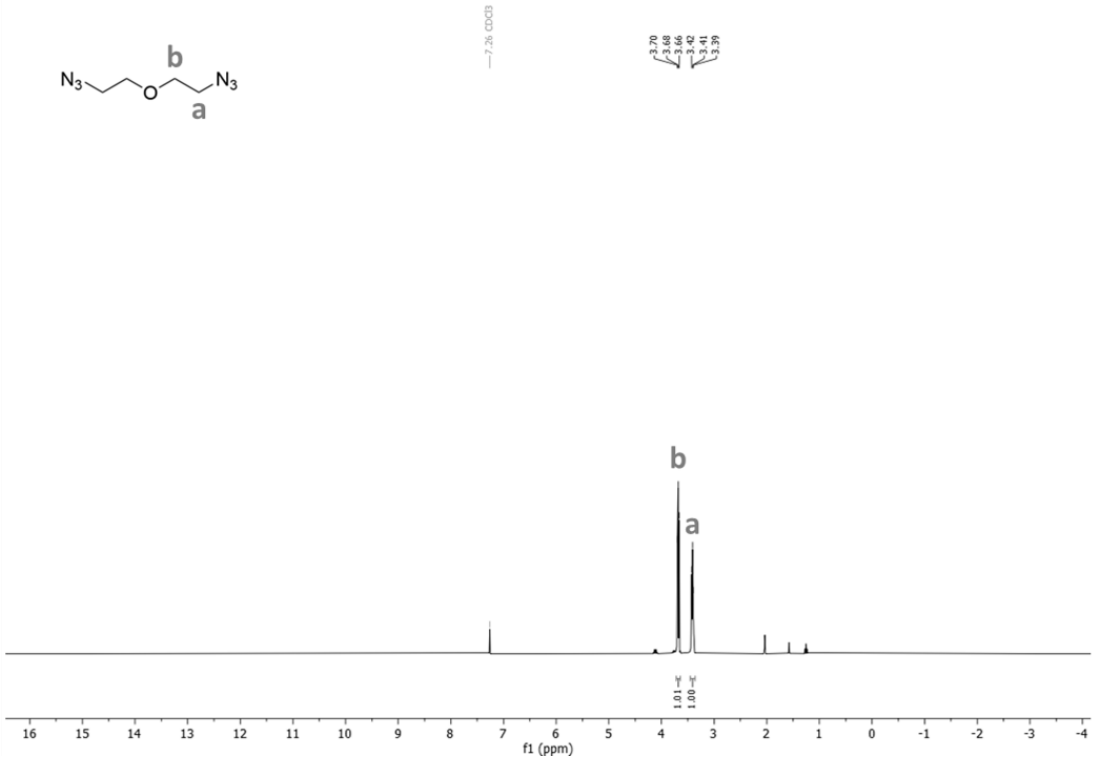

Figure S320: ^{1}H NMR spectrum of **44** ($CDCl_3$, 300 MHz).

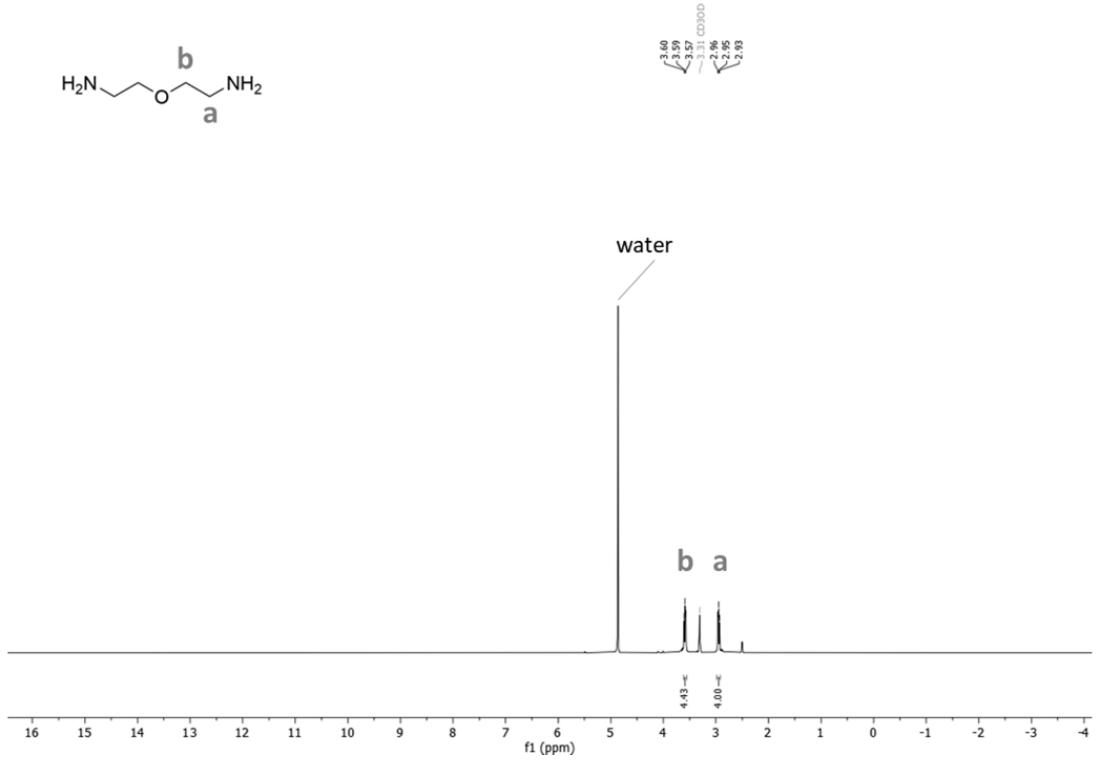

Figure S321: ^{1}H NMR spectrum of **O** ($CDCl_3$, 300 MHz).

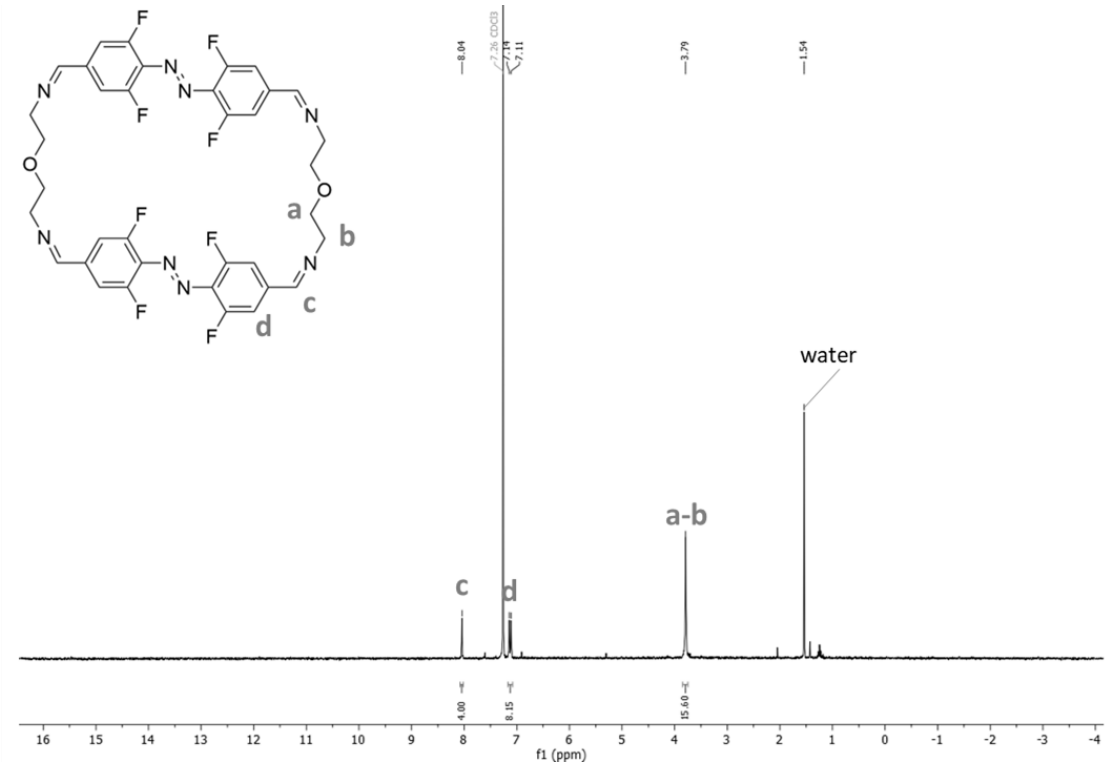

Figure S322: ^{1}H NMR spectrum of *E,E*-**A^{2}O^{2}** ($CDCl_3$, 300 MHz).

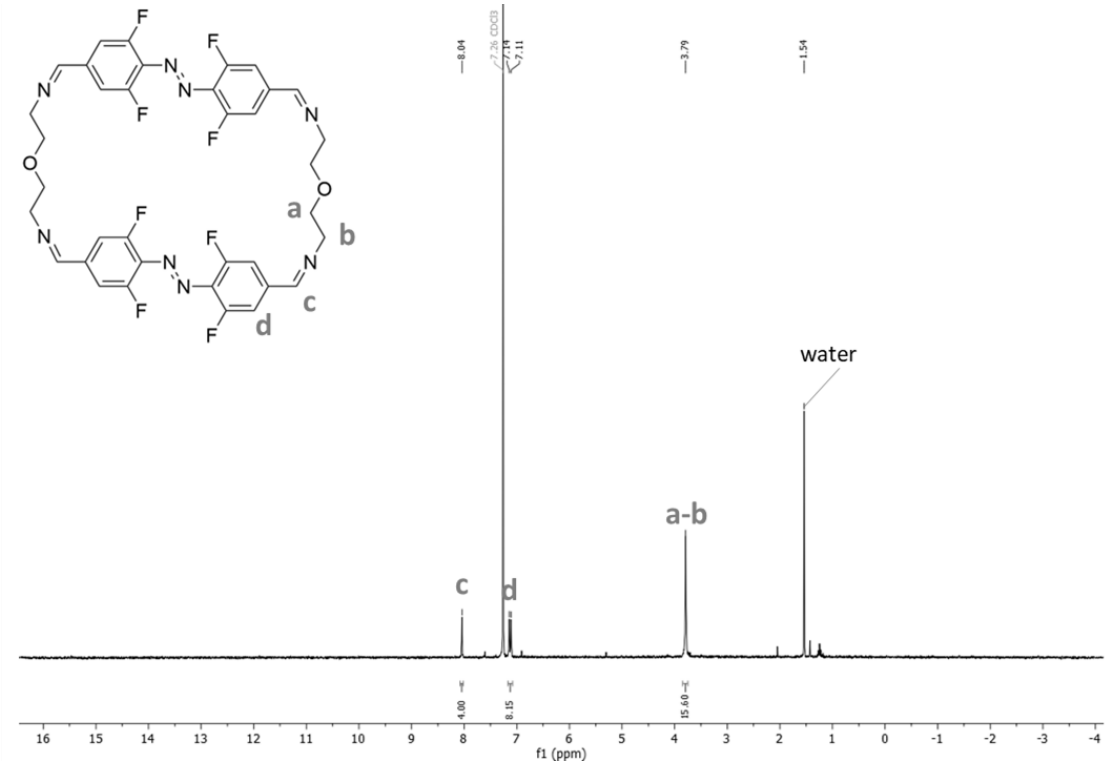

Figure S323: ^{19}F{^{1}H} NMR spectrum of *E,E*-**A^{2}O^{2}** ($CDCl_3$, 282 MHz).

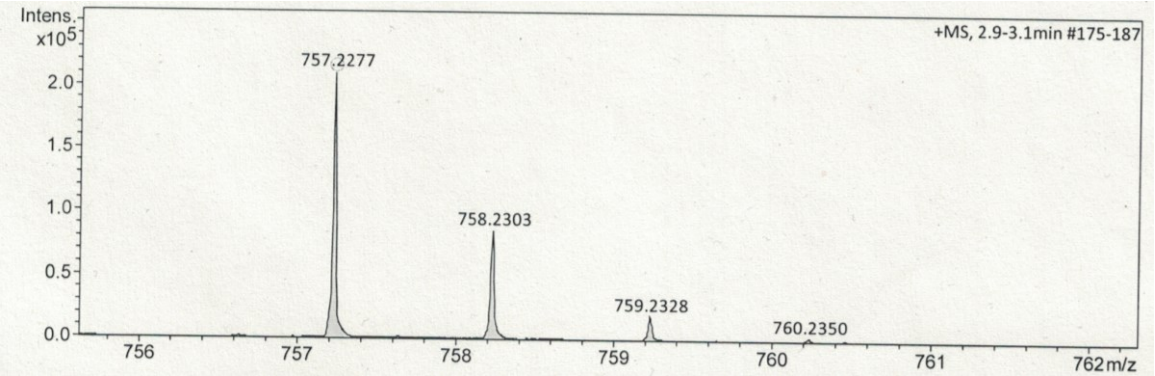

Figure S324: ESI-HR-mass spectrum of *E,E*-**A²O²**.

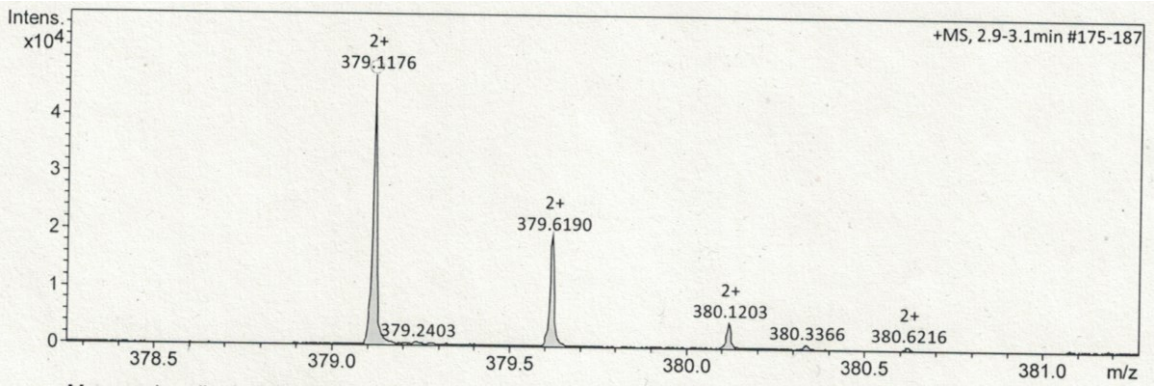

Figure S325: ESI-HR-mass spectrum of *E,E*-**A²O²**.

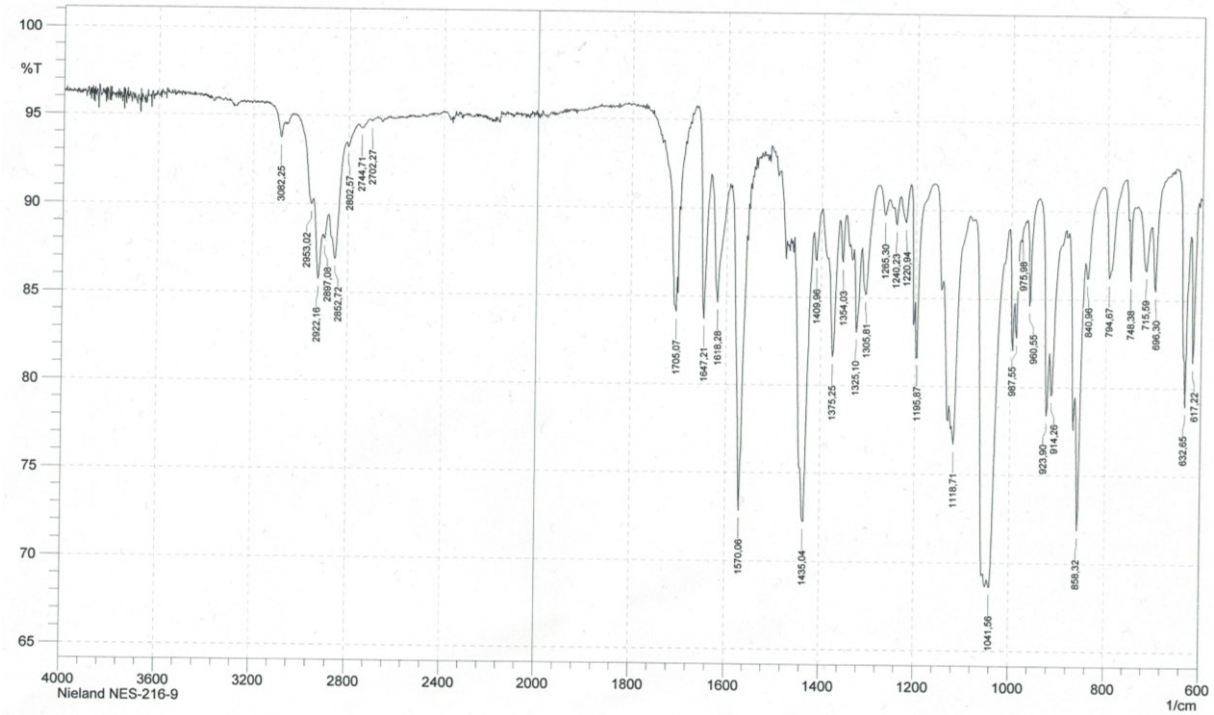

Figure S326: IR spectrum of *E,E*-**A²O²**.

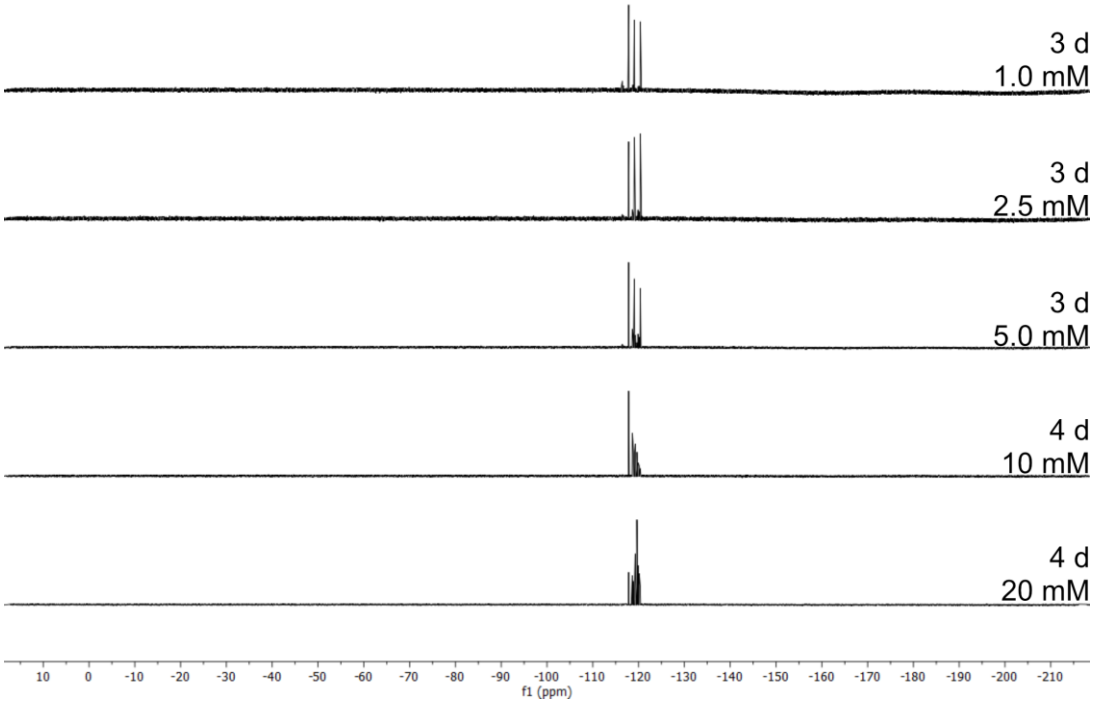

Figure S327: Comparison of $^{19}F\{^{1}H\}$ NMR spectra ($CDCl_3$, 282 MHz) of *E*-**A** and **Pr** at different concentrations after stirring in the dark.

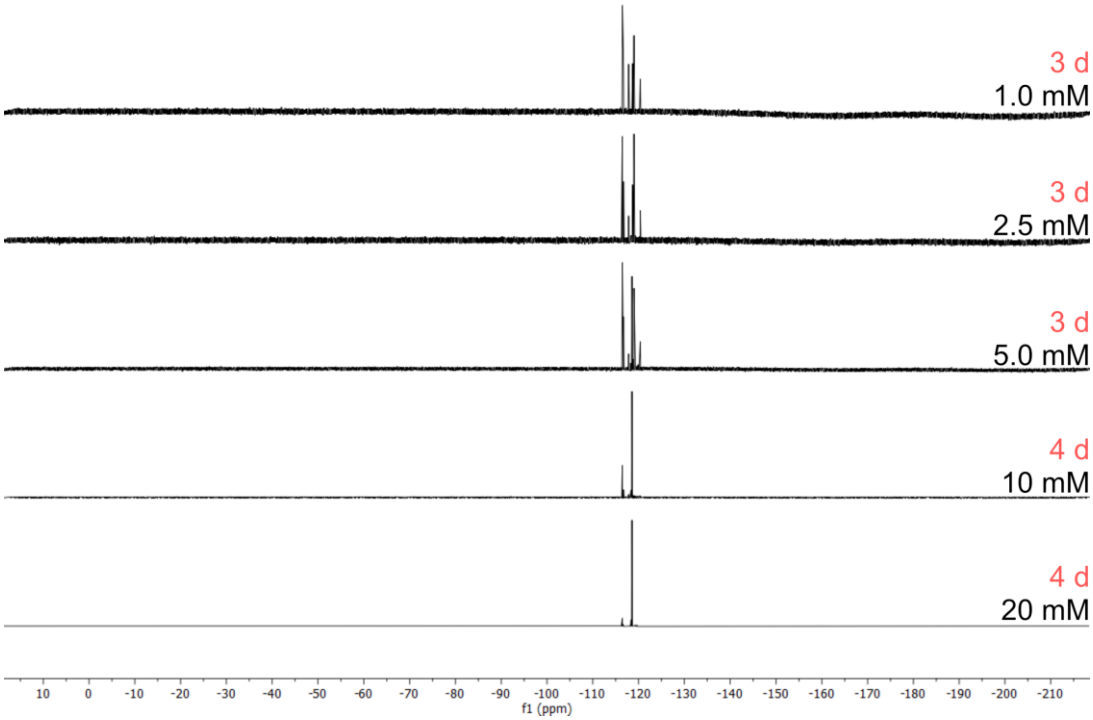

Figure S328: Comparison of $^{19}F\{^{1}H\}$ NMR spectra ($CDCl_3$, 282 MHz) of *E*-**A** and **Pr** at different concentrations after stirring under irradiation with red light (660 nm).

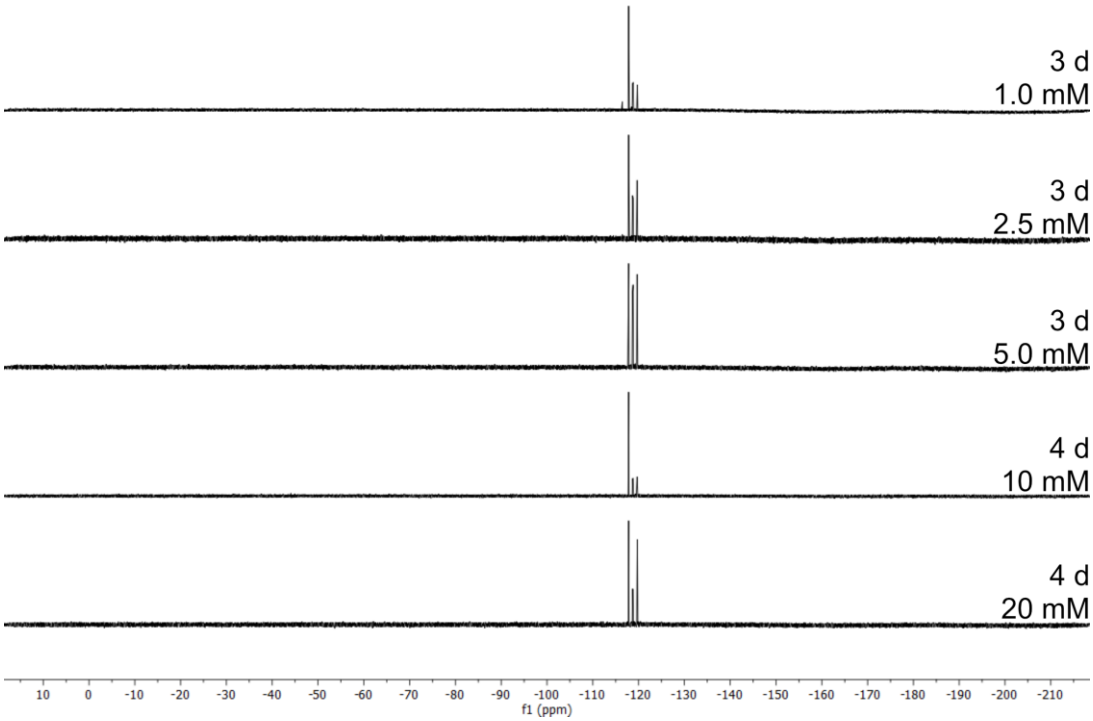

Figure S329: Comparison of $^{19}F\{^{1}H\}$ NMR spectra ($CDCl_3$, 282 MHz) of *E*-**A** and **B** at different concentrations after stirring in the dark.

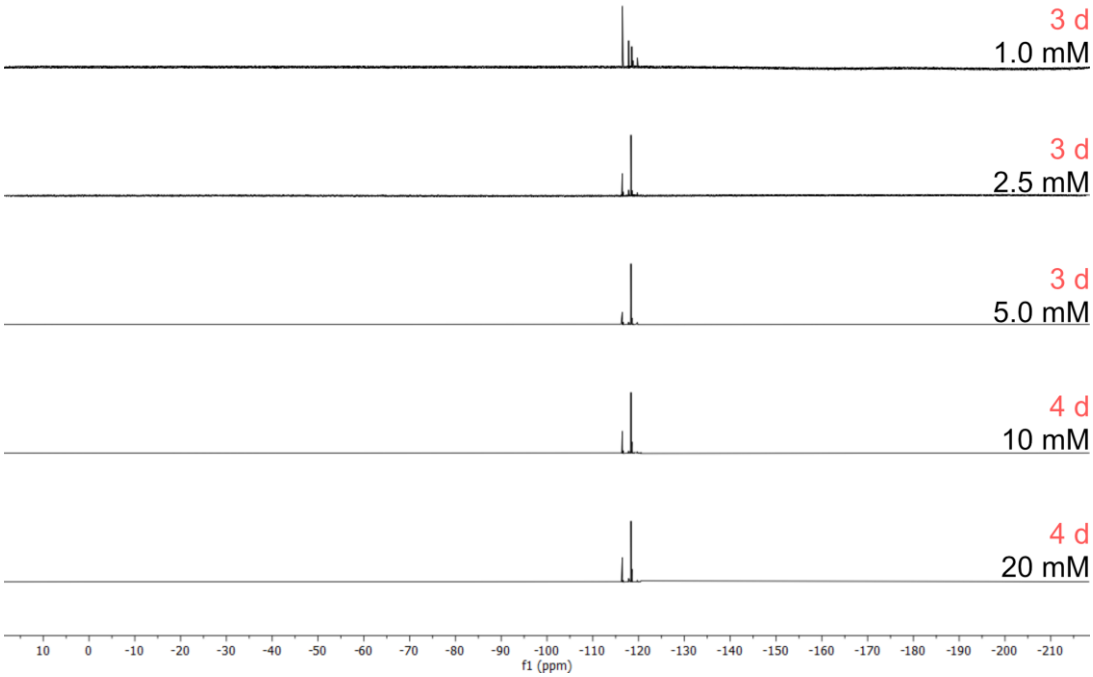

Figure S330: Comparison of $^{19}F\{^{1}H\}$ NMR spectra ($CDCl_3$, 282 MHz) of *E*-**A** and **B** at different concentrations after stirring under irradiation with red light (660 nm).

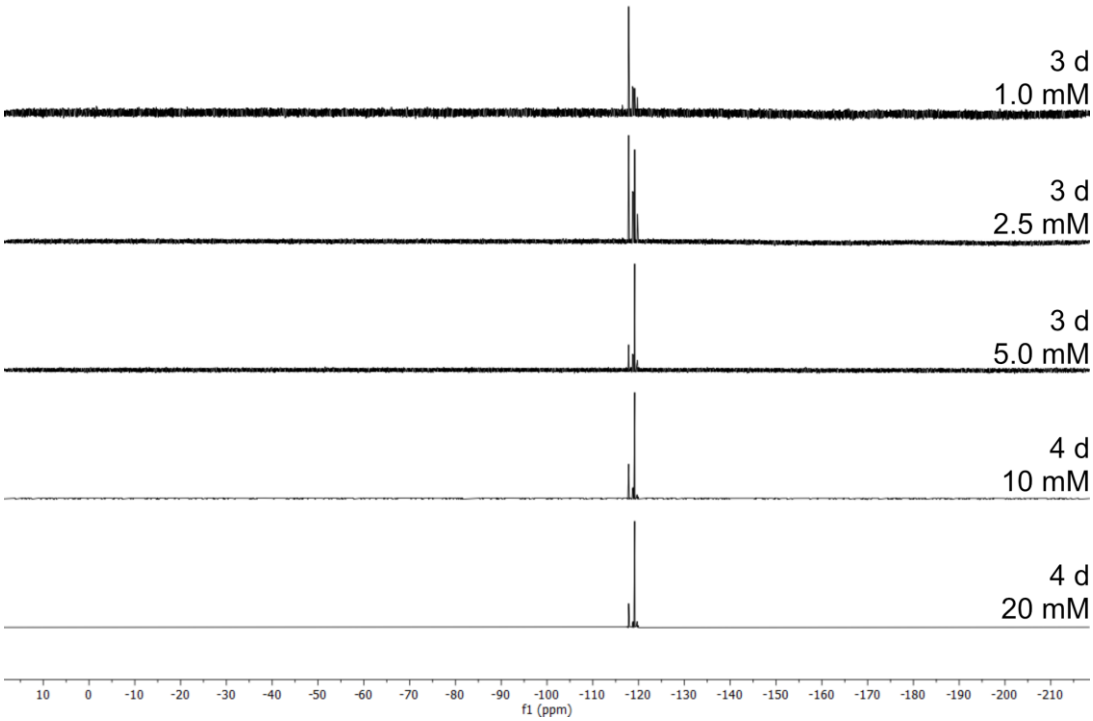

Figure S331: Comparison of $^{19}F\{^{1}H\}$ NMR spectra ($CDCl_3$, 282 MHz) of *E*-**A** and **Pe** at different concentrations after stirring in the dark.

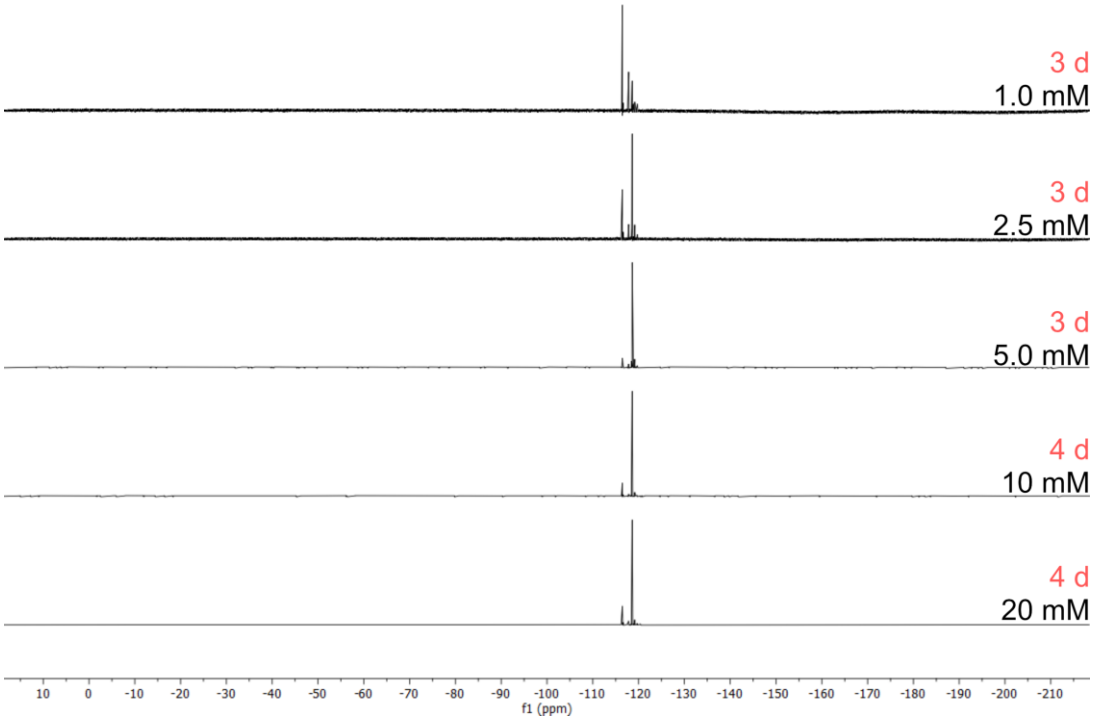

Figure S332: Comparison of $^{19}F\{^{1}H\}$ NMR spectra ($CDCl_3$, 282 MHz) of *E*-**A** and **Pe** at different concentrations after stirring under irradiation with red light (660 nm).

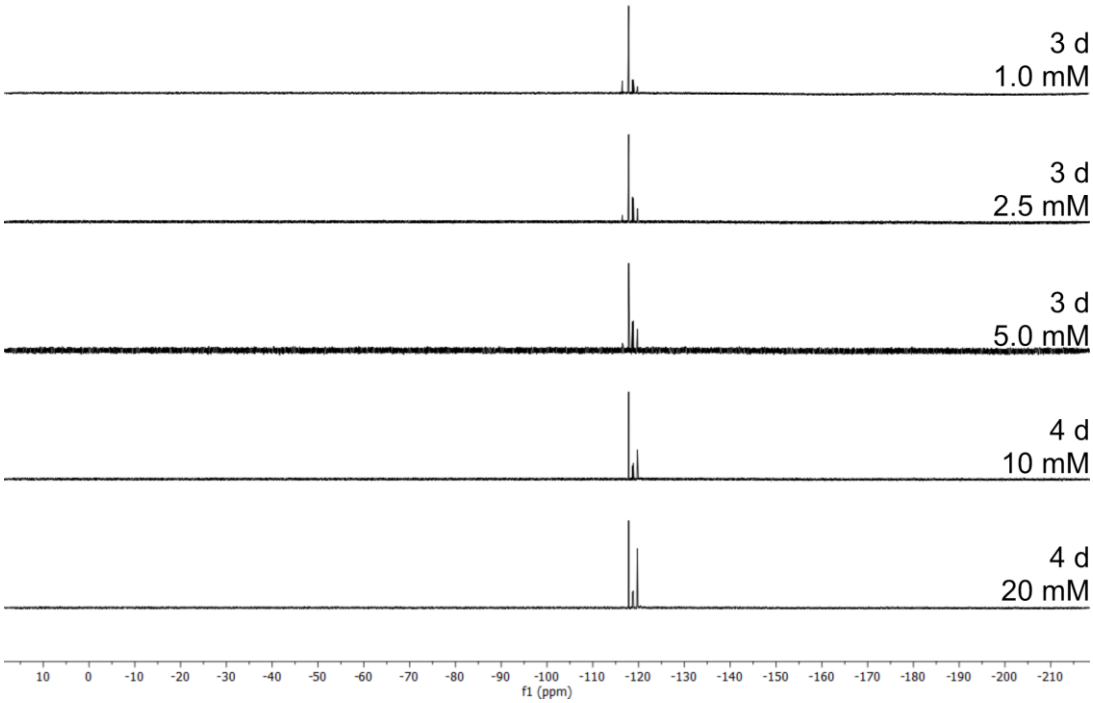

Figure S333: Comparison of $^{19}F\{^{1}H\}$ NMR spectra ($CDCl_3$, 282 MHz) of *E*-**A** and **H** at different concentrations after stirring in the dark.

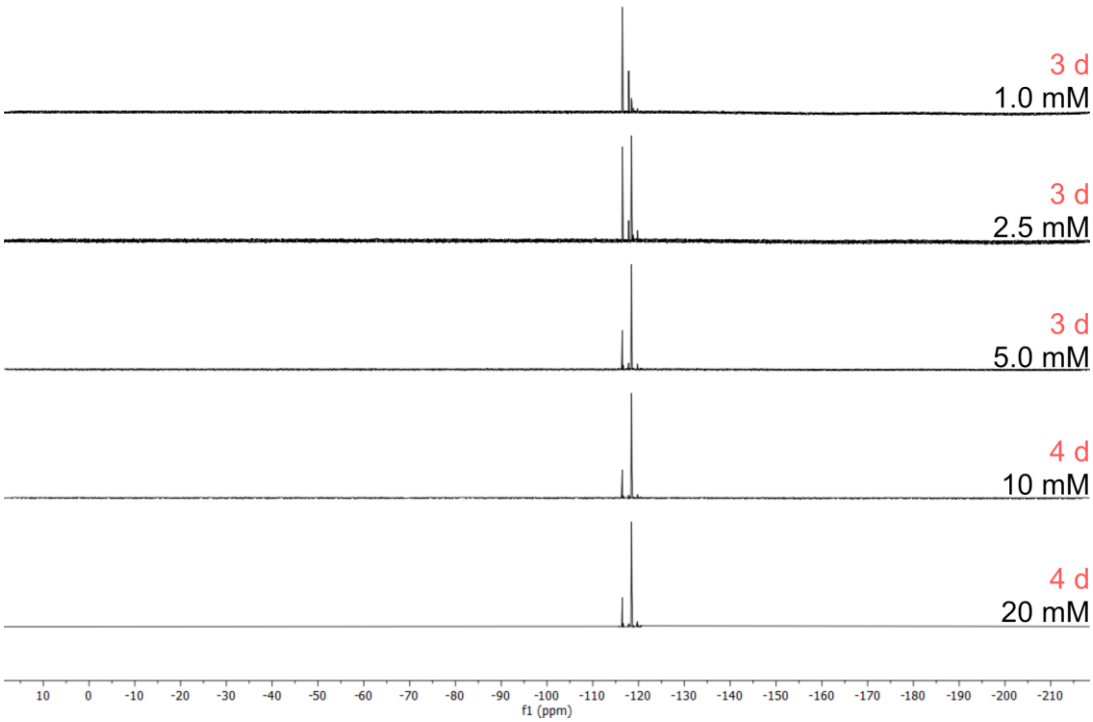

Figure S334: Comparison of $^{19}F\{^{1}H\}$ NMR spectra ($CDCl_3$, 282 MHz) of *E*-**A** and **H** at different concentrations after stirring under irradiation with red light (660 nm).

6.7 Spectra for 4.3.4

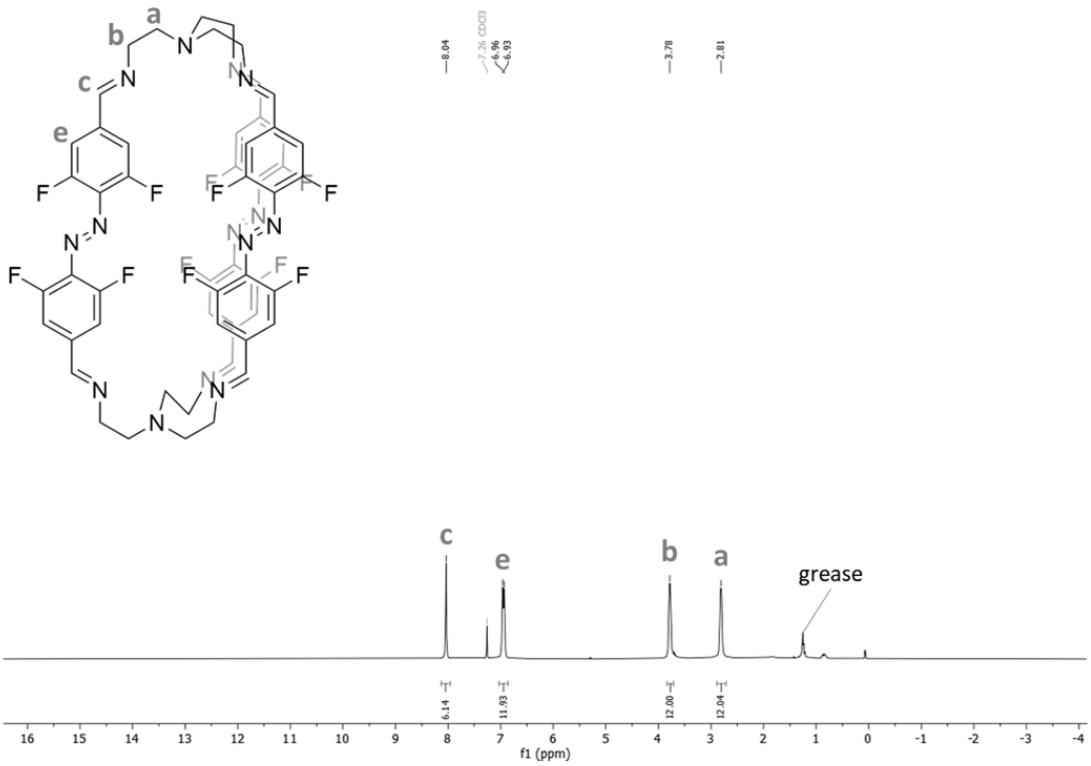

Figure S335: ^{1}H NMR spectrum of *E*,*E*,*E*-**A^{3}Tren^{2}** ($CDCl_3$, 300 MHz).

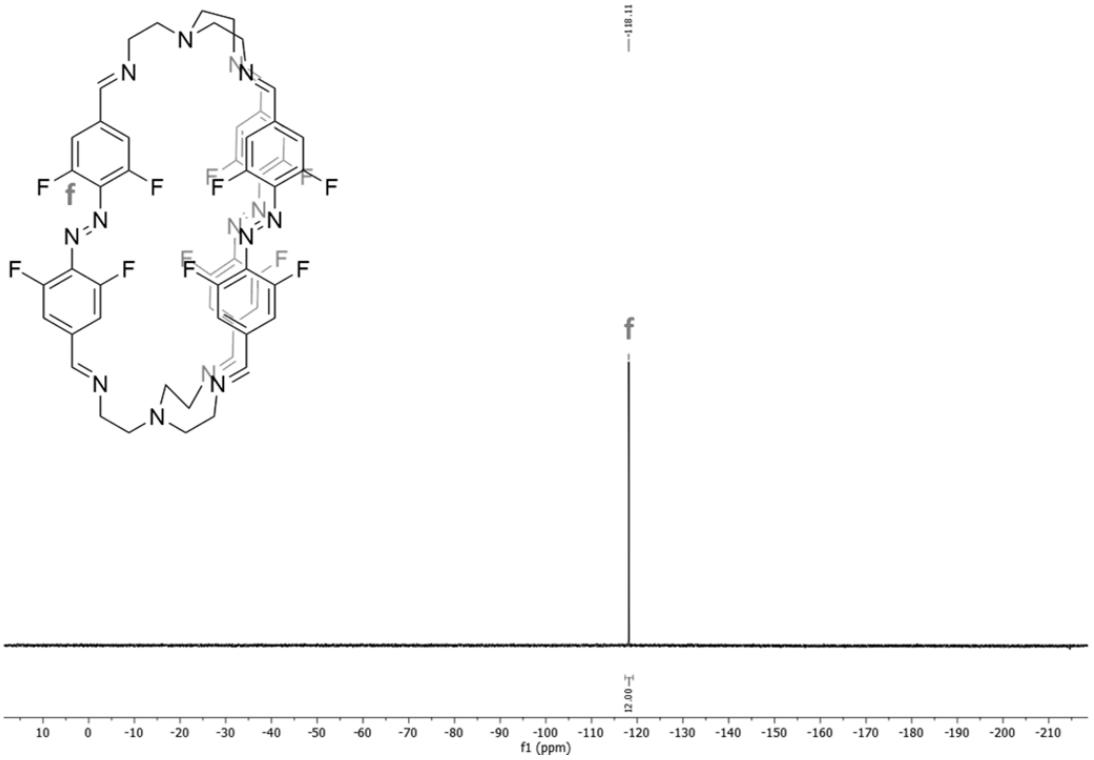

Figure S336: ^{19}F{^{1}H} NMR spectrum of *E*,*E*,*E*-**A^{3}Tren^{2}** ($CDCl_3$, 282 MHz).

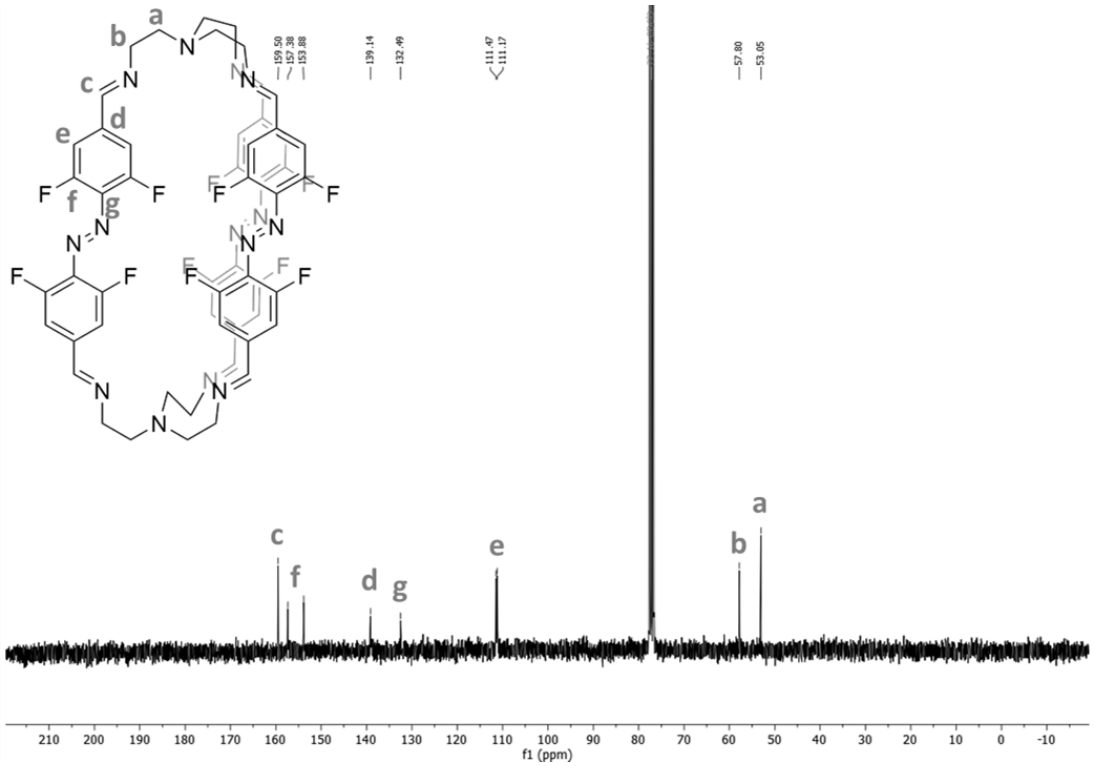

Figure S337: $^{13}C\{^{1}H\}$ NMR spectrum of *E*,*E*,*E*-**A^{3}Tren^{2}** ($CDCl_3$, 75 MHz).

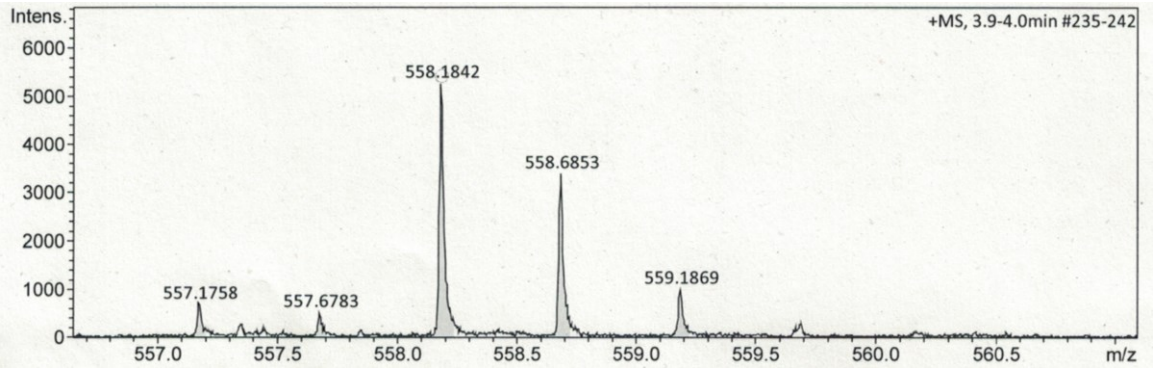

Figure S338: ESI-HR-mass spectrum of *E*,*E*,*E*-**A^{3}Tren^{2}**.

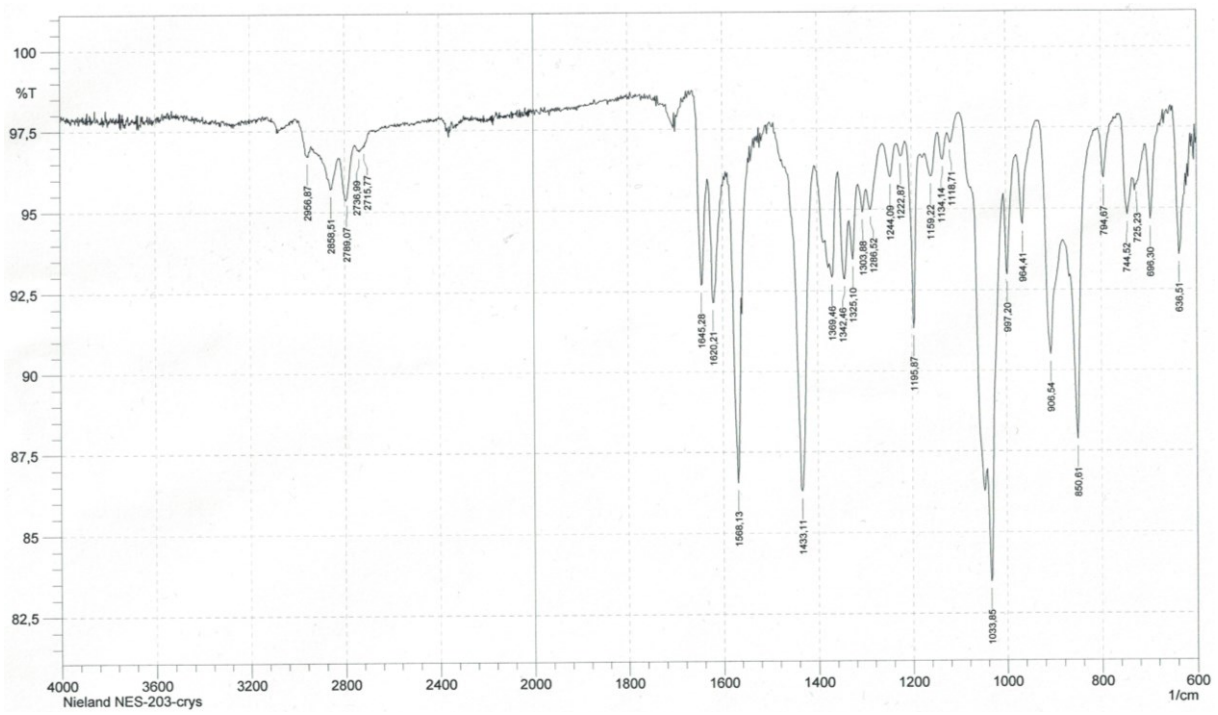

Figure S339: IR spectrum of *E*,*E*,*E*-**A^{3}Tren^2**.

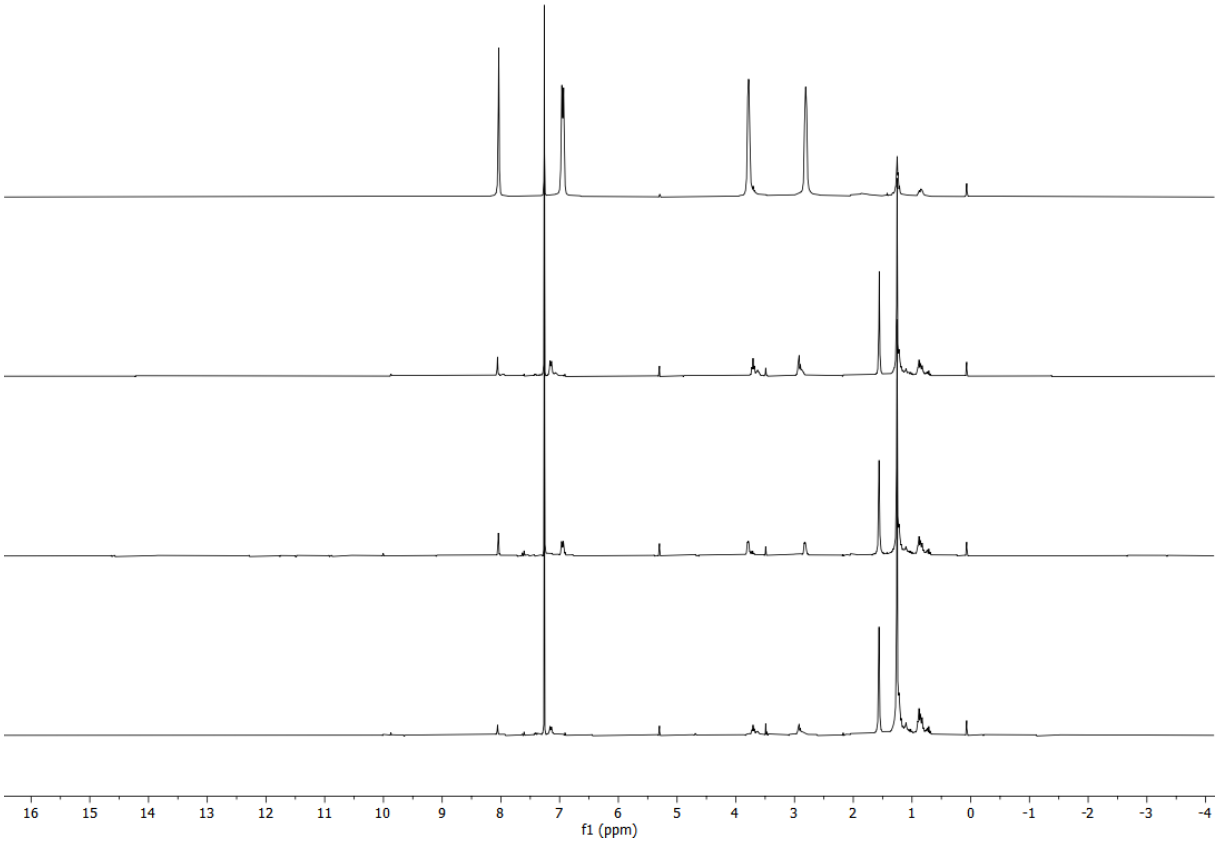

Figure S340: ^{1}H NMR spectrum of *E*,*E*,*E*-**A^{3}Tren^2** in the dark, after irradiation with red light for 5 days, after irradiation with UV light for 14 hours and again after irradiation with red light for 5 days (from top to bottom) ($CDCl_3$, 300 MHz).

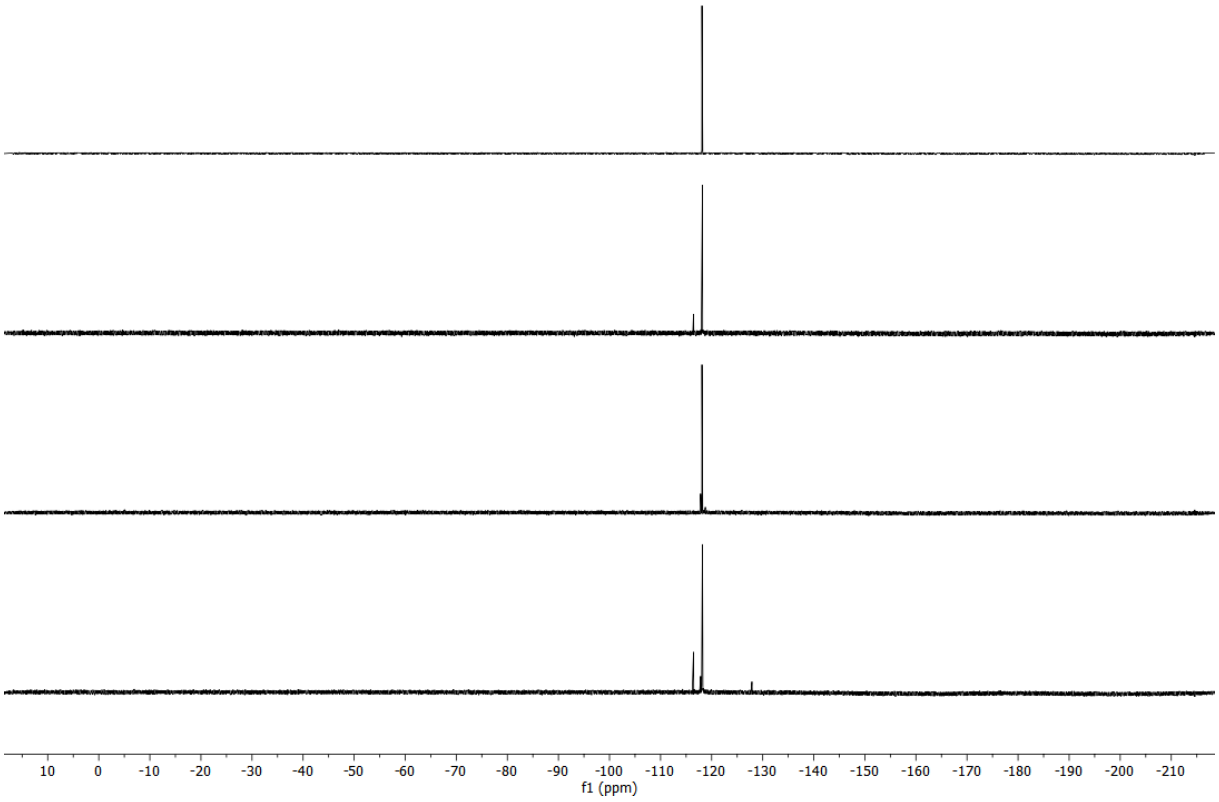

Figure S341: $^{19}F\{^{1}H\}$ NMR spectrum of *E,E,E*-**A^{3}Tren^{2}** in the dark, after irradiation with red light for 5 days, after irradiation with UV light for 14 hours and again after irradiation with red light for 5 days (from top to bottom) ($CDCl_3$, 282 MHz).

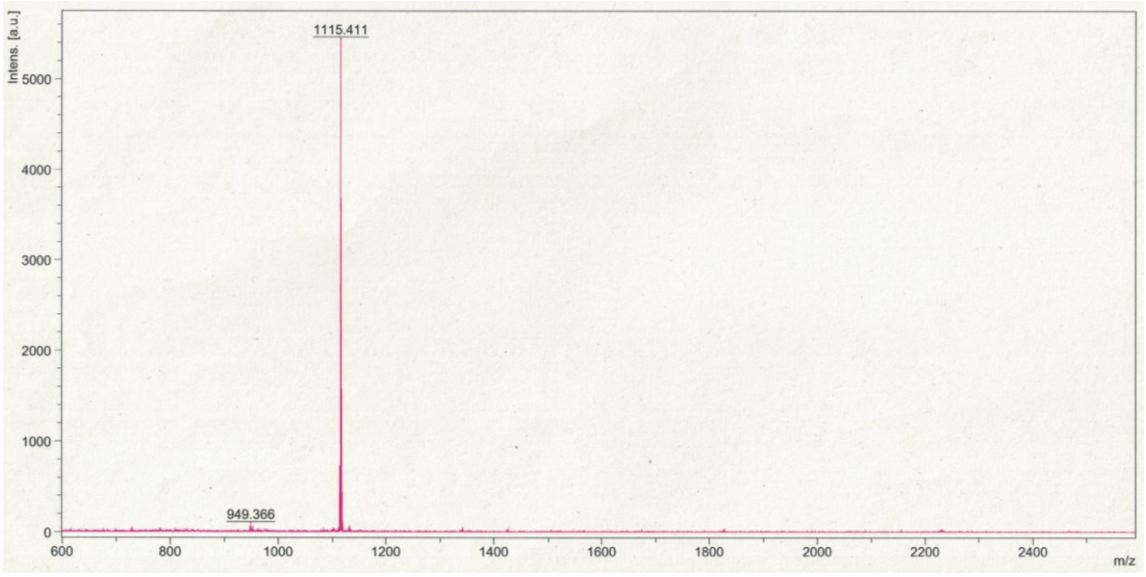

Figure S342: MALDI-mass spectrum of *E,E,E*-**A^{3}Tren^{2}** after irradiation with red light for 5 days.

7. Abbreviations

AT-IR	Attenuated transmission infrared spectroscopy
BET	Brunauer-Emmett-Teller
CCDC	Cambridge Crystallographic Data Center
DBU	1,8-Diazabicyclo[5.4.0]undec-7-ene
DCC	Dynamic covalent chemistry
DFT	Density functional theory
DMF	Dimethylformamide
DOSY	Diffusion ordered spectroscopy
ESI	Electron spray ionisation
HRMS	High resolution mass spectroscopy
LAG	Liquid assisted grinding
MALDI	Matrix assisted laser desorption ionisation
MOF	Metal-organic framework
NBS	*N*-Bromosuccinimide
NCS	*N*-Chlorosuccinimide
NMR	Nuclear magnetic resonance
TBA	Tribromoacetic acid
TCA	Trichloroacetic acid
TGA	Thermogravimetrical analysis
TLC	Thin layer chromatography
PSS	Photostationary state
PXRD	Powder X-ray diffraction

8. Selbstständigkeitserklärung

Ich versichere an Eides Statt, dass die Dissertation von mir selbständig und ohne unzulässige fremde Hilfe unter Beachtung der „Grundsätze zur Sicherung guter wissenschaftlicher Praxis an der Heinrich-Heine-Universität Düsseldorf“ erstellt worden ist.
Düsseldorf, den XX.05.2023

Esther J. G. Nieland